THE UNIVERSITY OF CHICAGO

ORDERED MONOLAYERS AND SUPRAMOLECULAR ASSEMBLIES ON 2D TMDS AND GRAPHITE USING MONOMERIC AND DIMERIC PORPHYRINS

A DISSERTATION SUBMITTED TO

THE FACULTY OF THE DIVISION OF THE PHYSICAL SCIENCES

IN CANDIDACY FOR THE DEGREE OF

DOCTOR OF PHILOSOPHY

DEPARTMENT OF CHEMISTRY

BY

ANDREW PETER GRORUD

CHICAGO, ILLINOIS

MARCH 2024

TABLE OF CONTENTS

Page

LIST OF FIGURES

LIST OF TABLES

LIST OF CHARTS

Chart **Page**

LIST OF SCHEMES

Scheme **Page**

LIST OF EQUATIONS

ACKNOWLDEGMENTS

I would like to begin by thanking my advisor, Professor Mike Hopkins, for his support, patience, and guidance throughout my time in graduate school. I've learned so much not only about how to be a good scientist, but also how to think about complex problems and be an all-around decent human being. I would also like to thank my undergraduate advisor, Professor Ben Lovaasen, in whose laboratory I first had the chance to do research and where I realized I wanted to pursue a Ph.D in chemistry. I would also like to thank Professor John Anderson and Professor Dmitri Talapin for serving on my dissertation committee.

I want to thank all of the members of the Hopkins group that I had the opportunity to work alongside. Judith Kamm got me started on this project and taught me so much when I had never thought about surface chemistry or had any idea what STM stood for. Ayush Gupta and I joined the Hopkins group at the same time and it was great to have a constant friend for navigating graduate school, laboratory moves, and a pandemic. Hunter Vibbert was incredibly supportive in getting acclimated to life in graduate school and to the Hopkins group and has continued to provide support even after he graduated. I've also enjoyed working with Mark Westwood, Chris Hansen, Kate Rawe, and Alpesh Sharma.

My family deserves a special thanks for their love and support as I worked on my Ph.D. My parents, Scott and Shelly Grorud, were incredibly supportive and helped me get through the times when I wasn't sure I was cut out for graduate school. They also provided endless conversation while I commuted, listening patiently to my ramblings even though I'm sure they contained far more chemistry than they ever cared to know. Kirsten and Jared Noetzel were also a huge support and while Soren doesn't know it yet, he has provided so much joy for me over the past year. I'd also like to thank Bob and Liza Brightly for their support and encouragement. My

friends in Chicago and beyond were also incredibly important, whether it was playing a board game, grabbing a meal, or just simply having an open door to get away from the lab for a few hours.

Finally, I'd like to thank Kathryn. She has walked beside me every step of the way through this program and I can never fully explain the depths to which her love and support has sustained and carried me. I certainly would not be where I am today without her.

to Kathryn

ABSTRACT

The development of general methods for the organization of molecules on technologically relevant materials enables the exploration of properties and functions that are not present in either the molecules or the materials alone. Bottom-up self-assembly of molecules is an especially promising approach for achieving these hybrid molecule–material systems with nanoscale precision. A modular approach to bottom-up self-assembly, where a functional group is attached to a molecular platform which forms ordered monolayers, seeks to expand the applicability of bottom-up self-assembly to a wide-range of molecules by decoupling the formation of ordered structures from the function in these systems. The central hypothesis of this work is that ordered porphyrin monolayers can serve as molecular platforms for modular self-assembly, enabling the incorporation of diverse molecular functionality onto wide array of materials.

This work describes the functionalization of materials using ordered porphyrin monolayers utilizing two approaches. The first approach explores the surface chemistry of metalloporphyrins on 2D TMDs. The effect of the metal center in a series of M(OEP) complexes (M = Ni, Zn, H_2 and Ga(Cl)), the peripheral substituents, the surface composition, and the deposition conditions on resulting porphyrin monolayers are explored *via* scanning tunneling microscopy at the solid–liquid interface. Computational chemistry was also utilized to explore the thermodynamics of self-assembly and electronic consequences of the formation of these interfaces. Finally, a modular self-assembly approach is described, where an electroactive ligand (ferrocene) was covalently attached to a five-coordinate gallium porphyrin, demonstrating the organization of a functional molecule on a 2D TMD.

The second approach explores using ordered monolayers of porphyrin dimers as a template for the organization of fullerenes. The synthesis of a series of cofacial porphyrin dimers,

$(Ga(OEP))_2(\mu\text{-}R)$, is described; the molecular structures and physical properties of these multi-porphyrin systems were investigated. The surface chemistry of these cofacial porphyrin dimers was then explored both as pristine monolayers and as a template to form bicomponent monolayers containing fullerene. The thermodynamics of the supramolecular organization of fullerenes were explored using computational chemistry for both the dimeric porphyrin systems along with a series of monomeric porphyrin systems, Ga(OEP)(R), containing axial fullerene affinity groups leading towards a method for computationally screening candidates for modular self-assembly.

CHAPTER 1

Introduction

The research projects described in this thesis are motivated by the expectation that incorporation of diverse molecular functionality into hierarchical structures on technologically relevant materials presents a tremendous opportunity to integrate the vast tunability of molecule structures and properties with the addressable length scales and processibility of the materials.[1] Such systems allow for exploration of collective properties or emergent phenomena that would not be expected from the individual components, with a wide array of potential applications.[1-3] The realization of such hybrid materials will require general methods for controlling the nanoscale organization of these molecules in three dimensions over comparatively large areas.[4-8] Bottom-up self-assembly of molecules on surfaces presents an opportunity for achieving this organization with nanoscale periodicity on mesoscopic scales. Described below are considerations that informed the approaches adopted in this research.

Self-assembled molecular structures typically rely either on the terminus of a molecule chemisorbed to the surface with the remainder of the molecule extending off the surface, such as in alkane thiols on gold,[9] or on non-covalent interactions among the peripheral substituents of molecules physiosorbed to the surface, resulting in an essentially two-dimensional (2D) monolayer. As non-covalent interactions are, in principle, surface agnostic, 2D physiosorbed monolayers provide a promising method for organizing molecules on a wide array of surfaces. Despite the substantial catalog of molecules that have been observed to form 2D monolayers, the formation of ordered structures under ambient conditions has typically relied on high-symmetry molecules possessing planar cores and/or long alkyl chains that provide strong adsorbate–surface or adsorbate–adsorbate interactions.[10-14] Decoupling the propensity to self-assemble from the

desired functionality would enable the use of molecules that on their own would not be expected to form highly ordered 2D monolayers (Figure 1.1). In this modular approach, the assembling molecule serves as a platform to which a functional group can be attached by means of a linker that is oriented orthogonal to the surface and the assembling molecule. Variation of the length of the linker enables organization off the surface and thus full three-dimensional (3D) control over the placement of the functional molecules. There are several examples of systems that achieve these goals, including triazatriangulenium derivatives,[15-21] Janus tectons,[22-26] and previous work in our group utilizing 5-coordinate porphyrins.[27,28]

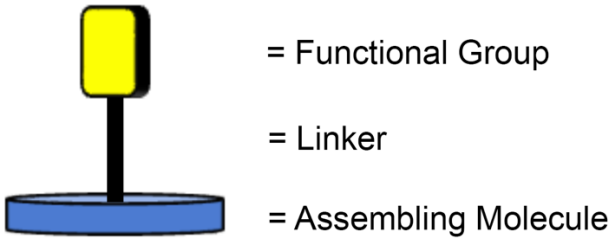

Figure 1.1. Cartoon depiction of modular self-assembly approach.

Porphyrins are of particular interest as candidates to serve as the assembling molecule in these systems (Figure 1.2). First and foremost, there have been a multitude of studies demonstrating the propensity of porphyrins to form ordered adlayers on a variety of substrates, including highly oriented pyrolytic graphite and metallic surfaces.[29-32] They also possess an extensive library of peripheral substituents that provide a means of altering the structure and density of the resulting monolayer.[33-35] Furthermore, synthetic methods to install a wide variety of metal centers are known,[36] including 5-coordinate metals[37] that provide an attachment point for the linker and axial ligand. Finally, porphyrins possess rich and controllable electronic and optical properties that could offer additional functionality irrespective of the functional group.[38-42]

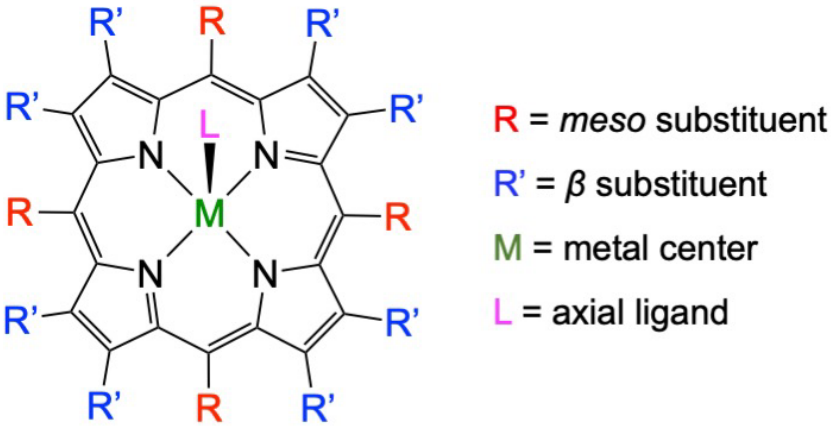

Figure 1.2. Generic structure of porphyrin demonstrating different substitutional points.

2D materials are important substrates for modular self-assembly because of their diverse electronic properties and atomically thin nature, which makes them extremely sensitive to surface modifications. Among these materials 2D transition-metal dichalcogenides (TMDs) have garnered significant interest as they possess fundamentally important and technologically relevant properties.[43-45] Chemical functionalization of 2D TMDs has been extensively explored as a means of tuning the optical or electronic properties of the materials.[1-3] Multiple strategies for achieving chemical functionalization have been investigated, including thick, unstructured molecular coatings on the surface of the 2D TMD(Figure 1.3a),[3] covalent attachment of functional molecules (Figure 1.3b),[3,46-49] and ordered molecular monolayers (Figure 1.3c).[50,51] Examples of ordered molecular monolayers are much less common than the thick coating or covalent attachment approaches, though several examples of a modular approach using phthalocyanine[52] or the previously mentioned triazatriangulenium[17,18] platform to incorporate photoactive azobenzenes using a dative or covalent attachment strategy, respectively, have been reported. The desire for a highly ordered molecule–substrate interface has also received renewed attention, as molecular orientation has been shown to have a tremendous impact on the resulting properties of these hybrid

systems, such as the distinct optical properties of a 2D TMD–phthalocyanine interface when the phthalocyanine is oriented face-on versus edge-on with respect to the surface.[53]

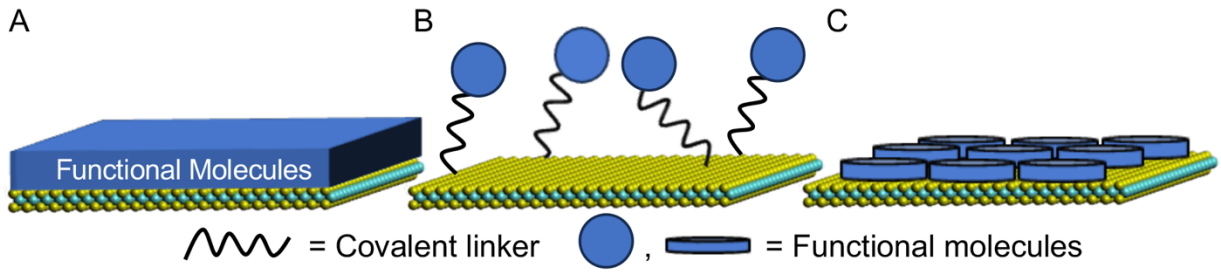

Figure 1.3. Representation of common strategies for functionalizing 2D TMDs. (a) Thick physisorbed molecular coatings; (b) covalently bound functional molecules; (c) ordered molecular adlayers.

While these examples have demonstrated that ordered molecular monolayers are possible on 2D TMDs, systematic studies exploring the relationship between the molecular structure and the ordered monolayer structure on 2D TMDs are lacking. Therefore, our first goal will be to systematically investigate the surface chemistry of porphyrins on 2D TMDs exploring the effect of the metal center and the peripheral substituents (Figure 1.4a). As transition metals are known to coordinate to the chalcogen atoms at the surface of TMDs,[54] the potential exists for metal–S interactions to influence the structure of the molecular monolayer. Octaethylporphyrins (OEP) with varying metal centers (M = Ni, Zn, and Ga(Cl)) and as the free base will be utilized to investigate these effects, as they are well-known to form ordered monolayers at the solid–liquid[55,56] and solid–air[57] interface on HOPG driven by van der Waals interactions between the ethyl substituents of the porphyrins, resulting in highly stable monolayers with structures that are independent of both the metal center and axial ligand.[55-58]

After investigation of the effects of the metal center, a study of peripheral substituents will take place to determine whether the relationships between the porphyrin structure and the resulting monolayer that enable a wide range of patterns and molecular densities on HOPG and metallic

substrates extend to 2D TMDs. Etioporphyrins (β substituents = 4 CH_3, 4 CH_2CH_3) and *meso*-tetradecylporphyrins (*meso* substituents = *n*-$C_{10}H_{21}$) will be investigated as we expect them to form monolayers that are more and less dense, respectively, than OEP. Upon completion of the systematic study of self-assembled porphyrin monolayers on 2D TMDs, we will seek to demonstrate that our approach can be used to create arrays of functional molecules with the periodicity of porphyrin monolayers (Figure 1.4b).

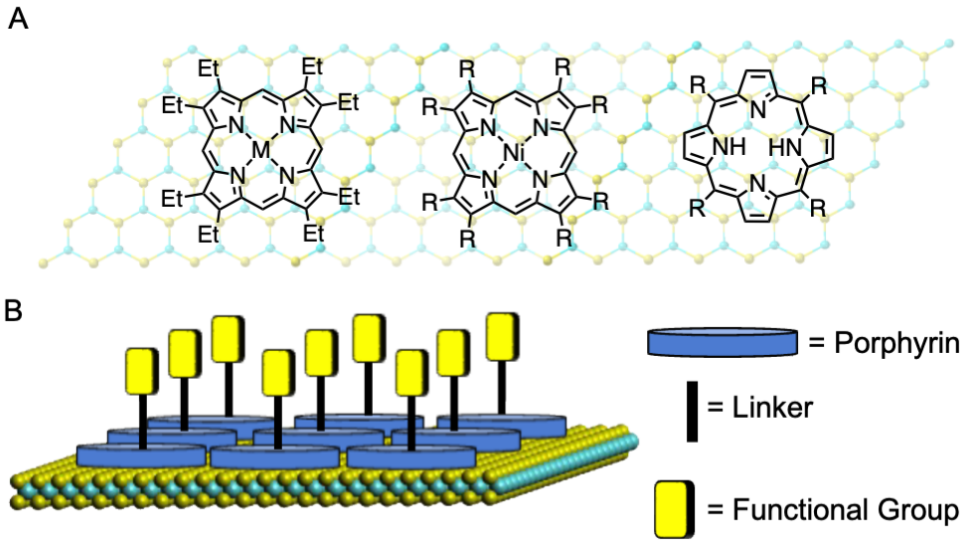

Figure 1.4. Depiction of approaches towards functionalizing 2D TMDs with self-assembled porphyrin monolayers. (a) Systematic study of the effects of metal centers (left) and peripheral substituents (center and right) on 2D TMDs; (b) 5-coordinate porphyrins to incorporate functional axial ligands.

While investigations on 2D TMDs will focus on incorporating functionality through covalently linking functional molecules to the metalloporphyrin, an alternative approach can be envisioned where the axial ligand of the porphyrin is an affinity group forming a supramolecular template for functional molecules. This provides a complementary approach for forming ordered adlayers of molecules which are otherwise challenging to incorporate into covalent-type systems. One such class of molecules that is of significant interest using this supramolecular approach is fullerenes and related derivatives. The electronic and optical properties of fullerenes have made

them useful in a variety of devices, including solar cells and optoelectronics.[59-61] These applications often require the fullerenes to be organized with respect to other electroactive components; however, fullerenes do not form stable highly ordered monolayers on their own,[62] and covalent functionalization of fullerenes is both challenging and can cause the properties of the pristine fullerene or desired derivative to be altered.[63] In order to address these problems, molecular monolayers that can template the formation of ordered arrays of fullerenes in a host–guest type architecture have been investigated.[64-68] While many of the previous motifs have relied on porous networks of molecules on surfaces, previous research in our group has found that a modular approach using a polyaromatic hydrocarbon axial ligand attached to a Ga(OEP) porphyrin forming a corral-like structure on the surface is capable of templating the formation of an ordered overlayer of fullerene (Figure 1.5a).[27]

We hypothesized that a similar strategy using cofacial porphyrin dimers bridged by a bidentate affinity group would incorporate fullerenes into the cavities formed between the two cofacial porphyrins in monolayer structure (Figure 1.5b), presenting an alternate vault-like structural motif to that of the corrals. Given suitable porphyrin–porphyrin spacing, these vault-like systems may exhibit greater stability for fullerenes, as interactions with the off-surface capping porphyrin would be expected in addition to the affinity group and the surface bound porphyrin present in corrals. We would also expect these structures to kinetically trap the fullerenes within the cavity once the monolayer has formed. Finally, the off-surface porphyrin presents an opportunity for incorporating additional functionality, such as by using a six-coordinate metal center for the capping porphyrin allowing *post-hoc* functionalization of the monolayer.

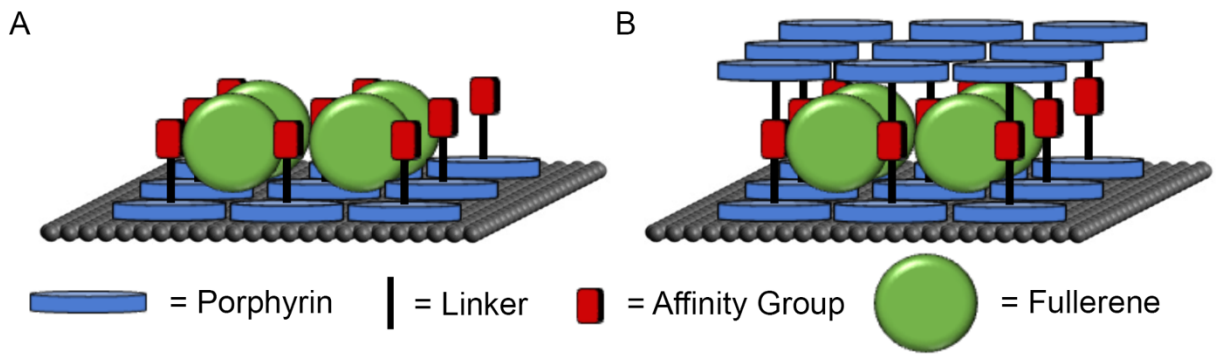

Figure 1.5. Approaches towards supramolecular organization of fullerene using porphyrin adlayers. (a) Corral-like structures of 5-coordinate porphyrins containing an axial affinity group; (b) vault-like structures of cofacial 5-coordinate porphyrin dimers bridged by an axial affinity group.

The first step to creating such systems is synthesizing the requisite cofacial porphyrin dimers. A multitude of cofacial porphyrin dimers have been studied, as interesting physical phenomena arise as a result of porphyrin–porphyrin interactions.[69,70] These systems most commonly use either flexible aliphatic or rigid aromatic substituents on the periphery of the porphyrin to link the macrocycles.[71,72] We envisioned a series of cofacial porphyrin dimers of varying heights and affinities for fullerene that adopt a less common structural motif, where the porphyrins are bridged through metal centers (Figure 1.6),[73,74] in our case gallium metal centers. This allows for the porphyrin to retain the peripheral substituents that are requisite for forming self-assembled monolayers. As the formation of these cofacial porphyrin dimers may lead to porphyrin–porphyrin interactions, the molecular structures and electronic properties of these complexes will be investigated through a variety of physical measurements and theoretical calculations.

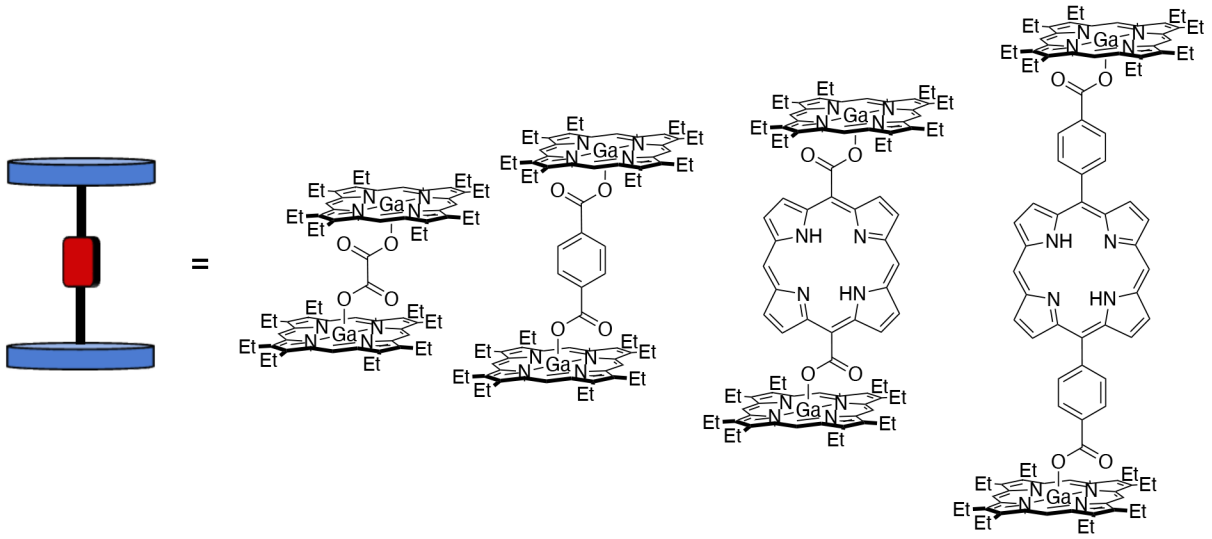

Figure 1.6. Cartoon depiction and molecular structures of cofacial porphyrin dimers.

Finally, we will investigate the surface chemistry of the cofacial porphyrin dimers and the ability to template fullerene organization. Examples of ordered monolayers of porphyrin or phthalocyanine dimers are known; however, these systems possess very small porphyrin–porphyrin (or phthalocyanine–phthalocyanine) separations (3.3–3.5 Å).[75,76] In contrast, the cofacial dimers we have envisioned are expected to exhibit much larger porphyrin–porphyrin separations (7.7–24.5 Å). While previous work in our group has demonstrated that neither tall axial ligands (oligo-phenylene-ethylene ligands) nor sterically bulky ligands (fullerene derivatives) prevent the formation of ordered porphyrin monolayers,[28] the combination of both the height of the bridging ligand and the steric bulk of the off-surface porphyrin has not been investigated; therefore, we will first determine whether the cofacial porphyrin dimers will form stable ordered monolayers on HOPG. Subsequently, the codeposition of[73,74] fullerenes with the porphyrin dimers will be examined to determine whether bicomponent monolayers can be formed.

Underlying the whole of this work is the complex process of self-assembly, which relies on finely balanced thermodynamics and kinetics in order to form highly ordered monolayers.[77-81]

Therefore, understanding how subtle changes to molecular structures, to molecule–surface interactions, or to the environment under which self-assembly occurs can alter the structures or stabilities of the ordered monolayers is vital towards realizing the goal of using molecular self-assembly as a means of incorporating diverse molecular functionality onto surfaces. As the study of the thermodynamics of self-assembly is challenging experimentally,[82-87] particularly under ambient conditions, computational chemistry has been utilized to interrogate structures and stabilities of ordered molecular monolayers.[88,89] Dispersion-corrected plane-wave density functional theory has been the method of choice, as it can accurately describe the non-covalent forces that dominate molecular overlayers on surfaces and account for the periodic adsorbate–adsorbate interactions that dictate the 2D and 3D supramolecular structures in these systems.[90-92] We anticipated that such computational approaches could provide insight into the systems described heretofore and sought to adapt and develop methods to tease out these subtle differences.

The central hypothesis of this work is that ordered porphyrin monolayers provide a surface-agnostic method for introducing diverse molecular functionality onto surfaces. Towards this end we seek to answer two questions: (1) Can porphyrins serve as platforms for modular self-assembly on 2D materials; and (2) Can monolayers of dimeric cofacial porphyrins be used to template the non-covalent organization of fullerenes?

Chapter 2 describes efforts towards answering the first question. We pursued a systematic study of the surface chemistry of metalloporphyrins on 2D TMDs, first investigating the effects of the metal center in a series of M(OEP) complexes (OEP = octaethylporphyrin; M = Ni, Zn, H_2, Ga(Cl)) and subsequently the effects of peripheral substituents, surface composition, and deposition conditions. We also describe efforts using computational chemistry to quantify the thermodynamics underlying these ordered monolayers and the electronic consequences of the

formation of these interfaces. Finally, we describe the synthesis and surface chemistry of Ga(OEP)(O_2CFc) (Fc = ferrocene), establishing the periodic organization of an electroactive functional molecule on a 2D TMD.

In Chapters 3 and 4, efforts to answer the second question are described. Chapter 3 explores the synthesis of a series of cofacial porphyrin dimers and uses spectroscopic methods and theoretical calculations to establish their molecular structures and explore the physical properties of the multi-porphyrin systems. Chapter 4 describes the surface chemistry of these cofacial porphyrin dimers both as pristine monolayers and as a template for forming bicomponent monolayers with fullerene encapsulated within the cavity formed by the cofacial porphyrin dimers. Again, computational chemistry explores the thermodynamics and structures of these systems and is utilized for interpreting experimental observations of these complex systems.

Finally, in Chapter 5, the computational approaches that play a supporting role in Chapters 2 and 4 become the central focus. We describe calculations investigating the thermodynamics and structures of a series of corral-like Ga(OEP)(R) monolayers with axial affinity groups that have previously been observed to template the organization of fullerenes. We report that these thermodynamic calculations can successfully predict the relative energies of these systems, leading towards a method for screening systems designed for modular self-assembly.

1.1 References

1. Gobbi, M.; Orgiu, E.; Samori, P. When 2D Materials Meet Molecules: Opportunities and Challenges of Hybrid Organic/Inorganic Van Der Waals Heterostructures. *Adv. Mater.* **2018**, *30*, 1706103.

2. Amsterdam, S. H.; Marks, T. J.; Hersam, M. C. Leveraging Molecular Properties to Tailor Mixed-Dimensional Heterostructures Beyond Energy Level Alignment. *J. Phys. Chem. Lett.* **2021**, *12*, 4543–4557.

3. Bertolazzi, S.; Gobbi, M.; Zhao, Y. D.; Backes, C.; Samori, P. Molecular Chemistry Approaches for Tuning the Properties of Two-Dimensional Transition Metal Dichalcogenides. *Chem. Soc. Rev.* **2018**, *47*, 6845–6888.

4. Mohnani, S.; Bonifazi, D. Supramolecular Architectures of Porphyrins on Surfaces: The Structural Evolution from 1D to 2D to 3D to Devices. *Coord. Chem. Rev.* **2010**, *254*, 2342–2362.

5. Sosa-Vargas, L.; Kim, E.; Attias, A. J. Beyond "Decorative" 2D Supramolecular Self-Assembly: Strategies Towards Functional Surfaces for Nanotechnology. *Mater. Horiz.* **2017**, *4*, 570–583.

6. Brill, A. R.; Koren, E.; de Ruiter, G. Molecular Functionalization of 2D Materials: From Atomically Planar 2D Architectures to Off-Plane 3D Functional Materials. *J. Mater. Chem. C* **2021**, *9*, 11569–11587.

7. Xie, R. B.; Hu, Y.; Lee, S. L. A Paradigm Shift from 2D to 3D: Surface Supramolecular Assemblies and Their Electronic Properties Explored by Scanning Tunneling Microscopy and Spectroscopy. *Small* **2023**, 2300413.

8. Parviz, B. A.; Ryan, D.; Whitesides, G. M. Using Self-Assembly for the Fabrication of Nano-Scale Electronic and Photonic Devices. *IEEE T. Adv. Packag.* **2003**, *26*, 233–241.

9. Love, J. C.; Estroff, L. A.; Kriebel, J. K.; Nuzzo, R. G.; Whitesides, G. M. Self-Assembled Monolayers of Thiolates on Metals as a Form of Nanotechnology. *Chem. Rev.* **2005**, *105*, 1103–1169.

10. Mali, K. S.; Adisoejoso, J.; Ghijsens, E.; De Cat, I.; De Feyter, S. Exploring the Complexity of Supramolecular Interactions for Patterning at the Liquid-Solid Interface. *Acc. Chem. Res.* **2012**, *45*, 1309–1320.

11. Kudernac, T.; Lei, S. B.; Elemans, J. A. A. W.; De Feyter, S. Two-Dimensional Supramolecular Self-Assembly: Nanoporous Networks on Surfaces. *Chem. Soc. Rev.* **2009**, *38*, 402–421.

12. Goronzy, D. P.; Ebrahim, M.; Rosei, F.; Arramel; Fang, Y.; De Feyter, S.; Tait, S. L.; Wang, C.; Beton, P. H.; Wee, A. T. S.; Weiss, P. S.; Perepichka, D. F. Supramolecular Assemblies on Surfaces: Nanopatterning, Functionality, and Reactivity. *ACS Nano* **2018**, *12*, 7445–7481.

13. De Feyter, S.; De Schryver, F. C. Self-Assembly at the Liquid/Solid Interface: STM Reveals. *J. Phys. Chem. B* **2005**, *109*, 4290–4302.

14. Barth, J. V. Molecular Architectonic on Metal Surfaces. *Annu. Rev. Phys. Chem.* **2007**, *58*, 375–407.

15. Kuhn, S.; Baisch, B.; Jung, U.; Johannsen, T.; Kubitschke, J.; Herges, R.; Magnussen, O. Self-Assembly of Triazatriangulenium-Based Functional Adlayers on Au(111) Surfaces. *Phys. Chem. Chem. Phys.* **2010**, *12*, 4481–4487.

16. Baisch, B.; Raffa, D.; Jung, U.; Magnussen, O. M.; Nicolas, C.; Lacour, J.; Kubitschke, J.; Herges, R. Mounting Freestanding Molecular Functions onto Surfaces: The Platform Approach. *J. Am. Chem. Soc.* **2009**, *131*, 442–443.

17. Brill, A. R.; Kafri, A.; Mohapatra, P. K.; Ismach, A.; de Ruiter, G.; Koren, E. Modulating the Optoelectronic Properties of MoS_2 by Highly Oriented Dipole-Generating Monolayers. *ACS Appl. Mater. Interfaces* **2021**, *13*, 32590–32597.

18. Brill, A. R.; Kuntumalla, M. K.; de Ruiter, G.; Koren, E. Formation of Highly Ordered Self-Assembled Monolayers on Two-Dimensional Materials Via Noncovalent Functionalization. *ACS Appl. Mater. Interfaces* **2020**, *12*, 33941–33949.

19. Lemke, S.; Chang, C. H.; Jung, U.; Magnussen, O. M. Reversible Potential-Induced Switching of Alkyl Chain Aggregation in Octyl-Triazatriangulenium Adlayers on Au(111). *Langmuir* **2015**, *31*, 3115–3124.

20. Otte, F. L.; Lemke, S.; Schütt, C.; Krekiehn, N. R.; Jung, U.; Magnussen, O. M.; Herges, R. Ordered Monolayers of Free-Standing Porphyrins on Gold. *J. Am. Chem. Soc.* **2014**, *136*, 11248–11251.

21. Jung, U.; Kuhn, S.; Cornelissen, U.; Tuczek, F.; Strunskus, T.; Zaporojtchenko, V.; Kubitschke, J.; Herges, R.; Magnussen, O. Azobenzene-Containing Triazatriangulenium Adlayers on Au(111): Structural and Spectroscopic Characterization. *Langmuir* **2011**, *27*, 5899–5908.

22. Du, P.; Bléger, D.; Charra, F.; Bouchiat, V.; Kreher, D.; Mathevet, F.; Attias, A. J. A Versatile Strategy Towards Non-Covalent Functionalization of Graphene by Surface- Confined Supramolecular Self-Assembly of Janus Tectons. *Beilstein J. Nanotechnol.* **2015**, *6*, 632–639.

23. Bléger, D.; Mathevet, F.; Kreher, D.; Attias, A. J.; Bocheux, A.; Latil, S.; Douillard, L.; Fiorini-Debuisschert, C.; Charra, F. Janus-Like 3D Tectons: Self-Assembled 2D Arrays of Functional Units at a Defined Distance from the Substrate. *Angew. Chem. Int. Ed.* **2011**, *50*, 6562–6566.

24. Du, P.; Kreher, D.; Mathevet, F.; Maldivi, P.; Charra, F.; Attias, A. J. Surface-Confined Supramolecular Self-Assembly of Molecular Nanocranes for Chemically Lifting and Positioning C_{60} above a Conducting Substrate. *ChemPhysChem* **2015**, *16*, 3774–3778.

25. Le Liepvre, S.; Du, P.; Kreher, D.; Mathevet, F.; Attias, A. J.; Fiorini-Debuisschert, C.; Douillard, L.; Charra, F. Fluorescent Self-Assembled Molecular Monolayer on Graphene. *ACS Photonics* **2016**, *3*, 2291–2296.

26. Valásek, M.; Mayor, M. Spatial and Lateral Control of Functionality by Rigid Molecular Platforms. *Chem. – Eur. J.* **2017**, *23*, 13538–13548.

27. Kamm, J. M. Ph. D. Thesis. The University of Chicago, Chicago, IL, 2017.

28. Lau, W.-Y. Ph. D. Thesis. The University of Chicago, Chicago, IL, 2016.

29. Otsuki, J. STM Studies on Porphyrins. *Coord. Chem. Rev.* **2010**, *254*, 2311–2341.

30. Auwarter, W.; Ecija, D.; Klappenberger, F.; Barth, J. V. Porphyrins at Interfaces. *Nat. Chem.* **2015**, *7*, 105–120.

31. Gottfried, J. M. Surface Chemistry of Porphyrins and Phthalocyanines. *Surf. Sci. Rep.* **2015**, *70*, 259–379.

32. Bonifazi, D.; Mohnani, S.; Llanes-Pallas, A. Supramolecular Chemistry at Interfaces: Molecular Recognition on Nanopatterned Porous Surfaces. *Chem. – Eur. J.* **2009**, *15*, 7004–7025.

33. Lindsey, J. S. Synthetic Routes to *meso*-Patterned Porphyrins. *Acc. Chem. Res.* **2010**, *43*, 300-311.

34. Synthesis and Organic Chemistry. In *The Porphyrin Handbook*; Kadish, K. M., Smith, K. M., Guilard, R., Eds.; Academic Press: San Diego, CA, 2000.

35. Hiroto, S.; Miyake, Y.; Shinokubo, H. Synthesis and Functionalization of Porphyrins through Organometallic Methodologies. *Chem. Rev.* **2017**, *117*, 2910–3043.

36. Adler, A. D.; Longo, F. R.; Kampas, F.; Kim, J. On the Preparation of Metalloporphyrins. *J. Inorg. Nucl. Chem.* **1970**, 2443–2445.

37. Kadish, K. M.; Cornillon, J. L.; Coutsolelos, A.; Guilard, R. Synthesis, Electrochemistry, and Ligand-Addition Reactions of Gallium(III) Porphyrins. *Inorg. Chem.* **1987**, *26*, 4167–4173.

38. Jurow, M.; Schuckman, A. E.; Batteas, J. D.; Drain, C. M. Porphyrins as Molecular Electronic Components of Functional Devices. *Coord. Chem. Rev.* **2010**, *254*, 2297–2310.

39. Li, L. L.; Diau, E. W. G. Porphyrin-Sensitized Solar Cells. *Chem. Soc. Rev.* **2013**, *42*, 291–304.

40. Zhang, W.; Lai, W. Z.; Cao, R. Energy-Related Small Molecule Activation Reactions: Oxygen Reduction and Hydrogen and Oxygen Evolution Reactions Catalyzed by Porphyrin- and Corrole-Based Systems. *Chem. Rev.* **2017**, *117*, 3717–3797.

41. Senge, M. O.; Fazekas, M.; Notaras, E. G. A.; Blau, W. J.; Zawadzka, M.; Locos, O. B.; Mhuircheartaigh, E. M. N. Nonlinear Optical Properties of Porphyrins. *Adv. Mater.* **2007**, *19*, 2737–2774.

42. Beletskaya, I.; Tyurin, V. S.; Tsivadze, A. Y.; Guilard, R.; Stern, C. Supramolecular Chemistry of Metalloporphyrins. *Chem. Rev.* **2009**, *109*, 1659–1713.

43. Tan, C. L.; Cao, X. H.; Wu, X. J.; He, Q. Y.; Yang, J.; Zhang, X.; Chen, J. Z.; Zhao, W.; Han, S. K.; Nam, G. H.; Sindoro, M.; Zhang, H. Recent Advances in Ultrathin Two-Dimensional Nanomaterials. *Chem. Rev.* **2017**, *117*, 6225–6331.

44. Lin, Z.; McCreary, A.; Briggs, N.; Subramanian, S.; Zhang, K. H.; Sun, Y. F.; Li, X. F.; Borys, N. J.; Yuan, H. T.; Fullerton-Shirey, S. K.; Chernikov, A.; Zhao, H.; McDonnell, S.; Lindenberg, A. M.; Xiao, K.; LeRoy, B. J.; Drndic, M.; Hwang, J. C. M.; Park, J.; Chhowalla, M.; Schaak, R. E.; Javey, A.; Hersam, M. C.; Robinson, J.; Terrones, M. 2D Materials Advances: From Large Scale Synthesis and Controlled Heterostructures to Improved Characterization Techniques, Defects and Applications. *2D Mater.* **2016**, *3*, 42001.

45. Zeng, M. Q.; Xiao, Y.; Liu, J. X.; Yang, K.; Fu, L. Exploring Two-Dimensional Materials toward the Next-Generation Circuits: From Monomer Design to Assembly Control. *Chem. Rev.* **2018**, *118*, 6236–6296.

46. Canton-Vitoria, R.; Scharl, T.; Stergiou, A.; Cadranel, A.; Arenal, R.; Guldi, D. M.; Tagmatarchis, N. Ping-Pong Energy Transfer in Covalently Linked Porphyrin-MoS2 Architectures. *Angew. Chem., Int. Ed.* **2020**, *59*, 3976–3981.

47. Vallan, L.; Canton-Vitoria, R.; Gobeze, H. B.; Jang, Y.; Arenal, R.; Benito, A. M.; Maser, W. K.; D'Souza, F.; Tagmatarchis, N. Interfacing Transition Metal Dichalcogenides with Carbon Nanodots for Managing Photoinduced Energy and Charge-Transfer Processes. *J. Am. Chem. Soc.* **2018**, *140*, 13488–13696.

48. Chen, X.; McAteer, D.; McGuinness, C.; Godwin, I.; Coleman, J. N.; McDonald, A. R. Ru^{II} Photosensitizer-Functionalized Two-Dimensional MoS_2 for Light-Driven Hydrogen Evolution. *Chem. - Eur. J.* **2018**, *24*, 351–355.

49. Presolski, S.; Pumera, M. Covalent Functionalization of MoS_2. *Mater. Today* **2016**, *19*, 140–145.

50. Park, J. H.; Sanne, A.; Guo, Y. Z.; Amani, M.; Zhang, K. H.; Movva, H. C. P.; Robinson, J. A.; Javey, A.; Robertson, J.; Banerjee, S. K.; Kummel, A. C. Defect Passivation of

Transition Metal Dichalcogenides Via a Charge Transfer Van Der Waals Interface. *Sci. Adv.* **2017**, *3*, e170166.

51. Song, Z. B.; Schultz, T.; Ding, Z. J.; Lei, B.; Han, C.; Amsalem, P.; Lin, T. T.; Chi, D. Z.; Wong, S. L.; Zheng, Y. J.; Li, M. Y.; Li, L. J.; Chen, W.; Koch, N.; Huang, Y. L.; Wee, A. T. S. Electronic Properties of a 1D Intrinsic/P-Doped Heterojunction in a 2D Transition Metal Dichalcogenide Semiconductor. *ACS Nano* **2017**, *11*, 9128–9135.

52. Wang, Y.; Iglesias, D.; Gali, S. M.; Beljonne, D.; Samori, P. Light-Programmable Logic-in-Memory in 2D Semiconductors Enabled by Supramolecular Functionalization: Photoresponsive Collective Effect of Aligned Molecular Dipoles. *ACS Nano* **2021**, *15*, 13732–13741.

53. Padgaonkar, S.; Amsterdam, S. H.; Bergeron, H.; Su, K.; Marks, T. J.; Hersam, M. C.; Weiss, E. A. Molecular-Orientation-Dependent Interfacial Charge Transfer in Phthalocyanine/MoS2 Mixed-Dimensional Heterojunctions. *J .Phys. Chem. C* **2019**, *123*, 13337–13343.

54. Backes, C.; Berner, N. C.; Chen, X.; Lafargue, P.; LaPlace, P.; Freeley, M.; Duesberg, G. S.; Coleman, J. N.; McDonald, A. R. Functionalization of Liquid-Exfoliated Two-Dimensional 2H-MoS_2. *Angew. Chem. Int. Ed.* **2015**, *54*, 2638–2642.

55. Ogunrinde, A.; Hipps, K. W.; Scudiero, L. A Scanning Tunneling Microscopy Study of Self-Assembled Nickel(II) Octaethylporphyrin Deposited from Solutions on HOPG. *Langmuir* **2006**, *22*, 5697–5701.

56. Kamm, J. M.; Iverson, C. P.; Lau, W. Y.; Hopkins, M. D. Axial Ligand Effects on the Structures of Self-Assembled Gallium–Porphyrin Monolayers on Highly Oriented Pyrolytic Graphite. *Langmuir* **2016**, *32*, 487–495.

57. Scudiero, L.; Barlow, D. E.; Hipps, K. W. Scanning Tunneling Microscopy, Orbital-Mediated Tunneling Spectroscopy, and Ultraviolet Photoelectron Spectroscopy of Nickel(II) Octaethylporphyrin Deposited from Vapor. *J. Phys. Chem. B* **2002**, *106*, 996–1003.

58. Friesen, B. A.; Bhattarai, A.; Mazur, U.; Hipps, K. W. Single Molecule Imaging of Oxygenation of Cobalt Octaethylporphyrin at the Solution/Solid Interface: Thermodynamics from Microscopy. *J. Am. Chem. Soc.* **2012**, *134*, 14897–14904.

59. Verner, R. F.; Benvegnu, C. *Handbook on Fullerene Synthesis, Properties and Applications.* Nova Science Publishers: New York, 2012.

60. Langa, F.; Nierengarten, J.-F. *Fullerenes : Principles and Applications.* 2nd ed.; Royal Society of Chemistry: Cambridge, 2011.

61. Prato, M. [60]Fullerene Chemistry for Materials Science Applications. *J. Mat. Chem.* **1997**, *7*, 1097–1109.

62. Szuba, S.; Czajka, R.; Kasuya, A.; Wawro, A.; Rafii-Tabar, H. Observation of C_{60} Film Formation on a Highly Oriented Pyrolitic Graphite Substrate Via Scanning Tunnelling Microscopy. *Appl. Surf. Sci.* **1999**, *144-45*, 648–652.

63. Paukov, M.; Kramberger, C.; Begichev, I.; Kharlamova, M.; Burdanova, M. Functionalized Fullerenes and Their Applications in Electrochemistry, Solar Cells, and Nanoelectronics. *Materials* **2023**, *16*, 1276.

64. Gonzalez, J. D. C.; Iyoda, M.; Rabe, J. P. Templated Bilayer Self-Assembly of Fully Conjugated π-Expanded Macrocyclic Oligothiophenes Complexed with Fullerenes. *Nat. Commun.* **2017**, *8*, 14717.

65. Kawano, S.; Nakaya, M.; Saitow, M.; Ishiguro, A.; Yanai, T.; Onoe, J.; Tanaka, K. Thermally Stable Array of Discrete C_{60}s on a Two-Dimensional Crystalline Adlayer of Macrocycles Both in Vacuo and under Ambient Pressure. *J. Am. Chem. Soc.* **2022**, *144*, 6749–6758.

66. Piot, L.; Silly, F.; Tortech, L.; Nicolas, Y.; Blanchard, P.; Roncali, J.; Fichou, D. Long-Range Alignments of Single Fullerenes by Site-Selective Inclusion into a Double-Cavity 2D Open Network. *J. Am. Chem. Soc.* **2009**, *131*, 12864–12865.

67. Theobald, J. A.; Oxtoby, N. S.; Phillips, M. A.; Champness, N. R.; Beton, P. H. Controlling Molecular Deposition and Layer Structure with Supramolecular Surface Assemblies. *Nature* **2003**, *424*, 1029–1031.

68. Yoshimoto, S.; Honda, Y.; Ito, O.; Itaya, K. Supramolecular Pattern of Fullerene on 2D Bimolecular “Chessboard" Consisting of Bottom-up Assembly of Porphyrin and Phthalocyanine Molecules. *J. Am. Chem. Soc.* **2008**, *130*, 1085–1092.

69. Le Mest, Y.; L’Her, M.; Hendricks, N. H.; Kim, K.; Collman, J. P. Electrochemical and Spectroscopic Properties of Dimeric Cofacial Porphyrins with Nonelectroactive Metal Centers - Delocalization Processes in the Porphyrin π-Cation-Radical Systems. *Inorg. Chem.* **1992**, *31*, 835–847.

70. Fletcher, J. T.; Therien, M. J. Extreme Electronic Modulation of the Cofacial Porphyrin Structural Motif. *J. Am. Chem. Soc.* **2002**, *124*, 4298–4311.

71. Harvey, P. D.; Stern, C.; Gros, C. P.; Guilard, R. The Photophysics and Photochemistry of Cofacial Free Base and Metallated Bisporphyrins Held Together by Covalent Architectures. *Coord. Chem. Rev.* **2007**, *251*, 401–428.

72. Pognon, G.; Wytko, J. A.; Weiss, J. Synthesis and Properties of Covalent Cofacial Bisporphyrins. *Targets Heterocycl. Syst.* **2008**, *11*, 21–43.

73. Guchhait, T.; Sasmal, S.; Khan, F. S. T.; Rath, S. P. Oxo- and Hydroxo-Bridged Diiron(III) Porphyrin Dimers: Inorganic and Bio-Inorganic Perspectives and Effects of Intermacrocyclic Interactions. *Coord. Chem. Rev.* **2017**, *337*, 112–144.

74. Kumar, P. P.; Maiya, B. G. Aluminium(III) Porphyrin Based Dimers and Trimers: Synthesis, Spectroscopy and Photochemistry. *New J. Chem.* **2003**, *27*, 619–625.

75. Otsuki, J. STM Studies on Double- and Triple-Decker Porphyrin and Phthalocyanine Complexes. *Supramol. Chem.* **2011**, *23*, 169–182.

76. Takami, T.; Ye, T.; Pathem, B. K.; Arnold, D. P.; Sugiura, K.; Bian, Y. Z.; Jiang, J. Z.; Weiss, P. S. Manipulating Double-Decker Molecules at the Liquid–Solid Interface. *J. Am. Chem. Soc.* **2010**, *132*, 16460–16466.

77. Mali, K. S.; De Feyter, S. Principles of Molecular Assemblies Leading to Molecular Nanostructures. *Philos. Trans. R. Soc., A* **2013**, *371*, 20120304.

78. Mali, K. S.; Pearce, N.; De Feyter, S.; Champness, N. R. Frontiers of Supramolecular Chemistry at Solid Surfaces. *Chem. Soc. Rev.* **2017**, *46*, 2520–2542.

79. Mazur, U.; Hipps, K. W. Kinetic and Thermodynamic Processes of Organic Species at the Solution-Solid Interface: The View through an STM. *Chem. Commun.* **2015**, *51*, 4737–4749.

80. Reimers, J. R. How Equilibrium Gets Mimicked During Kinetic and Thermodynamic Control in Porphyrin and Phthalocyanine Self-Assembled Monolayers. *Langmuir* **2018**, *34*, 18–22.

81. Mali, K. S.; De Feyter, S. Principles of Molecular Assemblies Leading to Molecular Nanostructures. *Philos. Trans. R. Soc., A* **2013**, *371*, 11981– 11985.

82. Song, W. T.; Martsinovich, N.; Heckl, W. M.; Lackinger, M. Born-Haber Cycle for Monolayer Self-Assembly at the Liquid-Solid Interface: Assessing the Enthalpic Driving Force. *J Am Chem Soc* **2013**, *135*, 14854–14862.

83. Gurdumov, K.; Mazur, U.; Hipps, K. W. Self-Assembly Dynamics and Stability through Concentration Control at the Solution/HOPG Interface. *J. Phys. Chem. C* **2022**, *126*, 12916–12927.

84. Gurdumov, K.; Mazur, U.; Hipps, K. W. Influences on the Dynamics and Stability of Self-Assembly: Solvent, Substrate, and Concentration. *J. Phys. Chem. C* **2022**, *126*, 19904–19915.

85. Bhattarai, A.; Marchbanks-Owens, K.; Mazur, U.; Hipps, K. W. Influence of the Central Metal Ion on the Desorption Kinetics of a Porphyrin from the Solution/HOPG Interface. *J. Phys. Chem. C* **2016**, *120*, 18140–18150.

86. Bhattarai, A.; Mazur, U.; Hipps, K. W. Desorption Kinetics and Activation Energy for Cobalt Octaethylporphyrin from Graphite at the Phenyloctane Solution-Graphite Interface: An STM Study. *J .Phys. Chem. C* **2015**, *119*, 9386–9394.

87. Reimers, J. R.; Panduwinata, D.; Visser, J.; Chin, Y.; Tang, C.; Goerigk, L.; Ford, M. J.; Baker, M.; Sum, T. J.; Coenen, M. J. J.; Hendriksen, B. L. M.; Elemans, J. A. A. W.; Hush, N. S.; Crossley, M. J. From Chaos to Order: Chain-Length Dependence of the Free Energy of Formation of Meso-Tetraalkylporphyrin Self-Assembled Monolayer Polymorphs. *J. Phys. Chem. C* **2016**, *120*, 1739–1748.

88. Chilukuri, B.; Mazur, U.; Hipps, K. W. Effect of Dispersion on Surface Interactions of Cobalt(II) Octaethylporphyrin Monolayer on Au(111) and HOPG(0001) Substrates: A Comparative First Principles Study (Vol 16, Pg 14096, 2014). *Phys. Chem. Chem. Phys.* **2014**, *16*, 20250–20250.

89. Reimers, J. R.; Panduwinata, D.; Visser, J.; Chin, Y.; Tang, C. G.; Goerigk, L.; Ford, M. J.; Sintic, M.; Sum, T. J.; Coenen, M. J. J.; Hendriksen, B. L. M.; Elemans, J. A. A. W.; Hush, N. S.; Crossley, M. J. A Priori Calculations of the Free Energy of Formation from Solution of Polymorphic Self-Assembled Monolayers. *Proc. Natl. Acad. Sci. U.S.A.* **2015**, *112*, E6101–E6110.

90. Chilukuri, B.; Mazur, U.; Hipps, K. W. Structure, Properties, and Reactivity of Porphyrins on Surfaces and Nanostructures with Periodic DFT Calculations. *Appl. Sci.* **2020**, *10*, 740.

91. Grimme, S.; Hansen, A.; Brandenburg, J. G.; Bannwarth, C. Dispersion-Corrected Mean-Field Electronic Structure Methods. *Chem. Rev.* **2016**, *116*, 5105–5154.

92. Kratzer, P.; Neugebauer, J. The Basics of Electronic Structure Theory for Periodic Systems. *Front. Chem.* **2019**, *7*, 1–18.

CHAPTER 2

Surface Functionalization of Monolayer Transition-Metal Dichalcogenides by Ordered Assemblies of Metalloporphyrins under Ambient Conditions

2.1. Introduction

Two-dimensional materials such as monolayer molybdenum disulfide (1L-MoS_2) and other transition metal dichalcogenides (TMDs) are subjects of intensive study due to their fundamentally important and potentially technologically relevant properties.[1-3] Realization of 1L-TMD based technologies will require the development of approaches to modify and control their electronic properties. Towards this end, several approaches to chemically functionalizing TMDs have been explored, including introducing heteroatoms into the TMD structure,[1,4] covalent modification using the chalcogen atoms as ligands for transition metals[5] or as attachment points for organic molecules,[5-9] and through non-covalent surface adsorption of molecules.[5,10,11] Among these methods non-covalent functionalization provides the distinct advantage of modifying the electronic properties of the TMD while leaving the structure and composition of the material intact.[5]

While significant effort has been devoted to non-covalent molecular functionalization of TMDs for tuning their electronic properties,[5] including using both porphyrins[12] and phthalocyanines,[13-15] the majority of examples have used many-layer molecular coatings for which the structure and state of molecular ordering at the TMD–molecule interface are unknown. The supramolecular functionalization of the surfaces of 1L-TMDs by ordered molecular monolayers has been comparatively much less explored, but should afford similar opportunities for modifying and controlling the electronic properties of TMDs, while providing a constant TMD–molecule interface and tunable molecular density to allow understanding and rational control of the extent

of electronic modification with high precision. One such approach towards these ordered interfaces is through the use of 2D polymers, where a recent example incorporated metalloporphyrins into 2D covalent or coordinate organic frameworks that could be stacked onto TMDs to create van der Waals heterostructures.[11] Self-assembled molecular monolayers offer another approach towards achieving ordered supramolecular functionalization, where incorporation of a vast array of chemical functionalities and the formation of a large variety of structures with significant variation in their density has been demonstrated on other atomically flat substrates.[16,17] In this vein, there have been several studies of the formation, structures, and electronic consequences of self-assembled molecular monolayers on 1L-TMDs under ultra-high vacuum (UHV) conditions, using titanyl phthalocyanine,[13] thiophenes,[18] PTCDA,[19] and fullerenes.[20-22] Additionally, an example of varying the molecular density of an ordered adlayer to alter the degree of electronic modification of graphene has been demonstrated using alkylamines of varying chain lengths under ambient conditions.[23] While UHV approaches have the advantage that their rigorously controlled conditions facilitate precision physical studies of the resulting functionalized material, they are limited to volatile molecular adsorbants and are not readily scalable. Preparing self-assembled molecular monolayers on 1L-TMDs by solution deposition under ambient conditions, as is well established on other atomically smooth surfaces[17,24] such as highly ordered pyrolytic graphite (HOPG), would couple the rich possibilities for electronic control and hierarchical assembly of TMDs with ease of fabrication and scalability.

Porphyrins are of particular interest as candidates for forming self-assembled molecular monolayers on 1L-TMDs under ambient conditions because their have been many studies demonstrating monolayer formation on other atomically smooth surfaces, particularly HOPG, and because of their rich physical properties and extensive library of peripheral substituents.[25-29]

Additionally, thin coatings of closely related phthalocyanines on MoS_2 display charge transfer between metallophthalocyanines and TMD[30] that is dependent on molecular orientation[31] and the identity of the metal center,[32] highlighting the need to bridge the well-developed understanding of molecular monolayers on atomically smooth surfaces with the possibilities of electronic modification at the molecule–TMD interface. Among porphyrins, 5-coordinate metalloporphyrins are of particular interest because the axial ligand provides a site to which other functional molecules can be bound, including those that, on their own, would not be expected to form ordered structures; the porphyrin anchor in these systems would allow for a vast number of molecules to form ordered monolayers on the surface of TMDs for development of hierarchical structures and materials.[33] Along this latter line, there have been several recent examples utilizing a similar approach to attach azobenzene to preformed molecular monolayers of either phthalocyanines[34] or triazatriangulene[35,36] on MoS_2, which display photoresponsive modulation of the electronic properties of MoS_2. Molecules with frontier orbitals residing near the mid-gap of the valence band and conduction band of TMDs would be ideal candidates for introducing favorable electronic band–orbital alignments that are not possible with porphyrins alone. These considerations motivated us to study the surface chemistry of porphyrins with 1L-TMDs under ambient conditions.

Given the structural and electronic differences between HOPG and 1L-TMDs, the potential parallels in their supramolecular surface chemistry is unclear. Supramolecular surface chemistry studies comparing HOPG and TMDs have reported instances where the ordered molecular assemblies have the same structure on both surfaces,[18,37-50] different structures,[38,40,41,43,45,51-57] or have been observed to selectively form on one substrate, with the structure on HOPG predicting that on bulk TMDs approximately half of the time.[58,59] Additionally, a study comparing bulk MoS_2

to trilayer (3L) MoS_2 under ambient conditions showed a distinct decrease in the ability to characterize order on 3L-MoS_2, possibly due to the decreased layer number.[42] Given these examples, there is significant uncertainty as to whether porphyrins will exhibit similar or divergent behavior on TMDs compared with HOPG. Understanding the relationships between formation and structure of molecular monolayers on 1L-TMDs and the large body of examples on HOPG would unlock a wide array of possibilities for supramolecular surface chemistry on 1L-MoS_2. In order to provide a direct comparison, porphyrins whose ordered assemblies on HOPG have been characterized will be studied under identical conditions.

In order to elucidate design principles for ordered assemblies on 1L-MoS_2, we investigated via scanning tunneling microscopy (STM) the molecular overlayers formed by porphyrins with varied substituents, using solution deposition methods under ambient conditions and probing typically at the solid–liquid interface. The compounds chosen (Chart 2.1a) include octaethylporphyrins (OEP) in which a metal center is absent (H_2OEP), a metal is present and possesses either a high (Zn(OEP)) or low (Ni(OEP)) binding constant for axial ligation, and is 5-coordinate (Ga(OEP)Cl), which produces a domed rather than planar structure. The conditions under which these OEP compounds form monolayers on HOPG and the resulting structures are well understood.[33,60] In addition, nickel(etioporphyrin I) (Ni(Etio), Chart 2.1b) and *meso*-tetradecylporphyrin ($H_2TC_{10}P$, Chart 2.1c) were studied, as representative examples of porphyrins with more compact structures and long alkyl side chains, respectively, in order to probe the effect of substituents on monolayer deposition, structure, and density. For Ni(OEP), the surface chemistry with 1L-WSe_2 was also investigated to determine whether surface functionalization can be applied to TMDs more generally. Supporting these experimental observations are a series of DFT calculations aimed at determining the adsorption sites and energies of the aforementioned

M(OEP) compounds on 1L-MoS_2. DFT calculations using the same methodology were also performed for the M(OEP) compounds on HOPG to provide a comparison between the substrates. Finally, ferrocene was incorporated into the axial ligand of Ga(OEP)(O_2CFc) (Chart 2.1d) to determine whether porphyrin monolayers enable support of additional functional moieties on TMDs. We report that all compounds self-assemble into molecular monolayers on these TMD surfaces upon deposition from solution under ambient conditions.

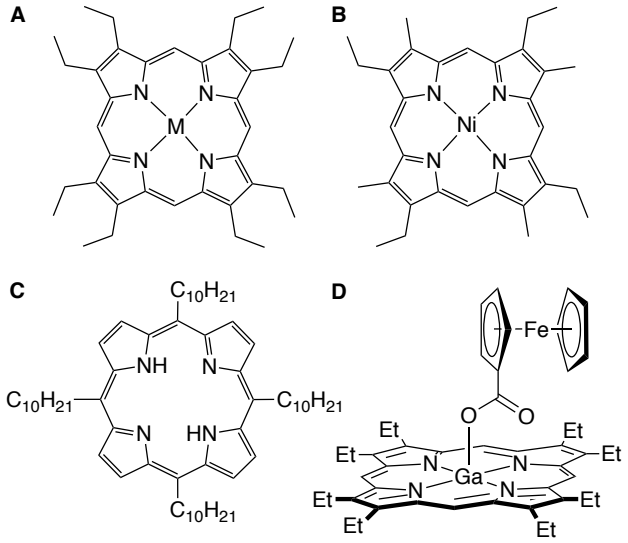

Chart 2.1. Porphyrins studied on monolayer TMDs. (a) M(OEP) (M = Ni, Zn, H_2) or M(OEP)X (M = Ga, X = Cl); (b) Ni(Etio); (c) $H_2TC_{10}P$; (d) Ga(OEP)(O_2CFc).

2.2. Experimental Section

2.2.1. General Procedures. Toluene, THF, diethyl ether, and acetonitrile (HPLC grade, stored under nitrogen) were purified by passing them under nitrogen pressure through an anaerobic, stainless-steel system consisting of either two 4.5 × 24 in. (1 gal) columns of activated A2 alumina (THF, CH_3CN) or one column of activated A2 alumina and one column of activated BASF R3-11 catalyst (toluene, pentane).[61] Ga(OEP)Cl[62] (OEP = octaethylporphyrin) and $H_2TC_{10}P$[63] (*meso*-tetra(*n*-$C_{10}H_{21}$)porphyrin) were synthesized according to standard procedures. Ga(OEP)(OH) was synthesized according to a method previously developed in our lab.[64] Other

chemicals were obtained from commercial sources and used as received. ^{1}H and ^{13}C NMR spectra were recorded at room temperature using a Bruker DMX 500 MHz NMR spectrometer. NMR chemical shifts were measured relative to solvent resonances.[65] Laser-desorption-ionization mass spectra were obtained using a Bruker UltrafleXtreme MALDI-TOF/TOF mass spectrometer on samples deposited without a matrix; the Bruker peptide calibration standard II (750–3150 Da) was used as the calibrant.

2.2.2. STM Sample Preparation. 1L-MoS_2 and 1L-WSe_2 samples were generously provided by Prof. Jiwoong Park's research group; these were grown on fused-silica substrates by metal-organic chemical vapor deposition.[66] The wafers were cut with a diamond-tipped pen to give samples with dimensions of roughly 0.75 cm × 0.75 cm. 1L-MoS_2 and 1L-WSe_2 were delaminated from their growth substrate by immersion in water[67] and transferred to a silicon wafer coated with a 6 nm Ti adhesion layer and 100 nm of polycrystalline Au. The samples were mounted to 12 mm diameter metal specimen discs with colloidal silver paste (PELCO, Ted Pella, Inc.), ensuring that electrical contact is made between the gold and the disc. HOPG (SPI-2 grade, SPI supplies) and bulk MoS_2 (2D Semiconductors) substrates were mounted to 12 mm diameter metal specimen discs with colloidal silver paste. The surface of the HOPG or bulk MoS_2 substrate was cleaved with adhesive tape prior to deposition. One drop of a 1-phenyloctane or tetradecane solution of the porphyrin (0.5 mM unless otherwise noted) was deposited onto the surface of the MoS_2, WSe_2, or HOPG. The STM tip was then engaged through the drop and the compound imaged at the solid–liquid interface. A Ni(OEP) monolayer studied at the solid–air interface was prepared by immersing the mounted 1L-MoS_2 into a 0.5 mM solution of Ni(OEP) in toluene for 30 minutes. Samples were then rinsed three times in neat toluene and dried under vacuum before STM imaging.

2.2.3. STM Measurements. STM images were acquired using a Digital Instruments Nanoscope IIIa standalone STM. Tips were either mechanically cut from $Pt_{0.8}Ir_{0.2}$ wire (Goodfellow) or obtained as 8 mm pre-cut $Pt_{0.8}Ir_{0.2}$ probes (Bruker). All measurements were taken at room temperature in constant-current mode. For each sample, an image of the underlying MoS_2 monolayer, WSe_2 monolayer, or HOPG was acquired. The data for the porphyrin overlayers were corrected after acquisition for instrumental drift in the SPIP software package[68] using the lattice parameters of the substrate as a reference.[69] Data analyses were performed using Gwyddion software.[70] Images were flattened, low-pass filtered, and sharpened by adjusting the contrast. Reported lattice parameters are averages of those determined from consecutive up- and down-scan images. For each of these images, the unit-cell distances were determined from the average distances of 100 sets of 5 consecutive porphyrin molecules, and the unit-cell angle was the average of 40 measurements. All images shown in the text are uncorrected images.

2.2.4. Preparation of Ga(OEP)(O_2CFc) (Fc = FeCp(C_5H_4)). This compound has been previously prepared in our group, but was reported to be impure.[64] To a stirred solution of Ga(OEP)(OH) (0.314 g, 0.507 mmol) in THF (25 mL) at room temperature was added a solution of ferrocene carboxylic acid (0.128 g, 0.556 mmol) in THF (15 mL). The solution was stirred for 2.5 h. The color of the dark pink solution did not change during this time. The solvent was removed under vacuum, and the crude product was suspended with stirring in a mixture of diethyl ether (20 mL) and acetonitrile (40 mL) to remove excess ferrocene carboxylic acid. The volume was reduced to 40 mL under vacuum and the product was collected as a pink powder (0.315 g, 0.379 mmol, 75% yield). The compound was recrystallized by diffusion of pentane into a toluene solution of the compound, which provided crystals suitable for X-ray crystallography. ^{1}H NMR (C_6D_6, 500.13 MHz, Figure 2.1): δ 10.49 (s, 4 H, *meso* H), 4.02 (complex m, 16 H, C$\underline{H_2}$CH$_3$), 2.83, (t, 2 H, Fc),

2.72, (s, 5 H, Fc), 2.61, (t, 2 H, Fc), 1.88 (t, 24 H, $CH_2C\underline{H}_3$). $^{13}C\{^1H\}$ NMR (C_6D_6, 125.77 MHz, Figure 2.2): δ 166.57 (CO_2), 147.06 (α), 142.66 (β), 97.79 (meso), 75.48 (Fc), 69.23 (Fc), 68.79 (Fc), 68.56 (Fc), 20.25 ($\underline{C}H_2CH_3$), 18.79 ($CH_2\underline{C}H_3$). LDI-TOF MS (*m/z*): $[M]^+$ = 830.240, predicted = 830.277; $[M–O_2CFc]^+$ = 601.295, predicted = 601.282.

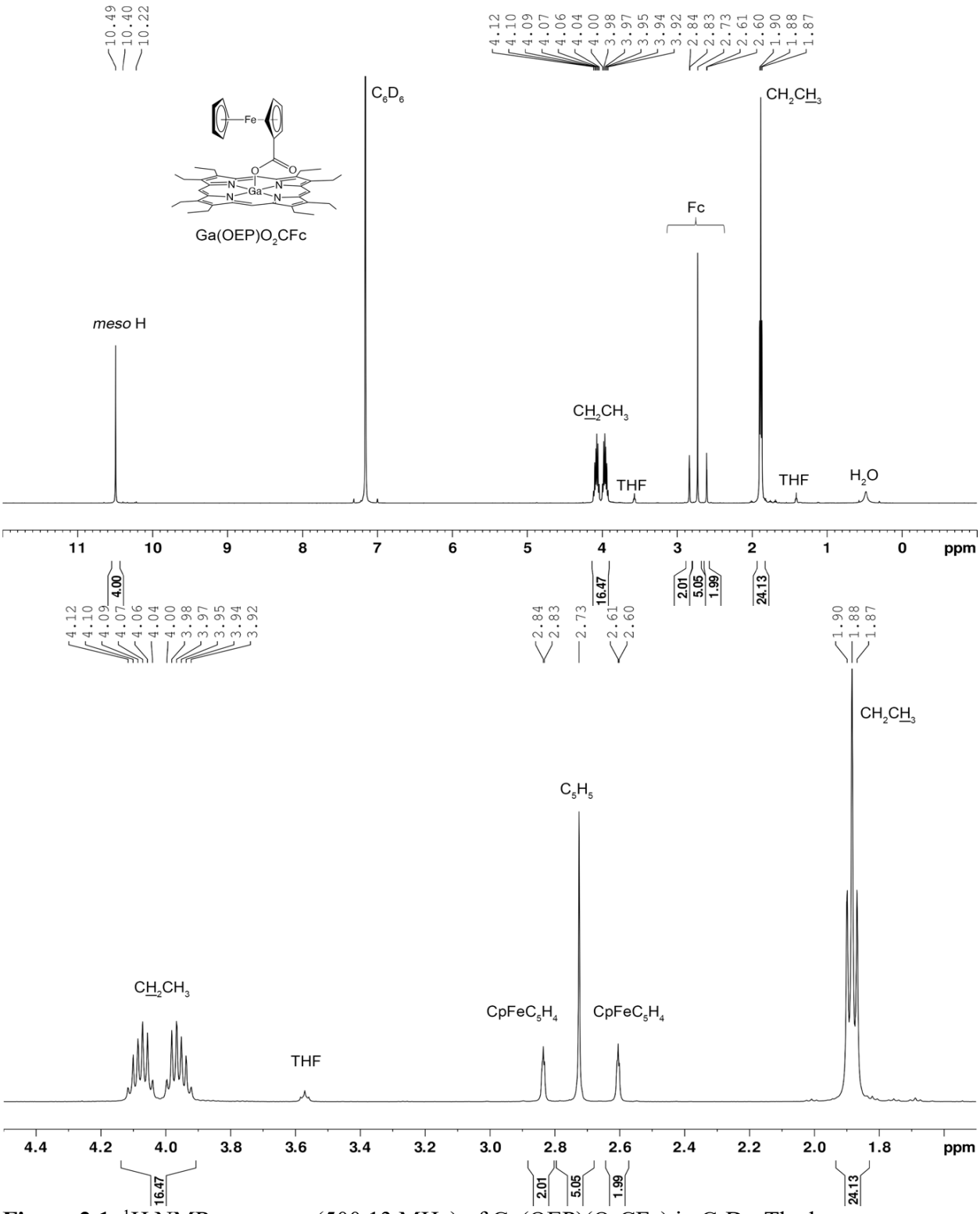

Figure 2.1. ^{1}H NMR spectrum (500.13 MHz) of Ga(OEP)(O_2CFc) in C_6D_6. The bottom spectrum is an expansion of the upper spectrum.

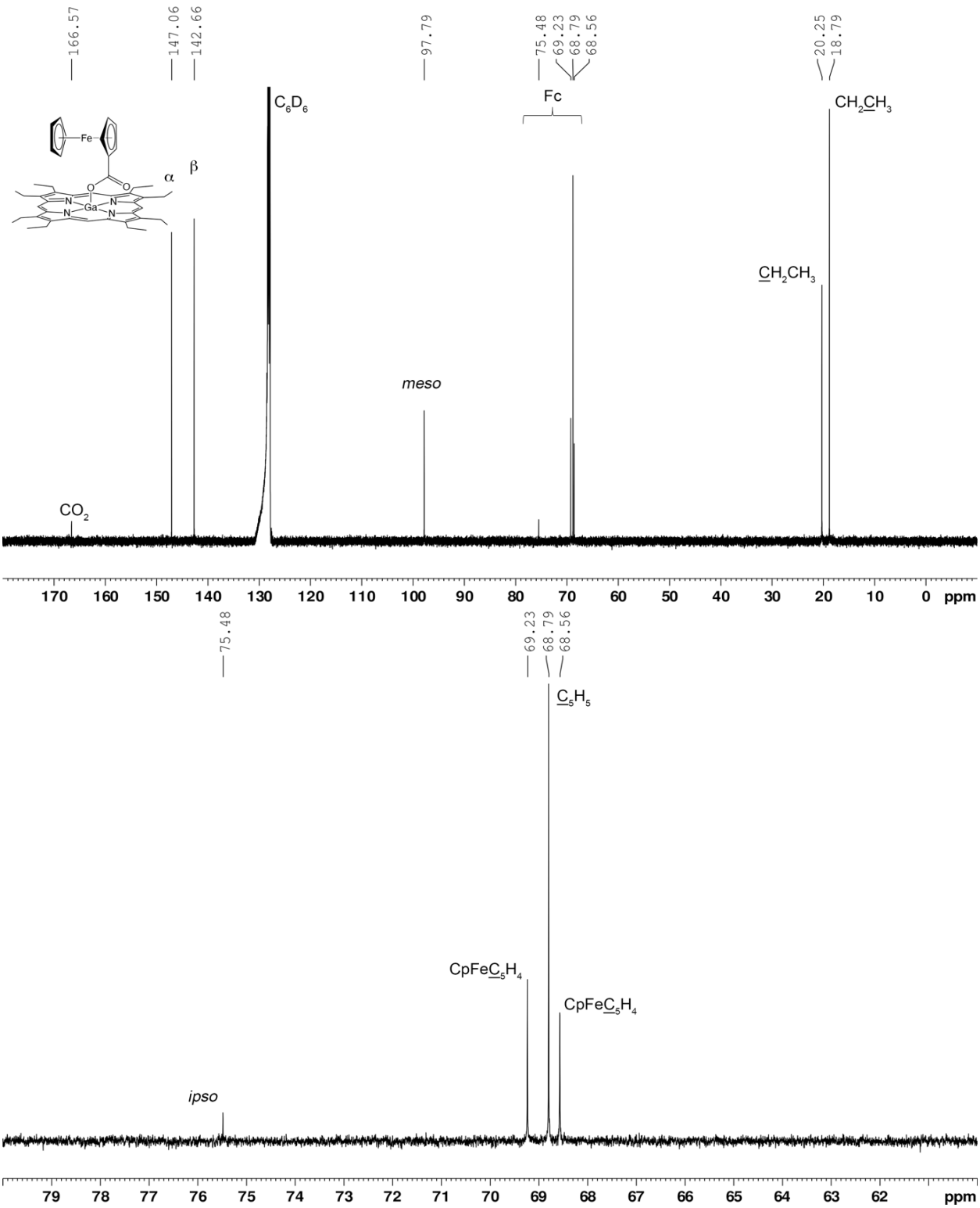

Figure 2.2. $^{13}C\{^{1}H\}$ NMR spectrum (125.77 MHz) of Ga(OEP)(O_2CFc) in C_6D_6. The bottom spectrum is an expansion of the upper spectrum.

2.2.5. Single Crystal X-Ray Diffraction. Diffraction data were measured at 100 K on a Bruker D8 VENTURE diffractometer equipped with a microfocus Mo-target X-ray tube (λ = 0.71073 Å) and PHOTON 100 CMOS detector. Data were collected using ω scans to survey a hemisphere of reciprocal space. Data reduction and integration were performed with the Bruker APEX3 software package (Bruker AXS, version 2015.5-2, 2015). Data were scaled and corrected for absorption effects using the multi-scan procedure as implemented in SADABS (Bruker AXS, version 2014/5).[71] The structure was solved by SHELXT (Version 2014/5)[72] and refined by a full-matrix least-squares procedure using OLEX2 (XL refinement program version 2017/1).[73,74] All atoms were refined with anisotropic thermal parameters. All hydrogen atoms were observed in the difference Fourier map and were included to refinement without any additional restraints. Crystallographic data and details of the data collection are listed in Table 2.1.

Table 2.1. Crystal Data and Structure Refinement Parameters for Ga(OEP)(O_2CFc).

Empirical formula	$C_{47}H_{53}FeGaN_4O_2$
Formula weight	831.50
Temperature/K	100(2)
Crystal system	monoclinic
Space group	*Cc*
a/Å	20.189(3)
b/Å	21.494(3)
c/Å	10.4422(12)
α/°	90
β/°	116.209(3)
γ/°	90
Volume/Å^3	4065.4(9)
Z	4
ρ_{calc}g/cm^3	1.359
μ/mm^{-1}	1.063
F(000)	1744.0
Crystal size/mm^3	0.31 × 0.21 × 0.11
Radiation	MoKα (λ = 0.71073)
2Θ range for data collection/°	4.35 to 52.198
Index ranges	$-24 \le h \le 24$, $-26 \le k \le 26$, $-12 \le l \le 12$
Reflections collected	33600
Independent reflections	7785 [R_{int} = 0.0763, R_{sigma} = 0.0865]
Data/restraints/parameters	7785/2/505
Goodness-of-fit on F^2	1.032
Final R indexes [I>=2σ (I)]	R_1 = 0.0511, wR_2 = 0.0735
Final R indexes [all data]	R_1 = 0.0790, wR_2 = 0.0812
Largest diff. peak/hole / e Å^{-3}	0.82/–0.61

$R_{int} = \Sigma| F_o^2 - \langle F_o^2 \rangle | / \Sigma | F_o^2|$

$R1 = \Sigma \, | \, |F_o| - |F_c| \, | \, / \Sigma \, |F_o|$

$wR2 = [\Sigma \, [w \, (F_o^2 - F_c^2)^2] / \Sigma \, [w \, (F_o^2)^{\,2}]]^{1/2}$

Goodness-of-fit = $[\Sigma \, [w \, (F_o^2 - F_c^2)^{\,2}] / (n-p)^{1/2}$

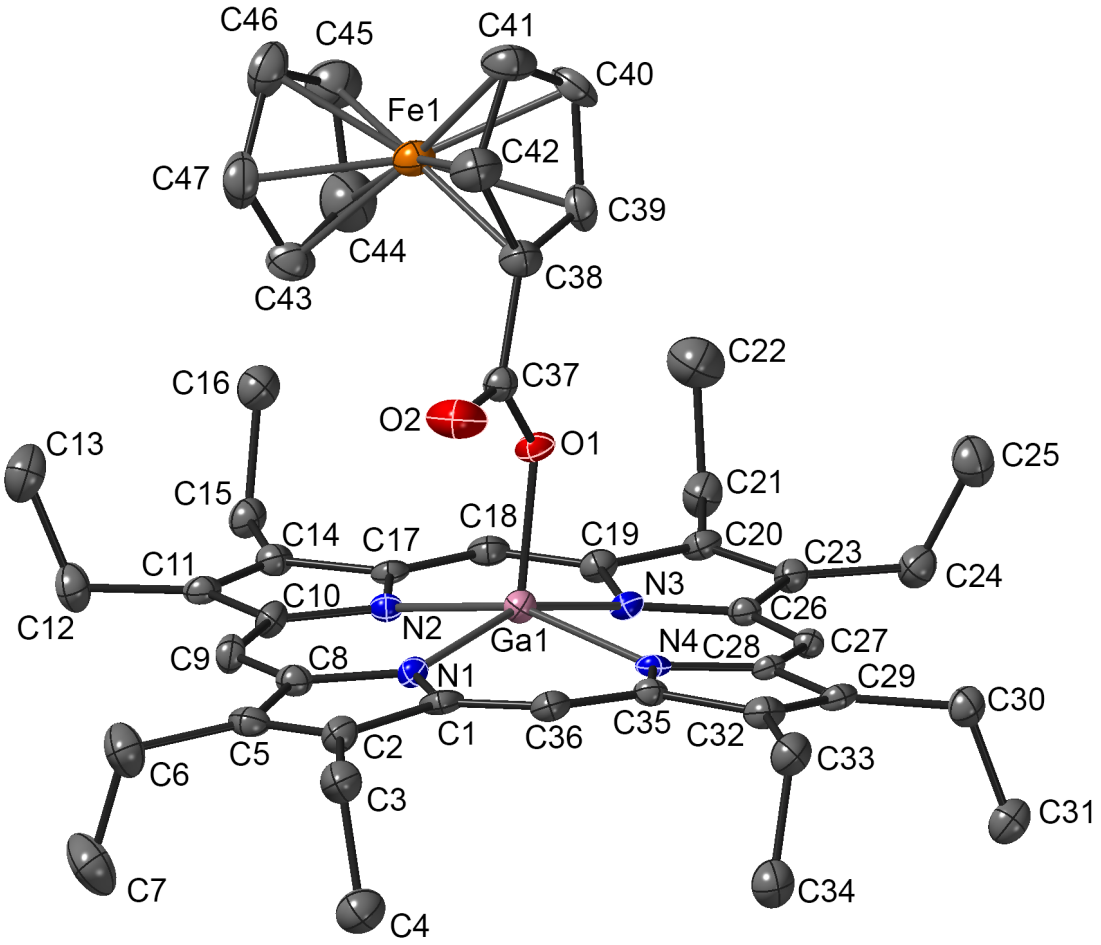

Figure 2.3. Molecular structure of Ga(OEP)(O_2CFc) as determined by X-ray crystallography (50% probability ellipsoids). Hydrogen atoms are not shown.

Table 2.2. Bond Lengths (Å) for Ga(OEP)(O_2CFc).

Atom	Atom	Length/Å	Atom	Atom	Length/Å
Ga1	O1	1.875(4)	C11	C12	1.507(8)
Ga1	N1	2.019(5)	C11	C14	1.360(9)
Ga1	N2	2.040(5)	C12	C13	1.533(9)
Ga1	N3	2.044(5)	C14	C15	1.499(8)
Ga1	N4	2.035(5)	C14	C17	1.459(8)
Fe1	C38	2.019(6)	C15	C16	1.527(9)
Fe1	C39	2.032(8)	C17	C18	1.373(8)
Fe1	C40	2.051(7)	C18	C19	1.378(8)
Fe1	C41	2.046(6)	C19	C20	1.451(8)
Fe1	C42	2.038(7)	C20	C21	1.504(8)
Fe1	C43	2.033(7)	C20	C23	1.356(8)
Fe1	C44	2.026(7)	C21	C22	1.538(9)
Fe1	C45	2.042(7)	C23	C24	1.501(8)
Fe1	C46	2.036(7)	C23	C26	1.447(8)
Fe1	C47	2.036(6)	C24	C25	1.537(9)
O1	C37	1.297(7)	C26	C27	1.382(8)
O2	C37	1.226(7)	C27	C28	1.368(8)
N1	C1	1.390(7)	C28	C29	1.442(8)
N1	C8	1.390(8)	C29	C30	1.508(8)
N2	C10	1.379(8)	C29	C32	1.363(8)
N2	C17	1.384(8)	C30	C31	1.515(9)
N3	C19	1.375(7)	C32	C33	1.511(8)
N3	C26	1.378(7)	C32	C35	1.436(8)
N4	C28	1.389(7)	C33	C34	1.528(9)
N4	C35	1.373(7)	C35	C36	1.381(8)
C1	C2	1.447(8)	C37	C38	1.496(8)
C1	C36	1.365(8)	C38	C39	1.420(9)
C2	C3	1.497(8)	C38	C42	1.419(9)
C2	C5	1.364(9)	C39	C40	1.417(8)
C3	C4	1.521(9)	C40	C41	1.418(10)
C5	C6	1.508(9)	C41	C42	1.429(9)
C5	C8	1.451(8)	C43	C44	1.414(10)
C6	C7	1.525(9)	C43	C47	1.418(12)
C8	C9	1.357(8)	C44	C45	1.380(10)
C9	C10	1.380(8)	C45	C46	1.410(10)
C10	C11	1.442(8)	C46	C47	1.423(11)

Table 2.3. Bond Angles (°) for Ga(OEP)(O_2CFc).

Atom	Atom	Atom	Angle/°	Atom	Atom	Atom	Angle/°
O1	Ga1	N1	110.86(18)	C8	C9	C10	126.6(6)
O1	Ga1	N2	98.79(18)	N2	C10	C9	124.1(5)
O1	Ga1	N3	91.66(17)	N2	C10	C11	110.0(5)
O1	Ga1	N4	101.70(17)	C9	C10	C11	125.9(6)
N1	Ga1	N2	88.12(19)	C10	C11	C12	124.8(6)
N1	Ga1	N3	157.5(2)	C14	C11	C10	107.9(5)
N1	Ga1	N4	87.84(19)	C14	C11	C12	127.2(6)
N2	Ga1	N3	87.35(19)	C11	C12	C13	112.2(5)
N4	Ga1	N2	159.22(19)	C11	C14	C15	129.9(6)
N4	Ga1	N3	88.61(18)	C11	C14	C17	106.0(5)
C38	Fe1	C39	41.0(3)	C17	C14	C15	124.1(6)
C38	Fe1	C40	68.5(3)	C14	C15	C16	112.5(5)
C38	Fe1	C41	68.8(2)	N2	C17	C14	110.2(5)
C38	Fe1	C42	40.9(2)	C18	C17	N2	125.3(6)
C38	Fe1	C43	107.4(3)	C18	C17	C14	124.4(6)
C38	Fe1	C44	124.7(3)	C17	C18	C19	125.2(6)
C38	Fe1	C45	160.8(3)	N3	C19	C18	125.1(5)
C38	Fe1	C46	156.9(3)	N3	C19	C20	110.5(5)
C38	Fe1	C47	120.8(3)	C18	C19	C20	124.4(5)
C39	Fe1	C40	40.6(2)	C19	C20	C21	124.5(5)
C39	Fe1	C41	68.6(3)	C23	C20	C19	106.3(5)
C39	Fe1	C42	69.0(3)	C23	C20	C21	129.2(5)
C39	Fe1	C43	120.7(3)	C20	C21	C22	112.0(5)
C39	Fe1	C45	124.1(3)	C20	C23	C24	128.5(5)
C39	Fe1	C46	161.1(3)	C20	C23	C26	107.4(5)
C39	Fe1	C47	156.2(4)	C26	C23	C24	123.9(5)
C41	Fe1	C40	40.5(3)	C23	C24	C25	112.8(5)
C42	Fe1	C40	68.5(3)	N3	C26	C23	109.9(5)
C42	Fe1	C41	40.9(3)	N3	C26	C27	124.8(5)
C42	Fe1	C45	157.0(3)	C27	C26	C23	125.3(5)
C43	Fe1	C40	156.0(4)	C28	C27	C26	126.8(5)
C43	Fe1	C41	162.1(3)	N4	C28	C29	110.0(5)
C43	Fe1	C42	124.8(3)	C27	C28	N4	124.5(5)
C43	Fe1	C45	67.8(3)	C27	C28	C29	125.6(5)
C43	Fe1	C46	68.2(3)	C28	C29	C30	124.8(5)
C43	Fe1	C47	40.8(3)	C32	C29	C28	106.6(5)
C44	Fe1	C39	107.1(3)	C32	C29	C30	128.6(6)
C44	Fe1	C40	120.8(3)	C29	C30	C31	113.2(5)
C44	Fe1	C41	155.7(3)	C29	C32	C33	128.4(5)

Table 2.3, continued. Bond Angles (°) for Ga(OEP)(O_2CFc).

C44	Fe1	C42	161.9(3)	C29	C32	C35	107.3(5)
C44	Fe1	C43	40.8(3)	C35	C32	C33	124.1(5)
C44	Fe1	C45	39.6(3)	C32	C33	C34	111.1(5)
C44	Fe1	C46	67.7(3)	N4	C35	C32	110.4(5)
C44	Fe1	C47	68.6(4)	N4	C35	C36	124.1(5)
C45	Fe1	C40	108.0(3)	C36	C35	C32	125.3(5)
C45	Fe1	C41	121.6(3)	C1	C36	C35	126.0(6)
C46	Fe1	C40	125.0(3)	O1	C37	C38	113.0(5)
C46	Fe1	C41	108.1(3)	O2	C37	O1	126.0(5)
C46	Fe1	C42	121.7(3)	O2	C37	C38	121.0(5)
C46	Fe1	C45	40.5(3)	C37	C38	Fe1	123.3(4)
C47	Fe1	C40	161.9(4)	C39	C38	Fe1	70.0(4)
C47	Fe1	C41	125.0(4)	C39	C38	C37	126.8(6)
C47	Fe1	C42	107.4(4)	C42	C38	Fe1	70.3(4)
C47	Fe1	C45	68.5(4)	C42	C38	C37	124.6(6)
C47	Fe1	C46	40.9(3)	C42	C38	C39	108.6(6)
C37	O1	Ga1	128.1(4)	C38	C39	Fe1	69.0(4)
C1	N1	Ga1	126.4(4)	C40	C39	Fe1	70.4(5)
C8	N1	Ga1	127.3(4)	C40	C39	C38	107.7(6)
C8	N1	C1	105.7(5)	C39	C40	Fe1	69.0(5)
C10	N2	Ga1	126.9(4)	C39	C40	C41	108.4(6)
C10	N2	C17	105.9(5)	C41	C40	Fe1	69.6(4)
C17	N2	Ga1	125.8(4)	C40	C41	Fe1	69.9(4)
C19	N3	Ga1	125.5(4)	C40	C41	C42	107.9(6)
C19	N3	C26	105.9(5)	C42	C41	Fe1	69.2(4)
C26	N3	Ga1	126.1(4)	C38	C42	Fe1	68.8(4)
C28	N4	Ga1	126.8(4)	C38	C42	C41	107.4(6)
C35	N4	Ga1	126.5(4)	C41	C42	Fe1	69.8(4)
C35	N4	C28	105.7(5)	C44	C43	Fe1	69.3(4)
N1	C1	C2	110.5(5)	C44	C43	C47	107.9(7)
C36	C1	N1	124.8(5)	C47	C43	Fe1	69.7(4)
C36	C1	C2	124.6(5)	C43	C44	Fe1	69.9(4)
C1	C2	C3	124.3(5)	C45	C44	Fe1	70.8(4)
C5	C2	C1	106.5(5)	C45	C44	C43	108.8(7)
C5	C2	C3	129.0(5)	C44	C45	Fe1	69.5(4)
C2	C3	C4	112.0(5)	C44	C45	C46	108.4(7)
C2	C5	C6	128.8(6)	C46	C45	Fe1	69.5(4)
C2	C5	C8	107.6(5)	C45	C46	Fe1	70.0(4)
C8	C5	C6	123.4(6)	C45	C46	C47	108.2(8)
C5	C6	C7	111.8(5)	C47	C46	Fe1	69.5(4)

Table 2.3, continued. Bond Angles (°) for Ga(OEP)(O_2CFc).

N1	C8	C5	109.6(5)	C43	C47	Fe1	69.5(4)
C9	C8	N1	124.9(6)	C43	C47	C46	106.8(8)
C9	C8	C5	125.5(6)	C46	C47	Fe1	69.6(4)

2.2.6. Density Functional Theory (DFT) Calculations. Calculations were performed using plane-wave density functional theory (PW-DFT) within Quantum Espresso (version 6.1)[75] unless otherwise noted. The generalized gradient approximation in the optB86b-vdW[76,77] formulation was used for most systems. This models the exchange and correlation interactions using the optB86[78] functional and the dispersion interactions with the vdw-DF[79-82] method, which has been previously shown to provide accurate results for MoS_2.[83] A small subset of calculations were performed using the revPBE[84] functional in conjunction with the vdw-DF method. Optimized norm-conserving Vanderbilt (ONCV) pseudopotentials were used.[85,86] A wavefunction cutoff energy of 60 Ry was used. The wavefunctions were sampled at the Γ point for isolated porphyrins and systems involving MoS_2, or at a *k*-point grid of 2 × 2 × 1 using the Monkhorst and Pack[87] method for systems involving HOPG. Gaussian smearing with a width of 0.001 Ry was included to ensure smooth convergence of the self-consistent field (SCF). Structures and adsorption energies were tested for convergence with respect to the wavefunction cutoff energy, *k*-points and smearing width. Geometry optimizations were performed with convergence thresholds on the total energy and total forces of 10^{-4} Ry and 10^{-3} Ry for the ionic minimization and 10^{-8} Ry for the electronic energy during the SCF process. These functionals, pseudopotentials and numerical parameters were chosen based on a series of test calculations that are detailed in Section 6.1.1.

HOPG and MoS_2 substrates were constructed from their bulk crystal structures as 8 × 8 × 2 (HOPG) and 6 × 6 × 2 (MoS_2) supercells in the *a, b, c* directions, respectively, to give 4-layer (4L) slabs. 1L- and 2L-MoS_2 were built by deleting three and two layers, respectively, from the

4L-MoS_2 slab. A vacuum layer of 30 Å in the *c* direction was added to avoid interactions within the periodic system. The structures of isolated porphyrin molecules were first calculated in Gaussian09[88] using the B3P86 functional,[89,90] LANL2DZ effective core potential basis set[91,92] for Ga, Zn and Ni atoms, and the 6-31G* basis set for all other atoms, with the ethyl groups oriented in an all "up" conformation, as has been previously described.[33] The optimized geometries obtained from the molecular DFT calculations were used as starting points for the PW-DFT calculations, which were optimized without constraints on any atoms. The optimizations of the isolated porphyrins were carried out in a 30 Å × 30 Å × 30 Å cell to ensure that the porphyrins were isolated with respect to periodic images.

Interfacial porphyrin–surface systems were built by inserting the optimized structure obtained from the isolated porphyrin calculation onto the surface of the optimized structure of MoS_2 or HOPG. The initial geometry of the interface was defined such that the distance between the $C_{20}N_4$ plane of the porphyrin and the plane of the topmost sulfur or carbon atoms was either 3.30 Å or 3.35 Å, respectively, in accord with expectation based on van der Waals radii. For interfaces involving 1L- or 2L-MoS_2, all atoms were allowed to relax; for 4L interfaces of both MoS_2 and HOPG, the porphyrin and the top two layers of the MoS_2 or HOPG were allowed to relax while the bottom two layers were frozen in the optimized positions for the free substrate. The dependence of the optimized geometry and adsorption energy on the number of MoS_2 layers is discussed in Section 6.1.2. Cell parameters for all systems are listed in Table 2.4.

Table 2.4. Lattice Parameters of Simulation Cells for PW-DFT Calculations of Porphyrins, Substrates, and Porphyrin/Substrate Assemblies.

System	*a* (Å)	*b* (Å)	*c* (Å)	*α* (°)	*β* (°)	*γ* (°)
Isolated Porphyrin	30	30	30	90	90	90
4L HOPG and 4L HOPG/Porphyrin	19.65	19.65	43.42	90	90	120
1L MoS_2 and 1L MoS_2/Porphyrin	18.98	18.98	34.60	90	90	120
2L MoS_2 and 2L MoS_2/Porphyrin	18.98	18.98	40.30	90	90	120
4L MoS_2 and 4L MoS_2/Porphyrin	18.98	18.98	51.70	90	90	120

2.3. Results and Discussion

2.3.1. STM Imaging of M(OEP) Monolayers on MoS_2 and HOPG. Deposition of 1-phenyloctane solutions (0.5 mM) of Ni(OEP) onto 1L-MoS_2 on gold at room temperature results in the rapid formation of self-assembled, ordered monolayers of Ni(OEP), as revealed by STM imaging at the solid–liquid interface. These deposition conditions are comparable to those that lead to formation of Ni(OEP) monolayers on HOPG.[33,93,94] Large ordered arrays of Ni(OEP) (minimum 50 nm × 50 nm) form within 5 minutes of deposition, as shown in Figure 2.4a–c. A higher-resolution STM image for Ni(OEP) on 1L-MoS_2 is shown in Figure 2.4b. The porphyrins appear as ring-like features approximately 1 nm in diameter in corrected images, consistent with alignment of the porphyrin plane parallel to the surface as shown in the height profile in Figure 2.4f. The ring-type structure has also been observed for Ni(OEP) on Au (111) under UHV conditions[95] and on HOPG at both the solid–air[60] and solid–liquid interface.[33,60] The ethyl side-chains of the porphyrins have not been imaged in our experiments, though Scudiero, *et al*., have found that on Au (111) (where UHV conditions allow side-chain imaging) M(OEP) compounds exhibit multiple rotational orientations in the unit cell.[95] Building a space-filling model of Ni(OEP) in the monolayer structure (Figure 2.4d) suggests that the M(OEP) may adopt multiple rotational orientations on 1L-MoS_2 in order to minimize steric repulsion between the ethyl side-chains of adjacent molecules. The possibility that the porphyrin monolayers might be directly supported on

the Au conduction layer was excluded by the observations that variation of the STM bias voltage allowed sequential imaging of both the porphyrin and the underlying MoS_2 (Figure 2.1d), showing it to always be present, and that deposition of Ni(OEP) on a bare Au substrate under the same experimental conditions did not result in formation of porphyrin monolayers. To additionally confirm that the Au conduction layer is not necessary for the formation of Ni(OEP) monolayers, a solution of Ni(OEP) deposited onto bulk MoS_2 under the same conditions as above also results in formation of a Ni(OEP) monolayer (Figure 2.5) similar to those on 1L-MoS_2.

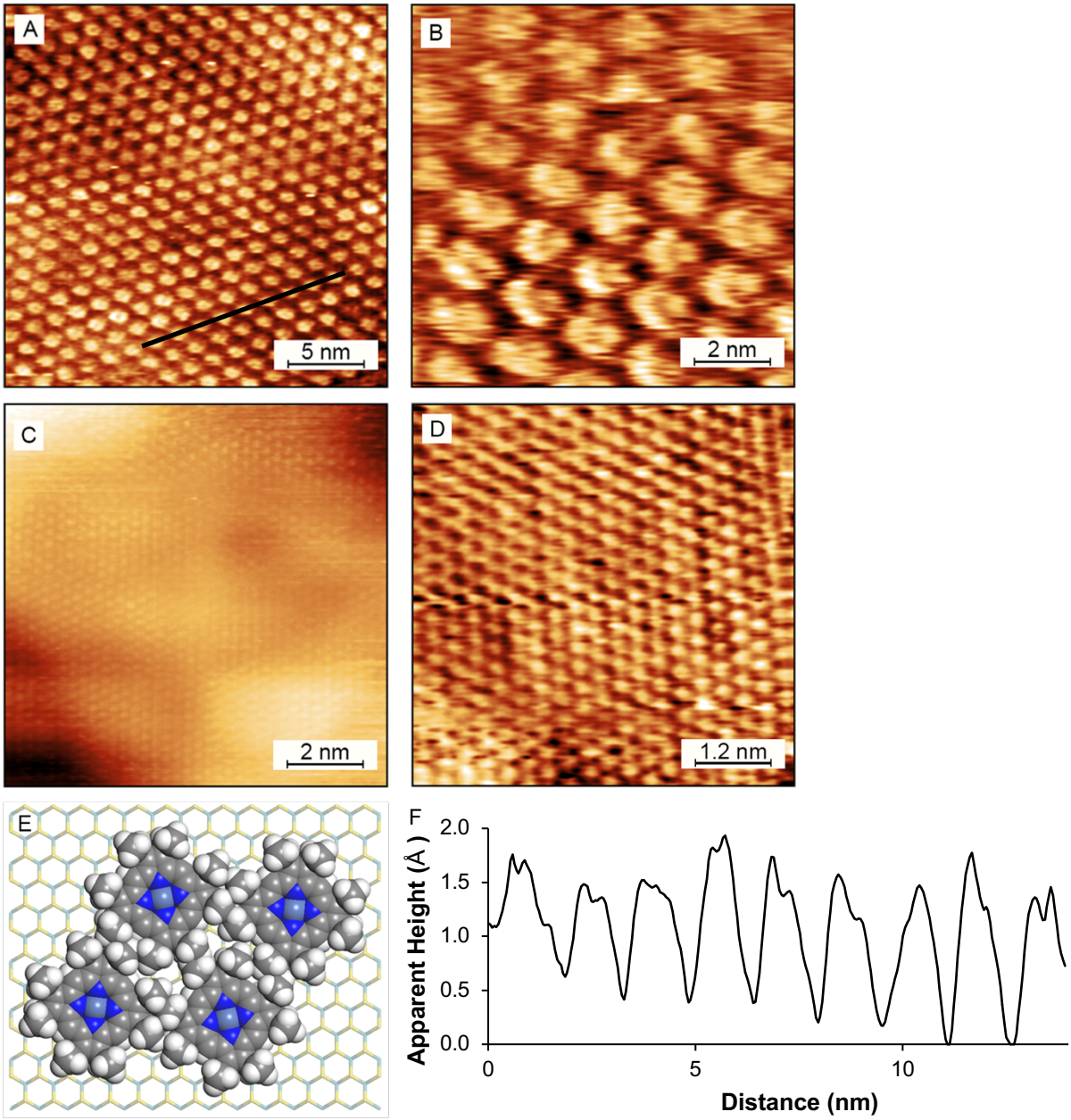

Figure 2.4. STM images, structural model and cross-sectional profile of Ni(OEP) monolayers on 1L-MoS_2 at the solid–liquid interface (0.5 mM, 1-phenyloctane); (a) Ni(OEP) (25 nm × 25 nm, I = 60 pA, V = –1500 mV); (b) Ni(OEP) (10 nm × 10 nm, I = 60 pA, V = –1500 mV); (c) Ni(OEP) (50 nm × 50 nm, I = 150 pA, V = –1500 mV); (d) MoS_2 imaged beneath a monolayer of Ni(OEP) (6 nm × 6 nm, I = 80 pA, V = –400 mV); (e) possible arrangement of Ni(OEP) on monolayer MoS_2; (f) Cross-sectional profile taken along the black line in STM image (a).

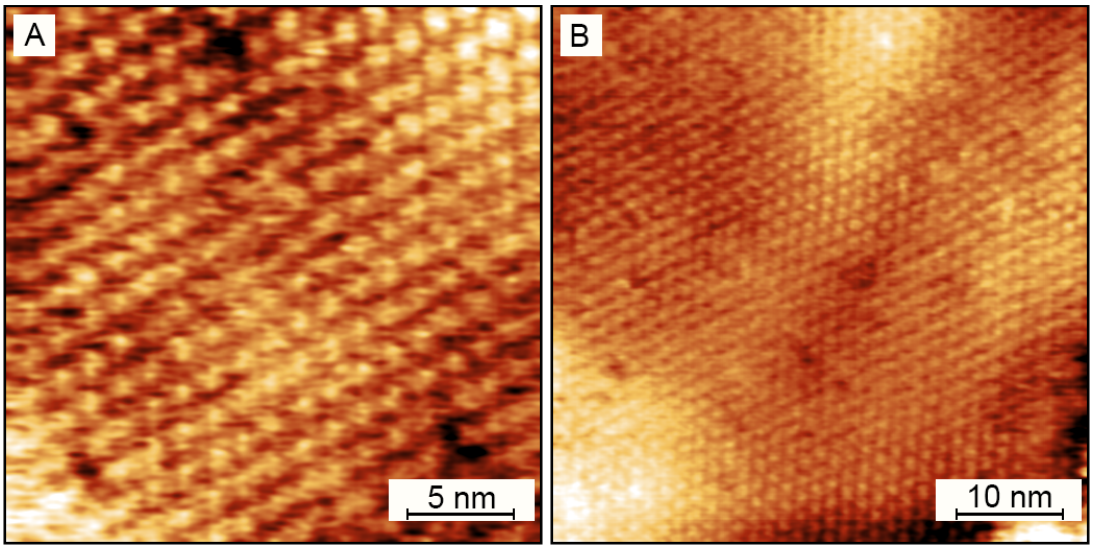

Figure 2.5. STM images of Ni(OEP) (0.5 mM in 1-phenyloctane) on bulk MoS_2 at the solid–liquid interface: (a) 25 nm × 25 nm (I = 150 pA, V = –1500 mV); (b) 50 nm × 50 nm (I = 150 pA, V = –1500 mV).

In order to test the dependence of monolayer formation and structure on the porphyrin metal center, 1-phenyloctane solutions (0.5 mM) of the octaethylporphyrins Zn(OEP), Ga(OEP)Cl, and H_2OEP were also deposited onto 1L-MoS_2. All M(OEP)s are observed by STM to form monolayers with ring-like features similar to those for Ni(OEP), and are stable over the course of several hours of continuous STM imaging (Figure 2.6). The less pronounced features for Ga(OEP)Cl (Figure 2.6b) compared with the other M(OEP)s is the result of the low current setpoints that were required to obtain these images. Ga(OEP)Cl monolayers could not be imaged at higher current setpoints, with only HOPG being observed. STM maging of other M(OEP)s at the low current setpoints used for Ga(OEP)Cl resulted in images with similar resolution to Figure 2.6b.

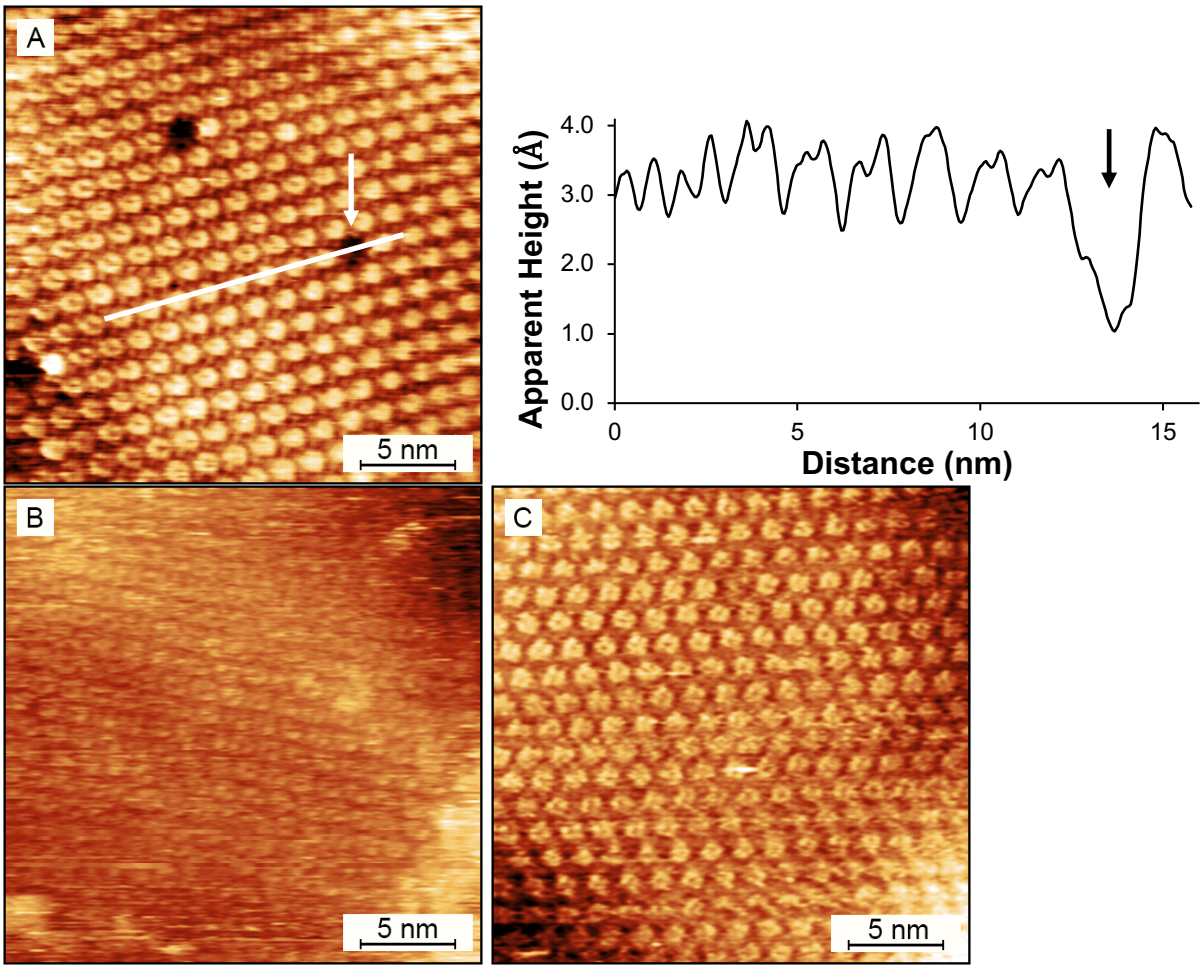

Figure 2.6. STM images of M(OEP) monolayers on monolayer MoS_2 at the solid–liquid interface (0.5 mM in 1-phenyloctane): (a) Left, Zn(OEP) (25 nm × 25 nm, I = 60 pA, V = –1500 mV) and Right, cross-sectional profile of Zn(OEP) taken along the white line , with a vacancy marked on both figures by an arrow; (b) Ga(OEP)Cl (25 nm × 25 nm, I = 12 pA, V = –1200 mV) from Ref. 64; (c) H_2OEP (25 × 25 nm, I = 150 pA, V = –1500 mV).

Measurements of the lattice constants of the M(OEP) monolayers (Table 2.5) show that all exhibit a pseudohexagonal geometry and unit cell dimensions that are identical to each other within experimental error (a = 1.35–1.39 nm, b = 1.33–1.36 nm, Γ = 63–68°). This indicates that the structure of the porphyrin monolayer is not affected by the presence or absence of the metal center (H_2OEP vs M(OEP)), the identity of the metal (Ni(OEP) vs Zn(OEP)), the planarity of the porphyrin (domed Ga(OEP)Cl vs planar M(OEP)), or possible axial interactions between the sulfur lone pairs of MoS_2 and the Zn center of Zn(OEP), which is known to form five-coordinate

complexes with sulfur compounds.[96] The unit-cell dimensions of the M(OEP) monolayers on MoS_2 are experimentally indistinguishable from those observed on HOPG under similar ambient conditions (Figure 2.7), despite the grossly different molecular and electronic structures that these surfaces present to the porphyrins.

Table 2.5. Unit-Cell Parameters of M(OEP) Monolayers on Monolayer MoS_2 and HOPG at the Solid–Liquid Interface.

	Ni(OEP)		H_2OEP		Zn(OEP)		Ga(OEP)Cl	
parameter	MoS_2	HOPG[a]	MoS_2	HOPG[b]	MoS_2	HOPG[b]	MoS_2[c]	HOPG[a]
a (nm)	1.39 (4)	1.39 (2)	1.38 (2)	1.38 (2)	1.37 (3)	1.37 (4)	1.35 (1)	1.37 (2)
b (nm)	1.33(4)	1.35 (3)	1.35 (2)	1.36 (2)	1.36 (3)	1.35 (2)	1.33 (2)	1.34 (2)
Γ (deg)	65 (5)	64 (2)	63 (3)	65 (1)	66 (2)	68 (1)	68 (1)	67 (1)

[a] From Ref. 33. [b] From data shown in Figure 2.7. [c] From Ref. 64.

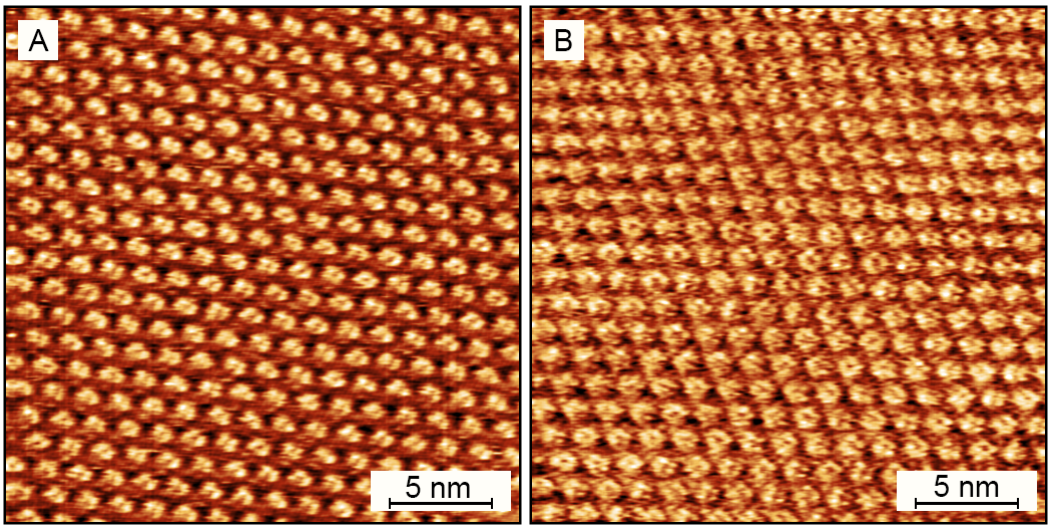

Figure 2.7. STM images (25 nm × 25 nm) of Zn(OEP) and H_2OEP monolayers on HOPG at the solid–liquid interface (0.5 mM in 1-phenyloctane): (a) Zn(OEP) (I = 30 pA, V = –700 mV); (b) H_2OEP (I = 30 pA, V = –600 mV).

2.3.2. STM Imaging of Porphyrin Monolayers on 1L TMDs and HOPG with Variations of Porphyrin, TMD, and Deposition Conditions. In order to explore the generality of this method for TMD functionalization, variations to the TMD, porphyrin, and deposition conditions were investigated. Solution deposition of Ni(OEP) onto 1L-WSe_2 also produced ordered, large-scale ordered molecular monolayers that are stable over several hours of STM

imaging (Figure 2.8a). The Ni(OEP) molecules are again observed as ring-like structures, and the monolayer possesses the same lattice constants as observed on 1L-MoS_2 (Table 2.6). The observation that the monolayer also forms on 1L-WSe_2 suggests that ambient-condition supramolecular surface functionalization will extend to the other TMD compositions that are available (MX_2: M = Mo, W; X = S, Se, Te).[97] Modifications to the peripheral substituents of the porphyrins were also introduced to probe the robustness of the approach and the effects of these groups on the structures of the arrays. On other surfaces, the nature of the porphyrin side chains is found to control the structure, dimensions, and stability of the monolayer.[98-100] Ni(etioporphyrin I) (Ni(Etio), Chart 2.1b) was investigated as an example of a porphyrin with more-compact side chains than OEP, and free-base *meso*-tetradecylporphyrin ($H_2TC_{10}P$, Chart 2.1c) was studied to explore the effects of long alkyl side chains. Both porphyrins are observed to form ordered monolayers on 1L-MoS_2 at the solid–liquid interface upon deposition from solution. The monolayer of Ni(Etio) (Figure 2.8b) displays a pseudohexagonal geometry with slightly smaller cell lengths than those observed for M(OEP) compounds (Table 2.6), consistent with its more compact structure; the structure is also quantitatively similar to that found for the compound on HOPG (Figure 2.9 and Table 2.7).[101] Interestingly, monolayers of $H_2TC_{10}P$ on MoS_2 were not detected when it was deposited from 1-phenyloctane solution (0.01 mM– 0.75 mM), but they were observed when tetradecane was used as the solvent. The $H_2TC_{10}P$ monolayers exhibit a lamellar structure, with rows of bright features arising from the porphyrin ring and dark stripes where the decyl chains are inferred to be located (Figure 2.8c). The density of $H_2TC_{10}P$ on the surface, 0.41 molecules/nm^2, is observed to be the same on MoS_2 and HOPG (Tables 2.6 and 2.7) and is significantly smaller than for M(OEP) and Ni(Etio) (0.58–0.60 molecules/nm^2 and 0.65 molecules/nm^2 respectively). These observations demonstrate that side-chain variation provides a

mechanism to control the structure and dimensions of porphyrin overlayers on 1L-MoS_2 and, by inference, other TMDs. Finally, variations to the deposition conditions were introduced to test whether ordered monolayers of porphyrins form on MoS_2 under technologically relevant conditions, at the solid–air interface. These samples were dosed by immersing the 1L-MoS_2 wafer in a 0.5 mM solution of NiOEP in toluene. The samples were rinsed three times with neat toluene and dried under vacuum before being imaged by STM at the solid–air interface under ambient conditions. Monolayers of Ni(OEP) readily form at the solid–air interface (Figure 2.8d) and are observed to have an identical unit cell to M(OEP) monolayers characterized at the solid–liquid interface (Table 2.6). These observations indicate that ordered monolayers of OEPs can be formed under technologically relevant conditions. Additionally, it suggests that the structures of monolayers deposited by immersion dosing and characterized at the solid–air can be inferred from those measured the less challenging solid–liquid interface.[102]

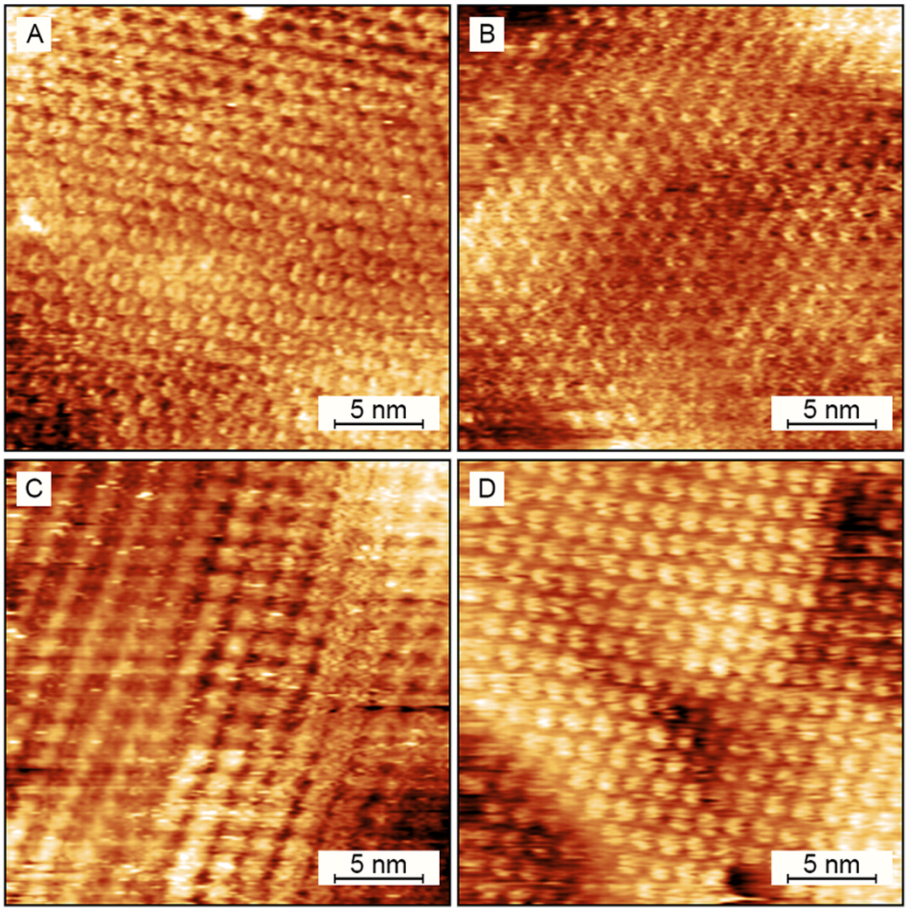

Figure 2.8. STM images (25 nm × 25 nm) of various porphyrin monolayers on monolayer TMDs: (a) Ni(OEP) on WSe_2 (I = 500 pA, V = –1800 mV, 0.5 mM in 1-phenyloctane); (b) Ni(Etio) on MoS_2 (I = 100 pA, V = –1400 mV, 0.5 mM in 1-phenyloctane); (c) $H_2TC_{10}P$ on MoS_2 (I = 10 pA, V = –1450 mV, 0.75 mM in tetradecane); (d) Ni(OEP) on MoS_2 (I = 8 pA, V = –1600 mV, solid–air interface).

Table 2.6. Unit-Cell Parameters of Ni(OEP), Ni(Etio), and $H_2TC_{10}P$ on TMDs.

	Ni(OEP)	Ni(Etio)	$H_2TC_{10}P$	Ni(OEP)
parameter	WSe_2	MoS_2	MoS_2	MoS_2 (solid–air)
a (nm)	1.39 (4)	1.33 (3)	1.38 (3)	1.39 (3)
b (nm)	1.33 (4)	1.30 (3)	1.76 (5)	1.36 (4)
Γ (deg)	66 (2)	63 (1)	88 (1)	69 (6)
Density (molecules/nm²)	0.59	0.65	0.41	0.57

Table 2.7. Unit-Cell Parameters of Ni(Etio) and $H_2TC_{10}P$ on HOPG.

parameter	Ni(Etio)	$H_2TC_{10}P$
a (nm)	1.31 (3)	1.37 (4)
b (nm)	1.29 (2)	1.75 (5)
Γ (deg)	66 (2)	86 (2)
Density (molecules/nm²)	0.65	0.42

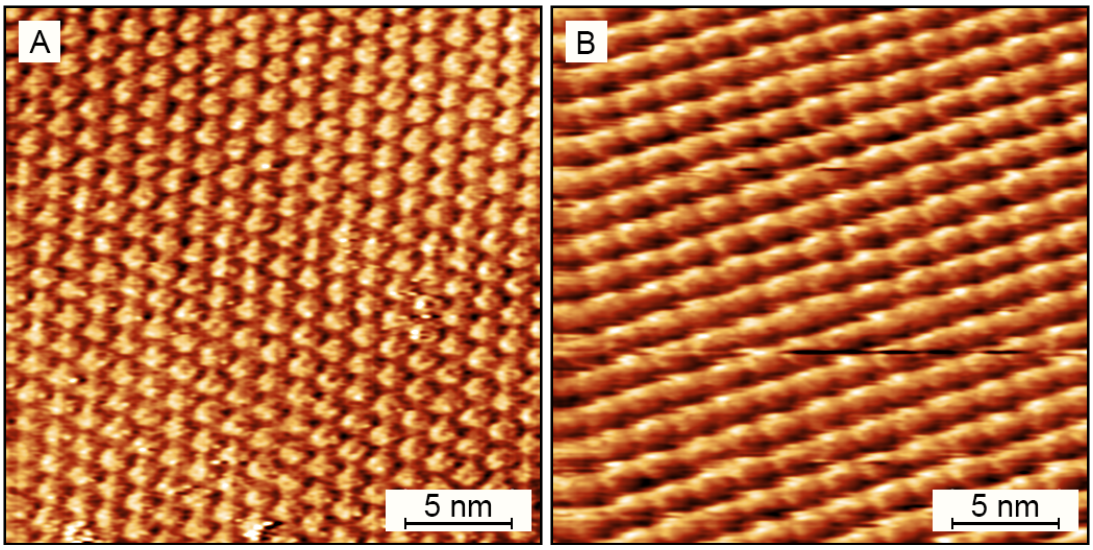

Figure 2.9. STM images (25 nm × 25 nm) of Ni(Etio), and $H_2TC_{10}P$ monolayers on HOPG at the solid–liquid interface: (a) Ni(Etio) (0.5 mM in 1-phenyloctane, I = 750 pA, V = –700 mV); (b) $H_2TC_{10}P$ (0.75 mM in tetradecane, I = 25 pA, V = –1400 mV).

2.3.3. DFT Determination of Adsorption Energies of M(OEP) Monolayers on 1L MoS_2 and HOPG. To gain further insight into the formation of self-assembled OEP monolayers, a series of DFT calculations were performed to determine the optimized structures and adsorption energies of porphyrins on 1L-MoS_2. The adsorption energies were determined according to Equation 2.1:

$$E_{ads} = E_{Int} - E_S - E_P \tag{2.1}$$

where E_{ads} is the adsorption energy of the porphyrin molecule on the substrate in the gas phase and E_{Int}, E_S, and E_P are the total energies of the optimized substrate–porphyrin interface, the isolated substrate and the isolated porphyrin, respectively. This approach has been used previously to calculate the adsorption energies of porphyrins and phthalocyanines on various substrates.[32,103-105] While this approach does not include the solvation energies for the porphyrin, substrate, or porphyrin–substrate assembly, the differences in these energies are expected to be minimal across the series of closely related M(OEP) complexes.

The adsorption energy of Ni(OEP) on 1L-MoS_2 was calculated with Ni placed at three high-symmetry MoS_2 sites and for three rotational conformers between periodic limits at each site (Figure 2.10). The binding sites are denoted Center, in which Ni is above a Mo atom; Top, in which Ni is over an S atom; and Bridge, where Ni is between two S atoms. The calculations show the adsorption energy exhibits a minimal dependence on the binding site or rotational conformation, ranging from –3.16 eV to –3.33 eV (Table 2.8), with the orientation denoted Bridge 22.5˚ being slightly favored. Given that the range of adsorption energies across all binding sites is only spanned 0.17 eV, is is likely that under the experimental deposition and imaging conditions (from solution at room temperature), the observed structure is not driven by the preferred site and orientation..[106] Detailed structural parameters of the calculated structures at each of these binding sites are discussed in Chapter 6.

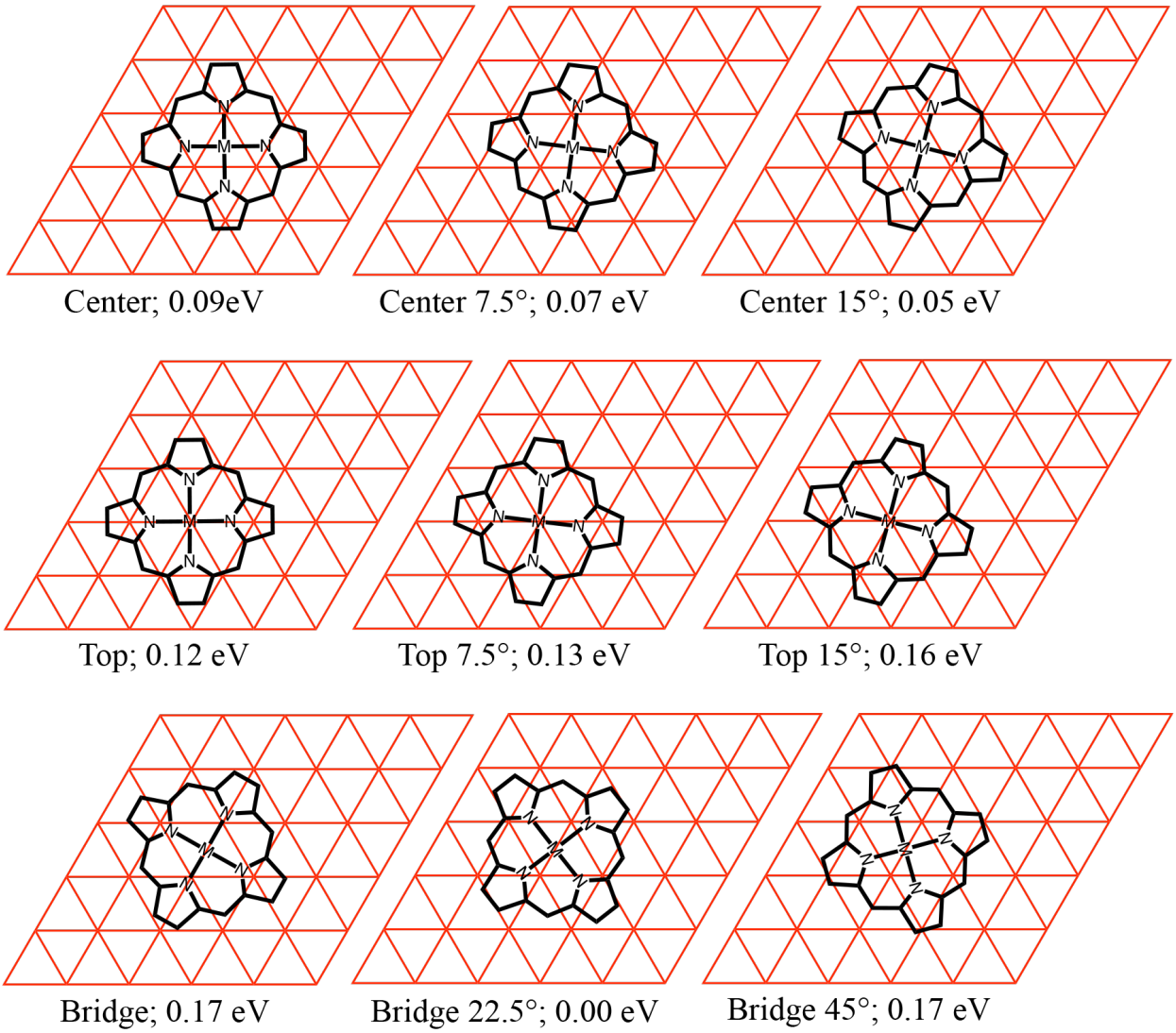

Figure 2.10. Relative calculated adsorption energies of Ni(OEP) for different binding sites and orientations on 1L-MoS_2, referenced to the lowest-energy configuration (Bridge 22.5° site). Sulfur atoms lie at the vertices of the underlying red grid. For a given site, angles indicate the rotation of the porphyrin relative to the orientation on the left side of each row. Hydrogen atoms and ethyl groups are not shown for clarity.

Table 2.8. Calculated Adsorption Energy of Ni(OEP) for Different Binding Sites and Orientations on 1L-MoS_2.

Binding Site	Adsorption Energy (eV)
Center 0˚	–3.23
Center 7.5°	–3.25
Center 15°	–3.28
Top 0˚	–3.21
Top 7.5°	–3.20
Top 15°	–3.17
Bridge 0˚	–3.16
Bridge 22.5°	–3.33
Bridge 45°	–3.16

The adsorption energies of Zn(OEP), H_2OEP and Ga(OEP)Cl were calculated at the lowest energy rotational conformers at each binding site for Ni(OEP) (Bridge 22.5˚, Center 15˚, and Top 0˚) and are found to have similar adsorption energies as Ni(OEP) (Table 2.9). All OEPs are roughly co-planar with the surface at a separation of approximately 3.30 Å (Figure 2.11) and do not show substantial distortion from planarity. Notably, H_2OEP shows the largest adsorption energy at the Center 15° binding site, in contrast with other M(OEP)s which all find the Bridge 22.5° binding site to be the most stable, though the energy differences between the binding sites are small. In sum, the small differences among the calculated adsorption energies across the range of porphyrins, binding sites, and rotational orientations indicate that the adsorption is driven principally by dispersion interactions between the surface and the porphyrin macrocycle and that interactions between the metal center and the sulfur atoms are to be too small to affect monolayer structure.

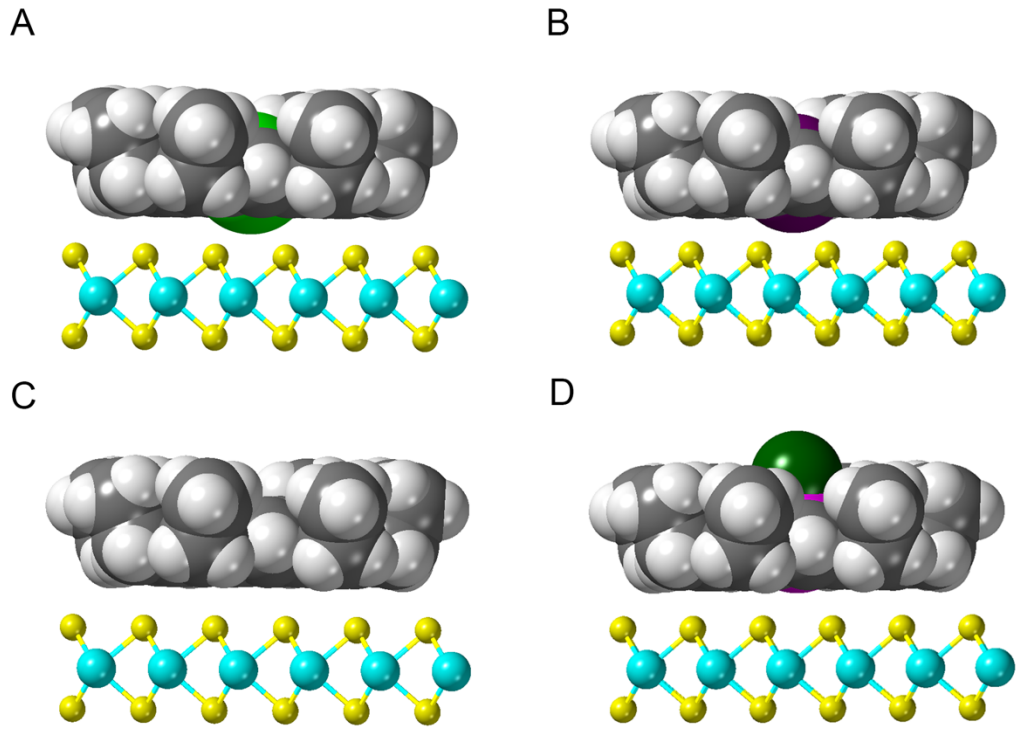

Figure 2.11. Calculated structures of (a) Ni(OEP), (b) Zn(OEP), (c) H_2OEP, and (d) Ga(OEP)Cl on 1L MoS_2 at the Bridge 22.5° binding site.

Table 2.9. Calculated Adsorption Energies for Zn(OEP), H_2OEP, and Ga(OEP)Cl on 1L-MoS_2 for the Minimum-Energy Orientations of Ni(OEP) at each Binding Site.

	Adsorption Energy (eV)		
Binding Site	Zn(OEP)	H_2OEP	Ga(OEP)Cl
Center 15°	–3.25	–3.20	–3.20
Top 0˚	–3.23	–3.18	–3.18
Bridge 22.5°	–3.30	–3.07	–3.27

Given the structural similarity between self-assembled monolayers of porphyrins on 1L-MoS_2 and HOPG, the optimized geometry and adsorption energy of Ni(OEP), Zn(OEP), H_2OEP, and Ga(OEP)Cl were also calculated on 4L graphite using the same methodology. The optimized structures are found to be similar to those on 1L-MoS_2, with an adsorbate–surface distance slightly larger than on 1L-MoS_2. While the increase in this distance seems counterintuitive given the larger van der Waals radius of sulfur compared to carbon, the larger separation between sulfur atoms in MoS_2 (3.16 Å) compared to the separation between carbon atoms in graphite (1.42 Å) allows the

best-fit plane of the $C_{20}N_4$ porphyin nuclei to be closer to the best-fit plane of the sulfur atoms in MoS_2 than to the carbon atoms in graphite. The adsorption energies are calculated to be roughly 10% larger on 4L graphite than on 1L-MoS_2 (Table 2.10). These small differences support our experimental observations that the self-assembly of porphyrins on these surfaces is similar.

Table 2.10. Calculated Adsorption Energies and Adsorbate–Surface Distances for Ni(OEP), Zn(OEP), H_2OEP, and Ga(OEP)Cl on 4L Graphite.

parameter	Ni(OEP)	Zn(OEP)	H_2OEP	Ga(OEP)Cl
Adsorption energy (eV)	–3.61	–3.61	–3.58	–3.60
Adsorbate–surface distance (Å)[a]	3.34	3.34	3.36	3.36

[a] Determined from the planes of best fit of the top layer of C atoms and the $C_{20}N_4$ macrocycle.

Finally, given that porphyrins and phthalocyanines have previously been used as molecular dopants for 1L-TMDs[13] and that self-assembled monolayers have the potential to tune the degree of doping through the alteration of both the electronic properties of the porphyrin and surface density of the molecules, the charge density difference (CDD) was calculated for OEPs on 1L-MoS_2 to determine the effect of the metal center (Figure 2.12).

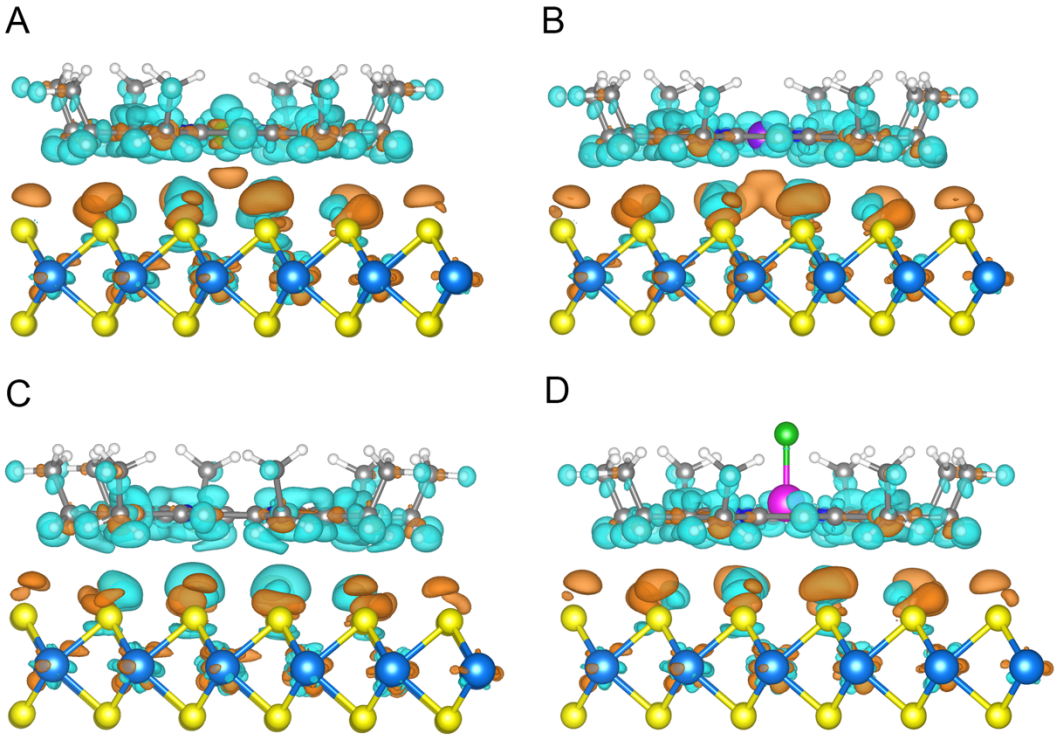

Figure 2.12. CDD plot of (a) Ni(OEP), (b) Zn(OEP), (c) H_2OEP, and (d) Ga(OEP)Cl on 1L MoS_2 at the Bridge 22.5° binding site, plotted at an isosurface corresponding to 0.002 $e^-/Å^3$; orange and cyan regions indicate the accumulation and loss of charge density, respectively.

In order to determine the net direction of charge transfer, the CDD was quantified according to Equation (2.2)

$$\rho_{diff(Z)} = \rho_{Int} - \rho_S - \rho_P \tag{2.2}$$

where $\rho_{diff(Z)}$ is the CDD averaged over the *xy*-plane and ρ_{Int}, ρ_S, and ρ_P are the charge densities of the interface, surface, and porphyrin, respectively. The results of the plane-averaged CDD are plotted against the *z*-axis in Figure 2.13. These plots show little variation between the calculated CDD at each of the individual binding sites. All OEPs are determined to donate charge density to 1L-MoS_2, in agreement with previous calculations using metallophthalocyanines.[32,104] Integration of these plots allow for an estimate of the magnitude of site-averaged charge redistribution per porphyrin, which ranges from 0.16 e^-/molecule (Ga(OEP)Cl) to 0.19 e^-/molecule (Ni(OEP))

(Table 2.11). The deconvolution of the contributions from the various moieties of the metalloporphyrin is discussed in Section 6.1.6. Given the experimental unit cell, these values correspond to roughly 1×10^{13} e^-/molecule, on the same order of magnitude as other non-covalent molecular dopants,[5] though it should be emphasized that the value calculated under gas-phase conditions on pristine 1L-MoS_2 is likely an overestimate compared to experimental conditions. As there are only small differences in charge redistribution between the various OEPs, tuning the surface density of the porphyrins as demonstrated both above on MoS_2 and in the literature on HOPG,[107] along with peripheral substitution of the porphyrin,[108] are likely to induce larger differences in the charge redistribution.

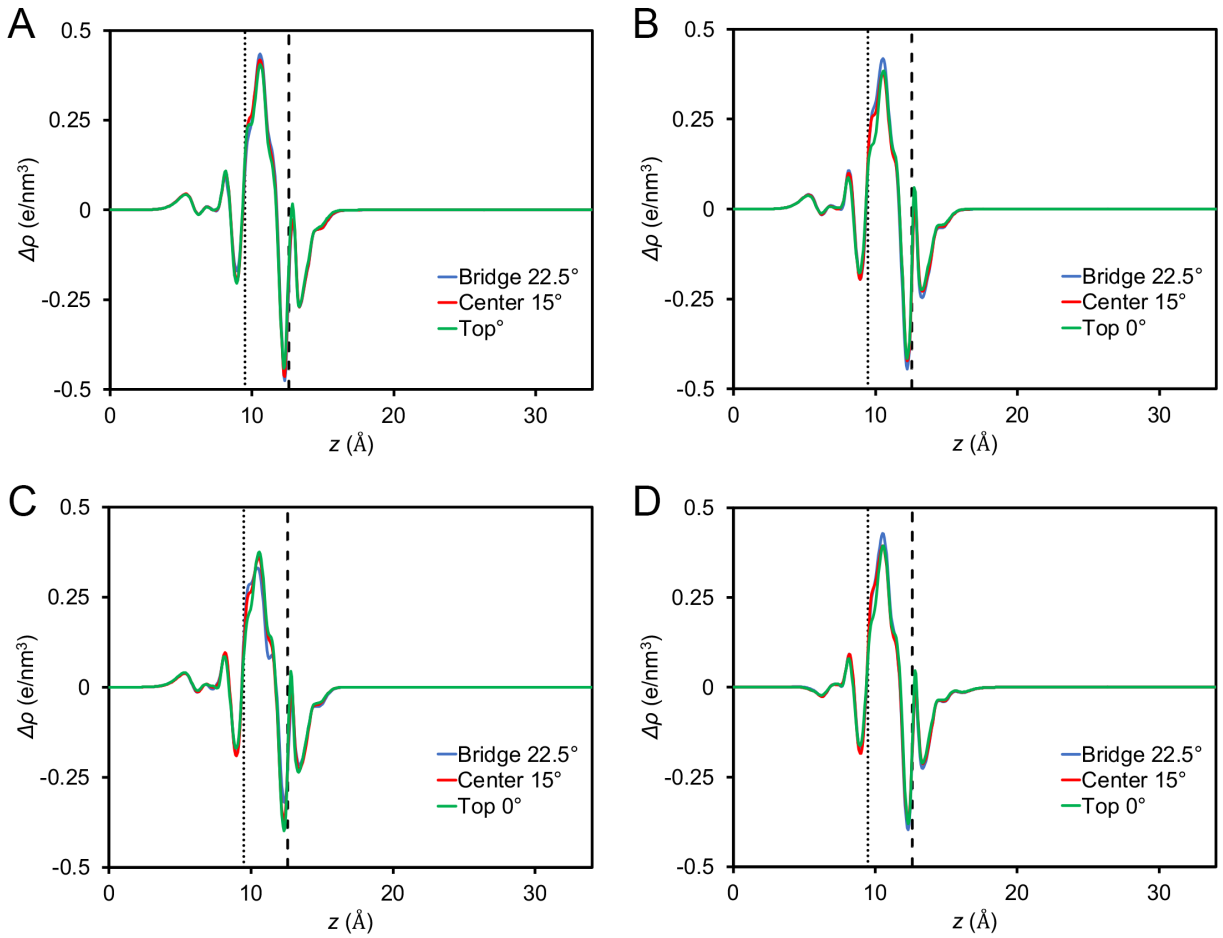

Figure 2.13. Plane-averaged (x, y) charge density difference at the lowest-energy porphyrin orientations at each site for (a) Ni(OEP), (b) Zn(OEP), (c) H_2OEP, and (d) Ga(OEP)Cl on 1L-MoS_2. The charge density difference is the y-axis and the z-coordinate of the corresponding unit cell is the x-axis. The dotted and dashed lines correspond to the planes-of-best-fit of the top layer of S atoms and the C, N, H atoms of the OEP (excluding the CH_3 groups) respectively.

Table 2.11. Plane-Averaged (x, y) Charge Density Differences (CDD) for M(OEP)s on 1L $MoS_2$for the Lowest-Energy Porphyrin Orientation at each Site.

	CDD (e^-/molecule)				
OEP	Center 15°	Top 0°	Bridge 22.5°	Average	Average (e^-/cm^2)
Ni(OEP)	–0.19	–0.20	–0.20	–0.20	-1.2×10^{13}
Zn(OEP)	–0.18	–0.17	–0.20	–0.19	-1.1×10^{13}
H_2OEP	–0.17	–0.17	–0.16	–0.17	-1.0×10^{13}
Ga(OEP)Cl	–0.16	–0.15	–0.18	–0.16	-9.5×10^{12}

2.3.4. STM Imaging of a Porphyrin Monolayer incorporating an Axial Ferrocene Ligand. Beyond the structural and electronic parameter space afforded by variation of the porphyrin peripheral substituents and central metal, 5-coordinate porphyrins of the type Ga(OEP)X additionally provide the opportunity to incorporate independent functional molecules on TMDs via the X ligand. In Ga(OEP)X monolayers the axial X ligands are arrayed perpendicular to the TMD surface,[33] opening the possibility of using these monolayers to both organize supported functional molecules on TMDs in manners not possible without these supports, and exert control over their lateral spacing and distance from the surface. Ferrocene is one functional molecule of interest owing to its electrochemically reversible redox chemistry and attendant applications in charge storage and in molecular switches,[109,110] and has previously been targeted for incorporation into ordered molecular assemblies.[111] Ferrocene was incorporated as an axial ligand in the complex Ga(OEP)(O_2CFc) (Fc = $CpFeC_5H_4$; Chart 2.1d) and shown to exhibit the expected structure byX-ray crystallography (Figure 2.3). Deposition of Ga(OEP)(O_2CFc) from 1-phenyloctane on 1L-MoS_2 produces monolayers of the compound that can be imaged by STM at the solid–liquid interface (Figure 2.14a). Based on the crystallographic data for the compound, the ferrocene units are supported with the Fe center approximately 5.36 Å above the contact plane of the monolayer. Strikingly, these images have only been observed using positive STM bias voltages, in contrast to imaging conditions used for other porphyrins in this study. Possibly for this reason, the images are less distinct than those observed for other OEP compounds, but the characteristic ring-shaped feature indicates the presence of an ordered array of surface-adsorbed porphyrin rings and orthogonal axial ligand, as illustrated in Figure 2.14b.

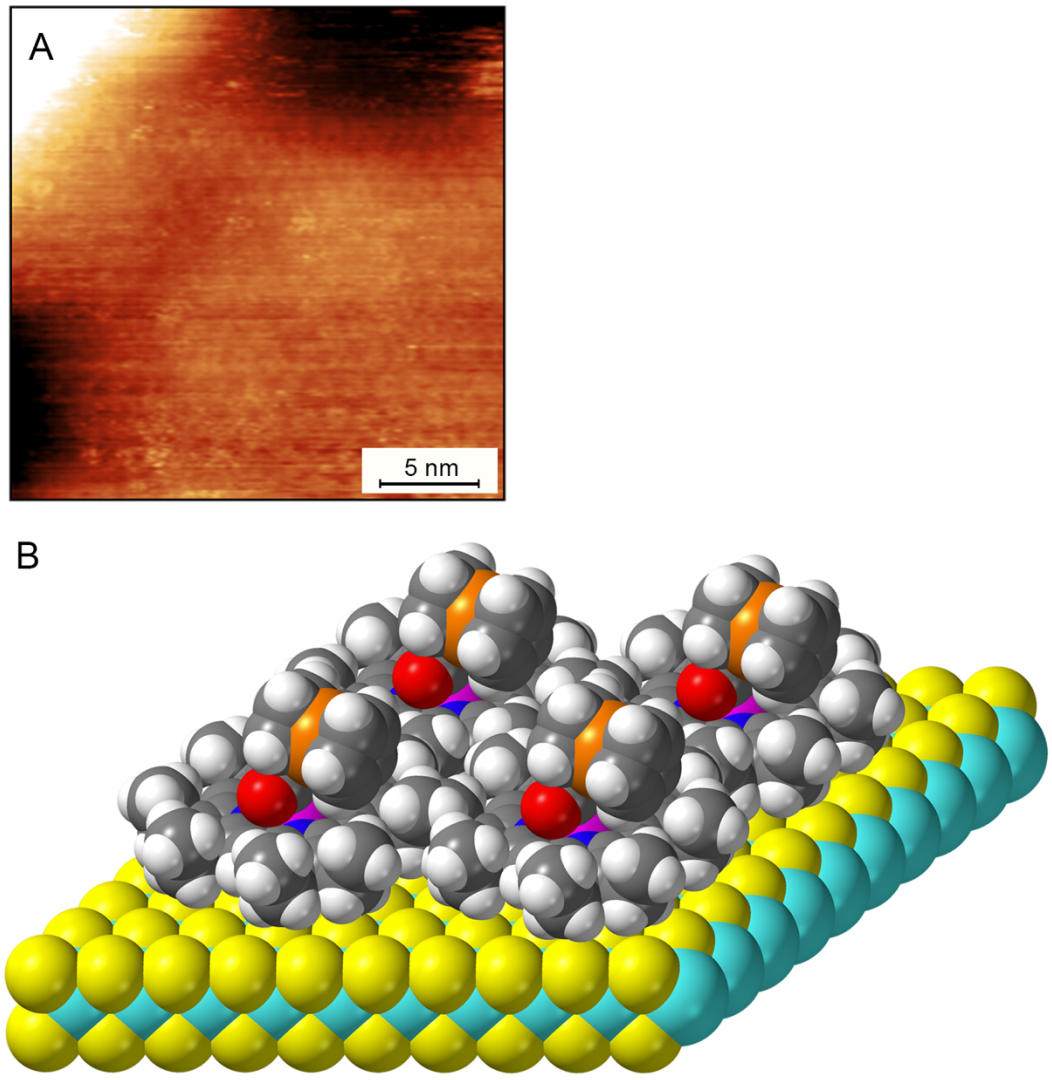

Figure 2.14. (a) STM image of Ga(OEP)(O_2CFc) on 1L-MoS_2 at the solid–liquid interface (25 × 25 nm, I = 300 pA, V = 1550 mV, 0.5 mM in 1-phenyloctane). (b) Representation of Ga(OEP)(O_2CFc) on 1L-MoS_2.

2.4. Conclusions

We have found that solution deposition of porphyrins with a variety of peripheral substituents and metal centers onto 1L-TMDs under ambient conditions results in their self-assembly into face-down, highly ordered monolayers. The porphyrin arrays are observed immediately, are typically expansive, and are stable for hours under continuous STM imaging. The inherent structural fidelity of the porphyrin arrays in a given system, and that observed using

various metal centers, makes porphyrin monolayers an ideal system for isolating the effects of molecular density and redox potential on non-covalent electronic modification of monolayer TMDs. Additionally, the structures exhibited by the arrays are similar to those observed on HOPG, indicating that the supramolecular surface chemistry of porphyrins on HOPG is an effective predictor for that on 1L-TMDs and, thus, the extensive work toward elucidating design principles for porphyrin monolayers on HOPG forms a basis for development and utilization of this interfacial chemistry on TMDs. Moreover, DFT calculations support both the observed stability of porphyrin monolayers on 1L-MoS_2 and their similarity to porphyrin monolayers on HOPG. The observation that ferrocene-containing Ga(OEP)(O_2CFc) also forms a monolayer opens the possibility of a more general approach to developing hybrid materials from TMDs and functional molecules, within which the base porphyrins control spatial organization and density and the functional subunit introduces independent properties.

2.5. References

1. Lin, Z.; McCreary, A.; Briggs, N.; Subramanian, S.; Zhang, K. H.; Sun, Y. F.; Li, X. F.; Borys, N. J.; Yuan, H. T.; Fullerton-Shirey, S. K.; Chernikov, A.; Zhao, H.; McDonnell, S.; Lindenberg, A. M.; Xiao, K.; LeRoy, B. J.; Drndic, M.; Hwang, J. C. M.; Park, J.; Chhowalla, M.; Schaak, R. E.; Javey, A.; Hersam, M. C.; Robinson, J.; Terrones, M. 2D Materials Advances: From Large Scale Synthesis and Controlled Heterostructures to Improved Characterization Techniques, Defects and Applications. *2D Mater.* **2016**, *3*, 42001.

2. Tan, C. L.; Cao, X. H.; Wu, X. J.; He, Q. Y.; Yang, J.; Zhang, X.; Chen, J. Z.; Zhao, W.; Han, S. K.; Nam, G. H.; Sindoro, M.; Zhang, H. Recent Advances in Ultrathin Two-Dimensional Nanomaterials. *Chem. Rev.* **2017**, *117*, 6225–6331.

3. Zeng, M. Q.; Xiao, Y.; Liu, J. X.; Yang, K.; Fu, L. Exploring Two-Dimensional Materials toward the Next-Generation Circuits: From Monomer Design to Assembly Control. *Chem. Rev.* **2018**, *118*, 6236–6296.

4. Zhang, X.; Lai, Z. C.; Ma, Q. L.; Zhang, H. Novel Structured Transition Metal Dichalcogenide Nanosheets. *Chem. Soc. Rev.* **2018**, *47*, 3301–3338.

5. Bertolazzi, S.; Gobbi, M.; Zhao, Y. D.; Backes, C.; Samori, P. Molecular Chemistry Approaches for Tuning the Properties of Two-Dimensional Transition Metal Dichalcogenides. *Chem. Soc. Rev.* **2018**, *47*, 6845–6888.

6. Chen, X.; McAteer, D.; McGuinness, C.; Godwin, I.; Coleman, J. N.; McDonald, A. R. Ru^{II} Photosensitizer-Functionalized Two-Dimensional MoS_2 for Light-Driven Hydrogen Evolution. *Chem. - Eur. J.* **2018**, *24*, 351–355.

7. Vallan, L.; Canton-Vitoria, R.; Gobeze, H. B.; Jang, Y.; Arenal, R.; Benito, A. M.; Maser, W. K.; D'Souza, F.; Tagmatarchis, N. Interfacing Transition Metal Dichalcogenides with Carbon Nanodots for Managing Photoinduced Energy and Charge-Transfer Processes. *J. Am. Chem. Soc.* **2018**, *140*, 13488–13696.

8. Presolski, S.; Pumera, M. Covalent Functionalization of MoS_2. *Mater. Today* **2016**, *19*, 140–145.

9. Canton-Vitoria, R.; Scharl, T.; Stergiou, A.; Cadranel, A.; Arenal, R.; Guldi, D. M.; Tagmatarchis, N. Ping-Pong Energy Transfer in Covalently Linked Porphyrin-MoS2 Architectures. *Angew. Chem., Int. Ed.* **2020**, *59*, 3976–3981.

10. Zhang, H. Y.; Choi, J.; Ramani, A.; Voiry, D.; Natoli, S. N.; Chhowalla, M.; McMillin, D. R.; Choi, J. H. Engineering Chemically Exfoliated Large-Area Two-Dimensional MoS_2 Nanolayers with Porphyrins for Improved Light Harvesting. *ChemPhysChem* **2016**, *17*, 2854–2862.

11. Zhong, Y.; Cheng, B. R.; Park, C.; Ray, A.; Brown, S.; Mujid, F.; Lee, J. U.; Zhou, H.; Suh, J.; Lee, K. H.; Mannix, A. J.; Kang, K.; Sibener, S. J.; Muller, D. A.; Park, J. Wafer-Scale Synthesis of Monolayer Two-Dimensional Porphyrin Polymers for Hybrid Superlattices. *Science* **2019**, *366*, 1379–1384.

12. Molina-Mendoza, A. J.; Vaquero-Garzon, L.; Leret, S.; de Juan-Fernandez, L.; Perez, E. M.; Castellanos-Gomez, A. Engineering the Optoelectronic Properties of MoS_2 Photodetectors through Reversible Noncovalent Functionalization. *Chem. Commun.* **2016**, *52*, 14365–14368.

13. Park, J. H.; Sanne, A.; Guo, Y. Z.; Amani, M.; Zhang, K. H.; Movva, H. C. P.; Robinson, J. A.; Javey, A.; Robertson, J.; Banerjee, S. K.; Kummel, A. C. Defect Passivation of Transition Metal Dichalcogenides via a Charge Transfer Van Der Waals Interface. *Sci. Adv.* **2017**, *3*, e170166.

14. Choi, J.; Zhang, H. Y.; Choi, J. H. Modulating Optoelectronic Properties of Two Dimensional Transition Metal Dichalcogenide Semiconductors by Photoinduced Charge Transfer. *ACS Nano* **2016**, *10*, 1671–1680.

15. Benjamin, C. J.; Zhang, S. K.; Chen, Z. H. Controlled Doping of Transition Metal Dichalcogenides by Metal Work Function Tuning in Phthalocyanine Compounds. *Nanoscale* **2018**, *10*, 5148–5153.

16. Kudernac, T.; Lei, S. B.; Elemans, J. A. A. W.; De Feyter, S. Two-Dimensional Supramolecular Self-Assembly: Nanoporous Networks on Surfaces. *Chem. Soc. Rev.* **2009**, *38*, 402–421.

17. Mali, K. S.; Adisoejoso, J.; Ghijsens, E.; De Cat, I.; De Feyter, S. Exploring the Complexity of Supramolecular Interactions for Patterning at the Liquid-Solid Interface. *Acc. Chem. Res.* **2012**, *45*, 1309–1320.

18. Liu, X. L.; Balla, I.; Sangwan, V. K.; Usta, H.; Facchetti, A.; Marks, T. J.; Hersam, M. C. Ultrahigh Vacuum Self-Assembly of Rotationally Commensurate C8-BTBT/MoS_2/Graphene Mixed-Dimensional Heterostructures. *Chem. Mater.* **2019**, *31*, 1761–1766.

19. Zheng, Y. J.; Huang, Y. L.; Chenp, Y. F.; Zhao, W. J.; Eda, G.; Spataru, C. D.; Zhang, W. J.; Chang, Y. H.; Li, L. J.; Chi, D. Z.; Quek, S. Y.; Wee, A. T. S. Heterointerface Screening Effects between Organic Monolayers and Monolayer Transition Metal Dichalcogenides. *ACS Nano* **2016**, *10*, 2476–2484.

20. Song, Z. B.; Schultz, T.; Ding, Z. J.; Lei, B.; Han, C.; Amsalem, P.; Lin, T. T.; Chi, D. Z.; Wong, S. L.; Zheng, Y. J.; Li, M. Y.; Li, L. J.; Chen, W.; Koch, N.; Huang, Y. L.; Wee, A. T. S. Electronic Properties of a 1D Intrinsic/P-Doped Heterojunction in a 2D Transition Metal Dichalcogenide Semiconductor. *ACS Nano* **2017**, *11*, 9128–9135.

21. Santos, E. J. G.; Scullion, D.; Chu, X. S.; Li, D. O.; Guisinger, N. P.; Wang, Q. H. Rotational Superstructure in Van Der Waals Heterostructure of Self-Assembled C_{60} Monolayer on the Wse_2 Surface. *Nanoscale* **2017**, *9*, 13245–13256.

22. Song, Z. B.; Wang, Q. X.; Li, M. Y.; Li, L. J.; Zheng, Y. J.; Wang, Z.; Lin, T. T.; Chi, D. Z.; Ding, Z. J.; Huang, Y. L.; Wee, A. T. S. Liquid-Solid Surface Phase Transformation of Fluorinated Fullerene on Monolayer Tungsten Diselenide. *Phys. Rev. B* **2018**, *97*, 134102.

23. Phillipson, R.; de la Rosa, C. J. L.; Teyssandier, J.; Walke, P.; Waghray, D.; Fujita, Y.; Adisoejoso, J.; Mali, K. S.; Asselierghs, I.; Huyghebaert, C.; Uji-i, H.; De Gendt, S.; Feyter, S. Tunable Doping of Graphene by Using Physisorbed Self-Assembled Networks. *Nanoscale* **2016**, *8*, 20017–20026.

24. De Feyter, S.; De Schryver, F. C. Self-Assembly at the Liquid/Solid Interface: STM Reveals. *J. Phys. Chem. B* **2005**, *109*, 4290–4302.

25. Otsuki, J. STM Studies on Porphyrins. *Coord. Chem. Rev.* **2010**, *254*, 2311–2341.

26. Auwarter, W.; Ecija, D.; Klappenberger, F.; Barth, J. V. Porphyrins at Interfaces. *Nat. Chem.* **2015**, *7*, 105–120.

27. Mohnani, S.; Bonifazi, D. Supramolecular Architectures of Porphyrins on Surfaces: The Structural Evolution from 1D to 2D to 3D to Devices. *Coord. Chem. Rev.* **2010**, *254*, 2342–2362.

28. Gottfried, J. M. Surface Chemistry of Porphyrins and Phthalocyanines. *Surf. Sci. Rep.* **2015**, *70*, 259–379.

29. Barth, J. V. Molecular Architectonic on Metal Surfaces. *Annu. Rev. Phys. Chem.* **2007**, *58*, 375–407.

30. Kafle, T. R.; Kattel, B.; Yao, P.; Zereshki, P.; Zhao, H.; Chan, W.-L. Effect of the Interfacial Energy Landscape on Photoinduced Charge Generation at the Znpc/MoS2 Interface. *J. Am. Chem. Soc.* **2019**, *141*, 11328–11336.

31. Padgaonkar, S.; Amsterdam, S. H.; Bergeron, H.; Su, K.; Marks, T. J.; Hersam, M. C.; Weiss, E. A. Molecular-Orientation-Dependent Interfacial Charge Transfer in Phthalocyanine/MoS2 Mixed-Dimensional Heterojunctions. *J .Phys. Chem. C* **2019**, *123*, 13337–13343.

32. Amsterdam, S. H.; Stanev, T. K.; Zhou, Q. F.; Lou, A. J. T.; Bergeron, H.; Darancet, P.; Hersam, M. C.; Stern, N. P.; Marks, T. J. Electronic Coupling in Metallophthalocyanine-Transition Metal Dichalcogenide Mixed-Dimensional Heterojunctions. *ACS Nano* **2019**, *13*, 4183–4190.

33. Kamm, J. M.; Iverson, C. P.; Lau, W. Y.; Hopkins, M. D. Axial Ligand Effects on the Structures of Self-Assembled Gallium-Porphyrin Monolayers on Highly Oriented Pyrolytic Graphite. *Langmuir* **2016**, *32*, 487–495.

34. Wang, Y.; Iglesias, D.; Gali, S. M.; Beljonne, D.; Samori, P. Light-Programmable Logic-in-Memory in 2D Semiconductors Enabled by Supramolecular Functionalization: Photoresponsive Collective Effect of Aligned Molecular Dipoles. *ACS Nano* **2021**, *15*, 13732–13741.

35. Brill, A. R.; Kuntumalla, M. K.; de Ruiter, G.; Koren, E. Formation of Highly Ordered Self-Assembled Monolayers on Two-Dimensional Materials via Noncovalent Functionalization. *ACS Appl. Mater. Interfaces* **2020**, *12*, 33941–33949.

36. Brill, A. R.; Kafri, A.; Mohapatra, P. K.; Ismach, A.; de Ruiter, G.; Koren, E. Modulating the Optoelectronic Properties of MoS_2 by Highly Oriented Dipole-Generating Monolayers. *ACS Appl. Mater. Interfaces* **2021**, *13*, 32590–32597.

37. Korolkov, V. V.; Svatek, S. A.; Summerfield, A.; Kerfoott, J.; Yang, L. X.; Taniguchi, T.; Watanabe, K.; Champness, N. R.; Besley, N. A.; Beton, P. H. Van Der Waals-Induced Chromatic Shifts in Hydrogen-Bonded Two-Dimensional Porphyrin Arrays on Boron Nitride. *ACS Nano* **2015**, *9*, 10347–10355.

38. Gobbi, M.; Bonacchi, S.; Lian, J. X.; Vercouter, A.; Bertolazzi, S.; Zyska, B.; Timpel, M.; Tatti, R.; Olivier, Y.; Hecht, S.; Nardi, M. V.; Beljonne, D.; Orgiu, E.; Samori, P. Collective Molecular Switching in Hybrid Superlattices for Light-Modulated Two-Dimensional Electronics. *Nat. Commun.* **2018**, *9*, 2661.

39. Verveniotis, E.; Okawa, Y.; Makarova, M. V.; Koide, Y.; Liu, J. W.; Smid, B.; Watanabe, K.; Taniguchi, T.; Komatsu, K.; Minari, T.; Liu, X. Y.; Joachim, C.; Aono, M. Self-Assembling Diacetylene Molecules on Atomically Flat Insulators. *Phys. Chem. Chem. Phys.* **2016**, *18*, 31600–31605.

40. Stecher, R.; Drewnick, F.; Gompf, B. Influence of Preparation Conditions on the Monolayer Structure: Bi- and Terthiophenes in Solution and Uhv. *Langmuir* **1999**, *15*, 6490–6494.

41. Davis, T. C.; Russell, S. R.; Claridge, S. A. Edge-on Adsorption of Multi-Chain Functional Alkanes Stabilizes Noncovalent Monolayers on MoS_2. *Chem. Commun.* **2018**, *54*, 11709–11712.

42. de la Rosa, C. J. L.; Phillipson, R.; Teyssandier, J.; Adisoejoso, J.; Balaji, Y.; Huyghebaert, C.; Radu, I.; Heyns, M.; De Feyter, S.; De Gendt, S. Molecular Doping of MoS_2 Transistors by Self-Assembled Oleylamine Networks. *Appl. Phys. Lett.* **2016**, *109*, 253112.

43. Ludwig, C.; Strohmaier, R.; Petersen, J.; Gompf, B.; Eisenmenger, W. Epitaxy and Scanning-Tunneling-Microscopy Image-Contrast of Copper Phthalocyanine on Graphite and MoS_2. *J. Vac. Sci. Technol., B: Microelectron. Nanometer Struct.--Process., Meas., Phenom.* **1994**, *12*, 1963–1966.

44. Strohmaier, R.; Ludwig, C.; Petersen, J.; Gompf, B.; Eisenmenger, W. STM Investigations of C_6br_6 on HOPG and MoS_2. *Surf. Sci.* **1994**, *318*, L1181–L1185.

45. Giancarlo, L. C.; Fang, H. B.; Rubin, S. M.; Bront, A. A.; Flynn, G. W. Influence of the Substrate on Order and Image Contrast for Physisorbed, Self-Assembled Molecular Monolayers: STM Studies of Functionalized Hydrocarbons on Graphite and MoS_2. *J. Phys. Chem. B* **1998**, *102*, 10255–10263.

46. Claypool, C. L.; Faglioni, F.; Matzger, A. J.; Goddard, W. A.; Lewis, N. S. Effects of Molecular Geometry on the STM Image Contrast of Methyl- and Bromo-Substituted Alkanes and Alkanols on Graphite. *J. Phys. Chem. B* **1999**, *103*, 9690–9699.

47. Strohmaier, R.; Ludwig, C.; Petersen, J.; Gompf, B.; Eisenmenger, W. STM Investigations of Ntcda on Weakly Interacting Substrates. *Surf. Sci.* **1996**, *351*, 292–302.

48. Walzer, K.; Sternberg, M.; Hietschold, M. Formation and Characterization of Coronene Monolayers on HOPG(0001) and MoS_2(0001): A Combined STM/Sts and Tight-Binding Study. *Surf. Sci.* **1998**, *415*, 376–384.

49. Gunther, C.; Karl, N.; Pflaum, J.; Strohmaier, R.; Gompf, B.; Eisenmenger, W.; Muller, M.; Mullen, K. Leed, STM, and Tds Studies of Ordered Thin Films of the Rhombus-Shaped Polycondensed Aromatic Hydrocarbon $C_{54}h_{22}$, on MoS_2, Ges, and Graphite. *Langmuir* **2005**, *21*, 656–665.

50. Nakaya, M.; Iwasa, T.; Tsunoyama, H.; Eguchi, T.; Nakajima, A. Heterodimerization via the Covalent Bonding of Ta@Si_{16} Nanoclusters and C_{60} Molecules. *J. Phys. Chem. C* **2015**, *119*, 10962–10968.

51. Cincotti, S.; Rabe, J. P. Self-Assembled Alkane Monolayers on $Mose_2$ and MoS_2. *Appl. Phys. Lett.* **1993**, *62*, 3531–3533.

52. Moltgen, H.; Kleinermanns, K.; Jesorka, A.; Schaffner, K.; Holzwarth, A. R. Self-Assembly of [Et,Et]-Bacteriochlorophyll C(F) on Highly Oriented Pyrolytic Graphite Revealed by Scanning Tunneling Microscopy. *Photochem. Photobiol.* **2002**, *75*, 619–626.

53. Iwakabe, Y.; Hara, M.; Kondo, K.; Tochigi, K.; Mukoh, A.; Garito, A. F.; Sasabe, H.; Yamada, A. 2 Types of Anchoring Structure in Smectic Liquid-Crystal Molecules. *Jpn. J. Appl. Phys., Part 2* **1990**, *29*, L2243–L2246.

54. Smith, D. P. E.; Heckl, W. M.; Klagges, H. A. Ordering of Alkylcyanobiphenyl Molecules at MoS_2 and Graphite Surfaces Studied by Tunneling Microscopy. *Surf. Sci.* **1992**, *278*, 166–174.

55. Ludwig, C.; Gompf, B.; Petersen, J.; Strohmaier, R.; Eisenmenger, W. STM Investigations of Ptcda and Ptcdi on Graphite and MoS_2 - a Systematic Study of Epitaxy and STM Image-Contrast. *Z. Phys. B: Condens. Matter* **1994**, *93*, 365–373.

56. Cincotti, S. R., J.P. *Supramol. Sci.* **1994**, *1*, 7–10.

57. Chen, J. J.; Zhu, E. B.; Liu, J.; Zhang, S.; Lin, Z. Y.; Duan, X. F.; Heinz, H.; Huang, Y.; De Yoreo, J. J. Building Two-Dimensional Materials One Row at a Time: Avoiding the Nucleation Barrier. *Science* **2018**, *362*, 1135–1139.

58. Afsharimani, N.; Minoia, A.; Volcke, C.; Surin, M.; Lazzaroni, R.; Balandier, J. Y.; Niebel, C.; Geerts, Y. H.; Nysten, B. Self-Assembly of Alkyl-Substituted Oligothiophenes on MoS_2: A Joint Experimental/Theoretical Study. *J. Phys. Chem. C* **2013**, *117*, 21743–21751.

59. Azumi, R.; Gotz, G.; Bauerle, P. Self-Assembly of Alkylsubstituted Oligothiophenes. *Synth. Met.* **1999**, *101*, 569–572.

60. Ogunrinde, A.; Hipps, K. W.; Scudiero, L. A Scanning Tunneling Microscopy Study of Self-Assembled Nickel(II) Octaethylporphyrin Deposited from Solutions on HOPG. *Langmuir* **2006**, *22*, 5697–5701.

61. Pangborn, A. B.; Giardello, M. A.; Grubbs, R. H.; Rosen, R. K.; Timmers, F. J. Safe and Convenient Procedure for Solvent Purification. *Organometallics* **1996**, *15*, 1518–1520.

62. Coutsolelos, A.; Guilard, R.; Bayeul, D.; Lecomte, C. Gallium(III) Porphyrins - Synthesis and Physicochemical Characteristics of Halogeno Gallium(III) Porphyrins X-Ray Crystal-Structure of Chloro-(5,10,15,20-Tetraphenylporphyrinato) Gallium(III). *Polyhedron* **1986**, *5*, 1157–1164.

63. Lindsey, J. S.; Schreiman, I. C.; Hsu, H. C.; Kearney, P. C.; Marguerettaz, A. M. Rothemund and Adler-Longo Reactions Revisited - Synthesis of Tetraphenylporphyrins under Equilibrium Conditions. *J. Org. Chem.* **1987**, *52*, 827–836.

64. Kamm, J. M. Ph. D. Thesis. The University of Chicago, Chicago, IL, 2017.

65. Fulmer, G. R.; Miller, A. J. M.; Sherden, N. H.; Gottlieb, H. E.; Nudelman, A.; Stoltz, B. M.; Bercaw, J. E.; Goldberg, K. I. NMR Chemical Shifts of Trace Impurities: Common Laboratory Solvents, Organics, and Gases in Deuterated Solvents Relevant to the Organometallic Chemist. *Organometallics* **2010**, *29*, 2176–2179.

66. Kang, K.; Xie, S. E.; Huang, L. J.; Han, Y. M.; Huang, P. Y.; Mak, K. F.; Kim, C. J.; Muller, D.; Park, J. High-Mobility Three-Atom-Thick Semiconducting Films with Wafer-Scale Homogeneity. *Nature* **2015**, *520*, 656–660.

67. Kang, K.; Lee, K. H.; Han, Y. M.; Gao, H.; Xie, S. E.; Muller, D. A.; Park, J. Layer-by-Layer Assembly of Two-Dimensional Materials into Wafer-Scale Heterostructures. *Nature* **2017**, *550*, 229–233.

68. *SPIP Software,* Version 6.0.9; Image Metrology A/S: Hørsholm, Denmark.

69. *MoS_2 Crystal Structure: Datasheet from "Pauling File Multinaries Edition – 2012" in Springermaterials.,* Springer-Verlag Berlin Heidelberg & Material Phases Data System (MPDS), Switzerland & National Institute for Materials Science (NIMS), Japan: https://materials.springer.com/isp/crystallographic/docs/sd_0309036 (accessed September 23, 2018)

70. Necas, D.; Klapetek, P. Gwyddion: An Open-Source Software for Spm Data Analysis. *Cent. Eur. J. Phys.* **2012**, *10*, 181–188.

71. Krause, L.; Herbst-Irmer, R.; Sheldrick, G. M.; Stalke, D. Comparison of Silver and Molybdenum Microfocus X-Ray Sources for Single-Crystal Structure Determination. *J. Appl. Crystallogr.* **2015**, *48*, 3–10.

72. Sheldrick, G. M. SHELXT - Integrated Space-Group and Crystal-Structure Determination. *Acta Crystallogr., Sect. A: Found. Adv.* **2015**, *71*, 3–8.

73. Dolomanov, O. V.; Bourhis, L. J.; Gildea, R. J.; Howard, J. A. K.; Puschmann, H. OLEX2: A Complete Structure Solution, Refinement and Analysis Program. *J. Appl. Crystallogr.* **2009**, *42*, 339–341.

74. Sheldrick, G. M. Crystal Structure Refinement with SHELXL. *Acta Crystallogr., Sect. C: Struct. Chem.* **2015**, *71*, 3–8.

75. Giannozzi, P.; Baroni, S.; Bonini, N.; Calandra, M.; Car, R.; Cavazzoni, C.; Ceresoli, D.; Chiarotti, G. L.; Cococcioni, M.; Dabo, I.; Dal Corso, A.; de Gironcoli, S.; Fabris, S.; Fratesi, G.; Gebauer, R.; Gerstmann, U.; Gougoussis, C.; Kokalj, A.; Lazzeri, M.; Martin-Samos, L.; Marzari, N.; Mauri, F.; Mazzarello, R.; Paolini, S.; Pasquarello, A.; Paulatto, L.; Sbraccia, C.; Scandolo, S.; Sclauzero, G.; Seitsonen, A. P.; Smogunov, A.; Umari, P.; Wentzcovitch, R. M. Quantum Espresso: A Modular and Open-Source Software Project for Quantum Simulations of Materials. *J. Phys.: Condens. Matter* **2009**, *21*, 395502.

76. Klimes, J.; Bowler, D. R.; Michaelides, A. Chemical Accuracy for the Van Der Waals Density Functional. *J. Phys.: Condens. Matter* **2010**, *22*, 022201.

77. Klimes, J.; Bowler, D. R.; Michaelides, A. Van Der Waals Density Functionals Applied to Solids. *Phys. Rev. B* **2011**, *83*, 195131.

78. Becke, A. D. On the Large-Gradient Behavior of the Density Functional Exchange Energy. *J. Chem. Phys.* **1986**, *85*, 7184–7187.

79. Thonhauser, T.; Zuluaga, S.; Arter, C. A.; Berland, K.; Schroder, E.; Hyldgaard, P. Spin Signature of Nonlocal Correlation Binding in Metal-Organic Frameworks. *Phys. Rev. Lett.* **2015**, *115*, 136402.

80. Thonhauser, T.; Cooper, V. R.; Li, S.; Puzder, A.; Hyldgaard, P.; Langreth, D. C. Van Der Waals Density Functional: Self-Consistent Potential and the Nature of the Van Der Waals Bond. *Phys. Rev. B* **2007**, *76*, 125112.

81. Langreth, D. C.; Lundqvist, B. I.; Chakarova-Kack, S. D.; Cooper, V. R.; Dion, M.; Hyldgaard, P.; Kelkkanen, A.; Kleis, J.; Kong, L. Z.; Li, S.; Moses, P. G.; Murray, E.; Puzder, A.; Rydberg, H.; Schroder, E.; Thonhauser, T. A Density Functional for Sparse Matter. *J. Phys.: Condens. Matter* **2009**, *21*, 084203.

82. Berland, K.; Cooper, V. R.; Lee, K.; Schroder, E.; Thonhauser, T.; Hyldgaard, P.; Lundqvist, B. I. Van Der Waals Forces in Density Functional Theory: A Review of the Vdw-Df Method. *Rep. Prog. Phys.* **2015**, *78*, 066501.

83. Peelaers, H.; Van de Walle, C. G. First-Principles Study of Van Der Waals Interactions in MoS_2 and Moo_3. *J. Phys.: Condens. Matter* **2014**, *26*, 305502.

84. Zhang, Y. K.; Yang, W. T. Comment on "Generalized Gradient Approximation Made Simple". *Phys. Rev. Lett.* **1998**, *80*, 890–890.

85. Hamann, D. R. Optimized Norm-Conserving Vanderbilt Pseudopotentials. *Phys. Rev. B* **2013**, *88*, 085117.

86. Schlipf, M.; Gygi, F. Optimization Algorithm for the Generation of Oncv Pseudopotentials. *Comput. Phys. Commun.* **2015**, *196*, 36–44.

87. Monkhorst, H. J.; Pack, J. D. Special Points for Brillouin-Zone Integrations. *Phys. Rev. B* **1976**, *13*, 5188–5192.

88. Frisch, M. J. T., G. W.; Schlegel, H. B.; Scuseria, G. E.; Robb, M. A.; Cheeseman, J. R.; Scalmani, G.; Barone, V.; Mennucci, B.; Petersson, G. A.; Nakatsuji, H.; Caricato, M.; Li, X.; Hratchian, H. P.; Izmaylov, A. F.; Bloino, J.; Zheng, G.; Sonnenberg, J. L.; Hada, M.; Ehara, M.; Toyota, K.; Fukuda, R.; Hasegawa, J.; Ishida, M.; Nakajima, T.; Honda, Y.; Kitao, O.; Nakai, H.; Vreven, T.; Montgomery, J. J. A.; Peralta, J. E.; Ogliaro, F.; Bearpark, M.; Heyd, J. J.; Brothers, E.; Kudin, K. N.; Staroverov, V. N.; Keith, T.; Kobayashi, R.; Normand, J.; Raghavachari, K.; Rendell, A.; Burant, J. C.; Iyengar, S. S.; Tomasi, J.; Cossi, M.; Rega, N.; Millam, J. M.; Klene, M.; Knox, J. E.; Cross, J. B.; Bakken, V.; Adamo, C.; Jaramillo, J.; Gomperts, R.; Stratmann, R. E.; Yazyev, O.; Austin, A. J.; Cammi, R.; Pomelli, C.; Ochterski, J. W.; Martin, R. L.; Morokuma, K.; Zakrzewski, V. G.; Voth, G. A.; Salvador, P.; Dannenberg, J. J.; Dapprich, S.; Daniels, A. D.; Farkas, O.; Foresman, J. B.; Ortiz, J. V.; Cioslowski, J.; Fox, D. J. *Gaussian 09,* Revision D.01; Gaussian, Inc.: Wallingford, CT. 2013.

89. Becke, A. D. Density-Functional Thermochemistry. III. The Role of Exact Exchange. *J. Chem. Phys.* **1993**, *98*, 5648–5652.

90. Perdew, J. P. Density-Functional Approximation for the Correlation-Energy of the Inhomogeneous Electron-Gas. *Phys. Rev. B* **1986**, *33*, 8822–8824.

91. Wadt, W. R.; Hay, P. J. Abinitio Effective Core Potentials for Molecular Calculations - Potentials for Main Group Elements Na to Bi. *J. Chem. Phys.* **1985**, *82*, 284–298.

92. Hay, P. J.; Wadt, W. R. Abinitio Effective Core Potentials for Molecular Calculations - Potentials for the Transition-Metal Atoms Sc to Hg. *J. Chem. Phys.* **1985**, *82*, 270–283.

93. Bhattarai, A.; Mazur, U.; Hipps, K. W. Desorption Kinetics and Activation Energy for Cobalt Octaethylporphyrin from Graphite at the Phenyloctane Solution-Graphite Interface: An STM Study. *J. Phys. Chem. C* **2015**, *119*, 9386–9394.

94. Oncel, N.; Bernasek, S. L. Ni(II)- and Vanadyloctaethylporphyrin Self-Assembled Layers Formed on Bare and 5-(Octadecyloxy)Isophthalic Acid Covered Graphite. *Langmuir* **2009**, *25*, 9290–9295.

95. Scudiero, L.; Barlow, D. E.; Hipps, K. W. Scanning Tunneling Microscopy, Orbital-Mediated Tunneling Spectroscopy, and Ultraviolet Photoelectron Spectroscopy of Nickel(II) Octaethylporphyrin Deposited from Vapor. *J. Phys. Chem. B* **2002**, *106*, 996–1003.

96. Vogel, G. C.; Searby, L. A. Lewis Acid-Base Interactions of Zinc Alpha, Beta, Gamma, Delta-Tetraphenylporphine with Several Neutral Donors. *Inorg. Chem.* **1973**, *12*, 936–939.

97. Wang, Q. H.; Kalantar-Zadeh, K.; Kis, A.; Coleman, J. N.; Strano, M. S. Electronics and Optoelectronics of Two-Dimensional Transition Metal Dichalcogenides. *Nat. Nano.* **2012**, *7*, 699–712.

98. Slater, A. G.; Hu, Y.; Yang, L.; Argent, S. P.; Lewis, W.; Blunt, M. O.; Champness, N. R. Thymine Functionalised Porphyrins, Synthesis and Heteromolecular Surface-Based Self-Assembly. *Chem. Sci.* **2015**, *6*, 1562–1569.

99. Qiu, X. H.; Wang, C.; Zeng, Q. D.; Xu, B.; Yin, S. X.; Wang, H. N.; Xu, S. D.; Bai, C. L. Alkane-Assisted Adsorption and Assembly of Phthalocyanines and Porphyrins. *J. Am. Chem. Soc.* **2000**, *122*, 5550–5556.

100. Lei, S. B.; Wang, C.; Yin, S. X.; Wang, H. N.; Xi, F.; Liu, H. W.; Xu, B.; Wan, L. J.; Bai, C. L. Surface Stabilized Porphyrin and Phthalocyanine Two-Dimensional Network Connected by Hydrogen Bonds. *J. Phys. Chem. B* **2001**, *105*, 10838–10841.

101. A monolayer of Ni(Etio) would be chiral if it consisted of molecules with exclusively left- or right-handed side-chain orientations, but the side chains could not be identified in the images.

102. STM characterization is typically less challenging at the solid–liquid interface, as compared to the solid-air interface, due to the self-healing nature of the system caused by the porphyrin containing solution in which the monolayer is imaged.

103. Chilukuri, B.; Mazur, U.; Hipps, K. W. Effect of Dispersion on Surface Interactions of Cobalt(II) Octaethylporphyrin Monolayer on Au(111) and HOPG(0001) Substrates: A Comparative First Principles Study. *Phys. Chem. Chem. Phys.* **2014**, *16*, 14096–14107.

104. Choudhury, P.; Ravavarapu, L.; Dekle, R.; Chowdhury, S. Modulating Electronic and Optical Properties of Monolayer MoS_2 Using Nonbonded Phthalocyanine Molecules. *J. Phys. Chem. C* **2017**, *121*, 2959–2967.

105. Reimers, J. R.; Panduwinata, D.; Visser, J.; Chin, Y.; Tang, C. G.; Goerigk, L.; Ford, M. J.; Sintic, M.; Sum, T. J.; Coenen, M. J. J.; Hendriksen, B. L. M.; Elemans, J. A. A. W.; Hush, N. S.; Crossley, M. J. A Priori Calculations of the Free Energy of Formation from Solution of Polymorphic Self-Assembled Monolayers. *Proc. Natl. Acad. Sci. U.S.A.* **2015**, *112*, E6101–E6110.

106. Hipps, K. W.; Mazur, U. Kinetic and Thermodynamic Control in Porphyrin and Phthalocyanine Self-Assembled Monolayers. *Langmuir* **2018**, *34*, 3–17.

107. Reimers, J. R.; Panduwinata, D.; Visser, J.; Chin, Y.; Tang, C. G.; Goerigk, L.; Ford, M. J.; Baker, M.; Sum, T. J.; Coenen, M. J. J.; Hendriksen, B. L. M.; Elemans, J. A. A. W.; Hush, N. S.; Crossley, M. J. From Chaos to Order: Chain-Length Dependence of the Free Energy of Formation of Meso-Tetraalkylporphyrin Self-Assembled Monolayer Polymorphs. *J. Phys. Chem. C* **2016**, *120*, 1739-1748.

108. Greulich, K.; Belser, A.; Bolke, S.; Gruninger, P.; Karstens, R.; Sattele, M. S.; Ovsyannikov, R.; Giangrisostomi, E.; Basova, T. V.; Klyamer, D.; Chasse, T.; Peisert, H. Charge Transfer from Organic Molecules to Molybdenum Disulfide: Influence of the Fluorination of Iron Phthalocyanine. *J. Phys. Chem. C* **2020**, *124*, 16990-16999.

109. Chidsey, C. E. D. Free-Energy and Temperature-Dependence of Electron-Transfer at the Metal-Electrolyte Interface. *Science* **1991**, *251*, 919–922.

110. Li, Q. L.; Mathur, G.; Homsi, M.; Surthi, S.; Misra, V.; Malinovskii, V.; Schweikart, K. H.; Yu, L. H.; Lindsey, J. S.; Liu, Z. M.; Dabke, R. B.; Yasseri, A.; Bocian, D. F.; Kuhr, W. G. Capacitance and Conductance Characterization of Ferrocene-Containing Self-Assembled Monolayers on Silicon Surfaces for Memory Applications. *Appl. Phys. Lett.* **2002**, *81*, 1494–1496.

111. El Garah, M.; Bonilla, A. S.; Ciesielski, A.; Gualandi, A.; Mengozzi, L.; Fiorani, A.; Iurlo, M.; Marcaccio, M.; Gutierrez, R.; Rapino, S.; Calvaresi, M.; Zerbetto, F.; Cuniberti, G.; Cozzi, P. G.; Paolucci, F.; Samori, P. Molecular Design Driving Tetraporphyrin Self-Assembly on Graphite: A Joint STM, Electrochemical and Computational Study. *Nanoscale* **2016**, *8*, 13678–13686.

CHAPTER 3

Synthesis, Structures, and Electronic Spectroscopy of Cofacial Gallium Porphyrin Dimers

3.1. Introduction

Multimeric porphyrin systems have been the object of a tremendous amount of research given their importance in photosynthetic systems,[1-6] their applications in catalysis,[7,8] and their use as components in molecular electronics and photonics.[9,10] As the structural relationship between porphyrin macrocycles in these systems is vital to engendering the desired collective properties, a variety of structural approaches for precisely tuning porphyrin–porphyrin interactions have been developed.[11] Limiting the scope of discussion to those compounds with a cofacial geometry, these approaches have included use of flexible aliphatic or rigid aromatic covalent bridges attached to the periphery of the porphyrin macrocycle (Figure 3.1a,b),[12,13] utilizing the metal center as the bridge (Figure 3.1c), in the case of sandwich type compounds,[14] or using 5-coordinate metalloporphyrins with axial bridging ligands (Figure 3.1d).[15-17]

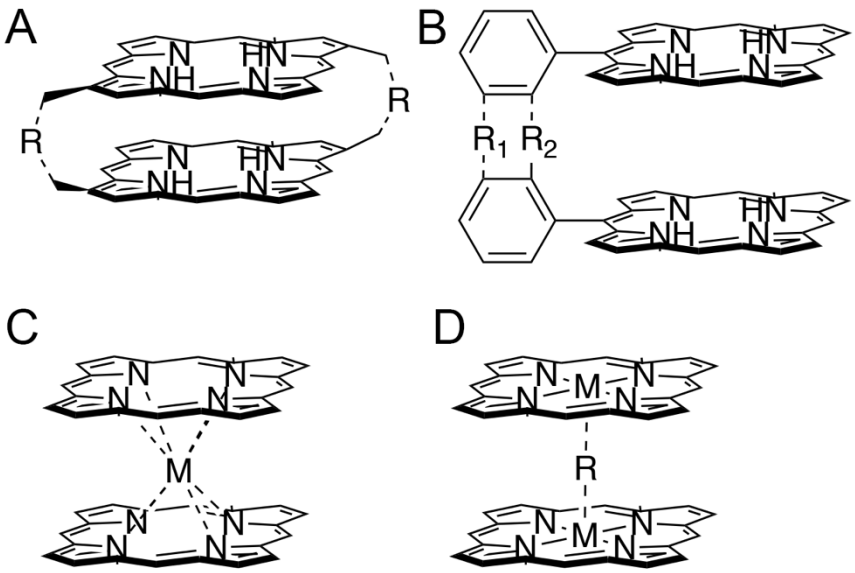

Figure 3.1. Selected binding motifs for cofacial porphyrin dimers including (a) flexible aliphatic linkages, (b) rigid aromatic linkages, (c) sandwich-type metallo-bis(porphyrins), and (d) axially ligand-bridged metalloporphyrins. For clarity, only peripheral substituents directly involved in the binding of the porphyrin macrocycles are shown.

Among these approaches, connecting the porphyrin macrocycles through the metal centers by means of a bridging ligand (Figure 3.1d) has the advantages of allowing for a large variety of porphyrin–porphyrin spacings, which are limited to a narrow range in sandwich-type complexes, and avoiding the often cumbersome and low-yield syntheses of covalently bridged porphyrins.[18-22] As our primary interest in these systems is as components in ordered surface arrays, connecting the porphyrins through the metal centers is also desirable because it leaves the monolayer-directing peripheral substituents intact. Therefore, we sought to investigate a general method for synthesizing cofacial ligand-bridged porphyrin dimers that could accommodate a wide variety of bridging groups.

We hypothesized that a condensation reaction between Ga(OEP)(OH) (OEP = octaethylporphyrin) and a dicarboxylic acid (Scheme 3.1) would lead to the formation of a cofacial dimeric complex of type $(Ga(OEP))_2$(μ-dicarboxylate), because monomeric 5-coordinate

porphyrin compounds with carboxylate ligands are well established.[23-31] Initial attempts at a similar reaction to form tetra-*n*-decyl porphyrin dimers of type $(Ga(TC_{10}P))_2(\mu\text{-dicarboxylate})$ were previously explored in our group with mixed success.[32] Building on this, a series of dicarboxylic acids were selected that would produce a wide range of porphyrin–porphyrin spacings in an extended Ga(OEP)-containing dimer. These $(Ga(OEP))_2(\mu\text{-dicarboxylate})$ compounds are shown in Figure 3.2.

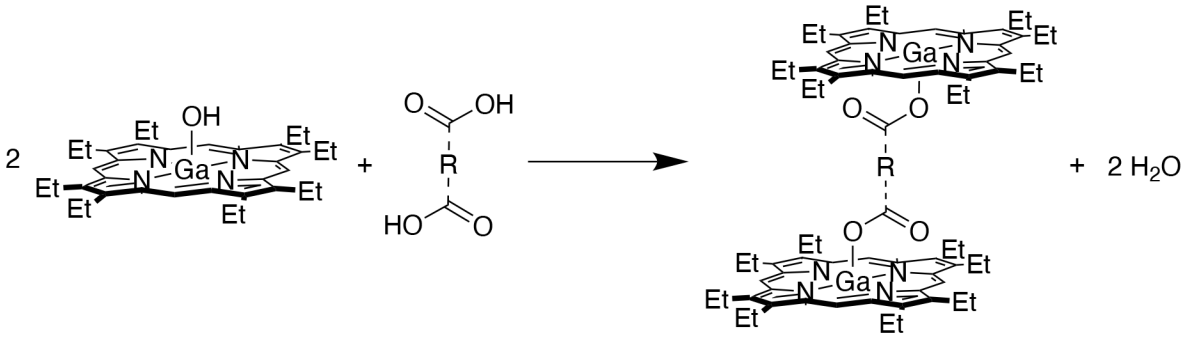

Scheme 3.1. Synthesis of $(Ga(OEP))_2(\mu\text{-}O_2CRCO_2)$ complexes.

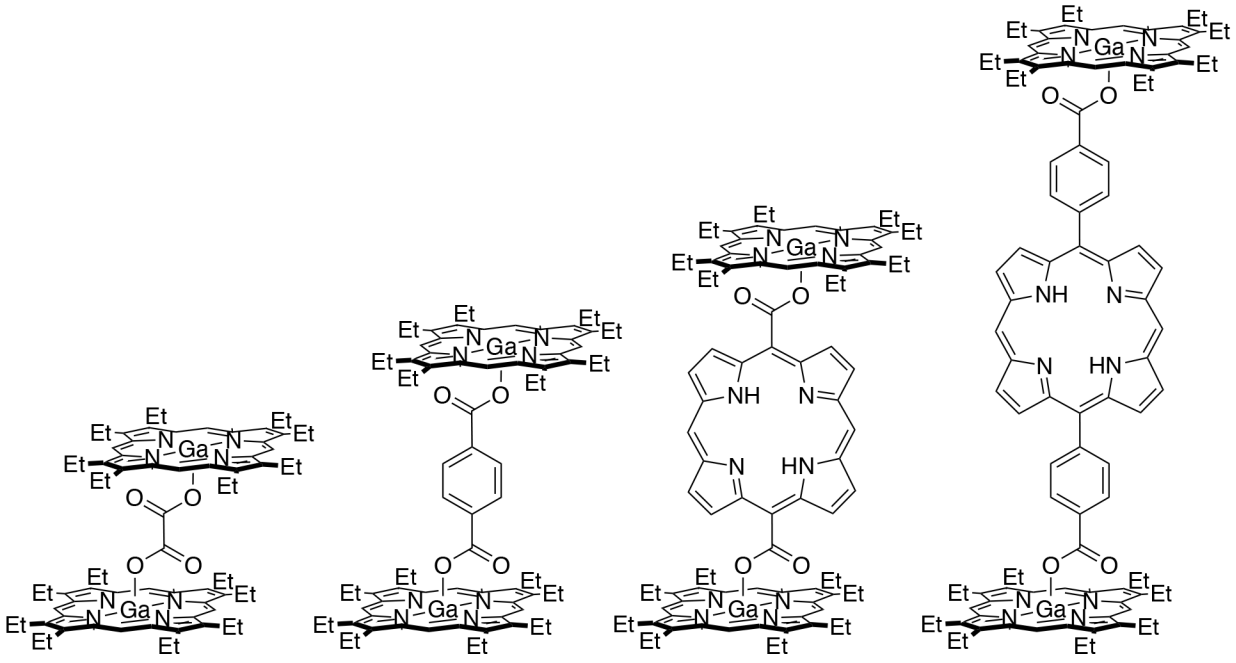

Figure 3.2. Cofacial $(Ga(OEP))_2(\mu\text{-dicarboxylate})$ dimers **1** (μ-oxalate), **2** (μ-terephthalate), **3** μ-BCP), and **4** (μ-BCPP) investigated in this chapter.

In this chapter, we describe the synthesis and properties of cofacial dimers **1**–**4** (Figure 3.2). The identity and purity of the complexes were established by an array of standard analytical methods, and their structures in the solid state, gas phase, and solution were established by a combination of single-crystal X-ray diffraction experiments, density functional theory calculations, and NMR and electronic spectroscopy, respectively. It was determined that the carboxylate linkers allow significant conformational flexibility, particularly for porphyrin- bridged **3** and **4**, and for **3** the solution structure was found to be solvent-dependent. The electronic interactions between porphyrin centers were investigated through electrochemical and electronic absorption and emission measurements. For porphyrin-bridged dimers **3** and **4**, excited-state energy transfer was observed.

3.2. Experimental Section

3.2.1. General Procedures. Toluene, THF, and pentane (HPLC-grade, stored under nitrogen, Sigma Aldrich) were purified by passing them under nitrogen pressure through an anaerobic, stainless-steel system consisting of either two 4.5 × 24 in. (1 gal) columns of activated A2 alumina (THF) or one column of activated A2 alumina and one column of activated BASF R3-11 catalyst (toluene, pentane).[33] CH_2Cl_2 and DMF (anhydrous grade, stored under nitrogen, Sigma Aldrich) were used as received. $CDCl_3$ used for NMR spectroscopy was stored over 3 Å molecular sieves and distilled under vacuum prior to use. CD_2Cl_2 and 1,2,4-trichlorobenzene-d_3 ($C_6D_3Cl_3$) were used as received. Ga(OEP)Cl[34], Ga(OEP)(OH),[35] dipyrromethane,[36] and 5,15-bis(4-carboxylphenyl)porphyrin (H_2BCPP)[37] were synthesized according to standard procedures. Other chemicals were obtained from commercial sources and used as received. All syntheses were carried out under a nitrogen atmosphere using standard

Schlenk techniques. ^{1}H NMR spectra were recorded on either a 400 MHz Bruker DRX spectrometer equipped with a BBO probe, using Topspin 1.3, or a 500 MHz Bruker Avance-II+ spectrometer equipped with a ^{1}H QNP probe, using Topspin 2.1. NMR samples were prepared in a glovebox under a nitrogen atmosphere. NMR chemical shifts were measured relative to solvent resonances.[38] HR-MS spectra were measured on an Agilent 6224 TOF-MS. Infrared spectra were measured with a Thermo Nicolet iS50 Advanced FT-IR with B-ATR.

3.2.2. Electronic Absorption and Emission Measurements. CH_2Cl_2 (≥99.9%, unstabilized, Fisher Chemical) and 1,2,4-trichlorobenzene (TCB) (99%, Oakwood Chemical) used for electronic absorption and emission measurements were degassed by three freeze-pump-thaw cycles (CH_2Cl_2) or by exposure to high vacuum for 30 min (TCB), placed under N_2, and then dried over 3 Å molecular sieves. Purified solvents were stored in the dark under N_2. Electronic-absorption spectra and -emission spectra were obtained in combination 1 cm and 1 mm path length cuvettes or 1 cm path length cuvettes, respectively, fitted with a J. Young tap. The cuvettes were cleaned by soaking for at least 18 h sequentially in HNO_3 (68% in H_2O, Certified ACS Plus, Fisher Chemical), 0.1 M KOH (85%, Oakwood Chemical) in H_2O, and water, washing with copious amounts of water between each step, and then oven-dried. Spectroscopic samples were prepared in a glovebox under N_2. Absorption spectra were recorded on a Cary 300 UV-visible spectrophotometer. Emission spectra were recorded on a PTI QuantMaster fluorimeter equipped with a Peltier-cooled R928 photomultiplier-tube detector. UV-vis spectra were recorded before and after measuring the emission spectrum to monitor for impurities resulting from degradation during measurement, to ensure they do not contribute to the emission spectrum. Emission and excitation spectra were corrected for detector and source response, respectively.

3.2.3. Electrochemical Measurements. Electrochemical measurements were performed at room temperature in a N_2 filled glovebox using a Bioanalytical Systems 100 B/W Electrochemical Workstation. A three-electrode configuration was used, with a working electrode (Bioanalytical Systems, platinum disk, area = 0.2 cm^2), auxiliary electrode (Bioanalytical Systems, platinum disk, area = 0.2 cm^2), and quasi-reference electrode (silver wire), which were polished prior to each experiment. Experiments were performed in CH_2Cl_2 containing 0.1 M $[N^nBu_4][PF_6]$ with ferrocene as an internal reference. CH_2Cl_2 was purified using the same procedure as for electronic absorption and emission measurements. $[N^nBu_4][PF_6]$ (98%, Oakwood Chemical) was recrystallized three times from 95% ethanol and dried under vacuum at 80° C for 24 h. Ferrocene (98%, Oakwood Chemical) was recrystallized three times from 95% ethanol and sublimed under vacuum. Potentials are referenced to the $FeCp_2^{0/+}$ couple. Square-wave voltammetry was performed using a frequency of 25 Hz and an amplitude of 50 mV. iR corrections were applied using the potentiostat software.

3.2.4. Synthesis and Characterization.

Preparation of (Ga(OEP))$_2$(μ-O_2CCO_2) (1). To a stirred, room-temperature solution of Ga(OEP)(OH) (0.075 g, 0.121 mmol) in THF (30 mL) was added oxalic acid (0.005 g, 0.056 mmol). The solution was stirred for 2 h, during which time a bright pink precipitate formed. The solvent volume was reduced to approximately 10 mL *in vacuo*. The product was collected as a pink powder (0.052 g, 0.040 mmol, 73% yield) and washed (3 × 5 mL) with toluene and pentane. The product was purified by recrystallization from CH_2Cl_2 layered with pentane and cooled to –40 °C. ^{1}H NMR ($CDCl_3$, 500.13 MHz, Figures 3.3 and 3.4): δ 9.75 (s, 8 H, *meso* H), 3.89 (complex m, 32 H, C$\underline{H}_2$CH$_3$), 1.71 (t, 48 H, CH$_2$C$\underline{H}_3$). IR (cm^{-1}, Figure 3.5): 1676 s (ν_{as} COO), 1234 s (ν_s COO). UV-vis (CH_2Cl_2; λ_{max}, nm (rel. int); Figure 3.6): 338 (5.9), 383 (25.0), 396 (100), 499

(0.5), 532 (3.6), 570 (5.4). The molecular ion of **1** was not observed by HR-MS; only the $[Ga(OEP)]^+$ cation was found.

Preparation of Ga(OEP)(O_2CCO_2H) (1m). To a stirred, room-temperature solution of oxalic acid (0.073 g, 0.81 mmol) in THF (50 mL) was added a solution of Ga(OEP)(OH) (0.025 g, 0.040 mmol) in THF (20 mL) dropwise over 5 min. The solution was stirred for 1 h; no precipitate was observed to form. The solvent was removed *in vacuo* and the remaining material was stirred in CH_2Cl_2 (15 mL) to extract the porphyrinic materials. The solution was filtered and the solvent was removed *in vacuo*. The product was suspended in toluene (2 mL), collected by filtration, and washed with toluene (2 × 2 mL) and pentane (2 × 2 mL) to obtain Ga(OEP)(O_2CCO_2H) as a pink powder (0.020 g, 0.029 mmol, 72% yield). Crystals suitable for X-ray diffraction were grown by diffusion between a solution of oxalic acid in THF layered on a solution of Ga(OEP)(OH) in toluene. ^1H NMR ($CDCl_3$, 400.20 MHz, Figure 3.7): δ 10.37 (s, 4 H, *meso* H), 4.20 (complex m, 16 H, $C\underline{H}_2CH_3$), 1.96 (t, 24 H, $CH_2C\underline{H}_3$). IR (cm^{-1}, Figure 3.8): 3300 w (ν OH), 1773 m (ν_{as} COO), 1663 m (ν_{as} COO), 1268 m (ν_s COO), 1251 m (ν_s COO). UV-vis (CH_2Cl_2; λ_{max}, nm (rel. int); Figure 3.9): 335 (4.6), 380 (11.6), 400 (100), 499 (0.5), 532 (3.4), 570 (5.2). The molecular ion of **1m** was not observed by HR-MS; only the $[Ga(OEP)]^+$ cation was found.

Preparation of (Ga(OEP))$_2$(μ-$O_2CC_6H_4CO_2$) (2). To a stirred, room-temperature solution of Ga(OEP)(OH) (0.150 g, 0.242 mmol) in DMF (60 mL) was added a solution of terephthalic acid (0.016 g, 0.096 mmol) in DMF (20 mL). The solution was stirred for 2 h, during which time a bright pink precipitate formed. The solvent was removed *in vacuo*. The crude product was suspended in toluene (10 mL), filtered, and washed (3 × 5 mL) with both toluene and pentane to provide the product as a pink powder. The product was then suspended in CH_2Cl_2 (20 mL) and

stirred for 0.5 h to remove small amounts of porphyrinic impurities. The product was collected, washed (3 × 5 mL) with toluene and pentane, and dried (0.078 g, 0.057 mmol, 59% yield). Crystals suitable for X-ray diffraction were grown by diffusion between a solution of terephthalic acid in THF layered on a solution of Ga(OEP)(OH) in CH_2Cl_2. ^{1}H NMR ($CDCl_3$, 500.13 MHz, Figures 3.10 and 3.11): δ 10.12 (s, 8 H, *meso* H), 4.02 (complex m, 32 H, C$\underline{H}_2$CH$_3$), 4.00 (s, 4 H, C_6H_4), 1.78 (t, 48 H, CH$_2$C$\underline{H}_3$).^{1}H NMR (CD_2Cl_2, 400.20 MHz. Figure 3.12): δ 10.20 (s, 8 H, *meso* H), 4.10 (complex m, 32 H, C$\underline{H}_2$CH$_3$), 3.94 (s, 4 H, C_6H_4), 1.81 (t, 48 H, CH$_2$C$\underline{H}_3$). HR-MS (CH_2Cl_2, 200 V, *m/z*, Figure 3.13): 1369.5822 ((M + H)$^+$, Calc. 1369.5840). IR (cm^{-1}, Figure 3.14): 1656 m (ν_{as} COO), 1282 m (ν_s COO). UV-vis (CH_2Cl_2; λ_{max}, nm (rel. int), Figure 3.15): 335 (5.5), 382 (15.6), 399 (100), 499 (0.5), 532 (3.8), 570 (5.8). UV-vis (TCB; λ_{max}, nm (rel. int), Figure 3.16): 336 (4.9), 384 (12.6), 404 (100), 501 (0.5), 534 (3.8), 572 (6.3).

Preparation of Ga(OEP)(O$_2$CPh). To a stirred, room-temperature solution of Ga(OEP)(OH) (0.050 g, 0.081 mmol) in toluene (25 mL) was added a solution of benzoic acid (0.015 g, 0.121 mmol) in toluene (20 mL). The solution was stirred for 1 h. The solvent was removed *in vacuo*. The crude product was suspended in diethyl ether (20 mL), filtered, and washed (3 × 5 mL) with diethyl ether and pentane to provide the product as a pink powder (0.027 g, 0.037 mmol, 46% yield). ^{1}H NMR (CD_2Cl_2, 500.13 MHz, Figures 3.17 and 3.18): δ 10.41 (s, 4 H, *meso* H), 6.61 (t, 1 H, *para* H), 6.29 (t, 2 H, *meta* H), 5.04 (d, 2 H, *ortho* H), 4.23 (complex m, 16 H, C$\underline{H}_2$CH$_3$), 1.96 (t, 24 H, CH$_2$C$\underline{H}_3$). IR (cm^{-1}, Figure 3.19): 1651 m (ν_{as} COO), 1339 m (ν_s COO). UV-vis (CH_2Cl_2; λ_{max}, nm (rel. int), Figure 3.20): 335 (4.4), 381 (11.3), 400 (100), 499 (0.4), 532 (3.3), 571 (5.0). UV-vis (TCB; λ_{max}, nm (rel. int), Figure 3.21): 336 (4.4), 384 (10.3), 405 (100), 500 (0.5), 534 (3.5), 572 (5.8). The molecular ion of Ga(OEP)(O$_2$CPh) was not observed by HR-MS; only the [Ga(OEP)]$^+$ cation was found.

Preparation of 5,15-Bis(4-ethoxycarbonyl)porphyrin (H_2BECP). H_2BECP was synthesized according to literature procedures. ^{1}H-NMR spectra match those previously reported.[39] UV-vis (CH_2Cl_2; λ_{max}, nm (rel. int), Figure 3.22): 400 (100), 500 (4.5), 537 (4.0). 576 (1.9), 630 (2.8). UV-vis (TCB; λ_{max}, nm (rel. int), Figure 3.23): 407 (100), 503 (4.6), 541 (4.3), 579 (3.0), 634 (3.1).

Preparation of 5,15-Bis(carboxyl)porphyrin (H_2BCP). This procedure is a modified version of a previously reported syntheses of 5,10,15,20-tetrakis(carboxyl)porphyrin[40] and H_2BCPP.[37,41] To a stirred, room temperature solution of H_2BECP (0.074 g, 0.163 mmol) in THF (21 mL) and MeOH (4 mL) was added an aqueous solution of KOH (4 mL, 2 M). The solution was refluxed for 17 h, after which it was allowed to cool to room temperature. The solution was acidified with an aqueous solution of HCl (6 mL, 2 M) and a dark purple powder precipitated from solution. The powder was washed successively with 2M HCl, H_2O, and CH_2Cl_2 to provide H_2BCP as a dark purple powder (0.040 g, 0.100 mmol, 62% yield). ^{1}H NMR (DMSO-d^6, 400.20 MHz, Figure 3.24): δ 14.66 (br s, 2H, COOH) 10.77 (s, 2 H, *meso* H), 9.77 (q, 8 H, *β* H), –3.48 (br s, 2 H, NH).

Preparation of (Ga(OEP))$_2$(μ-BCP) (3). To a stirred, room-temperature solution of Ga(OEP)(OH) (0.130 g, 0.210 mmol) in *N,N*-dimethylformamide (70 mL) was added H_2BCP (0.040 g, 0.100 mmol). The solution was stirred for 18 h, during which time a dark pink precipitate formed. The solvent was removed *in vacuo* at 35 ºC. The crude product was suspended in pentane, collected by filtration, and washed with pentane and toluene to provide (Ga(OEP))$_2$(BCP) as a dark pink powder (0.098 g, 0.061 mmol, 61% yield). The product was purified by stirring a suspension of the material in CH_2Cl_2 for 0.5 h, after which the product was collected by filtration and washed (3 × 5 mL) with CH_2Cl_2, toluene, and pentane. Crystals suitable for X-ray

crystallography were obtained from vapor diffusion of pentane into a solution of the compound in $CHCl_3$. ^{1}H NMR ($CDCl_3$, 500.13 MHz, Figures 3.25 and 3.26): δ 10.11 (s, 2 H, BCP *meso* H), 9.48 (s, 8 H, OEP *meso* H), 8.83 (d, 4 H, BCP *β* H), 6.32 (d, 4 H, BCP *β* H), 3.32 (complex m, 32 H, C$\underline{H}_2$CH$_3$), 1.52 (t, 48 H, CH$_2$C$\underline{H}_3$), –4.51 (br s, 2 H, BCPP NH). ^{1}H NMR ($C_6D_3Cl_3$, 500.13 MHz, Figures 3.27 and 3.28): δ 10.22 (s, 8 H, OEP *meso* H), 9.24 (s, 2 H, BCP *meso* H), 8.27 (d, 4 H, BCP *β* H), 6.13 (d, 4 H, BCP *β* H), 3.89 (complex m, 32 H, C$\underline{H}_2$CH$_3$), 1.78 (t, 48 H, CH$_2$C$\underline{H}_3$), –5.31 (br s, 2 H, BCP NH). HR-MS (CH_2Cl_2, 70 V, *m/z*, Figure 3.29): 1601.6571 ($(M + H)^+$, Calc. 1601.6593). IR (cm^{-1}, Figure 3.30): 1659 w (ν_{as} COO), 1298 w (ν_s COO). UV-vis (CH_2Cl_2; λ_{max}, nm (rel. int), Figure 3.31): 339 (12.3), 389 (75.9), 400 (100), 506 (3.5), 535 (6.6), 572 (9.8), 633 (0.3). UV-vis (TCB; λ_{max}, nm (rel. int), Figure 3.32): 338 (8.1), 403 (100), 506 (2.4), 535 (5.0), 573 (7.6), 634 (0.3).

Preparation of 5,15-Bis(4-methoxycarbonylphenyl)porphyrin (H_2BMCPP). This procedure is a modified version of previously reported syntheses of H_2BMCPP [41] and 5,15-bis(4-ethoxycarbonylphenyl)porphyrin.[37] To a room-temperature solution of dipyrromethane (0.422 g, 2.89 mmol) and 4-(methoxycarbonyl)benzaldehyde (0.474 g, 2.89 mmol) in anhydrous CH_2Cl_2 (350 mL) was added trifluoroacetic acid (230 μL, 3.00 mmol). The reaction was stirred in the dark for 17 h, during which time the solution turned very dark brown. To the reaction was added triethylamine (1.28 mL, 9.18 mmol) followed by *p*-chloranil (2.23 g, 9.08 mmol) and the mixture was refluxed for 90 min. The reaction mixture was allowed to cool to room temperature and filtered through silica gel (CH_2Cl_2). The solvent was removed *in vacuo* and the resulting residue was purified by column chromatography over silica gel (CH_2Cl_2). After removal of the volatile components, H_2BMCPP was obtained as a dark purple powder (0.359 g, 0.621 mmol, 41% yield). ^{1}H NMR spectra in $CDCl_3$ match those previously reported.[41] ^{1}H NMR (CD_2Cl_2, 500.13 MHz,

Figure 3.33): δ 10.40 (s, 2 H, *meso* H), 9.48 (d, 4 H, *β* H), 9.08 (d, 4 H, *β* H), 8.49 (d, 4 H, *ortho* H) 8.39 (d, 4 H, *meta* H), 4.12 (s, 6 H, CH_3), –3.17 (br s, 2 H, NH). UV-vis (CH_2Cl_2; λ_{max}, nm (rel. int), Figure 3.34): 365 (7.6), 389 (22.2), 408 (100), 502 (4.4), 537 (1.9), 575 (1.4), 630 (0.6). UV-vis (TCB; λ_{max}, nm (rel. int), Figure 3.35): 368 (6.0), 395 (20.1), 414 (100), 506 (4.0), 541 (1.9), 579 (1.3), 634 (0.5).

Preparation of (Ga(OEP))$_2$(μ-BCPP) (4). To a stirred, room-temperature solution of Ga(OEP)(OH) (0.163 g, 0.263 mmol) in *N,N*-dimethylformamide (60 mL) was added H_2BCPP (0.030 g, 0.106 mmol). The solution was heated to 35 ºC for 1 h, during which time a bright pink precipitate formed. The solvent was removed *in vacuo* at 35 ºC. The crude product was suspended in toluene, collected by filtration, and washed with toluene to obtain (Ga(OEP))$_2$(μ-BCPP) as a dark pink powder (0.112 g, 0.064 mmol, 60% yield). The ^{1}H NMR spectrum of the crude product indicated the presence of uncapped Ga(OEP)(BCPP) (~ 5%), so the material was dissolved in $CHCl_3$ to which Ga(OEP)(OH) (0.033 g, 0.053 mmol) was added and stirred for 1 h at room temperature. The volatile components were removed *in vacuo* and the material was suspended in toluene, collected by filtration, and washed (3 × 5 mL) with toluene and pentane to obtain (Ga(OEP))$_2$(μ-BCPP) as a dark pink powder (0.055 g, 0.031 mmol, 29% yield). Crystals suitable for X-ray crystallography were obtained from vapor diffusion of pentane into a solution of the compound in $CHCl_3$. ^{1}H NMR ($CDCl_3$, 500.13 MHz, Figures 3.36 and 3.37): δ 10.53 (s, 8 H, OEP *meso* H), 10.04 (s, 2 H, BCPP *meso* H), 9.08 (d, 4 H, BCPP *β* H), 8.32 (d, 4 H, BCPP *β* H), 7.16 (d, 4 H, *ortho* H) 5.47 (d, 4 H, *meta* H), 4.30 (complex m, 32 H, C$\underline{H}_2$CH$_3$), 2.02 (t, 48 H, CH$_2$C$\underline{H}_3$), –3.66 (br s, 2 H, BCPP NH). IR (cm^{-1}, Figure 3.38): 1665 w (ν_{as} COO), 1316 m (ν_s COO). UV-vis (CH_2Cl_2; λ_{max}, nm (rel. int), Figure 3.39): 336 (5.5), 380 (13.9), 401 (100), 411 (34.8), 503 (1.8), 533 (3.4), 571 (4.8), 633 (0.2). UV-vis (TCB; λ_{max}, nm (rel. int), Figure 3.40): 336 (4.3), 383 (11.3),

405 (100), 416 (33.6), 506 (1.7), 535 (3.2), 572 (5.0), 634 (0.1). The molecular ion of **4** was not observed by HR-MS; only the $[Ga(OEP)]^+$ cation was found.

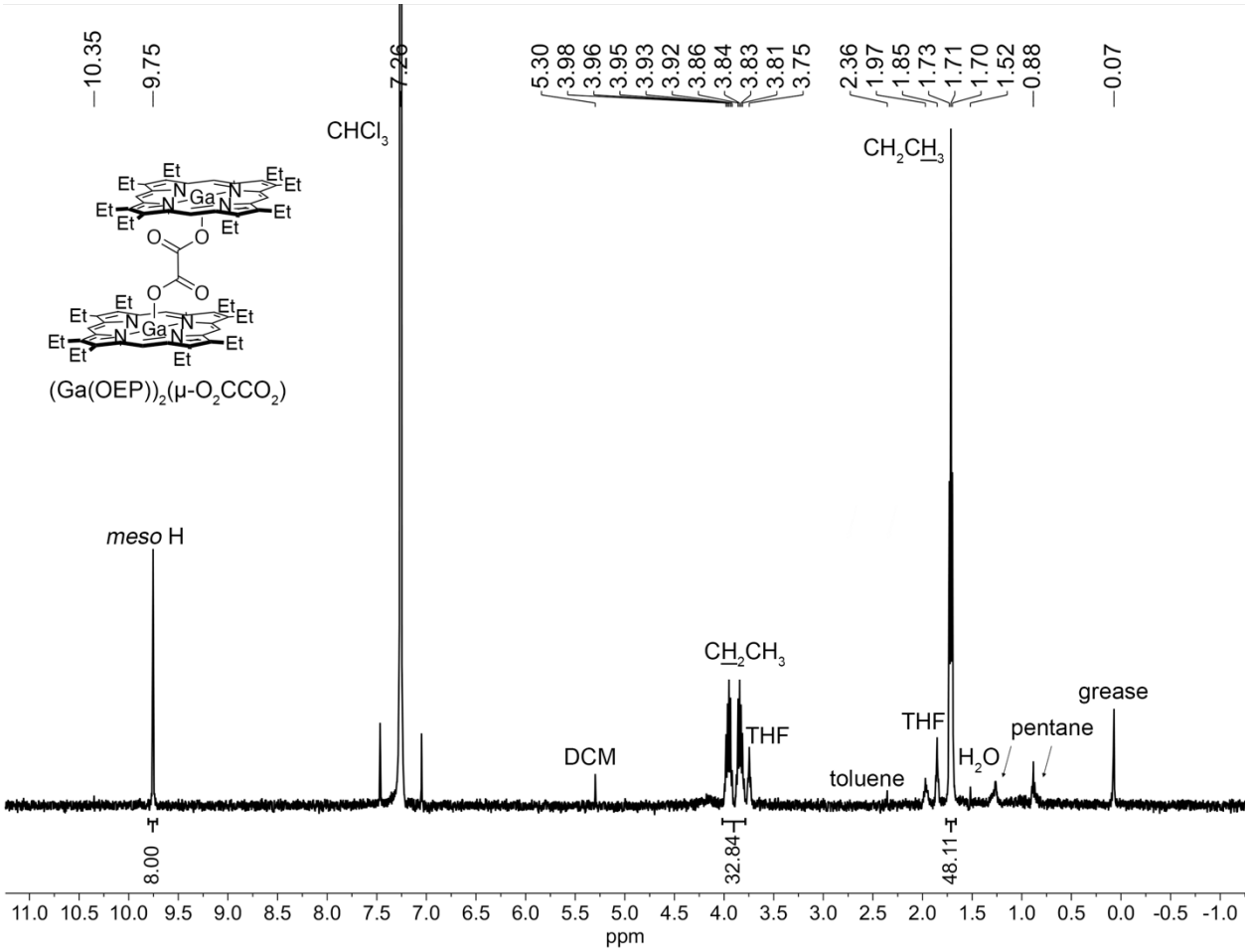

Figure 3.3. ^{1}H NMR spectrum (500.13 MHz) of $(Ga(OEP))_2(\mu\text{-}O_2CCO_2)$ (**1**) in $CDCl_3$.

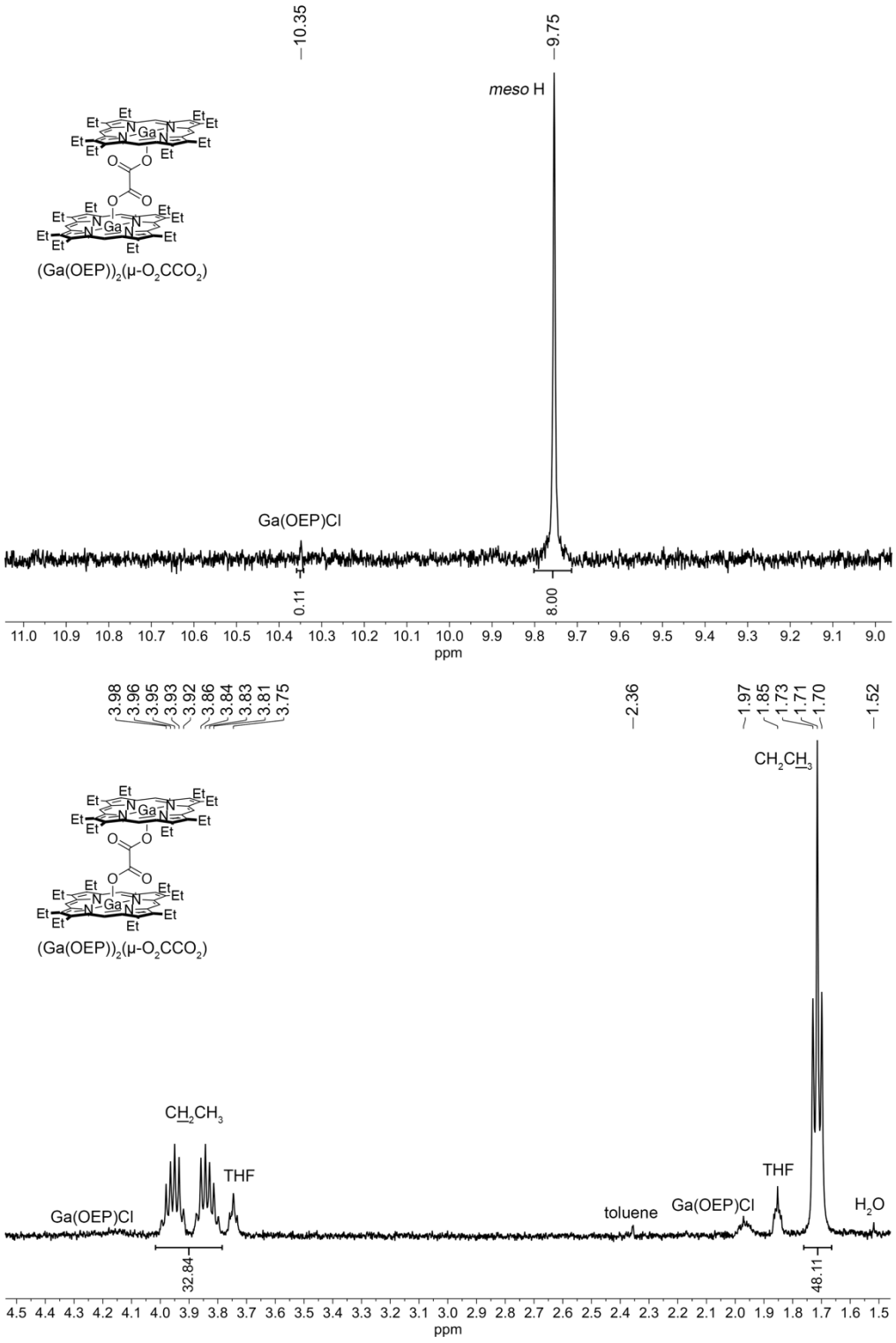

Figure 3.4. Expanded views of ^{1}H NMR spectra (500.13 MHz) of $(Ga(OEP))_2(\mu\text{-}O_2CCO_2)$ (**1**) in $CDCl_3$ shown in Figure 3.3.

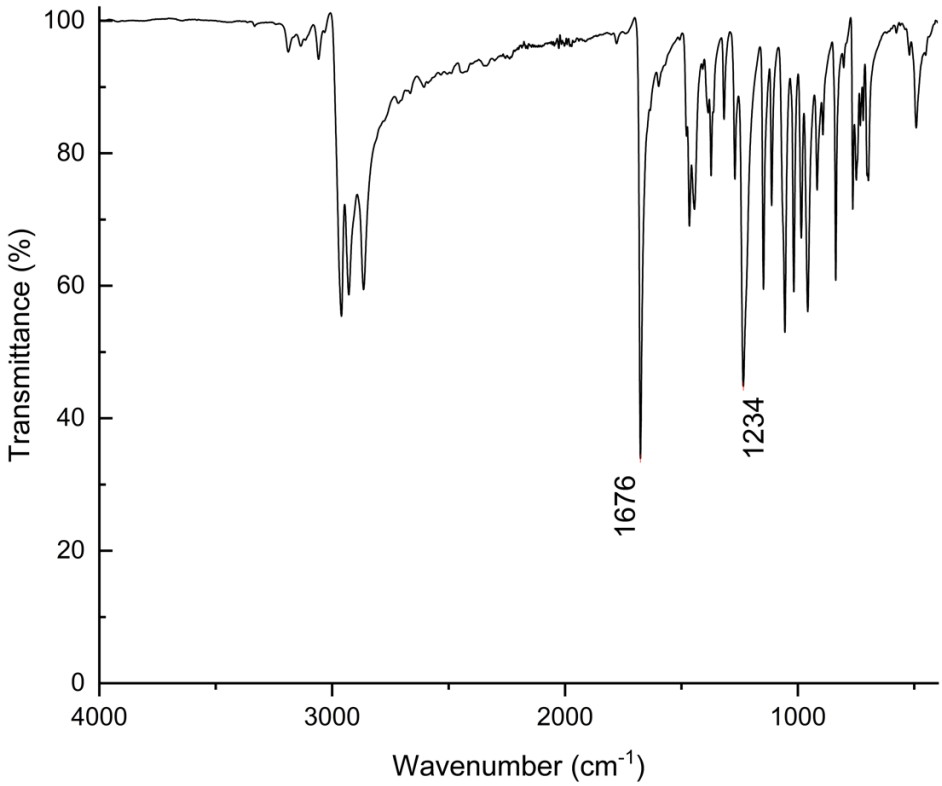

Figure 3.5. FT-IR spectrum of $(Ga(OEP))_2(\mu\text{-}O_2CCO_2)$ (**1**).

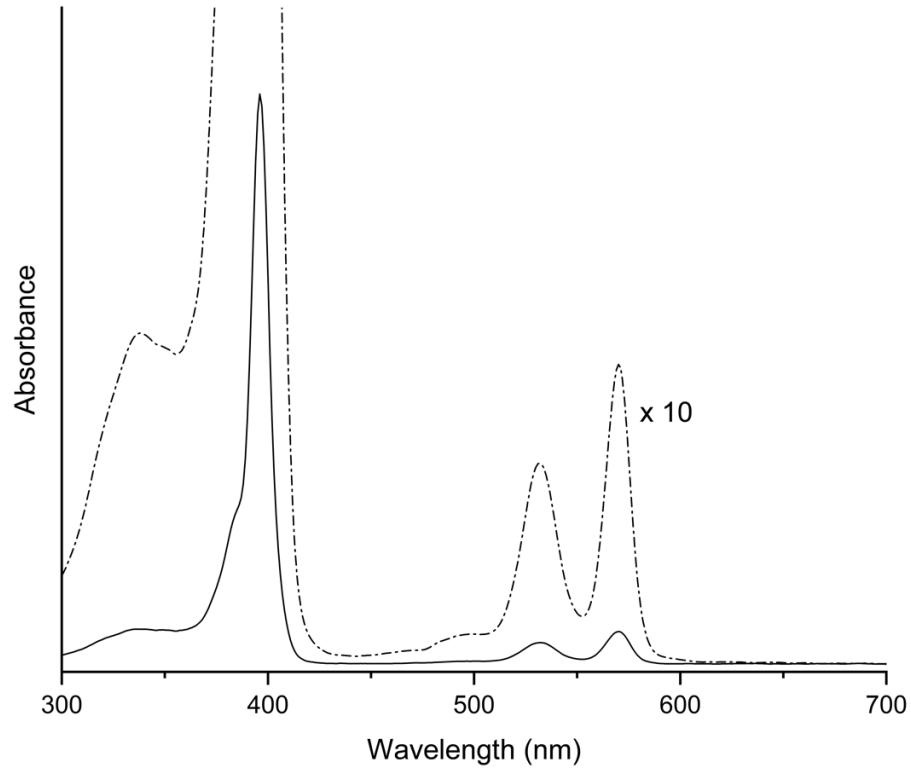

Figure 3.6. UV-Vis spectrum of $(Ga(OEP))_2(\mu\text{-}O_2CCO_2)$ (**1**) in CH_2Cl_2.

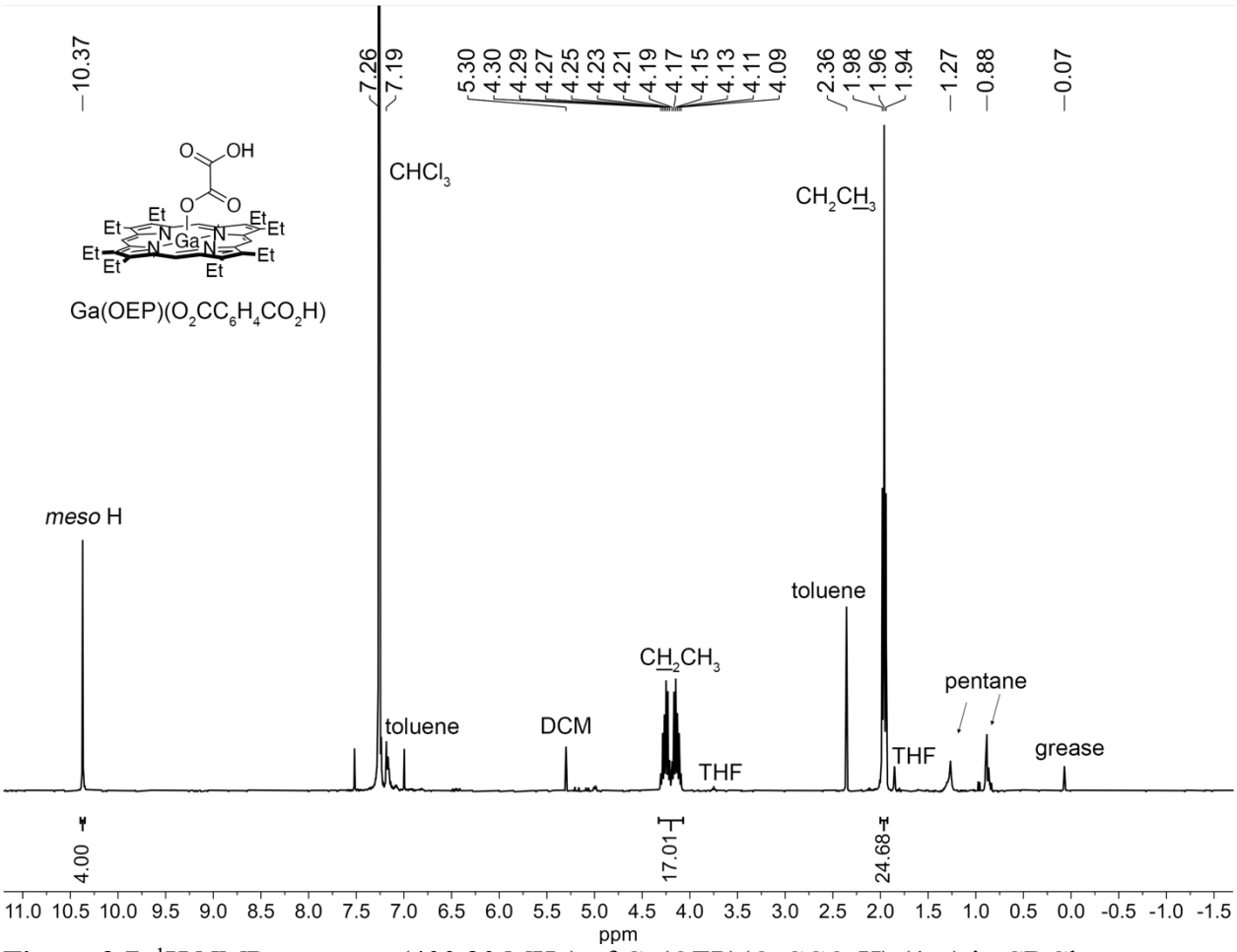

Figure 3.7. ^{1}H NMR spectrum (400.20 MHz) of Ga(OEP)(O_2CCO_2H) (**1m**) in $CDCl_3$.

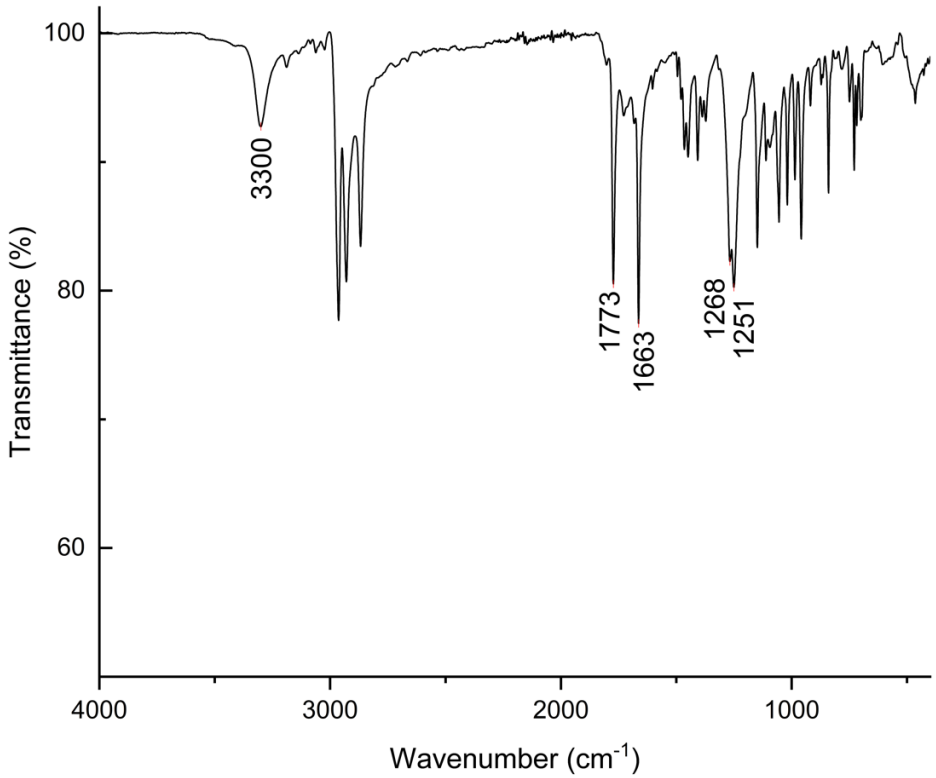

Figure 3.8. FT-IR spectrum of Ga(OEP)(O_2CCO_2H) (**1m**).

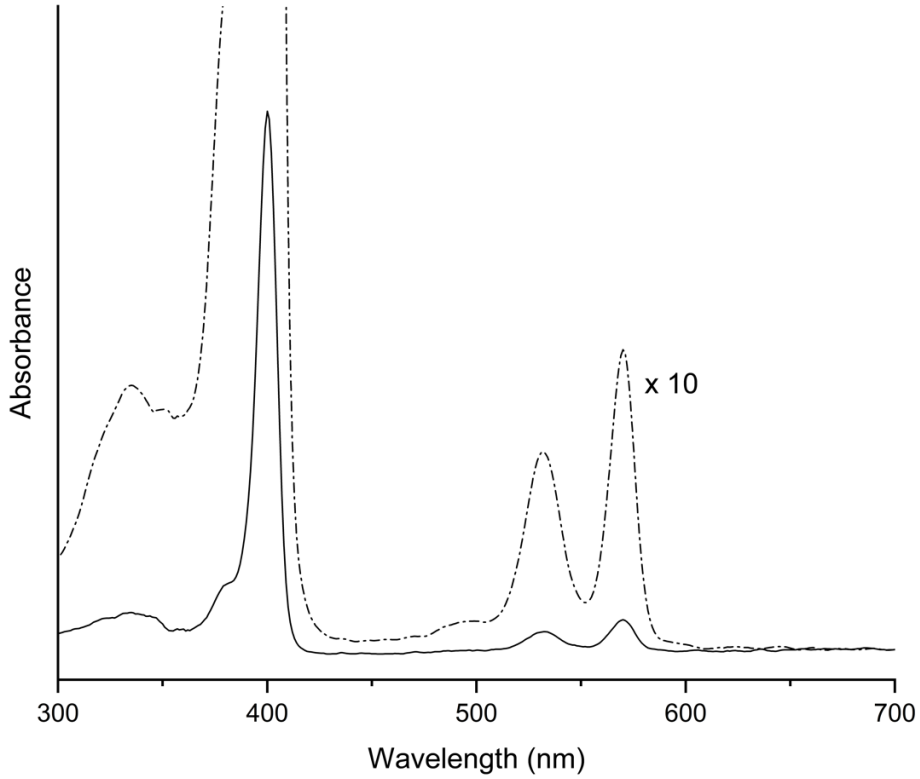

Figure 3.9. UV-Vis spectrum of Ga(OEP)(O_2CCO_2H) (**1m**) in CH_2Cl_2.

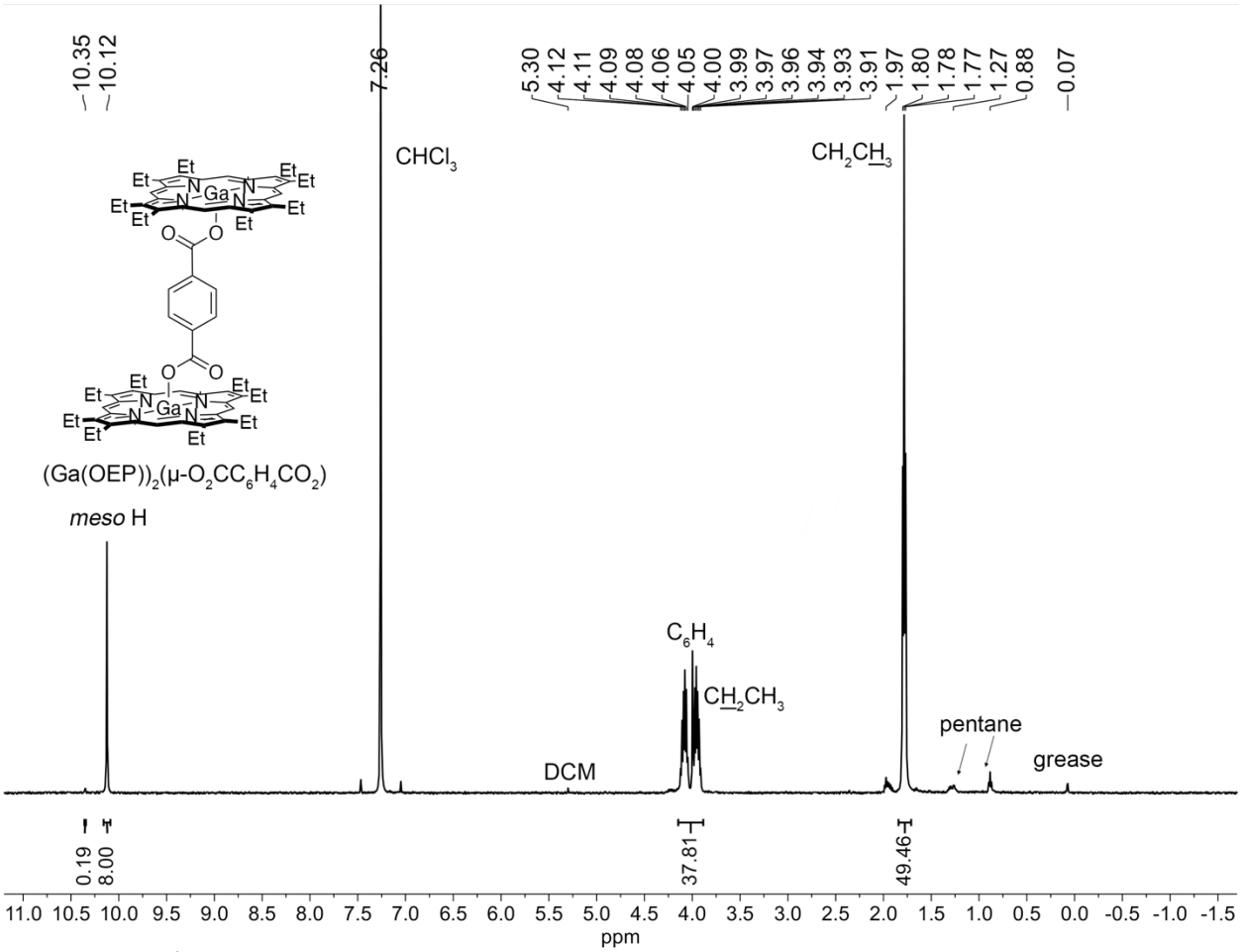

Figure 3.10. ^{1}H NMR spectra (500.13 MHz) of $(Ga(OEP))_2(\mu\text{-}O_2CC_6H_4CO_2)$ (**2**) in $CDCl_3$.

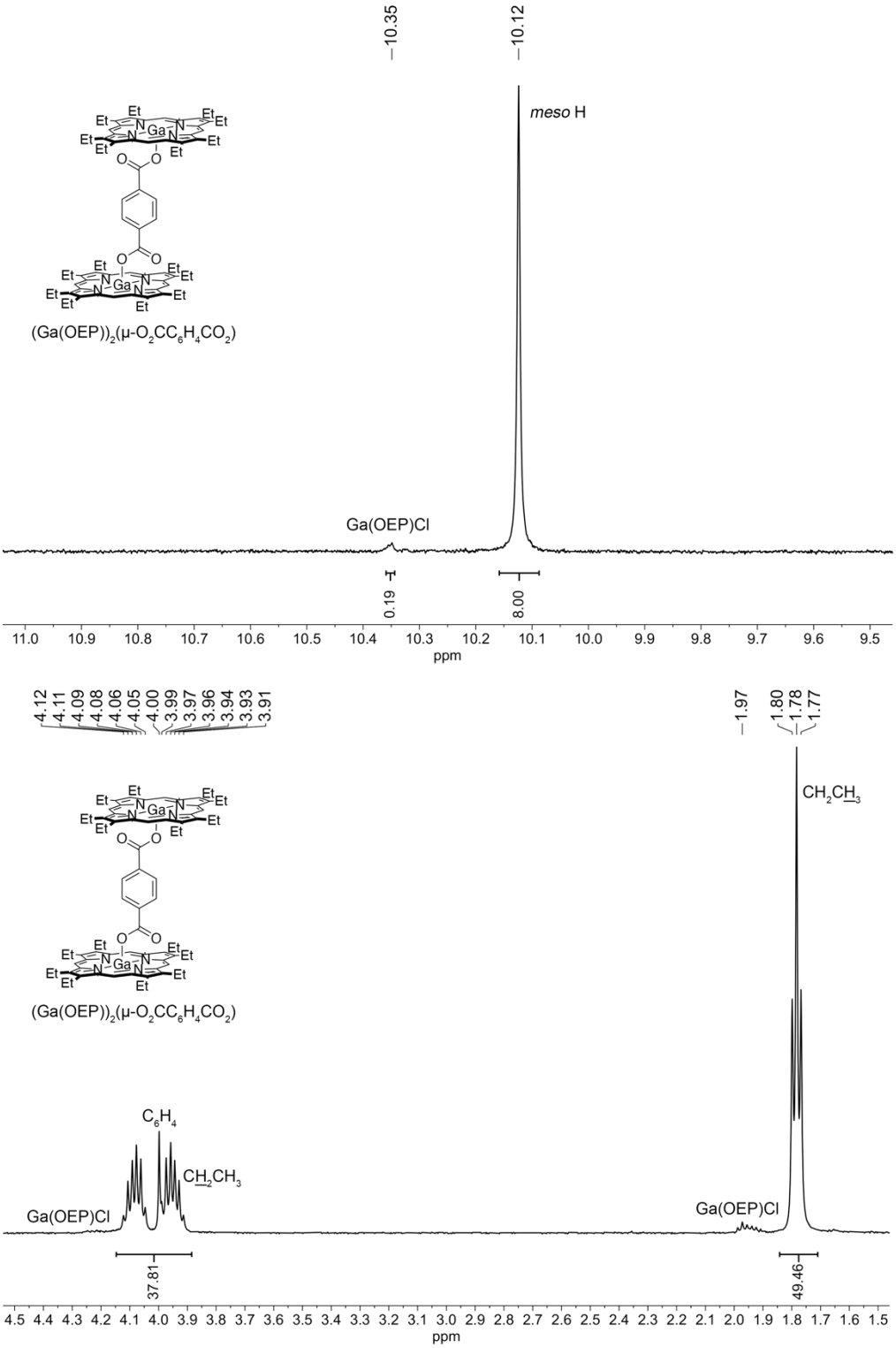

Figure 3.11. Expanded views of ^{1}H NMR spectra (500.13 MHz) of $(Ga(OEP))_2(\mu\text{-}O_2CC_6H_4CO_2)$ (**2**) in $CDCl_3$ shown in Figure 3.10.

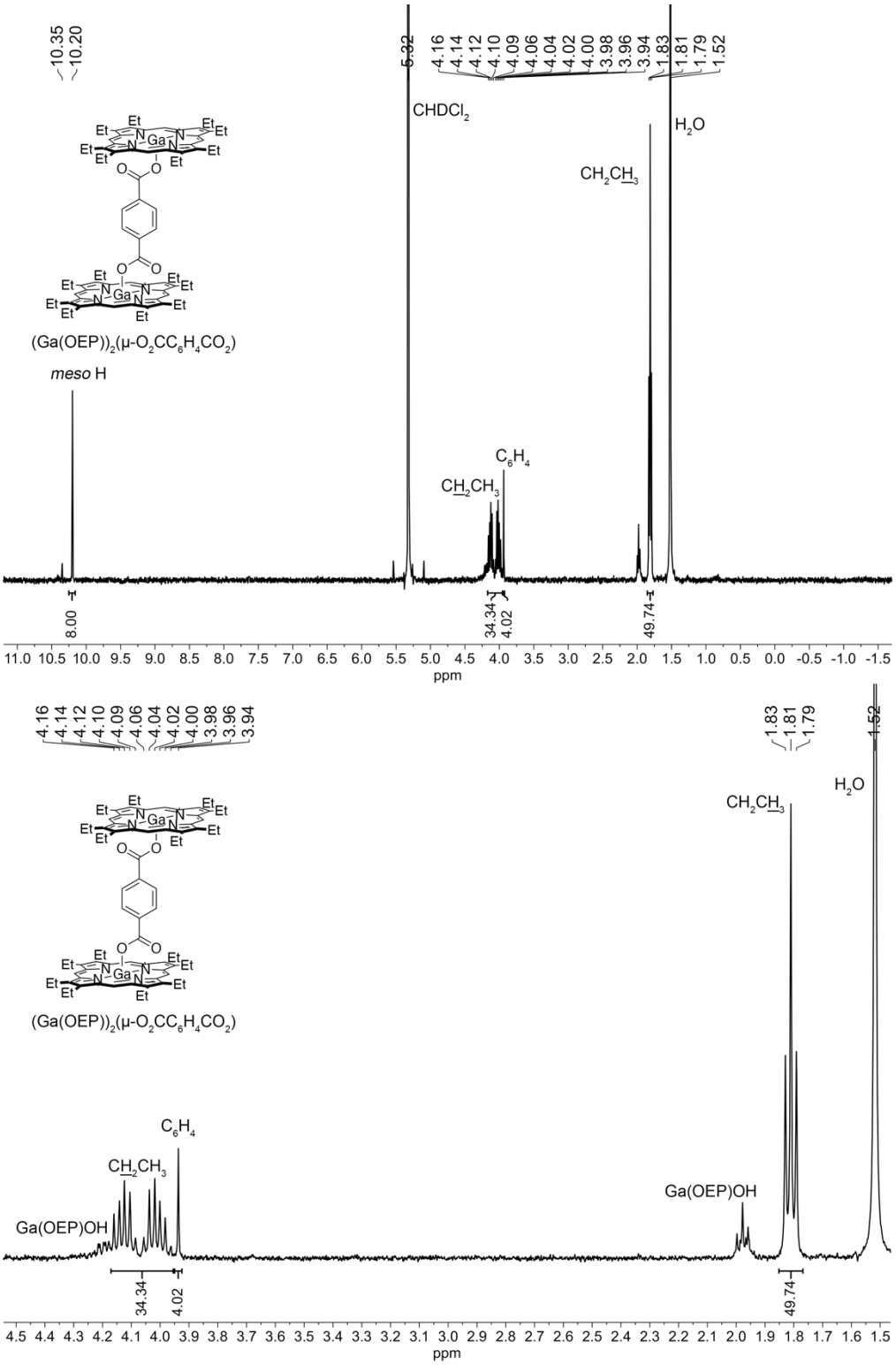

Figure 3.12. ^{1}H NMR spectra (400.20 MHz) of $(Ga(OEP))_2(\mu\text{-}O_2CC_6H_4CO_2)$ (**2**) in CD_2Cl_2. The bottom spectrum is an expansion of the upper spectrum.

Compound Table

Label	Tgt Score	Mass Error (ppm)	Tgt Formula	Obs. RT	Ref. Mass	Obs. Mass
Cpd 1: C80 H92 Ga2 N8 O4	95.78	0.12	C80 H92 Ga2 N8 O4	0.116	1366.5753	1366.5755

Obs. m/z	Obs. RT	Obs. Mass	Tgt Formula	Tgt Mass	Tgt Mass Error	Find Cpds Algorith
1369.5822	0.116	1366.5755	C80 H92 Ga2 N8 O4	1366.5753	0.12	Find By Formula

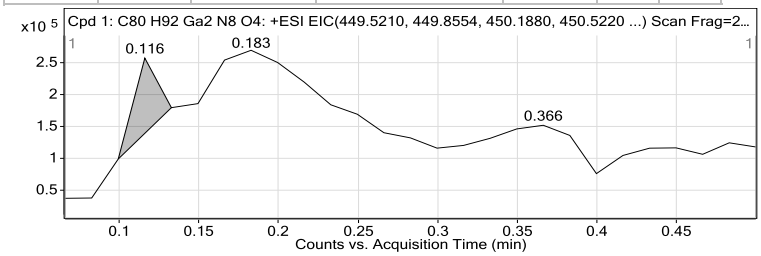

MS Zoomed Spectrum

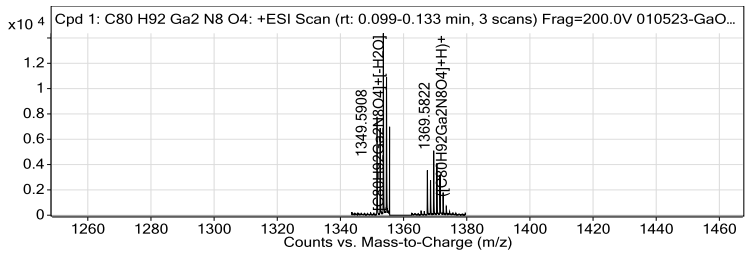

MS Spectrum Peak List

Obs. m/z	Charge	Abund	Formula	Ion/Isotope	Tgt Mass Error (ppm)
1348.6019	1	114.06	C80H92Ga2N8O4	M+[-H2O]	-27.97
1349.5908	1	204.04	C80H92Ga2N8O4	M+[-H2O]	-17.34
1367.5831	1	3571.13	C80H92Ga2N8O4	(M+H)+	-0.41
1368.5847	1	2794.64	C80H92Ga2N8O4	(M+H)+	0.78
1369.5822	1	5170.08	C80H92Ga2N8O4	(M+H)+	0.87
1370.5847	1	4096.77	C80H92Ga2N8O4	(M+H)+	0.67
1371.5844	1	3190.17	C80H92Ga2N8O4	(M+H)+	0.51
1372.5845	1	1800.16	C80H92Ga2N8O4	(M+H)+	1.27
1373.5864	1	730.96	C80H92Ga2N8O4	(M+H)+	1.5
1374.6139	1	295.67	C80H92Ga2N8O4	(M+H)+	-16.6

Figure 3.13. High-resolution mass spectrum of $(Ga(OEP))_2(\mu\text{-}O_2CC_6H_4CO_2)$ (**2**) (CH_2Cl_2, 200 V).

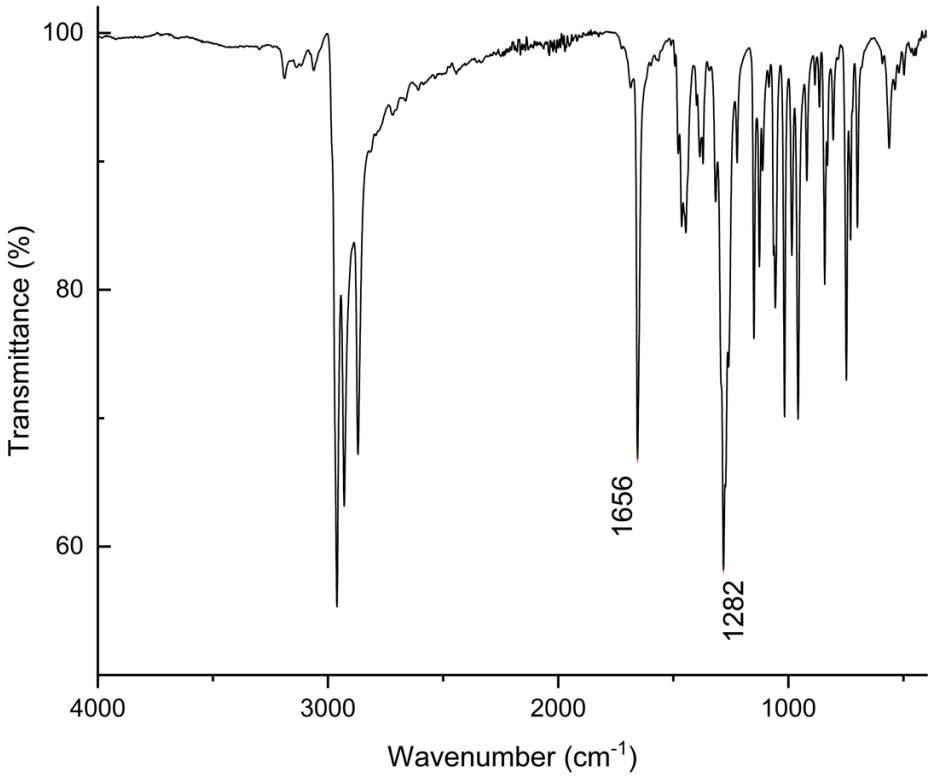

Figure 3.14. FT-IR spectrum of $(Ga(OEP))_2(\mu\text{-}O_2CC_6H_4CO_2)$ (**2**).

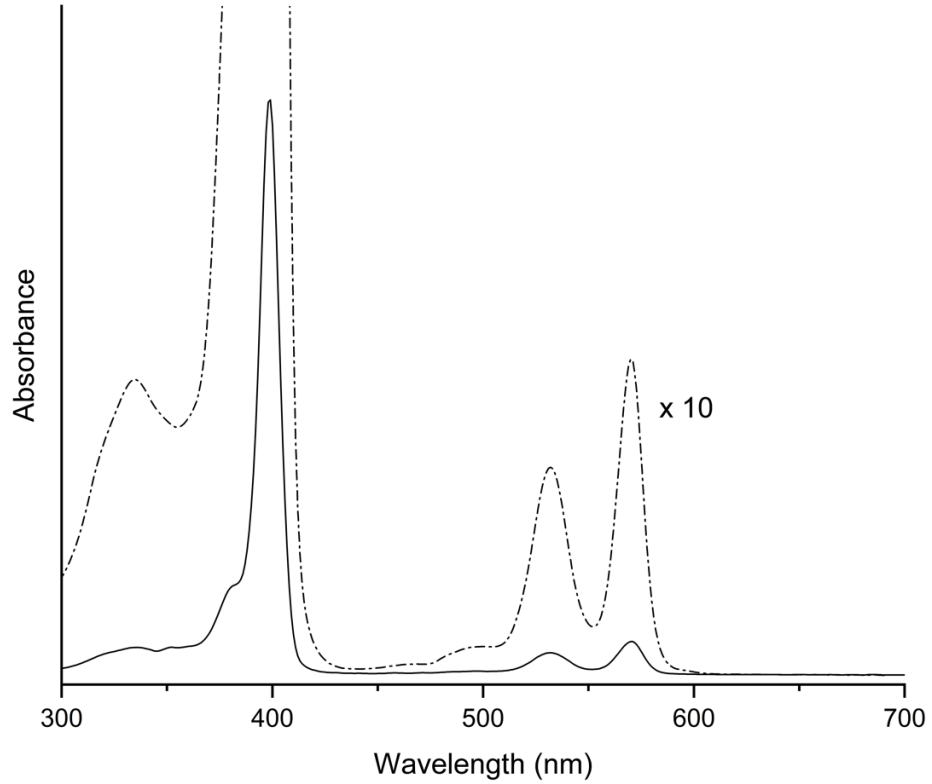

Figure 3.15. UV-Vis spectrum of $(Ga(OEP))_2(\mu\text{-}O_2CC_6H_4CO_2)$ (**2**) in CH_2Cl_2.

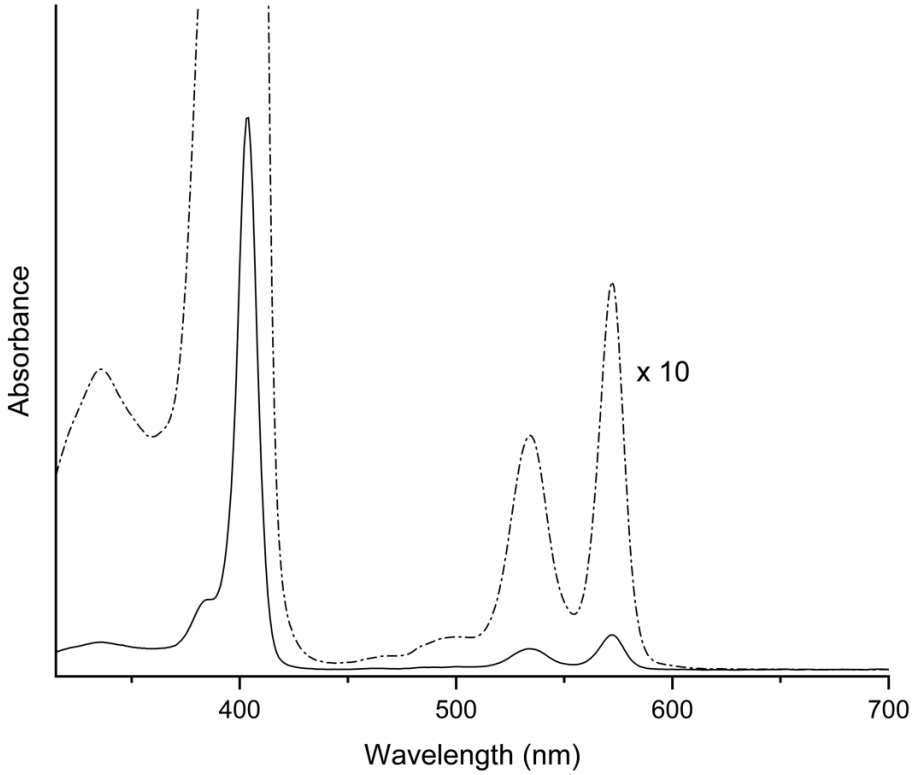

Figure 3.16. UV-Vis spectrum of $(Ga(OEP))_2(\mu\text{-}O_2CC_6H_4CO_2)$ (**2**) in TCB.

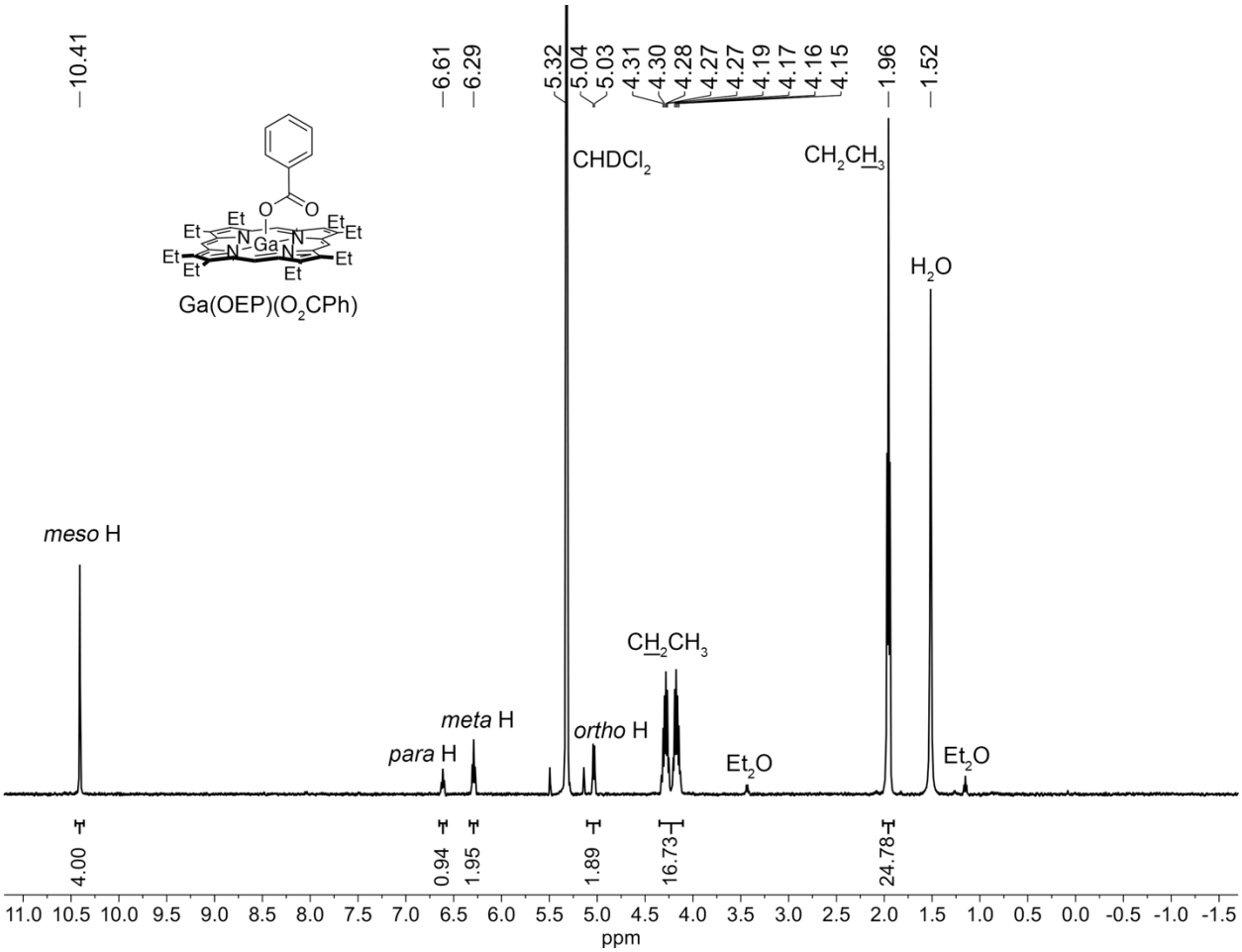

Figure 3.17. ^{1}H NMR spectra (500.13 MHz) of Ga(OEP)(O_2CPh) in CD_2Cl_2.

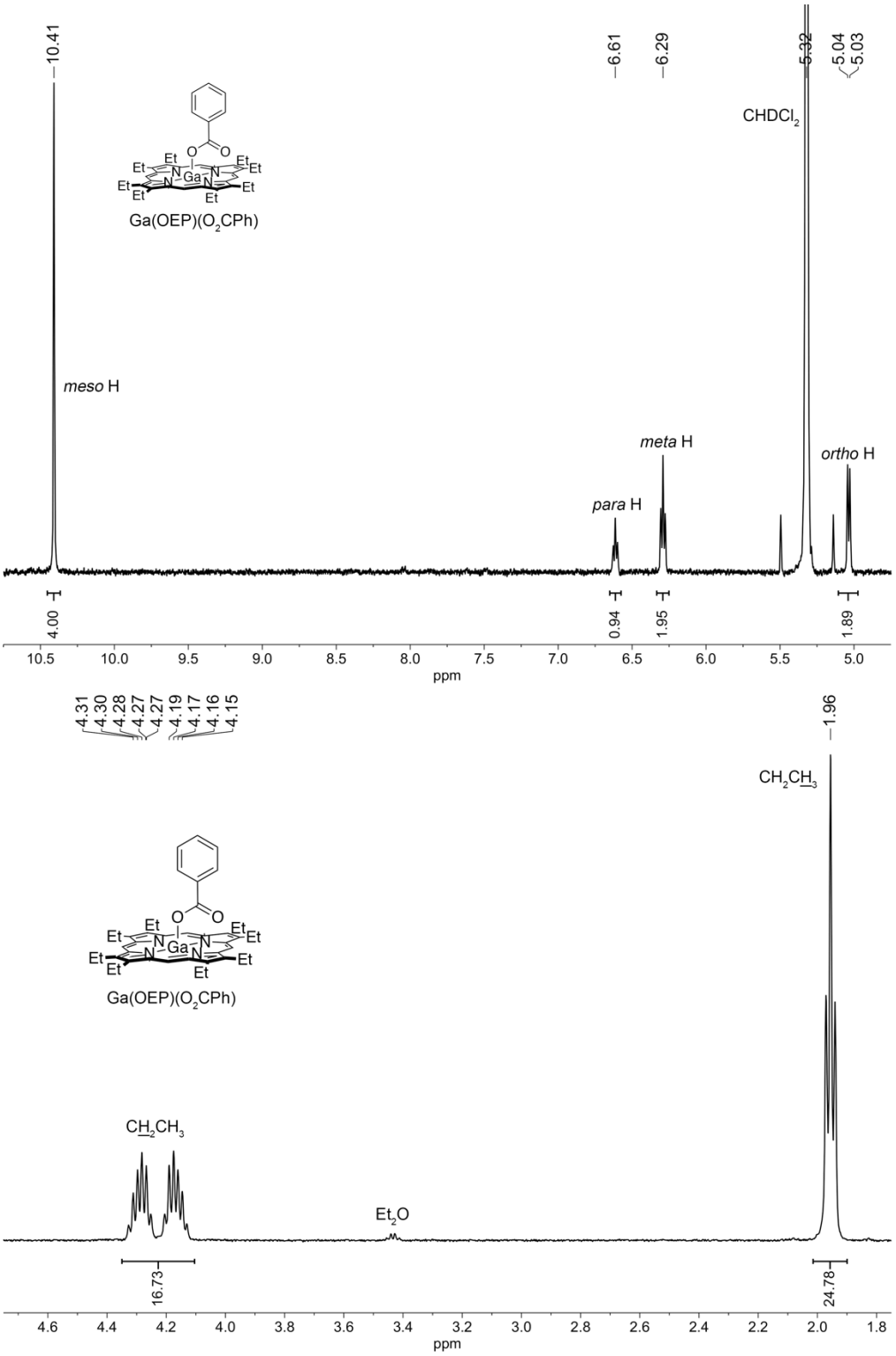

Figure 3.18. Expanded views of ^{1}H NMR spectra (500.13 MHz) of Ga(OEP)(O_2CPh) in CD_2Cl_2 shown in Figure 3.17.

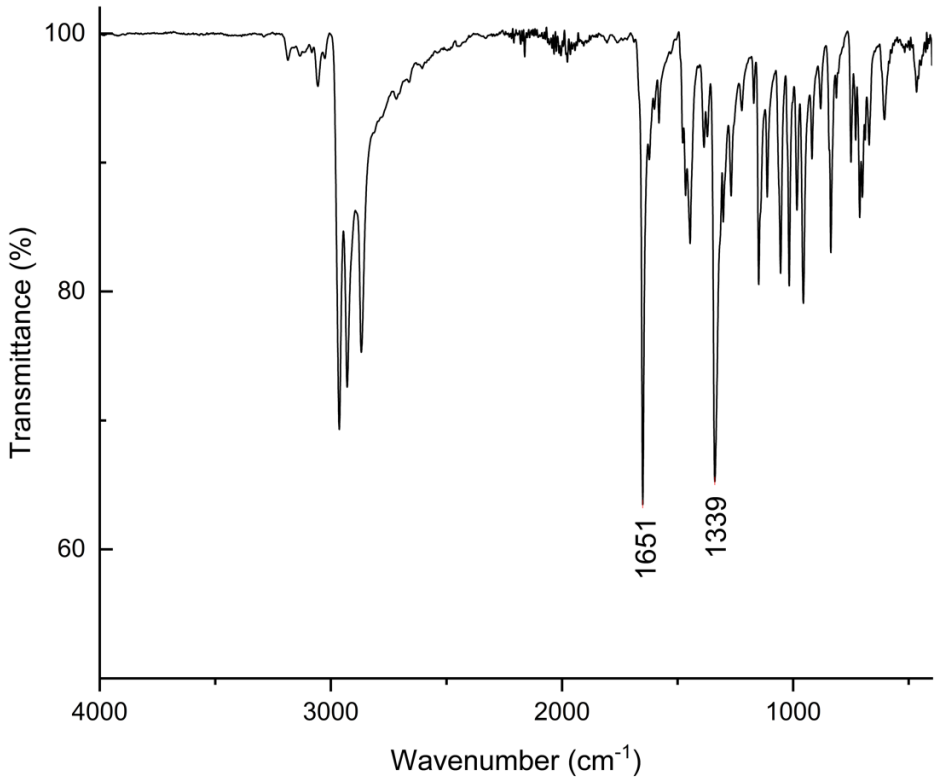

Figure 3.19. FT-IR spectrum of Ga(OEP)(O_2CPh).

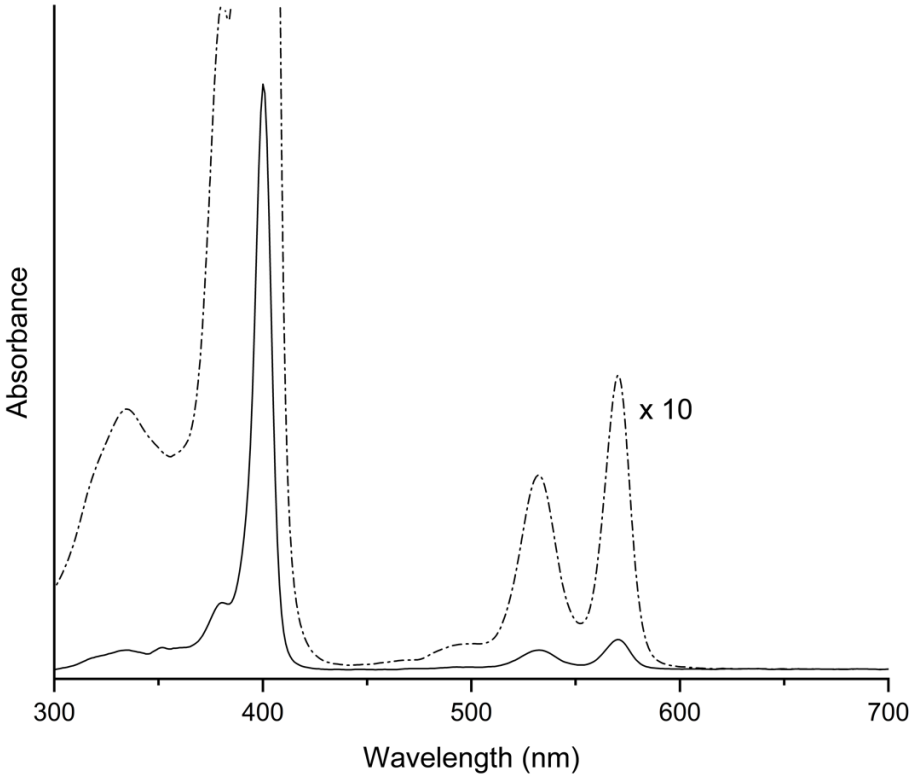

Figure 3.20. UV-Vis spectrum of Ga(OEP)(O_2CPh) in CH_2Cl_2.

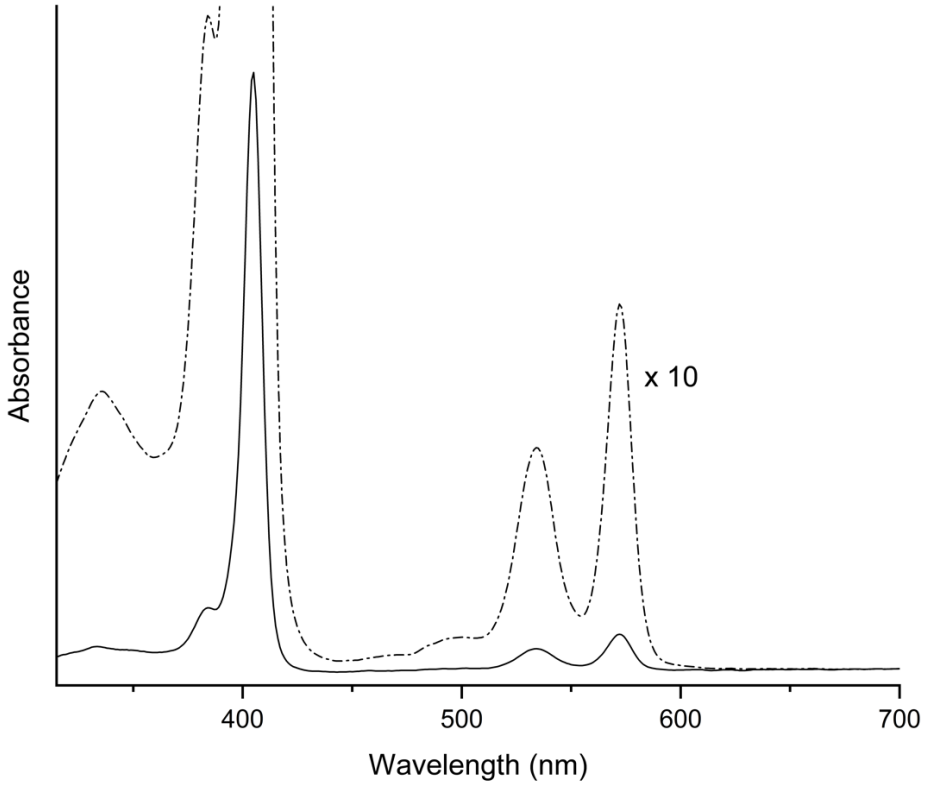

Figure 3.21. UV-Vis spectrum of Ga(OEP)(O_2CPh) in TCB.

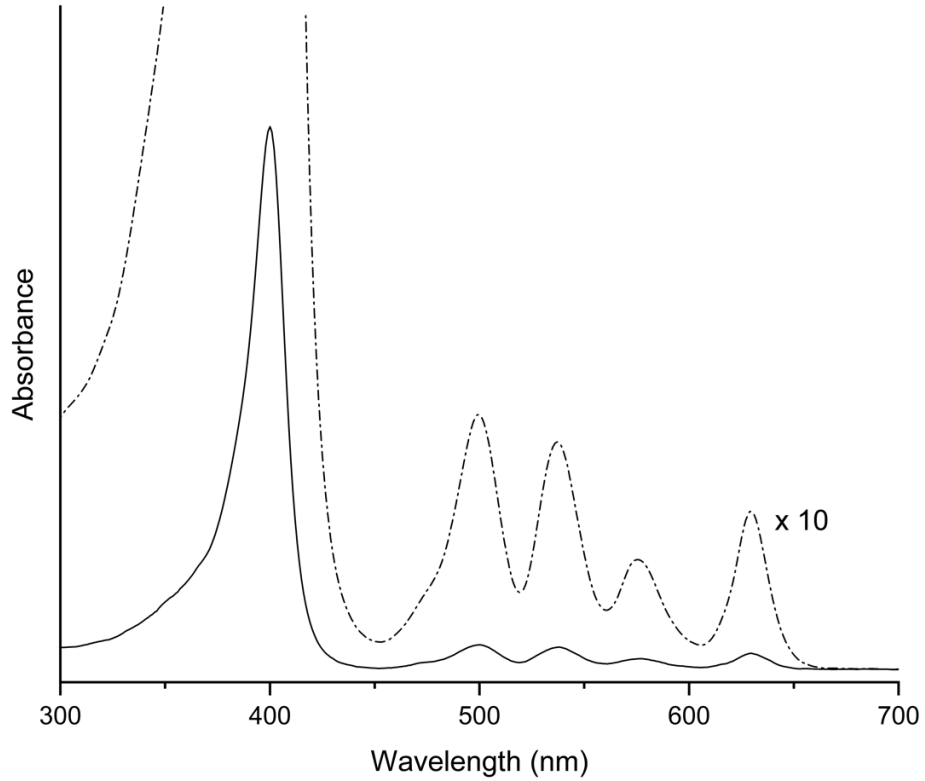

Figure 3.22. UV-Vis spectrum of H_2BECP in CH_2Cl_2.

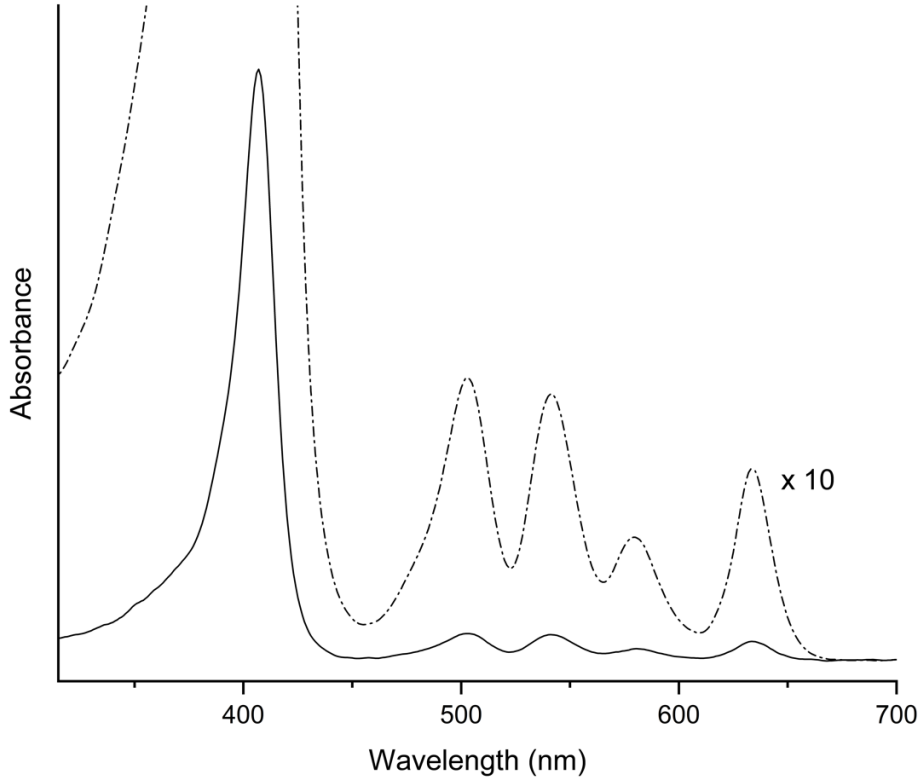

Figure 3.23. UV-Vis spectrum of H_2BECP in TCB.

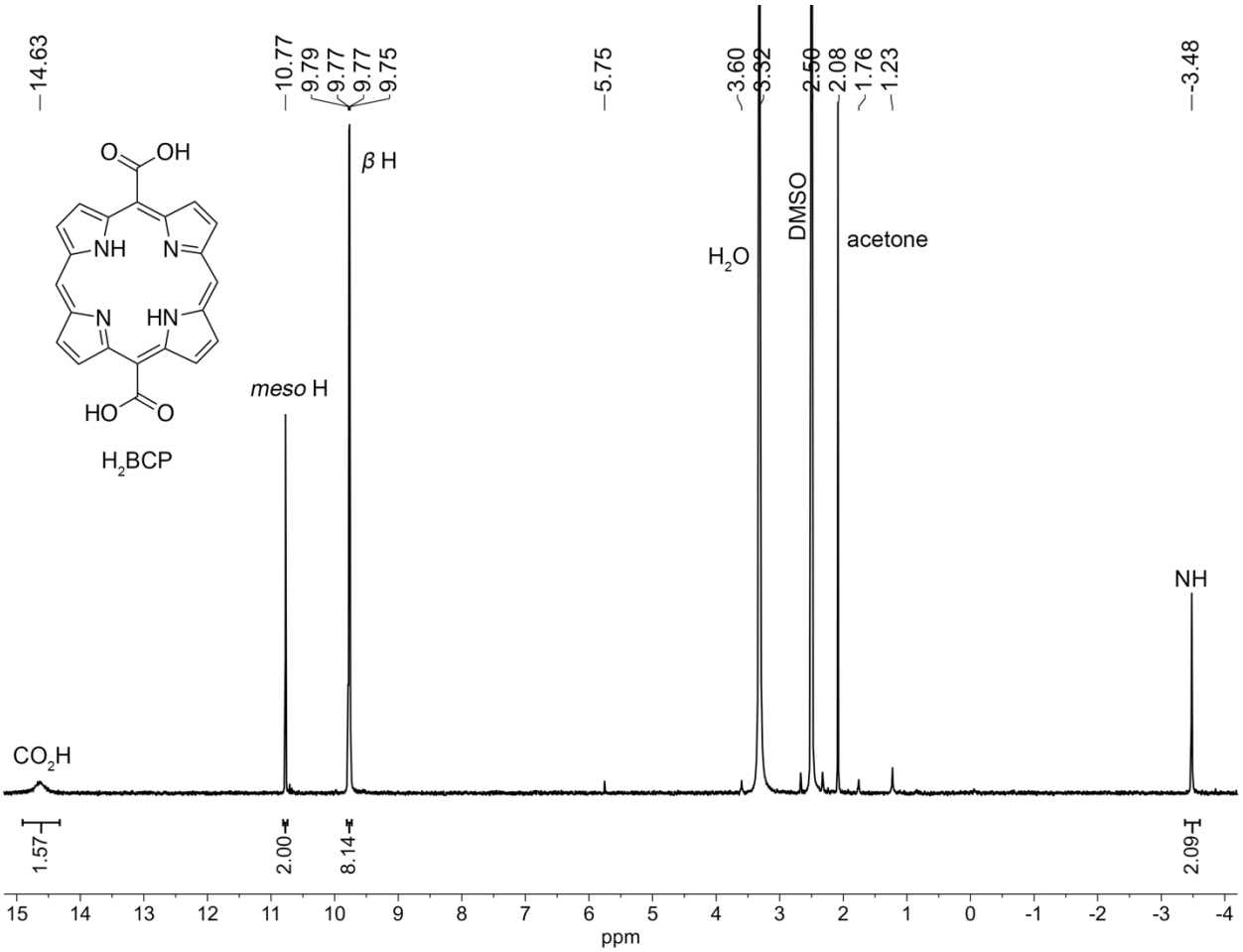

Figure 3.24. ^{1}H NMR spectra (400.20 MHz) of H_2BCP in DMSO-d^6.

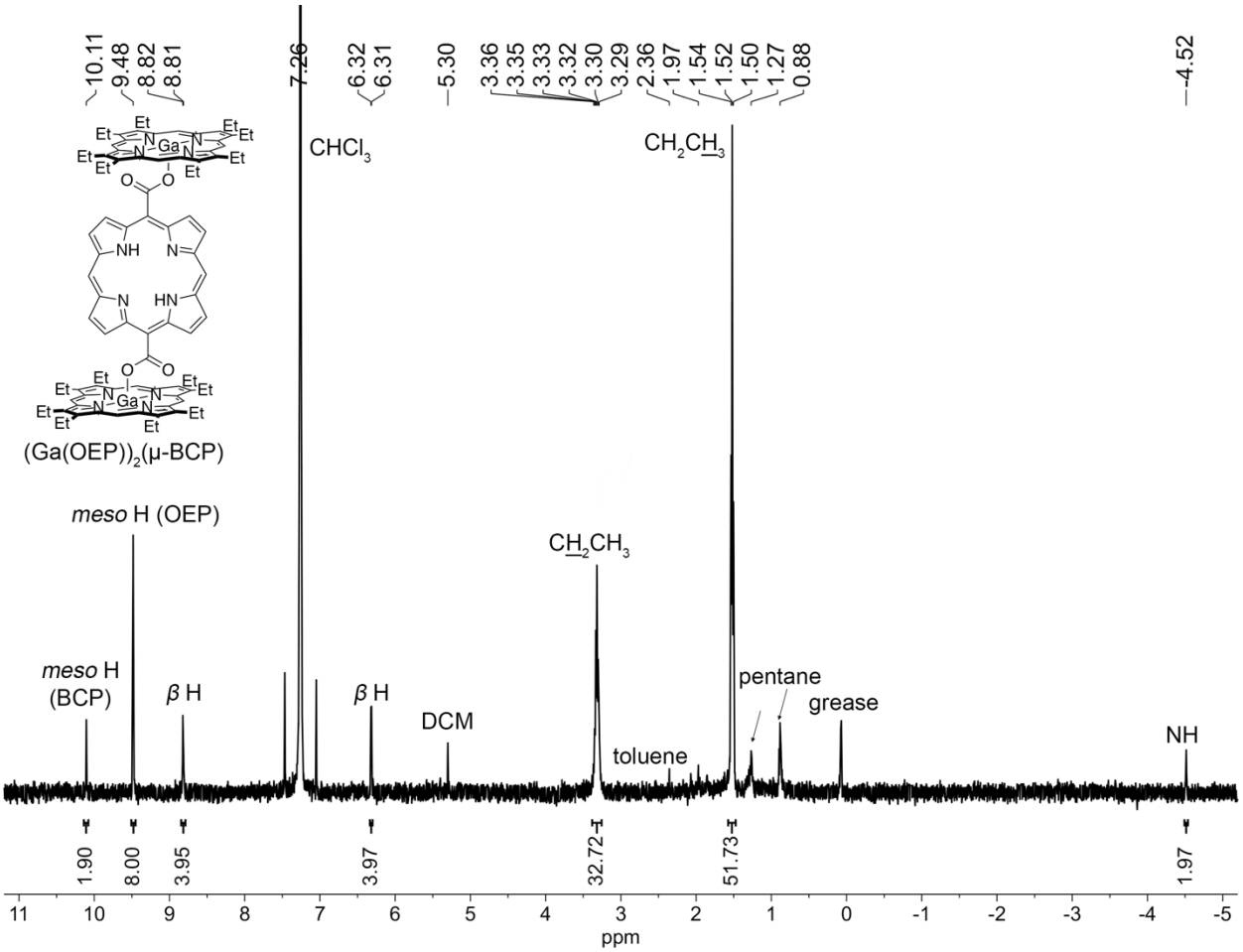

Figure 3.25. ^{1}H NMR spectra (500.13 MHz) of (Ga(OEP))$_2$(μ-BCP) (**3**) in $CDCl_3$.

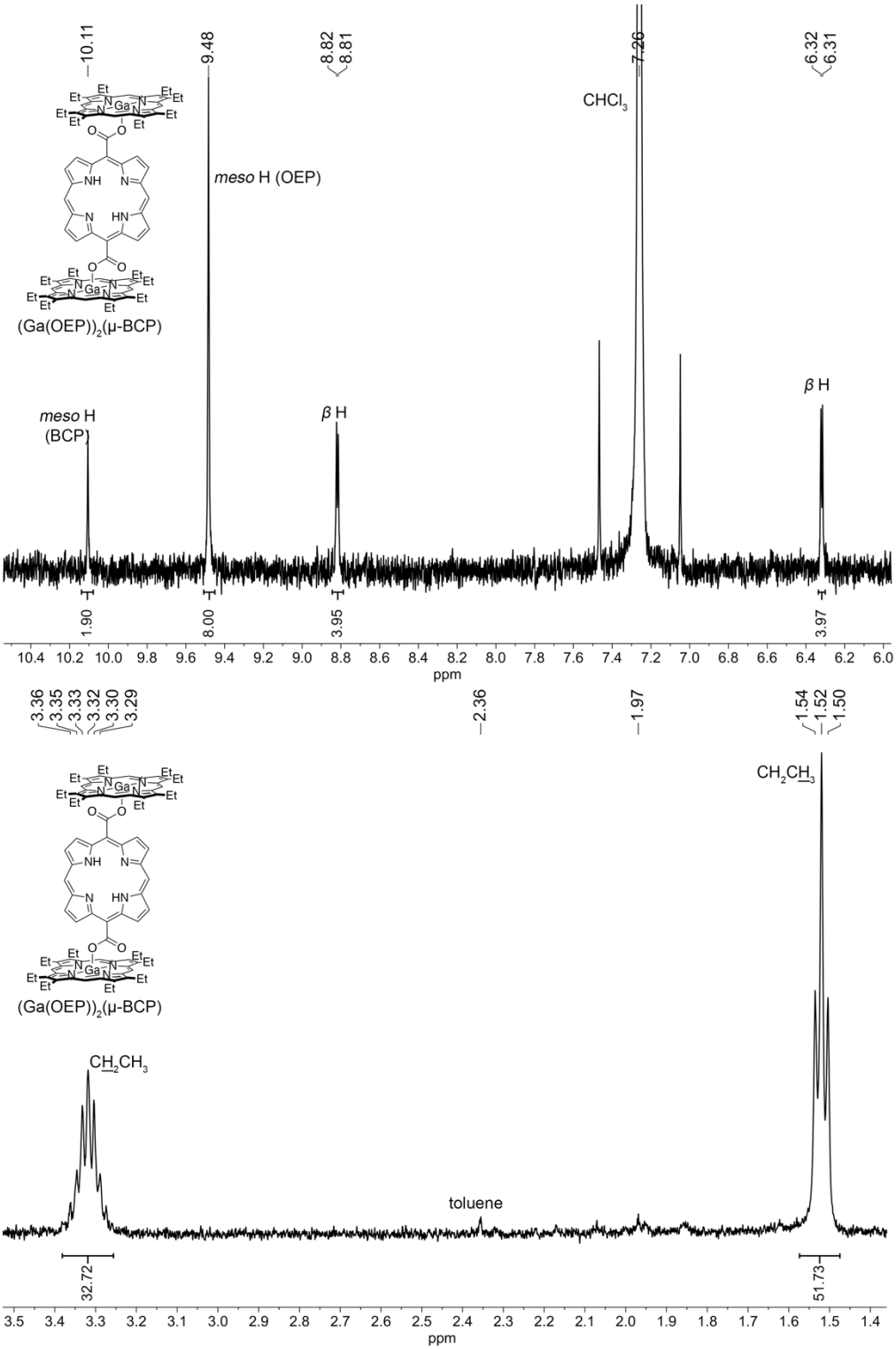

Figure 3.26. Expanded views of ^{1}H NMR spectra (500.13 MHz) of $(Ga(OEP))_2$(μ-BCP) (**3**) in $CDCl_3$ shown in Figure 3.25.

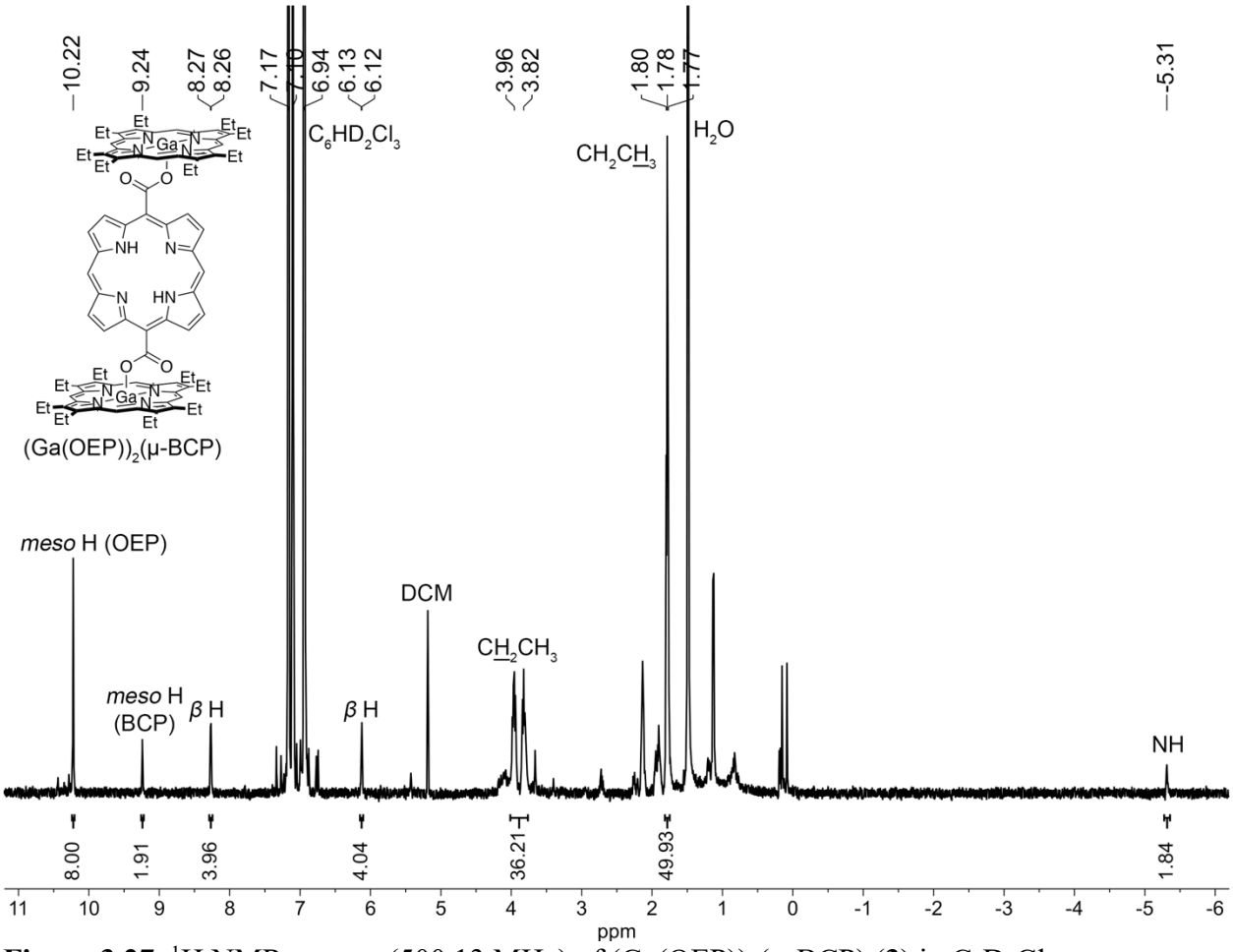

Figure 3.27. ^{1}H NMR spectra (500.13 MHz) of (Ga(OEP))$_2$(μ-BCP) (**3**) in $C_6D_3Cl_3$.

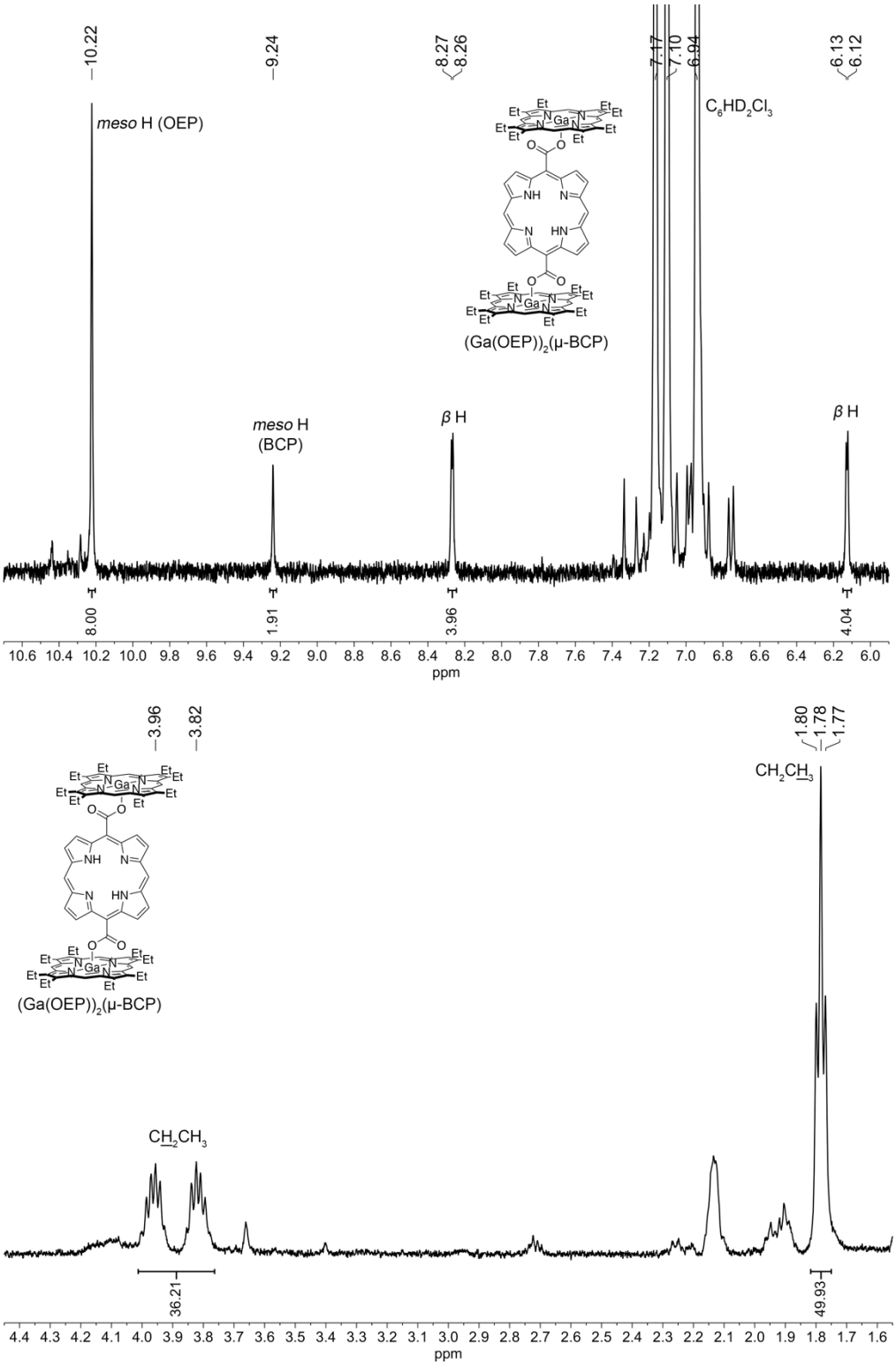

Figure 3.28. Expanded views of ^{1}H NMR spectra (500.13 MHz) of (Ga(OEP))$_2$(μ-BCP) (**3**) in $C_6D_3Cl_3$ shown in Figure 3.27.

Compound Table

Label	Tgt Score	Mass Error (ppm)	Tgt Formula	Obs. RT	Ref. Mass	Obs. Mass
Cpd 1: C94 H100 Ga2 N12 O4	97.99	-1.06	C94 H100 Ga2 N12 O4	0.219	1598.6502	1598.6485

Obs. m/z	Obs. RT	Obs. Mass	Tgt Formula	Tgt Mass	Tgt Mass Error	Find Cpds Algorith
1601.6571	0.219	1598.6485	C94 H100 Ga2 N12 O4	1598.6502	-1.06	Find By Formula

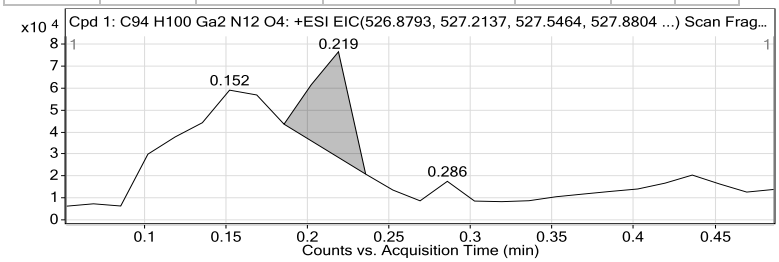

MS Zoomed Spectrum

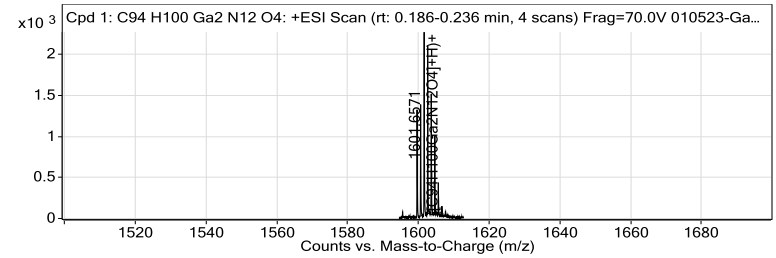

MS Spectrum Peak List

Obs. m/z	Charge	Abund	Formula	Ion/Isotope	Tgt Mass Error (ppm)
1599.6566	1	1331.36	C94H100Ga2N12O4	(M+H)+	0.53
1600.6596	1	1389.52	C94H100Ga2N12O4	(M+H)+	0.63
1601.6571	1	2313.63	C94H100Ga2N12O4	(M+H)+	1.04
1602.6575	1	2108.66	C94H100Ga2N12O4	(M+H)+	1.97
1603.6593	1	1520.7	C94H100Ga2N12O4	(M+H)+	0.85
1604.6613	1	1025.64	C94H100Ga2N12O4	(M+H)+	0.21
1605.6584	1	437.19	C94H100Ga2N12O4	(M+H)+	3.25
1606.6728	1	151.03	C94H100Ga2N12O4	(M+H)+	-4.16
1607.6596	1	82.4	C94H100Ga2N12O4	(M+H)+	5.77

Figure 3.29. High-resolution mass spectrum of $(Ga(OEP))_2(\mu\text{-BCP})$ (**3**) (CH_2Cl_2, 70 V).

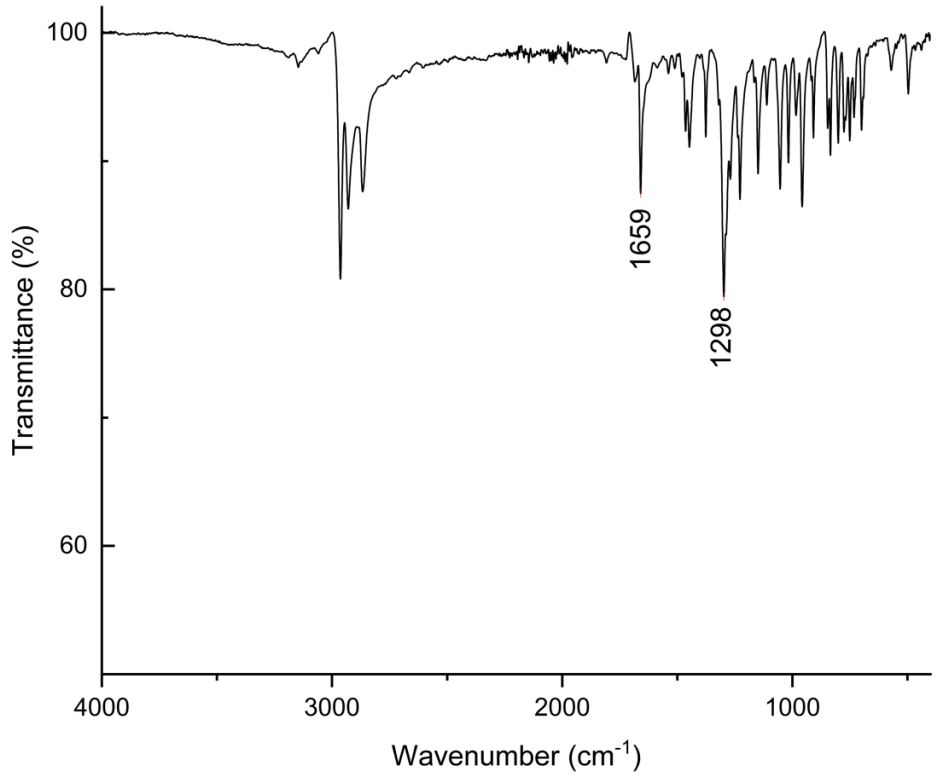

Figure 3.30. FT-IR spectrum of $(Ga(OEP))_2(\mu\text{-BCP})$ (**3**).

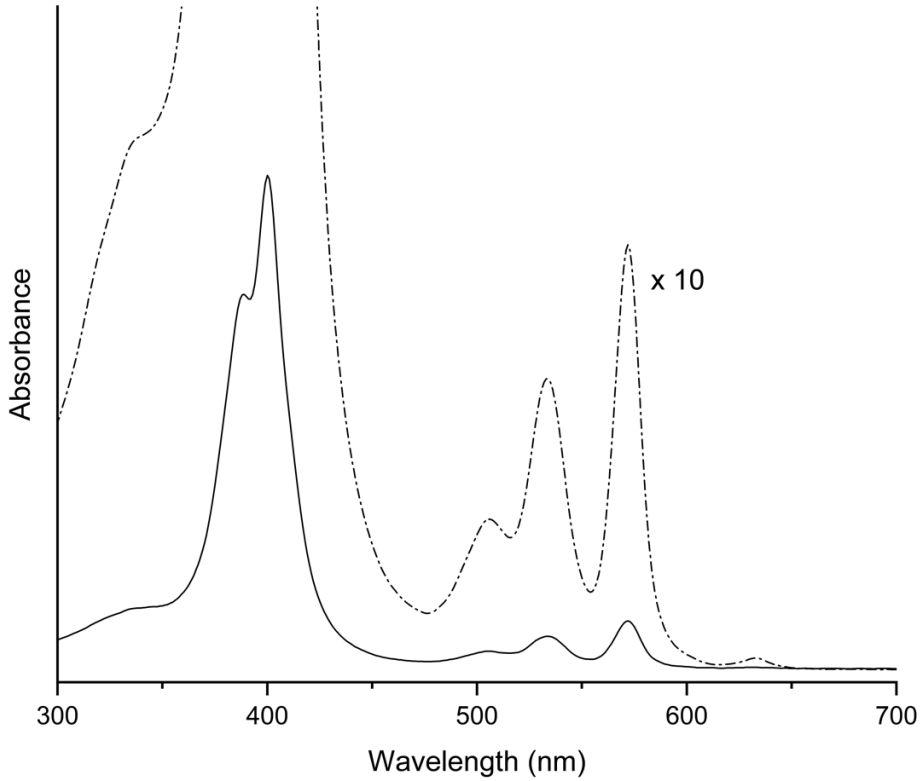

Figure 3.31. UV-Vis spectrum of $(Ga(OEP))_2(\mu\text{-BCP})$ (**3**) in CH_2Cl_2.

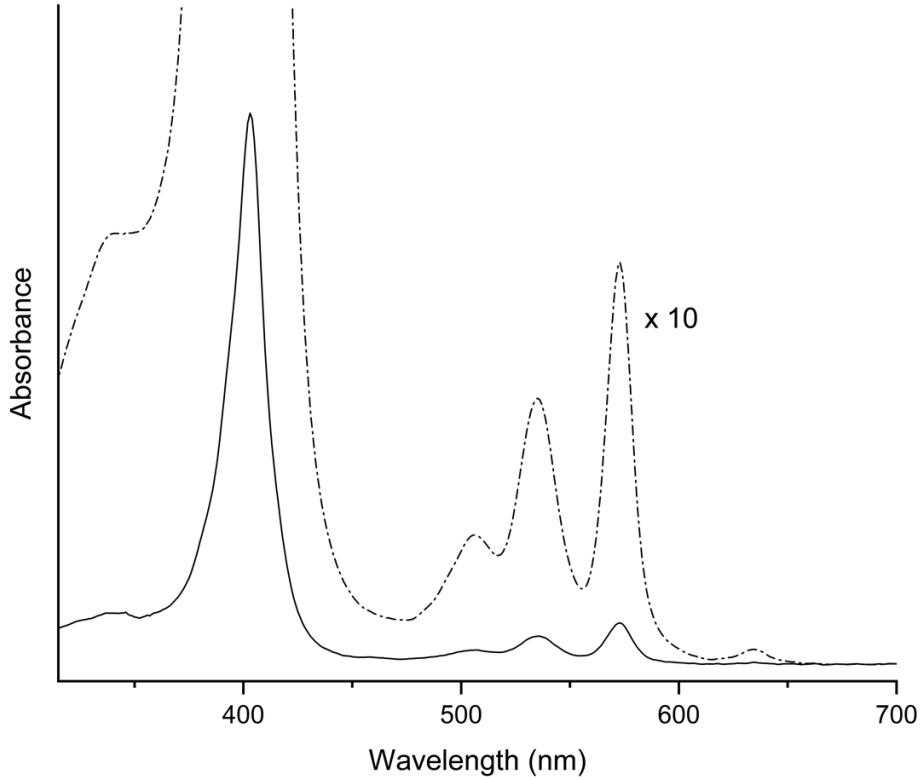

Figure 3.32. UV-Vis spectrum of $(Ga(OEP))_2(\mu\text{-BCP})$ (**3**) in TCB.

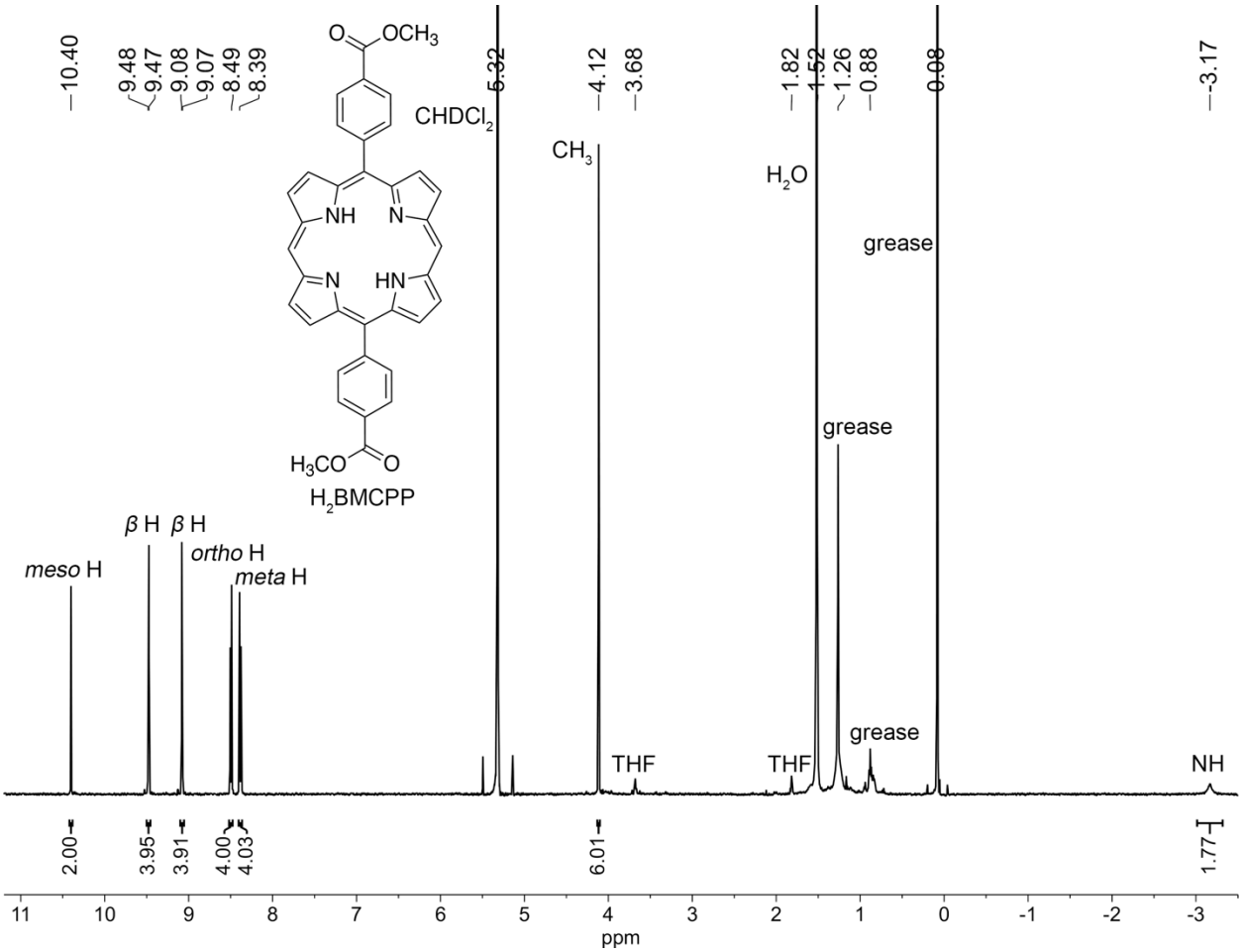

Figure 3.33. ^{1}H NMR spectra (500.13 MHz) of H_2BMCPP in CD_2Cl_2.

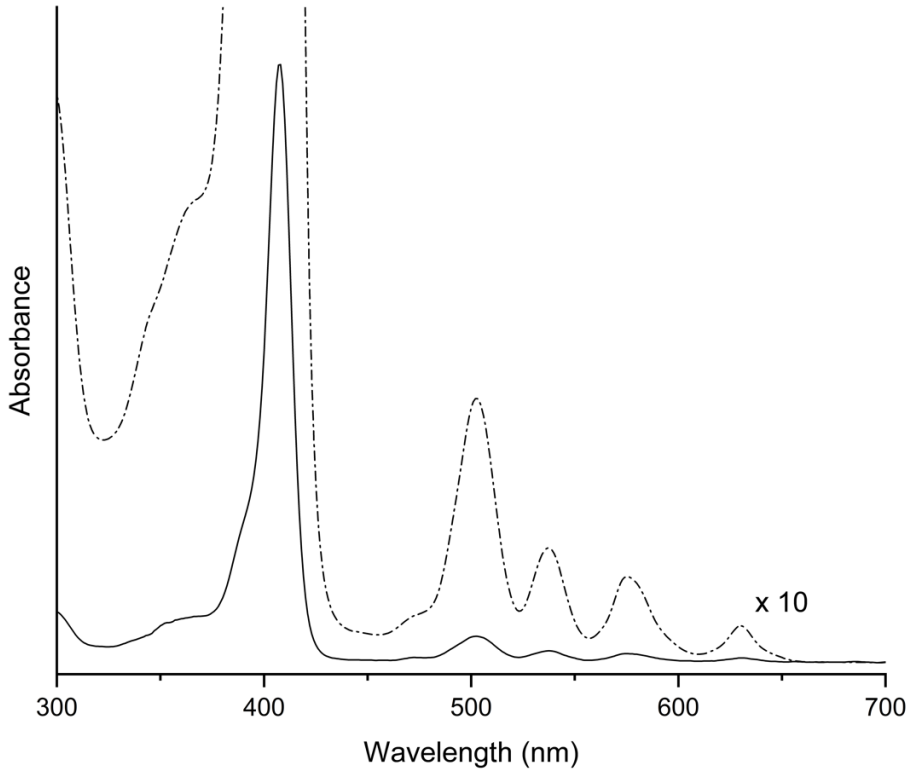

Figure 3.34. UV-Vis spectrum of H_2BMCPP in CH_2Cl_2.

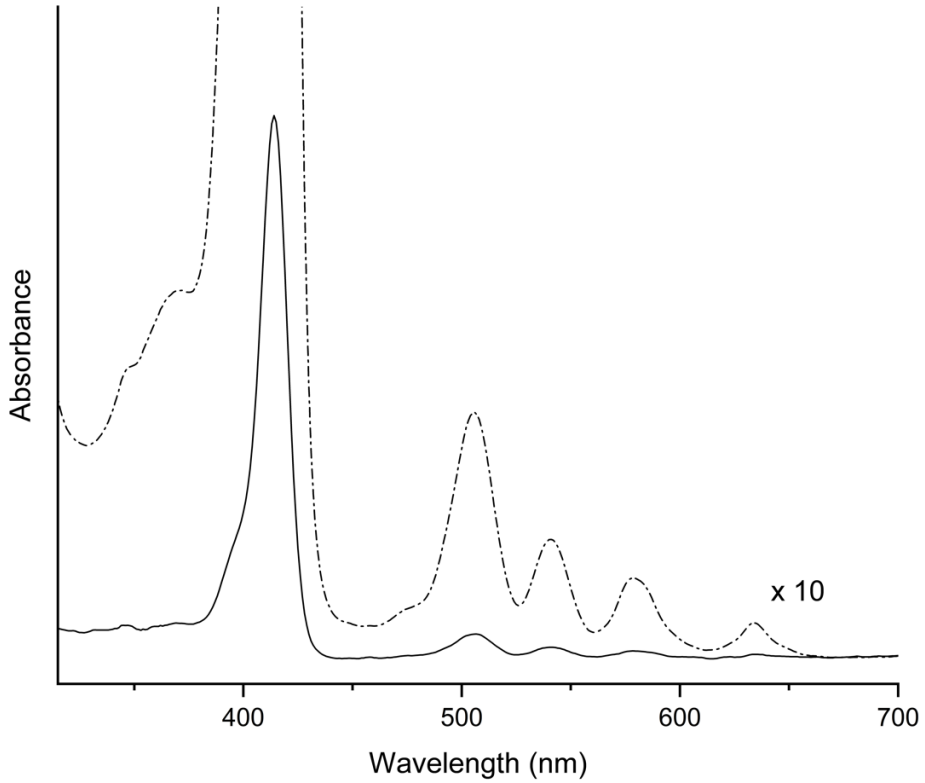

Figure 3.35. UV-Vis spectrum of H_2BMCPP in TCB.

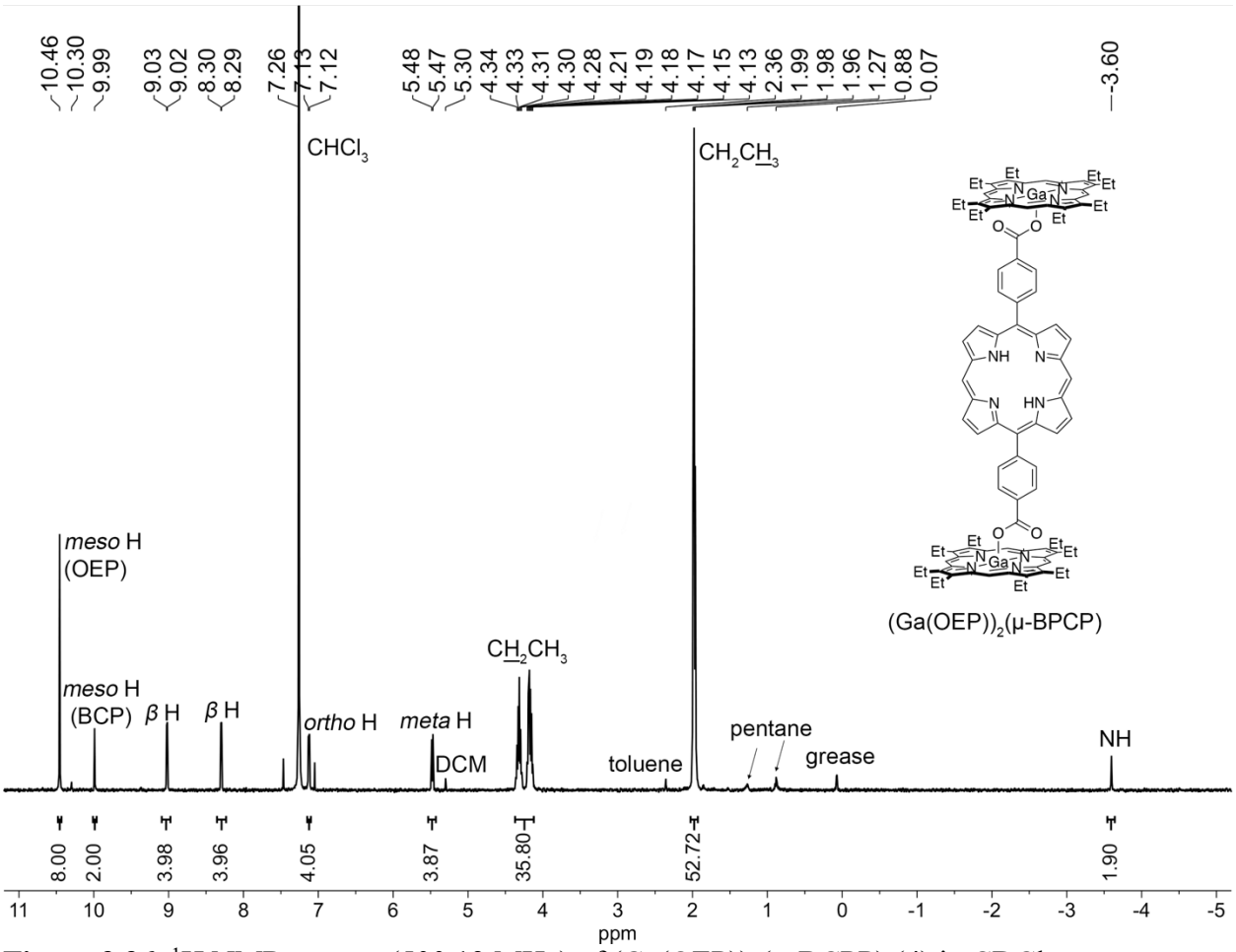

Figure 3.36. ^{1}H NMR spectra (500.13 MHz) of $(Ga(OEP))_2(\mu\text{-BCPP})$ (**4**) in $CDCl_3$.

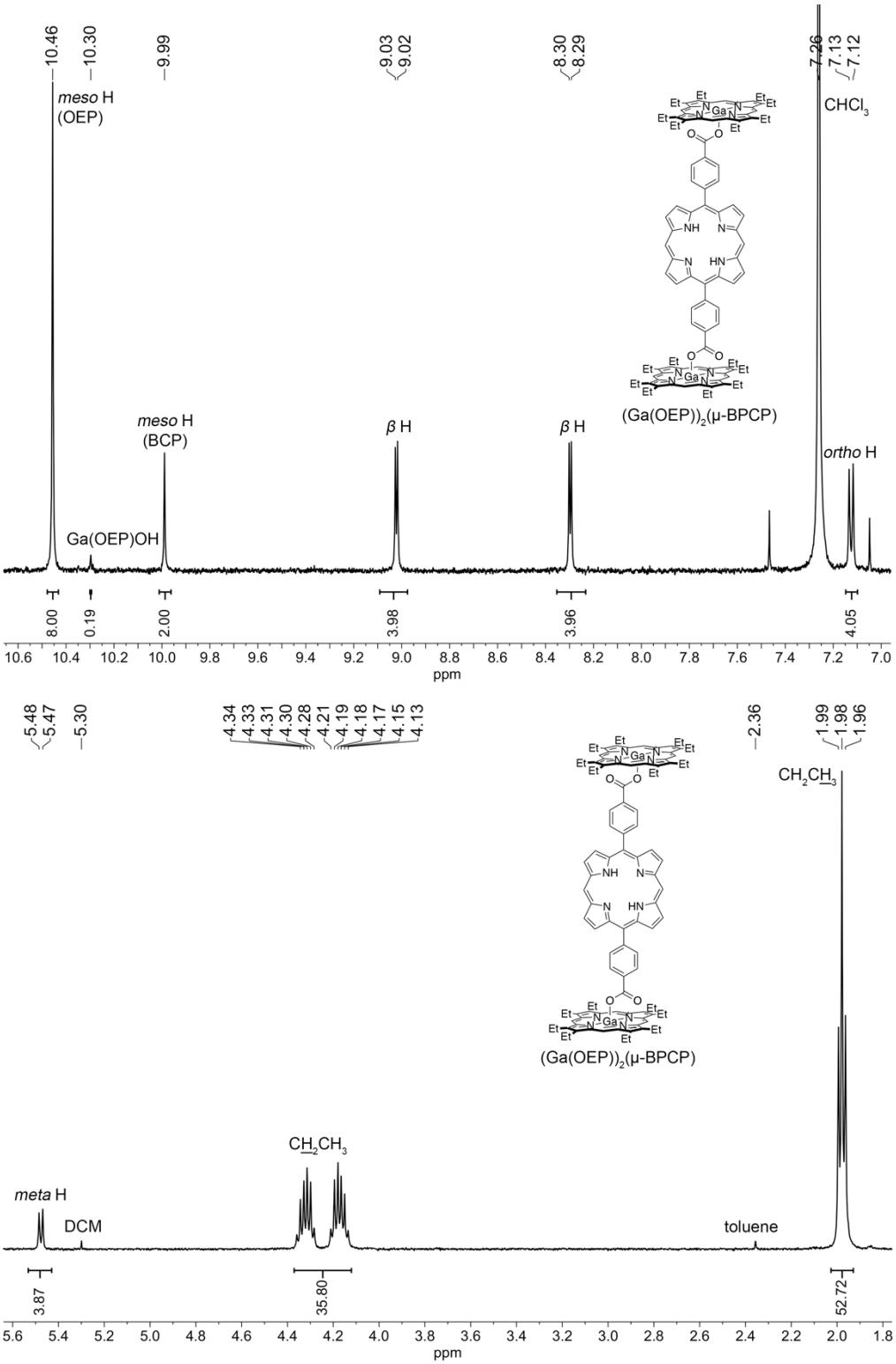

Figure 3.37. Expanded views of ^{1}H NMR spectra (500.13 MHz) of $(Ga(OEP))_2$(μ-BCPP) (**4**) in $CDCl_3$ shown in Figure 3.36.

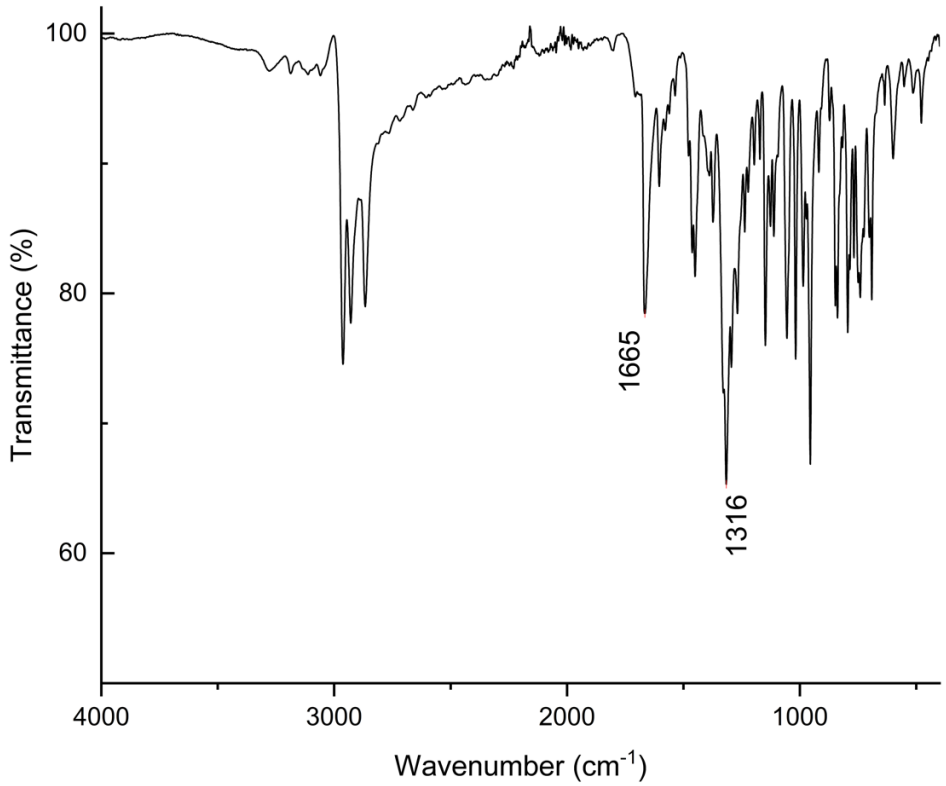

Figure 3.38. FT-IR spectrum of $(Ga(OEP))_2$(μ-BCPP) (**4**).

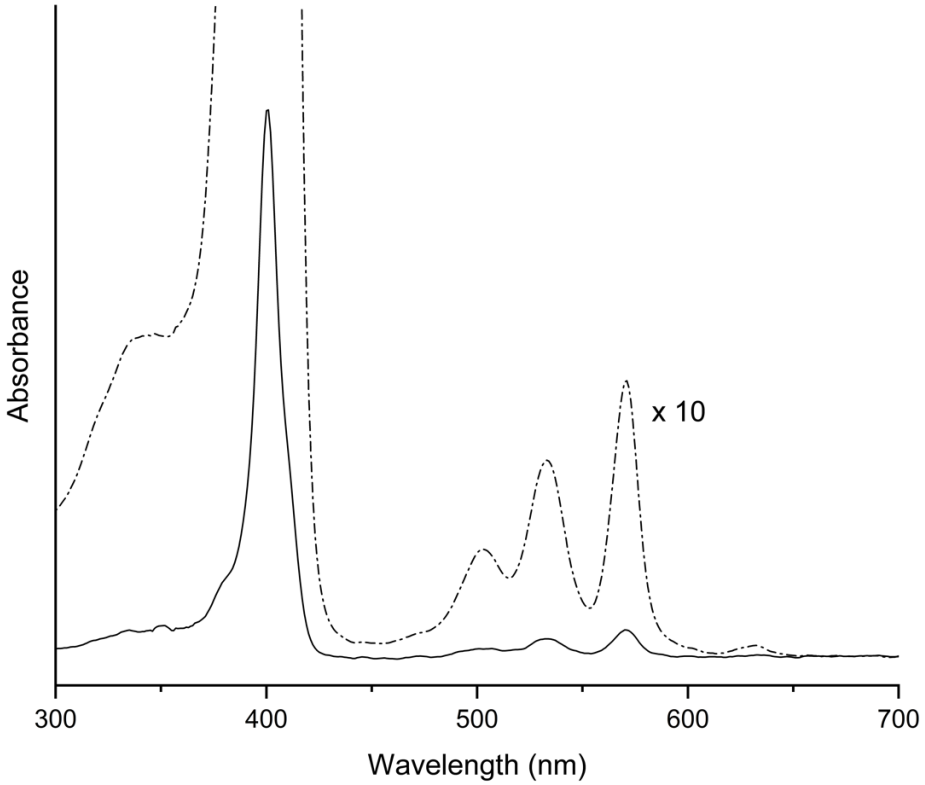

Figure 3.39. UV-Vis spectrum of $(Ga(OEP))_2$(μ-BCPP) (**4**) in CH_2Cl_2.

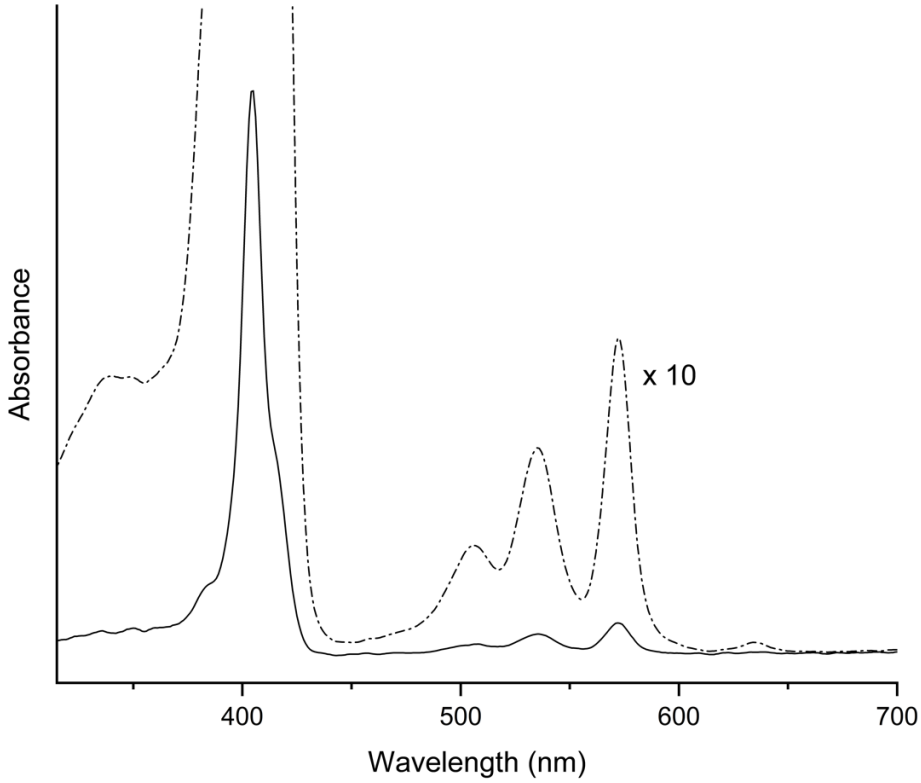

Figure 3.40. UV-Vis spectrum of $(Ga(OEP))_2$(μ-BCPP) (**4**) in TCB.

3.2.5. Single-Crystal X-Ray Diffraction Studies.

3.2.5.1. General Information. X-ray diffraction experiments were performed by Dr. Alexander Filatov. Diffraction data were measured at 100 K on a Bruker D8 VENTURE diffractometer equipped with a microfocus Mo-target X-ray tube (λ = 0.71073 Å) and PHOTON 100 CMOS detector. Data were collected using ω scans to survey a sphere of reciprocal space. Data reduction and integration were performed with the Bruker APEX3 software package (Bruker AXS, version 2017.3-0, 2018). Data were scaled and corrected for absorption effects using the multi-scan procedure as implemented in SADABS (Bruker AXS, version 2014/5).[42] The structure was solved by SHELXT (Version 2018/2)[43] and refined by a full-matrix least-squares procedure using OLEX2[44] (XL refinement program version 2018/3).[45] Crystallographic data and details of the data collection and structure refinement are listed in Table 3.1.

Table 3.1. Crystal Structure Data and Structure Refinement Parameters.

Parameter	**2**	**3**	**4**	**1m**
Empirical formula	$C_{80}H_{92}Ga_2N_8O_4$ • 2 C_4H_8O	$C_{94}H_{100}Ga_2N_{12}O_4$ • 6 $CHCl_3$	$C_{106}H_{106}Ga_2N_{12}O_4$ [a]	$C_{45}H_{53}GaN_4O_4$ • C_7H_8
Formula weight	1513.26	2317.50	1751.46	783.63
Temperature/K	100(2)	100(2)	100(2)	100(2)
Crystal system	triclinic	triclinic	monoclinic	triclinic
Space group	P-1	P-1	$P2_1/n$	P-1
a/Å	12.405(4)	13.569(2)	11.9700(13)	11.5348(15)
b/Å	13.173(4)	14.557(2)	64.065(7)	13.7755(18)
c/Å	13.652(4)	14.720(3)	13.3328(14)	14.289(2)
α/°	67.767(9)	89.692(4)	90	82.776(5)
β/°	68.107(9)	65.031(4)	106.424(3)	66.266(4)
γ/°	77.806(9)	84.204(4)	90	68.785(4)
Volume/$Å^3$	1909.8(10)	2620.1(8)	9807.1(18)	1937.0(5)
Z	1	1	4	2
$\rho_{calc}g/cm^3$	1.316	1.469	1.186	1.344
μ/mm^{-1}	0.766	1.030	0.606	0.760
F(000)	802.0	1190.0	3680.0	828.0
Crystal size/mm^3	0.18 × 0.11 × 0.09	0.283 × 0.084 × 0.076	0.24 × 0.148 × 0.074	0.261 × 0.056 × 0.048
2Θ range for data collection/°	5.078 to 50.148	4.29 to 50.244	4.238 to 50.118	4.394 to 50.33
Index ranges	$-14 \le h \le 14$ $-15 \le k \le 15$ $-16 \le l \le 16$	$-14 \le h \le 16$ $-17 \le k \le 17$ $0 \le l \le 17$	$-14 \le h \le 14$ $-76 \le k \le 76$ $-15 \le l \le 15$	$-13 \le h \le 12$ $-16 \le k \le 16$ $-17 \le l \le 17$
Reflections collected	19679	9246	107110	17814
Independent reflections[b]	6732 [R_{int} = 0.2175, R_{sigma} = 0.2261]	9246 [R_{int} = 0.0736, R_{sigma} = 0.0876]	17300 [R_{int} = 0.2020, R_{sigma} = 0.2397]	6888 [R_{int} = 0.0756, R_{sigma} = 0.0946]
Data / restraints / parameters	6732/60/477	9246/18/626	17300/57/1133	6888/368/565
Goodness-of-fit on F^2 [c]	1.022	1.019	1.026	1.022
Final R indexes [I>=2σ (I)][d,e]	R_1 = 0.0985, wR_2 = 0.1976	R_1 = 0.0715, wR_2 = 0.1580	R_1 = 0.0965, wR_2 = 0.1691	R_1 = 0.0541, wR_2 = 0.1041
Final R indexes [all data][d,e]	R_1 = 0.2080, wR_2 = 0.2478	R_1 = 0.1157, wR_2 = 0.1812	R_1 = 0.2088, wR_2 = 0.2043	R_1 = 0.0932, wR_2 = 0.1178

Table 3.1, continued. Crystal Structure Data and Structure Refinement Parameters.

Largest diff. peak/hole / e Å^{-3}	1.36/–0.84	0.89/–0.54	0.67/–0.81	0.44/–0.41

[a] Additional diffuse contribution to electron density was observed from solvent-filled voids. A solvent mask was calculated and revealed electron count consistent with partial occupancy of roughly 1.8 additional molecules of chloroform per asymmetric unit. [b] $R_{int} = \Sigma \mid F_o^2 - \langle F_o^2 \rangle \mid / \Sigma \mid F_o^2 \mid$. [c] Goodness-of-fit = $[\Sigma [w (F_o^2 - F_c^2)^2] / (n-p)]^{1/2}$; n: number of independent reflections; p: number of refined parameters. [d] $R_1 = \Sigma \mid \mid F_o \mid - \mid F_c \mid \mid / \Sigma \mid F_o \mid$. [e] $wR_2 = [\Sigma [w (F_o^2 - F_c^2)^2] / \Sigma [w (F_o^2)^2]]^{1/2}$

3.2.5.2. Specific Details for Structure Refinement of 2. All atoms were refined with anisotropic thermal parameters. All hydrogen atoms were included in idealized positions for structure factor calculations. Displacement parameter restraints such as SIMU 0.01 0.02 2 O3 > C44 and RIGU O3 > C44 were used for a co-crystallized solvent THF molecule.

3.2.5.3. Specific Details for Structure Refinement of 1m. All atoms were refined with anisotropic thermal parameters. All hydrogen atoms were included in idealized positions for structure factor calculations except that of an oxalate monoanion. In the structure, one of the ethyl groups and the solvent toluene molecule were found to be disordered. The refinement revealed an approximate 1:1 ratio of two parts. The disorder was modelled using appropriate geometric and displacement parameter restraints. The H atom (H4 connected to O4) was observed in the difference Fourier map and refined without imposing geometric restraints.

3.2.5.4. Specific Details for Structure Refinement of 3. All atoms were refined with anisotropic thermal parameters. All hydrogen atoms were included in idealized positions for structure factor calculations except the atom H5 connected to N5 which is refined without imposing restraints. The structure refined as a 2-component twin (as HKLF5) and the refined batch factor BASF = 0.1050(17). After twin refinement, the residual statistics improved from R_1 = 0.0877, wR_2 = 0.2218 for [I>=2σ (I)], R_1 = 0.1421, wR_2 = 0.2453 (all data), and largest diffraction

peak/hole 0.96/-0.59 e Å^{-3} to those listed in Table 3.1: R_1 = 0.0715, wR_2 = 0.1580 for [I>=2σ (I)], R_1 = 0.1157, wR_2 = 0.1812 (all data) and largest diffraction peak/hole 0.89/-0.54 e Å^{-3}.

3.2.5.5. Specific Details for Structure Refinement of 4. The crystal was weakly diffracting. The lowered diffraction power is due to co-crystallized solvents filling the pores and the extremely large unit cell with b > 64 Å. Data were collected using a very long collection time (120 seconds per frame). The solvent mask as implemented in OLEX2 was used. 416 electrons were found in a volume of 1768 Å^3 in 4 voids per unit cell. This is consistent with the presence of about 1.8 chloroform molecules per asymmetric unit. All atoms were refined with anisotropic thermal parameters.

3.2.6. Density Functional Theory Studies. Gas-phase geometry optimization calculations were performed in Gaussian 16.[46] The B3PW91 functional[47-51] with D3 dispersion corrections and Becke–Johnson damping[52] was utilized. A subset of calculations were performed without dispersion corrections, but were otherwise identical. The LANL2DZ effective core potential basis set[53,54] was used for Ga atoms; the 6-31G* basis set was used for all other atoms. Subsequent frequency calculations on the optimized structures revealed no imaginary frequencies, indicating the structures reside at potential-surface minima. Molecular models were built using CrystalMaker software.[55] The molecular orbital energy levels were determined using a single point energy calculation with the keyword **pop=full**; the resulting orbitals were rendered using IQmol software (www.iqmol.org) (isosurface = 0.02).

3.3. Results and Discussion

3.3.1. Synthesis and Characterization of Porphyrin Dimers and 1m. A general concern in syntheses of the type shown in Scheme 3.1 is that an experimental error in the 2:1 proportion of Ga(OEP)(OH) to dicarboxylic acid could lead to formation of Ga(OEP)(κ_1-dicarboxylate-H), if

the acid is in slight excess, or leave unreacted Ga(OEP)(OH), if the amount of acid is slightly deficient, with both side products potentially being difficult to separate from the desired dimer. While syntheses of monomeric porphyrins, such as that of Ga(OEP)(O_2CFc) in Chapter 2, use an excess of the carboxylic acid to ensure complete conversion of Ga(OEP)(OH) to the Ga(OEP)(O_2CR), we chose to explore conditions with a slight excess of Ga(OEP)(OH) for the dimeric syntheses to avoid formation of Ga(OEP)(κ_1-dicarboxylate-H), which was expected to be harder to separate from the dimeric complex than unreacted Ga(OEP)(OH). Based on the above rationale, reactions between the appropriate dicarboxylic acid and 2.1–2.5 equivalents of Ga(OEP)(OH) were employed and found to proceed at room temperature in THF (**1**) or DMF (**2**, **3**, and **4**), with solvent choice depending on the solubility of the diacid, providing the desired dimers in impure form. A light pink precipitate was observed to form as the reactions proceeded, indicative of the decreased solubility of the porphyrin dimers as compared to Ga(OEP)(OH). The crude products were found to be 85%–90% pure by ^{1}H-NMR spectroscopy, which also showed the presence of varying levels of Ga(OEP)(OH), Ga(OEP)Cl, and presumed monomeric Ga(OEP)(κ_1-dicarboxylate-H) derivatives, based on the diagnostic *meso*-H resonances described below. Despite much exploration of stoichiometries and reaction conditions, this initial level of purity could not be improved upon, and so considerable effort was devoted to developing purification procedures.

Removal of these impurities proceeded along several routes that were devised largely based on the varying solubility of **1**, **2**, **3**, and **4**, with particular attention paid to removing monomeric Ga(OEP)(κ_1-dicarboxylate-H) derivatives. The dimeric species are less soluble than the parent porphyrin and other monomeric impurities in all solvents employed during synthesis and purification of the complexes (CH_2Cl_2, $CHCl_3$, toluene, THF, DMF), with their relative solubility

being **1** >> **4** > **2** > **3**. This observation led to a straightforward purification route for **2** and **3**, which involved stirring a suspension of the crude product in CH_2Cl_2 to extract the impurities, followed by filtration and washing with toluene and pentane. ^{1}H-NMR spectra of **2** treated in this way (Figures 3.10 and 3.11) indicated that the purity had been improved to 96%, with the sole impurity being Ga(OEP)Cl. Attempts to further reduce the amount of this impurity by repeating the above treatments did not improve the purity of **2**. For **3**, the ^{1}H-NMR spectrum after treatment indicated a product with a purity of at least 99% (Figures 3.25 and 3.26). A small resonance (< 1% integrated intensity) at ca. 1.97 ppm corresponds to the OEP CH_3 resonance of a monomeric impurity, although it is not diagnostic as to which one. Attempts to treat **4** in a manner similar to **2** and **3** did not effectively remove the Ga(OEP)(κ_1-dicarboxylate-H) impurity due to the relatively higher solubility of **4**, and so an alternative approach was developed. Here, an additional 0.5 equivalent of Ga(OEP)(OH) was added to the crude product dissolved in $CHCl_3$ in order to react with the uncapped monomer impurity. After removal of the $CHCl_3$, the product was washed with toluene, in which **4** is only sparingly soluble, to remove the excess Ga(OEP)(OH). The *meso* region of the ^{1}H-NMR indicated that the material was 96% pure with a 4% Ga(OEP)(OH) impurity; no uncapped monomer remained (Figures 3.36 and 3.37). Attempts to further reduce the amount of Ga(OEP)(OH) impurity were unsuccessful. Compound **1** was recrystallized from CH_2Cl_2 layered with pentane at –40 °C, which resulted in a purity of 97% (Figures 3.3 and 3.4).

The dimeric composition of **1**–**4** was established by ^{1}H-NMR spectroscopy. The strong ring current (diamagnetic anisotropy) of porphyrins significantly affects the chemical shifts of nuclei located above the porphyrin plane, which, in the porphyrin dimers, includes the bridging ligand and the cofacial porphyrin. Thus, the deviations from the typical chemical shifts of the *meso* H, and to a lesser extent, the CH_2 and CH_3 resonances, relative to the typical porphyrin

Ga(OEP)(OH), together with those for the protons of the bridging ligands of **2**, **3**, and **4** relative to the free ligands, provide unique spectral fingerprints for the dimeric structures, as shown in Table 3.2 and Table 3.3. For **2**, **3**, and **4**, the possibility that the spectra could arise from the analogous uncapped monomers is precluded by the chemical shifts of the bridging ligands, which manifest bilateral symmetry about their midpoints in the dimers that would be absent in monomers. Specifically, the chemical equivalence of the C_6H_4 resonances in **2**, the β resonances in **3** and **4**, and the *o*-C_6H_4 and *m*-C_6H_4 resonances in **4** (Table 3.3) confirm the dimeric nature of these complexes; all would be expected to split into two sets of doublets given their varying distances from the plane of the Ga(OEP), as observed for a monomer such as Ga(OEP)(O_2CPh) (Figures 3.17 and 3.18) and in other axially ligated Ga(OEP) complexes.[56] For **1**, which does not have H atoms in the bridge, the dimeric nature is confirmed by the strong downfield shift observed for the porphyrin resonances of **1** as compared to Ga(OEP)(OH). To further confirm this, the uncapped monomeric derivative of compound **1**, Ga(OEP)(O_2CCO_2H) (**1m**), was synthesized. The synthesis proceeded by adding a solution of Ga(OEP)(OH) in THF dropwise to a stirred solution containing a large excess of oxalic acid in THF. The product was isolated from the excess oxalic acid by extracting the porphyrinic materials into CH_2Cl_2. ^{1}H-NMR spectra of **1m** exhibit chemical shifts that are distinct from those observed for compound **1**, with *meso*, CH_2, and CH_3 resonances at 10.37 ppm, 4.20 ppm, and 1.96 ppm, respectively; these are very similar to those of Ga(OEP)(OH) (δ 10.30, 4.16, 1.97; Table 3.2).

Table 3.2. ^{1}H-NMR Chemical Shifts (δ) for OEP for **1**–**4** and Ga(OEP)(OH) in $CDCl_3$.

Nuclei	**1**	**2**	**3**	**4**	Ga(OEP)(OH)
meso (OEP)	9.75	10.12	9.48	10.46	10.30
CH_2	3.89	4.03	3.32	4.25	4.16
CH_3	1.71	1.78	1.52	1.98	1.97

Table 3.3. ^{1}H-NMR Chemical Shifts for Bridging Ligands of **2**, **3**, **4** and Precursors in $CDCl_3$.

	δ (ppm)	
Nuclei (Complex)	Complex	Precursor[a]
C_6H_4 (**2**)	4.00	8.09
meso (**3** / **4**)	10.11 / 9.99	10.38 / 10.38
β1 (**3** / **4**)	8.82 / 9.03	9.70 / 9.45
β2 (**3** / **4**)	6.32 / 8.30	9.47 / 9.06
NH (**3** / **4**)	–4.52 / –3.60	–3.24 / –3.12
ortho (**4**)	7.13	8.44
meta (**4**)	5.48	8.34

[a] Precursor resonances are for dimethyl-terephthalate, H_2BECP,[39] and H_2BMCPP.[41]

Infrared (IR) spectra of **1** (Figure 3.5), **2** (Figure 3.14), **3** (Figure 3.30), and **4** (Figure 3.38) exhibit two stretches corresponding to the ν_{as}(COO) and ν_s(COO) modes of the carboxylate groups ranging from 1676 cm^{-1}–1656 cm^{-1} and 1316 cm^{-1}–1234 cm^{-1}, respectively (Table 3.4). The observation of large energy differences (> 200 cm^{-1}) between the asymmetric and symmetric stretches has previously been suggested to be indicative of a bis(monodentate) κ1:κ1 binding mode in bridging oxalates and of a monodentate binding mode in other carboxylate ligands.[57-60] The absence of stretches in the O–H region confirms the lack of substantial Ga(OEP)(OH) or free diacid in the material. In contrast, the IR spectrum of **1m** (Figure 3.8) exhibits two sets of ν_{as}(COO) and ν_s(COO) stretches along with the characteristic OH stretch at 3300 cm^{-1}, as would be expected given the chemical inequivalence of the ligating COO moieties and pendant COOH, respectively. Other features in the infrared spectra are consistent with those of metalloctaethylporphyrins.[61]

Table 3.4. IR Stretches (cm^{-1}) of ν_{as} (COO) and ν_s (COO) for **1**–**4**.

Compound	ν_{as} (COO) (cm^{-1})	ν_s (COO) (cm^{-1})
1	1676	1234
2	1656	1282
3	1659	1298
4	1665	1316

High-resolution mass spectrometry identified the molecular cation for complexes **2** (Figure 3.14) and **3** (Figure 3.29). For complexes **1** and **4**, no conditions were found under which the

molecular ion could be detected; only the $[Ga(OEP)]^+$ fragment was observed. The dimeric nature of these complexes was further confirmed by single crystal X-ray diffraction (SXRD) for **2**, **3**, and **4**, which are discussed in further detail below. No conditions were found for **1** that led to suitable crystals. The structure of **1m** was also determined (Figure 3.41, Table 3.5) and found to consist of a hydrogen-bonded dimer (*d*(OH···O = 2.765(4) Å), but is otherwise unexceptional.

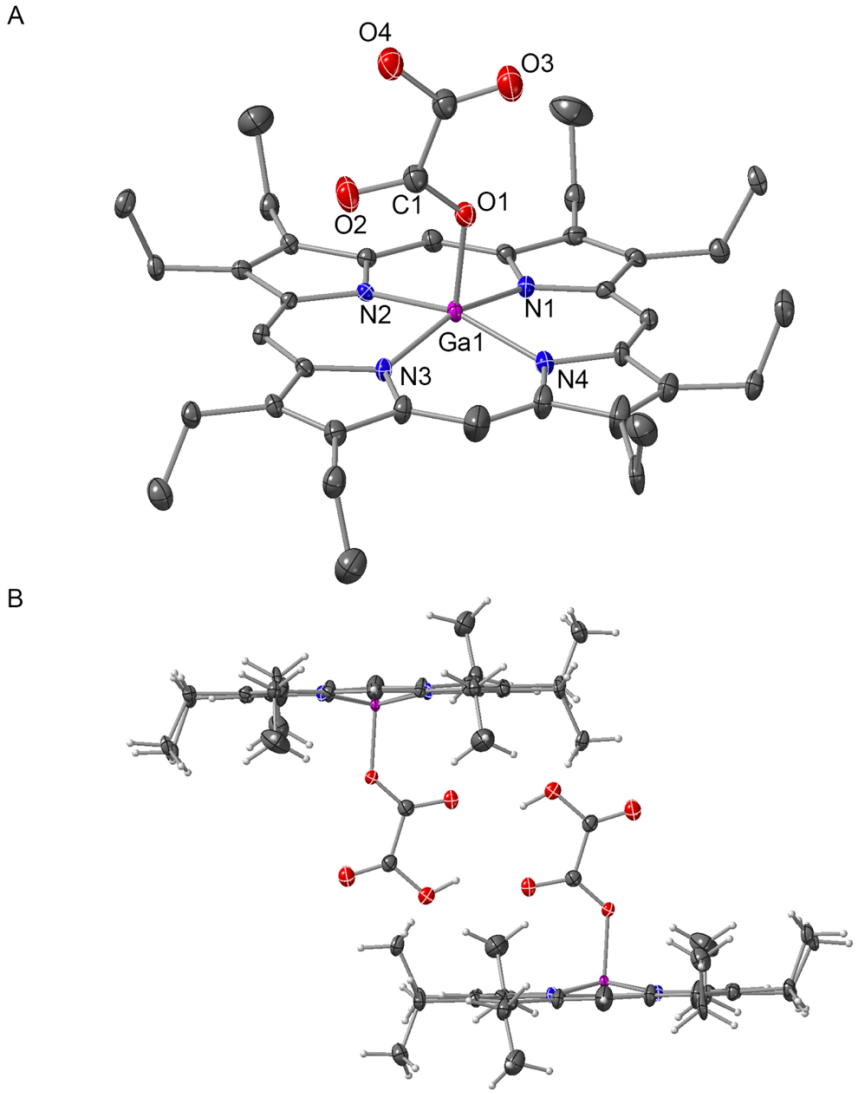

Figure 3.41. Molecular structure of **1m** as determined by X-ray crystallography (50% probability ellipsoids). (a) Molecular unit, hydrogen atoms are omitted for clarity; (b) Hydrogen-bonded dimer of **1m**.

3.3.2. Molecular Structures of Dimeric Porphyrin Complexes in the Solid State, Gas Phase, and Solution.

3.3.2.1. Single-Crystal X-Ray Diffraction Studies of Dimeric Porphyrin Complexes.

Molecular structures for **2**–**4** in the solid-state were investigated by means of single-crystal X-ray diffraction measurements; suitable crystals of **1** could not be obtained despite multiple attempts to grow them. The crystal structures confirm the dimer composition of the compounds but are markedly different from one another. The crystal structure of **2** (Figure 3.42, Table 3.5) conforms largely to expectation, exhibiting a structure in which the Ga(OEP) units are essentially parallel to each other. The terephthalate bridging ligand is approximately planar, although rather than adopting a roughly perpendicular configuration relative to the Ga(OEP) is oriented with the terephthalate and Ga(OEP) planes forming an angle 67.7°. This results in a porphyrin–porphyrin separation of 10.2 Å and an offset between the Ga–O axes. The Ga–O–C–O dihedral angle in **2** is –43.2°, which is near the typical range for M–O–C–O dihedral angles in other metalloporphyrin benzoates[62,63] and halobenzoates[64-66] (5° to 40°), though tungsten and molybdenum porphyrin benzoates have been observed with dihedral angles of 82.0° and 82.7°, respectively.[67]

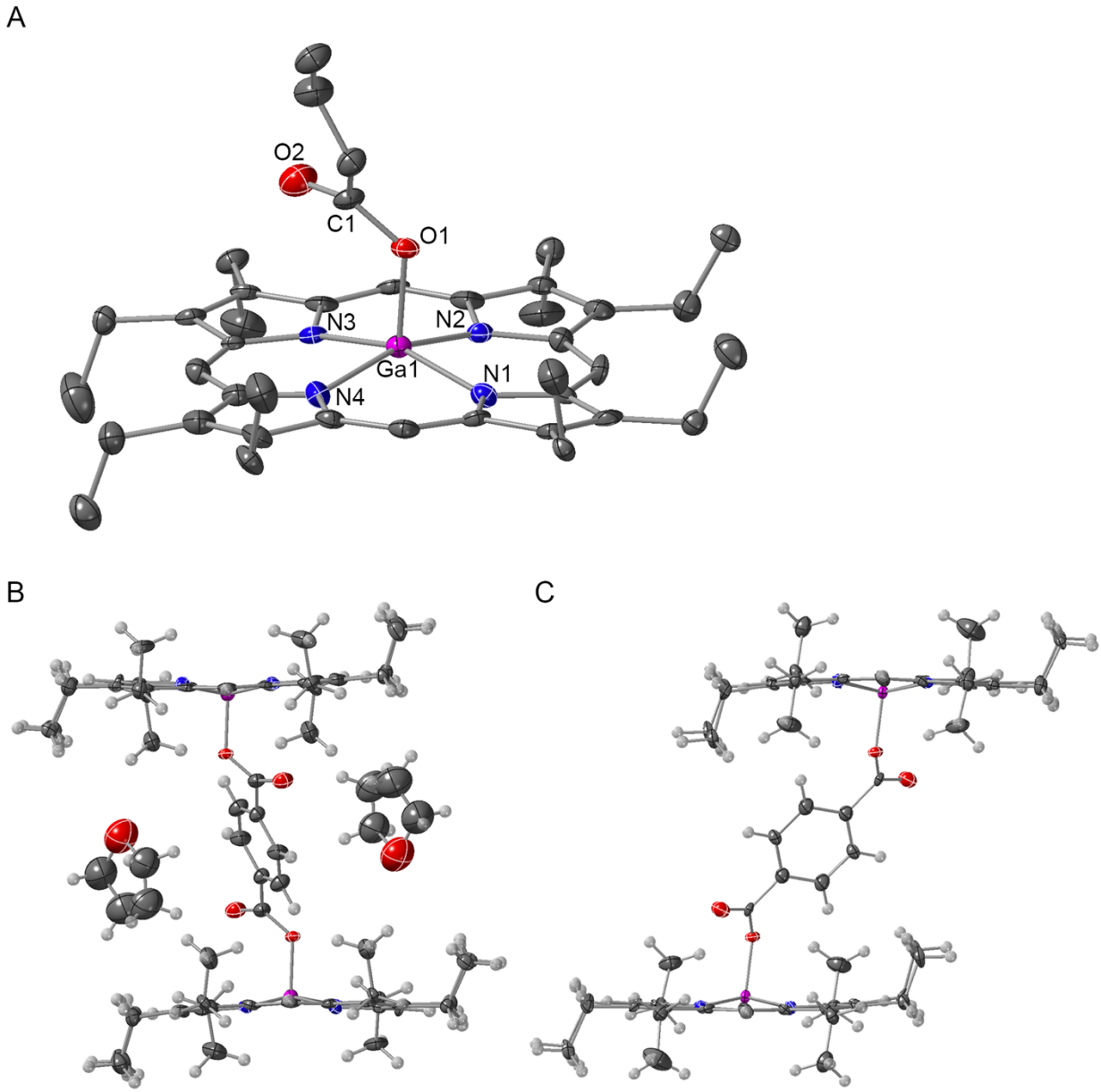

Figure 3.42. Structure of **2** as determined by X-ray crystallography (50% probability ellipsoids). (a) Asymmetric unit, hydrogen atoms are omitted for clarity; (b) Molecular dimer including interstitial THF; (c) Side-view of molecular dimer, interstitial THF omitted for clarity.

The crystal structure of **3** (Figure 3.43) is markedly different from that of **2,** exhibiting a tightly folded conformation with the bridging BCP porphyrin unit nearly parallel to the Ga(OEP) units. The distance between the planes of the Ga(OEP) and BCP units is 3.3 Å, which is van der Waals contact (Figure 3.43c), indicating that intramolecular π–π stacking interactions likely

stabilize this structure. The Ga–O–C–O dihedral angle required to accommodate this folded structure is 136.0°. This conformation of the carboxylate group is relatively unusual; the only porphyrin crystal structures containing a carboxylate axial ligand that we are aware of that possess a similar geometry are the structure and derivatives of β-hematin, Fe and Ga dimers of protoporphyrin IX, where the carboxylate substituents on the periphery of the porphyrins bridge the metal centers.[68-75] The mutual orientation of the Ga(OEP) and H_2BCP porphyrins is also similar to the structure of slipped cofacial porphyrin or corrole dimers containing nitrogenous bases as peripheral substituents on the porphyrin.[76-80] One final noteworthy feature of the structure is that the carboxylate geometry presents an exposed doubly bonded oxygen atom, which engages in hydrogen bonding with the co-crystallized $CHCl_3$ molecules (Figure 3.43b; d(O···H = 2.15 Å)).

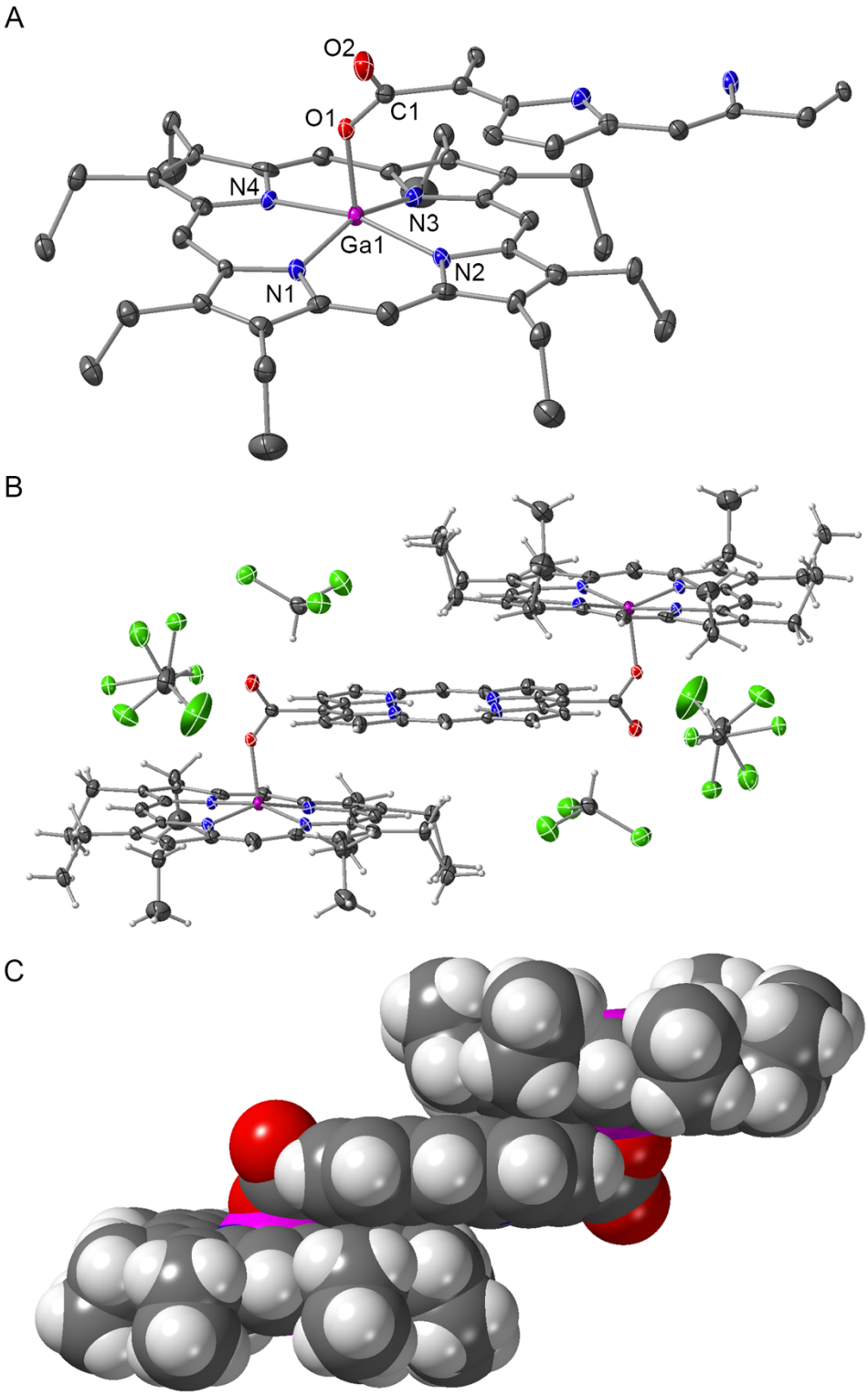

Figure 3.43. Structure of **3**, as determined by X-ray crystallography (50% probability ellipsoids): (a) asymmetric unit, with hydrogen atoms and cocrystallized $CHCl_3$ omitted for clarity; (b) dimer including cocrystallized $CHCl_3$ (c) space-filling model of dimer, cocrystallized $CHCl_3$ omitted for clarity.

The crystal structure of **4** (Figure 3.44) also reveals a folded structure with a much different Ga(OEP)–phenylcarboxylate geometry than **2**, although in this case the phenyl groups of the BCPP unit prevent the close intramolecular π–π stacking interactions between the porphyrin macrocycles found for **3**. The stability of this structure in the solid-state may be derived from intermolecular π–π stacking interactions between BCPP and Ga(OEP) units between adjacent molecules within the crystal (Figure 3.45). The distance between the planes of the H_2BCPP and Ga(OEP) $C_{20}N_4$ macrocycles in adjacent **4** complexes is 3.51 Å, which is near van der Waals contact.

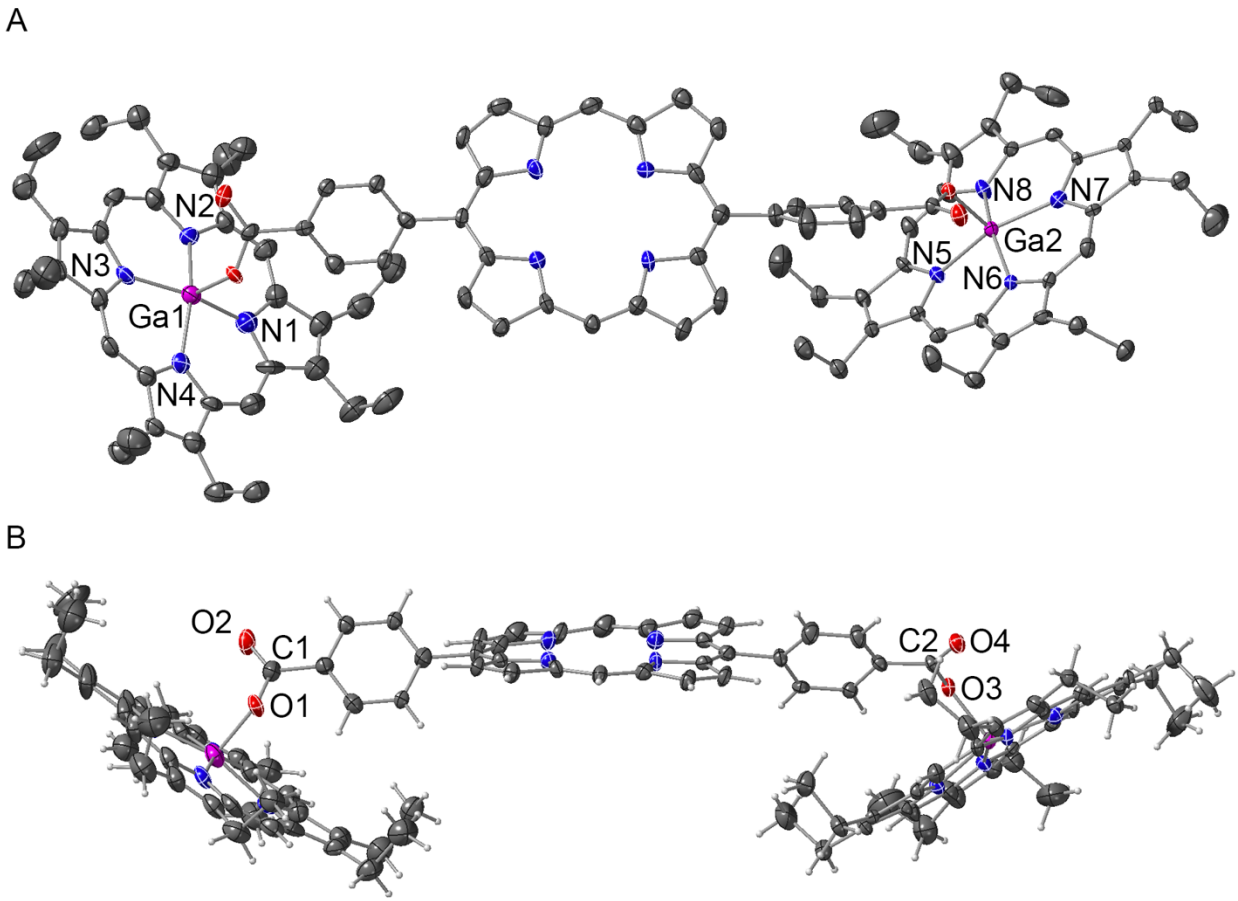

Figure 3.44. Structure of **4** as determined by X-ray crystallography (50% probability ellipsoids). (a) Molecular unit, hydrogen atoms are omitted for clarity; (b) Side-view of molecular unit.

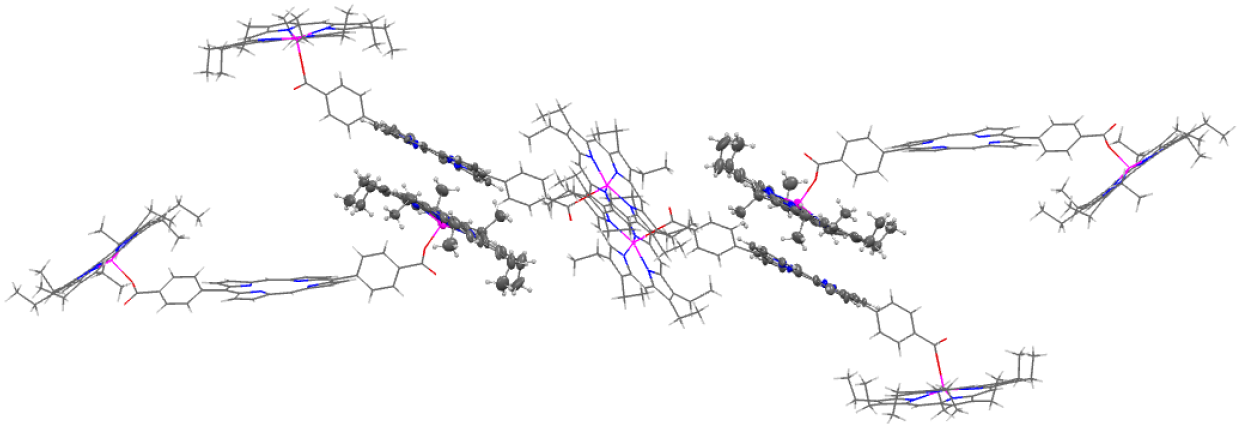

Figure 3.45. Packing of **4** showing intermolecular interactions between BCPP and Ga(OEP) units as determined by X-ray crystallography. The relevant BCPP and Ga(OEP) atoms are shown as 50% probability ellipsoids; all other atoms are shown with a wireframe model for clarity.

Table 3.5. Selected Bond Lengths (Å), Bond Angles (°), and Dihedral Angles (°) for Porphyrin Complexes.

Nuclei	**2**	**3**	**4**[a]	**1m**
Ga(1)–O(1) (Å)	1.889(5)	1.903(4)	1.876(4) / 1.896(4)	1.935(2)
Ga(1)–N(1) (Å)	2.030(7)	2.015(5)	2.043(6) / 2.035(5)	2.025(3)
Ga(1)–N(2) (Å)	2.012(7)	2.027(5)	2.018(5) / 2.015(5)	2.024(3)
Ga(1)–N(3) (Å)	2.024(7)	2.007(5)	1.996(6) / 2.021(5)	2.019(3)
Ga(1)–N(4) (Å)	2.031(7)	2.031(5)	2.012(6) / 2.028(5)	2.031(3)
N(1)–Ga(1)–O(1) (°)	93.1(3)	95.1(2)	93.4(2) / 94.30(18)	97.00(11)
N(2)–Ga(1)–O(1) (°)	101.2(2)	103.13(19)	103.3(2) / 101.16(18)	102.68(11)
N(3)–Ga(1)–O(1) (°)	106.0(2)	106.66(19)	103.4(2) / 105.78(18)	102.10(11)
N(4)–Ga(1)–O(1) (°)	96.2(2)	93.55(19)	95.8(2) / 97.00(19)	95.71(11)
Ga(1)–O(1)–C(1)–O(2) (°)	–43.2(12)	–136.0(6)	54.6(9) / 61.1(8)	5.7(6)

[a] The structure of **4** exhibits inequivalent Ga(OEP)(O_2C) subunits. The second value refers to the bond lengths and angles defined by Ga(2), O(3), N(5–8); the dihedral angle is defined by Ga(2), O(3), C(2) and O(4).

In contrast to the large differences among the overall and carboxylate coordination geometries of **2**, **3**, and **4**, the structures of the Ga(OEP) subunits in these compounds are relatively similar. The gallium atom for all three lies approximately 0.3 Å above the $C_{20}N_4$ plane of the porphyrin (Figure 3.46), consistent with observations for other Ga(OEP)X complexes.[81] In addition, the OEP macrocycles generally exhibit saddle-type distortions to various degrees, most

prominently in **3** and **4**. The planarity of the bridging porphyrin ligands in **3** and **4** is different, with the BCP unit in **3** remaining very flat, and the BCPP unit in **4** adopting a saddle-type distortion.

In sum, these crystals structures confirm the dimeric nature of the complexes and the κ1:κ1 binding mode of the carboxylate ligands but also demonstrate the conformational flexibility of the carboxylate linker, which allows for subtle intra- and intermolecular interactions to dictate the overall orientation of the complexes.

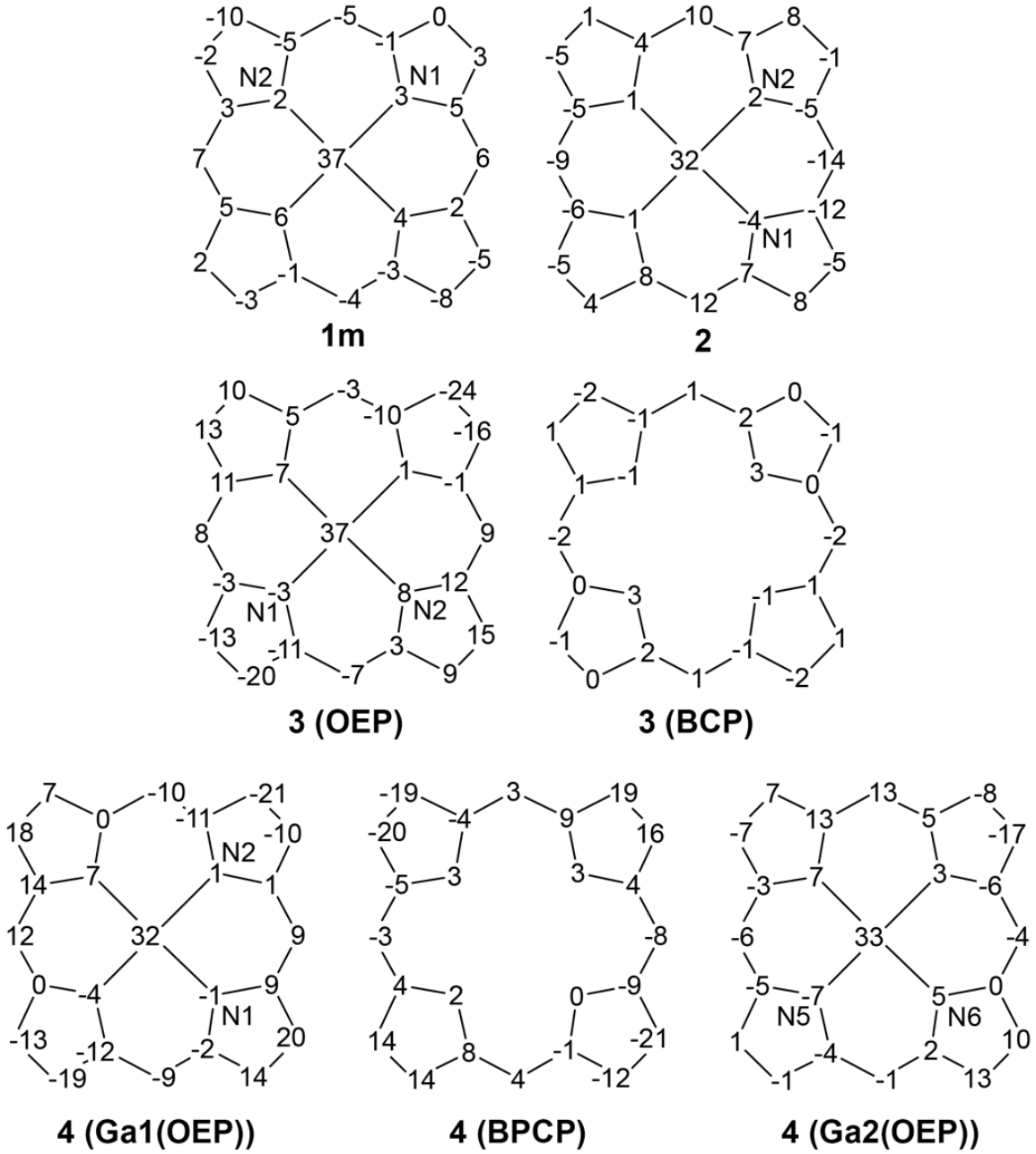

Figure 3.46. Displacements of Ga(OEP) and bridging porphyrin nuclei from the plane-of-best-fit of the $C_{20}N_4$ macrocycles from the crystallographic structure. Displacements are given in units of 0.01 Å.

3.3.2.2. Gas-Phase Structures of Dimeric Porphyrin Complexes Predicted from Density Functional Theory (DFT) Calculations. The molecular structures and conformational flexibility of the dimeric complexes in the gas phase, and of their monomeric counterparts, were

explored by means of DFT calculations, in order to predict the structure of **1** (for which crystallographic data are not available) and better understand the qualitatively different solid-state structures observed for **2**, **3**, and **4**. The optimized geometries of **1** and **2** are shown in Figure 3.47. The calculated structure of **1** exhibits $C_{20}N_4$ planes of the Ga(OEP)s canted at 15.3° with respect to one another. The O(1)–C–C–O(2) dihedral angle is calculated to be –106.9°; this is in reasonable agreement with similar copper, nickel, and zinc tetraaza-macrocycle complexes containing bridging oxalate ligands, which range from 101.7–103.5,[59,82,83] The calculated structure of **2** is similar to the crystal structure; the main differences are that the phenyl plane is perpendicular to the $C_{20}N_4$ porphyrin macrocycles, instead of at an angle of 67.7˚ as seen in the solid state, and the Ga–O–C angle is reduced from 127.7° in the solid-state structure to 122.7° in the calculated structure. These modest differences presumably reflect packing forces present in the crystal.

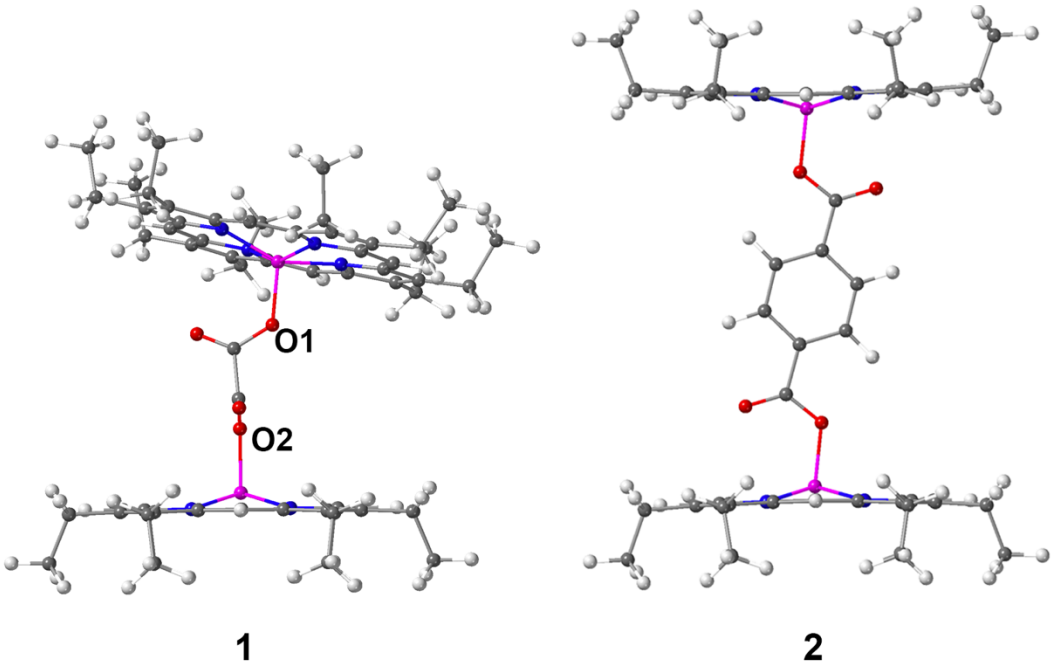

Figure 3.47. Ball-and-stick models of the gas-phase DFT calculated structures of **1** and **2.**

For the calculations of **3** and **4**, the geometry was optimized from two separate starting conformations: one from the crystallographically determined (folded) structure and the other from

a hypothetical extended (unfolded) geometry with the bridging porphyrin approximately perpendicular to the Ga(OEP) units, similar to the optimized structure for **2**. Local minima were found for both the extended and folded conformations of **3** (Figure 3.48) and **4** (Figure 3.49). In both cases, the geometry resembling the observed solid-state structure was calculated to be more stable than the fully extended structure (Table 3.6) when dispersion corrections were included in the calculation. The folded structure was not determined to be even locally stable in the absence of dispersion corrections (see Section 6.2.1). The relative energies of the folded conformers relative to the extended structures are –32.78 kcal/mol for **3** and –9.78 kcal/mol for **4**. The larger stabilization of the folded conformer found for **3** than **4** is almost certainly the result of the close intramolecular π–π stacking interactions in **3**, which are absent in **4**. Despite **4** appearing to be stabilized in the solid state mainly by intermolecular π–π stacking interactions, which do not exist in the gas-phase calculated structure, the folded structure of **4** is still calculated to be lower in energy than the extended structure. This may be a result of interactions between the phenyl groups and the Ga(OEP) macrocycles in this structure, as will be discussed later. The relative energies suggest that **3** and, to a lesser extent, **4** could retain their folded conformations in the gas and, possibly, solution phase.

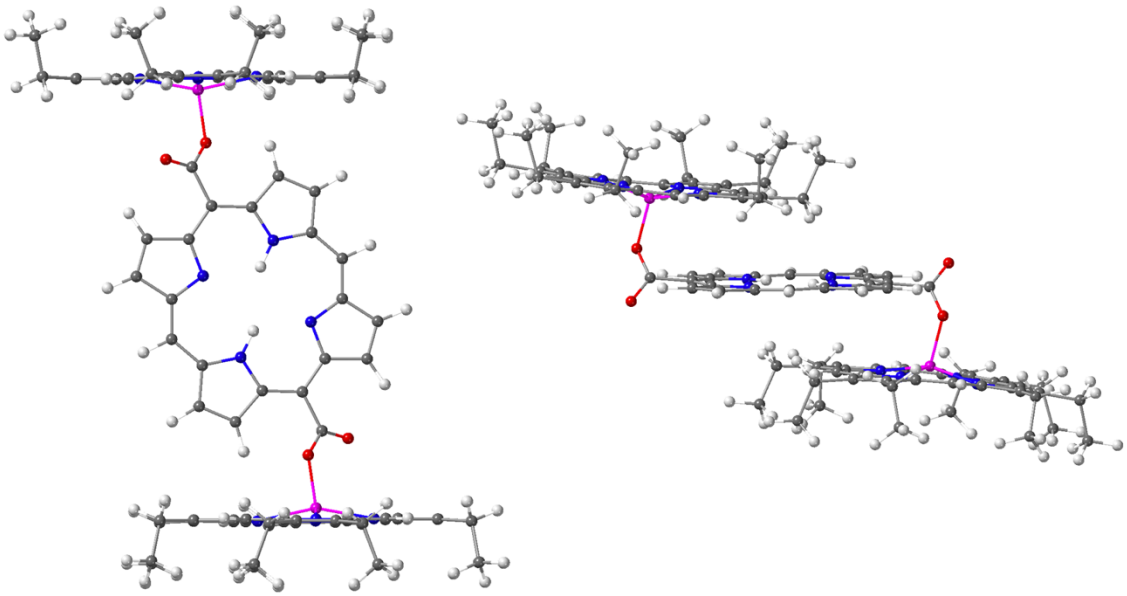

Figure 3.48. Ball-and-stick models of the gas-phase DFT calculated structures of **3** at local minimums in the extended and folded conformations.

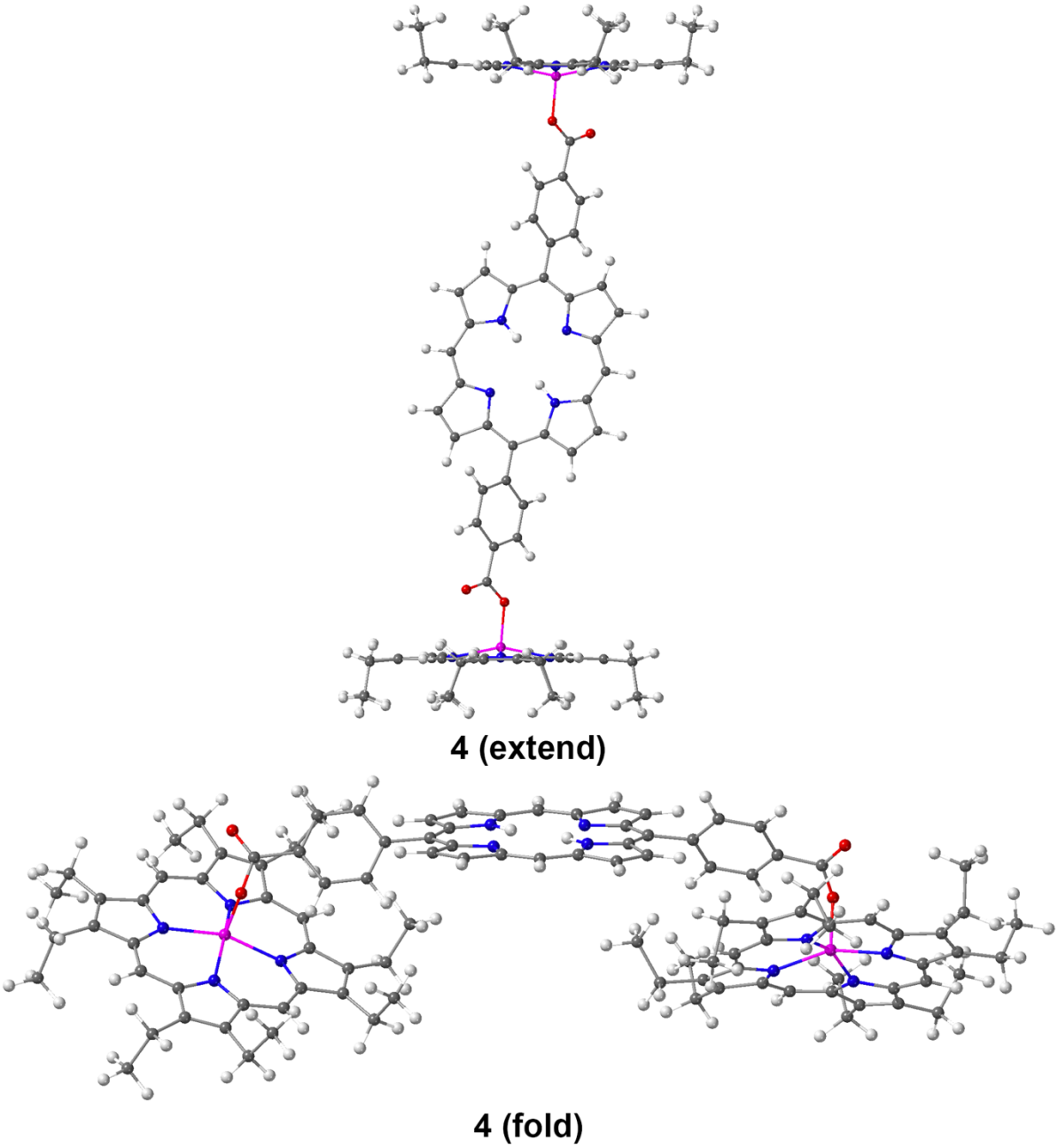

Figure 3.49. Ball-and-stick models of the gas-phase DFT calculated structures of **4**. Local minimums were found in extended (above) and folded (below) conformations.

Table 3.6. Relative Energies of **3** and **4** in Extended and Folded Conformations.

Conformation	**3** [a]	**4** [a]
Extend (kcal/mol)	0.00	0.00
Fold (kcal/mol)	–32.58	–9.78

[a] Energy of extended structures of both **3** and **4** are independently defined as 0.00 kcal/mol. The energies of **3** and **4** are not comparable.

Table 3.7. Selected Calculated (DFT) Bond Lengths (Å), Interporphyrin Distances (Å), Bond Angles (°), and Dihedral Angles (°) for Extended Porphyrin Complexes.[a]

Nuclei	**1**	**2**	**3** (Extend)	**4** (Extend)
Ga–O (Å)	1.860	1.853	1.858	1.857
Ga–N(1) (Å)	2.055	2.045	2.036	2.044
Ga–N(2) (Å)	2.055	2.045	2.045	2.044
Ga–N(3) (Å)	2.071	2.063	2.070	2.060
Ga–N(4) (Å)	2.071	2.063	2.051	2.060
$C_{20}N_4$–$C_{20}N_4$ (Å)[b]	7.6[c]	11.9	15.4	24.3
N(1)–Ga–O (°)	107.8	106.9	108.5	106.4
N(2)–Ga–O (°)	107.4	106.9	105.3	106.4
N(3)–Ga–O (°)	97.5	97.1	94.3	97.1
N(4)–Ga–O (°)	97.9	97.1	97.8	97.0
Ga–O–C–O (°)	2.4	0.0	–18.0	0.3

[a] The Ga(OEP) macrocycles in each porphyrin dimer complex are structurally identical; only one value for each quantity is listed that applies to both Ga(OEP) units. [b] Refers to the distance between the planes of best fit of the $C_{20}N_4$ macrocycles. [c] Reported value is the average distance of the $C_{20}N_4$ nuclei to the plane of best fit of the opposite $C_{20}N_4$ macrocycle.

Table 3.8. Selected Calculated (DFT) Bond Lengths (Å), Interporphyrin Distances (Å), Bond Angles (°), and Dihedral Angles (°) for Folded Porphyrin Complexes.

Nuclei	**3** (Fold)[a]	**4** (Fold)[b]
Ga–O (Å)	1.861	1.845
Ga–N(1) (Å)	2.044	2.038/2.065
Ga–N(2) (Å)	2.052	2.030/2.047
Ga–N(3) (Å)	2.047	2.054/2.039
Ga–N(4) (Å)	2.059	2.051/2.036
$(Ga)C_{20}N_4$–$(H_2)C_{20}N_4$ (Å)[c]	3.4[d]	3.6/4.0[d]
N(1)–Ga–O (°)	94.6	99.9/98.9
N(2)–Ga–O (°)	97.0	99.5/99.6
N(3)–Ga–O (°)	108.5	104.3/105.4
N(4)–Ga–O (°)	105.8	101.3/100.8
Ga–O–C–O (°)	–133.0	90.6/74.2
$(Ga)C_{20}N_4$–$(H_2)C_{20}N_4$ (°)[e]	5.8	35.5/30.5

[a] The two Ga(OEP) macrocycles in **3** (Fold) are structurally identical; only one value for each quantity is listed that applies to both Ga(OEP) units. [b] The two Ga(OEP) macrocycles in **4** (Fold) are inequivalent; two values for each quantity are listed with the first value referring to the Ga(OEP) unit on the left **4** (Fold) of Figure 3.49. [c] Refers to the distance between the planes of best fit of the Ga(OEP) $C_{20}N_4$ macrocycle ($(Ga)C_{20}N_4$) and the H_2BCP or H_2BCPP macrocycle ($(H_2)C_{20}N_4$). [d] Reported value is the average distance of the Ga(OEP) $C_{20}N_4$ nuclei to the plane of best fit of the H_2(BCP) $C_{20}N_4$ macrocycle. [e] Refers to the angle between the planes of best fit of the Ga(OEP) $C_{20}N_4$ macrocycle ($(Ga)C_{20}N_4$) and the H_2BCP or H_2BCPP macrocycle ($(H_2)C_{20}N_4$).

It is clear from crystal structures and the gas-phase calculations that the gallium–carboxylate geometry is highly flexible, such that the energetic penalty for rotating the carboxylate linkers must be smaller than the stabilization gained from other inter- and intramolecular interactions among the porphyrin macrocycles and bridging ligands. To quantify this, the relative energies of three model carboxylate complexes, Ga(OEP)(O_2CH), Ga(OEP)(O_2CCH_3), and Ga(OEP)(O_2CPh), were calculated as a function of Ga–O–C–O dihedral angle (Figure 3.50). Ga(OEP)(O_2CH) and Ga(OEP)(O_2CCH_3) both exhibit a minimum energy with a 0° Ga–O–C–O dihedral angle. The highest energy conformation is only 6–7 kcal/mol higher, at a Ga–O–C–O dihedral angle of 100° for Ga(OEP)(O_2CH) and 110° (with D3 dispersion) or 120° (without D3

dispersion) for Ga(OEP)(O_2CCH_3). The relative energy of Ga(OEP)(O_2CPh) with respect to the Ga–O–C–O dihedral angle is highly sensitive to the inclusion in the calculation of D3 dispersion correction, exhibiting with dispersion a minimum energy at 90° that is 0.8 kcal/mol lower in energy than at 0°. This orientation allows phenyl–porphyrin π–π stacking. The relatively flat relative energy surface calculated for Ga(OEP)(O_2CH) and Ga(OEP)(O_2CCH_3) and the phenyl–porphyrin interactions in Ga(OEP)(O_2CPh) demonstrate how the conformational flexibility of the carboxylate linker allows other intramolecular interactions to dictate the overall molecular structures. This also supports, as suggested above, phenyl–OEP interactions contributing to the lower energy for **4** in the folded structure compared to the extended structure, although the stabilization energy is not directly comparable as the ethyl groups are in different orientations.

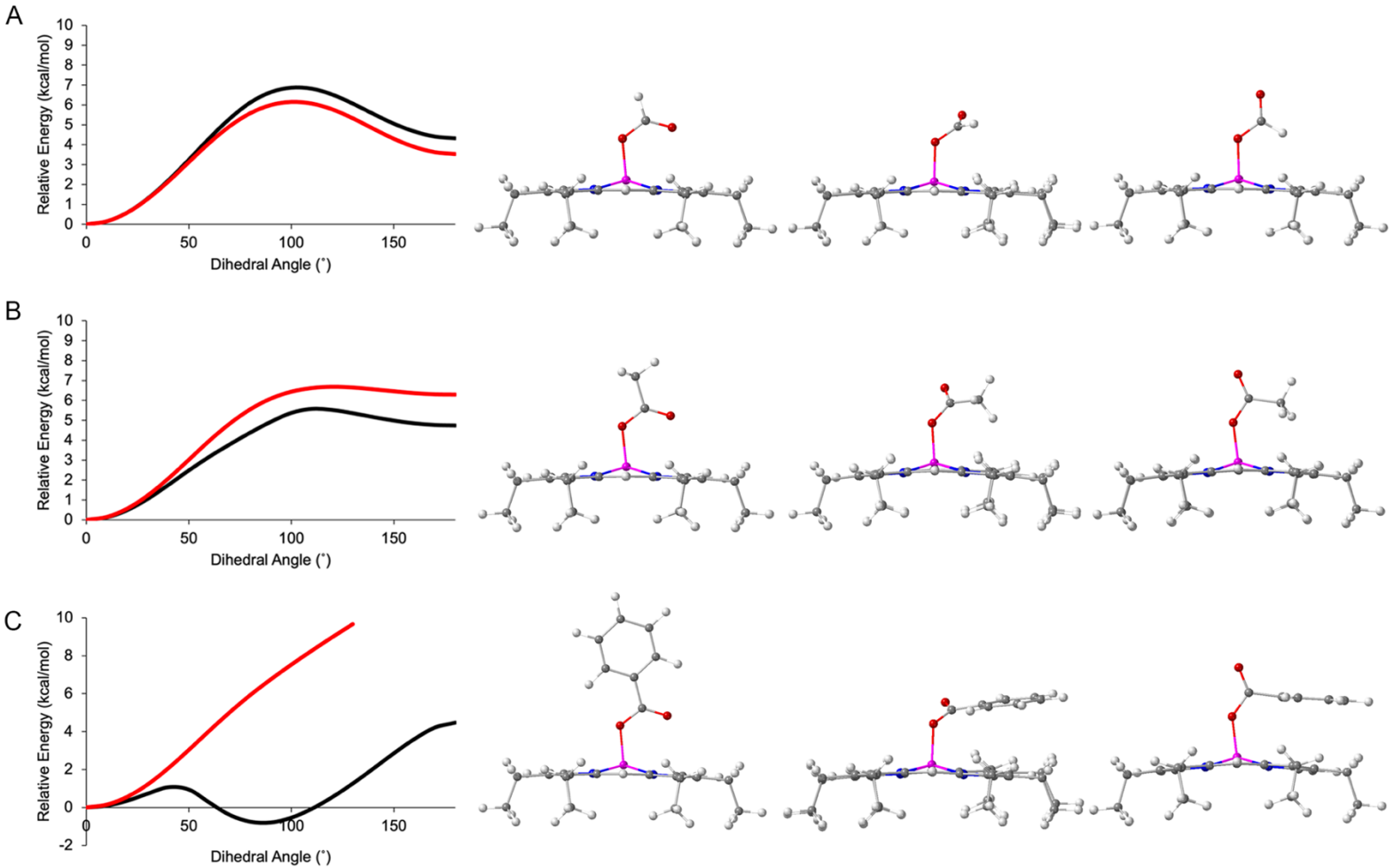

Figure 3.50. Relative energies and optimized geometries of (a) Ga(OEP)(O_2CH); (b) Ga(OEP)(O_2CCH_3); and (c) Ga(OEP)(O_2CPh) scanning the Ga–O–C–O dihedral angle. The graph (left) shows the relative energy of the Ga(OEP)(O_2CR) complex with dispersion corrections (black) and without dispersion corrections (red). Selected optimized geometries are shown with the Ga–O–C–O dihedral angle fixed at 0° (left), the structure with the maximum (Ga(OEP)(O_2CH) and Ga(OEP)(O_2CCH_3)) or minimum (Ga(OEP)(O_2CPh)) energy (center), and fixed at 180° (right).

3.3.2.3. Molecular Structures of Dimeric Porphyrin Complexes in Solution. The diverse solid-state structures exhibited by the porphyrin dimers, particularly the closely folded structure for **3**, and the general conformational flexibility exhibited by the carboxylate linkage, leaves open to question the structure(s) these compounds adopt in solution. This question was probed by ^{1}H-NMR and electronic-absorption spectroscopy.

3.3.2.3.1. Molecular Structures of Dimeric Porphyrin Complexes in Solution as Determined from ^{1}H-NMR Chemical Shifts. A number of empirical models have been developed for porphyrins and other aromatic systems that relate remote ring-current effects on a ^{1}H chemical shift to the distance and angle between the atom and the group with large diamagnetic anisotropy.[84-89] These methods can be used to calculate structural details for compounds in solution on the NMR time scale. In order to gain insight into the solution phase structures of the porphyrin dimers, we adopted a modified version of a point-dipole model that has previously been shown to provide good agreement between calculated and observed chemical shifts in axially coordinated porphyrins of known structure.[84,85] In this model the porphyrin macrocycle is divided into four 5-membered and four 6-membered loops; the ring current is represented by point-dipoles located at the center of each of these eight loops, with one above and one below the plane of the porphyrin, for a total of sixteen point dipoles. For the simplest case of complex **1**, the difference in the chemical shift of a given resonance between a "normal" monomeric porphyrin and a dimer in which the diamagnetic anisotropy of one porphyrin affects the nuclei of the other is provided by Equation 3.1,

$$\Delta\delta_R = \sum_{i=1,8} \frac{\mu_H\left\{1-\frac{3(z_{Por}\pm 0.64)^2}{r_{iR}{}^2}\right\}}{r_{iR}{}^3} + \sum_{j=1,8} \frac{\mu_P\left\{1-\frac{3(z_{Por}\pm 0.64)^2}{r_{jR}{}^2}\right\}}{r_{jR}{}^3} \qquad (3.1)$$

where $\Delta\delta_R$ is the calculated change in chemical shift of proton *R*, μ_H and μ_P are constants proportional to the magnetic moments of the hexagonal 6-membered and pentagonal 5-membered rings, respectively, z_{Por} is the distance from the proton to the plane of the opposing porphyrin, and r_{iR} and r_{jR} are the distances from proton *R* to point-dipole *i* and *j*, respectively (Figure 3.51). Note that the contributions from the porphyrins to which the protons are bonded are not included. The values of $\Delta\delta_R$ are calculated for a given static molecular structure and then averaged for any protons that are observed to be chemically equivalent.

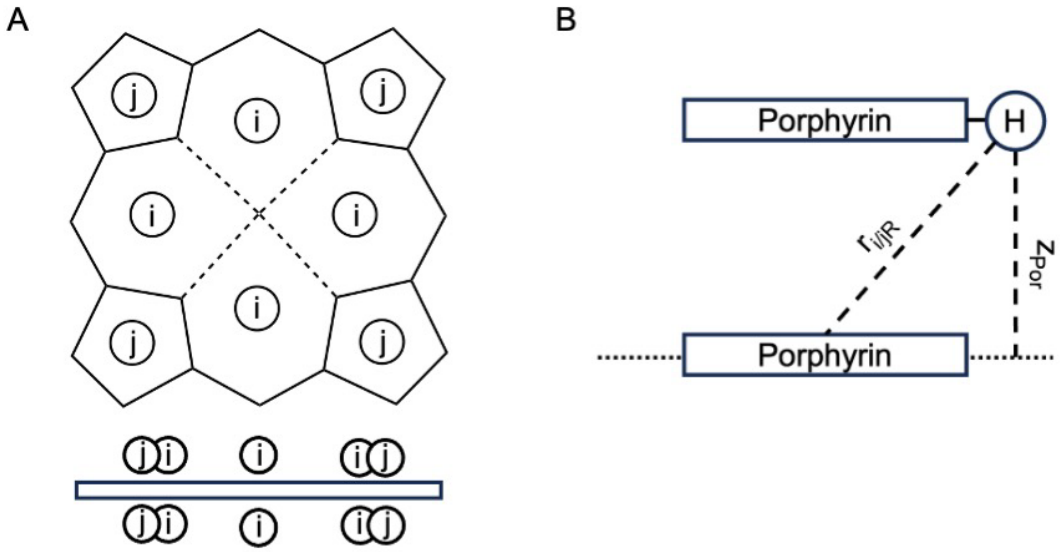

Figure 3.51. Diagram of point dipole model illustrating (a) top-view (above) and side-view (below) of sixteen point dipoles overlaid on a porphyrin macrocycle; (b) schematic of geometric parameters in Equation 3.1 for a system containing two cofacial porphyrins, showing $r_{i/jR}$ as the proton-to-dipole distance and z_{Por} as the proton-to-porphyrin plane distance.

An additional term is required to model complex **2**, because the diamagnetic anisotropy of the terephthalate phenyl ring also perturbs chemical shifts. This is described by Equation 3.2,

$$\Delta\delta_R = \sum_{i=1,8} \frac{\mu_H\left\{1-\frac{3(z_{Por}\pm 0.64)^2}{r_{iR}^2}\right\}}{r_{iR}^3} + \sum_{j=1,8} \frac{\mu_P\left\{1-\frac{3(z_{Por}\pm 0.64)^2}{r_{jR}^2}\right\}}{r_{jR}^3} + \frac{27.6\left\{1-\frac{3(z_{Ph})^2}{r_{PhR}^2}\right\}}{r_{PhR}^3} \qquad (3.2)$$

where z_{Ph} is the distance from the proton to the plane of the phenyl ring, and r_{PhR} is the distance from the proton to the point dipole at the center of the phenyl ring. These considerations also apply

to **3**, which contains three porphyrins, and **4**, which contains three porphyrins and two phenyl rings. Equations 3.3 and 3.4 describe **3** and **4**, respectively,

$$\Delta\delta_R = \sum_{k=1,2}\left[\sum_{i=1,8}\frac{\mu_H\left\{1-\frac{3(z_k\pm 0.64)^2}{r_{iR}{}^2}\right\}}{r_{iR}{}^3}+\sum_{j=1,8}\frac{\mu_P\left\{1-\frac{3(z_k\pm 0.64)^2}{r_{jR}{}^2}\right\}}{r_{jR}{}^3}\right] \quad (3.3)$$

$$\Delta\delta_R = \sum_{k=1,2}\left[\sum_{i=1,8}\frac{\mu_H\left\{1-\frac{3(z_k\pm 0.64)^2}{r_{iR}{}^2}\right\}}{r_{iR}{}^3}+\sum_{j=1,8}\frac{\mu_P\left\{1-\frac{3(z_k\pm 0.64)^2}{r_{jR}{}^2}\right\}}{r_{jR}{}^3}\right]+\sum_{l=1,2}\left[\frac{27.6\left\{1-\frac{3(z_l)^2}{r_{lR}{}^2}\right\}}{r_{lR}{}^3}\right] \quad (3.4)$$

where z_k is the distance from the proton to the plane of the *k*th porphyrin and z_l is the distance from the proton to the plane of the *l*th phenyl ring.

In order to use these equations to determine the solution-phase structures of the compounds, values of μ_H and μ_P are required. These were empirically determined from data for complexes **1** and **2**, which are expected to have less conformational flexibility than **3** and **4**, and by adopting Ga(OEP)(OH) as the reference compound for "normal" ^{1}H-NMR chemical shifts of the Ga(OEP) unit and dimethyl-terephthalate as the reference compound for the terephthalate ligand of **2**. The change to the chemical shift of a proton as a consequence of the dimeric structure is defined by Equation 3.5,

$$\Delta\delta_{Obs.} = \delta_{Obs.} - \delta_{Ref.} \quad (3.5)$$

where $\Delta\delta_{Obs.}$ is the observed change in the chemical shift for a specific proton, $\delta_{Obs.}$ is the chemical shift observed for that proton in the complex, and $\delta_{Ref.}$ is the chemical shift observed for the same proton in the reference compound. Globally fitting the values of $\Delta\delta_{Obs.}$ for **1** assuming the DFT optimized geometry and for **2** assuming the solid-state structure provides values for μ_H and μ_P of 20.0 Å^3 and 17.8 Å^3, respectively. Reasonably good agreement is found between observed and calculated values of $\Delta\delta$ across a wide range in chemical shifts (Table 3.9 and Table 3.10). This indicates that the molecular structures of **1** and **2** in solution, averaged on the NMR time scale, are

very similar to the extended geometries found for **1** in the gas phase from DFT calculations and experimentally for **2** in the solid state, in agreement with the assumptions behind the method. The empirically determined values of μ_H and μ_P are also in good agreement with previously determined values (19.3 Å^3 and 17.1 Å^3, respectively).[84]

Table 3.9. Observed and Calculated Changes in ^{1}H-NMR Chemical Shifts of **1**.

Resonance	**Δδ (Obs.)**	**Δδ (DFT)**
meso	–0.55	–0.47
CH_2	–0.27	–0.26
CH_3	–0.26	–0.25

Table 3.10. Observed and Calculated Changes in ^{1}H-NMR Chemical Shifts of **2**.

Resonance	**Δδ (Obs.)**	**Δδ (SXRD)**
meso	–0.18	–0.18
CH_2	–0.13	–0.20
CH_3	–0.19	–0.25
C_6H_4	–4.09	–4.09

The results for **1** and **2** allow prediction of the ^{1}H-NMR chemical shifts for **3** in different hypothetical geometries. Given the possibility that the closely folded solid-state structure of **3** persists in solution, the ^{1}H NMR spectra were measured in two solvents in which its solubility differs significantly, based on the hypothesis that differences in solubility might reflect differences in structure. These solvents were $CDCl_3$ and 1,2,4-trichlorobenzene-d_3, with the latter being the better solvent for **3** and the solvent used for surface chemistry experiments described in Chapter 4. The values of $\Delta\delta_{Obs.}$ found for the two solvents are distinctly different, as set out in Table 3.11, with the magnitudes in $CDCl_3$ compared with TCB-d_3 being larger for the *meso* (OEP), CH_2 (OEP), CH_3 (OEP) and *β2* (BCP) resonances but smaller for the *meso* (BCP), *β1* (BCP), and NH (BCP) resonances. In $CDCl_3$, the ^{1}H NMR-spectrum of **3** exhibits substantial upfield shifts for all resonances relative to reference values. The calculated values ($\Delta\delta_{Calc}$) for the folded conformer

observed in the crystal structure are of similar direction and magnitude to $\Delta\delta_{Obs.}$ except for *meso* (BCP), which is calculated to have a slight downfield shift ($\Delta\delta_{Obs.} = -0.29$, $\Delta\delta_{Calc} = 0.09$). The calculated shifts for the extended conformer of **3**, which is predicted by DFT to lie much higher in energy than the folded conformer in the gas phase, are in much poorer agreement with the observed values. While the calculation also predicts that the resonances on the H_2BCP subunit should show upfield shifts, the values are significantly different from $\Delta\delta_{Obs.}$, and, in disagreement with observation, predicts Ga(OEP) resonances should exhibit a downfield shift. The poor agreement between observed and calculated shifts for the extended conformer of **3** essentially rules out this being an important structure in $CDCl_3$ solution, whereas the comparatively good agreement between the calculated shifts for the folded conformer and the observed shifts in $CDCl_3$ suggests that **3** has a folded structure in this solvent.

In view of the one notable discrepancy for the folded structure of **3**, between observed and calculated values for *meso* (BCP) ($\Delta\delta_{Obs} = -0.29$, $\Delta\delta_{Calc} = 0.09$), calculations were performed to explore the sensitivity of the shifts to structural perturbations to the folded structure. There is too large a structural parameter space to use these methods to predict a definitive solution structure, but one example of a slightly distorted structure that provides closer agreement with observation is the hypothetical structure denoted Rot. in Figure 3.52, for which the planes of the Ga(OEP) units are rotated 5° further away from the H_2BCP unit than in the crystal structure such that the Ga(OEP) macrocycles are canted 8° with respect to the plane of the H_2BCP. The calculated shifts of this structure (Table 3.11) exhibit an upfield shift for *meso* (BCP), in roughly quantitative agreement with observation, and much better agreement for nearly all other chemical shifts. This is not intended to suggest that this perturbed structure is, in fact, the solution-state structure, but to

illustrate that the average solution structure in $CDCl_3$ is only slightly perturbed from the folded solid-state conformer.

Table 3.11. Observed and Calculated Changes in ^{1}H-NMR Chemical Shifts of **3**.[a]

Resonance	**Δδ Obs. ($CDCl_3$)**	**Δδ Obs. (TCB)**	**Δδ Calc. (SXRD)**	**Δδ Calc. (DFT-Extend)**	**Δδ Calc. (Rot.)**
meso H (OEP)	–0.82	–0.06	–1.03	0.12	–0.92
CH_2 (OEP)	–0.84	–0.19	–1.01	0.04	–0.79
CH_3 (OEP)	–0.45	–0.12	–0.59	0.01	–0.50
meso H (BCP)	–0.29	–1.14	0.09	–0.82	–0.23
β1 (BCP)[b]	–0.85	–1.43	–0.60	–0.94	–0.80
β2 (BCP)[b]	–3.17	–2.93	–3.51	–4.38	–3.53
NH (BCP)	–1.18	–2.19	–1.07	–1.76	–1.36

[a] Values δ_{Ref} used to determine δ_{Obs} for the BCP ligand are for the compound H_2BECP. [b] The H atoms *β1* and *β2* are those on the pyrrole groups nearest and farthest, respectively, from the carboxylate group.

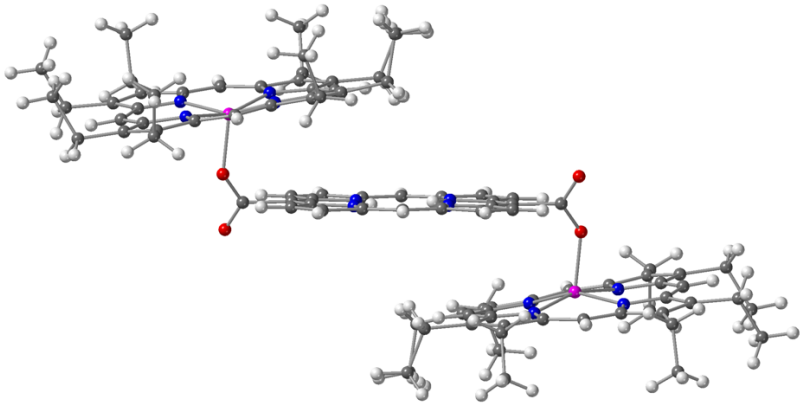

Figure 3.52. Ball-and-stick model of **3** with planes of OEP units rotated 5º away from BCP unit as compared to structure obtained by SXRD. Referred to in Table 3.11 as Rot.

The changes in the chemical shifts of **3** in TCB-d_3 are substantially different than those observed in $CDCl_3$ (Table 3.11), as noted above, with Ga(OEP) protons showing smaller downfield shifts and H_2BCP protons showing larger downfield shifts. These observations are inconsistent with the calculated values for the folded structure and much closer to the calculated shifts for the extended conformer. Of particular note is that the Ga(OEP) chemical shifts are very similar to the reference values, with observed and calculated Δδ values lying in the range –0.20 to

0.20, and sizable observed and calculated shifts for the BCP resonances. Overall agreement between observation and prediction for the extended structure is not as close as that found above for the folded conformer in $CDCl_3$ but the evidence strongly suggests that **3** adopts at least a partially unfolded conformation in TCB. The possibility of temperature-induced conformational changes of **3** in $CDCl_3$ and TCB was investigated by means of variable-temperature ^{1}H-NMR spectroscopy, although only minor changes were observed (Section 6.2.2).

The observed chemical shift differences for **4** in $CDCl_3$ (Table 3.12) are in good agreement with those calculated for the extended conformation predicted by DFT in the gas phase, and in poorer agreement with those calculated for the semi-folded structure observed in the solid state. Particularly diagnostic are the shifts for the Ga(OEP) unit and *meso* and *β2* of the BCPP unit. This result reinforces the observations from the crystal structure that the partial folding appeared to be stabilized by intermolecular porphyrin–porphyrin interactions, which are not present in dilute solution.

Table 3.12. Observed and Calculated Changes in ^{1}H-NMR Chemical Shifts of **4**.[a]

Resonance	**Δδ (Obs.)**	**Δδ (SXRD)**	**Δδ (DFT-Extend)**
meso H (OEP)	0.16	0.06	0.14
CH_2 (OEP)	0.09	–0.02	0.07
CH_3 (OEP)	0.01	–0.18	0.06
meso H (BCPP)	–0.36	0.09	–0.38
meta H (BCPP)	–2.86	–2.37	–2.49
ortho H (BCPP)	–1.31	–1.20	–1.12
β1 (BCPP)[b]	–0.40	–0.66	–0.47
β2 (BCPP)[b]	–0.73	–0.26	–0.88
NH (BCPP)	–0.38	–0.34	–0.58

[a] Values δ_{Ref} used to determine δ_{Obs} for the BCPP ligand are for the compound H_2BMCPP. [b] The H atoms *β1* and *β2* are those on the pyrrole groups nearest and farthest, respectively, from the carboxylate group.

In conclusion, interpretation of the ^{1}H-NMR chemical shifts indicates that **1**, **2**, and **4** adopt time-averaged extended structures in solution, whereas **3** is significantly folded in $CDCl_3$ solution and largely extended in TCB solution.

3.3.2.3.2. Molecular Structures of Dimeric Porphyrin Complexes in Solution Probed by Electronic-Absorption Spectroscopy. In general, the UV-vis spectra of porphyrin compounds exhibit absorption bands with characteristics that are specific to the porphyrin substituents and the presence and identity of the metal center, and which are known to be perturbed in specific ways by intermolecular porphyrin-porphyrin interactions such as those in solution-phase aggregates and condensed phases. Thus, the UV-vis spectra of **1**–**4** can provide insight into the solution-phase structures of the compounds that complements those gleaned from ^{1}H-NMR spectroscopy. These studies are also essential background for photoluminescence measurements described later in this chapter.

The expectation from the NMR studies is that the electronic spectra of **1**, **2**, and **4** should be consistent with these compounds possessing extended structures in solution, whereas those for **3** may be solvent dependent owing to the different structures present in $CDCl_3$ (and similar solvents) and TCB. This expectation is upheld. The basis for making these assessments is to compare the UV-Vis spectra of the dimeric complexes with those for mono-porphyrin model compounds to identify any changes associated with the dimer structure. All UV-Vis features are summarized in Table 3.13. The spectra of **1** and **1m** (Figure 3.53) are very similar to each other and to those of other Ga(OEP)X complexes,[90,91] displaying prominent Q-bands ($S_0 \rightarrow S_1$) at identical wavelengths (570, 532, and 499 nm) with comparable intensity patterns. The Soret band ($S_0 \rightarrow S_2$) of **1** is slightly blue shifted (by 4 nm) compared to the Soret band of **1m**. Cofacial porphyrin dimers tethered through organic peripheral meso or β linkages are also reported to

exhibit blue shifted Soret bands compared with their monomer subuits.[92-99] While the shift for **1** is relatively small compared to the tethered cofacial porphyrin dimers (8–21 nm), this is reasonable because the porphyrin–porphyrin separation in **1** (7.6 Å) is much larger than those in the tethered porphyrin dimers (4.3 to ~6.3 Å).[93] The UV-Vis spectrum of **2** is similarly consistent with an extended structure that lacks porphyrin–porphyrin interactions, based on the fact that its Q and Soret bands are nearly superimposable with those of the monomeric model compound Ga(OEP)(O_2CPh) (Figures 3.54 and 3.55), in both CH_2Cl_2 and TCB.

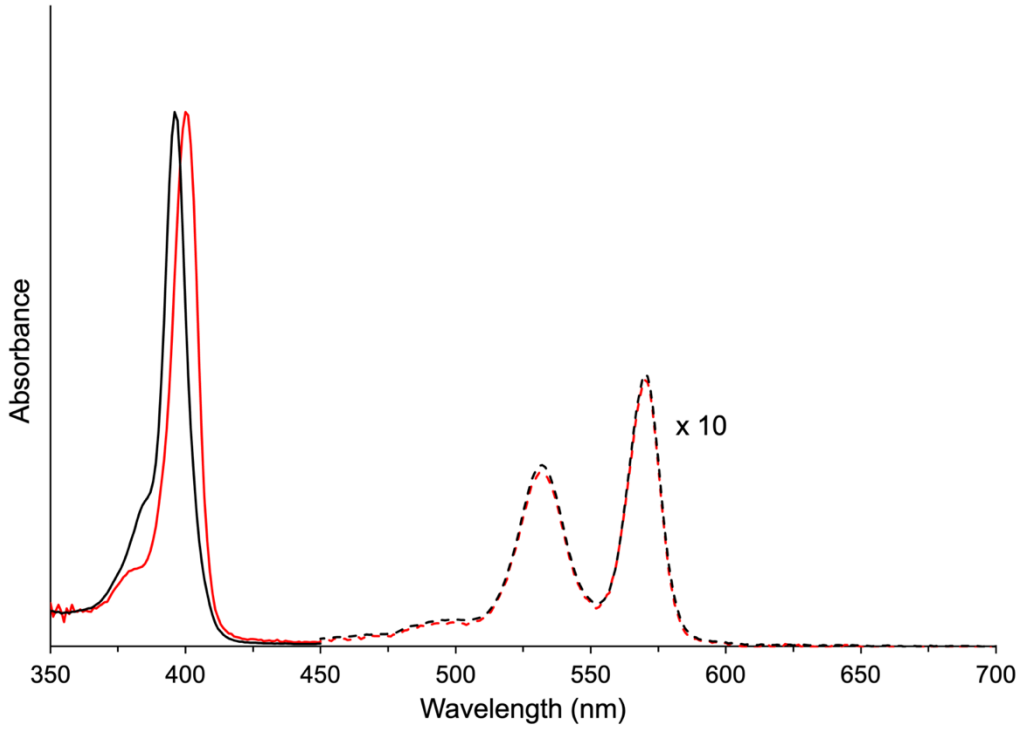

Figure 3.53. Overlay of UV-Vis spectrum of **1** (black) and **1m** (red) in CH_2Cl_2.

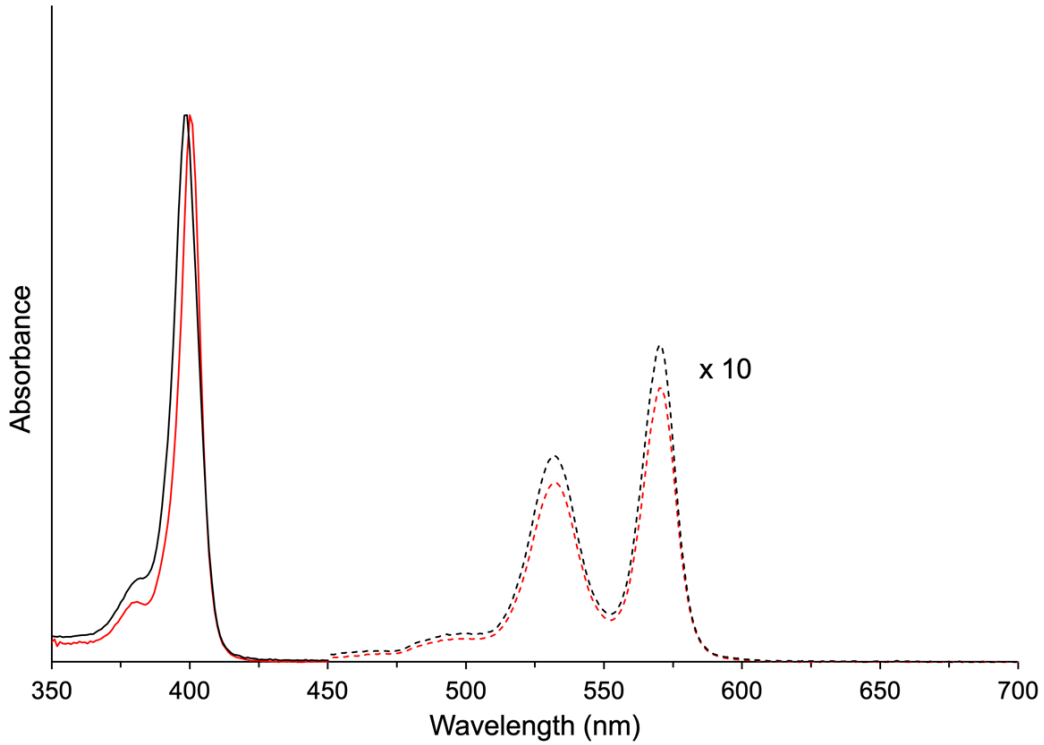

Figure 3.54. Overlay of UV-Vis spectrum of **2** (black) and Ga(OEP)(O_2CPh) (red) in CH_2Cl_2.

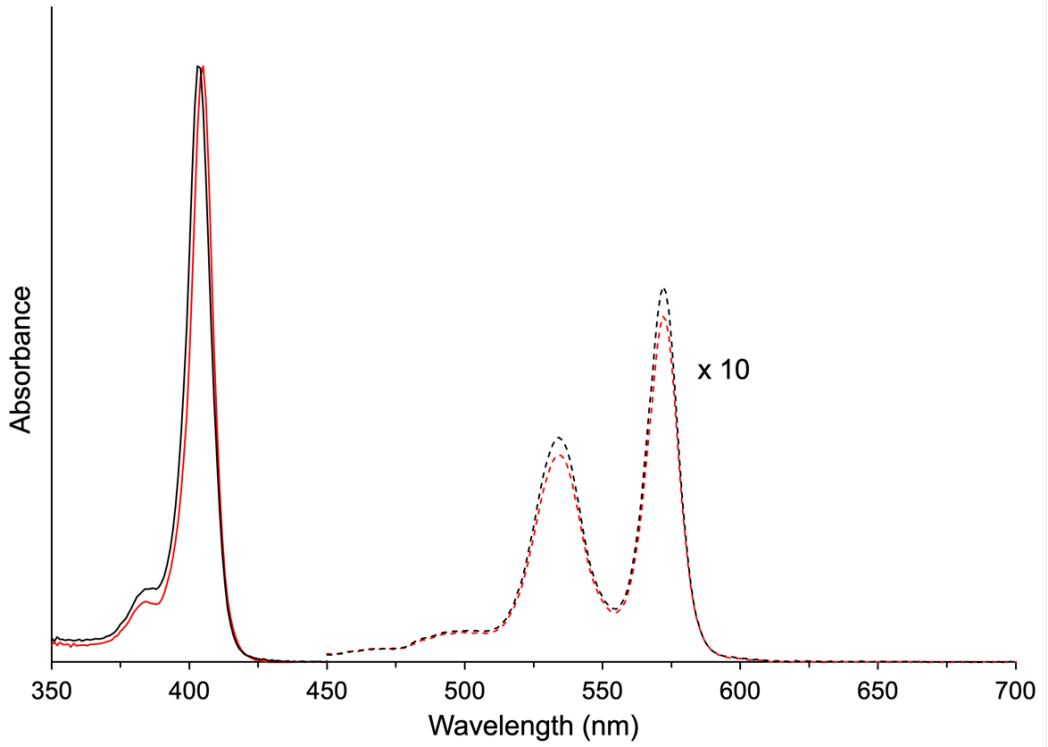

Figure 3.55. Overlay of UV-Vis spectrum of **2** (black) and Ga(OEP)(O_2CPh) (red) in TCB.

The UV-Vis spectra of **4** in CH_2Cl_2 and TCB are also fully consistent with this compound possessing an extended structure. The comparison to model compounds is somewhat less straightforward than for **1** and **2** because the BMCPP linker in **4** is formally a dicarboxylate dianion whereas its organic models are neutral. Nonetheless, fitting the spectrum of **4** as a sum of the nominal subunits Ga(OEP)(O_2CPh) and H_2BMCPP, with the relative weights determined by fitting to the Q-band region (450 nm–700 nm), provides fairly good agreement, though a very small reduction in the intensity of the Soret bands with respect to the Q-bands is observed in CH_2Cl_2 (Figure 3.56; spectrum in TCB, Figure 3.57). UV-Vis spectra of multi-porphyrin systems that are approximately the sum of the components are typical of orthogonal porphyrin dimers.[28,100,101] This observation is in agreement with the solution structure based on the ^{1}H-NMR data and further suggests that **4** is close to the extended complex in solution.

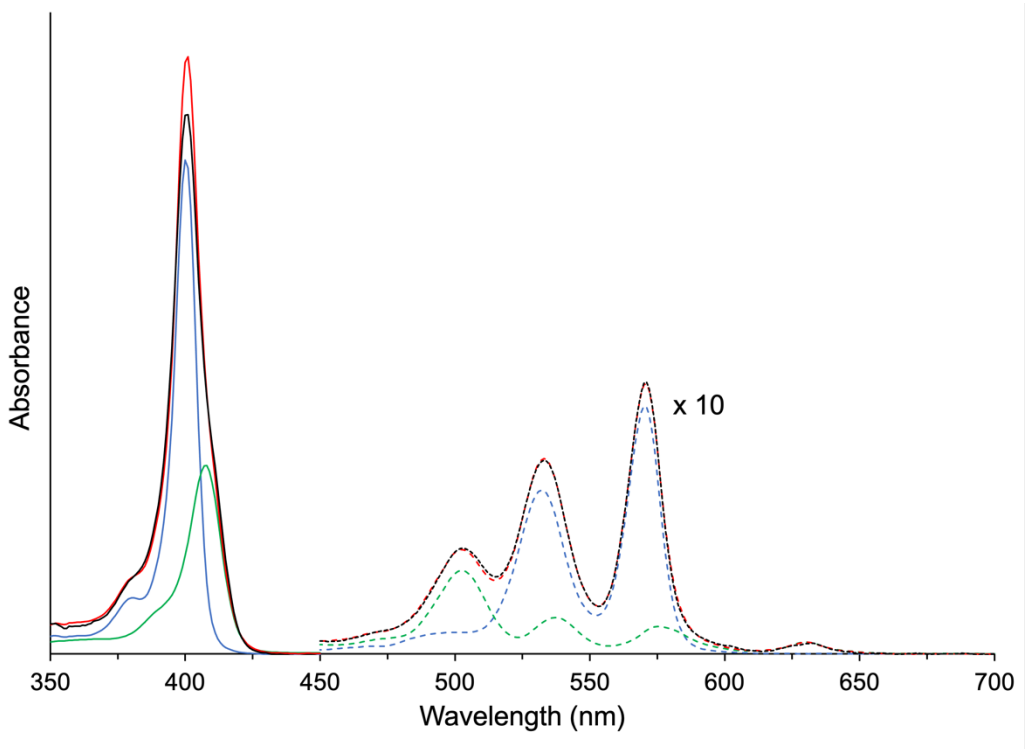

Figure 3.56. Overlay of UV-Vis spectrum of **4** (black), Ga(OEP)(O_2CPh) (blue), H_2BMCPP (green), and the sum of Ga(OEP)(O_2CPh) and H_2BMCPP (red) in CH_2Cl_2.

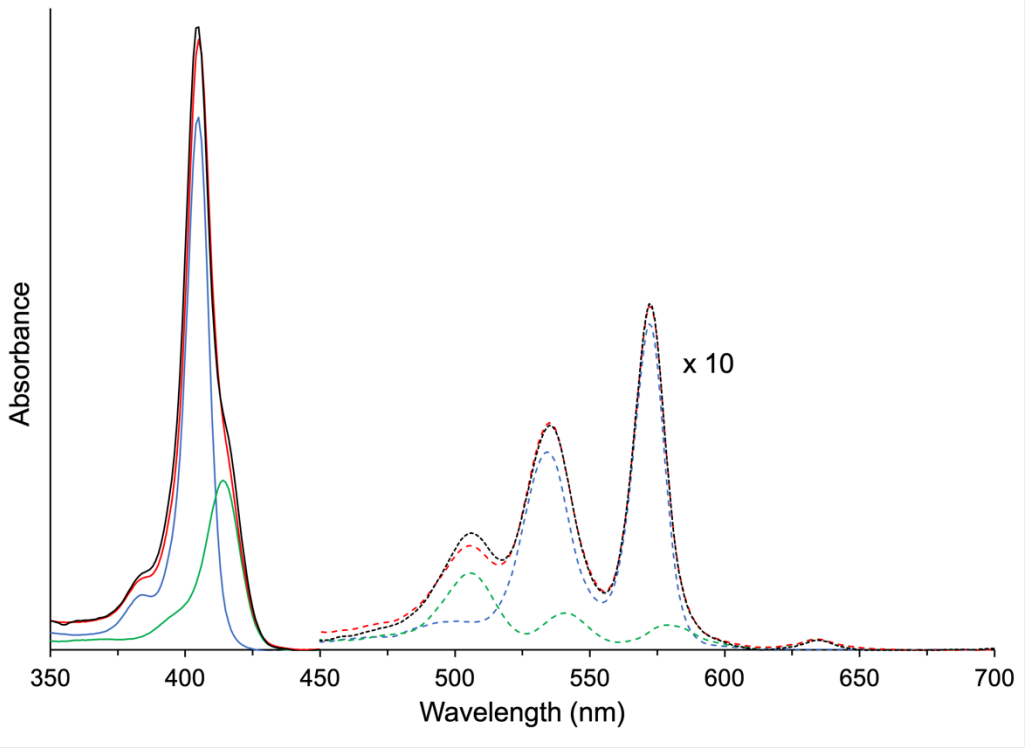

Figure 3.57. Overlay of UV-Vis spectrum of **4** (black), Ga(OEP)(O_2CPh) (blue), H_2BMCPP (green), and the sum of Ga(OEP)(O_2CPh) and H_2BMCPP (red) in TCB.

In contrast to the UV-Vis spectra for **1**, **2**, and **4**, the spectra for **3** are strongly solvent sensitive in a manner consistent with it possessing a solvent-dependent molecular structure. The spectrum in CH_2Cl_2, which based on ^{1}H NMR spectroscopic data should contain **3** in a folded structure similar to that observed in $CDCl_3$, exhibits four Q-bands, with the bands at 535 nm and 573 nm being the most intense, and an extremely broad Soret band at 400 nm that displays a prominent intense shoulder at 389 nm This spectrum was fit to a sum of the components Ga(OEP)(O_2CPh) and H_2BECP (Figure 3.58), in which the relative weights of the components were determined by the best fit to the Q-band region from 450 nm to 700 nm. Unlike for porphyrin-bridged dimer **4**, the fit does not exactly overlay the observed spectrum: there is an obvious redshift of the Q_y(1,0) band observed at 506 nm in **3** compared to that in H_2BECP and a slight redshift and marked intensity loss for the Q_x(0,0) band at 633 nm. Further, the Soret region of **3** shows a

significant loss in maximum intensity relative to the components, and its substantial broadening is not replicated. These features are consistent with the spectra of slipped cofacial porphyrin dimers,[76,77,102] and can be qualitatively understood using the molecular exciton model (Figure 3.59).[103] Because the porphyrin macrocycles in the solid-state and $CDCl_3$ solution structures of **3** are not perfectly coplanar (3° solid, ~8˚ solution), the Soret bands of both the Ga(OEP) and the H_2BCP components would be expected to split into a higher energy and lower energy transition. A small shift in the energy of the Soret band would also be expected due to the *xy* offset between the porphyrin macrocycles, although a significant change in λ_{max} is not observed for **3**. Because this model predicts four total Soret bands that also may be slightly shifted from their positions in the monomeric counterparts, a quantitative description of the Soret band is not possible and we are limited to noting that the significant broadening of the Soret band is consistent with a folded conformation.

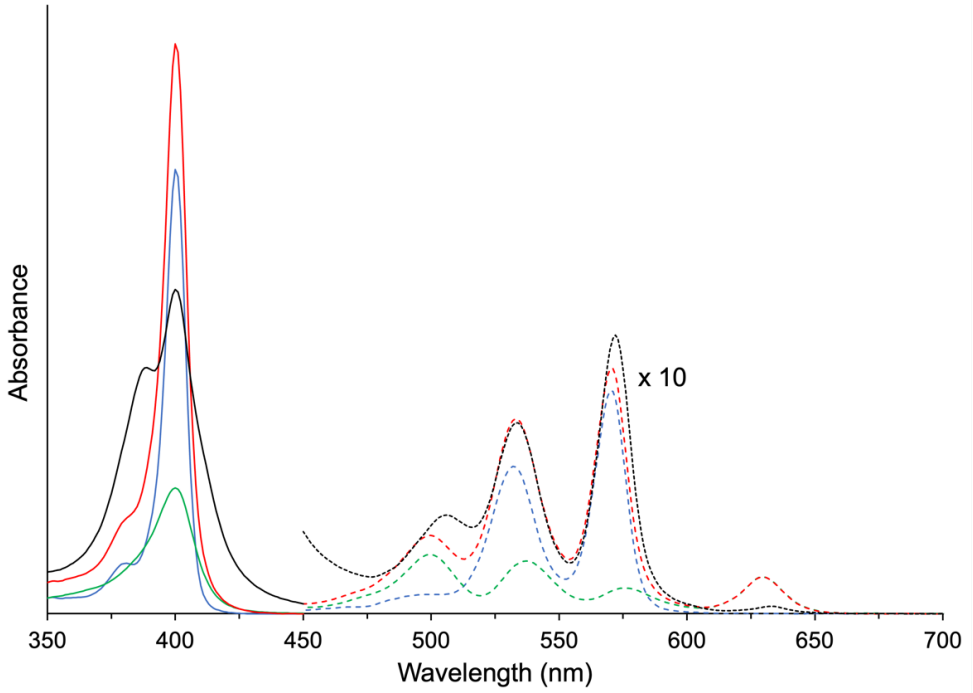

Figure 3.58. Overlay of UV-Vis spectrum of **3** (black), Ga(OEP)(O_2CPh) (blue), H_2BECP (green), and the sum of Ga(OEP)(O_2CPh) and H_2BECP (red) in CH_2Cl_2.

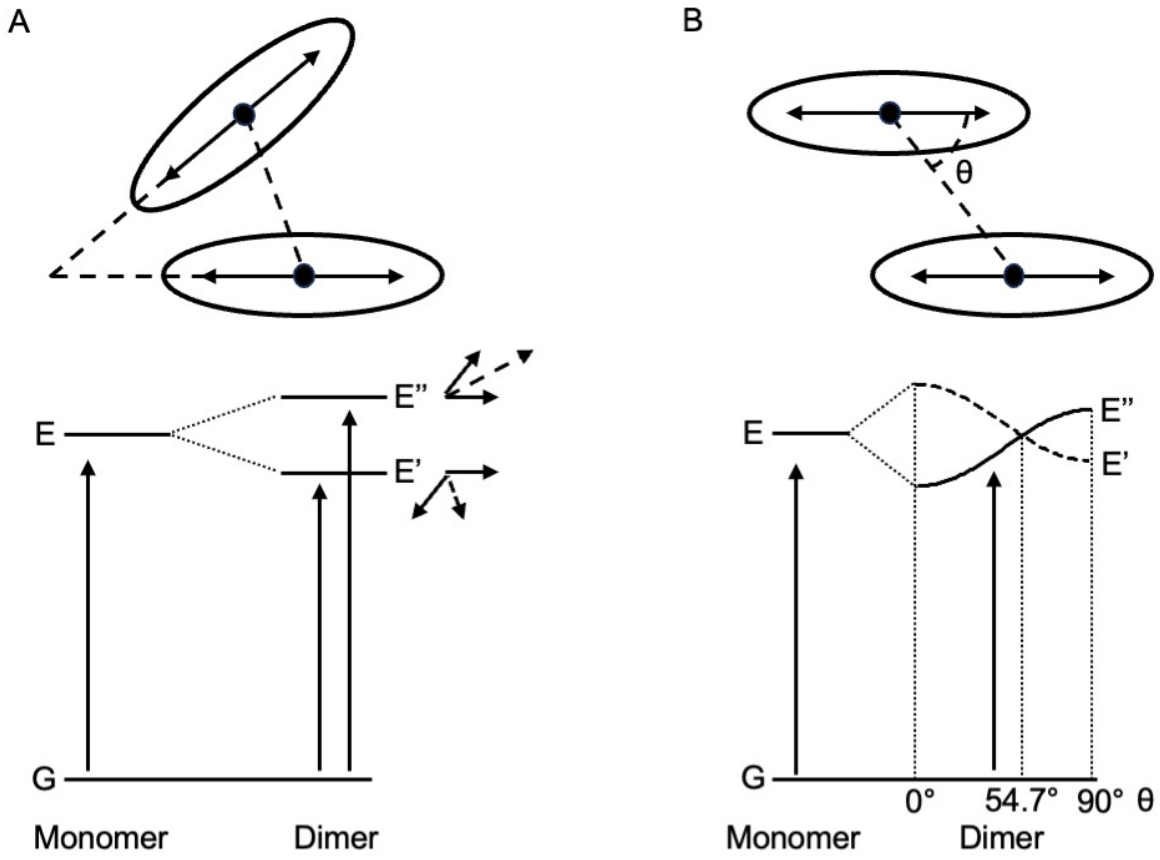

Figure 3.59. Qualitative energy diagrams of porphyrin monomers and dimers by the molecular exciton model showing effect of (a) canted porphyrins; (b) slipped cofacial porphyrins on the ground state and excited state energy levels. In both diagrams the ground states are denoted as G and the excited states are denoted as E for the monomer and E' and E'' for the dimer. The dipole phase relation of the excited states is shown to the right of E' and E'' in (a). θ refers to the angle formed by the porphyrin planes and an scalar connecting the centroids of the porphyrins in (b). The transition to E' is forbidden in (b). The diagrams are adapted from Ref. 103.

The UV-Vis spectrum of **3** in TCB exhibits a significantly narrower Soret band than in CH_2Cl_2, although this spectrum still cannot be described as the sum of the Ga(OEP)(O_2CPh) and H_2BECP spectra (Figure 3.60). The changes in the Q-bands are also less in TCB than in CH_2Cl_2. These observations are consistent with the ^{1}H-NMR data in TCB that suggest the complex adopts a structure that is unfolded to some degree, although the NMR data appear to be closer to the fully extended conformer than the UV-vis data. We do not have an explanation for the slightly different structural inferences provided by ^{1}H-NMR and UV-vis spectroscopy.

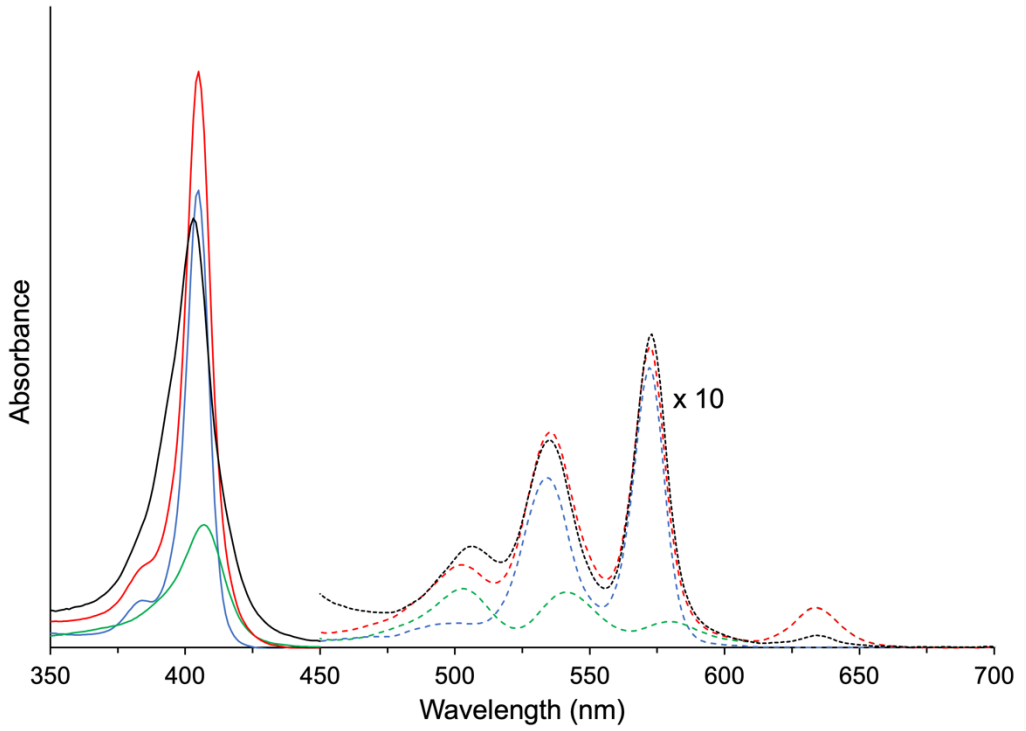

Figure 3.60. Overlay of UV-Vis spectrum of **3** (black), Ga(OEP)(O_2CPh) (blue), H_2BECP (green), and the sum of Ga(OEP)(O_2CPh) and H_2BECP (red) in TCB.

Table 3.13. Electronic-Absorption Band Maxima (nm) and Relative Intensities of Porphyrin Dimers and Model Compounds.

Complex	Solvent	λ, nm (rel. int.)
1	CH_2Cl_2	338 (5.9), 383 (25.0), 396 (100), 499 (0.5), 532 (3.6), 570 (5.4)
1m	CH_2Cl_2	335 (4.6), 380 (11.6), 400 (100), 499 (0.5), 532 (3.4), 570 (5.2)
2	CH_2Cl_2	335 (5.5), 382 (15.6), 399 (100), 499 (0.5), 532 (3.8), 570 (5.8)
	TCB	336 (4.9), 384 (12.6), 404 (100), 501 (0.5), 534 (3.8), 572 (6.3)
Ga(OEP)(O_2CPh)	CH_2Cl_2	335 (4.4), 381 (11.3), 400 (100), 499 (0.4), 532 (3.3), 571 (5.0)
	TCB	336 (4.4), 384 (10.3), 405 (100), 500 (0.5), 534 (3.5), 572 (5.8)
H_2BECP	CH_2Cl_2	400 (100), 500 (4.5), 537 (4.0). 576 (1.9), 630 (2.8)
	TCB	407 (100), 503 (4.6), 541 (4.3), 579 (3.0), 634 (3.1)
3	CH_2Cl_2	339 (12.3), 389 (75.9), 400 (100), 506 (3.5), 535 (6.6), 572 (9.8), 633 (0.3)
	TCB	338 (8.1), 403 (100), 506 (2.4), 535 (5.0), 573 (7.6), 634 (0.3)
H_2BMCPP	CH_2Cl_2	365 (7.6), 389 (22.2), 408 (100), 502 (4.4), 537 (1.9), 575 (1.4), 630 (0.6)
	TCB	368 (6.0), 395 (20.1), 414 (100), 506 (4.0), 541 (1.9), 579 (1.3), 634 (0.5)
4	CH_2Cl_2	336 (5.5), 380 (13.9), 401 (100), 411 (34.8), 503 (1.8), 533 (3.4), 571 (4.8), 633 (0.2)
	TCB	336 (4.3), 383 (11.3), 405 (100), 416 (33.6), 506 (1.7), 535 (3.2), 572 (5.0), 634 (0.1)

3.3.3. Electronic Structures and Properties of Dimeric Porphyrin Complexes.

3.3.3.1. DFT Calculations of the Electronic Structures of Dimeric Porphyrin Complexes. The porphyrinic frontier orbitals of the compounds were calculated by DFT to investigate whether they show important features that are a consequence of their particular molecular structures. Compounds **1** and **2** are discussed separately from the more complex porphyrin-bridged dimers **3** and **4**. Kohn-Sham orbitals were calculated at the optimized geometries for **1**, **1m**, **2** and Ga(OEP)(O_2CPh) (Table 3.14). Under D_{4h} symmetry, the four frontier ("Gouterman") orbitals of a metalloporphyrin are expected to consist of two closely spaced filled orbitals (HOMO and HOMO–1) and a doubly degenerate LUMO (Figure 3.61, left). A porphyrin

dimer with non-interacting orbitals should exhibit double this set of orbitals at the same energies, with the monomer HOMO becoming a dimer pair labeled HOMO and HOMO–1, the monomer HOMO–1 becoming a dimer pair denoted HOMO–2 and HOMO–3, and the monomer degenerate LUMO/LUMO+1 becoming in the dimer LUMO/LUMO+1/LUMO+2/LUMO+3 (Figure 3.61, center). If the orbitals are strongly interacting the degenerate occupied and unoccupied orbitals are expected become non-degenerate (Figure 3.61, right).

Table 3.14. Frontier Orbital Energies (eV) of **1**, **1m**, **2**, and Ga(OEP)(O_2CPh).

Orbital	**1**	**1m**	**2**	**Ga(OEP)(O_2CPh)**
LUMO+3	–1.975		–2.061	
LUMO+2	–1.976		–2.061	
LUMO+1	–1.980	–2.362	–2.065	–2.170
LUMO	–1.980	–2.366	–2.065	–2.173
HOMO	–4.919	–5.300	–4.997	–5.106
HOMO–1	–4.919	–5.494	–4.998	–5.281
HOMO–2	–4.954		–5.168	
HOMO–3	–5.075		–5.170	

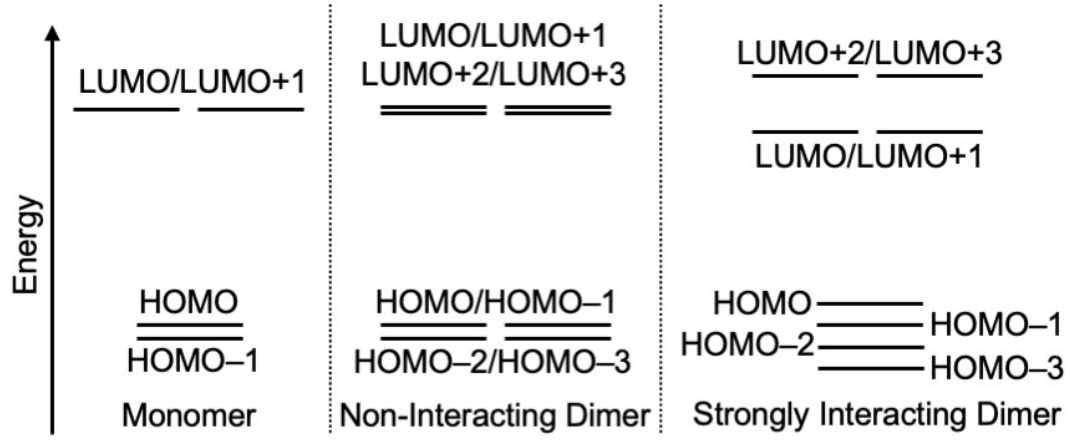

Figure 3.61. Qualitative molecular orbital diagram of the frontier orbitals for a porphyrin monomer (left), a non-interacting porphyrin dimer (center), and a strongly interacting porphyrin dimer (right).

Based on the orbital energies of **1**, the porphyrin-porphyrin interactions are fairly small. The HOMO/HOMO–1 pair of **1** are isoenergetic, the HOMO–2/HOMO–3 pair are split by 121

meV, and the LUMO-through-LUMO+3 set of orbitals span only a 5 meV range. These small splittings are qualitatively consistent with the small shift in the Soret band of **1** relative to **1m** (by 30 meV) noted earlier. Complex **2** exhibits splittings of ≤ 4 meV across the various pairs of orbitals, consistent with even smaller interporphyrin interactions.

For **3** and **4**, the extended and folded conformers are calculated to possess significantly different electronic structures. The extended conformers of **3** and **4** are essentially the sum of the components, with the calculated orbitals having entirely Ga(OEP) or H_2BCP/H_2BCPP parentage; selected examples are plotted in Figure 3.62 and Figure 3.63, respectively. The energies of the first six occupied and unoccupied calculated orbitals, along with the energies of H_2BECP and H_2BMCPP ligands are found in Table 3.15. Similar to **2**, two pairs of isoenergetic occupied orbitals and four nearly isoenergetic unoccupied orbitals of primarily Ga(OEP) parentage are calculated, along with two occupied and two unoccupied orbitals of H_2BCP or H_2BCPP parentage. In contrast, molecular orbitals of the folded structures of **3** and **4** that possess the appropriate symmetry are calculated to be significantly delocalized across both the Ga(OEP) and either H_2BCP or H_2BCPP units, respectively. This delocalization results in the loss of degeneracy of both the occupied and unoccupied orbital energies. The calculated molecular orbitals suggest that the physical properties of **3** and **4** should be substantially altered if they adopt the folded conformation.

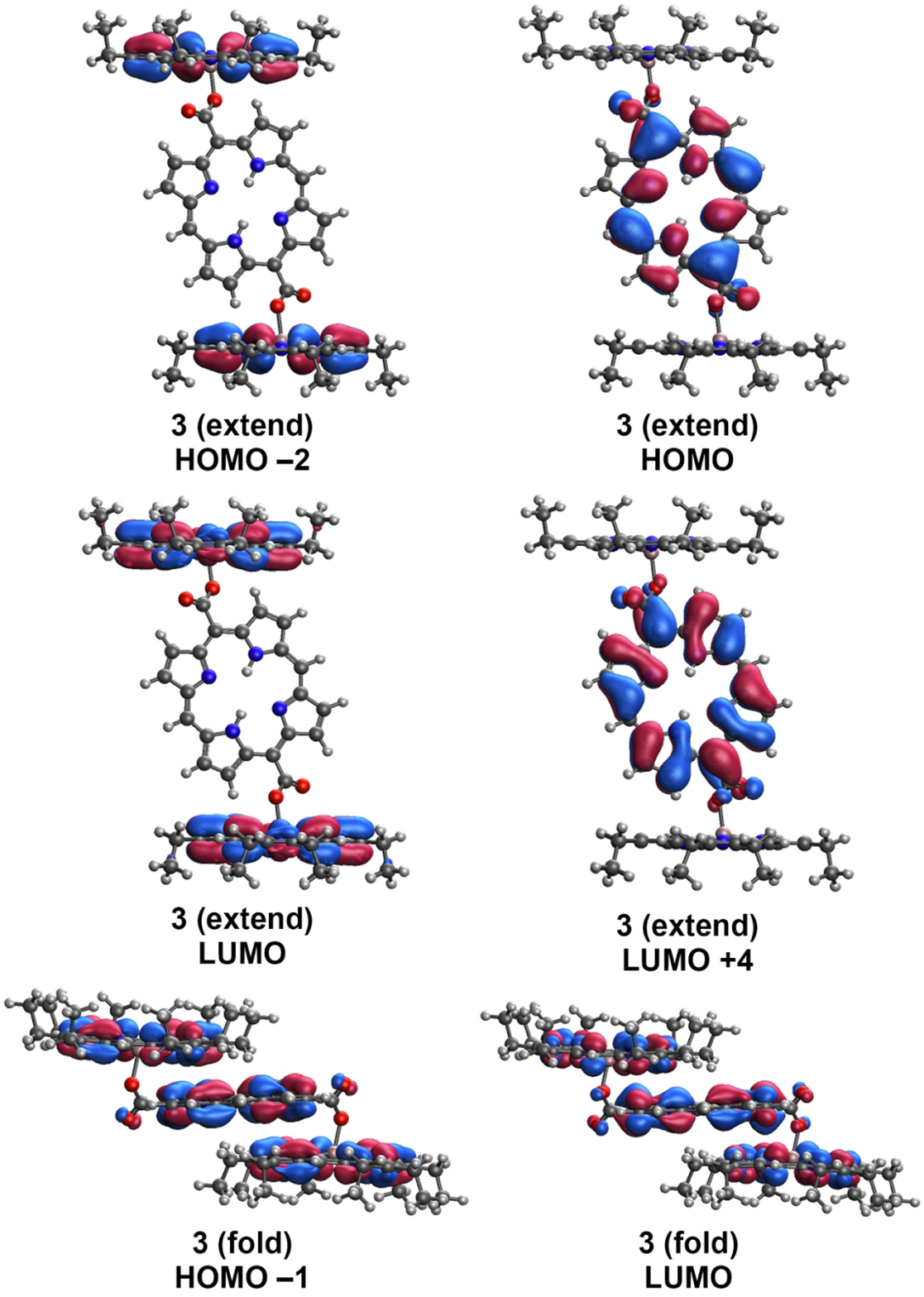

Figure 3.62. Highest occupied and lowest unoccupied molecular orbitals of primarily Ga(OEP) and H_2BCP parentage of **3** (extend). Selected occupied and unoccupied molecular orbitals with both Ga(OEP) and H_2BCP parentage of **3** (fold).

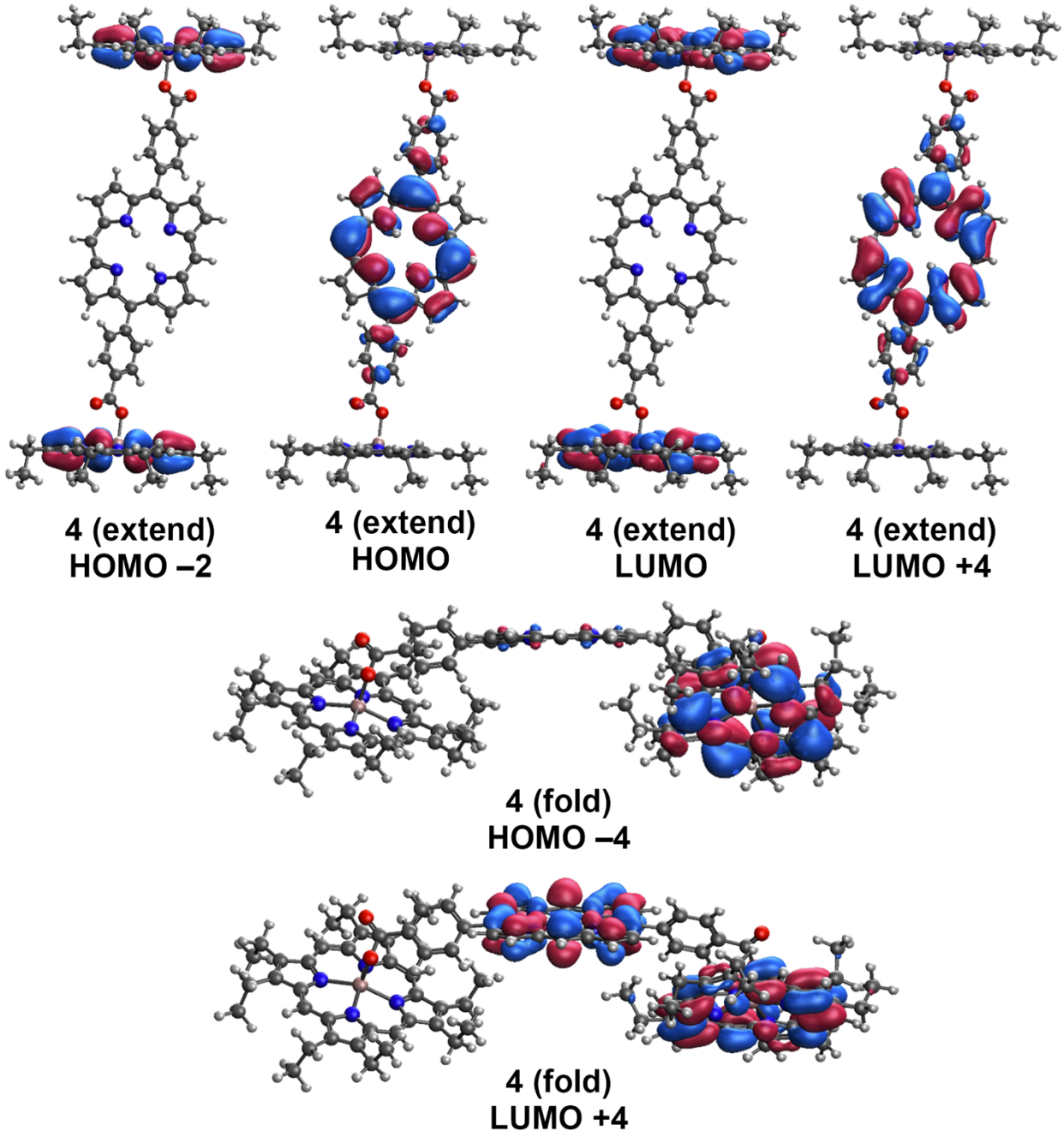

Figure 3.63. Highest occupied and lowest unoccupied molecular orbitals of primarily Ga(OEP) and H_2BCPP parentage of **4** (extend). Selected occupied and unoccupied molecular orbitals with both Ga(OEP) and H_2BCPP parentage of **4** (fold).

Table 3.15. Frontier Orbital Energies (eV) and Parentage of **3** and **4** in Extended and Folded Conformers and H_2BECP and H_2BMCPP.

	Orbital Energy (eV) (Parentage)					
Orbital	**3 (Extend)**	**3 (Fold)**	H_2BECP	**4 (Extend)**	**4 (Fold)**	H_2BMCPP
LUMO+5	–1.606 (H_2BCP)	–2.095 (OEP/H_2BCP)		–2.004 (H_2BCPP)	–2.262 (OEP/H_2BCPP)	
LUMO+4	–1.851 (H_2BCP)	–2.177 (OEP/H_2BCP)		–2.068 (H_2BCPP)	–2.263 (OEP/H_2BCPP)	
LUMO+3	–2.190 (OEP)	–2.200 (OEP)		–2.183 (OEP)	–2.274 (OEP/H_2BCPP)	
LUMO+2	–2.190 (OEP)	–2.223 (OEP/H_2BCP)		–2.183 (OEP)	–2.284 (OEP)	
LUMO+1	–2.205 (OEP)	–2.239 (OEP)	–2.552	–2.187 (OEP)	–2.290 (OEP)	–2.501
LUMO	–2.207 (OEP)	–2.354 (OEP/H_2BCP)	–2.996	–2.187 (OEP)	–2.361 (OEP/H_2BCPP)	–2.640
HOMO	–4.614 (H_2BCP)	–4.981 (BCP)	–5.691	–4.810 (H_2BCPP)	–5.033 (H_2BCPP)	–5.370
HOMO–1	–4.700 (H_2BCP)	–5.064 (OEP/H_2BCP)	–5.729	–5.103 (H_2BCPP)	–5.199 (OEP)	–5.611
HOMO–2	–5.134 (OEP)	–5.143 (OEP)		–5.120 (OEP)	–5.217 (OEP)	
HOMO–3	–5.136 (OEP)	–5.264 (OEP/H_2BCP)		–5.121 (OEP)	–5.366 (OEP/H_2BCPP)	
HOMO–4	–5.305 (OEP)	–5.297 (OEP/H_2BCP)		–5.298 (OEP)	–5.374 (OEP/H_2BCPP)	
HOMO–5	–5.308 (OEP)	–5.341 (OEP/H_2BCP)		–5.298 (OEP)	–5.403 (OEP)	

3.3.3.2. Electrochemical Studies. The electrochemistry of the porphyrin dimers was studied to explore whether their redox potentials manifest effects of porphyrin–porphyrin interactions. These would be expected to be largest for **1**, which has the shortest porphyrin–porphyrin distance among dimers with extended structures, and **3**, which is folded in low-polarity solvents such as CH_2Cl_2 and $CHCl_3$. The electrochemical properties of the porphyrin dimer complexes were investigated by means of square-wave voltammetry in CH_2Cl_2. This method was employed instead of cyclic voltammetry (CV) because the low solubility of the compounds limited the quality of the CV data. We will utilize the descriptors of Le Mest *et al.,*[92] common to the electrochemistry of porphyrin dimers, to describe the various features, *i.e.* an oxidative or reductive *process* refers to abstraction or addition of one electron per porphyrin ring, respectively; *features* refer to individual resolvable waves regardless of the number of electrons. The potentials of all redox features are set out in Table 3.16.

The redox potentials of **1** were observed to manifest porphyrin–porphyrin interactions. The oxidative scan of **1** exhibits three features (Figure 3.64a). The first two oxidation features are at 0.431 V and 0.595 V vs. $FeCp_2^{0/+}$. These potentials bracket the first oxidation of **1m** at 0.544 V (Figure 3.65a). The third oxidative feature of **1** is observed at 1.031 V, very similar to **1m** (1.028 V). The relative areas of the first and second oxidative features of **1** compared to that of the third oxidative feature suggests that the first and second features represent a sequential one-electron steps and the third oxidation may be a simultaneous two-electron oxidation or two sequential one-electron steps with a ΔE too small to be resolved. The fact that the third oxidative feature is broad (FWHM = 170 mV) compared to both the first and second oxidation features (FWHM = 131 mV) and to the internal ferrocene standard (FWHM = 139 mV) suggests that two sequential one-electron steps is more likely. In the reductive scan of **1** (Figure 3.64b), only one feature is observed

at –1.887 V. This potential is negative by 55 mV from that of **1m** at –1.832 V (Figure 3.65b). The feature is also broader than that for the ferrocene internal standard, which may indicate that the reduction process takes place as two non-resolvable one-electron steps. In summary, the notable features of the electrochemistry of **1** are the splitting of the first oxidation process, the lack of resolved splitting on the second oxidative process and the first reductive process, and the shifts of the first oxidation feature to a less positive potential and first reduction to a more negative potential as compared to **1m**. Understanding these features requires consideration of the interactions between the two porphyrin rings.

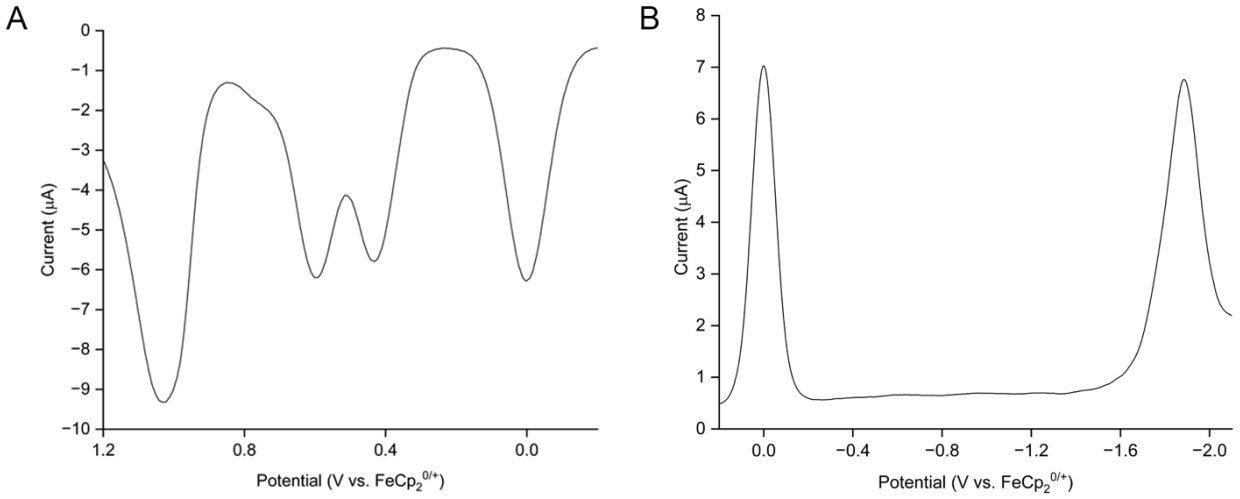

Figure 3.64. Square-wave voltammograms (frequency = 25 Hz, amplitude = 50 mV) of **1** in CH_2Cl_2 with 0.1 M $(NBu_4)(PF_6)$. (a) oxidative scan; (b) reductive scan.

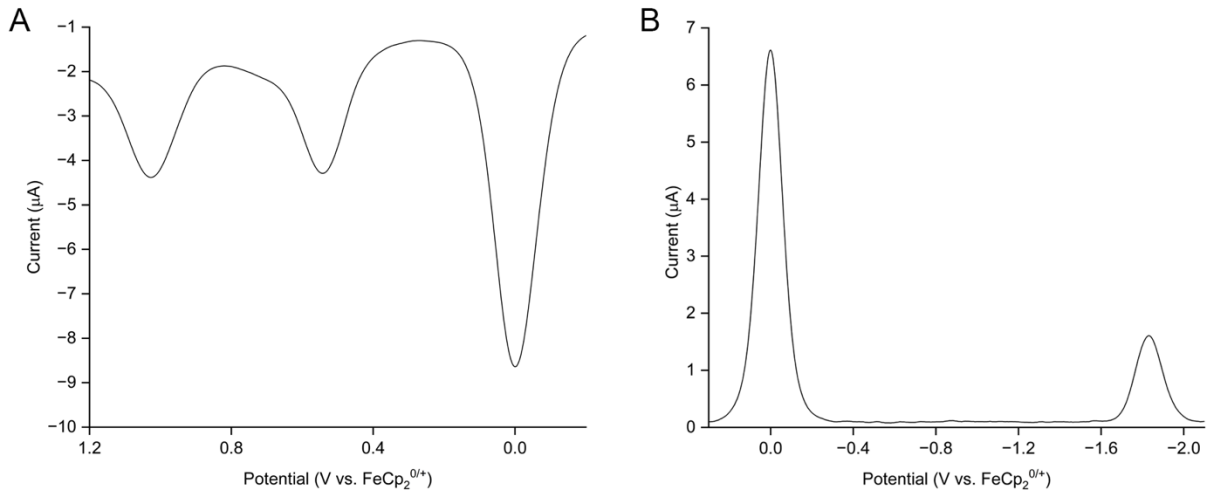

Figure 3.65. Square-wave voltammograms (frequency = 25 Hz, amplitude = 50 mV) of **1m** in CH_2Cl_2 with 0.1 M $(NBu_4)(PF_6)$. (a) oxidative scan; (b) reductive scan.

Two possible explanations for the differences between the redox properties of **1** and **1m** are that they reflect for the dimer (1) Coulombic effects between the two porphyrin rings upon introduction of charge, or (2) orbital interactions between the porphyrin rings resulting in delocalized redox events. In the limit of two porphyrin rings without orbital mixing where Coulombic repulsion dominates, the positive charge on the first oxidized porphyrin should increase the first oxidation potential of the other porphyrin. The splitting between the first oxidation potentials of the two porphyrins, ΔE, can be modeled using a dielectric continuum model[104-106] captured in Equation 3.6,

$$\Delta E = \frac{1}{(4\pi\varepsilon\varepsilon_o\varepsilon R_{ij})} + 36\ mV \tag{3.6}$$

where ε is the dielectric constant of the solution (solvent plus electrolyte), ε_o is the vacuum permittivity constant, and R_{ij} is the distance between the planes of the two porphyrins. The dielectric constant of neat CH_2Cl_2 is 8.93;[107] it will be larger for a solution containing 0.1 M $[NBu_4][PF_6]$. This latter dielectric constant has not been reported, but it has for CH_2Cl_2 containing either 0.1 M $[NBu_4][BF_4]$ (ε = 14.1)[108] or 0.1 M $[NBu_4][ClO_4]$ (ε = 12.5).[109] Experiments by Geiger

et al. indicate that [NBu_4][PF_6] in CH_2Cl_2 likely increases ε by less than the other electrolytes, suggesting that $8.93 < \varepsilon < 12.5$.[110] Based on these values and the porphyrin–porphyrin separation calculated by DFT (7.6 Å), the predicted Δ*E* would be 188 mV–248 mV. This range is larger than the experimentally observed Δ*E* of 164 mV. A key physical deficiency in this model is that it is strictly applicable to point dipoles, whereas a porphyrin cation will be diffuse due to π-delocalization, which may contribute to the overestimation of the predicted Δ*E*. Further, it does not explain why the first oxidation potential of **1** is less positive, why the first reduction potential of **1** is more negative than that of **1m**, or why the splitting is not observed in the second oxidation feature or the reduction feature, which, while broader than the ferrocene reference, nonetheless must possess values of Δ*E* of only ~80 mV based on their FWHM.

An alternative explanation is that the splitting of the first oxidation process into two features is caused by orbital interactions between porphyrin rings (Figure 3.61, left) that lead to the formation of delocalized π-radical cations.[77,92,95,111-114] The shifts in the first oxidation process and the first reduction process are also consistent with these systems, where a shift of 130 mV for the first oxidation potential to less positive potentials and a shift of 200 mV for the first reduction potential to more negative potentials was observed for a $(Zn)_2$ cofacial porphyrin with a spacing of 3.80 Å.[92] However, the separation between the porphyrin planes in **1** is larger than those of other systems. Electron paramagnetic resonance[92,113] or NIR spectroelectrochemical measurements[112,113] have previously been used to gain insight into the extent of delocalization and could help to identify the origin of the effect, though regardless of the explanation, these observations certainly confirm the dimeric nature of **1**.

The electrochemical features of **2** (Figure 3.66) can be explained analogously to **1**. No splitting of the first oxidation process is observed, though this feature along with the first reductive

feature are broadened with respect to the internal ferrocene standard suggesting a potential two step processes. The second oxidation process appears as a single peak, presumably a one-step two electron process. The further separation between the porphyrin rings (11.9 Å) in **2** as compared to **1** would limit the splitting regardless of whether it results from Coulombic repulsion or the coupling between the porphyrin rings, so the non-resolvable redox processes are not surprising. Deconvoluting the first oxidation feature with two gaussian functions, with FWHMs equal to the second oxidation process and the ferrocene internal standard (125 mV), results in a ΔE of roughly 60 mV, smaller than what would be predicted for a separation of using the dielectric continuum model (133–172 mV), though the same caveats with respect to the diffuse nature of the porphyrin orbitals as **1** would apply here.

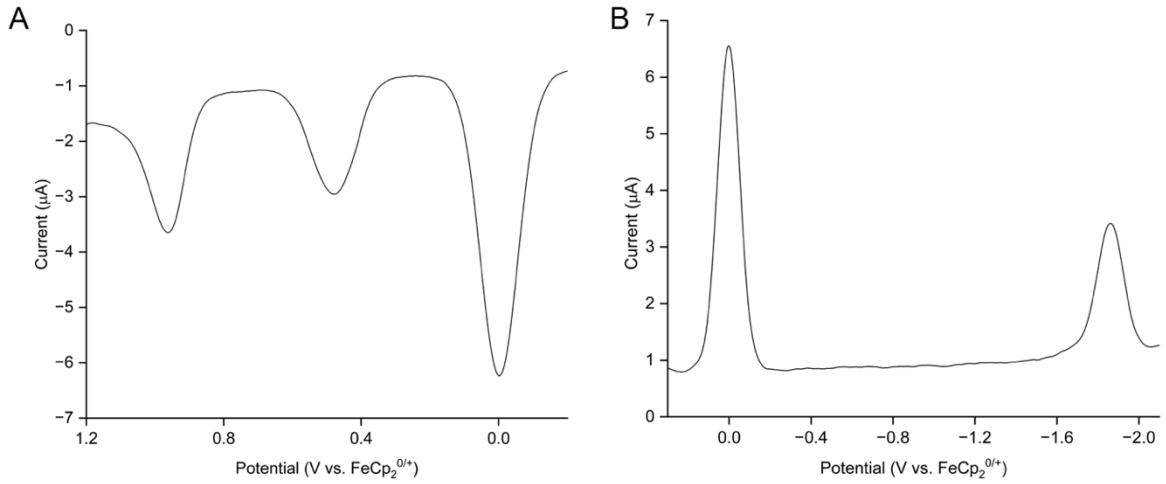

Figure 3.66. Square-wave voltammograms (frequency = 25 Hz, amplitude = 50 mV) of **2** in CH_2Cl_2 with 0.1 M $(NBu_4)(PF_6)$. (a) oxidative scan; (b) reductive scan.

The electrochemistry of **3** and **4** are expected to exhibit redox features corresponding to both the Ga(OEP) unit and the bridging porphyrin H_2BCP and H_2BCPP for **3** and **4**, respectively. As the folded structure of **3** would be expected to result in strong interporphyrin interactions that may complicate the interpretation of the redox features, the electrochemistry of **4** will be discussed first. The square-wave voltammogram of **4** (Figure 3.67a) exhibits three oxidative features at 0.524

V, 0.672 V, and 1.052 V. The first oxidation potential is consistent with being localized on the Ga(OEP) because it is similar to that of Ga(OEP)(O_2CCH_3) (0.550 V), and the second oxidation potential is localized on the H_2BCPP unit based on the lower intensity of this feature and the agreement with the first oxidation potential of H_2BMCPP (Figure 3.68a; 0.644 V). The relative area of the third oxidation feature compared to the first and second oxidation features suggests that it is localized on the H_2BCPP unit, though the Ga(OEP) unit also would be expected to be oxidized near this potential given the oxidation potentials observed for Ga(OEP)(O_2CCH_3) and **2**. As **4** is unfolded in CH_2Cl_2, the electrochemistry is expected to be similar to the sum of its constituent parts, as has been observed for other porphyrin dimers and trimers containing orthogonal porphyrin units.[101] The reductive scan of **4** (Figure 3.67b) exhibits two partially overlapping features at –1.552 V and –1.764 V; the first reductive feature is consistent with H_2BMCPP (Figure 3.68b; –1.516 V), the second reductive feature exhibits a relative area roughly twice that of the first reductive feature consistent with being localized on the Ga(OEP)(O_2CCH_3) and is shifted to a potential 56 mV less negative than Ga(OEP)(O_2CCH_3).

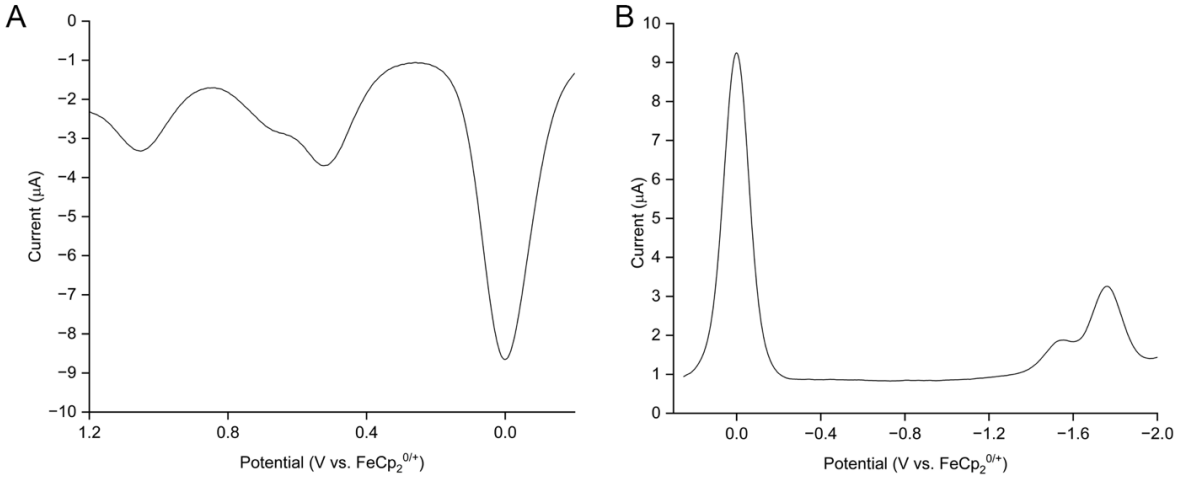

Figure 3.67. Square-wave voltammograms (frequency = 25 Hz, amplitude = 50 mV) of **4** in CH_2Cl_2 with 0.1 M (NBu_4)(PF_6). (a) oxidative scan; (b) reductive scan.

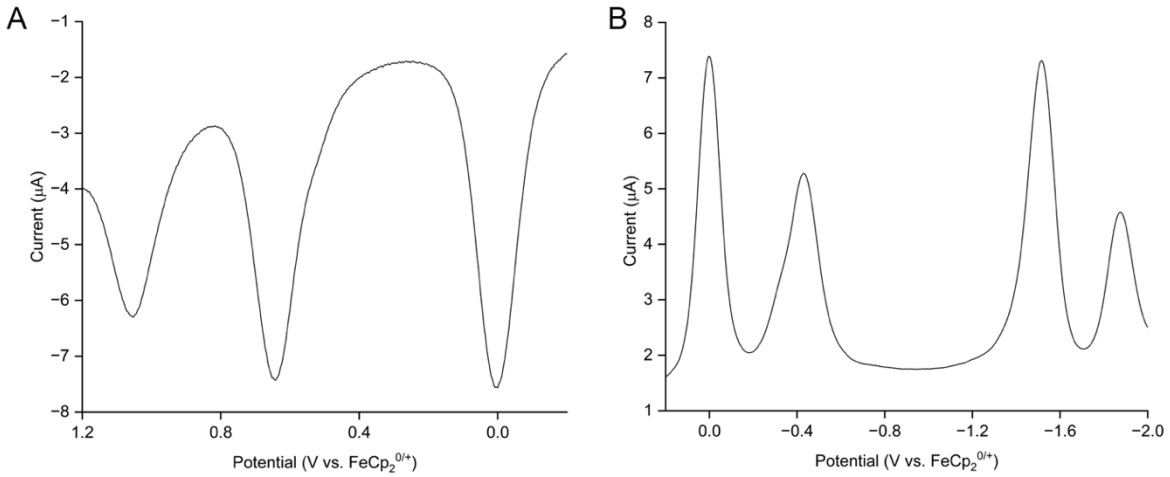

Figure 3.68. Square-wave voltammograms (frequency = 25 Hz, amplitude = 50 mV) of H_2BMCPP in CH_2Cl_2 with 0.1 M (NBu_4)(PF_6). (a) oxidative scan; (b) reductive scan.

The square-wave voltammogram of **3** (Figure 3.69a) reveals three oxidative features at 0.524 V, 0.744 V, and 1.040 V, that are consistent with the oxidations of monomeric counterparts, Ga(OEP)(O_2CCH_3) and H_2BECP (Figure 3.70a). These potentials are very similar to **4**, with the second oxidation potential shifted by 72 mV, which is in agreement with the observed shift between H_2BECP and H_2BMCPP (68 mV). The relative area of the third oxidation potential suggests it is localized on the Ga(OEP) unit, in agreement with the lack of an observed second oxidation of H_2BECP near this potential. The apparent similarity of the electrochemistry of **3** and its constituent parts is surprising given the proximity of the porphyrin rings in the folded conformation observed in CH_2Cl_2, where effects of greater magnitude to those for **1** would be expected. The apparent lack of electrostatic repulsion or porphyrin ring interactions may indicate that the complex unfolds upon oxidation, though typically π-radical cations are stabilized by porphyrin–porphyrin ring interactions, even forming supramolecular dimers in solution and the solid-state.[115-118] The reductive scan of **3** (Figure 3.69b) exhibits two features at –1.636 V and –1.864 V. The voltammogram also exhibits a large rising baseline as the potentials become more negative. The first and second reductions can be tentatively assigned to H_2BCP and Ga(OEP) based

on the observation that H_2BECP (Figure 3.70b) is more easily reduced than Ga(OEP)(O_2CCH_3) and the greater relative area of the second reduction feature compared to the first reduction feature. These assignments would indicate that the first reduction potential is 400 mV negative of the first reduction potential of H_2BECP and the second reduction potential is shifted 44 mV to more negative potentials than Ga(OEP)(O_2CCH_3). The reductive features, then, are not definitively suggestive of either a folded or an unfolded conformation, because the strongly shifted H_2BCP reduction would be expected for a folded conformation and the minimally shifted Ga(OEP) reduction for an unfolded conformation. Furthermore, we currently do not understand the large rising baseline observed at very negative voltage. Voltammetry at more negative voltages could be helpful in confirming the identity of these features and understanding the rising baseline, though we are limited by the electrochemical window of CH_2Cl_2 and the very limited solubility of **3** in other common electrochemical solvents.

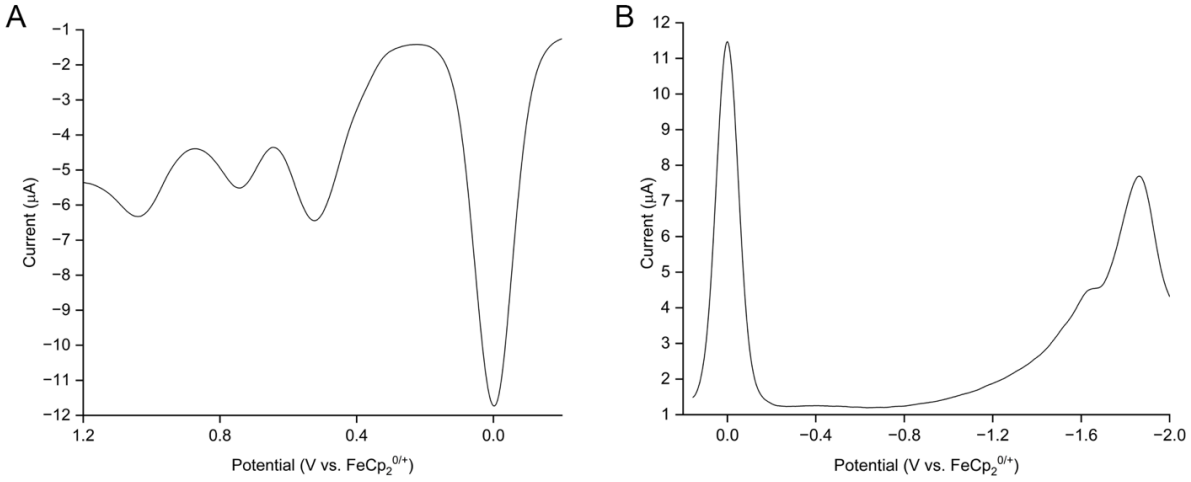

Figure 3.69. Square-wave voltammograms (frequency = 25 Hz, amplitude = 50 mV) of **3** in CH_2Cl_2 with 0.1 M (NBu_4)(PF_6). (a) oxidative scan; (b) reductive scan.

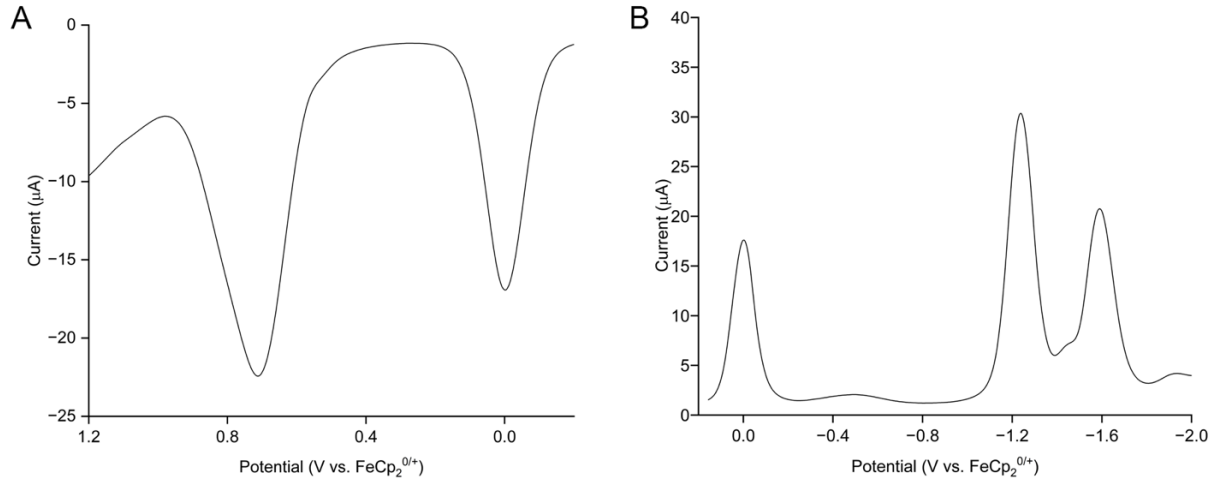

Figure 3.70. Square-wave voltammograms (frequency = 25 Hz, amplitude = 50 mV) of H_2BECP in CH_2Cl_2 with 0.1 M (NBu_4)(PF_6). (a) oxidative scan; (b) reductive scan.

Table 3.16. Oxidation and Reduction Features (V vs. $FcCp_2^{0/+}$) of Porphyrin Dimers and Precursors in CH_2Cl_2.

	Voltage (V vs. $FcCp_2^{0/+}$)					
Complex	Ox. 1	Ox. 2	Ox. 3	Red. 1	Red. 2	Red. 3
1	0.431	0.595	1.031	–1.887		
1m	0.544	1.028		–1.832		
2	0.480	0.964		–1.860		
Ga(OEP)(O_2CCH_3)[a]	0.550	0.980		–1.820		
H_2BECP	0.712			–1.236	–1.588	
3	0.524	0.744	1.040	–1.636	–1.864	
H_2BMCPP	0.644	1.056		–0.432[b]	–1.516	–1.876
4	0.524	0.672	1.052	–1.552	–1.764	

[a] From Ref. 90, measurements in CH_2Cl_2 with 0.1 M [NBu_4][ClO_4], referenced to $FeCp_2^{0/+}$ couple. [b] This feature is a result of an unidentified impurity as it exhibited batch to batch intensity dependence, though it has been observed in all samples of H_2BMCPP.

3.3.3.3. Fluorescence Spectroscopy. The emission spectra of the dimeric complexes and their monomeric counterparts were studied to further probe for inter-porphyrin interactions. Emission spectra were obtained using an excitation wavelength of 530 nm, which for multi-porphyrin compounds **3** and **4** provides excitation for both the Ga(OEP) and bridging porphyrins. Emission features for all dimers and monomeric counterparts are listed in Table 3.17. The spectra of **1** (Figure 3.71) and **2** (Figure 3.73) in CH_2Cl_2 are essentially indistinguishable from those for

the porphyrin monomer **1m** (Figure 3.72) and Ga(OEP)(O_2CPh) (Figure 3.75), indicating they do not manifest porphyrin–porphyrin interactions. They exhibit a prominent band at 574 nm, a second band at 630 nm that is roughly half as intense, and a tail out to approximately 750 nm. These spectra are in general agreement with those for other Ga(OEP)L complexes.[119] The spectra in TCB for **2** (Figure 3.74) and Ga(OEP)(O_2CPh) (Figure 3.76) are red-shifted by 2 nm, similar to the observation in the UV-vis spectra. The fact that the fluorescence spectra of **1** and **2** do not exhibit effects due to porphyrin–porphyrin interactions is consistent with observations for other metalloporphyrin dimers, where effects are observed only when the porphyrin–porphyrin separation is less than 5 Å.[93]

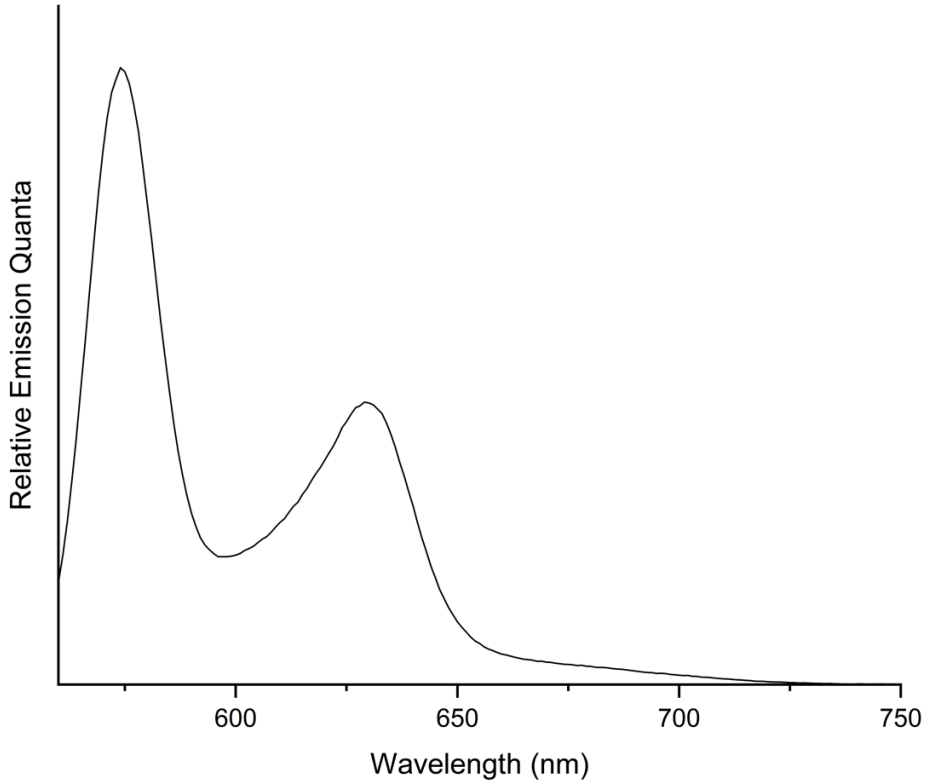

Figure 3.71. Emission spectrum of $(Ga(OEP))_2(\mu\text{-}O_2CCO_2)$ (**1**) in CH_2Cl_2 (λ_{ex} = 530 nm).

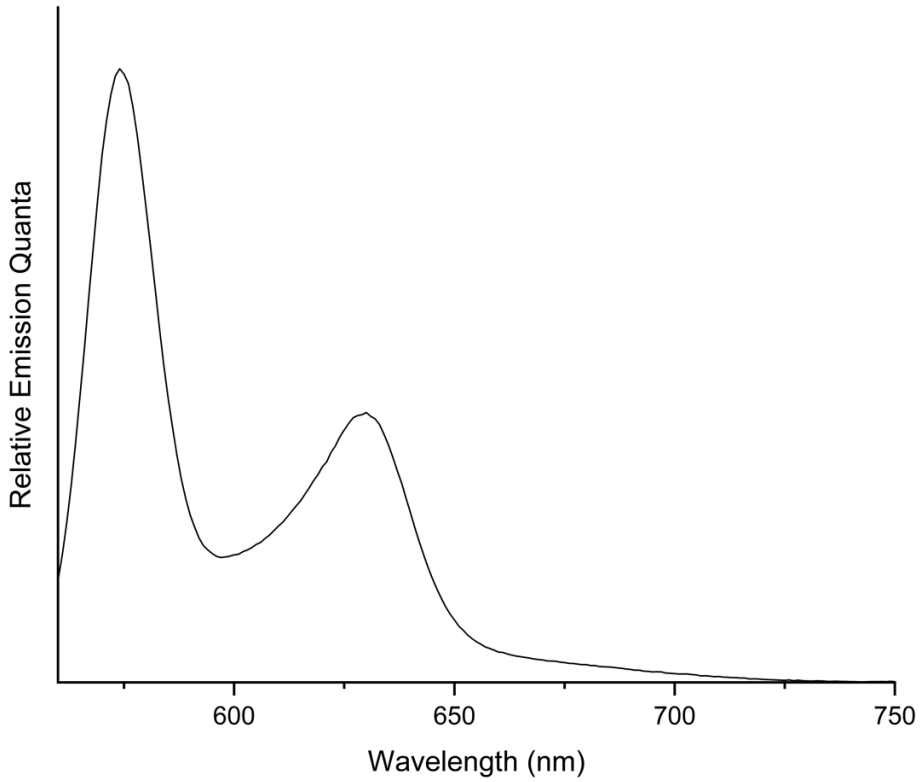

Figure 3.72. Emission spectrum of Ga(OEP)(O_2CCO_2H) (**1m)** in CH_2Cl_2 (λ_{ex} = 530 nm).

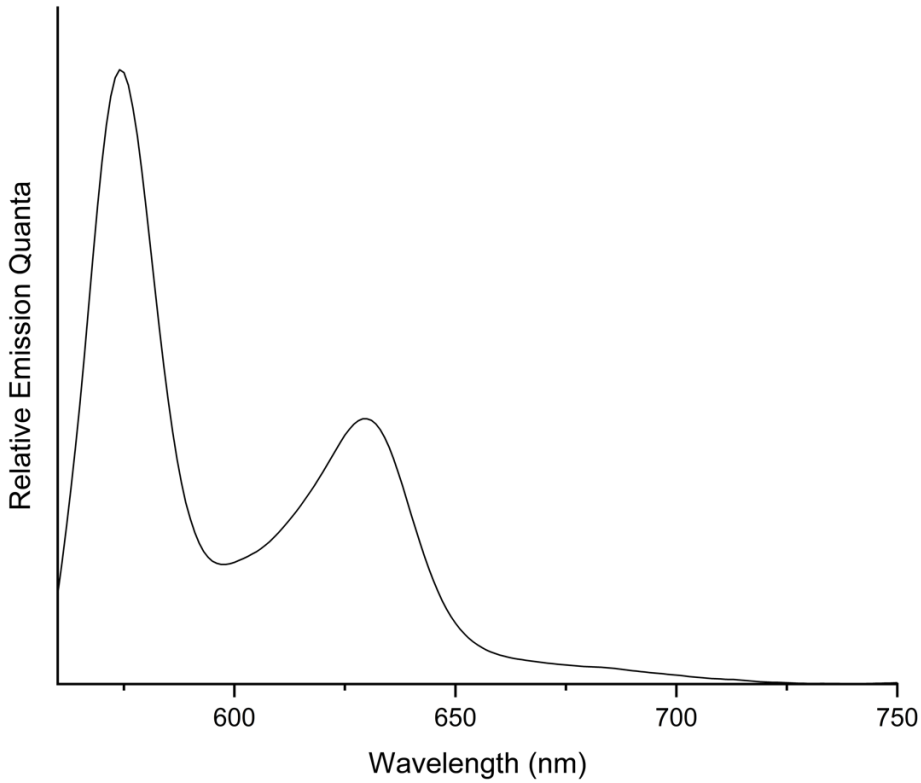

Figure 3.73. Emission spectrum of $(Ga(OEP))_2(\mu\text{-}O_2CC_6H_4CO_2)$ (**2**) in CH_2Cl_2 (λ_{ex} = 530 nm).

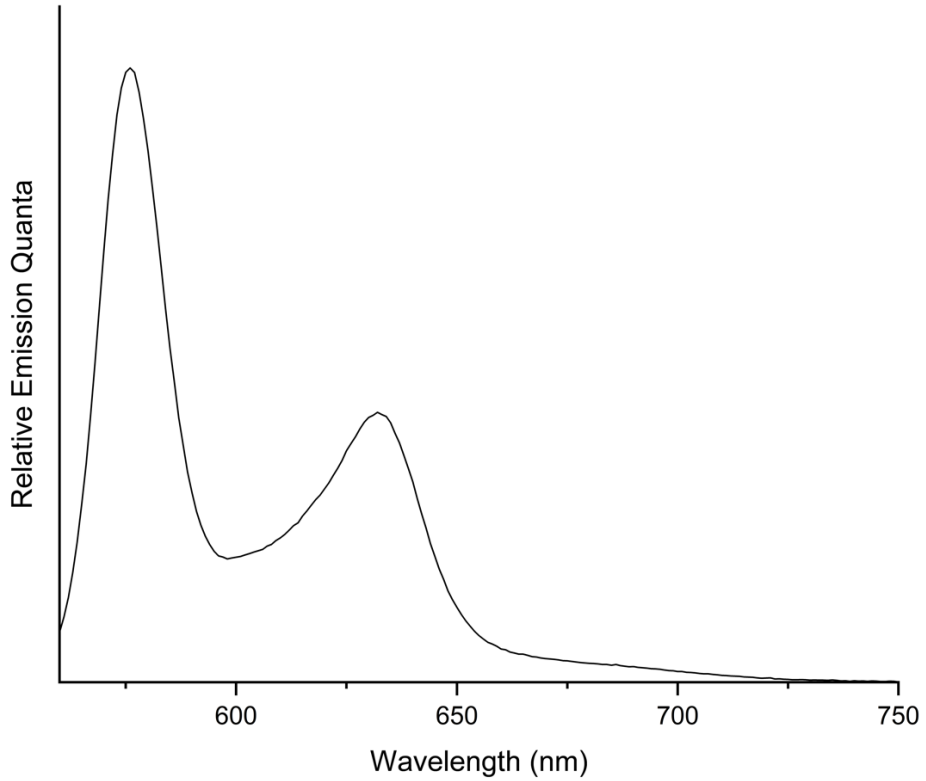

Figure 3.74. Emission spectrum of $(Ga(OEP))_2(\mu\text{-}O_2CC_6H_4CO_2)$ (**2**) in TCB (λ_{ex} = 530 nm).

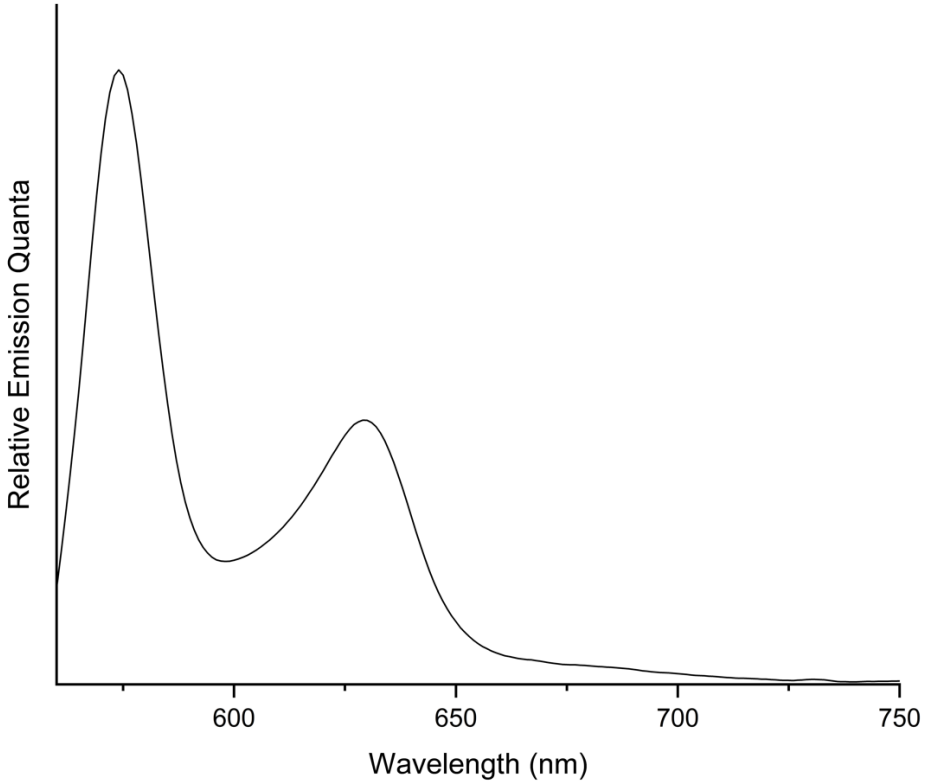

Figure 3.75. Emission spectrum of $Ga(OEP)(O_2CPh)$ in CH_2Cl_2 (λ_{ex} = 530 nm).

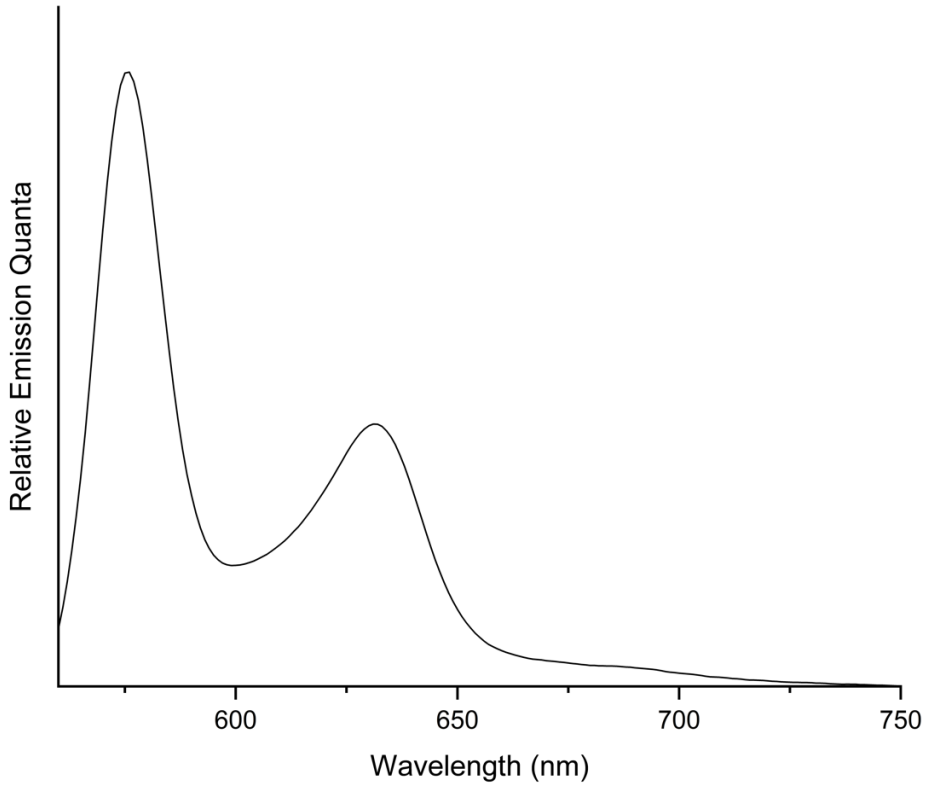

Figure 3.76. Emission spectrum of Ga(OEP)(O_2CPh) in TCB (λ_{ex} = 530 nm).

The emission spectra for **3** and **4** are more complex than those for **1** and **2** because they contain two different porphyrins with distinct absorption-band maxima. This makes their emission intensity profiles dependent on excitation wavelength and potentially subject to intramolecular excited-state energy-transfer processes. The spectra of **4** are discussed first because, unlike **3**, its molecular structure is not solvent dependent. The emission bands of **4** in CH_2Cl_2 (Figure 3.77) are observed at 574, 635, and 700 nm. These are quite close to expectation from the emission maxima of the model compounds for its components, namely Ga(OEP)(O_2CPh) (Figure 3.75; 574 and 630 nm) and H_2BMCPP (Figure 3.79; 635 and 699 nm), allowing the 574 nm band to be assigned to the Ga(OEP) unit, the 635 nm band as having contributions from both Ga(OEP) and the bridging H_2BCPP units but being dominated by the latter, given its closer wavelength agreement, and the 699 nm band arising from H_2BCPP. Given that excitation at 530 nm is largely absorbed by the

Ga(OEP) center, the prominence of the H_2BCPP contributions to the emission spectrum is suggestive of Ga(OEP)→H_2BCPP singlet–singlet energy transfer. The observations for **4** (Figure 3.78) and model compounds in TCB solution (Figures 3.76 and 3.80 for Ga(OEP)(O_2CPh) and H_2BMCPP, respectively) are similar to those in CH_2Cl_2, as expected.

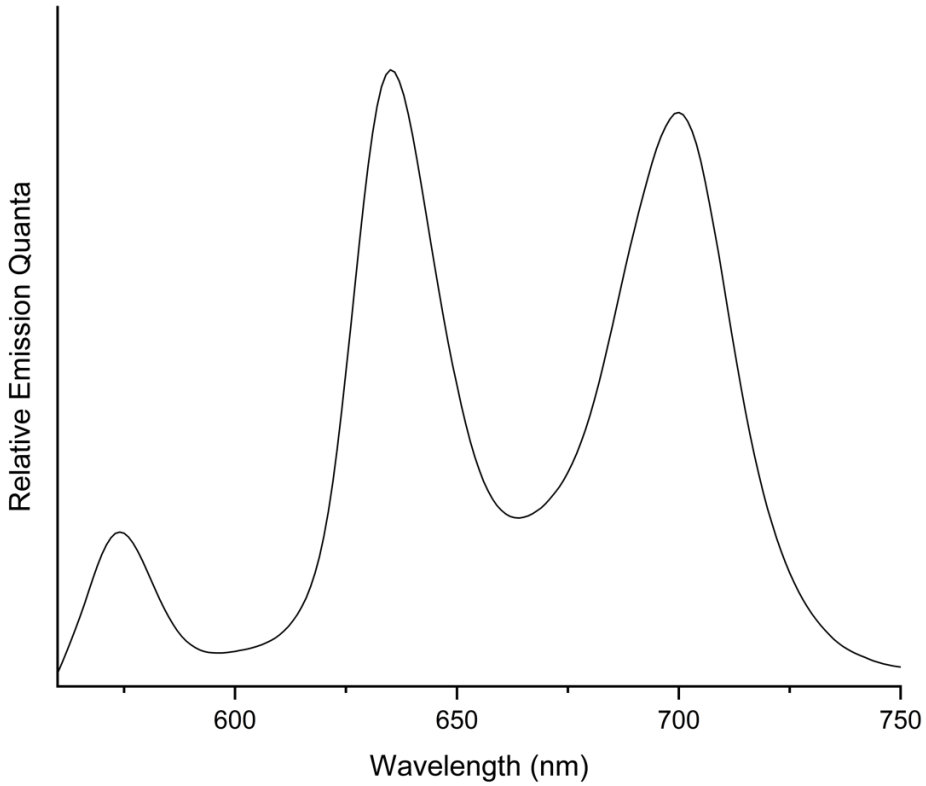

Figure 3.77. Emission spectrum of (Ga(OEP))$_2$(μ-BCPP) (**4**) in CH_2Cl_2 (λ_{ex} = 530 nm).

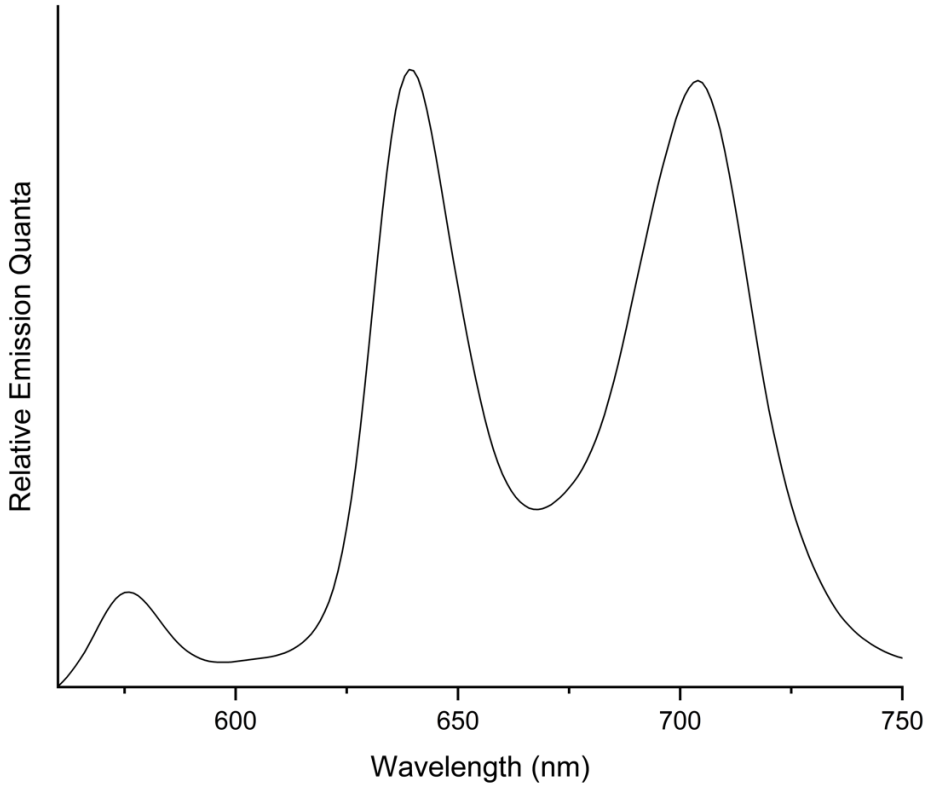

Figure 3.78. Emission spectrum of $(Ga(OEP))_2$(μ-BCPP) (**4**) in TCB (λ_{ex} = 530 nm).

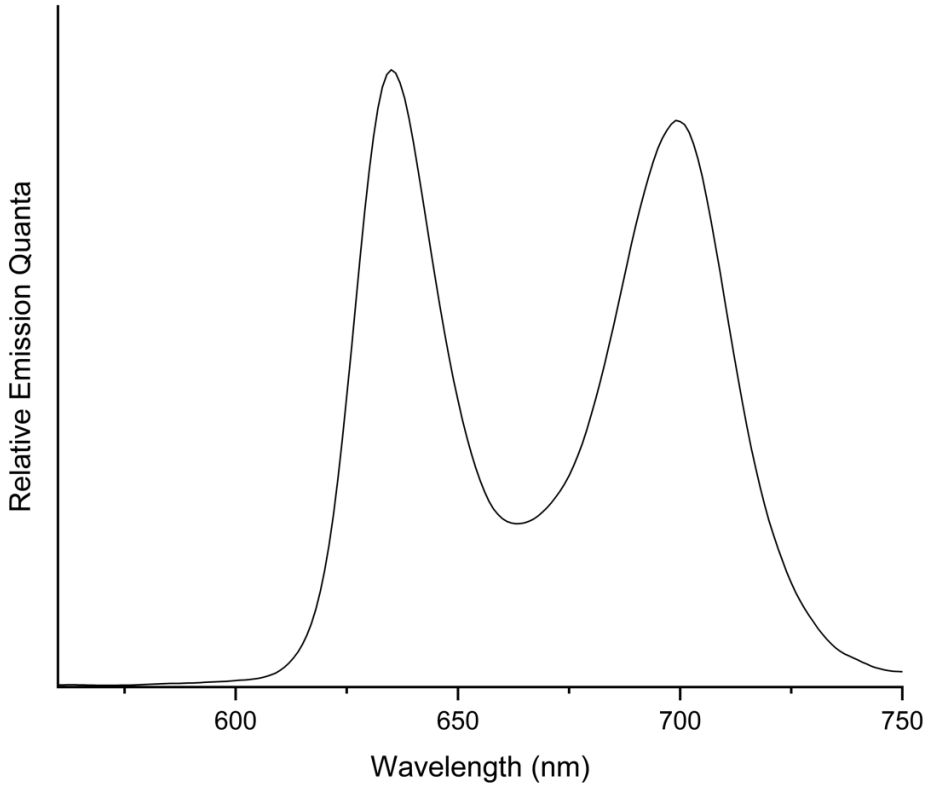

Figure 3.79. Emission spectrum of H_2BMCPP in CH_2Cl_2 (λ_{ex} = 530 nm).

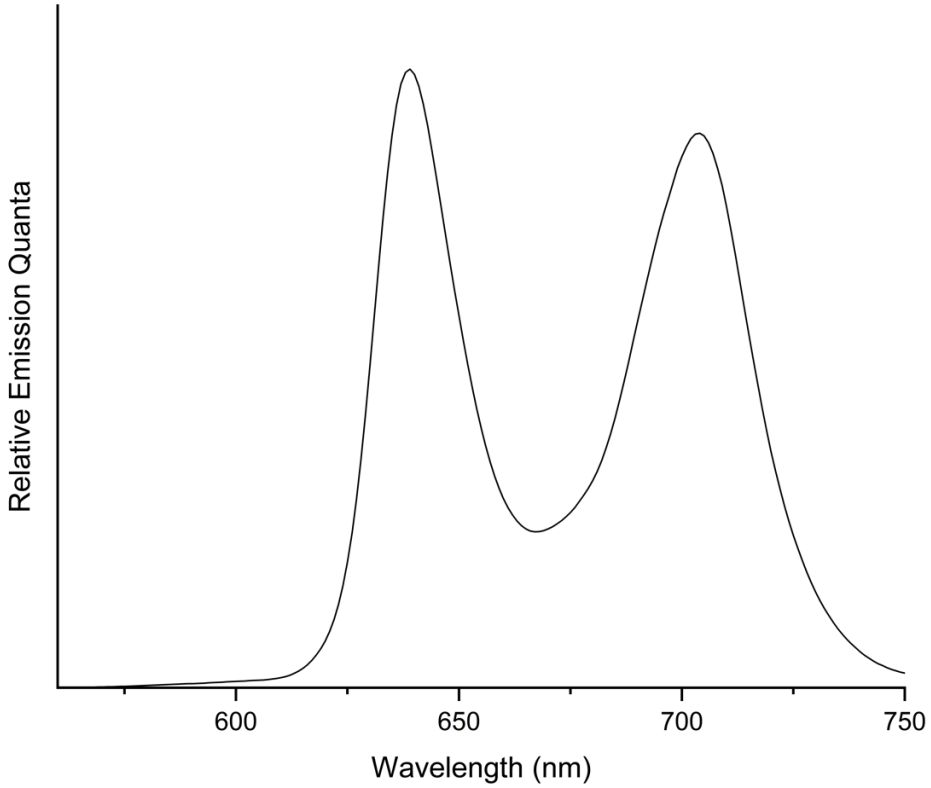

Figure 3.80. Emission spectrum of H_2BMCPP in TCB (λ_{ex} = 530 nm).

In order to investigate energy transfer further, excitation spectra were obtained at an emission monitoring of 710 nm, where only the H_2BCPP unit exhibits emission. In CH_2Cl_2 the excitation spectrum exhibits a weak band at 626 nm, corresponding to the H_2BCPP-derived absorption band at 634 nm, and strong bands near 530 nm and 570 nm (Figure 3.81). Based on the intensity of the 626 nm band, the bands at 530 and 570 nm are far too intense to be consistent with H_2BCPP absorption and instead are clearly dominated by absorption bands of the Ga(OEP) unit that maximize at these wavelengths. These bands are significantly more intense than the band at 500 nm, which is attributable to the absorption of H_2BCPP at 502 nm. These characteristics (and nearly identical ones in TCB solution, Figure 3.82) indicate the operation of facile Ga(OEP)→H_2BCPP energy transfer in **4**. Interporphyrin singlet–singlet energy transfer has been observed in other orthogonal mixed metallo- and free-base porphyrin dimers and trimers.[28,100,101]

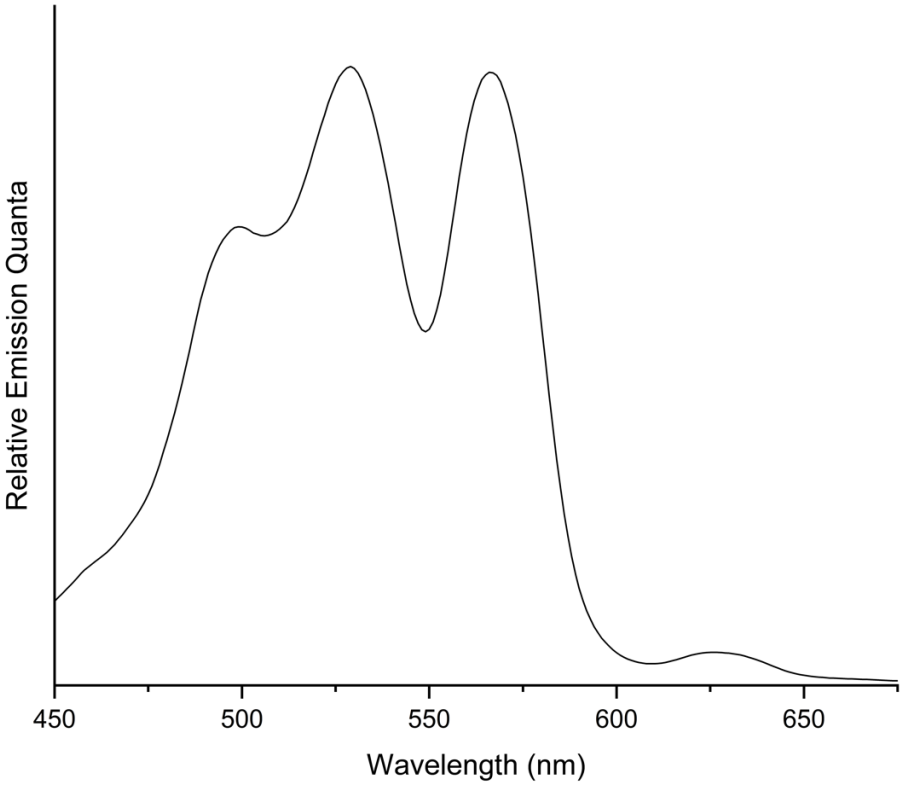

Figure 3.81. Excitation spectrum of $(Ga(OEP))_2(\mu\text{-BCPP})$ (**4**) in CH_2Cl_2 (λ_{em} = 710 nm).

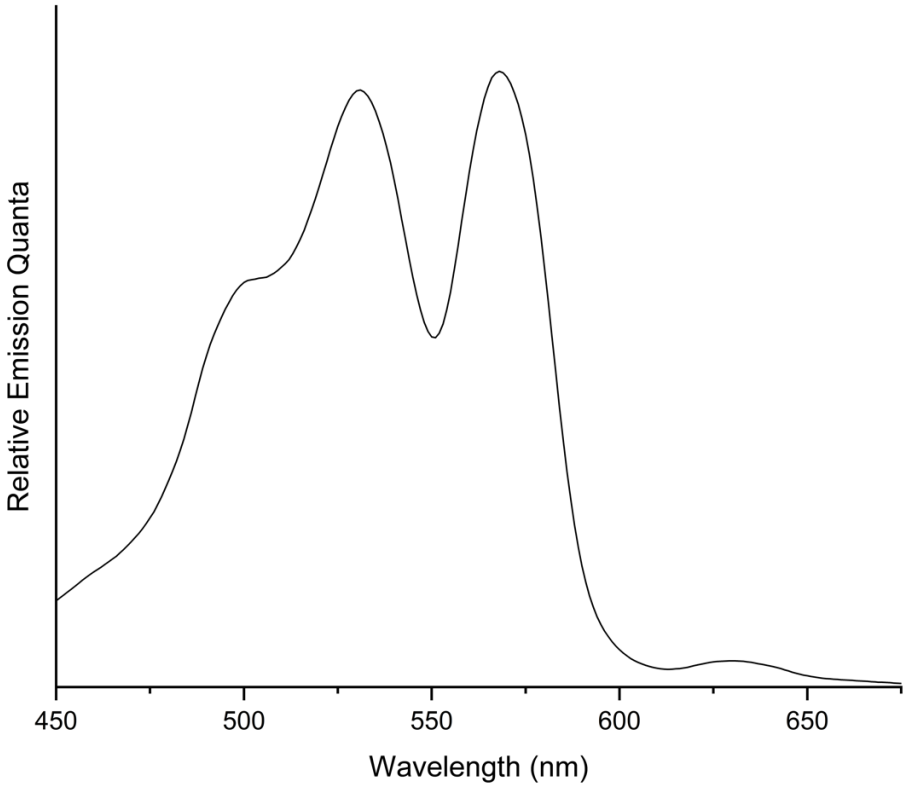

Figure 3.82. Excitation spectrum of $(Ga(OEP))_2(\mu\text{-BCPP})$ (**4**) in TCB (λ_{em} = 710 nm).

The emission spectra for **3** resemble those for **4** but with differences arising from the fact that it is folded in CH_2Cl_2 solution and unfolded in TCB solution. Like **4**, the emission spectra of **3** in both solvents (Figures 3.83 and 3.84) exhibit three bands, at 574 nm (in CH_2Cl_2; 576 nm in TCB), 635 nm (639 nm TCB), and 705 nm (both solvents). As found for **4**, the 574/576 nm band is coincident with a band for the Ga(OEP) unit, the 635/639 nm band contains contributions from the bridging H_2BCP (638/644 nm; Figures 3.85 and 3.86)) and Ga(OEP) (630/632 nm) units, and the 705 nm band is due to the H_2BCP. In contrast to these similarities, the relative intensities of the three bands are substantially different in the two solvents. In TCB, in which **3** has an unfolded structure, the band at 576 nm is weak relative to the other two bands. The overall emission profile is qualitatively similar to that for **4** in CH_2Cl_2 and TCB, and similarly suggestive of analogous Ga(OEP)→H_2BCP energy transfer. In CH_2Cl_2, however, the 574 nm band is stronger than the other two bands. While this seemingly suggests energy transfer is comparatively inefficient, the folded conformation may also substantially alter the fluorescence profile. Studies of cofacial porphyrin dimers with rigid aromatic spacers (Figure 3.1b) containing two free-base porphyrins ($(H_2)_2$) or two zinc porphyrins ($(Zn)_2$) have demonstrated that the fluorescence quantum yield is substantially quenched as the porphyrin–porphyrin separation decreases because interporphyrin interactions increase the non-radiative decay rate.[93,120] The molecular structure of **3** in the folded conformation exhibits distinct environments for H_2BCP and Ga(OEP), where H_2BCP is surrounded by two Ga(OEP) porphyrins, while the Ga(OEP) porphyrins each exhibit close porphyrin–porphyrin interactions on only one face (Figure 3.43c). This may lead to differential quenching of the H_2BCP and Ga(OEP) fluorescence. The 5 nm redshift of the 705 nm band of **3** compared to H_2BECP (700 nm) in CH_2Cl_2 is indicative of significant porphyrin–porphyrin interactions; redshifts of 5 nm and 12 nm in the emission bands were observed for $(H_2)_2$ porphyrin

dimers at separations of 4.32 Å and 3.80 Å, respectively, compared to the monomeric porphyrin.[93] In contrast, no shift is observed for the 574 nm Ga(OEP) emission compared to Ga(OEP)(O_2CPh), indicating that porphyrin–porphyrin interactions may alter the fluorescence of H_2BCP more significantly than Ga(OEP). As the fluorescence profile of **3** in CH_2Cl_2 does not unequivocally demonstrate energy transfer, excitation spectra of **3** were obtained. Excitation spectra of **3** in CH_2Cl_2 (Figure 3.87) and TCB (Figure 3.88) are qualitatively similar to each other and to those of **4**, with the spectra being dominated by the Ga(OEP) absorption bands near 530 nm and 570 nm, despite the emission being entirely from H_2BCP at the emission monitoring of 710 nm. The bands at 500 nm (in CH_2Cl_2; 500 nm in TCB) and 629 nm (629 nm in TCB) correspond to the free base absorption bands at 506 nm (506 nm in TCB) and 633 nm (634 nm in TCB). These characteristics indicate the operation of facile Ga(OEP)→H_2BCP energy transfer in **3** in both CH_2Cl_2 and TCB.

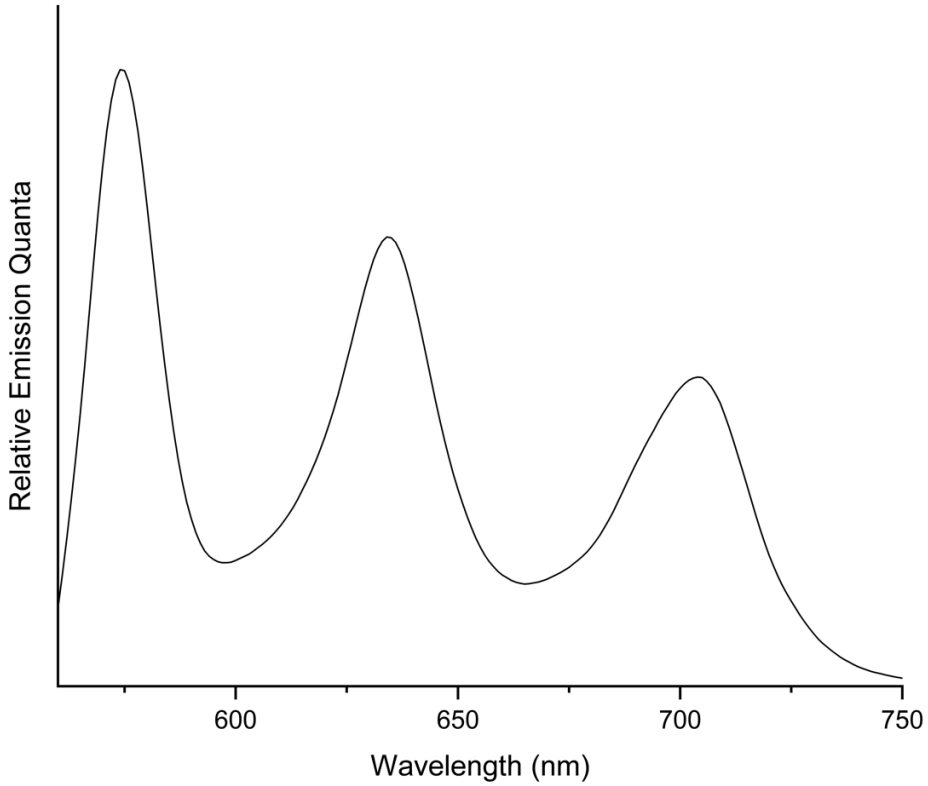

Figure 3.83. Emission spectrum of $(Ga(OEP))_2$(μ-BCP) (**3**) in CH_2Cl_2 (λ_{ex} = 530 nm).

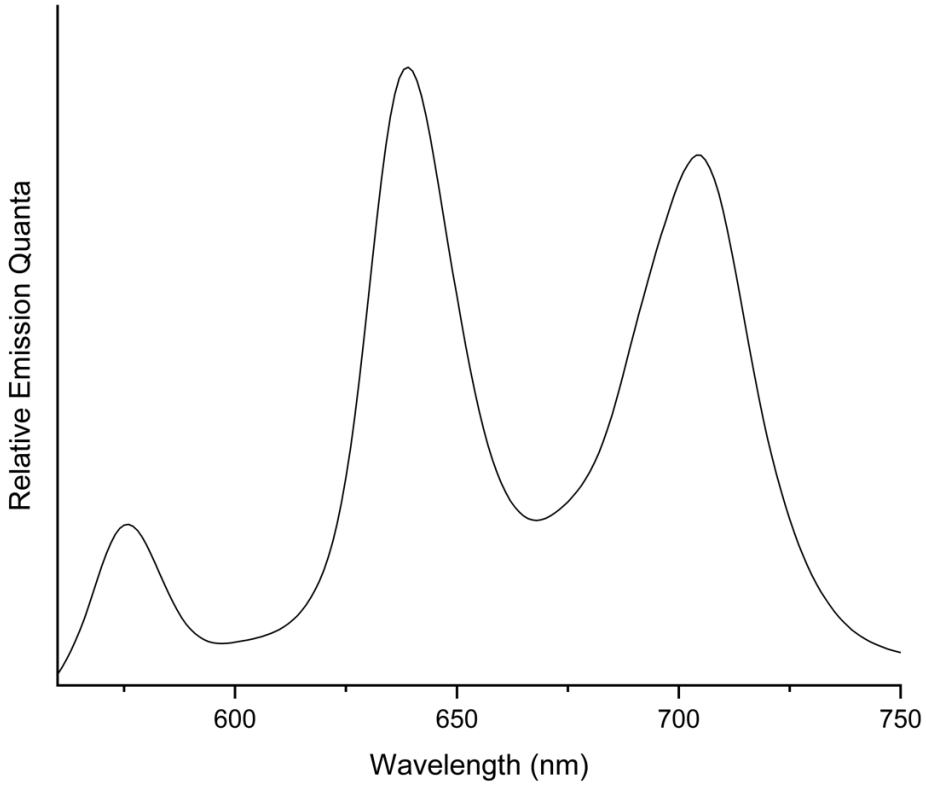

Figure 3.84. Emission spectrum of $(Ga(OEP))_2(\mu\text{-BCP})$ (**3**) in TCB (λ_{ex} = 530 nm).

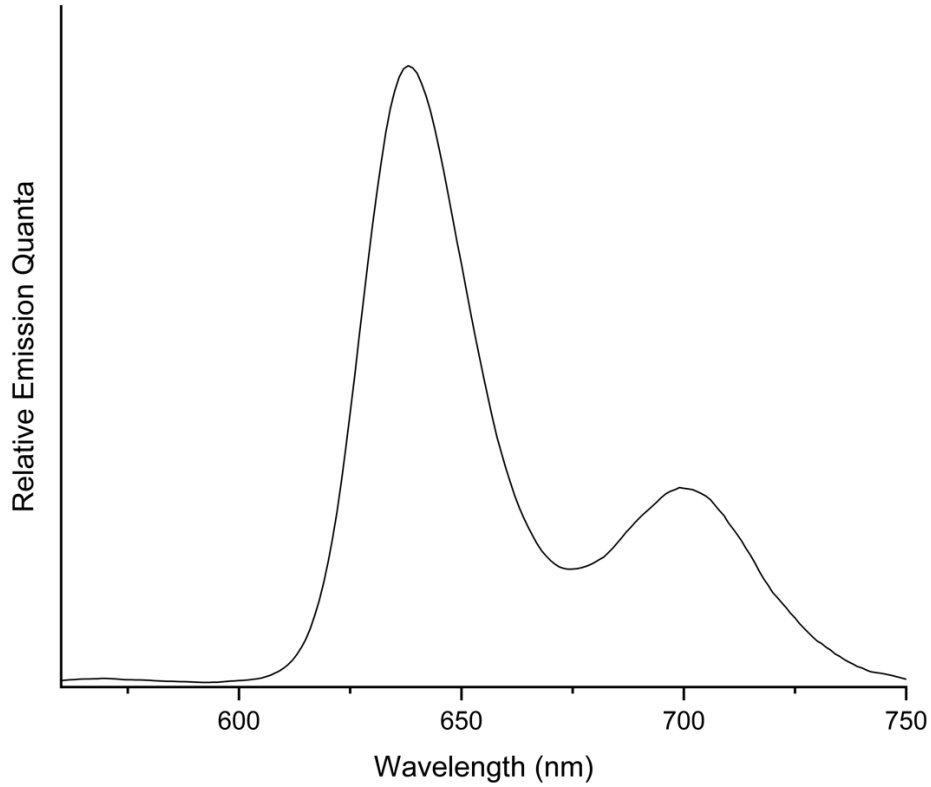

Figure 3.85. Emission spectrum of H_2BECP in CH_2Cl_2 (λ_{ex} = 530 nm).

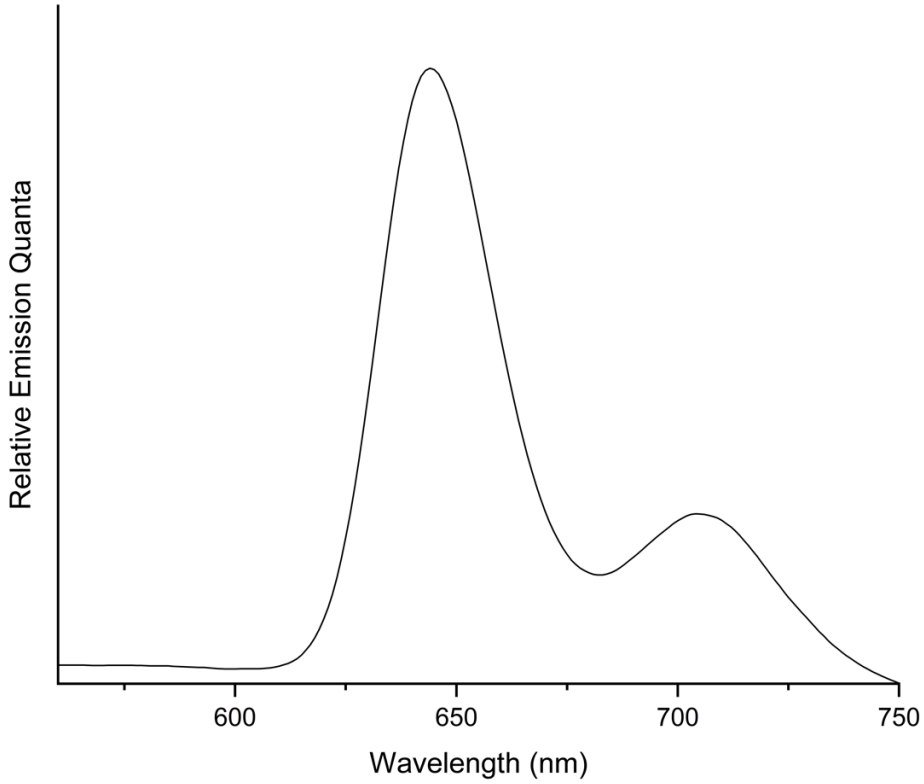

Figure 3.86. Emission spectrum of H_2BECP in TCB (λ_{ex} = 530 nm).

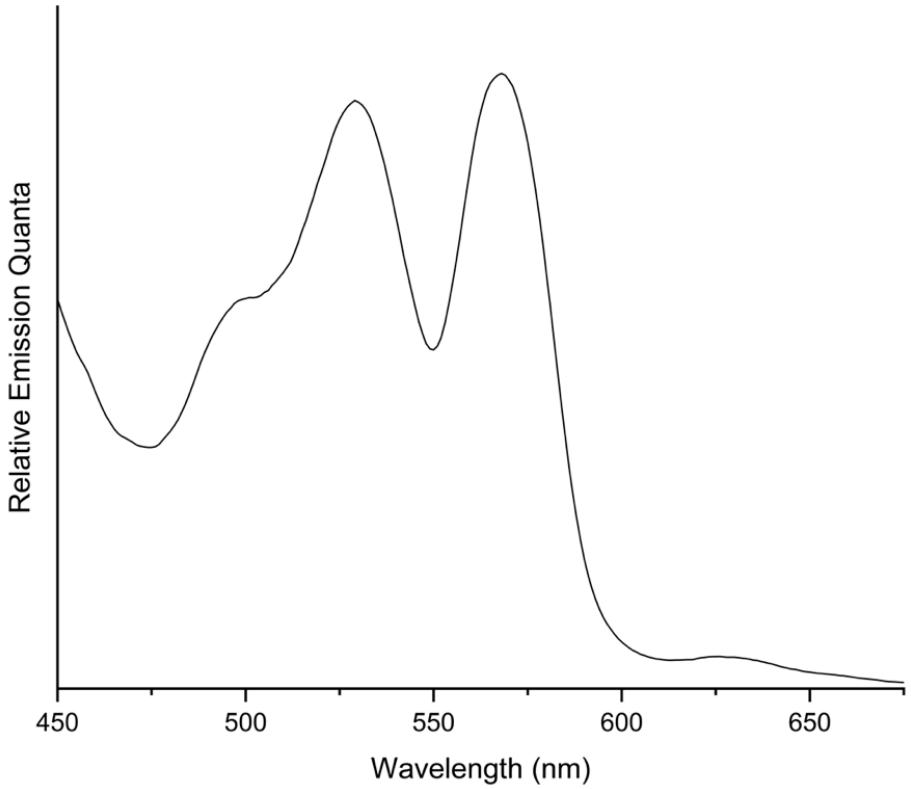

Figure 3.87. Excitation spectrum of $(Ga(OEP))_2$(μ-BCP) (**3**) in CH_2Cl_2 (λ_{em} = 710 nm).

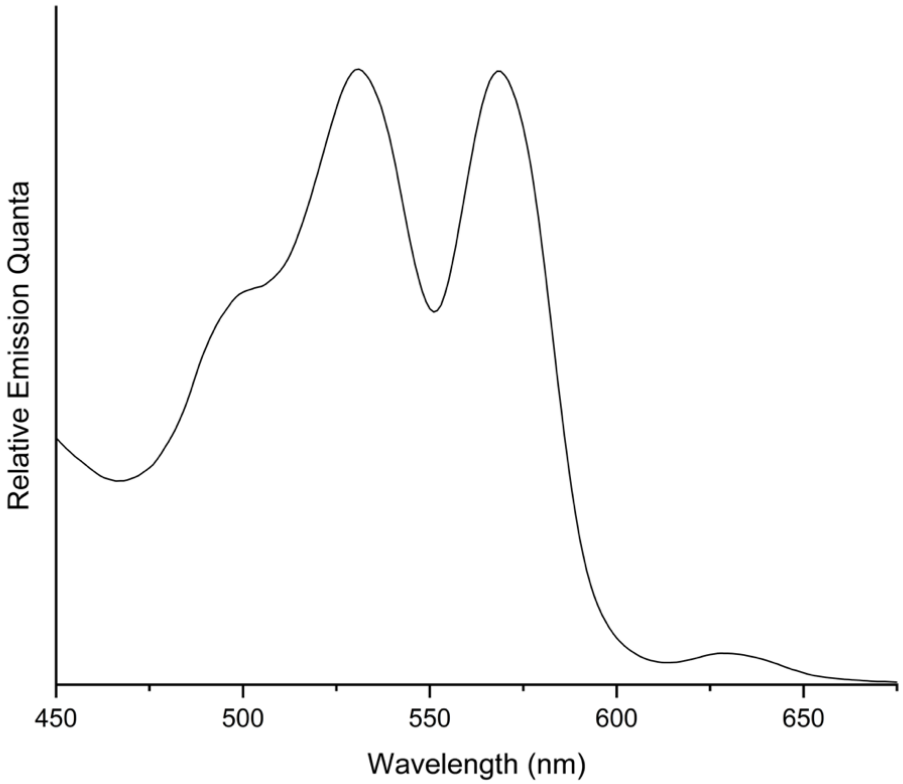

Figure 3.88. Excitation spectrum of $(Ga(OEP))_2(\mu\text{-BCP})$ (**3**) in TCB (λ_{em} = 710 nm).

Table 3.17. Emission Band Maxima (nm) and Relative Intensities.

Complex	Solvent	λ, nm (rel. int.)
1	CH_2Cl_2	574 (100), 630 (45.7)
1m	CH_2Cl_2	574 (100), 630 (44.1)
2	CH_2Cl_2	574 (100), 630 (43.2)
	TCB	576 (100), 632 (44.0)
Ga(OEP)(O_2CPh)	CH_2Cl_2	574 (100), 630 (43.6)
	TCB	576 (100), 632 (42.9)
H_2BECP	CH_2Cl_2	638 (100), 700 (36.0)
	TCB	644 (100), 705 (34.8)
3	CH_2Cl_2	574 (100), 635 (73.0), 705 (51.4)
	TCB	576 (28.1), 639 (100), 705 (86.5)
H_2BMCPP	CH_2Cl_2	635 (100), 699 (93.5)
	TCB	639 (100), 704 (90.7)
4	CH_2Cl_2	574 (26.4), 635 (100), 700 (93.3)
	TCB	576 (16.8), 639 (100), 704 (98.6)

3.4. Conclusions

A series of cofacial gallium porphyrin dimers utilizing dicarboxylate bridging ligands have been synthesized and characterized. A model for the chemical shifts of these compounds that uses the diamagnetic anisotropy of the porphyrin to provide general conformational analysis of solution state structures indicates **3** is folded in $CDCl_3$ because of the presence of strong intramolecular π–π interactions observed in the crystal structure, but exhibits an extended structure in TCB. These findings are confirmed by electronic-absorption spectra for **3** in these solvents. Compounds **1**, **2**, and **4** exhibit extended structures in solution, based on similar analyses.

The effect of dimerization on the electrochemical properties was investigated. Notably, **1** exhibits clear evidence of perturbation from the monomer **1m,** consistent with porphyrin–porphyrin interaction; future investigations could seek to determine the origin of this effect, including electron paramagnetic resonance or NIR spectroelectrochemical measurements. Electronic emission and excitation spectra of **3** and **4** both exhibit clear evidence of energy transfer from the OEP to the free-base bridging porphyrins. Future efforts will be directed towards quantifying this energy transfer using time-resolved measurements.

While the dimeric porphyrin complexes that have been synthesized here were selected in order to exhibit a wide range of porphyrin–porphyrin separations, the simple synthetic requirement of a ligand containing two sterically unencumbered carboxylic acids suggests that a wide variety of bridging ligands could be incorporated. One interesting route would be to incorporate bridging ligands that exhibit complementary functionality to the porphyrins, such as a catalyst that could be photosensitized by the porphyrin. Furthermore, there is significant synthetic space to explore, including utilizing six-coordinate metalloporphyrins to form extended structures or developing different binding motifs, expanding the scope of these systems beyond carboxylate-based linkers.

3.5. References

1. Deisenhofer, J.; Epp, O.; Miki, K.; Huber, R.; Michel, H. X-Ray Structure-Analysis of a Membrane-Protein Complex - Electron-Density Map at 3Å Resolution and a Model of the Chromophores of the Photosynthetic Reaction Center from *Rhodopseudomonas-Viridis*. *J. Mol. Biol.* **1984**, *180*, 385-398.

2. Chang, C. H.; Tiede, D.; Tang, J.; Smith, U.; Norris, J.; Schiffer, M. Structure of *Rhodopseudomonas-Sphaeroides* R-26 Reaction Center. *FEBS Lett.* **1986**, *205*, 82–86.

3. Allen, J. P.; Feher, G.; Yeates, T. O.; Komiya, H.; Rees, D. C. Structure of the Reaction Center from *Rhodobacter Sphaeroides* R-26: The Cofactors. *Proc. Natl. Acad. Sci. U. S. A.* **1987**, *84*, 5730–5734.

4. Feher, G.; Allen, J. P.; Okamura, M. Y.; Rees, D. C. Structure and Function of Bacterial Photosynthetic Reaction Centers. *Nature* **1989**, *339*, 111–116.

5. Panda, M. K.; Ladomenou, K.; Coutsolelos, A. G. Porphyrins in Bio-Inspired Transformations: Light-Harvesting to Solar Cell. *Coord. Chem. Rev.* **2012**, *256*, 2601–2627.

6. Otsuki, J. Supramolecular Approach Towards Light-Harvesting Materials Based on Porphyrins and Chlorophylls. *J. Mater. Chem. A* **2018**, *6*, 6710–6753.

7. Rosenthal, J.; Nocera, D. G. Role of Proton-Coupled Electron Transfer in O–O Bond Activation. *Acc. Chem Res.* **2007**, *40*, 543–553.

8. Afanasiev, P.; Sorokin, A. B. μ-Nitrido Diiron Macrocyclic Platform: Particular Structure for Particular Catalysis. *Acc. Chem. Res.* **2016**, *49*, 583–593.

9. Lu, H.; Kobayashi, N. Optically Active Porphyrin and Phthalocyanine Systems. *Chem. Rev.* **2016**, *116*, 6184–6261.

10. Anderson, H. L. Building Molecular Wires from the Colours of Life: Conjugated Porphyrin Oligomers. *Chem. Commun.* **1999**, 2323–2330.

11. Beletskaya, I.; Tyurin, V. S.; Tsivadze, A. Y.; Guilard, R.; Stern, C. Supramolecular Chemistry of Metalloporphyrins. *Chem. Rev.* **2009**, *109*, 1659–1713.

12. Pognon, G.; Wytko, J. A.; Weiss, J. Synthesis and Properties of Covalent Cofacial Bisporphyrins. *Targets Heterocycl. Syst.* **2008**, *11*, 21–43.

13. Harvey, P. D.; Stern, C.; Gros, C. P.; Guilard, R. The Photophysics and Photochemistry of Cofacial Free Base and Metallated Bisporphyrins Held Together by Covalent Architectures. *Coord. Chem. Rev.* **2007**, *251*, 401–428.

14. Vargas-Zuniga, G. I.; Boreen, M. A.; Mangel, D. N.; Arnold, J.; Sessler, J. L. Porphyrinoid Actinide Complexes. *Chem. Soc. Rev.* **2022**, *51*, 3735–3758.

15. Kobuke, Y. Porphyrin Supramolecules by Self-Complementary Coordination. In *Non-Covalent Multi-Porphyrin Assemblies*; Alessio, E., Ed. Vol. 121; Springer Berlin Heidelberg: Berlin, Heidelberg, 2006; pp 49–104.

16. Guchhait, T.; Sasmal, S.; Khan, F. S. T.; Rath, S. P. Oxo- and Hydroxo-Bridged Diiron(III) Porphyrin Dimers: Inorganic and Bio-Inorganic Perspectives and Effects of Intermacrocyclic Interactions. *Coord. Chem. Rev.* **2017**, *337*, 112–144.

17. Satake, A.; Kobuke, Y. Artificial Photosynthetic Systems: Assemblies of Slipped Cofacial Porphyrins and Phthalocyanines Showing Strong Electronic Coupling. *Org. Biomol. Chem.* **2007**, *5*, 1679–1691.

18. Chang, C. J.; Deng, Y. Q.; Heyduk, A. F.; Chang, C. K.; Nocera, D. G. Xanthene-Bridged Cofacial Bisporphyrins. *Inorg. Chem.* **2000**, *39*, 959–966.

19. Deng, Y. Q.; Chang, C. J.; Nocera, D. G. Direct Observation of the "Pac-Man" Effect from Dibenzofuran-Bridged Cofacial Bisporphyrins. *J. Am. Chem. Soc.* **2000**, *122*, 410–411.

20. Chang, C. K.; Abdalmuhdi, I. A Biphenylenediporphyrin - 2 Cofacially Arranged Porphyrins with a Biphenylene Bridge. *Angew. Chem., Int. Ed. Engl.* **1984**, *23*, 164–165.

21. Chang, C. K.; Abdalmuhdi, I. Anthracene Pillared Cofacial Diporphyrin. *J. Org. Chem.* **1983**, *48*, 5388–5390.

22. Collman, J. P.; Denisevich, P.; Konai, Y.; Marrocco, M.; Koval, C.; Anson, F. C. Electrode Catalysis of the 4-Electron Reduction of Oxygen to Water by Dicobalt Face-to-Face Porphyrins. *J. Am. Chem. Soc.* **1980**, *102*, 6027–6036.

23. Poddutoori, P. K.; Lim, G. N.; Vassiliev, S.; D'Souza, F. Ultrafast Charge Separation and Charge Stabilization in Axially Linked ‘Tetrathiafulvalene-Aluminum(III) Porphyrin-Gold(III) Porphyrin' Reaction Center Mimics. *Phys. Chem. Chem. Phys.* **2015**, *17*, 26346–26358.

24. Poddutoori, P. K.; Sandanayaka, A. S. D.; Zarrabi, N.; Hasobe, T.; Ito, O.; van der Est, A. Sequential Charge Separation in Two Axially Linked Phenothiazine-Aluminum(III) Porphyrin-Fullerene Triads. *J. Phys. Chem. A* **2011**, *115*, 709–717.

25. Poddutoori, P. K.; Sandanayaka, A. S. D.; Hasobe, T.; Ito, O.; van der Est, A. Photoinduced Charge Separation in a Ferrocene-Aluminum(III) Porphyrin-Fullerene Supramolecular Triad. *J. Phys. Chem. B* **2010**, *114*, 14348–14357.

26. Poddutoori, P. K.; Bregles, L. P.; Lim, G. N.; Boland, P.; Kerr, R. G.; D'Souza, F. Modulation of Energy Transfer into Sequential Electron Transfer Upon Axial Coordination of Tetrathiafulvalene in an Aluminum(III) Porphyrin-Free-Base Porphyrin Dyad. *Inorg. Chem.* **2015**, *54*, 8482–8494.

27. Zarrabi, N.; Obondi, C. O.; Lim, G. N.; Seetharaman, S.; Boe, B. G.; D'Souza, F.; Poddutoori, P. K. Charge-Separation in Panchromatic, Vertically Positioned Bis(Donor Styryl)BODIPY–Aluminum(III) Porphyrin–Fullerene Supramolecular Triads. *Nanoscale* **2018**, *10*, 20723–20739.

28. Amati, A.; Cavigli, P.; Demitri, N.; Natali, M.; Indelli, M. T.; Iengo, E. Sn(IV) Multiporphyrin Arrays as Tunable Photoactive Systems. *Inorg. Chem.* **2019**, *58*, 4399–4411.

29. Amati, A.; Cavigli, P.; Kahnt, A.; Indelli, M. T.; Iengo, E. Self-Assembled Ruthenium(II)Porphyrin-Aluminium(III)Porphyrin-Fullerene Triad for Long-Lived Photoinduced Charge Separation. *J. Phys. Chem. A* **2017**, *121*, 4242–4252.

30. Davidson, G. J. E.; Lane, L. A.; Raithby, P. R.; Warren, J. E.; Robinson, C. V.; Sanders, J. K. M. Coordination Polymers Based on Aluminum(III) Porphyrins. *Inorg. Chem.* **2008**, *47*, 8721–8726.

31. Bagaki, A.; Gobeze, H. B.; Charalambidis, G.; Charisiadis, A.; Stangel, C.; Nikolaou, V.; Stergiou, A.; Tagmatarchis, N.; D'Souza, F.; Coutsolelos, A. G. Axially Assembled Photosynthetic Antenna-Reaction Center Mimics Composed of Boron Dipyrromethenes, Aluminum Porphyrin, and Fullerene Derivatives. *Inorg. Chem.* **2017**, *56*, 10268–10280.

32. Lau, W.-Y. Ph. D. Thesis. The University of Chicago, Chicago, IL, 2016.

33. Pangborn, A. B.; Giardello, M. A.; Grubbs, R. H.; Rosen, R. K.; Timmers, F. J. Safe and Convenient Procedure for Solvent Purification. *Organometallics* **1996**, *15*, 1518–1520.

34. Coutsolelos, A.; Guilard, R.; Bayeul, D.; Lecomte, C. Gallium(III) Porphyrins - Synthesis and Physicochemical Characteristics of Halogeno Gallium(III) Porphyrins X-Ray Crystal-Structure of Chloro-(5,10,15,20-Tetraphenylporphyrinato) Gallium(III). *Polyhedron* **1986**, *5*, 1157–1164.

35. Grorud, A. P. K., J. M.; Mujid, F.; Park, J.; Hopkins, M. D. Self-Assembly of Porphyrin Monolayers on Monolayer Transition Metal Dichalcogenides under Ambient Conditions. *In Preparation*

36. Laha, J. K.; Dhanalekshmi, S.; Taniguchi, M.; Ambroise, A.; Lindsey, J. S. A Scalable Synthesis of *meso*-Substituted Dipyrromethanes. *Org. Process Res. Dev.* **2003**, *7*, 799–812.

37. Marschner, S. M.; Haldar, R.; Fuhr, O.; Woll, C.; Brase, S. Modular Synthesis of *trans*-A_2b_2 - Porphyrins with Terminal Esters: Systematically Extending the Scope of Linear Linkers for Porphyrin-Based MOFs. *Chem. – Eur. J.* **2021**, *27*, 1390–1401.

38. Fulmer, G. R.; Miller, A. J. M.; Sherden, N. H.; Gottlieb, H. E.; Nudelman, A.; Stoltz, B. M.; Bercaw, J. E.; Goldberg, K. I. NMR Chemical Shifts of Trace Impurities: Common Laboratory Solvents, Organics, and Gases in Deuterated Solvents Relevant to the Organometallic Chemist. *Organometallics* **2010**, *29*, 2176–2179.

39. Terazono, Y.; North, E. J.; Moore, A. L.; Moore, T. A.; Gust, D. Base-Catalyzed Direct Conversion of Dipyrromethanes to 1,9-Dicarbinols: A [2+2] Approach for Porphyrins. *Org. Lett.* **2012**, *14*, 1776–1779.

40. Shi, L.; Jiang, Y. Y.; Jiang, T.; Yin, W.; Yang, J. P.; Cao, M. L.; Fang, Y. Q.; Liu, H. Y. Water-Soluble Manganese and Iron Mesotetrakis(Carboxyl)Porphyrin: DNA Binding, Oxidative Cleavage, and Cytotoxic Activities. *Molecules* **2017**, *22*, 1084.

41. Lu, K. D.; He, C. B.; Lin, W. B. Nanoscale Metal-Organic Framework for Highly Effective Photodynamic Therapy of Resistant Head and Neck Cancer. *J. Am. Chem. Soc.* **2014**, *136*, 16712–16715.

42. Krause, L.; Herbst-Irmer, R.; Sheldrick, G. M.; Stalke, D. Comparison of Silver and Molybdenum Microfocus X-Ray Sources for Single-Crystal Structure Determination. *J. Appl. Crystallogr.* **2015**, *48*, 3–10.

43. Sheldrick, G. M. SHELXT – Integrated Space-Group and Crystal-Structure Determination. *Acta Crystallogr., Sect. A: Found. Adv.* **2015**, *71*, 3–8.

44. Dolomanov, O. V.; Bourhis, L. J.; Gildea, R. J.; Howard, J. A. K.; Puschmann, H. OLEX2: A Complete Structure Solution, Refinement and Analysis Program. *J. Appl. Crystallogr.* **2009**, *42*, 339–341.

45. Sheldrick, G. M. Crystal Structure Refinement with SHELXL. *Acta Crystallogr., Sect. C: Struct. Chem.* **2015**, *71*, 3–8.

46. Frisch, M. J.; Trucks, G. W.; Schlegel, H. B.; Scuseria, G. E.; Robb, M. A.; Cheeseman, J. R.; Scalmani, G.; Barone, V.; Petersson, G. A.; Nakatsuji, H.; Li, X.; Caricato, M.; Marenich, A. V.; Bloino, J.; Janesko, B. G.; Gomperts, R.; Mennucci, B.; Hratchian, H. P.; Ortiz, J. V.; Izmaylov, A. F.; Sonnenberg, J. L.; Williams; Ding, F.; Lipparini, F.; Egidi, F.; Goings, J.; Peng, B.; Petrone, A.; Henderson, T.; Ranasinghe, D.; Zakrzewski, V. G.; Gao, J.; Rega, N.; Zheng, G.; Liang, W.; Hada, M.; Ehara, M.; Toyota, K.; Fukuda, R.; Hasegawa, J.; Ishida, M.; Nakajima, T.; Honda, Y.; Kitao, O.; Nakai, H.; Vreven, T.; Throssell, K.; Montgomery Jr., J. A.; Peralta, J. E.; Ogliaro, F.; Bearpark, M. J.; Heyd, J. J.; Brothers, E. N.; Kudin, K. N.; Staroverov, V. N.; Keith, T. A.; Kobayashi, R.; Normand, J.; Raghavachari, K.; Rendell, A. P.; Burant, J. C.; Iyengar, S. S.; Tomasi, J.; Cossi, M.;

Millam, J. M.; Klene, M.; Adamo, C.; Cammi, R.; Ochterski, J. W.; Martin, R. L.; Morokuma, K.; Farkas, O.; Foresman, J. B.; Fox, D. J. *Gaussian 16 Rev. A.03,* Wallingford, CT. 2016.

47. Perdew, J. P.; Burke, K.; Wang, Y. Generalized Gradient Approximation for the Exchange-Correlation Hole of a Many-Electron System. *Phys. Rev. B* **1996**, *54*, 16533–16539.

48. Perdew, J. P.; Chevary, J. A.; Vosko, S. H.; Jackson, K. A.; Pederson, M. R.; Singh, D. J.; Fiolhais, C. Erratum: Atoms, Molecules, Solids, and Surfaces - Applications of the Generalized Gradient Approximation for Exchange and Correlation. *Phys. Rev. B* **1993**, *48*, 4978–4978.

49. Perdew, J. P.; Chevary, J. A.; Vosko, S. H.; Jackson, K. A.; Pederson, M. R.; Singh, D. J.; Fiolhais, C. Atoms, Molecules, Solids, and Surfaces - Applications of the Generalized Gradient Approximation for Exchange and Correlation. *Phys. Rev. B* **1992**, *46*, 6671–6687.

50. Perdew, J. P. In *Electronic Structure of Solids '91*; Ziesche, P., Eschrig, H., Eds.; Vol. 11; Akademie Verlag: Berlin, 1991.

51. Burke, K.; Perdew, J. P.; Wang, Y. In *Electronic Density Functional Theory: Recent Progress and New Directions*; Dobson, J. F., Vignale, G., Das, M. P., Eds.; Plenum: 1998.

52. Grimme, S.; Ehrlich, S.; Goerigk, L. Effect of the Damping Function in Dispersion Corrected Density Functional Theory. *J. Comput. Chem.* **2011**, *32*, 1456–1465.

53. Hay, P. J.; Wadt, W. R. Abinitio Effective Core Potentials for Molecular Calculations - Potentials for the Transition-Metal Atoms Sc to Hg. *J. Chem. Phys.* **1985**, *82*, 270–283.

54. Wadt, W. R.; Hay, P. J. Abinitio Effective Core Potentials for Molecular Calculations - Potentials for Main Group Elements Na to Bi. *J. Chem. Phys.* **1985**, *82*, 284–298.

55. Palmer, D. C. *Crystalmaker,* Version 10.6.5; CrystalMaker Software Ltd: Begbroke, Oxfordshire, England.

56. Kamm, J. M. Ph. D. Thesis. The University of Chicago, Chicago, IL, 2017.

57. Deacon, G. B.; Phillips, R. J. Relationships between the Carbon-Oxygen Stretching Frequencies of Carboxylato Complexes and the Type of Carboxylate Coordination. *Coord. Chem. Rev.* **1980**, *33*, 227–250.

58. Das, N.; Ghosh, A.; Arif, A. M.; Stang, P. J. Self-Assembly of Neutral Platinum-Based Supramolecular Ensembles Incorporating Oxocarbon Dianions and Oxalate. *Inorg. Chem.* **2005**, *44*, 7130–7137.

59. Kim, J. C.; Cho, J. H.; Lough, A. J. Syntheses, Isolation, and Structures of Nickel(II) and Copper(II) Coordination Polymers with a Tetraaza Macrocyclic Ligand. *Inorg. Chim. Acta.* **2001**, *317*, 252–258.

60. Li, M. X.; Xie, G. Y.; Jin, S. L.; Gu, Y. D.; Chen, M. Q.; Liu, J.; Xu, Z.; You, X. Z. Synthesis and Magnetic Properties of Novel Maleato-Bridged Cyclic Tetranuclear Manganese(II) Complexes: Crystal Structure of $[Mn_4(M\text{-}Maleate)_2(Bipy)_8](Clo4)(4)\bullet(Meoh)_2(H_2o)_2$. *Polyhedron* **1996**, *15*, 535–539.

61. Boucher, L. J.; Katz, J. J. Infared Spectra of Metalloporphyrins (4000–160 cm-1). *J. Am. Chem. Soc.* **1967**, *89*, 1340–1345.

62. Wang, N.; Lei, H. T.; Zhang, Z. Y.; Li, J. F.; Zhang, W.; Cao, R. Electrocatalytic Hydrogen Evolution with Gallium Hydride and Ligand-Centered Reduction. *Chem. Sci.* **2019**, *10*, 2308-2314.

63. Natali, M.; Amati, A.; Demitri, N.; Iengo, E. Photoinduced Electron vs. Concerted Proton Electron Transfer Pathways in Sn^{IV} $(L\text{-}Tryptophanato)_2$ Porphyrin Conjugates. *Chem. – Eur. J.* **2021**, *27*, 7872–7881.

64. Rani, J.; Raveendran, A.; Sushila; Chaudhary, A.; Panda, M. K.; Patra, R. Polymorphism in Sn(IV)-Tetrapyridyl Porphyrins with a Halogenated Axial Ligand: Structural, Photophysical, and Morphological Study. *Cryst. Growth & Des.* **2018**, *18*, 1437–1447.

65. Siddiqui, R.; Rani, J.; Akshita; Dhamija, S.; Shivam, K.; Kagra, D.; Sharma, P.; Venugopalan, P.; Patra, R. Homo- and Hetero-Halogen Interaction Based Molecular Associations in Wheel-Axle Topology Derived Sn(IV) Porphyrin Complexes: An Experimental and Theoretical Analysis. *CrystEngComm* **2023**, 4946–4959.

66. Satoh, W.; Masumoto, S.; Shimizu, M.; Yamamoto, Y.; Akiba, K. Synthesis of Unsymmetrically Substituted Antimony(V) Tetraphenylporphyrins. *B. Chem. Soc. Jpn.* **1999**, *72*, 459–463.

67. Nandi, G.; Sarkar, S. Solid-State Synthesis of Molybdenum and Tungsten Porphyrins and Aerial Oxidation of Coordinated Benzenethiolate to Benzenesulfonate. *Inorg. Chem.* **2012**, *51*, 6412–6420.

68. Pagola, S.; Stephens, P. W.; Bohle, D. S.; Kosar, A. D.; Madsen, S. K. The Structure of Malaria Pigment B-Haematin. *Nature* **2000**, *404*, 307–310.

69. Bohle, D. S.; Dodd, E. L.; Stephens, P. Structure of Malaria Pigment and Related Propanoate-Linked Metalloporphyrin Dimers. *Chem. Biodiversity* **2012**, *9*, 1891–1902.

70. Bohle, D. S.; Dodd, E. L.; Kosar, A. J.; Sharma, L.; Stephens, P. W.; Suárez, L.; Tazoo, D. Soluble Synthetic Analogues of Malaria Pigment: Structure of Mesohematin Anhydride

and Its Interaction with Chloroquine in Solution. *Angew. Chem., Int. Ed.* **2011**, *50*, 6151–6154.

71. Dodd, E. L.; Bohle, D. S. Orienting the Heterocyclic Periphery: A Structural Model for Chloroquine's Antimalarial Activity. *Chem. Commun.* **2014**, *50*, 13765–13768.

72. Kuter, D.; Suarez, L.; Dodd, E. L.; Noll, B. C.; Stephens, P. W.; Bohle, D. S. Hydrating the Bispropionate Notch in Malaria Pigment: A New Structural Motif in the Iron(III)(Deuteroporphyrin) Dimer. *Chem. – Eur. J.* **2019**, *25*, 4373–4378.

73. Bohle, D. S.; Dodd, E. L. [Gallium(III) Protoporphyrin IX]: A Soluble Diamagnetic Model for Malaria Pigment. *Inorg. Chem.* **2012**, *51*, 4411–4413.

74. Gildenhuys, J.; le Roex, T.; Egan, T. J.; de Villiers, K. A. The Single Crystal X-Ray Structure of β-Hematin Dmso Solvate Grown in the Presence of Chloroquine, a β-Hematin Growth-Rate Inhibitor. *J. Am. Chem. Soc.* **2013**, *135*, 1037–1047.

75. Klonis, N.; Dilanian, R.; Hanssen, E.; Darmanin, C.; Streltsov, V.; Deed, S.; Quiney, H.; Tilley, L. Hematin-Hematin Self-Association States Involved in the Formation and Reactivity of the Malaria Parasite Pigment, Hemozoin. *Biochemistry* **2010**, *49*, 6804–6811.

76. Fukushima, K.; Funatsu, K.; Ichimura, A.; Sasaki, Y.; Suzuki, M.; Fujihara, T.; Tsuge, K.; Imamura, T. Synthesis and Properties of Rhodium(III) Porphyrin Cyclic Tetramer and Cofacial Dimer. *Inorg. Chem.* **2003**, *42*, 3187–3193.

77. Funatsu, K.; Imamura, T.; Ichimura, A.; Sasaki, Y. Novel Cofacial Ruthenium(II) Porphyrin Dimers and Tetramers. *Inorg. Chem.* **1998**, *37*, 4986–4995.

78. Kalita, D.; Morisue, M.; Kobuke, Y. Synthesis and Electrochemical Properties of Slipped-Cofacial Porphyrin Dimers of Ferrocene-Functionalized Zn-Imidazolyl-Porphyrins as Potential Terminal Electron Donors in Photosynthetic Models. *New J. Chem.* **2006**, *30*, 77–92.

79. Kobuke, Y.; Miyaji, H. Supramolecular Organization of Imidazolyl-Porphyrin to a Slipped Cofacial Dimer. *J. Am. Chem. Soc.* **1994**, *116*, 4111–4112.

80. Sharma, V. K.; Mahammed, A.; Mizrahi, A.; Morales, M.; Fridman, N.; Gray, H. B.; Gross, Z. Dimeric Corrole Analogs of Chlorophyll Special Pairs. *J. Am. Chem. Soc.* **2021**, *143*, 9450–9460.

81. Kamm, J. M.; Iverson, C. P.; Lau, W. Y.; Hopkins, M. D. Axial Ligand Effects on the Structures of Self-Assembled Gallium–Porphyrin Monolayers on Highly Oriented Pyrolytic Graphite. *Langmuir* **2016**, *32*, 487–495.

82. Park, H.; Kim, J. C.; Lough, A. J.; Lee, B. M. One-Dimensional Macrocyclic Zinc(II) Coordination Polymer Containing an Unusual Bis-Monodentate Oxalate Bridge. *Inorg. Chem. Commun.* **2007**, *10*, 303–306.

83. Kim, J. A.; Park, H.; Kim, J. C.; Lough, A. J.; Pyun, S. Y.; Roh, J.; Lee, B. M. 1D Copper(II) and Zinc(II) Coordination Polymers Containing an Unusual Twisted Oxalate Bridge. *Inorg. Chim. Acta.* **2008**, *361*, 2087–2093.

84. Abraham, R. J.; Bedford, G. R.; Mcneillie, D.; Wright, B. The NMR Spectra of the Porphyrins 16 – Zinc(II) *meso*-Tetraphenylporphyrin (Zn Tpp) as a Diamagnetic Shift Reagent. A Quantitative Ring Current Model. *Org. Magn. Reson.* **1980**, *14*, 418–425.

85. Abraham, R. J.; Fell, S. C. M.; Smith, K. M. The N.M.R Spectra of Porphyrins 13 – a Ring Current Model for Porphyrin and Chlorin (7,8-Dihydroporphyrin) Rings. *Org. Magn. Reson.* **1977**, *9*, 367–373.

86. Perkins, S. J. Ring Current Models for the Heme Ring in Cytochrome-C. *J. Magn. Reson.* **1980**, *38*, 297–312.

87. Gao, Y. Z.; Walter, V.; Ferguson, M. J.; Tykwinski, R. R. Hierarchical Synthesis, Structure, and Photophysical Properties of Gallium- and Ruthenium-Porphyrins with Axially Bonded Azo Ligands. *Chem. – Eur. J.* **2020**, *26*, 16712–16720.

88. Iwamoto, H.; Fukazawa, Y. Ring Current Models of Porphyrin and Conformational Analysis of the Dicarboxylate Complex of Sn Porphyrin. *Heterocycles* **2008**, *75*, 1711–1723.

89. Johnson, C. E.; Bovey, F. A. Calculation of Nuclear Magnetic Resonance Spectra of Aromatic Hydrocarbons. *J. Chem. Phys.* **1958**, *29*, 1012–1014.

90. Kadish, K. M.; Cornillon, J. L.; Coutsolelos, A.; Guilard, R. Synthesis, Electrochemistry, and Ligand-Addition Reactions of Gallium(III) Porphyrins. *Inorg. Chem.* **1987**, *26*, 4167–4173.

91. Kadish, K. M.; Boisseliercocolios, B.; Coutsolelos, A.; Mitaine, P.; Guilard, R. Electrochemistry and Spectroelectrochemistry of Gallium(III) Porphyrins - Redox Properties of 5-Coordinate Ionic and σ-Bonded Complexes. *Inorg. Chem.* **1985**, *24*, 4521–4528.

92. Le Mest, Y.; L'Her, M.; Hendricks, N. H.; Kim, K.; Collman, J. P. Electrochemical and Spectroscopic Properties of Dimeric Cofacial Porphyrins with Nonelectroactive Metal Centers - Delocalization Processes in the Porphyrin π-Cation-Radical Systems. *Inorg. Chem.* **1992**, *31*, 835–847.

93. Faure, S.; Stern, C.; Guilard, R.; Harvey, P. D. Role of the Spacer in the Singlet-Singlet Energy Transfer Mechanism (Förster vs. Dexter) in Cofacial Bisporphyrins. *J. Am. Chem. Soc.* **2004**, *126*, 1253–1261.

94. Buchler, J. W.; Decian, A.; Fischer, J.; Kihnbotulinski, M.; Paulus, H.; Weiss, R. Cerium(IV) Bis(Octaethylporphyrinate) and Dicerium(III) Tris(Octaethylporphyrinate) - Parents of a New Family of Lanthanoid Double-Decker and Triple-Decker Molecules. *J. Am. Chem. Soc.* **1986**, *108*, 3652–3659.

95. Fletcher, J. T.; Therien, M. J. Extreme Electronic Modulation of the Cofacial Porphyrin Structural Motif. *J. Am. Chem. Soc.* **2002**, *124*, 4298–4311.

96. Guilard, R.; Lopez, M. A.; Tabard, A.; Richard, P.; Lecomte, C.; Brandes, S.; Hutchison, J. E.; Collman, J. P. Synthesis and Characterization of Novel Cobalt Aluminum Cofacial Porphyrins - 1st Crystal and Molecular-Structure of a Heterobimetallic Biphenylene Pillared Cofacial Diporphyrin. *J. Am. Chem. Soc.* **1992**, *114*, 9877–9889.

97. Kadish, K. M.; Moninot, G.; Hu, Y.; Dubois, D.; Ibnlfassi, A.; Barbe, J. M.; Guilard, R. Double-Decker Actinide Porphyrins and Phthalocyanines - Synthesis and Spectroscopic Characterization of Neutral, Oxidized, and Reduced Homoleptic and Heteroleptic Complexes. *J Am. Chem. Soc.* **1993**, *115*, 8153–8166.

98. Schaverien, C. J.; Orpen, A. G. Chemistry of (Octaethylporphyrinato)Lutetium and (Octaethylporphyrinato)Yttrium Complexes - Synthesis and Reactivity of (OEP)MX Derivatives and the Selective Activation of O2 by (OEP)Y(μ-Me)$_2$AlMe$_2$. *Inorg. Chem.* **1991**, *30*, 4968–4978.

99. Scheidt, W. R.; Cheng, B.; Safo, M. K.; Cukiernik, F.; Marchon, J. C.; Debrunner, P. G. New Class of Bridged Diiron(III) Complexes with a Single Hydroxo Bridge - the Preparation and Structure of (M-Hydroxo)Bis((Octaethylporphinato)Iron(III)) Perchlorate. *J. Am. Chem. Soc.* **1992**, *114*, 4420–4421.

100. Giribabu, L.; Rao, T. A.; Maiya, B. G. "Axial-Bonding"-Type Hybrid Porphyrin Arrays: Synthesis, Spectroscopy, Electrochemistry, and Singlet State Properties. *Inorg. Chem.* **1999**, *38*, 4971–4980.

101. Kumar, P. P.; Maiya, B. G. Aluminium(III) Porphyrin Based Dimers and Trimers: Synthesis, Spectroscopy and Photochemistry. *New J. Chem.* **2003**, *27*, 619–625.

102. Matano, Y.; Matsumoto, K.; Terasaka, Y.; Hotta, H.; Araki, Y.; Ito, O.; Shiro, M.; Sasamori, T.; Tokitoh, N.; Imahori, H. Synthesis, Structures, and Properties of *meso*-Phosphorylporphyrins: Self-Organization through P–Oxo–Zinc Coordination. *Chem. – Eur. J.* **2007**, *13*, 891–901.

103. Kasha, M.; Rawls, H. R.; Ashraf El-Bayoumi, M. The Exciton Model in Molecular Spectroscopy. *Pure Appl. Chem.* **1965**, *11*, 371–392.

104. Ferrere, S.; Elliott, C. M. Electrochemical Studies of Structurally Related Triply-Bridged Dinuclear Tris(Bipyridine)Iron(II) Complexes - an Electrostatic Model for Site-Site Interaction. *Inorg. Chem.* **1995**, *34*, 5818–5824.

105. Richardson, D. E.; Taube, H. Determination of $E_2° - E_1°$ in Multistep Charge-Transfer by Stationary-Electrode Pulse and Cyclic Voltammetry - Application to Binuclear Ruthenium Ammines. *Inorg. Chem.* **1981**, *20*, 1278–1285.

106. Ammar, F.; Saveant, J. M. Convolution Potential Sweep Voltammetry II. Multistep Nernstian Waves. *J. Electroanal. Chem.* **1973**, *47*, 215–221.

107. Laboratory Solvents and Other Liquid Reagents. In *CRC Handbook of Chemistry and Physics,* 101st ed.; Rumble, J. R., Bruno, T. J., Doa, M. J. ed.; CRC Press 2020.

108. Bao, D. D.; Millare, B.; Xia, W.; Steyer, B. G.; Gerasimenko, A. A.; Ferreira, A.; Contreras, A.; Vullev, V. I. Electrochemical Oxidation of Ferrocene: A Strong Dependence on the Concentration of the Supporting Electrolyte for Nonpolar Solvents. *J. Phys. Chem. A* **2009**, *113*, 1259–1267.

109. Sigvartsen, T.; Gestblom, B.; Noreland, E.; Songstad, J. Conductometric and Dielectric Behavior of Solutions of Tetrabutylammonium Perchlorate in Solvents of Low and Medium Permittivity. *Acta. Chem. Scand.* **1989**, *43*, 103–115.

110. Barrière, F.; Geiger, W. E. Use of Weakly Coordinating Anions to Develop an Integrated Approach to the Tuning of $\Delta E_{1/2}$ Values by Medium Effects. *J. Am. Chem. Soc.* **2006**, *128*, 3980–3989.

111. Cowan, J. A.; Sanders, J. K. M. Synthesis and Electrochemical Properties of Some Metalated and Peripherally Substituted Porphyrin Co-Facial Dimers. *J. Chem. Soc., Perkin Trans. 1* **1987**, 2395–2402.

112. Dinolfo, P. H.; Lee, S. J.; Coropceanu, V.; Brédas, J. L.; Hupp, J. T. Borderline Class II/III Ligand-Centered Mixed Valency in a Porphyrinic Molecular Rectangle. *Inorg. Chem.* **2005**, *44*, 5789–5797.

113. Takai, A.; Gros, C. P.; Barbe, J. M.; Guilard, R.; Fukuzumi, S. Enhanced Electron-Transfer Properties of Cofacial Porphyrin Dimers through π-π Interactions. *Chem. – Eur. J.* **2009**, *15*, 3110–3122.

114. Yamashita, K.; Kuramochi, N.; Van, H. P. Q.; Furutani, K.; Ogawa, T.; Sugiura, K. Efficient Synthesis of Arylenedioxy-Bridged Porphyrin Dimers through Catalyst-Free Nucleophilic Aromatic Substitution. *ChemPlusChem* **2020**, *85*, 217–226.

115. Scheidt, W. R.; Buentello, K. E.; Ehlinger, N.; Cinquantini, A.; Fontani, M.; Laschi, F. Mixed-Valence Porphyrin π-Cation Radical Derivatives: Electrochemical Investigations. *Inorg. Chim. Acta.* **2008**, *361*, 1722-1727.

116. Li, M.; Neal, T. J.; Wyllie, G. R. A.; Oliver, A. G.; Schulz, C. E.; Scheidt, W. R. Metalloporphyrin Mixed-Valence π-Cation Radicals: [Fe(OxoOEC$^{\bullet/2}$)(Cl)]$SbCl_6$, Structure, Magnetic Properties, and Near-IR Spectra. *Inorg. Chem.* **2011**, *50*, 9114–9121.

117. Brancato-Buentello, K. E.; Kang, S. J.; Scheidt, W. R. Metalloporphyrin Mixed-Valence π-Cation Radicals: Solution Stability and Properties. *J. Am. Chem. Soc.* **1997**, *119*, 2839–2846.

118. Scheidt, W. R.; BrancatoBuentello, K. E.; Song, H. S.; Reddy, K. V.; Cheng, B. S. Metalloporphyrin Mixed-Valence π-Cation Radicals: Solid-State Structures. *Inorg. Chem.* **1996**, *35*, 7500–7507.

119. Ohno, O.; Kaizu, Y.; Kobayashi, H. Luminescence of Some Metalloporphins Including the Complexes of the IIIb Metal Group. *J. Chem. Phys.* **1985**, *82*, 1779–1787.

120. Bolze, F.; Gros, C. P.; Drouin, M.; Espinosa, E.; Harvey, P. D.; Guilard, R. Fine Tuning of the Photophysical Properties of Cofacial Diporphyrins via the Use of Different Spacers. *J. Organomet. Chem.* **2002**, *643*, 89–97.

CHAPTER 4

Self-assembly of Cofacial Porphyrin Dimers on HOPG: Double-Decker Monolayers for Intercalation of C_{60}

4.1. Introduction

The development of methods for organizing functional molecules and nanoparticles on atomically smooth surfaces with nanoscale precision promises applications in on-surface synthesis, catalysis, quantum information science, and optoelectronics.[1-8] Supramolecular self-assembly provides a means towards achieving this goal whether the self-assembled systems are functional themselves[9-13] or serve as a template for further functionalization, such as through covalent modification of the surface[14-16] or non-covalent organization of functional components, as in host–guest type networks.[17-21] In Chapter 2, two approaches towards patterning functional molecules were explored on monolayer TMDs, investigating the self-assembly of metalloporphyrins and of 5-coordinate metalloporphyrins modified with a covalently bound redox-active ligand. In this chapter, we turn our attention towards host–guest type systems.

Surface-confined host–guest systems have been utilized for the confinement of a wide variety of guest species and have been investigated under conditions ranging from low-temperature ultra-high vacuum (LT-UHV) to the solid–liquid interface at ambient temperature.[22-27] These systems have often utilized a host species that forms a porous network on atomically flat surfaces; both porphyrins[18,20] and, to a much greater degree, fullerenes[17,18,28-49] have been investigated as guest species in these systems. The particular interest in fullerenes as a guest species has arisen for a number of reasons. First, given the electronic and optical properties of pristine fullerenes and their numerous derivatives, they have often been a target for incorporation into a variety of devices including solar cells, optoelectronics, and as molecular qubits, which often require the fullerenes

to possess spatial periodicity or be organized with respect to other electroactive components.[50-57] Second, incorporation by non-covalent methods allows for the use of synthetically scalable pristine fullerenes with their attendant properties or specific derivatives with desired properties, as opposed to covalent assembly methods which require fullerene tethers that can be both synthetically challenging to install and result in the modification of fullerene properties. Third, fullerenes are only known to form monolayers without a template under limited conditions,[58-62] and often suffer from instability or the formation of multilayers.[60]

Host–guest supramolecular networks specifically targeting fullerenes as guests have utilized a variety of strategies. One approach has utilized porous networks of molecular tectons (Figure 4.1a), such as carboxylic acids,[17,28-34] other hydrogen bonded networks[18,35] and covalent organic frameworks (COFs).[36-39] A second approach has explored pre-fabricated porous molecules that form ordered assemblies (Figure 4.1b), such as oligothiophenes,[17,33,40,41] and shape-persistent macrocycles.[42-44] Another approach is to employ organic molecules onto which fullerene can directly adsorb (Figure 4.1c). Porphyrins have been targeted for use as hosts in these types of systems given their known affinity for fullerenes in both the solution[63-65] and solid state,[66-69] but fullerene incorporation has only been observed under UHV,[45-48] electrochemical conditions,[49] or as a bicomponent guest within a porous network.[18] Despite the incorporation of fullerenes into these systems, many of the host networks fall short of an ideal system, exhibiting non-specific adsorption of the guest,[18,29,33-40,43,48,49] demanding deposition and imaging conditions,[17,18,34,35,43,45-48] or low guest incorporation.[28-30,41,48] Previous research in our group sought to develop a new assembly motif to address these issues using 5-coordinate gallium porphyrins with axial fullerene affinity groups such as pyrenes, thiophenes, or porphyrins to induce assembly of fullerenes into the corral-like structure formed by the axial ligand, with the structure defined by the surface

porphyrin unit-cell (Figure 4.1d). In contrast to previous approaches, the surface structures of these systems would be highly tunable using the well-established relationships between the peripheral substituents of the porphyrin and monolayer structure, capable of producing patterns with varying periodicity or altering the size of the corral to accommodate various guests. The axial ligand could also be altered independently to tune the guest affinity in search of highly stable specific guest adsorption. Deposition of these complexes with C_{60} resulted in selective adsorption of the fullerene into the nano-corral under ambient conditions.[70] However, these systems still suffered from a significant fraction of empty adsorption sites even at high fullerene concentrations, and desorption/adsorption events were observed on the STM time scale at the solid–liquid interface.

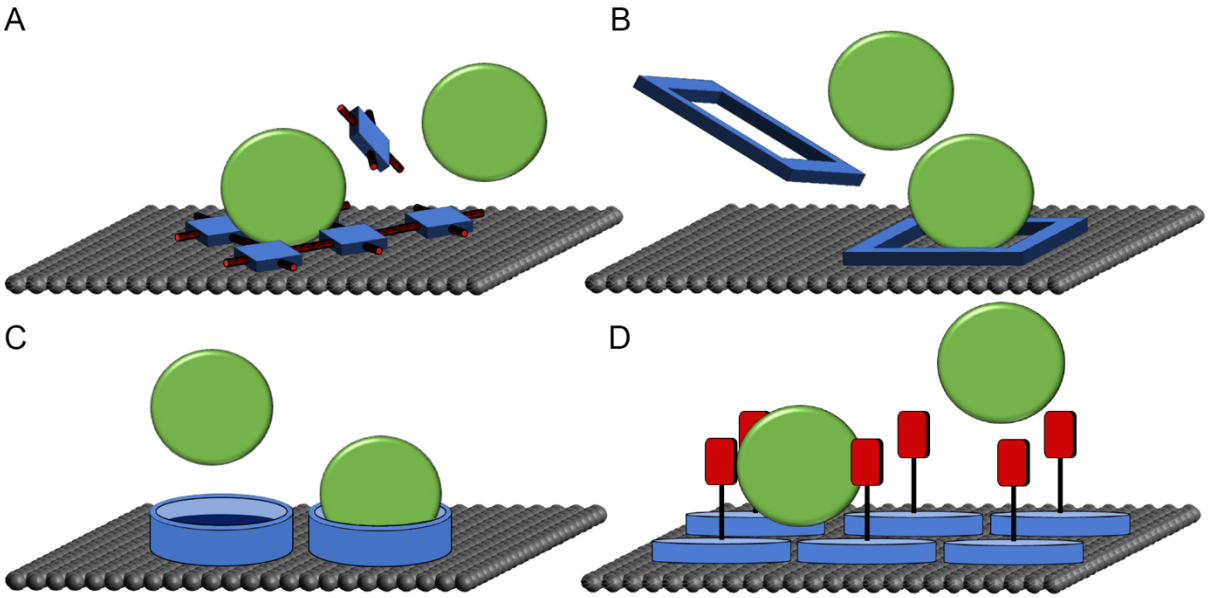

Figure 4.1. Cartoon depiction of literature approaches for organizing fullerene using host-guest type architectures. (a) Fullerene adsorbed within porous network formed from assembled molecular tectons; (b) fullerene adsorbed within pore of pre-fabricated molecule adsorbed on the surface; (c) fullerene adsorbed directly onto adsorbed molecule; (d) fullerene adsorbed onto molecular adlayer with axial affinity groups.

Building on this approach, we hypothesized that a monolayer of porphyrin dimers, such as those synthesized in Chapter 3, would be an attractive system to template the organization of

fullerenes into the nanocavities formed upon monolayer formation, as illustrated in Figure 4.2, where one porphyrin dictates self-assembly on the surface and the other is supported above the surface. A bridging ligand between these two porphyrins serves as both a fullerene affinity group and as a spacer to tailor the distance between the porphyrins, and thus the *z*-dimension of the nanocavity, resulting in a structure that is more reminiscent of fullerenes encapsulated within MOFs[71,72] than surface-confined porous networks. This type of nanocavity then exhibits the previous advantages of the nano-corral approach along with potential improvements of providing greater interaction with the fullerene due to the off-surface capping porphyrin and a structure that is expected to kinetically trap the fullerene upon incorporation into the lattice, preventing desorption even under thermodynamically unfavorable conditions.[73-75] Furthermore, these systems have the potential for additional derivatization; one can envision a heterometallic porphyrin dimer, where a six-coordinate metal would enable *post-hoc* functionalization of the monolayer.

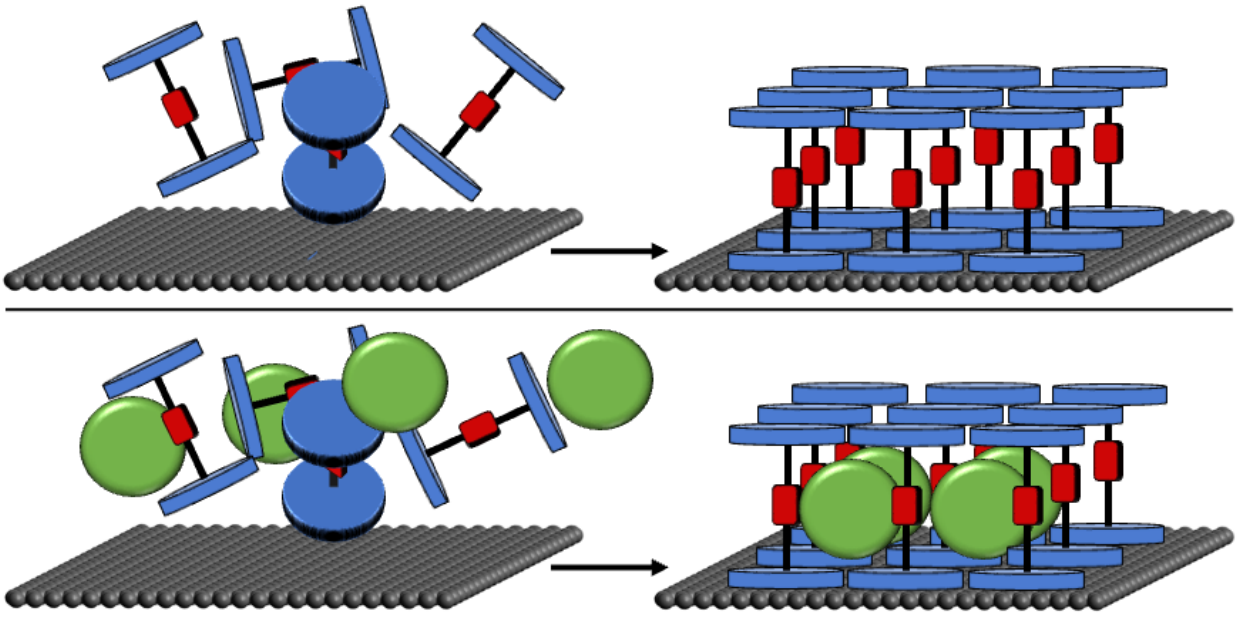

Figure 4.2. Cartoon depiction of self-assembly processes of the pristine porphyrin dimers (above) and mixtures of porphyrin dimers and C_{60} (below) investigated in this study.

While the self-assembly of 4-coordinate metalloporphyrins on atomically flat surfaces has been extensively studied along with, to a lesser extent, 5-coordinate metalloporphyrins, the self-assembly of porphyrin dimers is comparatively much less studied. Several examples of porphyrin and related phthalocyanine dimers have been examined under both UHV and ambient conditions, though these have typically involved "sandwich-type" complexes of the form Por-Ln-Por where Ln is a metal center from the lanthanide series and Por are porphyrins or the related phthalocyanines; the macrocycles in these systems are essentially in van der Waals contact, separated by 3.3–3.5 Å.[76-83] To the best of our knowledge, the only reports of ligand-bridged metalloporphyrins studied by STM are the several reports of transiently observed μ-oxo manganese porphyrin dimers.[84,85] As the porphyrin dimers studied here (Chart 4.1) are significantly larger than those described previously in the literature and, as established in Chapter 3, possess significant structural flexibility, it is unknown whether stable monolayers of these complexes will form. Contributing to this uncertainty, recent work in our group examined several porphyrin dimers based on the tetradecylporphyrin and found that the formation of ordered monolayers was observed with a terephthalate bridging ligand, but not with a pyrene dicarboxylate ligand.[86] Therefore, the self-assembly of the pristine porphyrin dimers will be examined prior to the investigation of their ability to entrain fullerenes.

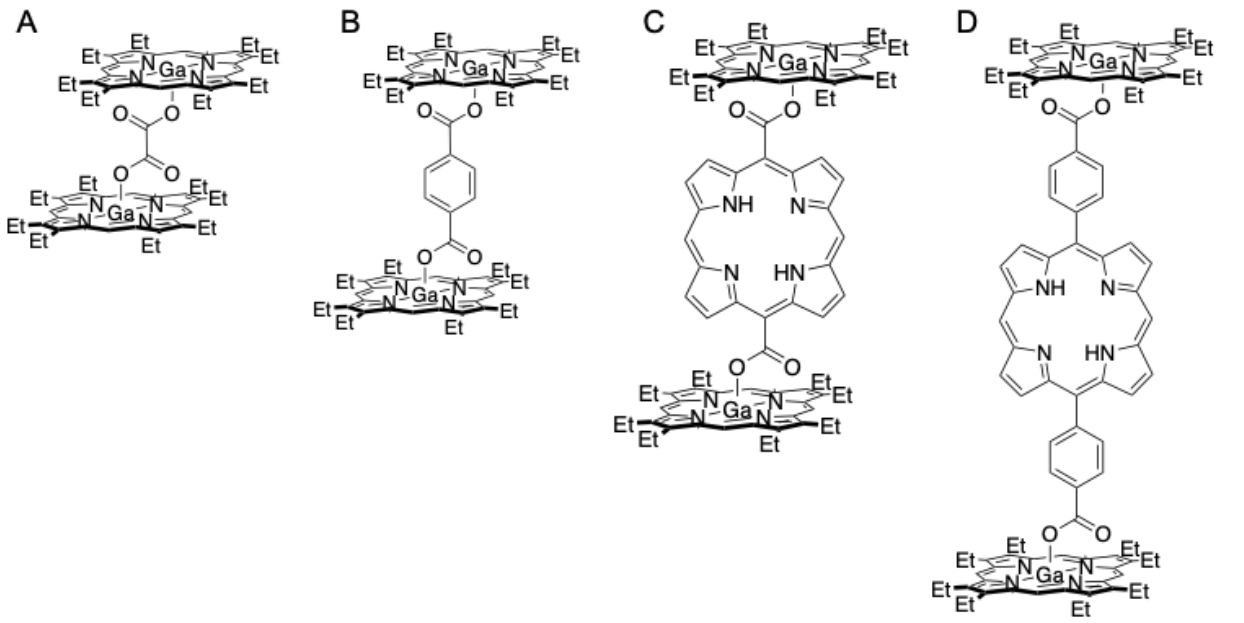

Chart 4.1. Porphyrin dimers studied on HOPG. (a) $(Ga(OEP))_2(\mu\text{-}O_2CCO_2)$ (**1**); (b) $(Ga(OEP))_2(\mu\text{-}O_2CC_6H_4CO_2)$ (**2**); (c) $(Ga(OEP))_2(\mu\text{-BCP})$ (**3**); (d) $(Ga(OEP))_2(\mu\text{-BPCP})$ (**4**). Porphyrin dimers are shown in a fully extended geometry for clarity of the bridging ligand.

In this chapter, the propensity of porphyrin dimers **1**–**4** to form stable ordered monolayers on HOPG at the solid–liquid interface was investigated by STM. For **2**–**4**, which are predicted to form a nanocavity of a suitable size for C_{60}, the co-deposition of the porphyrin dimers and C_{60} was subsequently explored. The bridging ligands in these systems are expected to engender the formed nanocavities with distinct combinations of size and fullerene affinity, ranging from nanocavities that are well-suited to the size of the fullerene but with low fullerene affinity (**2**), both well-suited to the size of the fullerene and with high fullerene affinity (**3**), and poorly suited to the size of the fullerene, but with high fullerene affinity (**4**), allowing for the exploration of how these variables affect the effectiveness of these complexes as templates for fullerene organization. In support of the STM studies, DFT calculations were utilized to determine the adsorption energy of C_{60} in these systems and simulate STM images.

4.2. Experimental Section

4.2.1. Materials. Compounds **1**, **2**, **3**, and **4** were synthesized as described in Chapter 3. 1,2,4-Trichlorobenzene (99%, Oakwood Chemical), C_{60} (99.9%, SES Research), and hexanes (ACS Certified, Fisher Chemical) were used as received.

4.2.2. STM Measurements. Highly oriented pyrolytic graphite (HOPG) (SPI-2 grade, SPI supplies) substrates were mounted to metal specimen discs (12 mm diameter, 0.91 mm thickness) with colloidal silver paste (PELCO, Ted Pella). The surface of the HOPG substrate was cleaved with adhesive tape prior to deposition. 4 μL of a 1,2,4-trichlorobenzene solution containing the porphyrin complex or a pre-mixed solution of the porphyrin complex and C_{60} was deposited onto the surface of the HOPG. STM data were acquired using a Digital Instruments Nanoscope IIIa standalone STM. Tips were either mechanically cut from $Pt_{0.8}Ir_{0.2}$ wire (Goodfellow) or obtained as 8 mm pre-cut $Pt_{0.8}Ir_{0.2}$ probes (Bruker). STM studies of molecular monolayers on HOPG were undertaken at room temperature in constant-current mode at the HOPG–1,2,4-trichlorobenzene interface. Measurements of the underlying HOPG in these samples were obtained in constant-height mode. For each sample where a unit cell is reported, an image of the underlying graphite was acquired in both up- and down-scan directions of the STM. The data for the porphyrin overlayers were corrected after acquisition for instrumental drift in the SPIP software package[87] using a correction factor obtained from the image of the underlying graphite in the same scan direction and the lattice parameters of graphite. Data analyses were performed using Gwyddion software.[88] Images were flattened, low-pass filtered, and sharpened by adjusting the contrast. Reported lattice parameters are averages of those determined from consecutive up- and down-scan images. For each of these images, the unit-cell distances were determined from the average

distances of 100 sets of 5 consecutive porphyrin molecules, and the unit-cell angle was the average of 40 measurements.

4.2.3. Single-Crystal X-Ray Diffraction Studies.

4.2.3.1. General Information. Crystals of **2**•$(C_{60})_2$•$C_6H_3Cl_3$ were grown at room temperature by vapor diffusion of hexanes into a solution of 1.0 equivalent of **2** and 0.9 equivalents of C_{60} in 1,2,4-trichlorobenzene.X-ray diffraction experiments were performed by Dr. Alexander Filatov. Diffraction data were measured at 100 K on a Bruker D8 VENTURE diffractometer equipped with a microfocus Mo-target X-ray tube (λ = 0.71073 Å) and PHOTON 100 CMOS detector. Data were collected using ω scans to survey a sphere of reciprocal space. Data reduction and integration were performed with the Bruker APEX3 software package (Bruker AXS, version 2017.3-0, 2018). Data were scaled and corrected for absorption effects using the multi-scan procedure as implemented in SADABS (Bruker AXS, version 2014/5).[89] The structure was solved by SHELXT (Version 2018/2)[90] and refined by a full-matrix least-squares procedure using OLEX2[91] (XL refinement program version 2018/3)[92] Crystallographic data and details of the data collection and structure refinement are listed in Table 4.1.

Table 4.1. Crystal Data and Structure Refinement for **2**•$(C_{60})_2$•$C_6H_3Cl_3$.

Empirical formula[a]	$C_{80}H_{92}Ga_2N_8O_4$ • 2 C_{60} • $C_6H_3Cl_3$
Formula weight	2991.68
Temperature/K	100(2)
Crystal system	triclinic
Space group	P-1
a/Å	13.659(3)
b/Å	13.670(3)
c/Å	21.741(4)
α/°	95.677(4)
β/°	105.073(4)
γ/°	115.329(4)
Volume/Å^3	3438.8(11)
Z	1
ρ_{calc}g/cm^3	1.445
μ/mm^{-1}	0.522
F(000)	1532.0
Crystal size/mm^3	0.25 × 0.137 × 0.094
Radiation	MoKα (λ = 0.71073)
2Θ range for data collection/°	4.58 to 50.554
Index ranges	-16 ≤ h ≤ 16, -16 ≤ k ≤ 16, -26 ≤ l ≤ 26
Reflections collected	29629
Independent reflections[b]	12408 [R_{int} = 0.1006, R_{sigma} = 0.1763]
Data/restraints/parameters	12408/1403/1002
Goodness-of-fit on F^2 [c]	1.068
Final R indexes [I>=2σ (I)][d,e]	R_1 = 0.1500, wR_2 = 0.2928
Final R indexes [all data][d,e]	R_1 = 0.2193, wR_2 = 0.3232
Largest diff. peak/hole / e Å^{-3}	0.83/-1.06

[a] Additional diffuse contribution to electron density was observed from solvent filled voids. A solvent mask was calculated and revealed electron count consistent with partial occupancy of 2 additional molecules of hexanes per formula unit. [b] $R_{int} = \Sigma | F_o^2 - \langle F_o^2 \rangle | / \Sigma | F_o^2 |$. [c] Goodness-of-fit = $[\Sigma [w (F_o^2 - F_c^2)^2] / (n-p)]^{1/2}$; n: number of independent reflections; p: number of refined parameters. [d] $R_1 = \Sigma | | F_o | - | F_c | | / \Sigma | F_o |$. [e] $wR_2 = [\Sigma [w (F_o^2 - F_c^2)^2] / \Sigma [w (F_o^2)^2]]^{1/2}$

4.2.3.2. Structure Refinement. All atoms were refined with anisotropic thermal parameters except those of C_{60}, which were severely disordered. The terephthalate ligand and interstitial 1,2,4-trichlorobenzene also exhibited disorder. All three moieties were modeled with

two orientations (Figure 4.3). Some geometric and thermal parameter restraints were utilized to model the disordered units. The crystal also contained disordered solvent molecules located in large solvent accessible voids. The diffuse contribution to scattering was accounted for by applying a solvent mask algorithm[93] as implemented in OLEX2. The algorithm located voids centered at (–0.111 0.359 0.750) and (0.111 0.641 0.250), each with a volume of 176 Å^3 and an electron count of 42. This is consistent with a partially occupied hexane molecule.

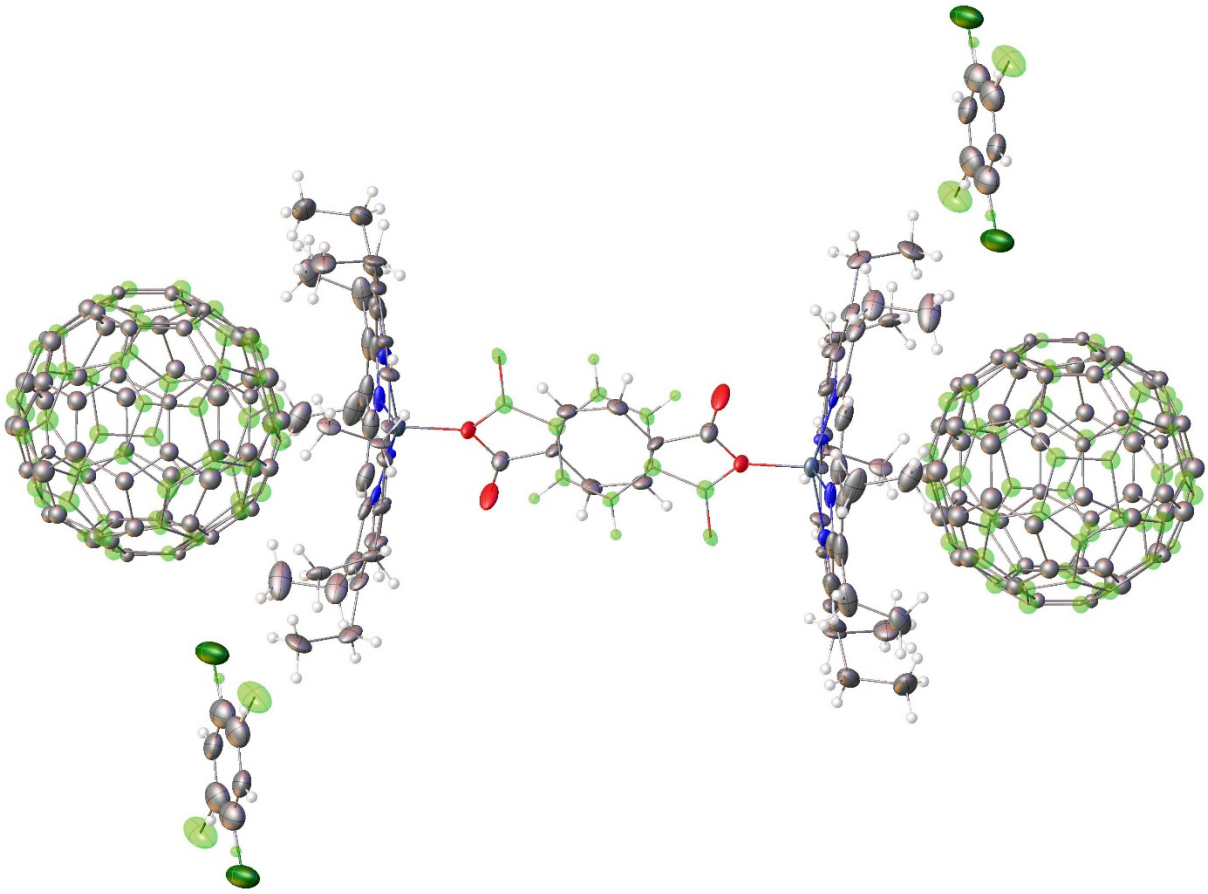

Figure 4.3. Molecular structure **2**•$(C_{60})_2$•$C_6H_3Cl_3$ as determined by X-ray crystallography (50% probability ellipsoids). Both orientations used to model the C_{60}, terephthalate and 1,2,4-trichlorobenzene are shown.

4.2.4. DFT Methodology. Calculations of porphyrin complexes with and without C_{60} were performed for gas-phase systems using plane-wave density functional theory (PW-DFT) within Quantum Espresso (version 6.1).[94] The generalized gradient approximation in the optB86b-vdW[95,96] formulation was used. This models the exchange and correlation interactions using the optB86[97] functional and the dispersion interactions with the vdw-DF[98-101] method. Optimized norm-conserving Vanderbilt (ONCV) pseudopotentials were used.[102,103] A wavefunction cutoff energy of 60 Ry was used and the wavefunctions were sampled at the Γ point. Gaussian smearing with a width of 0.001 Ry was included to ensure smooth convergence of the self-consistent field (SCF). Structures and adsorption energies were tested for convergence with respect to the wavefunction cutoff energy, *k*-points, and smearing width. Geometry optimizations were performed with convergence thresholds on the total energy and total forces of 10^{-4} Ry and 10^{-3} Ry, respectively, for the ionic minimization and 10^{-8} Ry for the electronic energy during the SCF process. The *x* and *y* dimensions of the simulation cells were defined as the smallest integer multiple of the experimentally determined unit cells that contained the appropriate periodicity; in most systems this was a 1 × 1 unit cell. For several systems a 2 × 2 unit cell was utilized to isolate a non-periodic structure or for a structure with a larger periodicity. For all systems a vacuum layer of 30 Å in the *c* direction was added to avoid interactions within the periodic system. The optimization of isolated C_{60} was carried out in a 30 Å × 30 Å × 30 Å cell to ensure isolation with respect to periodic images. Cell parameters for all systems are listed in Table 4.2. The influence of HOPG on the geometry of the porphyrin complex was accounted for by first calculating the optimized structure of the porphyrin complexes in the presence of a 1L graphene sheet. The structure of the graphene-adsorbed porphyrin was frozen in its optimized geometry and the graphene was removed for all subsequent calculations to reduce the computational cost. STM

images were simulated using the Tersoff–Hamann approximation[104] and utilized a *k*-point grid of 1 × 1 × 1 using the Monkhorst and Pack[105] method. A single layer of graphene was added into these systems after optimizing the structure of the porphyrin and fullerene, after which the electronic structure was recalculated in order to properly align the Fermi level of the system with experimental systems. The *z*-coordinate for simulating these images passed through the plane of the upper porphyrin, which was chosen after various *z*-coordinates were tested; the results of these benchmarking calculations are discussed in Chapter 6.3.1. Molecular models were built using CrystalMaker software.[106] Simulated STM images were plotted using OriginPro software.[107]

Table 4.2. Lattice Parameters of Simulation Cells and Number of Porphyrin Complexes for PW-DFT Calculations of Porphyrins and Porphyrin/Fullerene Assemblies.

System	*a* (Å)	*b* (Å)	*c* (Å)	*α* (°)	*β* (°)	*γ* (°)	*N*[a]
Isolated C_{60}	30.00	30.00	30.00	90	90	90	*n/a*
2 and **2**:C_{60}	14.90	14.90	45.00	90	90	90	1
2 and **2**:C_{60} (Tilt)	29.80	29.80	45.00	90	90	90	1
2 and **2**:C_{60} (Vacancy)	29.80	29.80	45.00	90	90	90	3
3 and **3**:C_{60}	14.90	14.90	51.00	90	90	90	1
4 and **4**:C_{60}	14.90	14.90	60.00	90	90	90	1

[a] Number of porphyrin complexes within the PW-DFT simulation cell. All simulations included either zero or one C_{60}.

For each gas-phase calculation, the solvation energy was determined with a corresponding condensed-phase calculation in Gaussian16 using the B3P86 functional,[108,109] LANL2DZ effective core potential basis set[110,111] for Ga atoms, and the 6-31G* basis set for all other atoms. The optimized geometries obtained from the gas-phase PW-DFT calculations were used to construct supercells (if applicable) to explicitly model all interactions between C_{60} and the porphyrin dimer. Solvation energies were computed using the SMD module. The solvent parameters used for 1,2,4-trichlorobenzene are listed in Table 4.3. A similar approach has been used to calculate adsorption energies of porphyrins on HOPG in 1,2,4-trichlorobenzene.[112]

Table 4.3. SMD Solvent Parameters for 1,2,4-Trichlorobenzene.

Parameter	value
ε	2.24[a]
n^2	2.47[a]
α	0.00[b]
β	0.04[b]
γ	56.3[c]
Φ	0.667
Ψ	0.333
r	1.98

[a] From Ref. 113. [b] From Ref. 114. [c] From Ref. 115.

4.3. Results and Discussion

4.3.1. Self-Assembly and STM Imaging of Porphyrin Dimer Monolayers on HOPG.

The deposition of 4 μL of a 0.5 mM solution of **1**, **2**, **3**, and **4** in 1,2,4-trichlorobenzene (TCB) onto the basal plane of HOPG under ambient conditions results in self-assembly of ordered monolayers of the porphyrins, which are observed immediately upon engaging the STM tip (Figure 4.4). The arrays formed by **1**, **2**, and **4** (Figure 4.4a, b, and d) span domains of at least 50 nm × 50 nm. While monolayers of **3** have not been observed with complete coverage over a 50 nm × 50 nm domain, continuous coverage of **3** along the fast-scan axis (horizontal) of the STM over 50 nm (Figure 4.4c) suggests that the smaller extent of domains of **3** observed along the slow-scan axis (vertical) of the STM is either an imaging artifact or due to delamination of the monolayer of **3** during imaging. None of the samples exhibit features consistent with formation of multilayers, *e.g.*, regions with features of similar size and periodicity, but exhibiting greater apparent height.

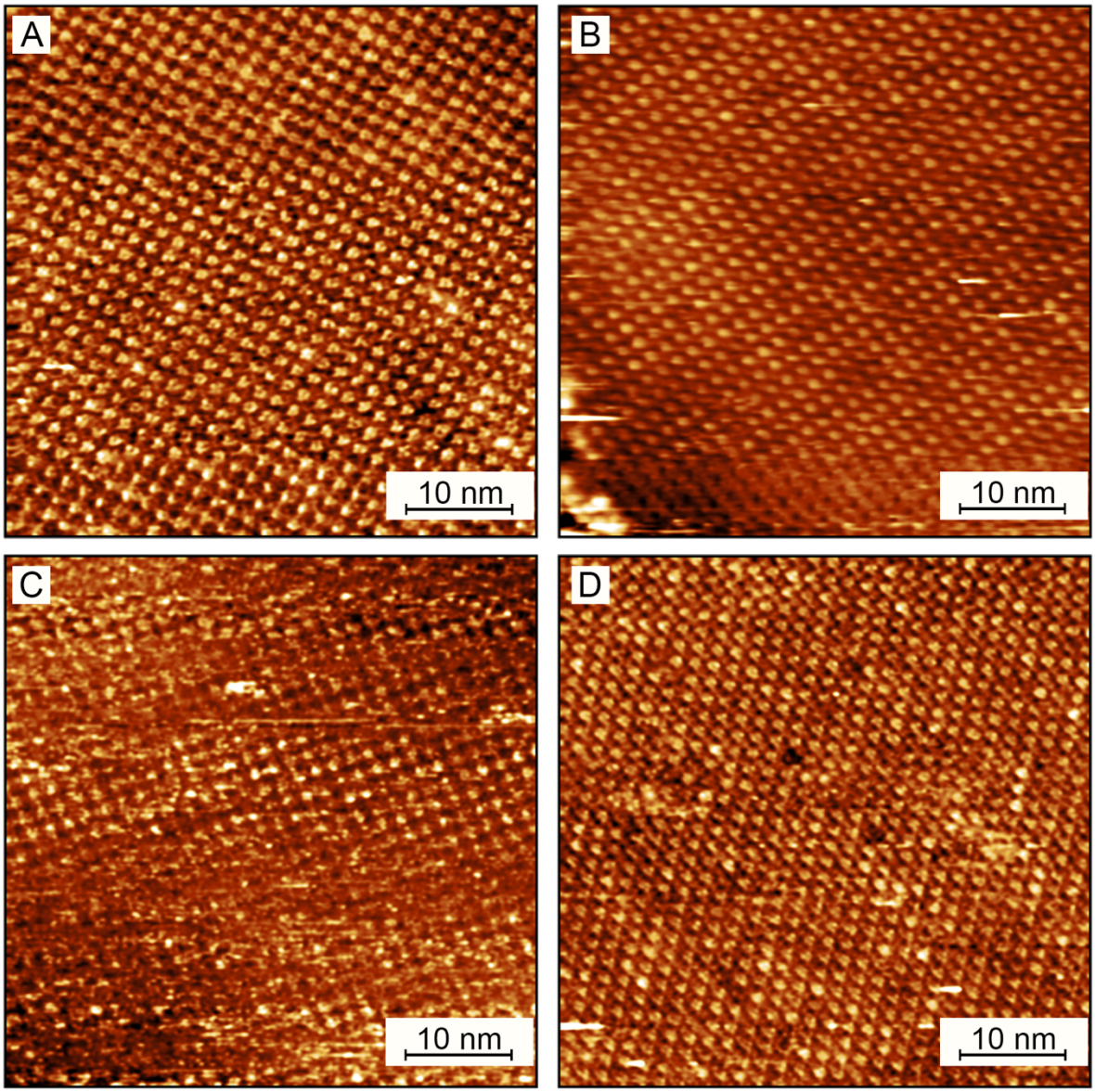

Figure 4.4. Large-scale STM images (50 nm × 50 nm) of monolayers of **1**, **2**, **3**, and **4** on HOPG at the solid–liquid interface (TCB, 0.5 mM): (a) **1**, I = 40 pA, V = –900 mV; (b) **2**, I = 40 pA, V = –700 mV; (c) **3**, I = 100 pA, V = –1100 mV; (d) **4**, I = 40 pA, V = –700 mV.

In smaller-scale images of the monolayers, individual molecules appear as ring-like features similar to those seen in previous studies of 5-coordinate gallium porphyrins on HOPG at the solid–liquid interface (Figure 4.5).[116] Unit-cell analyses (Table 4.4) show that all porphyrin monolayers exhibit a square lattice of approximate dimension 1.50 nm × 1.50 nm. The unit-cell parameters are statistically indistinguishable from each other and from those found for Ga(OEP)Cl

(Table 4.4) and previously reported for Co(OEP) HOPG in TCB solvent.[112] This indicates that the porphyrin molecules within monolayers of **1**–**4** are arranged such that one gallium porphyrin unit of the dimer is adsorbed face-on to HOPG, with the second porphyrin being supported above the surface by the bridging ligand. Cross-sectional profiles reveal apparent heights that range from 0.04–0.15 nm. These apparent heights are considerably shorter than the calculated heights of the fully extended dimers (0.77–2.45 nm; see Chapter 3, Table 3.7), but because STM data are a convolution of both the physical and electronic structure, apparent heights frequently diverge from actual heights; thus, it is not possible to deduce the porphyrin–porphyrin face-to-face distance in the monolayer from these data.[84,116,117]

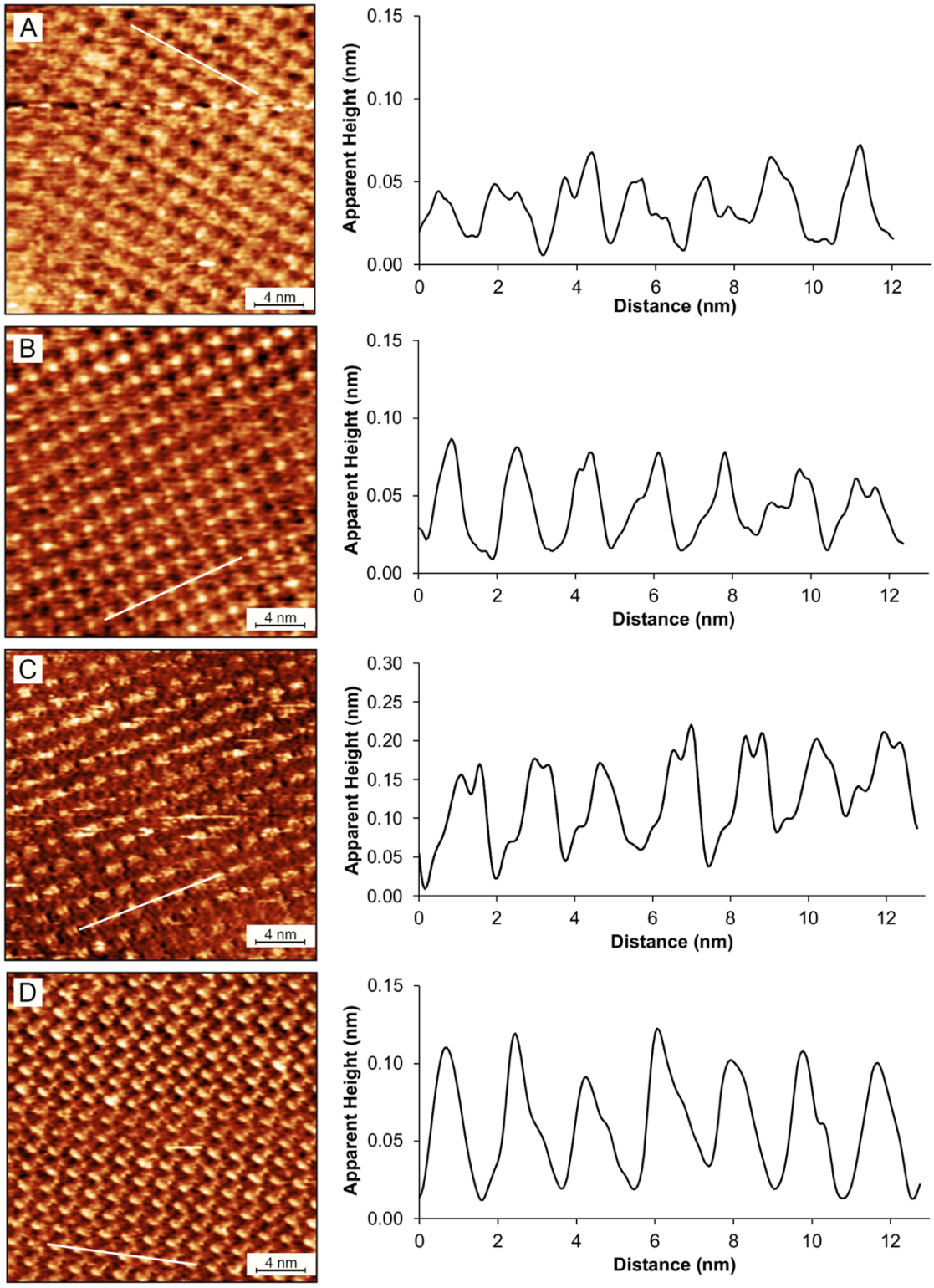

Figure 4.5. STM images (25 nm × 25 nm) and cross-sectional profiles of monolayers of **1**, **2**, **3**, and **4** on HOPG at the solid–liquid interface (TCB, 0.5 mM): (a) **1**, I = 40 pA, V = –900 mV; (b) **2**, I = 40 pA, V = –700 mV; (c) **3**, I = 100 pA, V = –1100 mV; (d) **4**, I = 40 pA, V = –700 mV. The cross-sectional profiles are taken along the white lines shown in the STM image.

Table 4.4. Unit-Cell Parameters of Monolayers of Porphyrin Dimers on HOPG at the Solid–Liquid Interface.

Parameter	**1**	**2**	**3**	**4**	**Ga(OEP)Cl**
a (nm)	1.50 (3)	1.48 (3)	1.50 (3)	1.50 (2)	1.50 (3)
b (nm)	1.50 (3)	1.47 (3)	1.49 (3)	1.49 (5)	1.45 (3)
Γ (deg)	90 (3)	89 (1)	90 (1)	90 (3)	91 (1)

The square lattice observed in these systems contrasts with the pseudo-hexagonal lattice observed for monolayers of 4- and 5-coordinate porphyrins deposited on HOPG from 1-phenyloctane, as reported in Chapter 2 and numerous other studies. A recent study by Gurdumov, *et al.*, of Co(OEP) in TCB on HOPG showed that the stabilization of the square pseudopolymorph is a result of co-adsorption of TCB, which through STM imaging was observed to adsorb coplanar with HOPG in the vacancy at the center of each Co(OEP) unit cell.[112] TCB has also been observed to co-adsorb within other molecular monolayers.[118-122] In the present study, STM current corresponding to TCB was not observed in any of the images of **1**–**3**. To understand whether the absence of TCB features is due to differences between the experimental conditions of the present and previous studies or, instead, is a consequence of the fact that **1**–**3** are porphyrin dimers rather than monomers, a systematic study of the bias-voltage dependence of STM images of monolayers of Ni(OEP) on HOPG at the TCB–solid interface was conducted (Section 6.3.2). Features attributable to co-adsorbed TCB within monolayers of Ni(OEP) can be observed in the bias-voltage regime in which the images of **1–3** were obtained. We conclude that absence of TCB features in the STM images of **1**–**3** is the result of their dimer structures, imaging of which requires an STM tip height too far from the co-adsorbed TCB to allow its observation.

STM images of monolayers of **4** differ from those for **1**–**3** because they exhibit small, periodic features between the porphyrin features that constitute the square lattice (Figure 4.6). The features are observed as two narrow peaks located ~0.5 nm and ~1 nm from the preceding

porphyrin feature along the diagonal of the unit cell. They are not centered within the square lattice of **4**, and therefore are not due to co-adsorbed TCB. While some porphyrins are known to assemble on HOPG at the solid–liquid or solid–air interface in an edge-on orientation,[123-127] an edge-on orientation of **4** would require the features to be separated by approximately 2.5 nm, inconsistent with the observed spacing. One possible explanation for this observation is that it arises from an offset of the upper and lower porphyrin macrocycles allowing simultaneous STM imaging of both and/or the bridging porphyrin.

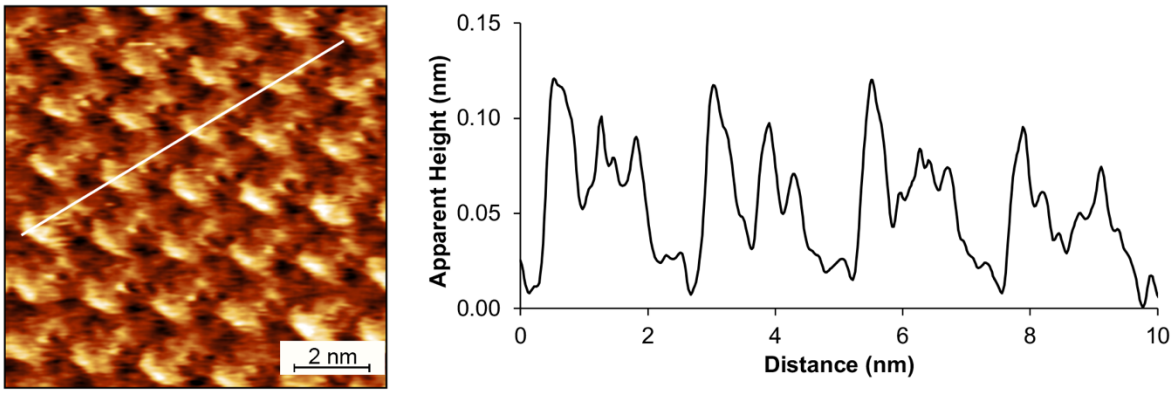

Figure 4.6. Small-scale STM image (10 nm × 10 nm) and cross-sectional profile of **4** monolayer on HOPG at the solid–liquid interface (TCB, 0.5 mM,) $I = 40$ pA, $V = -700$ mV.

The possibility that the STM images for **1**–**4** instead exhibit a monolayer formed from impurities was considered because the procedures for synthesizing and purifying the compounds provides them in 96–99% purity (see Chapter 3). Given that the concentration of **1**–**4** employed for STM measurements is 0.5 mM, the concentration of porphyrinic impurities in these samples would range from roughly 5–20 μM; thus, the possibility that the monolayers observed using samples of **1**–**4** consist entirely of Ga(OEP)X impurities is remote. To confirm this, the concentration threshold for STM detection of a monolayer of Ga(OEP)Cl in TCB on HOPG was investigated and determined to be roughly 1.0 mM (Section 6.3.3), which is 2–3 orders of magnitude higher than the concentration of these impurities in samples of **1**–**4**. While this excludes

the formation of complete monolayers porphyrin impurities, the possibility that some porphyrinic impurities may be incorporated into the monolayer cannot be rigorously excluded. No obvious defects consistent with impurities have been observed.

To gain insight into the possible 3D structures of the monolayers, PW-DFT geometry optimizations were performed for **1**–**4** utilizing the average experimental lattice parameters to establish the simulation cell. The resulting structures are shown in Figure 4.7. In these calculations, the structure of the surface-adsorbed gallium octaethylporphyrin was frozen in an ethyl-up conformation; all other atoms were optimized without constraint. One caveat of note is that these calculations are for the gas phase and therefore do not account for solvation effects that may play a role in determining molecular geometries. The calculated structures of **1** and **2** (Figure 4.7a and b) predict the second porphyrin is supported above the surface with the bridging ligand roughly perpendicular to the cofacial octaethylporphyrins. For the porphyrin-bridged complexes **3** and **4** the bridging ligand adopt a canted conformation with respect to the surface-bound porphyrin, although, as noted in Chapter 3, the Ga–carboxylate linkage is quite flexible and a number of other porphyrin conformations presumably are similar in energy. The angle between the planes-of-best-fit of the surface-confined octaethylporphyrin and the bridging porphyrin ligand in **3** is 80º (Figure 4.7c). To the preceding point, local minimums can be found for a monolayer of **4** in two conformations, one with an angle between the surface-confined and bridging porphyrins of 59º (Figure 4.7d), resulting in a significant offset between the two cofacial octaethylporphyrins (Figure 4.7e). The other structure adopts a conformation with an angle of 77º (Figure 4.7f), similar to the conformation of **3**. Notably, the structure in Figure 4.7d and e is determined to be 0.24 eV more stable than the structure in Figure 4.7f. Such a structure could be envisioned as presenting three

distinct STM-imageable porphyrins, consistent with the experimental data for the monolayer of **4** showing two features with a distinct periodic relationship to the main porphyrin square lattice.

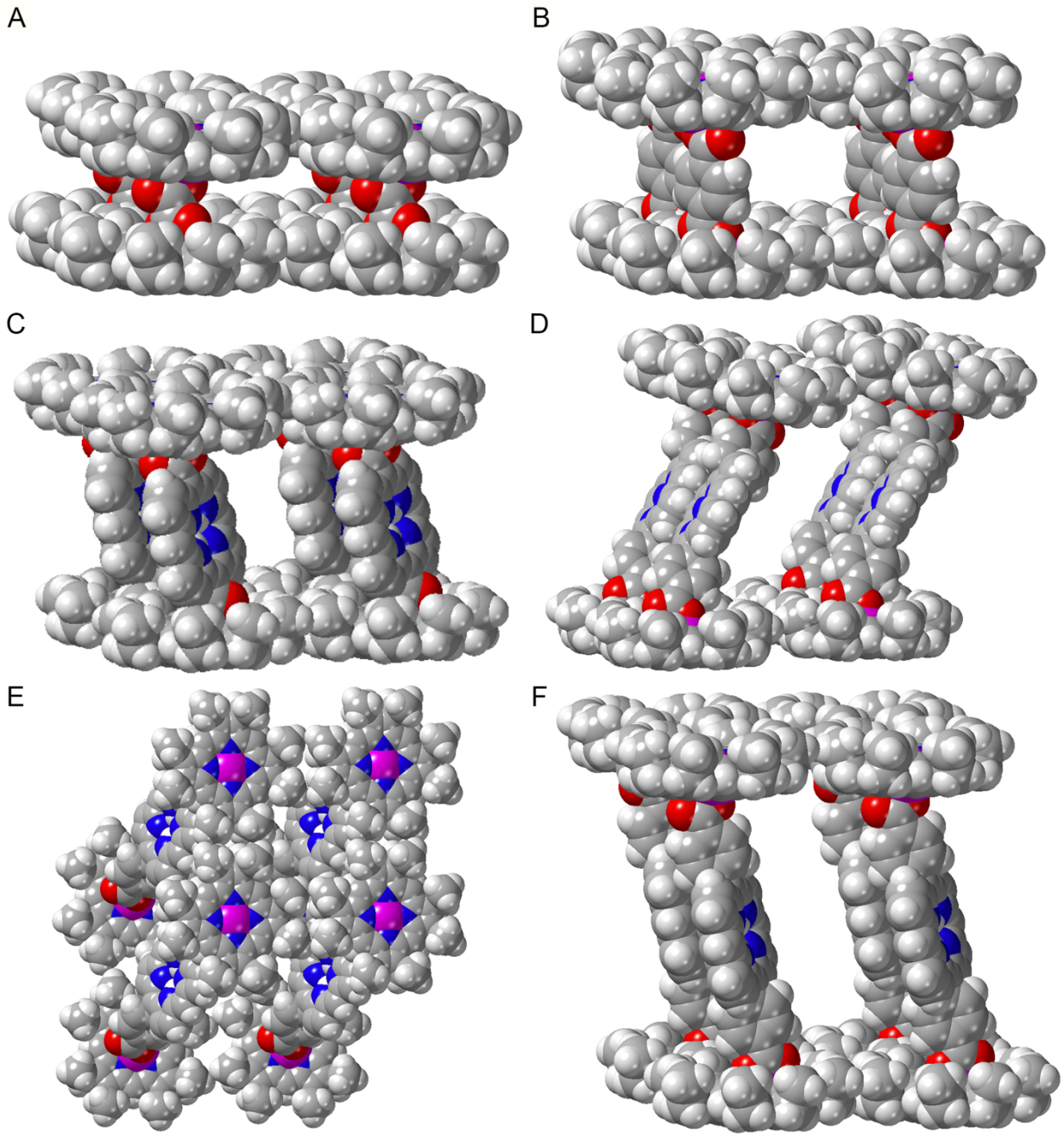

Figure 4.7. CPK Models of the DFT calculated structures of porphyrin monolayers of (a) **1**; (b) **2**; (c) **3**; (d) side-view of lowest energy structure of **4**; (e) top-view of lowest energy structure of **4**; (f) alternate structure of **4**.

4.3.2. STM Imaging of Monolayers of 2 Containing Intercalated C_{60}. Co-deposition of premixed TCB solutions of **2** and C_{60} onto HOPG results in self-assembly of ordered overlayers that exhibit STM images that are distinct from those observed for **2** in the absence of C_{60} (Figure 4.8). Qualitatively, the images exhibit interpenetrating square lattices of brighter and dimmer features. The cross-sectional profile shows that these correspond, respectively, to a taller and broader feature that appears similar to the porphyrin signals observed in monolayers of **2,** and a distinct shorter and narrower feature. The relative height of the shorter and narrower features compared to the taller and broader features is sample dependent but both features are always present when **2** and C_{60} are co-deposited. Structural analysis of the unit cells (Table 4.5) defined by the two features indicates they have the same lattice parameters, which are indistinguishable from those of a monolayer of pure **2**. In order to determine which feature corresponds to **2**, an analysis of the apparent height and apparent width of features in the monolayers of **2**:C_{60} and **2** was conducted (Table 4.6). The apparent heights of the features cannot distinguish the various species, but the apparent widths demonstrate that the broader feature likely corresponds to **2**. This means that the additional feature is attributable to one of three possible molecules: (1) a second porphyrin; (2) TCB, as observed previously for monolayers of Co(OEP) and in our laboratory for Ni(OEP) but, importantly, not for **1**–**4**; or (3) C_{60} contained within the interstices of the double-decker monolayer.

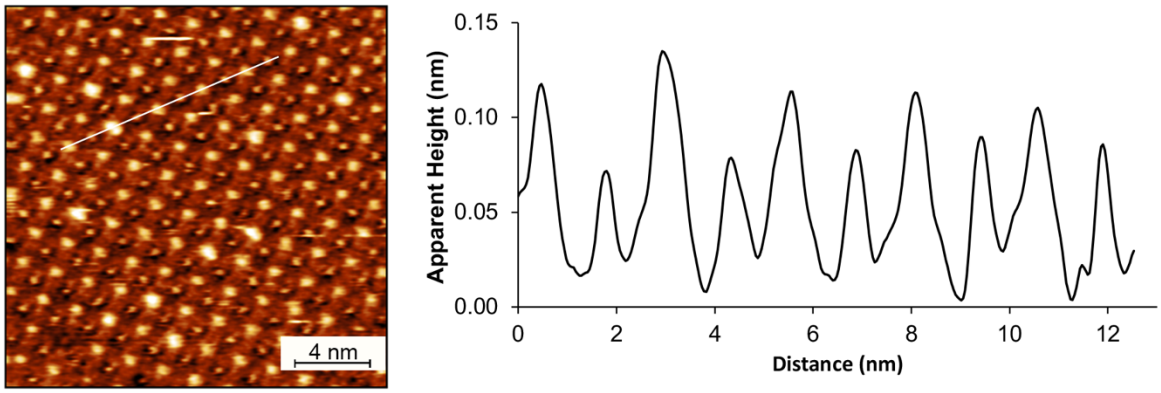

Figure 4.8. STM image (20 nm × 20 nm) and cross-sectional profile of monolayer of co-deposited **2** and C_{60} on HOPG at the solid–liquid interface (TCB, [**2**] = 0.5 mM, [C_{60}] = 1.0 mM; I = 50 pA, V = –900 mV).

Table 4.5. Unit-Cell Parameters of Monolayers of Co-Deposited **2** and C_{60} on HOPG at the Solid–Liquid Interface.

parameter	**Brighter Features**	**Dimmer Features**
a (nm)	1.49 (2)	1.49 (2)
b (nm)	1.48 (3)	1.48 (2)
Γ (deg)	89 (1)	89 (1)

Table 4.6. Apparent Height (Å) and Width (nm) of STM features in Monolayers of Co-Deposited **2**:C_{60} and Pristine **2**.

	2:C_{60}[a]		**2**[b]
parameter	**Broad Feature**	**Narrow Feature**	
Apparent Height (Å)	0.8 (0.2)	0.6 (0.1)	0.7 (0.2)
Apparent Width (nm)	1.3 (0.2)	0.9 (0.1)	1.6 (0.2)

[a] Based on data shown in Figure 4.6. [b] Based on data obtained across multiple trials including data shown in Figure 4.3b.

The STM data for the monolayer formed on HOPG when **2** and C_{60} are co-deposited is interpreted as arising of a lattice of **2** containing one interstitial C_{60} guest molecule in each unit cell, based on the following reasoning. The possibility noted above that the dimmer feature arises from a second porphyrin is excluded the center-to-center distance between the large and small features of approximately 1 nm; this is too small to accommodate a porphyrin, which will have a van der Waals diameter of approximately 1.2 nm. A second alternative, that the interpenetrating features arise from co-adsorbed TCB, is unlikely because they are only observed when **2** and C_{60}

are codeposited and not in the monolayer of pristine **2**, nor in monolayers of **1**, **3**, or **4**. Furthermore, STM images (Figure 4.9a) and cross-sectional profiles of a smaller region of the monolayer formed by co-deposited **2** and C_{60} exhibit occasional vacancies in the positions of both C_{60} and **2**, as shown in the cross-sectional profiles (Figure 4.9c, top and middle profiles, respectively). In the vacancy of **2**, a feature is still observed, but its height and width are significantly smaller than for the other features corresponding to **2** in this image. Notably, the feature appears similar to other shorter and narrower features in the image. As reports of monolayers of TCB in the absence of a co-adsorbed species are not known, and the interactions between TCB and adjacent **2** in the monolayer at this position would be minimal given the large distance (~0.75 nm), TCB is an unlikely source of the current observed within the vacancy of **2**. This also suggests that, more generally, the shorter and narrower features are not attributable to TCB, given the similar appearance. Though this feature could be a 5-coordinate porphyrin impurity adsorbed within the vacancy of **2**, no similar features are observed within the monolayer of pristine **2**, rendering this an unlikely explanation. Therefore, we conclude that the reasonable assignment of the smaller and narrower features consistent with the data is C_{60} contained within the interstices of the monolayer of **2**.

Large-scale images (Figure 4.9b) show that the monolayers of **2**:C_{60} are widespread, encompassing an area of at least 50 nm × 50 nm. Most of the vacancies observed within the monolayers are of **2**, whereas no vacancies over a region of the same size were observed within the monolayer of pristine **2**. These vacancies may result from the more complex nature of self-assembly for a bicomponent monolayer where vacant binding sites of **2** within the monolayer of **2**:C_{60} become inaccessible due to the steric bulk of C_{60}. A cross-sectional profile passing through both porphyrin and C_{60} features (Figure 4.9c, bottom profile) shows that, unlike the porphyrin

vacancy observed in the small-scale image, no feature is observed in this vacancy. Notably, C_{60} features are observed even at the C_{60} binding sites adjacent to vacancies of **2**, indicating that the adsorption of C_{60} is thermodynamically favorable even without the collective interactions of all four **2** expected in a complete unit cell. The incorporation of C_{60} is near the expected 1:1 ratio of C_{60} to **2**. This differs from previous corral-like structures where incorporation was below the expected 1:1 C_{60}: porphyrin ratio.[70] This increased incorporation of C_{60} may be a result of several factors, including a more energetically favorable adsorption site, a lack of steric hinderance from the bridging ligand, and the close-packed upper porphyrins of **2** within the monolayer preventing distortion of the terephthalate ligands towards C_{60} that, while increasing the adsorption energy of an individual fullerene, would induce an anti-cooperative effect in adjacent unit cells.

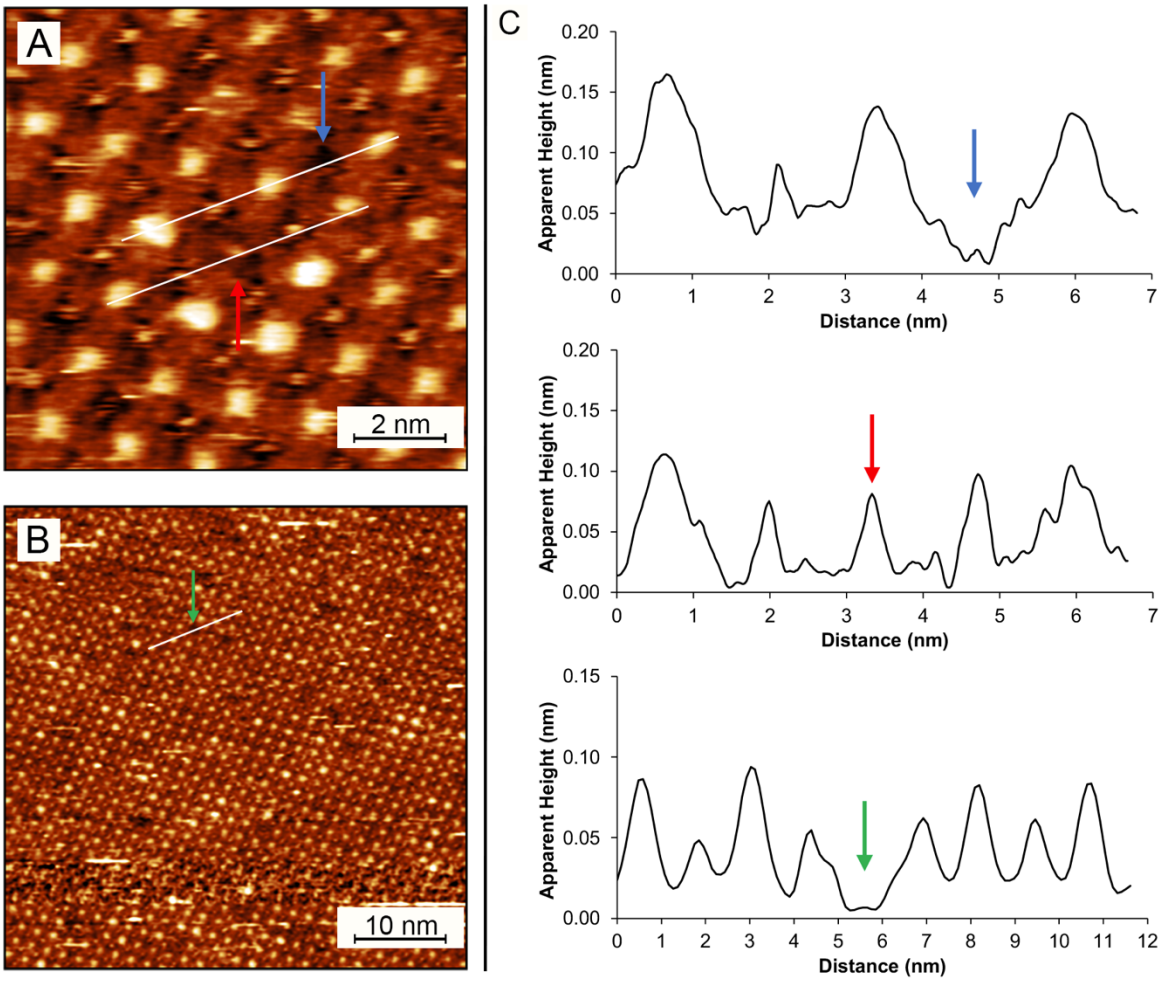

Figure 4.9. STM images and cross-sectional profiles of monolayer of co-deposited **2** and C_{60} on HOPG at the solid–liquid interface (TCB, [**2**] = 0.5 mM, [C_{60}] = 1.0 mM, I = 50 pA, V = –900 mV) (a) 10 nm × 10 nm; (b) 50 nm × 50 nm; (c) cross-sectional profiles along white lines in STM images. The arrows in the images and cross-sectional profiles denote vacancies (blue arrow, C_{60}; green and red arrows, **2**).

The bias-voltage dependence of STM images of monolayers of **2** and C_{60} is shown in Figure 4.10. At bias-voltages around –400 mV only **2** is observed. At intermediate bias-voltages around –650 mV, **2** is still clearly observed along with significant current in the interstitial regions where C_{60} was observed in Figure 4.8. The features are less resolved at these bias-voltages as there is less differentiation between features along the unit-cell axes. It is unclear whether the images in this intermediate bias-voltage range have contributions from C_{60} or are primarily **2** along with

contributions from the underlying HOPG. At the most negative bias-voltages investigated, above –900 mV, C_{60} is clearly resolved along with the bright **2** features.

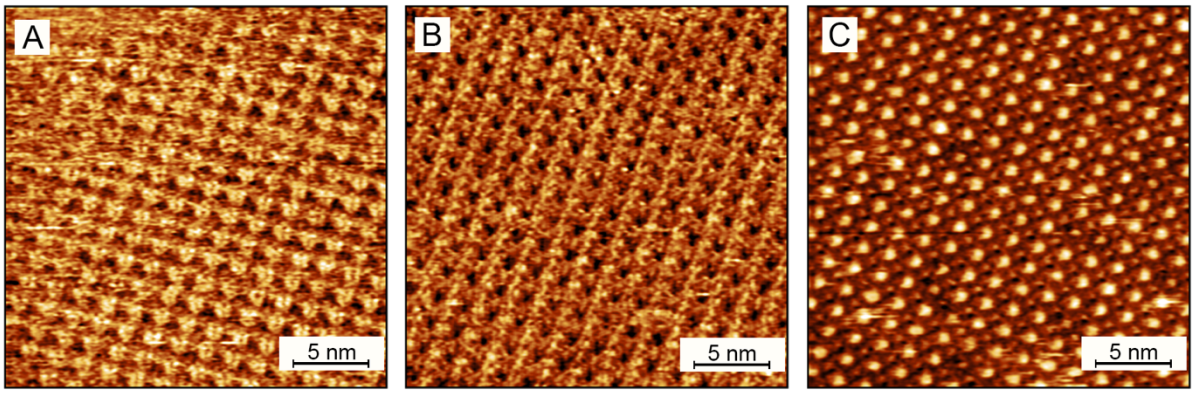

Figure 4.10. STM images of monolayer of co-deposited **2** and C_{60} on HOPG at the solid–liquid interface (1,2,4-TCB, [**2**] = 0.5 mM, [C_{60}] = 1.0 mM, 25 nm × 25 nm) (A) I = 50 pA, V = –400 mV; (B) I = 50 pA, V = –650 mV; (C) I = 50 pA, V = –1000 mV.

4.3.3. External Adsorption of C_{60} to the 2:C_{60} Layer. The STM images of **2**:C_{60} reveal that some of the porphyrin features appear substantially brighter than others (Figure 4.8). Analysis of consecutive STM images (Figure 4.11) show that a fraction of these brighter and broader features become dimmer on the successive image (t = n + 30 s), though in the majority of cases a new brighter and broader feature is observed for an adjacent or near-adjacent porphyrin feature. While these features could arise from variation in the electronic structure at specific adsorption sites on HOPG (*i.e.* a Moiré pattern), the seemingly random positions of the features are inconsistent with this explanation. The features could also arise from fluctuations in the monolayer–tip coupling, however, the persistence of some features between images and the correlated locations between the majority of others renders this explanation unlikely. We conclude that the most likely identity of these features is from the adsorption of C_{60} to the upper porphyrin of **2** with adsorption/desorption occurring within the time between STM images. The correlated locations from image to image suggest the possibility of C_{60} hopping between different upper porphyrin macrocycles, such a process has been observed previously with C_{60} hopping between

adjacent or near-adjacent cavities within nanoporous networks of trimesic acid, perylene derivatives, and porphyrins.[18,30,47]

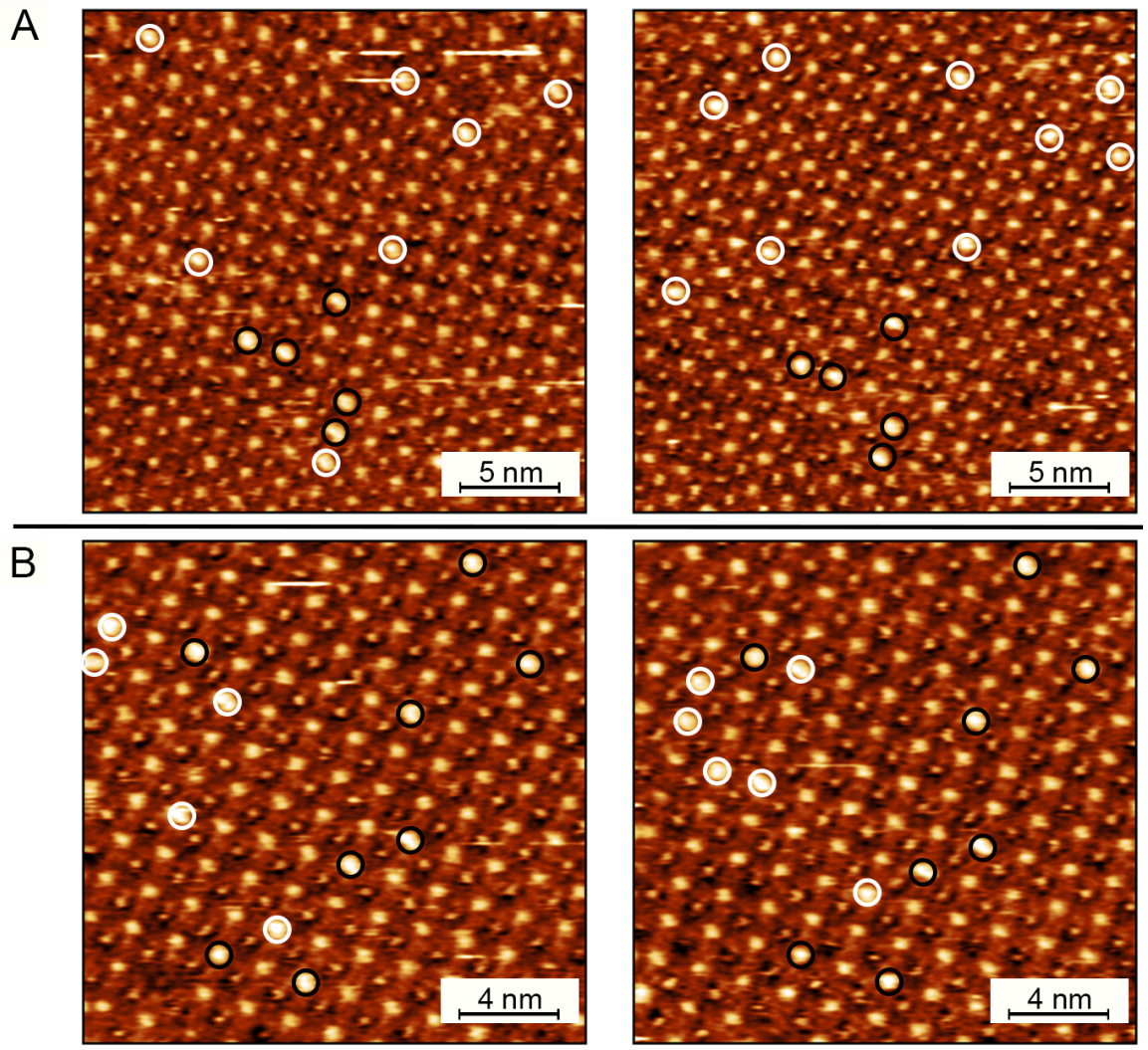

Figure 4.11. Sequential STM images of monolayers of co-deposited **2** and C_{60} on HOPG at the solid–liquid interface (TCB, [**2**] = 0.5 mM, [C_{60}] = 1.0 mM). The images on the left are taken immediately preceding those on the right. (a) I = 50 pA, V = –900 mV, 25 nm × 25 nm; (b) I = 50 pA, V = –900 mV, 20 nm × 20 nm. The black circles indicate bright features that appear similar across both images, the white circles indicate bright features that become dimmer in the opposite image. Bright features that are outside the scanning area in the opposite image, due to thermal drift, are not circled.

The propensity for the fullerene to bind with the OEP macrocycle was investigated by the growth of co-crystals of **2** and C_{60} from a solution in TCB with vapor diffusion of hexanes. While

structures of these co-crystals obtained by SXRD (Figure 4.3 and Figure 4.12) show significant disorder in both the C_{60} and terephthalate moieties, the interaction between the octaethylporphyrin macrocycles of **2** and C_{60} is clearly demonstrated and strongly suggests that this interaction could occur at least transiently on the surface.

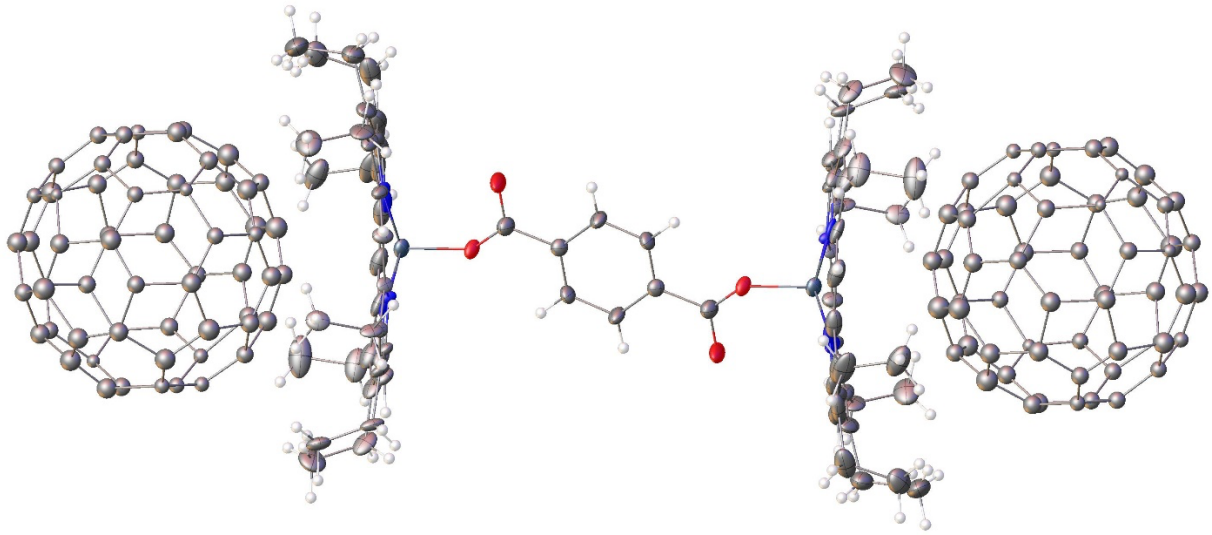

Figure 4.12. Structure co-crystal of **2** and C_{60} as determined by X-ray crystallography (50% probability ellipsoids). Only one orientation is shown for C_{60} and terephthalate moieties.

4.3.4. DFT Calculated Adsorption Energies of 2 and C_{60}. DFT calculations were performed to quantify the adsorption energy of C_{60} with **2** in various geometries relevant to the surface and in solution, in support of the qualitative observations made using STM. The gas-phase adsorption energy calculations were performed within the PW-DFT framework using the Quantum Espresso computational package with a similar methodology to that described in Chapter 2 according to Equation 4.1:

$$E_{ads(g)} = E_{\mathbf{2}:C60(g)} - E_{\mathbf{2}(g)} - E_{C60(g)} \quad (4.1)$$

Here, $E_{ads(g)}$ is the gas-phase adsorption energy of C_{60} within the monolayer formed by **2** and $E_{\mathbf{2}:C60(g)}$, $E_{\mathbf{2}(g)}$, $E_{C60(g)}$ are the gas-phase total energies of the supramolecular complex formed by **2**:C_{60}, **2** and C_{60} as calculated in the PW-DFT framework. The influence of the surface on the

geometry of **2** was accounted for by first optimizing **2** in the presence of a graphene sheet; the graphene-adsorbed porphyrin unit was then frozen in this optimized geometry for all subsequent calculations and the graphene was removed to substantially reduce the computational cost. This approach was utilized after a series of test calculations showed the impact of excluding the graphene was minimal (Section 6.4.1). The computational cost of including surface atoms is a well-known challenge and a recent approach has been developed that allows for modeling the surface–adsorbate interactions without explicit inclusion of the surface,[128] however it has not been implemented into the software package used here.

As a substantial difference in the solvation energy is expected between various structures of **2**:C_{60}, solvation effects were included using the SMD solvation module as implemented in the Gaussian 16 software package according to Equations 4.2 and 4.3:

$$E_{solv} = \Delta E^{G}_{2{:}C_{60}(g\rightarrow s)} - \Delta E^{G}_{\mathbf{2}(g\rightarrow s)} - \Delta E^{G}_{C_{60}(g\rightarrow s)} \tag{4.2}$$

$$\Delta E^{G}_{X(g\rightarrow s)} = E^{G}_{X(s)} - E^{G}_{X(g)} \tag{4.3}$$

Here, E_{solv} is the solvation energy associated with adsorption of C_{60} within the monolayer formed by **2**, $\Delta E^{G}_{2{:}C_{60}(g\rightarrow s)}$, $\Delta E^{G}_{\mathbf{2}(g\rightarrow s)}$, and $\Delta E^{G}_{C_{60}(g\rightarrow s)}$ are the solvation energies of the supramolecular complex formed by **2**:C_{60}, **2** and C_{60}, and $E^{G}_{X(s)}$ and $E^{G}_{X(g)}$ are the total energies from single point calculations in the gas and solvated phases at the PW-DFT optimized gas-phase geometry, respectively, using the Gaussian software package. The solvated-phase adsorption energy was then determined according to Equation 4.4:

$$E_{ads(s)} = E_{ads(g)} + E_{solv} \tag{4.4}$$

Here, $E_{ads(s)}$ is the solvated-phase adsorption energy. A similar approach for including solvation effects has recently been used to model porphyrin monolayers.[112]

The optimized structure of **2**:C_{60} in a monolayer-like geometry is shown in Figure 4.13. The energy of the system as a function of C_{60} within the unit cell of **2** is found to be at minimum at the center of the cell, where the main interactions of C_{60} are with the CH_2 groups of the upper porphyrin and the CH_3 groups of the lower porphyrin, the latter of which are forced to adopt the up-conformation on the surface. Notably, because the cleft between the upturned ethyl chains of the lower porphyrin and macrocycle of the upper porphyrin is too small to accommodate C_{60}, the terephthalate moieties remain quite far from the C_{60}; the closest approach to the fullerene are 5.2 Å and 6.6 Å for the edge-facing and plane-facing terephthalate moieties, respectively.

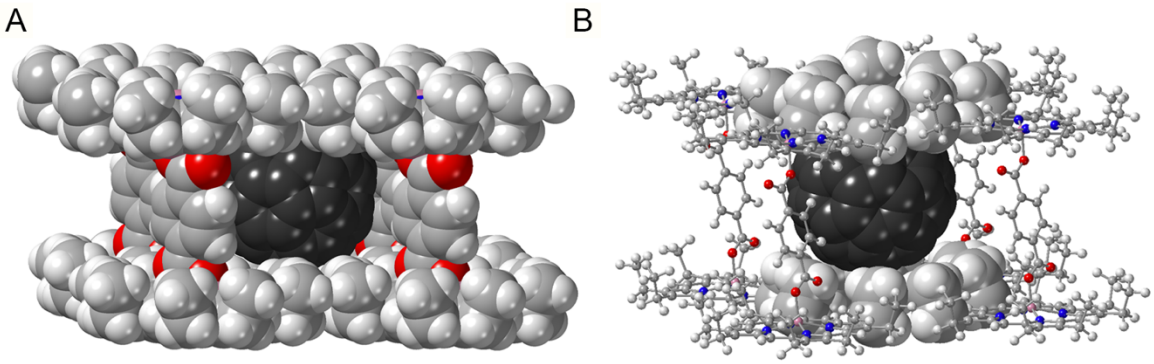

Figure 4.13. Calculated (DFT) structures of **2**:C_{60} at the center binding site (Center). The structure is shown in two renderings: (a) a CPK model; (b) Hybrid CPK and ball-and-stick model highlighting the binding pocket. Carbon atoms of **2** (light) and C_{60} (dark) are shown in different shades of gray for contrast.

The optimized geometries and adsorption energies of C_{60} with **2** in several alternate conformations were also calculated to determine the relative stability of these structures compared to the Center structure in Figure 4.13. In the first structure (Figure 4.14a, denoted Tilt) the upper porphyrin is canted with respect to the lower porphyrin in order to accommodate close-contact between C_{60} and the terephthalate bridging ligand. This structure could be relevant in solution or at certain edge sites of the monolayer, but it would be unlikely for this structure to be propagated throughout the monolayer because the tilt between the porphyrins would decrease the size of the

cavity and prevent adsorption of C_{60} at adjacent binding sites. The second structure (Figure 4.14b, denoted Upper) investigates the interaction of C_{60} with the macrocycle of the upper porphyrin, as suggested results in the bright and broad features observed in the STM image. The final structure (Figure 4.14c, denoted Vacancy) investigates the stability of C_{60} at the center of a unit cell of **2** containing one vacancy, as C_{60} was observed at many adsorption sites adjacent to a vacancy. The gas-phase adsorption energies, solvation energies and solvated-phase adsorption energies are listed in Table 4.7. The Center binding site is determined to be the most stable in both the gaseous and solvated phase. While the adsorption energy of the Upper site is only calculated to be 0.11 eV less stable than the Center site in the gas-phase, including solvation energy increases the difference in adsorption energy to 0.26 eV, demonstrating a substantial difference between these sites at the solid–TCB interface. The solvated-phase adsorption energy of C_{60} at the Vacancy site is –1.15 eV, approximately 80% of the complete Center site, and very similar to the Upper site after accounting for solvation. The relatively protected local environment at the Vacancy site provided by the partial monolayer of **2,** as compared to the Upper site, may contribute to the greater fraction of occupied vacancy sites versus upper sites. Overall, the stability of C_{60} at the Center adsorption site supports the interpretation of the small features within the STM images of **2** and C_{60}. As noted above, the adsorption energy at the Center binding site includes only minimal interaction with the terephthalate bridging moieties, suggesting that given a suitably sized cavity that allows for contact with both porphyrins, a bridging ligand with an affinity for C_{60} may not be required.

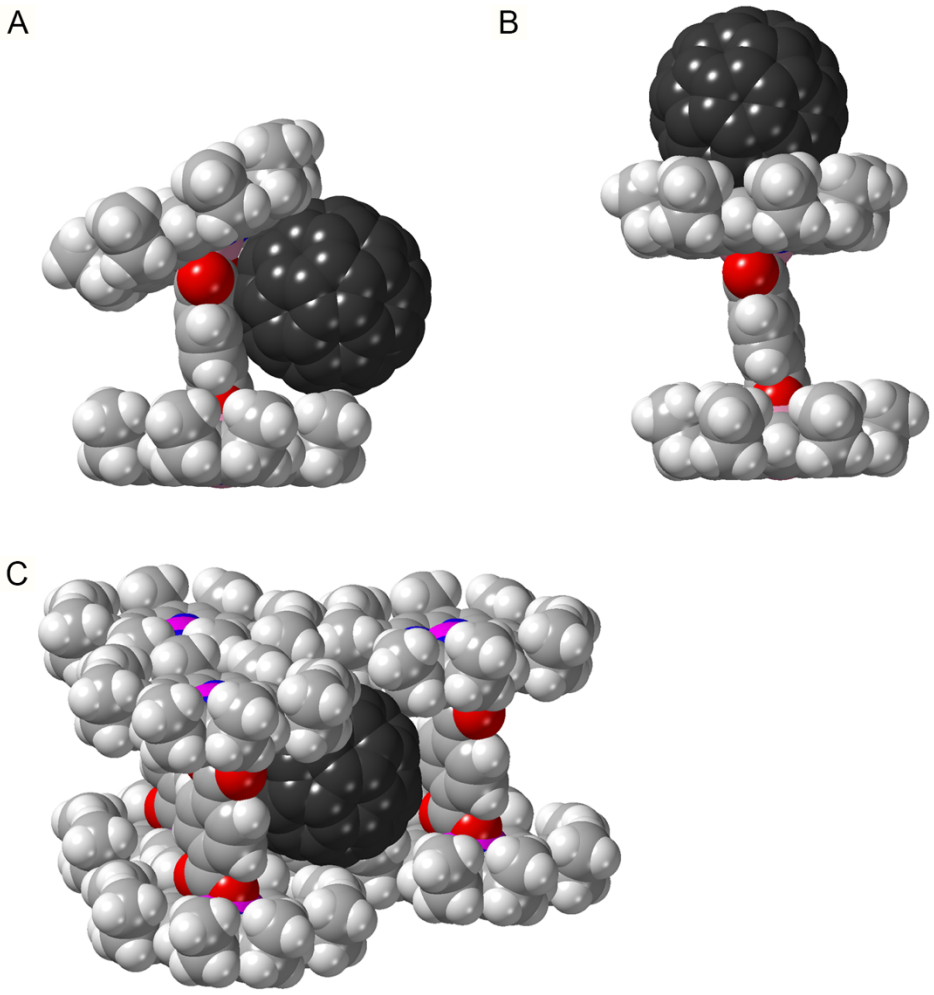

Figure 4.14. Space-filling models of alternate adsorption modes for **2**:C_{60} with (a) a tilted upper Ga(OEP) unit to accommodate the C_{60} (Tilt); (b) the C_{60} interacting with the face of the upper macrocycle (Upper); (c) the C_{60} at the center adsorption site with one **2** vacancy (Vacancy). Carbon atoms of **2** (light) and C_{60} (dark) are shown in different shades of gray for contrast.

Table 4.7. Calculated Gas-Phase Adsorption Energies, Solvation Energies, and Solvated-Phase Adsorption Energies for **2**:C_{60} at Various Geometries.

parameter	Center	Tilt	Upper	Vacancy
$\Delta E_{ads(g)}$ (eV)	–1.64	–1.30	–1.53	–1.35
ΔE_{solv} (eV)	0.22	0.37	0.36	0.20
$\Delta E_{ads(s)}$ (eV)	–1.42	–0.92	–1.17	–1.15

4.3.5. Simulated STM Images of Monolayers of 2 and 2:C_{60}. Simulated STM images of the monolayers of **2** and of **2**:C_{60} were calculated to determine whether they show the same bias-voltage dependence that was observed for the latter in the STM experiments. The STM images

were simulated using the Tersoff-Hamann approximation[104] with the *z*-coordinate set at the position of the $C_{20}N_4$ plane of the upper porphyrin. The choice of the *z*-coordinate is further discussed in Section 6.3.1. Simulated STM images of **2**:C_{60} (Figure 4.15a) and **2** (Figure 4.15b) show that at a bias-voltage of –400 mV the porphyrin is clearly observed for both **2** and **2**:C_{60}, whereas the C_{60} is very faint in **2**:C_{60}. At more negative bias-voltages, –900 mV and –1100 mV, the porphyrin remains nearly identical in both **2** and **2**:C_{60}, while the C_{60} feature in **2**:C_{60} becomes more prominent. The calculated bias-voltage dependence of C_{60} is in agreement with that observed by STM (Figures 4.8 and 4.10). Overall, the simulated STM images further support the identification of the features in experimental STM images of **2**:C_{60}.

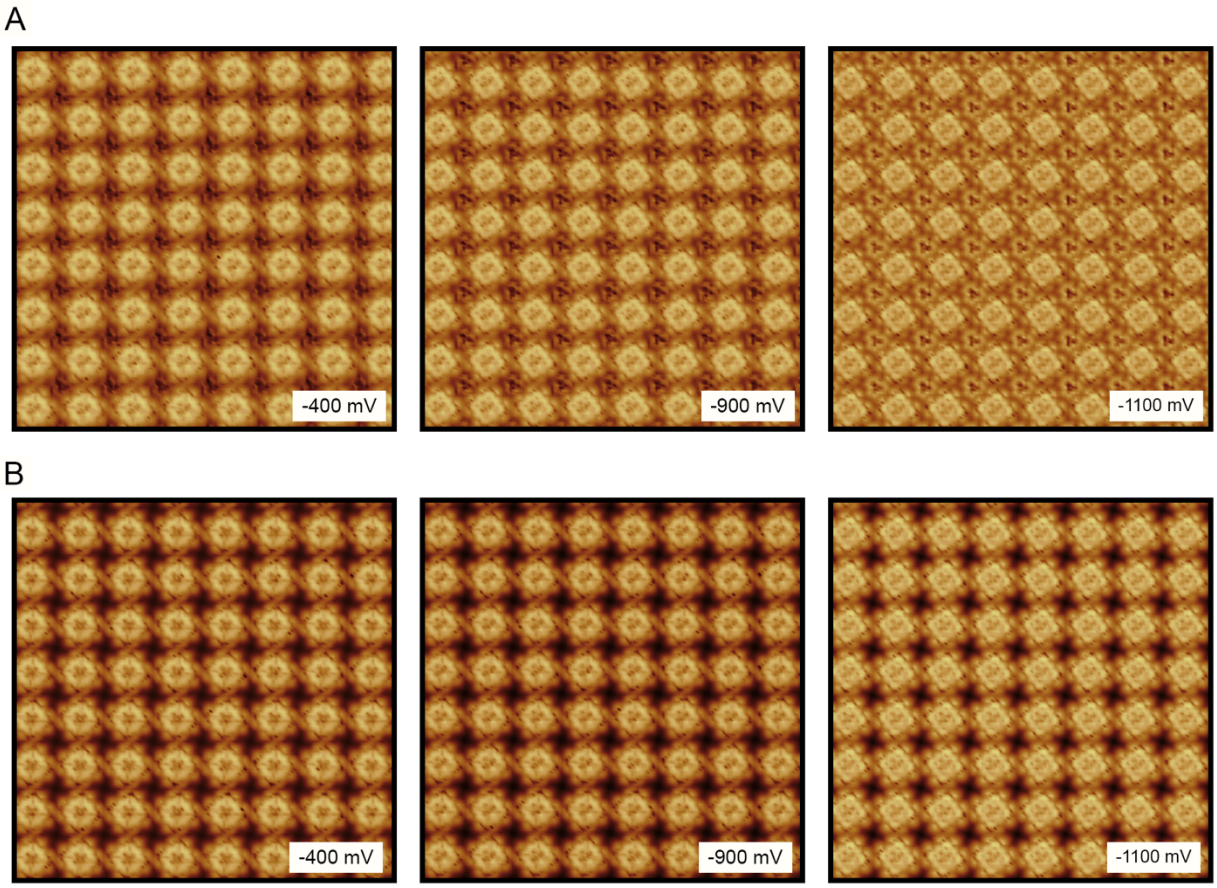

Figure 4.15. Simulated constant-current STM images at –400 mV (left), –900 mV (center), and –1100 mV (right) of (a) **2**:C_{60} and (b) **2**.

4.3.6. Investigation of Monolayers of 3:C_{60} and 4:C_{60}. Because **3** and **4** are also expected to have a significant affinity for C_{60}, co-deposition of the complexes and C_{60} to potentially form monolayers **3**:C_{60} and **4**:C_{60} was investigated. STM imaging of co-deposited **3** and C_{60} revealed only bare HOPG with no observation of monolayers of either **3**:C_{60} or **3**, despite use of identical conditions to those used to form monolayers of pristine **3**. The lack of monolayers of even pristine **3** in these systems indicates that the presence of C_{60} dramatically alters the thermodynamics of self-assembly in this system. Further investigation of this system should explore whether C_{60} induces conformational changes of **3** in solution that could prevent monolayer formation; this might be accomplished using UV-Vis and ^{1}H-NMR spectroscopy.

Co-deposition of **4** and C_{60} results in the formation of monolayers whose STM images differ from those for **4**, exhibiting four features across various bias-voltages (Figure 4.16). At a bias-voltage of –500 mV, two circular features are observed in the STM image and cross-sectional profile: a brighter and dimmer feature. The brighter feature appears at the center of the unit cell of the dimmer features (or *vice versa*). Similar features are observed at –700 mV and –900 mV, with the dimmer features becoming slightly brighter at –700 mV and both features showing an apparent height of approximately 0.05 nm at –900 mV. In addition, a much larger and brighter feature appears in the image obtained at –900 mV. A large change is noted at bias-voltages around –1100 mV, again brighter and dimmer circular features are observed; however, in these images rather than the brighter feature being in the center of a unit cell of the dimmer feature (or *vice versa*), the bright feature partially overlaps the dim feature offset along the unit cell vector. Similar to the image at –900 mV, large bright features are observed in several locations across the image. The unit cell, as defined by either the bright or the dim features in Figure 4.16a, was determined to be

approximately 1.50 nm × 1.50 nm with an angle of 88 degrees (Table 4.8), indistinguishable from any of the other systems studied here.

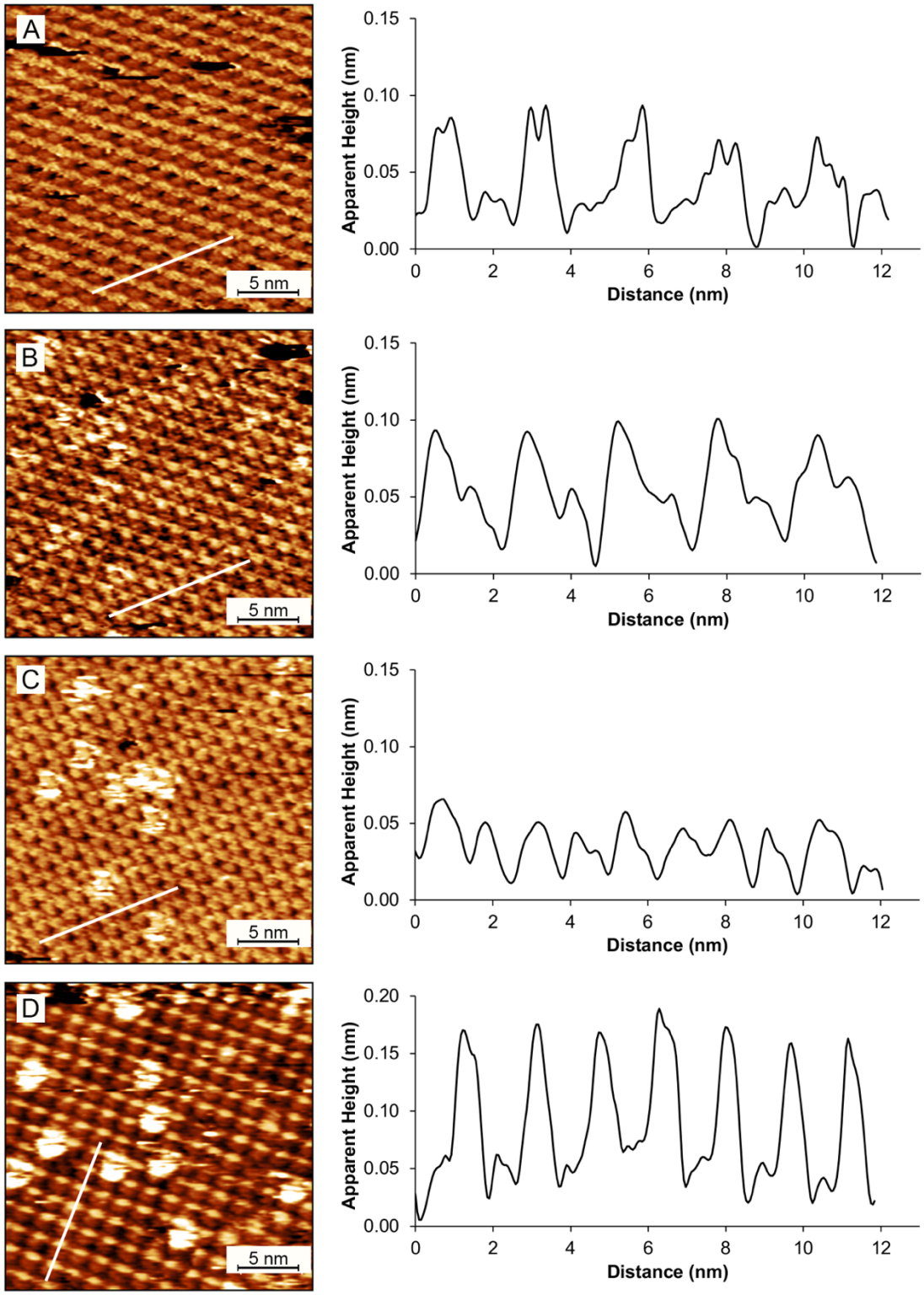

Figure 4.16. STM image and cross-sectional profile of monolayer of co-deposited **4** and C_{60} on HOPG at the solid–liquid interface (TCB, [**2**] = 0.5 mM, [C_{60}] = 2.5 mM, 25 nm × 25 nm, I = 20 pA) (a) V = –500 mV; (b) V = –700 mV; (c) V = –900 mV; (d) V = –1100 mV.

Table 4.8. Unit-Cell Parameters of Monolayers of **4**:C_{60} on HOPG at the Solid–Liquid Interface.

parameter	Bright Features[a]	Dim Features[a]
a (nm)	1.52 (3)	1.50 (2)
b (nm)	1.49 (8)	1.49 (6)
Γ (deg)	88 (1)	88 (1)

[a] From data in Figure 4.16a

Observations from pristine monolayers of **4** and the bicomponent system **2**:C_{60} allow for tentative assignment of these features. The bright and dim features observed at bias-voltages of –700 mV or less negative were assigned to the upper and lower porphyrins of **4**. This assignment is supported by the observations of the small features near the center of the unit cell in monolayers of pristine **4**, the similar width and profile of the bright and dim features, and the inability to image C_{60} at these bias-voltages in **2**:C_{60}. While these images appear similar to those of Ni(OEP) in TCB imaged in the same range of bias-voltages (Section 6.3.2), the disappearance of these features at more negative bias-voltages for **4**:C_{60}, unlike for the TCB features observed within the Ni(OEP) monolayer, demonstrate that TCB is not the source of these features. This suggests that **4** adopts a significantly distorted geometry where the upper porphyrin is offset from the lower porphyrin by roughly 1 nm in the *xy* plane, based on the unit cell. This offset is similar to that observed in monolayers of pristine **4**, though the multiple porphyrin features were not as clearly resolved in that system. The bright features along the unit cell axis observed at –1100 mV are assigned to C_{60} given the similar appearance of C_{60} at these bias-voltages in monolayers of **2**:C_{60}, with the dimmer features at these bias-voltages resulting from the lower porphyrin of **4**. The large and bright features clearly observed above –900 mV, may be a result of adsorption of C_{60} to the macrocycle of the upper porphyrin analogously to that observed in **2**:C_{60}. These features are clearly larger and brighter than those observed in Figure 4.8; currently, no clear justification for this change in appearance can be provided.

4.3.7. DFT Calculated Adsorption Energies of 3:C_{60} and 4:C_{60}. The adsorption energy of C_{60} was calculated for **3**:C_{60} and **4**:C_{60} to investigate the lack of formation of a bicomponent monolayer and the lowest energy on-surface geometry, respectively. The calculations were performed using the same methodology as that employed for **2**:C_{60}. Optimized structures of a surface-like **3**:C_{60} and two on-surface conformations of **4**:C_{60} are shown in Figure 4.17 with adsorption energies in Table 4.9. The space-filling model of **3**:C_{60} demonstrates the well-suited height of the cavity for the C_{60} if **3** adopts a fully extended configuration allowing for interaction with both the OEP and BCP subunits. The solvated-phase adsorption energy of C_{60} within the modeled **3**:C_{60} is significantly greater than that of **2**:C_{60}. Thus, the lack of an experimentally observed monolayer of **3**:C_{60} may be kinetically rather than thermodynamically disfavored.

Space-filling models of the optimized geometries of **4**:C_{60} where **4** is either in an extended or folded conformation are shown in Figure 4.17b. When **4** is extended the close contact between **4** and C_{60} is limited to the BPCP unit and the edge of the phenyl group of the BPCP on the adjacent **4**. In contrast, in the folded geometry, C_{60} is in close-contact with the porphyrin macrocycle of the linking BPCP unit, the adjacent phenyl group of the BPCP, and edge of the OEP of the neighboring **4** on the surface. These differences are borne out in the solvated-phase adsorption energy where the folded conformation is 0.23 eV more stable than the extended conformation.

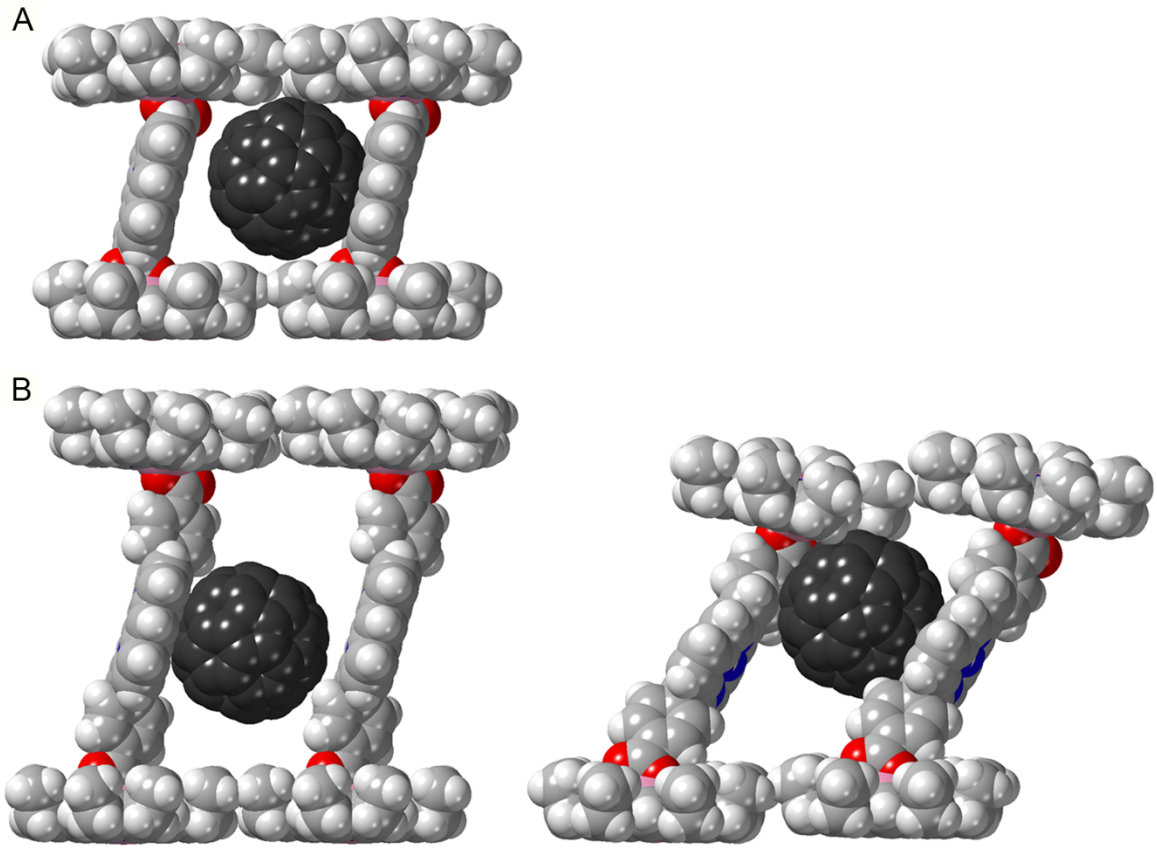

Figure 4.17. Space-filling models of (a) **3**:C_{60} and (b) **4**:C_{60} in extended (left) and folded (right) conformations. Carbon atoms of **2** (light) and C_{60} (dark) are shown in different shades of gray for contrast.

Table 4.9. Calculated Gas-Phase Adsorption Energies, Solvation Energies, and Solvated-Phase Adsorption Energies for **3**:C_{60} and **4**:C_{60}.

parameter	**3**:C_{60}	**4**:C_{60} (Extended)	**4**:C_{60} (Folded)
$\Delta E_{ads(g)}$ (eV)	–2.09	–1.38	–1.91
ΔE_{solv} (eV)	0.41	0.18	0.48
$\Delta E_{ads(s)}$ (eV)	–1.68	–1.20	–1.43

4.4. Conclusions

The surface chemistry of a series of co-facial porphyrin dimers has been investigated on HOPG. It was found that deposition of **1**–**4** onto HOPG results in formation of face-down, highly ordered monolayers generally consistent with those observed for 4-coordinate metalloporphyrins, despite the significant height and steric bulk presented by the linkers and non-surface bound porphyrins. Co-deposition of **2** or **4** with C_{60} results in the formation of bicomponent monolayers.

Bias-voltage dependence, DFT derived adsorption energies, and simulated STM images confirm that the second component in these systems is C_{60} entrained within the cavity formed by monolayers by the porphyrin complexes. The observation of identical structures formed by pristine monolayers of **1**–**4**, bicomponent monolayers **2**:C_{60} and **4**:C_{60}, and those of monomeric 4- and 5-coordinate metalloporphyrins under the same conditions suggests that the vast literature of self-assembled porphyrins and phthalocyanines on HOPG could be utilized in these types of systems, providing a method for substantially altering the size of the cavity to accommodate other small molecules or nanoparticles. Furthermore, the stability of C_{60} in the monolayer **2**:C_{60}, despite the apparent lack of interaction between the terephthalate moiety and the C_{60}, suggests that, with the appropriate porphyrin spacing, functional spacers such as photo- or redox-active linkers could be introduced.

4.5. References

1. Lehn, J. M. Toward Complex Matter: Supramolecular Chemistry and Self-Organization. *Proc. Natl. Acad. Sci. U. S. A.* **2002**, *99*, 4763–4768.

2. Goronzy, D. P.; Ebrahim, M.; Rosei, F.; Arramel; Fang, Y.; De Feyter, S.; Tait, S. L.; Wang, C.; Beton, P. H.; Wee, A. T. S.; Weiss, P. S.; Perepichka, D. F. Supramolecular Assemblies on Surfaces: Nanopatterning, Functionality, and Reactivity. *ACS Nano* **2018**, *12*, 7445–7481.

3. Held, P. A.; Fuchs, H.; Studer, A. Covalent-Bond Formation via on-Surface Chemistry. *Chem. – Eur. J.* **2017**, *23*, 5874–5892.

4. Xing, L. B.; Peng, Z. T.; Li, W. T.; Wu, K. On Controllability and Applicability of Surface Molecular Self-Assemblies. *Acc. Chem. Res.* **2019**, *52*, 1048–1058.

5. Wasielewski, M. R.; Forbes, M. D. E.; Frank, N. L.; Kowalski, K.; Scholes, G. D.; Yuen-Zhou, J.; Baldo, M. A.; Freedman, D. E.; Goldsmith, R. H.; Goodson, T.; Kirk, M. L.; McCusker, J. K.; Ogilvie, J. P.; Shultz, D. A.; Stoll, S.; Whaley, K. B. Exploiting Chemistry and Molecular Systems for Quantum Information Science. *Nat. Rev. Chem.* **2020**, *4*, 490–504.

6. Gobbi, M.; Orgiu, E.; Samori, P. When 2D Materials Meet Molecules: Opportunities and Challenges of Hybrid Organic/Inorganic Van Der Waals Heterostructures. *Adv. Mater.* **2018**, *30*, 1706103.

7. Amsterdam, S. H.; Marks, T. J.; Hersam, M. C. Leveraging Molecular Properties to Tailor Mixed-Dimensional Heterostructures Beyond Energy Level Alignment. *J. Phys. Chem. Lett.* **2021**, *12*, 4543–4557.

8. Munninghoff, J. A. W.; Elemans, J. A. A. W. Chemistry at the Square Nanometer: Reactivity at Liquid/Solid Interfaces Revealed with an STM. *Chem. Commun.* **2017**, *53*, 1769–1788.

9. Brill, A. R.; Kuntumalla, M. K.; de Ruiter, G.; Koren, E. Formation of Highly Ordered Self-Assembled Monolayers on Two-Dimensional Materials via Noncovalent Functionalization. *ACS Appl. Mater. Interfaces* **2020**, *12*, 33941–33949.

10. Brill, A. R.; Kafri, A.; Mohapatra, P. K.; Ismach, A.; de Ruiter, G.; Koren, E. Modulating the Optoelectronic Properties of MoS_2 by Highly Oriented Dipole-Generating Monolayers. *ACS Appl. Mater. Interfaces* **2021**, *13*, 32590–32597.

11. Zhao, Y. D.; Bertolazzi, S.; Samori, P. A Universal Approach toward Light Responsive Two-Dimensional Electronics: Chemically Tailored Hybrid Van Der Waals Heterostructures. *ACS Nano* **2019**, *13*, 4814–4825.

12. Wang, Y.; Iglesias, D.; Gali, S. M.; Beljonne, D.; Samori, P. Light-Programmable Logic-in-Memory in 2D Semiconductors Enabled by Supramolecular Functionalization: Photoresponsive Collective Effect of Aligned Molecular Dipoles. *ACS Nano* **2021**, *15*, 13732–13741.

13. Phillipson, R.; de la Rosa, C. J. L.; Teyssandier, J.; Walke, P.; Waghray, D.; Fujita, Y.; Adisoejoso, J.; Mali, K. S.; Asselierghs, I.; Huyghebaert, C.; Uji-i, H.; De Gendt, S.; Feyter, S. Tunable Doping of Graphene by Using Physisorbed Self-Assembled Networks. *Nanoscale* **2016**, *8*, 20017–20026.

14. Tahara, K.; Ishikawa, T.; Hirsch, B. E.; Kubo, Y.; Brown, A.; Eyley, S.; Daukiya, L.; Thielemans, W.; Li, Z.; Walke, P.; Hirose, S.; Hashimoto, S.; De Feyter, S.; Tobe, Y. Self-Assembled Monolayers as Templates for Linearly Nanopatterned Covalent Chemical Functionalization of Graphite and Graphene Surfaces. *ACS Nano* **2018**, *12*, 11520–11528.

15. Tahara, K.; Kubo, Y.; Hashimoto, S.; Ishikawa, T.; Kaneko, H.; Brown, A.; Hirsch, B. E.; De Feyter, S.; Tobe, Y. Porous Self-Assembled Molecular Networks as Templates for Chiral-Position-Controlled Chemical Functionalization of Graphitic Surfaces. *J. Am. Chem. Soc.* **2020**, *142*, 7699–7708.

16. Hashimoto, S.; Kaneko, H.; De Feyter, S.; Tobe, Y.; Tahara, K. Symmetry and Spacing Controls in Periodic Covalent Functionalization of Graphite Surfaces Templated by Self-Assembled Molecular Networks. *Nanoscale* **2022**, *14*, 12595–12609.

17. Gonzalez, J. D. C.; Iyoda, M.; Rabe, J. P. Templated Bilayer Self-Assembly of Fully Conjugated π-Expanded Macrocyclic Oligothiophenes Complexed with Fullerenes. *Nat. Commun.* **2017**, *8*, 14717.

18. Stohr, M.; Wahl, M.; Spillmann, H.; Gade, L. H.; Jung, T. A. Lateral Manipulation for the Positioning of Molecular Guests within the Confinements of a Highly Stable Self-Assembled Organic Surface Network. *Small* **2007**, *3*, 1336–1340.

19. Cui, D. L.; Ebrahimi, M.; Macleod, J. M.; Rosei, F. Template-Driven Dense Packing of Pentagonal Molecules in Monolayer Films. *Nano Lett.* **2018**, *18*, 7570–7575.

20. Wintjes, N.; Bonifazi, D.; Cheng, F. Y.; Kiebele, A.; Stohr, M.; Jung, T.; Spillmann, H.; Diederich, F. A Supramolecular Multiposition Rotary Device. *Angew. Chem., Int. Ed.* **2007**, *46*, 4089–4092.

21. Schmaltz, B.; Rouhanipour, A.; Rader, H. J.; Pisula, W.; Mullen, K. Filling the Cavity of Conjugated Carbazole Macrocycles with Graphene Molecules: Monolayers Formed by Physisorption Serve as a Surface for Pulsed Laser Deposition. *Angew. Chem., Int. Ed.* **2009**, *48*, 720–724.

22. Teyssandier, J.; De Feyter, S.; Mali, K. S. Host–Guest Chemistry in Two-Dimensional Supramolecular Networks. *Chem. Commun.* **2016**, *52*, 11465–11487.

23. Kudernac, T.; Lei, S. B.; Elemans, J. A. A. W.; De Feyter, S. Two-Dimensional Supramolecular Self-Assembly: Nanoporous Networks on Surfaces. *Chem. Soc. Rev.* **2009**, *38*, 3505–3505.

24. Bonifazi, D.; Mohnani, S.; Llanes-Pallas, A. Supramolecular Chemistry at Interfaces: Molecular Recognition on Nanopatterned Porous Surfaces. *Chem. – Eur. J.* **2009**, *15*, 7004–7025.

25. Zhang, X. M.; Zeng, Q. D.; Wang, C. Molecular Templates and Nano-Reactors: Two-Dimensional Hydrogen Bonded Supramolecular Networks on Solid/Liquid Interfaces. *RSC Adv.* **2013**, *3*, 11351–11366.

26. Stepanow, S.; Lingenfelder, M.; Dmitriev, A.; Spillmann, H.; Delvigne, E.; Lin, N.; Deng, X. B.; Cai, C. Z.; Barth, J. V.; Kern, K. Steering Molecular Organization and Host–Guest Interactions Using Two-Dimensional Nanoporous Coordination Systems. *Nat. Mater.* **2004**, *3*, 229–233.

27. Khan, S. B.; Lee, S. L. Supramolecular Chemistry: Host–Guest Molecular Complexes. *Molecules* **2021**, *26*, 3995.

28. Blunt, M. O.; Russell, J. C.; Gimenez-Lopez, M. D.; Taleb, N.; Lin, X. L.; Schroder, M.; Champness, N. R.; Beton, P. H. Guest-Induced Growth of a Surface-Based Supramolecular Bilayer. *Nat. Chem.* **2011**, *3*, 74–78.

29. den Boer, D.; Han, G. D.; Swager, T. M. Templating Fullerenes by Domain Boundaries of a Nanoporous Network. *Langmuir* **2014**, *30*, 762–767.

30. Griessl, S. J. H.; Lackinger, M.; Jamitzky, F.; Markert, T.; Hietschold, M.; Heckl, W. M. Room-Temperature Scanning Tunneling Microscopy Manipulation of Single C_{60} Molecules at the Liquid–Solid Interface: Playing Nanosoccer. *J. Phys. Chem. B* **2004**, *108*, 11556–11560.

31. Hu, Y.; Zeng, X. M.; Sahare, S.; Xie, R. B.; Lee, S. L. Flow-Induced-Crystallization: Tailoring Host–Guest Supramolecular Co-Assemblies at the Liquid–Solid Interface. *Nanoscale Adv.* **2022**, *4*, 3524–3530.

32. Li, M.; Deng, K.; Lei, S. B.; Yang, Y. L.; Wang, T. S.; Shen, Y. T.; Wang, C. R.; Zeng, Q. D.; Wang, C. Site-Selective Fabrication of Two-Dimensional Fullerene Arrays by Using a Supramolecular Template at the Liquid–Solid Interface. *Angew. Chem., Int. Ed.* **2008**, *47*, 6717–6721.

33. MacLeod, J. M.; Ivasenko, O.; Fu, C. Y.; Taerum, T.; Rosei, F.; Perepichka, D. F. Supramolecular Ordering in Oligothiophene–Fullerene Monolayers. *J. Am. Chem. Soc.* **2009**, *131*, 16844–16850.

34. Xu, B.; Tao, C. G.; Williams, E. D.; Reutt-Robey, J. E. Coverage Dependent Supramolecular Structures: C_{60} : Aca Monolayers on Ag(111). *J. Am. Chem. Soc.* **2006**, *128*, 8493–8499.

35. Theobald, J. A.; Oxtoby, N. S.; Phillips, M. A.; Champness, N. R.; Beton, P. H. Controlling Molecular Deposition and Layer Structure with Supramolecular Surface Assemblies. *Nature* **2003**, *424*, 1029–1031.

36. Cui, D.; MacLeod, J. M.; Ebrahimi, M.; Perepichka, D. F.; Rosei, F. Solution and Air Stable Host/Guest Architectures from a Single Layer Covalent Organic Framework. *Chem. Commun.* **2015**, *51*, 16510–16513.

37. Cui, D. L.; Ebrahimi, M.; Rosei, F.; Macleod, J. M. Control of Fullerene Crystallization from 2D to 3D through Combined Solvent and Template Effects. *J. Am. Chem. Soc.* **2017**, *139*, 16732–16740.

38. Cui, D. L.; MacLeod, J. M.; Rosei, F. Planar Anchoring of C_{70} Liquid Crystals Using a Covalent Organic Framework Template. *Small* **2019**, *15*, 1903294.

39. Plas, J.; Ivasenko, O.; Martsinovich, N.; Lackinger, M.; De Feyter, S. Nanopatterning of a Covalent Organic Framework Host–Guest System. *Chem. Commun.* **2016**, *52*, 68–71.

40. Mena-Osteritz, E.; Bauerle, P. Complexation of C_{60} on a Cyclothiophene Monolayer Template. *Adv. Mater.* **2006**, *18*, 447–451.

41. Piot, L.; Silly, F.; Tortech, L.; Nicolas, Y.; Blanchard, P.; Roncali, J.; Fichou, D. Long-Range Alignments of Single Fullerenes by Site-Selective Inclusion into a Double-Cavity 2D Open Network. *J. Am. Chem. Soc.* **2009**, *131*, 12864–12865.

42. Cui, K.; Schlutter, F.; Ivasenko, O.; Kivala, M.; Schwab, M. G.; Lee, S. L.; Mertens, S. F. L.; Tahara, K.; Tobe, Y.; Mullen, K.; Mali, K. S.; De Feyter, S. Multicomponent Self-Assembly with a Shape-Persistent N-Heterotriangulene Macrocycle on Au(111). *Chem. – Eur. J.* **2015**, *21*, 1652–1659.

43. Kawano, S.; Nakaya, M.; Saitow, M.; Ishiguro, A.; Yanai, T.; Onoe, J.; Tanaka, K. Thermally Stable Array of Discrete C_{60}s on a Two-Dimensional Crystalline Adlayer of Macrocycles Both in Vacuo and under Ambient Pressure. *J. Am. Chem. Soc.* **2022**, *144*, 6749–6758.

44. Pan, G. B.; Cheng, X. H.; Hoger, S.; Freyland, W. 2D Supramolecular Structures of a Shape-Persistent Macrocycle and Co-Deposition with Fullerene on HOPG. *J. Am. Chem. Soc.* **2006**, *128*, 4218–4219.

45. Bonifazi, D.; Spillmann, H.; Kiebele, A.; de Wild, M.; Seiler, P.; Cheng, F. Y.; Guntherodt, H. J.; Jung, T.; Diederich, F. Supramolecular Patterned Surfaces Driven by Cooperative Assembly of C_{60} and Porphyrins on Metal Substrates. *Angew. Chem., Int. Ed.* **2004**, *43*, 4759–4763.

46. Spillmann, H.; Kiebele, A.; Stohr, M.; Jung, T. A.; Bonifazi, D.; Cheng, F. Y.; Diederich, F. A Two-Dimensional Porphyrin-Based Porous Network Featuring Communicating Cavities for the Templated Complexation of Fullerenes. *Adv. Mater.* **2006**, *18*, 275–279.

47. Kiebele, A.; Bonifazi, D.; Cheng, F. Y.; Stohr, M.; Diederich, F.; Jung, T.; Spillmann, H. Adsorption and Dynamics of Long-Range Interacting Fullerenes in a Flexible, Two-Dimensional, Nanoporous Porphyrin Network. *ChemPhysChem* **2006**, *7*, 1462–1470.

48. Bonifazi, D.; Kiebele, A.; Stohr, M.; Cheng, F. Y.; Jung, T.; Diederich, F.; Spillmann, H. Supramolecular Nanostructuring of Silver Surfaces via Self-Assembly of [60]Fullerene and Porphyrin Modules. *Adv. Funct. Mater.* **2007**, *17*, 1051–1062.

49. Yoshimoto, S.; Honda, Y.; Ito, O.; Itaya, K. Supramolecular Pattern of Fullerene on 2D Bimolecular “Chessboard" Consisting of Bottom-up Assembly of Porphyrin and Phthalocyanine Molecules. *J. Am. Chem. Soc.* **2008**, *130*, 1085–1092.

50. Prato, M. [60]Fullerene Chemistry for Materials Science Applications. *J. Mat. Chem.* **1997**, *7*, 1097–1109.

51. Langa, F.; Nierengarten, J.-F. *Fullerenes : Principles and Applications.* 2nd ed.; Royal Society of Chemistry: Cambridge, 2011.

52. Verner, R. F.; Benvegnu, C. *Handbook on Fullerene Synthesis, Properties and Applications.* Nova Science Publishers: New York, 2012.

53. Baskar, A. V.; Benzigar, M. R.; Talapaneni, S. N.; Singh, G.; Karakoti, A. S.; Yi, J. B.; Al-Muhtaseb, A. H.; Ariga, K.; Ajayan, P. M.; Vinu, A. Self-Assembled Fullerene Nanostructures: Synthesis and Applications. *Adv. Funct. Mater.* **2022**, *32*, 2106924.

54. Morton, J. J. L.; Tyryshkin, A. M.; Ardavan, A.; Benjamin, S. C.; Porfyrakis, K.; Lyon, S. A.; Briggs, G. A. D. Bang–Bang Control of Fullerene Qubits Using Ultrafast Phase Gates. *Nat. Phys.* **2006**, *2*, 40–43.

55. Benjamin, S. C.; Ardavan, A.; Briggs, G. A. D.; Britz, D. A.; Gunlycke, D.; Jefferson, J.; Jones, M. A. G.; Leigh, D. F.; Lovett, B. W.; Khlobystov, A. N.; Lyon, S. A.; Morton, J. J. L.; Porfyrakis, K.; Sambrook, M. R.; Tyryshkin, A. M. Towards a Fullerene-Based Quantum Computer. *J. Phys.: Condens. Matter* **2006**, *18*, S867–S883.

56. Harneit, W. Fullerene-Based Electron-Spin Quantum Computer. *Phys. Rev. A* **2002**, *65*, 032322.

57. Zhou, S.; Yuan, J. Y.; Wang, Z. Y.; Ling, K.; Fu, P. X.; Fang, Y. H.; Wang, Y. X.; Liu, Z.; Porfyrakis, K.; Briggs, G. A. D.; Gao, S.; Jiang, S. D. Implementation of Quantum Level Addressability and Geometric Phase Manipulation in Aligned Endohedral Fullerene Qudits. *Angew. Chem., Int. Ed.* **2022**, *61*, e202115263.

58. Uemura, S.; Sakata, M.; Taniguchi, I.; Kunitake, M.; Hirayama, C. Novel "Wet Process" Technique Based on Electrochemical Replacement for the Preparation of Fullerene Epitaxial Adlayers. *Langmuir* **2001**, *17*, 5–7.

59. Uemura, S.; Samori, P.; Kunitake, M.; Hirayama, C.; Rabe, J. P. Crystalline C_{60} Monolayers at the Solid–Organic Solution Interface. *J. Mater. Chem.* **2002**, *12*, 3366–3367.

60. Szuba, S.; Czajka, R.; Kasuya, A.; Wawro, A.; Rafii-Tabar, H. Observation of C_{60} Film Formation on a Highly Oriented Pyrolitic Graphite Substrate via Scanning Tunnelling Microscopy. *Appl. Surf. Sci.* **1999**, *144-45*, 648–652.

61. Zhang, Y.; Gao, X. P.; Weaver, M. J. Scanning Tunneling Microscopy of C_{60} and C_{70} on Ordered Au(111) and Au(110): Molecular Structure and Electron Transmission. *J. Phys. Chem.* **1992**, *96*, 510–513.

62. Wilson, R. J.; Meijer, G.; Bethune, D. S.; Johnson, R. D.; Chambliss, D. D.; Devries, M. S.; Hunziker, H. E.; Wendt, H. R. Imaging C_{60} Clusters on a Surface Using a Scanning Tunneling Microscope. *Nature* **1990**, *348*, 621–622.

63. Wu, Z. Q.; Shao, X. B.; Li, C.; Hou, J. L.; Wang, K.; Jiang, X. K.; Li, Z. T. Hydrogen-Bonding-Driven Preorganized Zinc Porphyrin Receptors for Efficient Complexation of C_{60}, C_{70}, and C_{60} Derivatives. *J. Am. Chem. Soc.* **2005**, *127*, 17460–17468.

64. Bhattacharya, S.; Ujihashi, N.; Aonuma, S.; Kimura, T.; Komatsu, N. Spectral and Theoretical Studies on Effective and Selective Non-Covalent Interaction between Tetrahexylporphyrins and Fullerenes. *Spectrochim. Acta, Part A* **2007**, *68*, 495–503.

65. Tashiro, K.; Aida, T. Metalloporphyrin Hosts for Supramolecular Chemistry of Fullerenes. *Chem. Soc. Rev.* **2007**, *36*, 189–197.

66. Konarev, D. V.; Khasanov, S. S.; Saito, G.; Lyubovskaya, R. N. Design of Molecular and Ionic Complexes of Fullerene C_{60} with Metal(II) Octaethylporphyrins, M^{II}oep (M = Zn, Co, Fe, and Mn) Containing Coordination M–N(Ligand) and M–C(C_{60}^{-}) Bonds. *Cryst. Growth Des.* **2009**, *9*, 1170–1181.

67. Olmstead, M. M.; Costa, D. A.; Maitra, K.; Noll, B. C.; Phillips, S. L.; Van Calcar, P. M.; Balch, A. L. Interaction of Curved and Flat Molecular Surfaces. The Structures of Crystalline Compounds Composed of Fullerene (C_{60}, C_{60}o, C_{70}, and C_{120}o) and Metal Octaethylporphyrin Units. *J. Am. Chem. Soc.* **1999**, *121*, 7090–7097.

68. Ishii, T.; Aizawa, N.; Yamashita, M.; Matsuzaka, H.; Kodama, T.; Kikuchi, K.; Ikemoto, I.; Iwasa, Y. First Syntheses of Cocrystallites Consisting of Anti-Formed Metal Octaethylporphyrins with Fullerene C_{60}. *J. Chem. Soc., Dalton Trans.* **2000**, 4407–4412.

69. Kurotobi, K.; Murata, Y. A Single Molecule of Water Encapsulated in Fullerene C_{60}. *Science* **2011**, *333*, 613–616.

70. Kamm, J. M. Ph. D. Thesis. The University of Chicago, Chicago, IL, 2017.

71. Sun, D.; Tham, F. S.; Reed, C. A.; Boyd, P. D. W. Extending Supramolecular Fullerene–Porphyrin Chemistry to Pillared Metal–Organic Frameworks. *Proc. Natl. Acad. Sci. U. S. A.* **2002**, *99*, 5088–5092.

72. Feng, Y. Q.; Wang, T. S.; Li, Y. J.; Li, J.; Wu, J. Y.; Wu, B.; Jiang, L.; Wang, C. R. Steering Metallofullerene Electron Spin in Porous Metal Organic Framework. *J. Am. Chem. Soc.* **2015**, *137*, 15055–15060.

73. Gutzler, R.; Cardenas, L.; Rosei, F. Kinetics and Thermodynamics in Surface-Confined Molecular Self-Assembly. *Chem. Sci.* **2011**, *2*, 2290–2300.

74. Hipps, K. W.; Mazur, U. Kinetic and Thermodynamic Control in Porphyrin and Phthalocyanine Self-Assembled Monolayers. *Langmuir* **2018**, *34*, 3–17.

75. Reimers, J. R. How Equilibrium Gets Mimicked During Kinetic and Thermodynamic Control in Porphyrin and Phthalocyanine Self-Assembled Monolayers. *Langmuir* **2018**, *34*, 18–22.

76. Otsuki, J. STM Studies on Double- and Triple-Decker Porphyrin and Phthalocyanine Complexes. *Supramol. Chem.* **2011**, *23*, 169–182.

77. Komeda, T.; Isshiki, H.; Liu, J.; Katoh, K.; Yamashita, M. Variation of Kondo Temperature Induced by Molecule–Substrate Decoupling in Film Formation of Bis (Phthalocyaninato)Terbium(III) Molecules on Au(111). *ACS Nano* **2014**, *8*, 4866–4875.

78. Komeda, T.; Katoh, K.; Yamashita, M. Double-Decker Phthalocyanine Complex: Scanning Tunneling Microscopy Study of Film Formation and Spin Properties. *Prog. Surf. Sci.* **2014**, *89*, 127–160.

79. Mannini, M.; Bertani, F.; Tudisco, C.; Malavolti, L.; Poggini, L.; Misztal, K.; Menozzi, D.; Motta, A.; Otero, E.; Ohresser, P.; Sainctavit, P.; Condorelli, G. G.; Dalcanale, E.; Sessoli, R. Magnetic Behaviour of Tbpc2 Single-Molecule Magnets Chemically Grafted on Silicon Surface. *Nat. Commun.* **2014**, *5*, 4582.

80. Schwobel, J.; Fu, Y. S.; Brede, J.; Dilullo, A.; Hoffmann, G.; Klyatskaya, S.; Ruben, M.; Wiesendanger, R. Real-Space Observation of Spin-Split Molecular Orbitals of Adsorbed Single-Molecule Magnets. *Nat. Commun.* **2012**, *3*, 953.

81. Takami, T.; Ye, T.; Pathem, B. K.; Arnold, D. P.; Sugiura, K.; Bian, Y. Z.; Jiang, J. Z.; Weiss, P. S. Manipulating Double-Decker Molecules at the Liquid–Solid Interface. *J. Am. Chem. Soc.* **2010**, *132*, 16460–16466.

82. Rana, S.; Jiang, J. Z.; Korpany, K. V.; Mazur, U.; Hipps, K. W. STM Investigation of the Y[C6s-Pc](2) and Y[C4o-Pc](2) Complex at the Solution-Solid Interface: Substrate Effects, Submolecular Resolution, and Vacancies. *J. Phys. Chem. C* **2021**, *125*, 1421–1431.

83. Rana, S.; Johnson, K. N.; Gurdumov, K.; Mazur, U.; Hipps, K. W. Scanning Tunneling Microscopy Reveals Surface Diffusion of Single Double-Decker Phthalocyanine Molecules at the Solution/Solid Interface. *J. Phys. Chem. C* **2022**, *126*, 4140–4149.

84. den Boer, D.; Li, M.; Habets, T.; Iavicoli, P.; Rowan, A. E.; Nolte, R. J. M.; Speller, S.; Amabilino, D. B.; De Feyter, S.; Elemans, J. A. A. W. Detection of Different Oxidation States of Individual Manganese Porphyrins During Their Reaction with Oxygen at a Solid/Liquid Interface. *Nat. Chem.* **2013**, *5*, 621–627.

85. Li, M.; den Boer, D.; Iavicoli, P.; Adisoejoso, J.; Uji-i, H.; Van der Auweraer, M.; Amabilino, D. B.; Elemans, J. A. A. W.; De Feyter, S. Tip-Induced Chemical Manipulation of Metal Porphyrins at a Liquid/Solid Interface. *J. Am. Chem. Soc.* **2014**, *136*, 17418–17421.

86. Lau, W.-Y. Ph. D. Thesis. The University of Chicago, Chicago, IL, 2016.

87. *Spip Software,* Version 6.0.9; Image Metrology A/S: Hørsholm, Denmark.

88. Necas, D.; Klapetek, P. Gwyddion: An Open-Source Software for Spm Data Analysis. *Cent. Eur. J. Phys.* **2012**, *10*, 181–188.

89. Krause, L.; Herbst-Irmer, R.; Sheldrick, G. M.; Stalke, D. Comparison of Silver and Molybdenum Microfocus X-Ray Sources for Single-Crystal Structure Determination. *J. Appl. Crystallogr.* **2015**, *48*, 3–10.

90. Sheldrick, G. M. SHELXT – Integrated Space-Group and Crystal-Structure Determination. *Acta Crystallogr., Sect. A: Found. Adv.* **2015**, *71*, 3–8.

91. Dolomanov, O. V.; Bourhis, L. J.; Gildea, R. J.; Howard, J. A. K.; Puschmann, H. OLEX2: A Complete Structure Solution, Refinement and Analysis Program. *J. Appl. Crystallogr.* **2009**, *42*, 339–341.

92. Sheldrick, G. M. Crystal Structure Refinement with SHELXL. *Acta Crystallogr., Sect. C: Struct. Chem.* **2015**, *71*, 3–8.

93. Fenn, T. D.; Schnieders, M. J.; Brunger, A. T. A Smooth and Differentiable Bulk-Solvent Model for Macromolecular Diffraction. *Acta Crystallogr., Sect. D: Struct. Biol.* **2010**, *66*, 1024–1031.

94. Giannozzi, P.; Baroni, S.; Bonini, N.; Calandra, M.; Car, R.; Cavazzoni, C.; Ceresoli, D.; Chiarotti, G. L.; Cococcioni, M.; Dabo, I.; Dal Corso, A.; de Gironcoli, S.; Fabris, S.; Fratesi, G.; Gebauer, R.; Gerstmann, U.; Gougoussis, C.; Kokalj, A.; Lazzeri, M.; Martin-Samos, L.; Marzari, N.; Mauri, F.; Mazzarello, R.; Paolini, S.; Pasquarello, A.; Paulatto, L.; Sbraccia, C.; Scandolo, S.; Sclauzero, G.; Seitsonen, A. P.; Smogunov, A.; Umari, P.; Wentzcovitch, R. M. Quantum Espresso: A Modular and Open-Source Software Project for Quantum Simulations of Materials. *J. Phys.: Condens. Matter* **2009**, *21*, 395502.

95. Klimes, J.; Bowler, D. R.; Michaelides, A. Chemical Accuracy for the Van Der Waals Density Functional. *J. Phys.: Condens. Matter* **2010**, *22*, 022201.

96. Klimes, J.; Bowler, D. R.; Michaelides, A. Van Der Waals Density Functionals Applied to Solids. *Phys. Rev. B* **2011**, *83*, 195131.

97. Becke, A. D. On the Large-Gradient Behavior of the Density Functional Exchange Energy. *J. Chem. Phys.* **1986**, *85*, 7184–7187.

98. Thonhauser, T.; Zuluaga, S.; Arter, C. A.; Berland, K.; Schroder, E.; Hyldgaard, P. Spin Signature of Nonlocal Correlation Binding in Metal–Organic Frameworks. *Phys. Rev. Lett.* **2015**, *115*, 136402.

99. Thonhauser, T.; Cooper, V. R.; Li, S.; Puzder, A.; Hyldgaard, P.; Langreth, D. C. Van Der Waals Density Functional: Self-Consistent Potential and the Nature of the Van Der Waals Bond. *Phys. Rev. B* **2007**, *76*, 125112.

100. Langreth, D. C.; Lundqvist, B. I.; Chakarova-Kack, S. D.; Cooper, V. R.; Dion, M.; Hyldgaard, P.; Kelkkanen, A.; Kleis, J.; Kong, L. Z.; Li, S.; Moses, P. G.; Murray, E.; Puzder, A.; Rydberg, H.; Schroder, E.; Thonhauser, T. A Density Functional for Sparse Matter. *J. Phys.: Condens. Matter* **2009**, *21*, 084203.

101. Berland, K.; Cooper, V. R.; Lee, K.; Schroder, E.; Thonhauser, T.; Hyldgaard, P.; Lundqvist, B. I. Van Der Waals Forces in Density Functional Theory: A Review of the Vdw-Df Method. *Rep. Prog. Phys.* **2015**, *78*, 066501.

102. Hamann, D. R. Optimized Norm-Conserving Vanderbilt Pseudopotentials. *Phys. Rev. B* **2013**, *88*, 085117.

103. Schlipf, M.; Gygi, F. Optimization Algorithm for the Generation of Oncv Pseudopotentials. *Comput. Phys. Commun.* **2015**, *196*, 36–44.

104. Tersoff, J.; Hamann, D. R. Theory of the Scanning Tunneling Microscope. *Phys. Rev. B* **1985**, *31*, 805–813.

105. Monkhorst, H. J.; Pack, J. D. Special Points for Brillouin-Zone Integrations. *Phys. Rev. B* **1976**, *13*, 5188–5192.

106. Palmer, D. C. *Crystalmaker,* Version 10.6.5; CrystalMaker Software Ltd: Begbroke, Oxfordshire, England.

107. *Originpro,* Version 2022b; OriginLab Corporation: Northhampton, MA, USA.

108. Becke, A. D. Density-Functional Thermochemistry. III. The Role of Exact Exchange. *J. Chem. Phys.* **1993**, *98*, 5648–5652.

109. Perdew, J. P. Density-Functional Approximation for the Correlation-Energy of the Inhomogeneous Electron-Gas. *Phys. Rev. B* **1986**, *33*, 8822–8824.

110. Wadt, W. R.; Hay, P. J. Abinitio Effective Core Potentials for Molecular Calculations - Potentials for Main Group Elements Na to Bi. *J. Chem. Phys.* **1985**, *82*, 284–298.

111. Hay, P. J.; Wadt, W. R. Abinitio Effective Core Potentials for Molecular Calculations - Potentials for the Transition-Metal Atoms Sc to Hg. *J. Chem. Phys.* **1985**, *82*, 270–283.

112. Gurdumov, K.; Mazur, U.; Hipps, K. W. Self-Assembly Dynamics and Stability through Concentration Control at the Solution/HOPG Interface. *J. Phys. Chem. C* **2022**, *126*, 12916–12927.

113. Laboratory Solvents and Other Liquid Reagents. In *CRC Handbook of Chemistry and Physics,* 101st ed.; Rumble, J. R., Bruno, T. J., Doa, M. J. ed.; CRC Press 2020.

114. Abraham, M. H. Hydrogen-Bonding. 31. Construction of a Scale of Solute Effective or Summation Hydrogen-Bond Basicity. *J. Phys. Org. Chem.* **1993**, *6*, 660–684.

115. *1,2,4-Trichlorobenzene Data Sheet*. http://www.microkat.gr/msdspd90-99/1%2C2%2C4-Trichlorobenzene.html (accessed 2022-10-6).

116. Kamm, J. M.; Iverson, C. P.; Lau, W. Y.; Hopkins, M. D. Axial Ligand Effects on the Structures of Self-Assembled Gallium–Porphyrin Monolayers on Highly Oriented Pyrolytic Graphite. *Langmuir* **2016**, *32*, 487–495.

117. Barlow, D. E.; Hipps, K. W. A Scanning Tunneling Microscopy and Spectroscopy Study of Vanadyl Phthalocyanine on Au(111): The Effect of Oxygen Binding and Orbital Mediated Tunneling on the Apparent Corrugation. *J. Phys. Chem. B* **2000**, *104*, 5993–6000.

118. Gurdumov, K.; Mazur, U.; Hipps, K. W. Influences on the Dynamics and Stability of Self-Assembly: Solvent, Substrate, and Concentration. *J. Phys. Chem. C* **2022**, *126*, 19904–19915.

119. Cui, D.; MacLeod, J. M.; Ebrahimi, M.; Rosei, F. Selective Binding in Different Adsorption Sites of a 2D Covalent Organic Framework. *CrystEngComm* **2017**, *19*, 4927–4932.

120. Iritani, K.; Takeda, H.; Kather, M.; Yokoi, M.; Moeglen, M.; Ikeda, M.; Otsubo, Y.; Ozawa, Y.; Tahara, K.; Hirose, K.; De Feyter, S.; Tobe, Y. Electrostatically Driven Guest Binding in Self-Assembled Molecular Network of Hexagonal Pyridine Macrocycle at the Liquid/Solid Interface: Symmetry Breaking Induced by Coadsorbed Solvent Molecules. *Langmuir* **2019**, *35*, 15051–15062.

121. Lee, S.; Hirsch, B. E.; Liu, Y.; Dobscha, J. R.; Burke, D. W.; Tait, S. L.; Flood, A. H. Multifunctional Tricarbazolo Triazolophane Macrocycles: One-Pot Preparation, Anion Binding, and Hierarchical Self-Organization of Multilayers. *Chem. – Eur. J.* **2016**, *22*, 560–569.

122. Keller, T. J.; Bahr, J.; Gratzfeld, K.; Schonfelder, N.; Majewski, M. A.; Stepien, M.; Hoger, S.; Jester, S. S. Nanopatterns of Arylene-Alkynylene Squares on Graphite: Self-Sorting and Intercalation. *Beilstein J. Org. Chem.* **2019**, *15*, 1848–1855.

123. Adachi, K.; Hirose, T.; Matsuda, K. The Polymorphism of Porphyrin 2D Assemblies at the Liquid–Graphite Interface: The Effect of a Polar Solvent Additive and a Flexible Spacer on the Face-on and Edge-on Type Molecular Arrangements. *Chem. Commun.* **2019**, *55*, 8836–8839.

124. El Garah, M.; Bonilla, A. S.; Ciesielski, A.; Gualandi, A.; Mengozzi, L.; Fiorani, A.; Iurlo, M.; Marcaccio, M.; Gutierrez, R.; Rapino, S.; Calvaresi, M.; Zerbetto, F.; Cuniberti, G.; Cozzi, P. G.; Paolucci, F.; Samori, P. Molecular Design Driving Tetraporphyrin Self-Assembly on Graphite: A Joint STM, Electrochemical and Computational Study. *Nanoscale* **2016**, *8*, 13678–13686.

125. Gao, A. M.; Miao, X. R.; Liu, J.; Zhao, P.; Huang, J. W.; Deng, W. L. Two-Dimensional Self-Assembly of a Porphyrin–Polypyridyl Ruthenium(II) Hybrid on HOPG Surface through Metal–Ligand Interactions. *ChemPhysChem* **2010**, *11*, 1951–1955.

126. Sakano, T.; Hasegawa, J.; Higashiguchi, K.; Matsuda, K. Chronological Change from Face-on to Edge-on Ordering of Zinc-Tetraphenylporphyrin at the Phenyloctane–Highly Oriented Pyrolytic Graphite Interface. *Chem. – Asian J.* **2012**, *7*, 394–399.

127. Zhou, Y. S.; Wang, B.; Zhu, M. Z.; Hou, J. G. Observation of Co-Existence of 'Face-on' and 'Edge-on' Stacking Styles in a Porphyrin Monolayer. *Chem. Phys. Lett.* **2005**, *403*, 140–145.

128. Mason, S. E.; Beton, P. H.; Besley, N. A. Airbed: A Simplified Density Functional Theory Model for Physisorption on Surfaces. *J. Chem. Theory Comput.* **2019**, *15*, 5628–5634.

CHAPTER 5

Computational Investigation of the Optimized Structures and Adsorption Energies of C_{60} within Monolayers of Ga(OEP)(R)

5.1. Introduction

The formation of self-assembled structures on planar surfaces is a complex process whose outcome reflects a balance of thermodynamic and kinetic factors.[1-4] As previous studies have shown, the free energy available for self-assembled processes is often a fraction of the magnitude of the component enthalpic driving forces and entropic penalties.[4-7] For this reason, subtle changes to molecular structures or experimental deposition conditions can have significant effect on whether a monolayer forms and, if it does, its lattice structure and properties . Several of these effects have been noted in earlier chapters, such as the solvent dependent formation of monolayers of $H_2TC_{10}P$ noted in Chapter 2 and the solvent-dependent structures observed for OEP complexes noted in Chapter 4; they have also been identified in other self-assembled systems.[8-11] Understanding and predicting, computationally, the subtle differences that can lead to changes in the propensity for molecules to form ordered monolayers or the resulting structures offers a significant opportunity to focus experimental efforts on the most promising systems without having to synthesize, purify, and investigate the surface chemistry of potential candidates. Furthermore, computationally derived structures and energies can help interpret experimental data and suggest the dominance of kinetics or thermodynamics in these systems. In this chapter, we describe computational studies of the structures and adsorption energies of C_{60} adsorbed within monolayers of Ga(OEP)(R) complexes (Figure 5.1).

The rise of dispersion-corrected DFT has made it possible to accurately calculate adsorption energies of systems dominated by non-covalent interactions; however, a tremendous

diversity of approaches within this method exist.[12] Localized DFT has often been used to model solution-based supramolecular assemblies involving isolated molecular hosts and C_{60},[13] whereas plane-wave DFT is generally used for self-assembled extended systems on planar surfaces.[14] The use of plane-wave DFT allows for interactions between adjacent molecules to be modeled implicitly using periodic boundary conditions[15] and avoids the necessity of corrections for basis-set-superposition errors required for localized DFT,[16] both of which reduce the computational cost. As we are interested in adlayers of C_{60} adsorbed within a monolayer of porphyrins, rather than the interaction of C_{60} with an isolated molecule, plane-wave DFT methods will be utilized.

Solvation is also an important consideration in these systems, where significant differences in the solvent-exposed area of the C_{60} and axial ligand are expected based on both the identity and the orientation of the axial ligands with respect to the fullerenes. While continuum solvation models have been adapted for plane-wave DFT,[17] organic solvents have not been parameterized and would require benchmarking against a large series of experimental results. Recently, however, it has been shown that the calculation of the optimized structure and gas-phase adsorption energy can be decoupled from the calculation of solvation energy, and plane-wave DFT and localized DFT, respectively, can be used in conjunction.[5-7] A wide variety of organic solvents have been parameterized using continuum models in localized DFT, and it has been shown that the free-energy of small molecules adsorbed within a porphyrin monolayer can be accurately predicted;[7] a similar approach will be used here.

While a mature and robust model would primarily focus on screening candidates for self-assembled systems *a priori*, developing a framework that accurately describes systems that have been experimentally characterized is a prerequisite for establishing the utility of the model. The Ga(OEP)(R)•C_{60} host–guest bilayers developed in our group are a good test case because the

nature of R determines whether C_{60} is incorporated.[18] Monolayers assembled from Ga(OEP)(R) complexes exhibit a pseudohexagonal structure that is independent of the axial ligand with dimensions of approximately 1.39 nm × 1.36 nm and an angle of 66° (Figure 5.1). The two diagonal dimensions of this cell are 1.53 nm and 2.30 nm, which are commensurate with the C_{60} van der Waals diameter of approximately 1.1 nm. The axial ligand, R, extends perpendicular to the plane of the Ga(OEP), forming a corral in which C_{60} can adsorb. We sought to calculate the structures and adsorption energy of C_{60} within porphyrin monolayers that both do and do not incorporate C_{60} in order to determine whether this type of model could accurately predict the relative adsorption energies and gain insight into designing future systems.

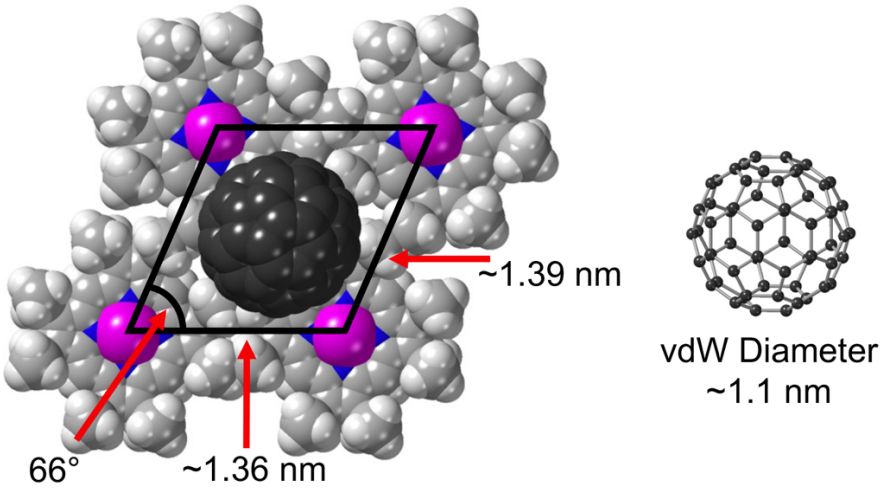

Figure 5.1. Molecular model of a Ga(OEP)(R) monolayer with adsorbed C_{60} (left) and molecular structure of C_{60} (right). The axial ligand is omitted for clarity.

Five Ga(OEP)(R) complexes (Figure 5.2) that have been investigated experimentally were studied. The axial ligands of the Ga(OEP)(R) complexes span heights ranging from ~8.1 Å (Ga(OEP)(CCPh)) to ~12.7 Å (Ga(OEP)(CC-2-Pyrene)) and varying affinities for C_{60}.[19-21] Monolayers of the both Ga(OEP)(CC-*n*-Pyrene) complexes have been observed to incorporate C_{60} and are expected to provide computational evidence for a significant affinity for C_{60}. The non-bilaterally symmetric (local C_s rather than C_{2v}) structure of the CC-1-pyrene axial ligand also

requires examination of a variety of axial ligand orientations around C_{60}. Ga(OEP)(CCPh) serves as an example of a monolayer that has not been observed to incorporate C_{60}. Ga(OEP)(CC-3-Thiophene) is investigated as thiophene is known to form complexes with C_{60},[22-24] along with the observation of adsorption of C_{60} within the monolayers under certain conditions. Ordered arrays of thiophene and C_{60} are also an intriguing technological target, given that thiophene is a common component with fullerenes in bulk heterojunction solar cells.[25] Finally, Ga(OEP)(CC-Tript) (Tript = 9-triptycene) was investigated as despite its known affinity for C_{60},[21,26] only sporadic incorporation of C_{60} into a monolayer of Ga(OEP)(CC-Tript) was observed. Given the qualitative structural similarity of the porphyrin complexes, the entropy of the self-assembled systems was not calculated; adsorption energies, rather than free energies, will be reported. The adsorption energy of C_{60} into a monolayer of Ga(OEP)(CCPh), which does not incorporate C_{60}, will be utilized as a benchmark for the approximate minimum driving force required to overcome these penalties. We report that the adsorption energies generally correlate with whether C_{60} is incorporated within the monolayers. Exploration of various binding sites reveals that highly ordered structures are lower in energy than structures that maximize the adsorption energy of individual C_{60} molecules. The structural factors that contribute to these results are discussed, along with how these observations can help to interpret experimental observations and suggest future lines of research.

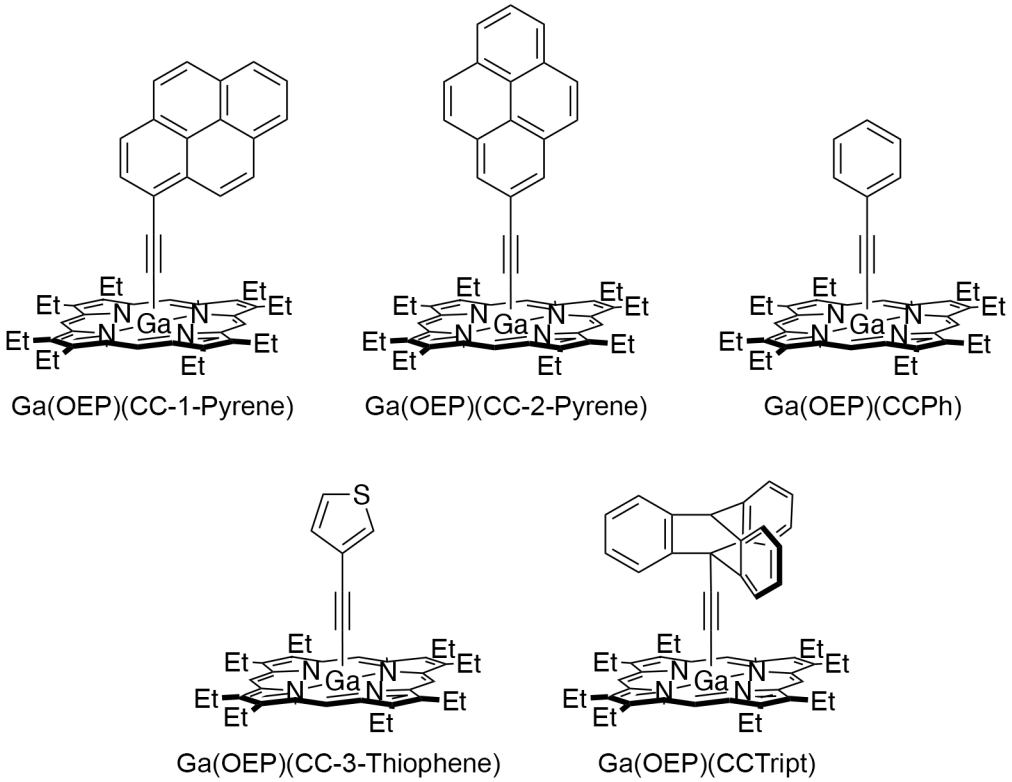

Figure 5.2. Ga(OEP)(R) complexes for which structures and adsorption energies of C_{60} will be calculated by means of DFT methods.

5.2. Experimental Section

The DFT methodology is very similar to that employed in Chapter 4. Calculations of Ga(OEP)(R) complexes with and without C_{60} were performed for gas-phase systems using plane-wave density functional theory (PW-DFT) within Quantum Espresso (version 6.1).[27] The generalized gradient approximation in the optB86b-vdW[28,29] formulation was used. This models the exchange and correlation interactions using the optB86[30] functional and the dispersion interactions with the vdw-DF[31-34] method. Optimized norm-conserving Vanderbilt (ONCV) pseudopotentials were used.[35,36] A wavefunction cutoff energy of 60 Ry was used and the wavefunctions were sampled at the Γ point. Gaussian smearing with a width of 0.001 Ry was included to ensure smooth convergence of the self-consistent field (SCF). Structures and adsorption energies were tested for convergence with respect to the wavefunction cutoff energy,

k-points, and smearing width. Geometry optimizations were performed with convergence thresholds on the total energy and total forces of 10^{-4} Ry and 10^{-3} Ry, respectively, for the ionic minimization and 10^{-8} Ry for the electronic energy during the SCF process. The *x* and *y* dimensions of the simulation cells were defined as the smallest integer multiple of the experimentally determined pseudohexagonal unit cell, 1.39 nm × 1.36 nm with an angle of 68°, that contained the appropriate periodicity. Generally, this was a 1 × 1 unit cell, however, for several systems a larger unit cell was utilized to model a structure where inequivalence of the axial ligands was necessary. For all systems a vacuum layer of at least 30 Å in the *c* direction was added to avoid interactions within the periodic system. The optimization of isolated C_{60} was carried out in a 30 Å × 30 Å × 30 Å cell to ensure isolation with respect to periodic images. Cell parameters for all systems are listed in Table 5.1. The influence of HOPG on the geometry of the Ga(OEP)(R) complex was accounted for by first calculating the optimized structure of the Ga(OEP)(R) in the presence of a 1L graphene sheet. The structure of the graphene-adsorbed Ga(OEP) subunit was frozen in its optimized geometry and the graphene was removed for all subsequent calculations. Justification for this approach is discussed in Section 6.4.1. The rotational orientation of C_{60} with respect to the axial ligands was not controlled in these calculations; the rotational dependence of the adsorption of C_{60} with a CC-1-Pyrene axial ligand is discussed in Section 6.4.2. Molecular models were built using CrystalMaker software.[37]

Table 5.1. Lattice Parameters of Simulation Cells and Number of Porphyrin Complexes for PW-DFT Calculations of Porphyrins and Porphyrin/Fullerene Assemblies.

System	*a* (Å)	*b* (Å)	*c* (Å)	*α* (°)	*β* (°)	*γ* (°)	N_{Por}[a]	N_{C60}[b]
Isolated C_{60}	30.00	30.00	30.00	90	90	90	*n/a*	1
Bridge and Center	13.60	13.90	45.00	90	90	68	1	1
Center Rotated	27.20	13.90	45.00	90	90	68	2	1
Maximum	27.20	27.80	45.00	90	90	68	4	1
Supercell	27.20	27.80	45.00	90	90	68	4	1 or 4

[a] Number of Ga(OEP)(R) complexes within the PW-DFT simulation cell. [b] Number of C_{60} within the PW-DFT simulation cell.

For each gas-phase calculation, the solvation energy was determined with a corresponding condensed-phase calculation in Gaussian16 using the B3P86 functional,[38,39] LANL2DZ effective core potential basis set[40,41] for Ga atoms, and the 6-31G* basis set for all other atoms. The optimized geometries obtained from the gas-phase PW-DFT calculations were used to construct supercells to explicitly model all interactions between C_{60} and the porphyrin dimer. Solvation energies were computed using the SMD module. The solvent parameters used for 1-phenyloctane are listed in Table 5.2. A similar approach has been used to calculate adsorption energies of M(OEP) on HOPG in toluene.[7] Both gas-phase and solvated-phase adsorption energies are reported; the solvated-phase adsorption energy will always be referenced unless explicitly noted otherwise.

Table 5.2. SMD Solvent Parameters for 1-Phenyloctane.

Parameter	value
ε	2.26[a]
n^2	2.205[a]
α	0.00[b]
β	0.15[b]
γ	43.47[c]
Φ	0.429
Ψ	0.00
r	2.20

[a] From Ref. 42. [b] From Ref. 43. [c] From Ref. 44.

5.3. Results and Discussion

5.3.1. Description of DFT Methodology. DFT calculations were performed to determine the optimized geometries and adsorption energies of C_{60} within monolayers of Ga(OEP)(R) complexes and investigate the effect of ligand identity and orientation. The calculations were performed using an identical methodology to those in Chapter 4. Briefly, the gas-phase adsorption energy was calculated to Equation 5.1:

$$E_{ads(g)} = E_{Ga(OEP)(R)\bullet C60(g)} - E_{Ga(OEP)(R)(g)} - E_{C60(g)} \quad (5.1)$$

Where $E_{ads(g)}$ is the gas-phase adsorption energy of C_{60} within the monolayer formed by the Ga(OEP)(R) complex and $E_{Ga(OEP)(R)\bullet C60(g)}$, $E_{Ga(OEP)(R)(g)}$, $E_{C60(g)}$ are the gas-phase total energies of C_{60} within the monolayer formed by the Ga(OEP)(R) complex, the monolayer of Ga(OEP)(R), and C_{60} as calculated in the PW-DFT framework. The influence of graphite on the optimized geometry of the Ga(OEP) subunit was modeled by first optimizing the Ga(OEP)(R) complex on a 1L sheet of graphene. The Ga(OEP) subunit was then frozen in all subsequent calculations. The contribution of graphite to the adsorption energy of C_{60} is not accounted for; this is justified in Section 6.4.1, as calculations of the adsorption energy of C_{60} within monolayers of select Ga(OEP)(R) monolayers adsorbed on 1L graphene demonstrate that inclusion of the surface adds only a small and nearly constant contribution to the adsorption energy.

Solvation effects were included using the SMD module in Gaussian 16 software package according to Equations 5.2 and 5.3:

$$E_{solv} = \Delta E^{G}_{Ga(OEP)(R)\bullet C_{60}(g\rightarrow s)} - \Delta E^{G}_{Ga(OEP)(R)(g\rightarrow s)} - \Delta E^{G}_{C_{60}(g\rightarrow s)} \quad (5.2)$$

$$\Delta E^{G}_{X(g\rightarrow s)} = E^{G}_{X(s)} - E^{G}_{X(g)} \quad (5.3)$$

Here, E_{solv} is the solvation energy associated with adsorption of C_{60} within the monolayer formed by Ga(OEP)(R), $\Delta E^{G}_{Ga(OEP)(R)\bullet C_{60}(g\rightarrow s)}$, $\Delta E^{G}_{Ga(OEP)(R)(g\rightarrow s)}$, and $\Delta E^{G}_{C_{60}(g\rightarrow s)}$ are the solvation

energies of C_{60} within the monolayer formed by Ga(OEP)(R), the monolayer of Ga(OEP)(R), and C_{60}, and $E^G_{X(s)}$ and $E^G_{X(g)}$ are the total energies from single-point calculations in the solvated and gas phases at the PW-DFT optimized gas-phase geometry, respectively, using the Gaussian 16 software package. The solvated-phase adsorption energy was then determined according to Equation 5.4:

$$E_{ads(solv)} = E_{ads(g)} + E_{solv} \tag{5.4}$$

Here, $E_{ads(s)}$ is the solvated-phase adsorption energy. This approach is depicted as a thermodynamic cycle of selected quantities in Equations 5.1 – 5.4 in Figure 5.3. A similar approach for including solvation effects has recently been used to model porphyrin monolayers.[7]

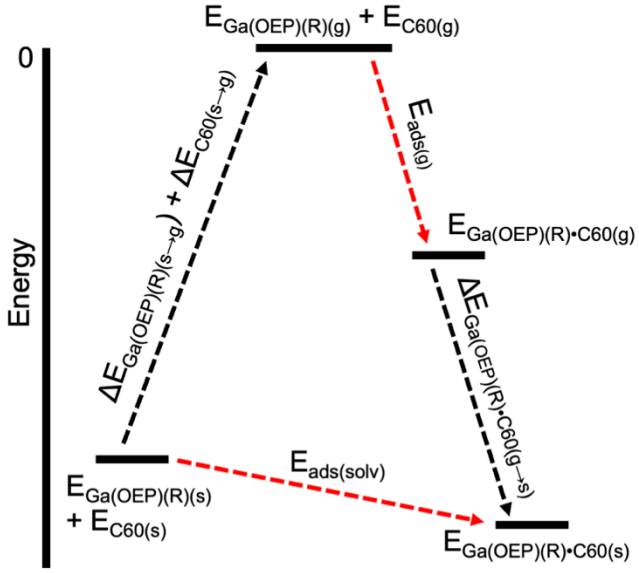

Figure 5.3. Depiction of thermodynamic cycle for calculating $E_{ads(solv)}$. The gas-phase ($E_{ads(g)}$) and solvated-phase ($E_{ads(solv)}$) adsorption energy are denoted with red arrows.

5.3.2. Optimized Geometries and Adsorption Energy of C_{60} within Ga(OEP)(CC-1-Pyrene) Monolayers. The optimized geometry and adsorption energy of C_{60} within monolayers of Ga(OEP)(CC-1-Pyrene) was determined for various hypothetical lattice sites and pyrene orientations as depicted in Figure 5.4. In the bridge site (Figure 5.4b), C_{60} is located along the short

unit-cell axis between two Ga(OEP) subunits; it is assumed that these present identical 1-pyrene orientations. In the center binding site the C_{60} resides site at the center of the Ga(OEP)(R) unit cell (Figure 5.4 c,d,e). Different pyrene orientations are possible due to the fact that it is not bilaterally symmetric, as defined above. The pyrene orientations can be identical (Figure 5.4c) or rotated 180° from one another in adjacent rows (designated as center rotated, Figure 5.4d). These structures are all tileable and not expected to substantially alter the adsorption energy of C_{60} at adjacent binding sites. An additional structure displays all 1-pyrene ligands oriented for maximum contact with the C_{60} (Figure 5.4e). While this structure would be expected to possess the strongest binding for C_{60}, it is not tileable and the adsorption energy at adjacent binding sites would likely be reduced (*vide infra*).

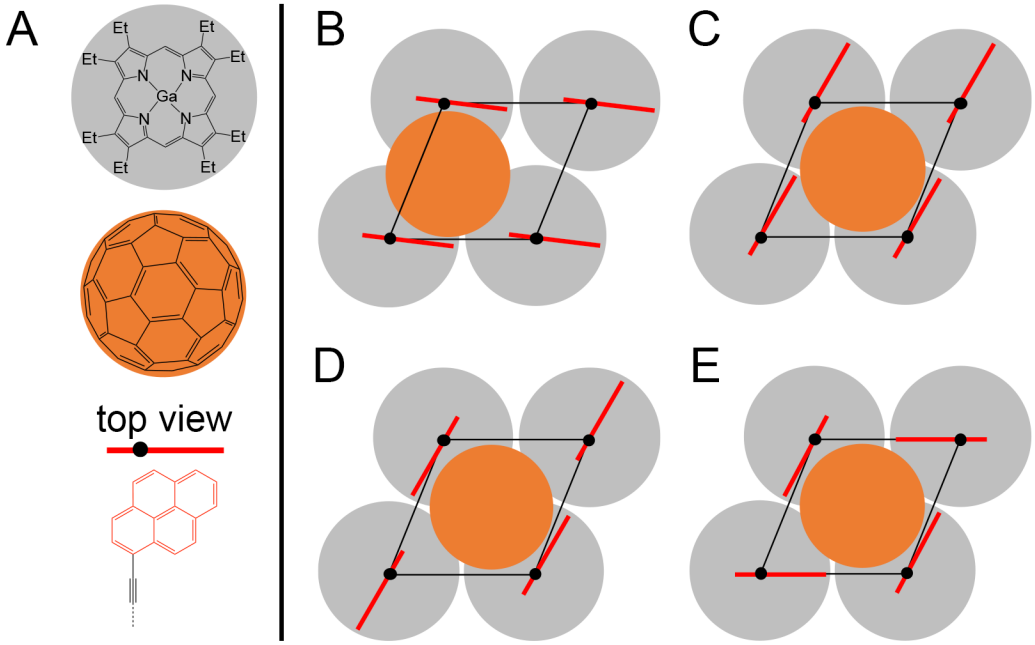

Figure 5.4. Depiction of (a) components and (b, c, d, e) possible binding sites for C_{60} with varying orientations of the axial ligand in Ga(OEP)(CC-1-Pyrene): (b) bridge binding site, (c) center binding site, (d) center binding site with alternating pyrene rotations, (e) center binding site with maximum pyrene–C_{60} contact.

The optimized structures and adsorption energies ($E_{ads(solv)}$) of the three tileable orientations are shown in Figure 5.5 and Table 5.2, respectively. The bridge binding site (Figure 5.5a) exhibits a structure that possesses two face-on 1-pyrene:C_{60} interactions, with the adsorption energy calculated to be –1.41 eV. The center binding site (Figure 5.5b) exhibits a smaller adsorption energy (–1.32 eV), which can be understood given that only one face-on 1-pyrene:C_{60} interaction is present, due to the non-bilaterally symmetric nature of 1-pyrene, with the other 1-pyrene:C_{60} interactions being edge-on. Deconvolution of the contributions from the axial ligands and the upturned ethyl chains of the Ga(OEP) subunit (Section 6.4.3) indicates that the differences in adsorption energy are a function of the axial ligands and not of differences in the CH_3:C_{60} interactions. The adsorption energy of the center rotated binding site (–1.39 eV) is roughly the same as for the bridge site; it similarly contains two face-on 1-pyrene:C_{60} interactions (Figure 5.5c), however, the adsorption energy in the gas-phase is likely overestimated, as the independent optimization of the axial ligands required to model this system allow both 1-pyrene ligands to tilt about 7° towards the C_{60}. The influence of independent optimization of axial ligands on the adsorption energy is discussed in Section 6.4.4, and we suggest that the bridge binding site is the lowest energy binding site of the tileable structures. The adsorption energy at the maximum contact binding site (Figure 5.6) is, as expected, more negative (by –0.27 eV) than the bridge binding site. In addition to the two face-on 1-pyrene:C_{60} interactions, two edge-on 1-pyrene:C_{60} interactions are also present at this orientation. While this initially suggests that the maximum binding site would be the most stable and observed experimentally, the parameter that governs a self-assembled system in thermodynamic equilibrium is not adsorption energy per C_{60}, but adsorption energy per unit area.[5] Therefore, direct comparison of the adsorption energy of the bridge binding site and the maximum binding site cannot be made without looking at an expanded view.

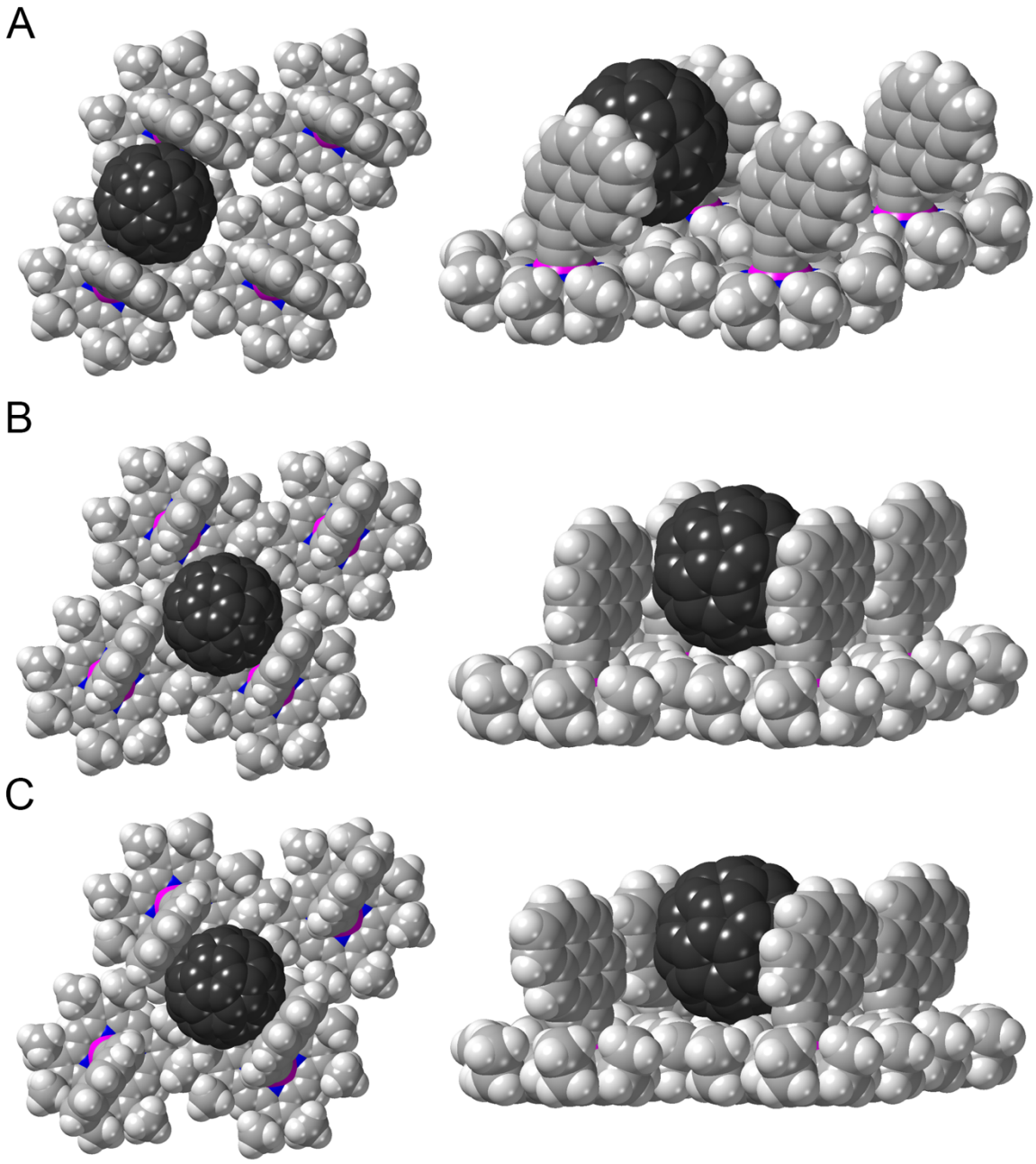

Figure 5.5. Space-filling models of Ga(OEP)(CC-1-Pyrene) with C_{60} from above (left) and side (right) views at the (a) Bridge, (b) Center and (c) Center Rotated binding sites.

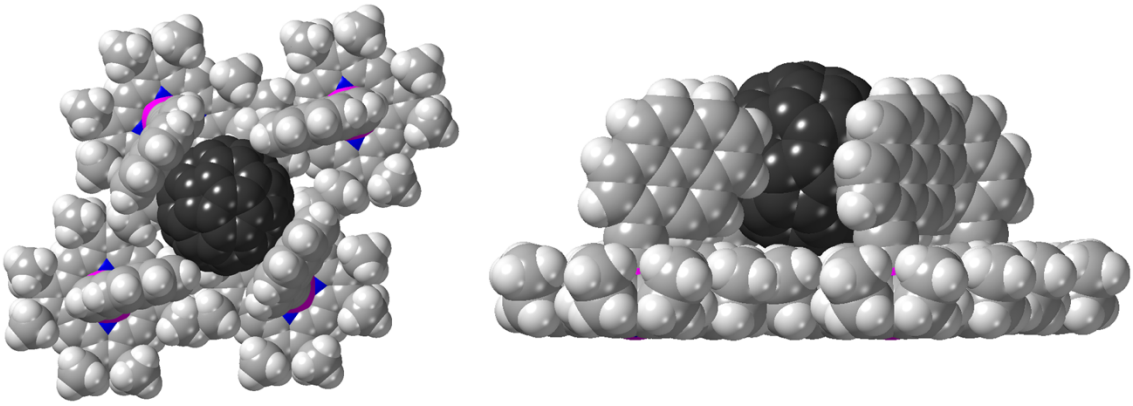

Figure 5.6. Space-filling models of Ga(OEP)(CC-1-Pyrene) with C_{60} from above (left) and side (right) views at the center binding site with CC-1-Pyrene units rotated for maximum contact with C_{60}.

Table 5.3. Adsorption Energy and Geometric Parameters of C_{60} within a Monolayer of Ga(OEP)(CC-1-Pyrene) at Various Binding Sites and Orientations.

Parameter	Bridge	Center	Center Rotated[c]	Maximum[c]
$E_{ads(gas)}$ (eV)	–1.77	–1.60	–1.79	–2.20
E_{solv} (eV)	0.36	0.28	0.40	0.52
$E_{ads(solv)}$ (eV)	–1.41	–1.32	–1.39	–1.68
Primary 1-Pyrene – C_{60} Distance (Å)[a]	3.34	3.64	2.89	2.97
Secondary 1-Pyrene – C_{60} Distance (Å)[a]	3.53	3.00[b]	3.02	3.12

[a] Calculated as the distance from the centroid of the ligand to the centroid of C_{60} minus the radius of C_{60} (0.35 Å). *n.b.* As the distance is not measured directly from nuclei to nuclei, values less than the sum of vdW radii are possible. The identity of the ligand designated as primary is the nearest ligand oriented face-on towards C_{60}. [b] Ligand is oriented edge-on towards C_{60}, distance is the shortest nuclei – nuclei distance, $H_{Ligand} – C_{C60}$. [c] Ligands are independently optimized.

A more complete comparison can be made by including the effect of the orientation of the 1-pyrene ligands at the maximum binding site on the adjacent binding sites. The repeating unit as a consequence of this orientation is a 2 × 2 cell with four possible C_{60} binding sites (Figure 5.7). The 1-pyrene orientations for the maximum binding site (site A) lead to binding sites containing four edge-on contacts (site B), two face-on contacts and no edge-on contacts (site C), and two edge-on contacts (site D). The optimized structure containing C_{60} at all four binding sites is shown in Figure 5.8. Notable is the implied instability of C_{60} at site D, given that the C_{60} relaxes to a position exhibiting close contact with the C_{60} at site B and a face-on 1-pyrene ligand (in the absence

of explicit solvent molecules in the calculation). The gas-phase adsorption energy of C_{60} at each of these sites was determined by removing the other three C_{60} molecules and calculating the energy of the system without re-optimization. The calculated energies (Table 5.4) demonstrate that while the ligand orientation leads to a greater gas-phase adsorption energy at site A, –2.20 eV, site C is similar to the center binding site, –1.60 eV, while site B and site D, each –1.37 eV, are destabilized with respect to all the tileable binding sites. The total gas-phase adsorption energy of C_{60} for the repeating unit is determined to –6.99 eV, which is greater than the sum of the deconvoluted sites due to C_{60} – C_{60} interactions. A direct comparison can now be made with the bridge binding site, where the adsorption energy for a 2 × 2 unit is –7.08 eV, assuming negligible C_{60} – C_{60} interactions, indicating that the thermodynamic minimum for the self-assembled system is the bridge binding site.

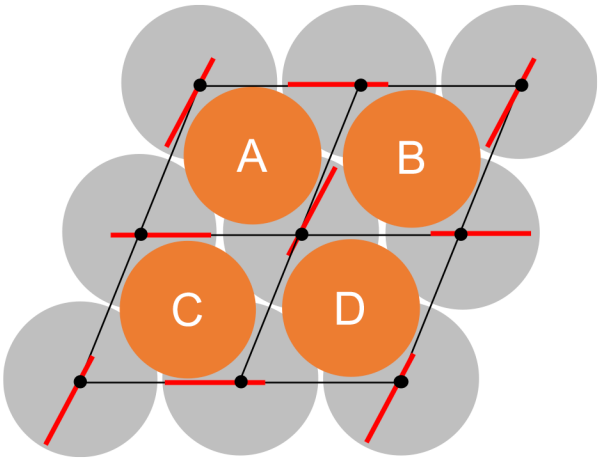

Figure 5.7. Depiction of axial ligand orientations in a 2 × 2 supercell of Ga(OEP)(CC-1-Pyrene) propagating those found surrounding C_{60} at binding site A.

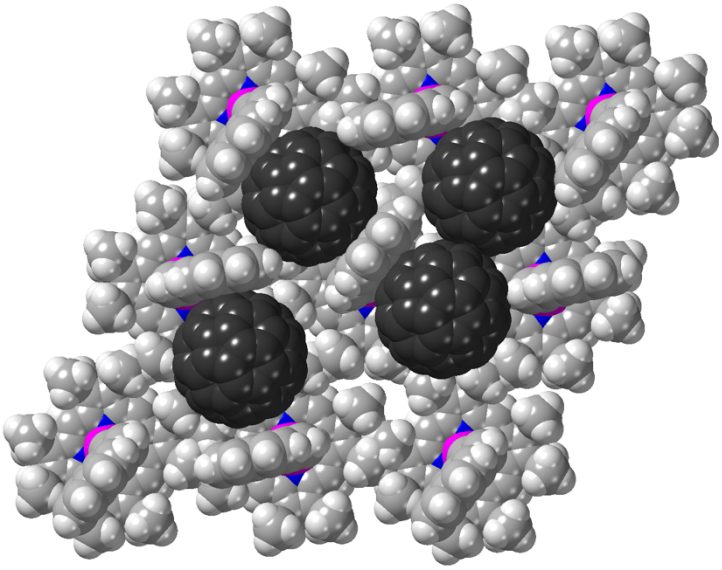

Figure 5.8. Space-filling models of the calculated structure of Ga(OEP)(CC-1-Pyrene) supercell with four C_{60} at the adsorption sites depicted in Figure 5.7.

Table 5.4. Adsorption Energy of C_{60} within a Monolayer of Ga(OEP)(CC-1-Pyrene) at Various Binding Sites.

Binding Site	$E_{ads(gas)}$ (eV)
Site A[a]	–2.20
Site B[b]	–1.37
Site C[b]	–1.60
Site D[b]	–1.37
All Sites[c]	–6.99

[a] From Table 5.3. [b] Determined in absence of C_{60} at other binding sites. [c] Calculated with all binding sites occupied.

Applying the information determined from these calculations to the experimental results suggests that the close-packed C_{60} features observed by STM for sequentially deposited Ga(OEP)(CC-1-Pyrene) and C_{60} have a small energetic preference (ca 0.1 eV) for adsorption at the bridge site. In addition to the close-packed structures, persistent isolated or clustered C_{60} features have been observed in these systems. While the thermodynamic minimum of the system may be with C_{60} adsorbed at the bridge site, many self-assembled systems form kinetically trapped structures.[45-47] We hypothesize that these features may be C_{60} kinetically trapped in a structure

resembling the maximum contact binding site in whole or in part for the isolated or clustered features, respectively, disfavoring adsorption at adjacent binding sites.

5.3.3. Optimized Geometries and Adsorption Energy of C_{60} within Ga(OEP)(CC-2-Pyrene) and Ga(OEP)(CCPh) Monolayers. Optimized structures and adsorption energies of C_{60} within monolayers of the complexes Ga(OEP)(CC-2-Pyrene) and Ga(OEP)(CCPh), which unlike Ga(OEP)(CC-1-Pyrene) have bilaterally symmetric axial ligands (local C_{2v} vs. C_s for CC-1-pyrene) were investigated at the bridge and center binding sites (Figure 5.9). The center rotated site does not exist for these compounds due to the symmetry of these axial ligands. Given that structures analogous to the maximum binding site of Ga(OEP)(CC-1-Pyrene) would require a significantly greater tilt of the axial ligands towards C_{60} than in Ga(OEP)(CC-1-Pyrene), exacerbating the destabilization of adjacent binding sites, the structure and adsorption energy at an analogous maximum binding site was not investigated.

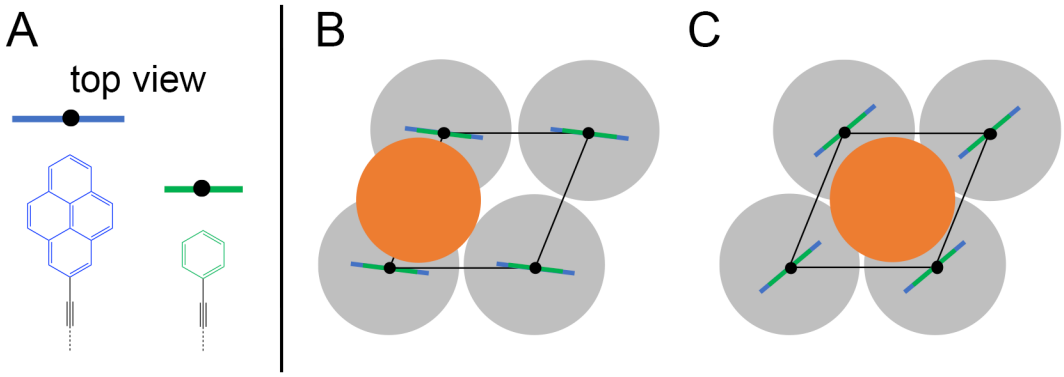

Figure 5.9. Depiction of (a) components and axial ligand orientations for Ga(OEP)(CC-2-Pyrene) and Ga(OEP)(CCPh) systems at the (b) bridge binding site and (c) center binding site.

The optimized structure of C_{60} at the bridge site of the Ga(OEP)(CC-2-Pyrene) monolayer (Figure 5.10a) exhibits two face-on 2-pyrene:C_{60} interactions; the adsorption energy (–1.36 eV; Table 5.5) is similar to that of Ga(OEP)(CC-1-Pyrene) (–1.41 eV) at this site. Deconvoluting the contributions of the CC-Pyrene ligands and the upturned ethyl groups (Section 6.4.3) suggests that

the interaction between the ethyl groups and C_{60} in Ga(OEP)(CC-2-Pyrene) is weaker than for Ga(OEP)(CC-1-Pyrene). This may arise because the centroid of the CC-1-Pyrene ligand lies roughly 1 Å closer to the porphyrin plane than the centroid of CC-2-Pyrene, allowing for better contact with the ethyl groups. The optimized structure of C_{60} at the center site of the Ga(OEP)(CC-2-Pyrene) (Figure 5.10b) shows two face-on 2-pyrene:C_{60} interactions, though the pyrene ligands remain further from the C_{60} than in Ga(OEP)(CC-1-Pyrene) system. As a result, the difference in adsorption energy at the center site compared to the bridge site in Ga(OEP)(CC-2-Pyrene) systems (0.19 eV) is roughly double that of Ga(OEP)(CC-1-Pyrene) (0.09 eV).

The optimized structure of C_{60} at the bridge site of the Ga(OEP)(CCPh) monolayer (Figure 5.11a) exhibits a significant tilt (10°) of the phenyl groups with respect to the plane of the porphyrin. This tilt is distinct from that observed for Ga(OEP)(CC-1-Pyrene), where both pyrene ligands tilted towards the C_{60}. Here, as the phenyl ligands are forced to adopt identical geometries, one phenyl ligand tilts towards the C_{60} and the other tilts away. This allows for a face-on interaction of the phenyl that leans away from C_{60} with the fullerene, as the significantly shorter height of the phenyl ligand leads to an offset of the heights of phenyl centroid and the C_{60} centroid of 1.5 Å that would result in a primarily edge-on contact if the phenyl ligand remained perpendicular to the plane of the porphyrin. The adsorption energy of C_{60} at the bridge site of Ga(OEP)(CCPh) (Table 5.5) indicates that the bridge site is 0.44 eV less stable than Ga(OEP)(CC-2-Pyrene). A calculation where the phenyl ligand is forced to remain orthogonal to the plane of the porphyrin exhibited a gas-phase adsorption energy reduced by 0.1 eV. The center binding of Ga(OEP)(CCPh) systems (Figure 5.11b) again exhibits a reduced adsorption energy compared to the bridge site, similar to Ga(OEP)(CC-*n*-Pyrene) systems. The phenyl ligand does not tilt at the center site, as it did at the bridge site; the justification for why the optimized structure does not contain this tilt is not currently

understood, though as it is not the minimum energy geometry it was not investigated further. As incorporation of C_{60} into Ga(OEP)(CCPh) has not been observed experimentally, this system suggests a lower bound on the adsorption energy required to incorporate C_{60} into Ga(OEP)(R) monolayers of ca. 0.9 eV, which could be used as a screening method for other axial ligands.

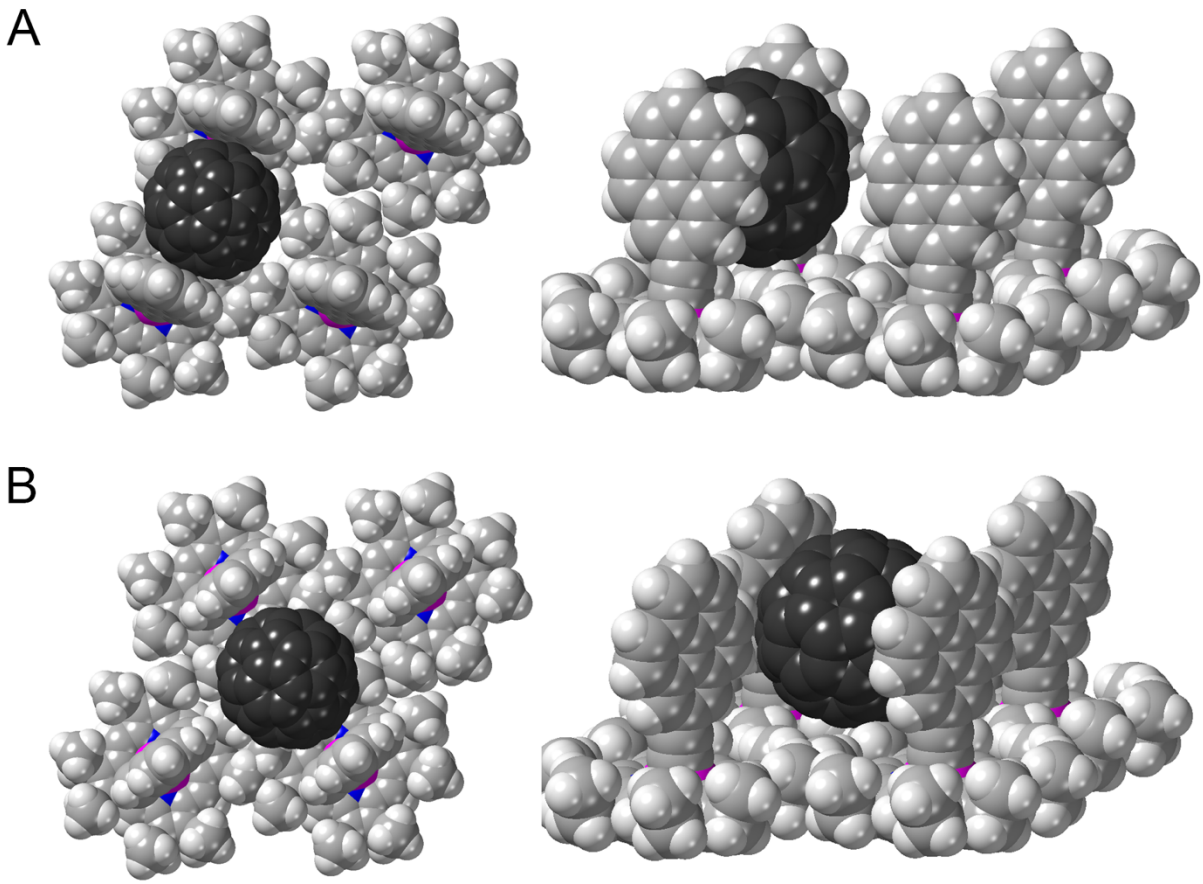

Figure 5.10. Space-filling models of Ga(OEP)(CC-2-Pyrene) with C_{60} from above (left) and side (right) views at the (a) Bridge, (b) Center binding sites.

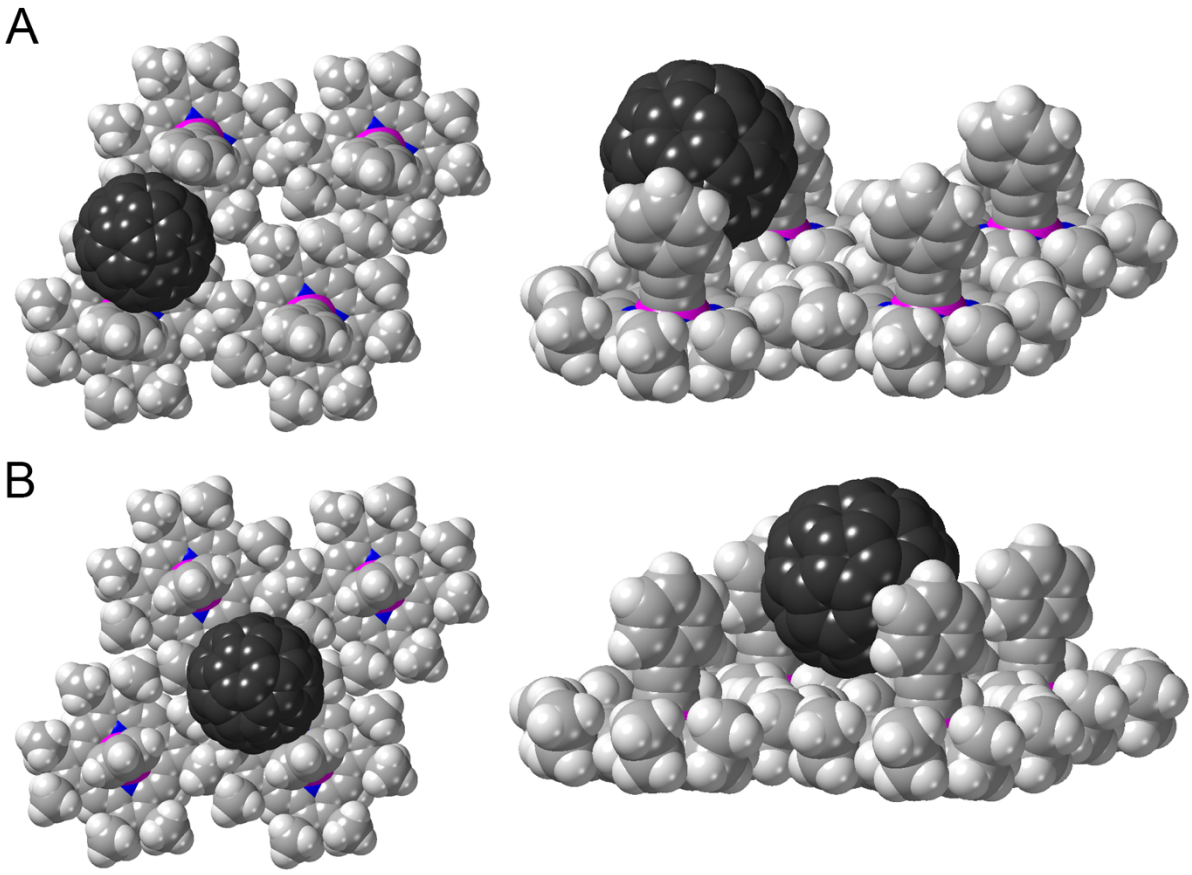

Figure 5.11. Space-filling models of Ga(OEP)(CCPh) with C_{60} from above (left) and side (right) views at the (a) Bridge, (b) Center binding sites.

Table 5.5. Adsorption Energy and Geometric Parameters of C_{60} within Monolayers of Ga(OEP)(CC-2-Pyrene) and Ga(OEP)(CCPh) at the Bridge and Center Binding Sites.

	Ga(OEP)(CC-2-Pyrene)		Ga(OEP)(CCPh)	
Parameter	Bridge	Center	Bridge	Center
$E_{ads(gas)}$ (eV)	–1.64	–1.27	–1.15	–0.95
E_{solv} (eV)	0.28	0.10	0.23	0.12
$E_{ads(solv)}$ (eV)	–1.36	–1.17	–0.92	–0.83
Primary Ligand – C_{60} Distance (Å)[a]	3.46	3.94	3.20	3.46
Secondary Ligand – C_{60} Distance (Å)[a]	3.52	4.21	3.44[b]	5.27

[a] Calculated as the distance from the centroid of the ligand to the centroid of C_{60} minus the radius of C_{60} (0.35 Å). *n.b.* As the distance is not measured directly from nuclei to nuclei values below the sum of the vdW radii are possible. The identity of the ligand designated as primary is the nearest ligand oriented face-on towards C_{60}. [b] Ligand is oriented edge-on towards C_{60}, distance is the shortest nuclei – nuclei distance, $C_{Ligand} - C_{C60}$.

5.3.4. Optimized Geometries and Adsorption Energy of C_{60} within Ga(OEP)(CC-3-Thiophene) and Ga(OEP)(CCTript) Monolayers. The optimized structure of C_{60} adsorbed at the bridge and center sites of a Ga(OEP)(CC-3-Thiophene) monolayer is shown in Figures 5.12a and b, respectively. The adsorption energy (Table 5.6) of C_{60} with Ga(OEP)(CC-3-Thiophene) at the bridge site is slightly more stable (–0.97 eV) than for Ga(OEP)(CCPh) (–0.92 eV). While the center site is less stable for Ga(OEP)(CC-3-Thiophene) than the bridge site, as has been determined for all systems, it is slightly less stable (–0.77 eV) than Ga(OEP)(CCPh) (–0.83 eV). The thiophene ligand does not adopt the tilted conformation exhibited by the phenyl ligand at the bridge site, which may be a result of optimizing the C_{60} – sulfur interaction. That the bridge binding site exhibits a slightly greater adsorption energy for C_{60} with Ga(OEP)(CC-3-Thiophene) than Ga(OEP)(CCPh) is qualitatively consistent with experimental results. In these experiments, the ratio of filled sites to unfilled sites in the Ga(OEP)(CC-3-Thiophene) systems was lower than Ga(OEP)(CC-Pyrene) systems, consistent with the significantly reduced adsorption energy going from Ga(OEP)(CC-Pyrene) to Ga(OEP)(CC-3-Thiophene) systems. We note that at high concentrations of C_{60} relative to Ga(OEP)(CC-3-Thiophene), a structure consistent with a multilayer of Ga(OEP)(CC-3-Thiophene) with C_{60} encapsulated between two Ga(OEP)(CC-3-Thiophene) molecules was observed. Unfortunately, the computational resources required to model such a multilayer are beyond our capabilities.

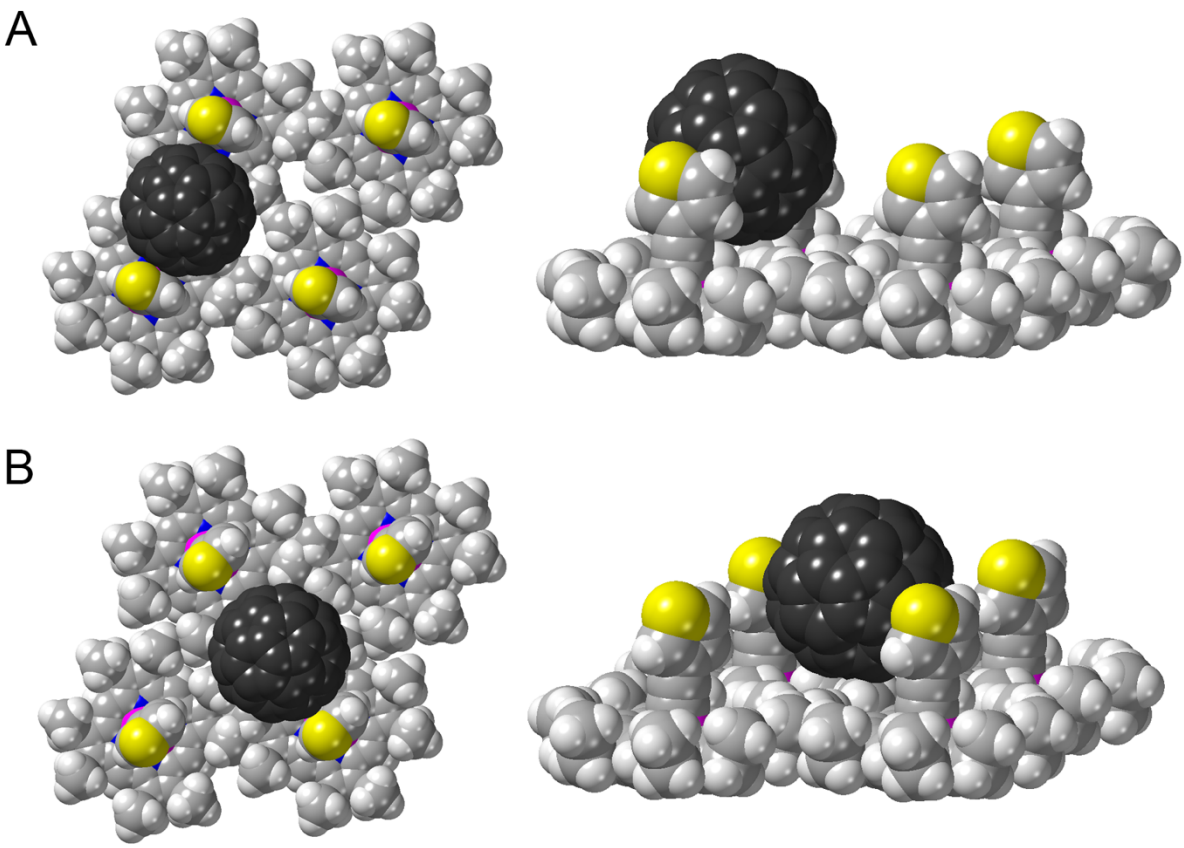

Figure 5.12. Space-filling models of Ga(OEP)(CC-3-Thiophene) with C_{60} from above (left) and side (right) views at the (a) Bridge, (b) Center binding sites.

Table 5.6. Adsorption Energy and Geometric Parameters of C_{60} within a Monolayer of Ga(OEP)(CC-3-Thiophene) at the Bridge and Center Binding Sites.

Parameter	Bridge	Center
$E_{ads(gas)}$ (eV)	–1.16	–0.89
E_{solv} (eV)	0.19	0.12
$E_{ads(solv)}$ (eV)	–0.97	–0.77
Primary Ligand – C_{60} Distance (Å)[a]	3.50	3.47
Secondary Ligand – C_{60} Distance (Å)[a]	3.50	5.16

[a] Calculated as the distance from the centroid of the ligand to the centroid of C_{60} minus the radius of C_{60} (0.35 Å). *n.b.* As the distance is not measured directly from nuclei to nuclei values below the sum of the vdW radii are possible. The identity of the ligand designated as primary is the nearest ligand oriented face-on towards C_{60}.

Ga(OEP)(CCTript) presents a distinct structure, as opposed to the planar axial ligands previously investigated. The 120° angle between the adjacent 6-membered rings results in a cleft well-suited for binding C_{60}. The optimized structure (Figure 5.13) demonstrates this, where C_{60}

has multiple face-on interactions with two triptycene ligands at the bridge site and an additional edge-on interaction with a third triptycene. The adsorption energy for C_{60} within the Ga(OEP)(CCTript) monolayer (Table 5.7) is nearly equal to the adsorption energy of the maximum binding site of the Ga(OEP)(CC-1-Pyrene) system, despite retaining a tileable structure. Interestingly, experimental investigation of this system has revealed only sporadic incorporation of C_{60} into the Ga(OEP)(CCTript) monolayer. Given the calculated results, we hypothesize that the triptycene ligands may adopt an orientation that blocks the C_{60} binding site upon formation of the Ga(OEP)(CCTript) monolayer. The ligands may be kinetically trapped in this orientation, which would prevent widespread adsorption of C_{60} upon sequential addition. This suggests that further investigation of this system is warranted using either a pre-mixed deposition method, to avoid preformation of the potentially sterically blocked binding sites, or deposition at elevated temperatures, in order to overcome the activation barrier for rearrangement of the triptycene ligands.

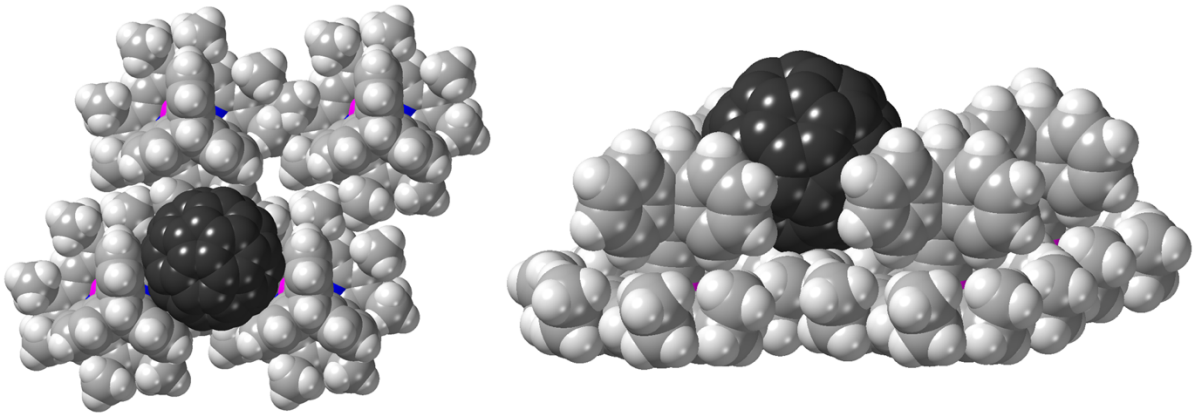

Figure 5.13. Space-filling models of Ga(OEP)(CC-3-Triptycene) with C_{60} from above (left) and side (right) views at the (a) Bridge, (b) Center binding sites.

Table 5.7. Adsorption Energy of C_{60} within a Monolayer of Ga(OEP)(CCTript) at the Bridge Binding Sites.

parameter	Bridge
$E_{ads(gas)}$ (eV)	–2.00
E_{solv} (eV)	0.37
$E_{ads(solv)}$ (eV)	–1.63

5.4. Conclusions

A method for computationally determining the adsorption energies of C_{60} within a variety of Ga(OEP)(R) monolayers has been investigated incorporating both dispersion interactions and solvation effects. Monolayers of Ga(OEP)(CC-1-Pyrene) and Ga(OEP)(CC-2-Pyrene) were both determined to have a significant affinity for C_{60}, in agreement with experimental results. The non-bilaterally symmetric structure of 1-pyrene required investigation of a variety of rotational conformers, demonstrating that a highly ordered structure with C_{60} adsorbed at the bridge site is slightly preferrable to one that maximizes the adsorption energy of a single C_{60} at the expense of adjacent binding sites. However, the large local adsorption energy may contribute to kinetically trapped states that reduce the fraction of C_{60} occupied binding sites. C_{60} was determined to be substantially less stable within a Ga(OEP)(CCPh) monolayer as compared to the pyrenyl systems, in accordance with the lack of experimentally observed adlayer formation. Significantly, the adsorption energy of C_{60} within the Ga(OEP)(CCPh) monolayer suggests a minimum threshold that could be used to screen potential axial ligands.

In the case of Ga(OEP)(CC-3-Thiophene), a slightly more favorable adsorption energy for C_{60} was found than for Ga(OEP)(CCPh), though it was significantly less stable than either of the Ga(OEP)(CC-Pyrene) systems, in agreement with experimental results. Ga(OEP)(CCTript) monolayers were found to have a substantial affinity for C_{60}, rivaling that of the maximized

conformer of Ga(OEP)(CC-1-Pyrene); the lack of widespread incorporation observed experimentally provides an impetus to reexamine this promising system.

These calculations have provided significant insight into the on-surface structures and adsorption energies of C_{60} within the Ga(OEP)(R) structures studied here and could be used to screen other similar systems; however, the utility of these calculations relies on the relative similarities of the axial ligands. Future attention should be turned towards incorporating entropic effects into these calculations so that free energies can be determined. This would provide a physically meaningful measure of stability, rather than relying on the comparison of relative adsorption energies, thus expanding the applicability of this method to a wide variety of hosts, guests, and structures.

5.5. References

1. Mali, K. S.; De Feyter, S. Principles of Molecular Assemblies Leading to Molecular Nanostructures. *Philos. Trans. R. Soc., A* **2013**, *371*, 20120304.

2. Mali, K. S.; Pearce, N.; De Feyter, S.; Champness, N. R. Frontiers of Supramolecular Chemistry at Solid Surfaces. *Chem. Soc. Rev.* **2017**, *46*, 2520–2542.

3. Mazur, U.; Hipps, K. W. Kinetic and Thermodynamic Processes of Organic Species at the Solution-Solid Interface: The View through an STM. *Chem. Commun.* **2015**, *51*, 4737–4749.

4. Reimers, J. R. How Equilibrium Gets Mimicked During Kinetic and Thermodynamic Control in Porphyrin and Phthalocyanine Self-Assembled Monolayers. *Langmuir* **2018**, *34*, 18–22.

5. Reimers, J. R.; Panduwinata, D.; Visser, J.; Chin, Y.; Tang, C. G.; Goerigk, L.; Ford, M. J.; Sintic, M.; Sum, T. J.; Coenen, M. J. J.; Hendriksen, B. L. M.; Elemans, J. A. A. W.; Hush, N. S.; Crossley, M. J. A Priori Calculations of the Free Energy of Formation from Solution of Polymorphic Self-Assembled Monolayers. *Proc. Natl. Acad. Sci. U.S.A.* **2015**, *112*, E6101–E6110.

6. Gurdumov, K.; Mazur, U.; Hipps, K. W. Influences on the Dynamics and Stability of Self-Assembly: Solvent, Substrate, and Concentration. *J. Phys. Chem. C* **2022**, *126*, 19904–19915.

7. Gurdumov, K.; Mazur, U.; Hipps, K. W. Self-Assembly Dynamics and Stability through Concentration Control at the Solution/HOPG Interface. *J. Phys. Chem. C* **2022**, *126*, 12916–12927.

8. Mali, K. S.; Schwab, M. G.; Feng, X. L.; Mullen, K.; De Feyter, S. Structural Polymorphism in Self-Assembled Networks of a Triphenylene Based Macrocycle. *Phys. Chem. Chem. Phys.* **2013**, *15*, 12495–12503.

9. Steeno, R.; Minoia, A.; Gimenez-Lopez, M. C.; Blunt, M. O.; Champness, N. R.; Lazzaroni, R.; Mali, K. S.; De Feyter, S. Molecular Dopant Determines the Structure of a Physisorbed Self-Assembled Molecular Network. *Chem. Commun.* **2021**, *57*, 1454–1457.

10. El Garah, M.; Bonilla, A. S.; Ciesielski, A.; Gualandi, A.; Mengozzi, L.; Fiorani, A.; Iurlo, M.; Marcaccio, M.; Gutierrez, R.; Rapino, S.; Calvaresi, M.; Zerbetto, F.; Cuniberti, G.; Cozzi, P. G.; Paolucci, F.; Samori, P. Molecular Design Driving Tetraporphyrin Self-Assembly on Graphite: A Joint STM, Electrochemical and Computational Study. *Nanoscale* **2016**, *8*, 13678–13686.

11. Iritani, K.; Takeda, H.; Kather, M.; Yokoi, M.; Moeglen, M.; Ikeda, M.; Otsubo, Y.; Ozawa, Y.; Tahara, K.; Hirose, K.; De Feyter, S.; Tobe, Y. Electrostatically Driven Guest Binding in Self-Assembled Molecular Network of Hexagonal Pyridine Macrocycle at the Liquid/Solid Interface: Symmetry Breaking Induced by Coadsorbed Solvent Molecules. *Langmuir* **2019**, *35*, 15051–15062.

12. Grimme, S.; Hansen, A.; Brandenburg, J. G.; Bannwarth, C. Dispersion-Corrected Mean-Field Electronic Structure Methods. *Chem. Rev.* **2016**, *116*, 5105–5154.

13. Grimme, S. Supramolecular Binding Thermodynamics by Dispersion-Corrected Density Functional Theory. *Chem. – Eur. J.* **2012**, *18*, 9955–9964.

14. Chilukuri, B.; Mazur, U.; Hipps, K. W. Structure, Properties, and Reactivity of Porphyrins on Surfaces and Nanostructures with Periodic DFT Calculations. *Appl. Sci.* **2020**, *10*, 740.

15. Kratzer, P.; Neugebauer, J. The Basics of Electronic Structure Theory for Periodic Systems. *Front. Chem.* **2019**, *7*, 1 – 18.

16. Kestner, N. R.; Combariza, J. E. Basis Set Superposition Errors: Theory and Practice. *Rev. Comput. Chem.* **1999**, *13*, 99– 32.

17. Andreussi, O.; Dabo, I.; Marzari, N. Revised Self-Consistent Continuum Solvation in Electronic-Structure Calculations. *J. Chem. Phys.* **2012**, *136*, 064102.

18. Kamm, J. M. Ph. D. Thesis. The University of Chicago, Chicago, IL, 2017.

19. Bhattacharya, S.; Nayak, S. K.; Chattopadhyay, S.; Banerjee, M.; Mukherjee, A. K. Study of Molecular Complex Formation between [60]Fullerene and Two Series of Donors by the NMR Method. *J. Phys. Chem. A* **2001**, *105*, 9865–9868.

20. Datta, K.; Banerjee, M.; Seal, B. K.; Mukherjee, A. K. Ground State Eda Complex Formation between [60]Fullerene and a Series of Polynuclear Aromatic Hydrocarbons. *J. Chem. Soc., Perkin Trans. 2* **2000**, 531–534.

21. Hu, S. Z.; Chen, C. F. Triptycene-Derived Oxacalixarene with Expanded Cavity: Synthesis, Structure and Its Complexation with Fullerenes C-60 and C-70. *Chem. Commun.* **2010**, *46*, 4199–4201.

22. Barendt, T. A.; Ball, M. L.; Xu, Q. Z.; Zhang, B. Y.; Fowler, B.; Schattman, A.; Ritter, V. C.; Steigerwald, M. L.; Nuckolls, C. Supramolecular Assemblies for Electronic Materials. *Chem. – Eur. J.* **2020**, *26*, 3744–3748.

23. Shimizu, H.; Park, K. H.; Otani, H.; Aoyagi, S.; Nishinaga, T.; Aso, Y.; Kim, D.; Iyoda, M. A Saturn-Like Complex Composed of Macrocyclic Oligothiophene and C-60 Fullerene: Structure, Stability, and Photophysical Properties in Solution and the Solid State. *Chem. – Eur. J.* **2018**, *24*, 3793–3801.

24. Shimizu, H.; Gonzalez, J. D. C.; Hasegawa, M.; Nishinaga, T.; Haque, T.; Takase, M.; Otani, H.; Rabe, J. P.; Iyoda, M. Synthesis, Structures, and Photophysical Properties of Pi-Expanded Oligothiophene 8-Mers and Their Saturn-Like C-60 Complexes. *J. Am. Chem. Soc.* **2015**, *137*, 3877–3885.

25. Lu, L. Y.; Zheng, T. Y.; Wu, Q. H.; Schneider, A. M.; Zhao, D. L.; Yu, L. P. Recent Advances in Bulk Heterojunction Polymer Solar Cells. *Chem. Rev.* **2015**, *115*, 12666–12731.

26. Konarev, D. V.; Drichko, N. V.; Lyubovskaya, R. N.; Shul'ga, Y. M.; Litvinov, A. L.; Semkin, V. N.; Dubitsky, Y. A.; Zaopo, A. Donor-Acceptor Interaction of Fullerene C-60 with Triptycene in Molecular Complex Tpc Center Dot C-60. *J. Mol. Struct.* **2000**, *526*, 25–29.

27. Giannozzi, P.; Baroni, S.; Bonini, N.; Calandra, M.; Car, R.; Cavazzoni, C.; Ceresoli, D.; Chiarotti, G. L.; Cococcioni, M.; Dabo, I.; Dal Corso, A.; de Gironcoli, S.; Fabris, S.; Fratesi, G.; Gebauer, R.; Gerstmann, U.; Gougoussis, C.; Kokalj, A.; Lazzeri, M.; Martin-Samos, L.; Marzari, N.; Mauri, F.; Mazzarello, R.; Paolini, S.; Pasquarello, A.; Paulatto, L.; Sbraccia, C.; Scandolo, S.; Sclauzero, G.; Seitsonen, A. P.; Smogunov, A.; Umari, P.; Wentzcovitch, R. M. Quantum Espresso: A Modular and Open-Source Software Project for Quantum Simulations of Materials. *J. Phys.: Condens. Matter* **2009**, *21*, 395502.

28. Klimes, J.; Bowler, D. R.; Michaelides, A. Chemical Accuracy for the Van Der Waals Density Functional. *J. Phys.: Condens. Matter* **2010**, *22*, 022201.

29. Klimes, J.; Bowler, D. R.; Michaelides, A. Van Der Waals Density Functionals Applied to Solids. *Phys. Rev. B* **2011**, *83*, 195131.

30. Becke, A. D. On the Large-Gradient Behavior of the Density Functional Exchange Energy. *J. Chem. Phys.* **1986**, *85*, 7184–7187.

31. Thonhauser, T.; Zuluaga, S.; Arter, C. A.; Berland, K.; Schroder, E.; Hyldgaard, P. Spin Signature of Nonlocal Correlation Binding in Metal–Organic Frameworks. *Phys. Rev. Lett.* **2015**, *115*, 136402.

32. Thonhauser, T.; Cooper, V. R.; Li, S.; Puzder, A.; Hyldgaard, P.; Langreth, D. C. Van Der Waals Density Functional: Self-Consistent Potential and the Nature of the Van Der Waals Bond. *Phys. Rev. B* **2007**, *76*, 125112.

33. Langreth, D. C.; Lundqvist, B. I.; Chakarova-Kack, S. D.; Cooper, V. R.; Dion, M.; Hyldgaard, P.; Kelkkanen, A.; Kleis, J.; Kong, L. Z.; Li, S.; Moses, P. G.; Murray, E.; Puzder, A.; Rydberg, H.; Schroder, E.; Thonhauser, T. A Density Functional for Sparse Matter. *J. Phys.: Condens. Matter* **2009**, *21*, 084203.

34. Berland, K.; Cooper, V. R.; Lee, K.; Schroder, E.; Thonhauser, T.; Hyldgaard, P.; Lundqvist, B. I. Van Der Waals Forces in Density Functional Theory: A Review of the Vdw-Df Method. *Rep. Prog. Phys.* **2015**, *78*, 066501.

35. Hamann, D. R. Optimized Norm-Conserving Vanderbilt Pseudopotentials. *Phys. Rev. B* **2013**, *88*, 085117.

36. Schlipf, M.; Gygi, F. Optimization Algorithm for the Generation of Oncv Pseudopotentials. *Comput. Phys. Commun.* **2015**, *196*, 36–44.

37. Palmer, D. C. *Crystalmaker,* Version 10.6.5; CrystalMaker Software Ltd: Begbroke, Oxfordshire, England.

38. Becke, A. D. Density-Functional Thermochemistry. III. The Role of Exact Exchange. *J. Chem. Phys.* **1993**, *98*, 5648–5652.

39. Perdew, J. P. Density-Functional Approximation for the Correlation-Energy of the Inhomogeneous Electron-Gas. *Phys. Rev. B* **1986**, *33*, 8822–8824.

40. Wadt, W. R.; Hay, P. J. Abinitio Effective Core Potentials for Molecular Calculations - Potentials for Main Group Elements Na to Bi. *J. Chem. Phys.* **1985**, *82*, 284–298.

41. Hay, P. J.; Wadt, W. R. Abinitio Effective Core Potentials for Molecular Calculations - Potentials for the Transition-Metal Atoms Sc to Hg. *J. Chem. Phys.* **1985**, *82*, 270–283.

42. Laboratory Solvents and Other Liquid Reagents. In *CRC Handbook of Chemistry and Physics,* 101st ed.; Rumble, J. R., Bruno, T. J., Doa, M. J. ed.; CRC Press 2020.

43. Abraham, M. H. Hydrogen-Bonding. 31. Construction of a Scale of Solute Effective or Summation Hydrogen-Bond Basicity. *J. Phys. Org. Chem.* **1993**, *6*, 660–684.

44. Prak, D. J. L.; Prak, P. J. L.; Cowart, J. S.; Trulove, P. C. Densities and Viscosities at 293.15–373.15 K, Speeds of Sound and Bulk Moduli at 293.15–333.15 K, Surface Tensions, and Flash Points of Binary Mixtures of *N*-Hexadecane and Alkylbenzenes at 0.1 MPa. *J. Chem. Eng. Data* **2017**, *62*, 1673–1688.

45. Jahanbekam, A.; Chilukuri, B.; Mazur, U.; Hipps, K. W. Kinetically Trapped Two-Component Self-Assembled Adlayer. *J. Phys. Chem. C* **2015**, *119*, 25364–25376.

46. Bhattarai, A.; Marchbanks-Owens, K.; Mazur, U.; Hipps, K. W. Influence of the Central Metal Ion on the Desorption Kinetics of a Porphyrin from the Solution/HOPG Interface. *J. Phys. Chem. C* **2016**, *120*, 18140–18150.

47. Bhattarai, A.; Mazur, U.; Hipps, K. W. Desorption Kinetics and Activation Energy for Cobalt Octaethylporphyrin from Graphite at the Phenyloctane Solution-Graphite Interface: An STM Study. *J .Phys. Chem. C* **2015**, *119*, 9386–9394.

CHAPTER 6

Supplementary Information

6.1. Chapter 2 Supplementary Information

6.1.1. Benchmarking DFT Functionals for Graphite, MoS_2, and Metalloporphyrins.

In order to make comparisons among DFT-calculated structures and adsorption energies of metalloporphyrins on MoS_2 and graphite, it is necessary to use a consistent density functional because calculated structures and energies can functional-dependent.[1] To test the suitability of functionals for these calculations, the structures of both 4L-MoS_2 and 4L-graphite were calculated and compared to their experimental crystal structures. Calculations with the optb86b were found to reproduce both the in-plane lattice parameter, angles and, importantly, the dispersion-dominated interplanar separation of a 4L-MoS_2 slab (Table 6.1) and 4L-graphite slab (Table 6.2). Notably, the commonly used dispersion-corrected functional, vdW-DF, overstimates interplane lattice parameter by more than 0.4 Å for the 4L graphite slab. Given this, the optb86b functional was used for all subsequent calculations.

Table 6.1. Experimental Lattice Parameters of MoS_2 and Calculated Lattice Parameters of 4L MoS_2.

Parameter	Experimental	DFT (optb86b)
a (nm)	0.316	0.316
c (nm)	1.232	1.230
Mo–S Bond Length (Å)	2.39	2.41
S–Mo–S Bond Angle (°)	80.3	81.5

Table 6.2. Experimental Lattice Parameters of HOPG and Calculated Lattice Parameters of 4L Graphite.

Parameter	Experimental	DFT (optb86b)	DFT (vdW-DF)
a (nm)	0.246	0.246	0.246
c (nm)	0.671	0.671	0.716
C–C bond length (Å)	1.42	1.42	1.42

Having determined an appropriate functional for the graphite and MoS_2 components of the systems, the suitability of this functional for metalloporphyrins was investigated. The structures of Ni(OEP) and Ga(OEP)Cl, representative examples of 4-coordinate and domed 5-coordinate metalloporphyrins, respectively, were calculated in PW-DFT using the optb86b functional. Selected bond lengths for Ni(OEP) and bond lengths and angles for Ga(OEP)Cl are listed in Tables 6.3 and 6.4, respectively. These values are in reasonably good agreement with those from crystal structures, with similar N–C bond lengths for both porphyrins. The Ni–N bond lengths are in good agreement, although a small elongation is observed in the calculated Ga–N bond lengths (~0.025 Å) along with an increase in the doming type distortion of the Ga center, as evidenced by the slightly larger average N–Ga–Cl angle (102.2° by DFT; 101.3° in crystal structure). It has been previously noted that these discrepancies may arise from intrinsic differences between the gas-phase equilibrium structure and the structure determined by single-crystal X-ray diffraction methods.[2] Given that the discrepancies between the calculated structures and the crystal structures are small relative to their respective values, the optb86b functional was determined to be suitable for metalloporphyrins and interfacial systems.

Table 6.3. Selected Bond Lengths (Å) for Ni(OEP) Calculated by PW-DFT and from Single-Crystal X-ray Diffraction Data.

Parameter	DFT (optb86b)	Experimental[a]
Ni–N(1)	1.952	1.958(4)
Ni–N(2)	1.952	1.946(4)
Ni–N(3)	1.952	1.958(4)
Ni–N(4)	1.952	1.946(4)
N–C (avg.)	1.382	1.385(10)

[a] Values from Ref. 3

Table 6.4. Selected Bond Lengths (Å) and Angles (°) for Ga(OEP)Cl Calculated by PW-DFT and from Single-Crystal X-ray Diffraction Data.

Parameter	DFT (optb86b)	Experimental[a]
Ga–N(1)	2.053	2.033(4)
Ga–N(2)	2.054	2.030(4)
Ga–N(3)	2.064	2.038(4)
Ga–N(4)	2.064	2.037(4)
Ga–Cl	2.237	2.2397(13)
N(1)–Ga–Cl	102.4	102.2(1)
N(2)–Ga–Cl	102.4	100.9(1)
N(3)–Ga–Cl	102.0	101.3(1)
N(4)–Ga–Cl	101.8	100.8(1)
N–C (avg.)	1.376	1.379(11)

[a] Values from Ref. 4.

6.1.2. Effect of Layer-Number on the Structure and Adsorption Energy of Ni(OEP) on MoS_2.

In addition to the calculations performed on the interface of Ni(OEP) and 1L-MoS_2, calculations were also conducted using 2L- and 4L-MoS_2 substrates with Ni(OEP) in order to address several questions. First, as comparisons between molecular monolayers on bulk substrates and 1L substrates are limited (see Chapter 2), these calculations can determine whether significant layer-number dependence would be expected to arise in the optimized structure or adsorption energy of molecular monolayers on MoS_2. Second, as the systems that were studied experimentally in Chapter 2 include supporting layers of polycrystalline Au beneath the 1L-MoS_2, these calculations serve as a proxy for the importance of including supporting layers. (While 1L-MoS_2 supported on few-layer Au would serve as a more effective system for testing this, modeling such a system is extremely computationally intensive due to the need for (a) fully relativistic pseudopotentials and (b) a larger unit cell to minimize the distortion applied to MoS_2 required to enforce periodicity in a cell containing the incommensurate lattices of MoS_2 and Au.[5]) It was determined that as the number of layers of MoS_2 increases from 1L to 2L, the separation between Ni(OEP) and MoS_2 decreases slightly (0.04 Å) and the nickel atom resides further below the $C_{20}N_4$

plane (0.015 Å for 1L; 0.027 Å for 2L; Figure 6.1a and b). Further, the adsorption energy in the system increased by 0.12 eV going from 1L- to 2L-MoS_2 (Table 6.5). The effects of two additional layers of MoS_2, from 2L to 4L (Figure 6.1c and Table 6.5), were comparatively small. It is unlikely that these small changes in the structure and adsorption energy with respect to the number of layers would significantly alter the stability or experimentally observed geometries of self-assembled monolayers of porphyrins on MoS_2. Therefore, all other calculations were carried out using 1L-MoS_2 given the significant savings of computational resources compared to using 2L-MoS_2.

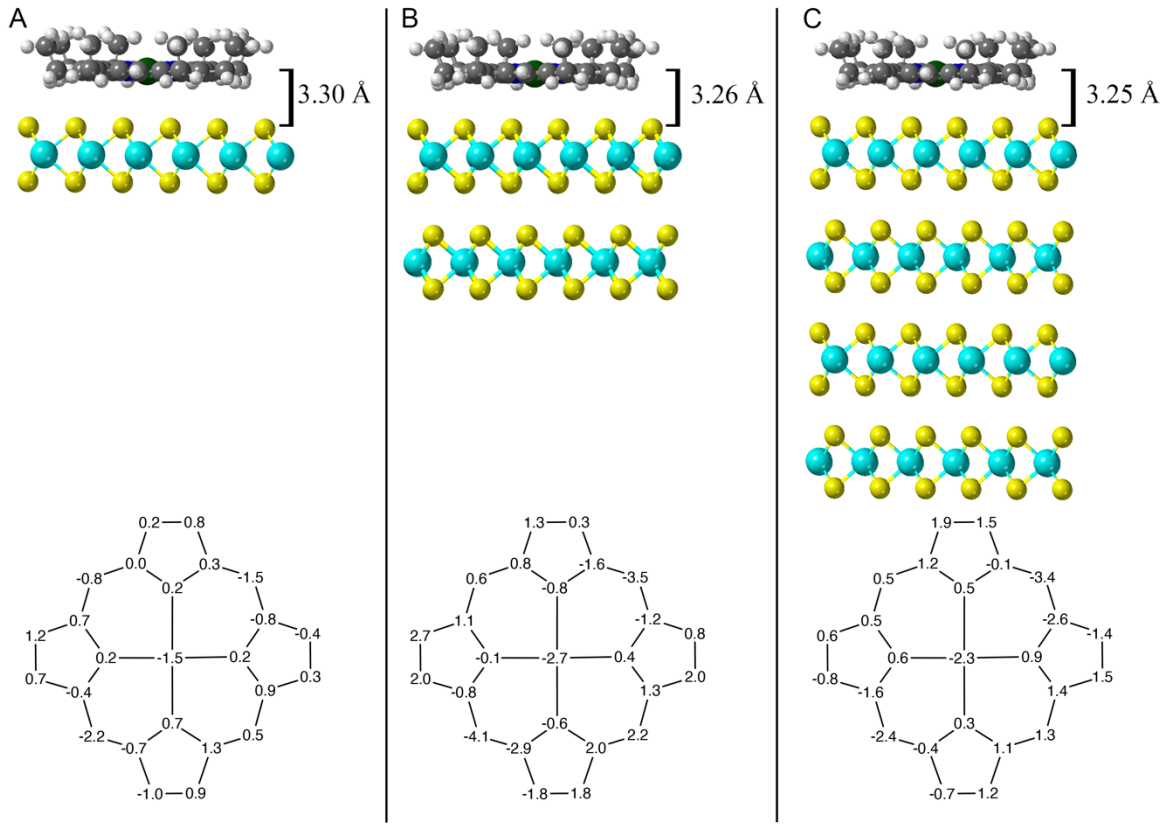

Figure 6.1. Calculated adsorbate–substrate distances of Ni(OEP) on MoS_2 (Bridge 22.5°) and displacements of the $C_{20}N_4Ni$ nuclei from the plane of best fit of the $C_{20}N_4$ macrocycle in units of 0.01 Å (bottom): (a) 1L MoS_2, (b) 2L MoS_2, and (c) 4L MoS_2. The adsorbate–surface distance is determined from the planes of best fit for the top layer of S atoms and the $C_{20}N_4Ni$ macrocycle.

Table 6.5. Calculated Adsorption Energy and Adsorbate–Surface Distance for Ni(OEP) on 1L, 2L and 4L MoS_2.

Parameter	1L MoS_2	2L MoS_2	4L MoS_2
Adsorption energy (eV)	–3.33	–3.45	–3.43
Adsorbate–surface distance (Å)[a]	3.30	3.26	3.25

[a] Determined from the planes of best fit of the top layer of S atoms and the $C_{20}N_4$ macrocycle.

6.1.3. Analysis of Structural Parameters of Ni(OEP) at Various Binding Sites on 1L-MoS_2 and Effect of Constrained Optimization. In an effort to understand the relative stability of the Bridge 22.5º binding site, structural parameters were extracted from the optimized geometry of Ni(OEP) on 1L-MoS_2 at each binding site (Table 6.6), specifically, the adsorbate–surface distance, the average S–metalloporphyrin atom distance, the number of close S–metalloporphyrin atom contacts, and the number of unique S–metalloporphyrin atom contacts. Each of these represent a method to quantify the contact between the surface S atoms and the metalloporphyrin atoms. The only structural parameter that is observed to correlate with adsorption energy is the inverse relationship between the average S–metalloporphyrin atom distance when comparing rotational conformers at a single binding site, though this correlation does not hold true when comparing the various binding sites. No single parameter or combination of parameters can be found that show a direct correlation with the adsorption energy when compared across all binding sites. The data suggest that a multitude of factors lead to the trends observed in the adsorption energy, including those not yet understood.

Table 6.6. Adsorption Energy and Various Structural Parameters of Ni(OEP) at Binding Sites on 1L-MoS_2.

Binding Site	Adsorption Energy (eV)	Adsorbate–surface distance (Å)[a]	Avg. S–$C_{20}N_4NiC_8$ Distance (Å)[b]	Close S–$C_{20}N_4NiC_8$ Contacts[c]	Unique S–$C_{20}N_4NiC_8$ Contacts[d]
Center	–3.23	3.28	3.50	43	16
Center 7.5°	–3.25	3.28	3.52	45	17
Center 15°	–3.28	3.28	3.55	51	18
Top	–3.21	3.29	3.53	43	17
Top 7.5°	–3.20	3.31	3.52	37	17
Top 15°	–3.17	3.31	3.50	35	15
Bridge	–3.16	3.31	3.52	46	18
Bridge 22.5°	–3.33	3.30	3.54	43	14
Bridge 45°	–3.16	3.30	3.52	43	18

[a] The adsorbate–surface distance is determined from the planes of best fit of the top layer of C atoms and the $C_{20}N_4$ macrocycle. [b] The average distance between C, N, Ni atoms and their nearest S contacts, excluding the CH_3 carbon atoms. [c] Total number of S–C, S–N, S–Ni distances within 110% of the sum of the S and C van der Waals radii (3.8 Å). [d] Number of unique S atoms within 110% of the sum of the S and C van der Waals radii (3.8 Å) of any C, N, Ni atoms.

Adsorption energies were also determined with geometric constraints to compare the relative adsorption energy of the binding sites in the absence of small structural differences between the substrate or the metalloporphyrin (Table 6.7). When the Mo and S nuclei were frozen in their optimized geometry from the isolated calculation, the adsorption energies are either identical or exhibit a minimal change (maximum 0.02 eV for Center 15°). The trends calculated for the adsorption energy amongst the various rotational conformers remain the same with the exceptions of the Center 7.5° and Center 15° sites being isoenergetic, though the adsorption energy differed by only 0.03 eV in the unconstrained system. If the entire system is frozen in its optimized geometry from the isolated systems with the adsorbate–surface distance fixed at 3.30 Å, the adsorption energies decrease at all binding sites compared to the unconstrained systems (0.02 eV – 0.04 eV), though the trends in the adsorption energies among the binding sites remain the same. This indicates that these small differences in adsorption energy are intrinsic to the specific binding sites.

Table 6.7. Adsorption Energy of Ni(OEP) at Various Binding Sites on 1L-MoS_2 with Various Geometrical Constraints.

Binding Site	Adsorption Energy (eV)[a]	Adsorption Energy (eV) OEP Relaxation[b]	Adsorption Energy (eV) No Relaxation[c,d]
Center	–3.23	–3.25	*N/A*
Center 7.5°	–3.25	–3.26	*N/A*
Center 15°	–3.28	–3.26	–3.26
Top	–3.21	–3.21	–3.17
Top 7.5°	–3.20	–3.19	*N/A*
Top 15°	–3.17	–3.16	*N/A*
Bridge	–3.16	–3.16	–3.14
Bridge 22.5°	–3.33	–3.32	–3.30
Bridge 45°	–3.16	–3.16	–3.13

[a] No constraints were placed on any nuclei. [b] Mo and S nuclei were frozen in their optimized geometries from the isolated MoS_2 monolayer calculation. [c] All nuclei were frozen in their optimized geometries from their respective isolated calculations. The adsorbate–surface distance, determined from the planes of best fit of the top layer of S atoms and the $C_{20}N_4$ macrocycle, was fixed at 3.30 Å for all systems. [d] Only tested at selected binding sites.

6.1.4. Adsorption Energy of Nickel(II) Porphine on Graphite and 1L MoS_2. The contribution of the peripheral substituents of the porphyrin to the adsorption energy was determined by comparing the adsorption energy of Ni(OEP) to nickel porphine (Ni(Por)) on 1L MoS_2 and graphite, where the eight ethyl groups in the β positions of the porphyrin are replaced by hydrogen atoms. The adsorption energy of Ni(Por) is significantly smaller on both graphite and 1L-MoS_2 than Ni(OEP), by 1.34 eV and 1.29 eV, respectively (Table 6.8; Tables 2.8 and 2.10 for Ni(OEP)). In agreement with the adsorption energies found for Ni(OEP), Ni(Por) exhibits a greater adsorption energy on graphite than on 1L-MoS_2. The difference between adsorption energies of Ni(OEP) and Ni(Por) can be used to estimate the contribution to adsorption energy from the CH_2 groups on each surface; f each CH_2 contributes 0.17 eV on graphite and 0.16 eV on 1L-MoS_2. This value is in reasonable agreement with temperature-programmed desorption measurements of the desorption barrier for *n*-alkanes, which range from 0.11 eV–0.15 eV per carbon for n = 3 – 8.[6,7] The higher values calculated for the CH_2 groups are not surprising as contributions from the

peripheral hydrogen atoms in the β positions of Ni(Por) are assumed to be zero. These observations, along with the small variations in adsorption energy in the series of M(OEP)s discussed in Chapter 2, indicate that despite the significant geometric and electronic differences of HOPG and MoS_2, the energetics of the adsorption of porphyrins are very similar. The isolation of the contribution of the metal center and the peripheral substituents indicate that this similarity is not a result of a fortuitous sum of discrepant constituent parts, but agrees for each component.

Table 6.8. Adsorption Energy of Ni(Por) on 4L Graphite and Monolayer MoS_2.

	Ni(Por)	
Parameter	4L Graphite	ML MoS_2
Adsorption energy (eV)	-2.27	-2.04
Adsorption energy difference from Ni(OEP) (eV)[a]	1.34	1.29
Adsorption energy per CH_2 (eV)[b]	-0.17	-0.16

[a] Compared to adsorption energy of Ni(OEP) on identical substrate. [b] Contribution of eight hydrogen atoms in β positions are not considered.

6.1.5. Deconvolution of Atomic and Constituent Contributions to Charge Density Differences. The contributions of the various atoms and moieties to the charge density difference (CDD) were determined according to Equation 6.1:

$$\delta_{diff} = \delta_{Int} - \delta_{S/P} \tag{6.1}$$

Where δ_{diff} is the difference in partial charge for an atom and δ_{Int} and $\delta_{S/P}$ are the partial charges of the same atom at the interface and in either the isolated surface (δ_S) or porphyrin (δ_P) structure. The partial atomic charges were determined using the DDEC6 program, which deconvolutes the atomic contributions from the PW-DFT calculated charge density.[8-13] The atomic and moietic contributions to the charge density difference for Ni(OEP), Zn(OEP), Ga(OEP)Cl and H_2OEP for the lowest energy rotational conformer at each binding site are shown in Tables 6.9, 6.10, 6.11, and 6.12, respectively. We note that the sums of the partial charges of the atoms or moieties are significantly larger than what was reported using the plane-averaged method in

Chapter 2 (Table 2.11). That the magnitude of CDD using the sum of partial charges is larger than when using the plane-averaged totals is expected, because when the charge density of the interface is plane-averaged, any overlapping charge density in the direction orthogonal to the plane will be canceled out. However, given the discrepancies between the two methods, we focus on the relative magnitudes of the partial atomic charges of the constituents.

Generally, the atomic contributions indicate that the vast majority of the charge donation from the OEPs to MoS_2 is from the macrocycle and CH_2 groups (75%–90%), as would be expected given their relative proximity to the surface, whereas the CH_3 groups far from the surface show a very small contribution. The only significant difference calculated between these systems is the role of the metal center. For Ni(OEP),Ni is calculated to account for approximately 10% of the total donated charge, whereas for other systems the metal contribution is either very small (3% for Zn(OEP)) or negligible (H_2OEP and Ga(OEP)Cl). These calculations further support the conclusion in Chapter 2, that while small metal-center dependent differences in the charge redistribution at the MoS_2 interface do exist, tuning the surface density of the porphyrins is likely to engender much larger differences between systems.

Table 6.9. Atomic Contributions to Charge Density Difference for Ni(OEP) on Monolayer MoS_2 at Various Binding Sites.

	CDD (e^-)			
Ni(OEP)	Center 15°	Top 0°	Bridge 22.5°	Average
Ni	–0.03	–0.04	–0.03	–0.03
$C_{20}N_4H_4$[a]	–0.17	–0.17	–0.17	–0.17
$(CH_2)_8$	–0.08	–0.07	–0.08	–0.08
$(CH_3)_8$	–0.04	–0.04	–0.04	–0.04
Total	–0.32	–0.32	–0.32	–0.32

[a] $C_{20}N_4H_4$ refers to the atoms of the porphyrin macrocycle, including the hydrogens attached to the *meso* carbons.

Table 6.10. Atomic Contributions to Charge Density Difference for Zn(OEP) on Monolayer MoS_2 at Various Binding Sites.

	CDD (e^-)			
Zn(OEP)	Center 15°	Top 0°	Bridge 22.5°	Average
Zn	–0.01	0.00	–0.01	–0.01
$C_{20}N_4H_4$[a]	–0.19	–0.19	–0.20	–0.19
$(CH_2)_8$	–0.09	–0.07	–0.09	–0.08
$(CH_3)_8$	–0.03	–0.03	–0.04	–0.04
Total	–0.32	–0.29	–0.34	–0.32

[a] $C_{20}N_4H_4$ refers to the atoms of the porphyrin macrocycle, including the hydrogens attached to the *meso* carbons.

Table 6.11. Atomic Contributions to Charge Density Difference for Ga(OEP)Cl on Monolayer MoS_2 at Various Binding Sites.

	CDD (e^-)			
Ga(OEP)Cl	Center 15°	Top 0°	Bridge 22.5°	Average
Ga	0.00	0.00	0.00	0.00
Cl	–0.01	–0.01	–0.01	–0.01
$C_{20}N_4H_4$[a]	–0.15	–0.17	–0.18	–0.17
$(CH_2)_8$	–0.10	–0.07	–0.08	–0.08
$(CH_3)_8$	–0.03	–0.03	–0.04	–0.03
Total	–0.29	–0.28	–0.31	–0.29

[a] $C_{20}N_4H_4$ refers to the atoms of the porphyrin macrocycle, including the hydrogens attached to the *meso* carbons.

Table 6.12. Atomic Contributions to Charge Density Difference for H_2OEP on Monolayer MoS_2 at Various Binding Sites.

	CDD (e^-)			
H_2OEP	Center 15°	Top 0°	Bridge 22.5°	Average
H_2	0.00	0.00	0.00	0.00
$C_{20}N_4H_4$[a]	–0.18	–0.19	–0.15	–0.17
$(CH_2)_8$	–0.08	–0.07	–0.11	–0.09
$(CH_3)_8$	–0.04	–0.03	–0.04	–0.04
Total	–0.30	–0.29	–0.30	–0.30

[a] $C_{20}N_4H_4$ refers to the atoms of the porphyrin macrocycle, including the hydrogens attached to the *meso* carbons.

6.2. Chapter 3 Supplementary Information

6.2.1. Effect of Dispersion Corrections on Relative Energy of Porphyrin Dimer Conformers.

The optimized geometries and energies of **3** and **4** were determined by DFT using the B3PW91 functional, either with or without D3 dispersion corrections. All other parameters of

the calculations were identical. It was found that when the geometries of **3** and **4** were optimized without the inclusion of dispersion corrections, the folded structures were not stable and would relax to the extended structures. The relative energies of the folded structures without dispersion corrections were determined by performing a single point energy calculation at the optimized geometry calculated with the inclusion of dispersion corrections. The relative energies (Table 6.13) show that for **3** and **4** the inclusion of D3 dispersion corrections results in the folded structure being more stable than the extended structure by 32.71 kcal/mol and 9.78 kcal/mol, respectively; without dispersion corrections, the extended structures are found to be more stable by roughly 26 kcal/mol in both cases. We find that dispersion corrections are vital for modeling the folded structures of **3** and **4** observed by X-ray crystallography and were included in all subsequent calculations of porphyrin dimer complexes.

Table 6.13. Relative Energy of Porphyrin Dimer Conformers with and without Inclusion of D3 Dispersion Corrections.

	3		**4**	
System	Extended[a]	Folded	Extended[a]	Folded
B3PW91-D3	0.00	–32.71	0.00	–9.78
B3PW91	0.00	25.91[b]	0.00	26.03[b]

[a] Energy of all extended structures are independently defined as 0.00 kcal/mol. The energies of **3** and **4** are not comparable. [b] Geometry optimizations without D3 dispersion corrections starting from the folded structures of **3** or **4** resulted in the extended structures. The energy of the folded structure was determined from a single point calculation at the optimized geometry found for the folded structure with D3 dispersion corrections.

6.2.2. Temperature Dependence of Molecular Structure of 3. Given the solvent dependent conformations that were observed for **3**, the possibility that the structure of **3** could also exhibit temperature dependence was investigated by means of variable-temperature ^{1}H-NMR (VT-NMR) spectroscopy in $CDCl_3$ and $C_6D_3Cl_3$. VT-NMR spectra of **3** in $CDCl_3$ from 25 °C to 50 °C are shown in Figure 6.2 and the changes in the chemical shifts of the resonances in Table 6.14. All shifts are reported relative to the $CHCl_3$ solvent residual at 25 °C (7.26 ppm). While $CHCl_3$ is

known to exhibit a temperature-dependent chemical shift due to the excitation of vibrational and rotational modes,[14] the assumption of a constant solvent residual allows for conformational changes of **3** to be isolated from changes in the chemical shift that would occur even without a major conformational change. The peak shape in these spectra is the result of poor shimming rather than degradation, as the solvent residual exhibits the same profile. As the temperature increases from 25 °C to 50 °C, downfield shifts of 0.10 ppm, 0.09 ppm, and 0.04 ppm are observed for the *meso* (OEP), CH_2, and CH_3 protons residing on the Ga(OEP) unit, respectively. Upfield shifts with increasing temperature are generally observed for the H_2BCP protons; the magnitude of the shifts varies between the protons with *meso* (BCP) (0.1 ppm) > *β1* (0.06 ppm) > *β2* (0.02 ppm) and no shift being observed for the NH protons. If these changes are compared to those calculated for the folded and extended structures of **3** (see Chapter 3, Table 3.11), it is observed that the directions of the shifts are consistent with those expected for moving from the folded conformer to the extended conformer, though the magnitudes of the changes are much smaller than would be predicted if **3** was completely extended. To ensure that these shifts were the result of conformational changes and not degradation, a ^{1}H-NMR spectrum was taken after cooling to 25 °C from elevated temperatures; the shifts were observed to return to the expected values for **3** at 25 °C, indicating that no substantial degradation took place. Overall, these results indicate that at elevated temperatures **3** may undergo small conformational changes towards an extended structure, but the conformation should still be considered as folded.

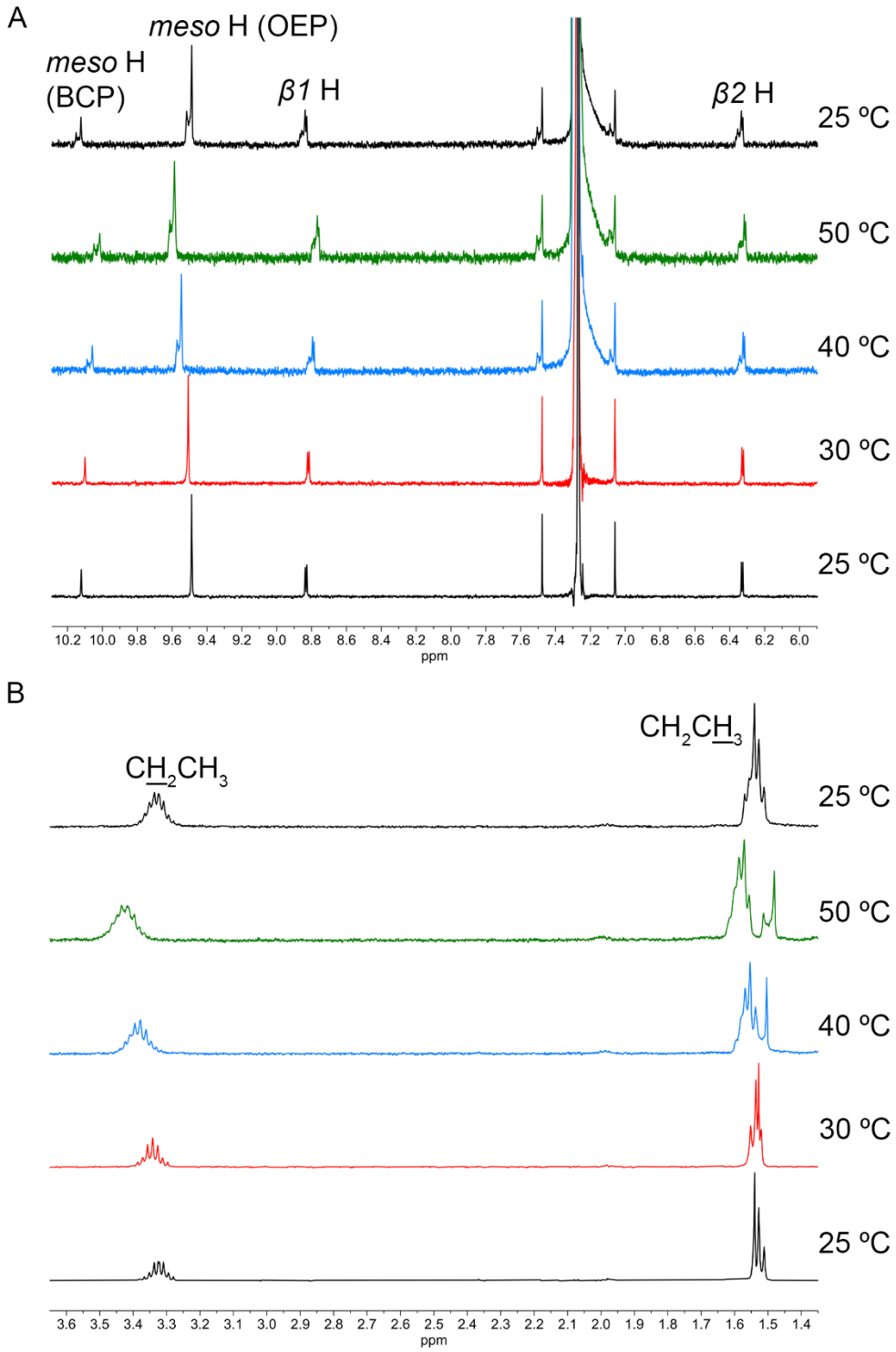

Figure 6.2. ^{1}H-NMR spectra (500.13 MHz) of **3** in $CDCl_3$ at various temperatures. Spectra are corrected to $CHCl_3$ solvent residual at 25 °C (7.26 ppm). (a) Aromatic region; (b) aliphatic region; (c) porphyrin NH region.

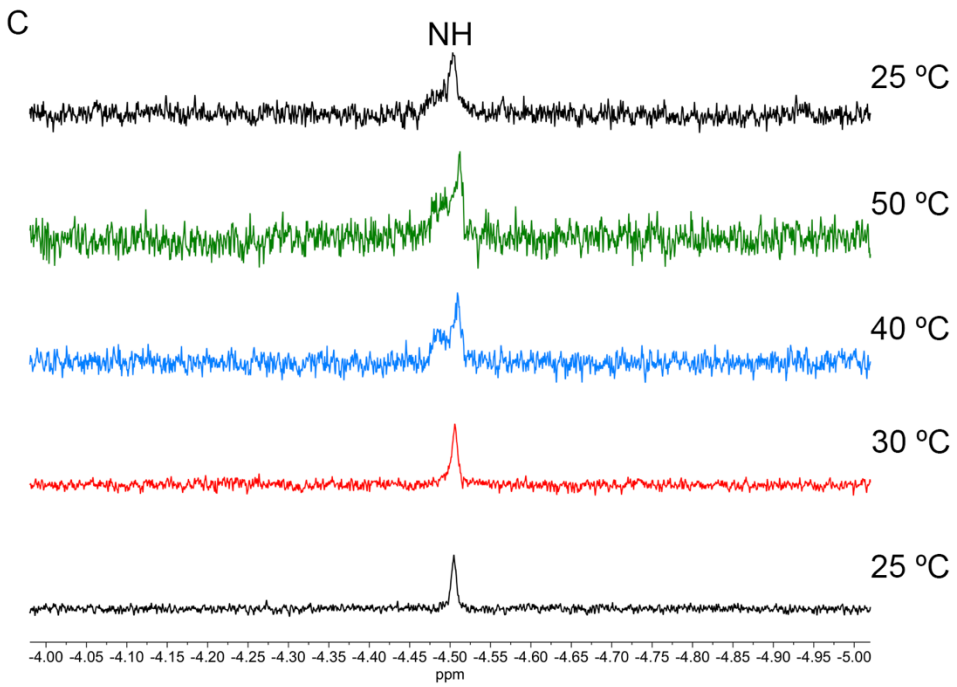

Figure 6.2, continued. ^{1}H-NMR spectra (500.13 MHz) of **3** in $CDCl_3$ at various temperatures. Spectra are corrected to $CHCl_3$ solvent residual at 25 °C (7.26 ppm). (a) Aromatic region; (b) aliphatic region; (c) porphyrin NH region.

Table 6.14. Temperature Dependence of ^{1}H-NMR Chemical Shifts of **3** in $CDCl_3$.[a]

Resonance	**25 °C**	**30 °C**	**40 °C**	**50 °C**	**25 °C**[c]
meso H (OEP)	9.48	9.50	9.54	9.58	9.48
CH_2 (OEP)	3.32	3.33	3.37	3.41	3.32
CH_3 (OEP)	1.52	1.53	1.54	1.56	1.52
meso H (BCP)	10.11	10.09	10.05	10.01	10.11
β1 (BCP)[b]	8.82	8.81	8.78	8.76	8.82
β2 (BCP)[b]	6.32	6.32	6.31	6.30	6.32
NH (BCP)	–4.52	–4.52	–4.52	–4.52	–4.52

[a] All shifts are reported with respect to the $CHCl_3$ solvent residual at 25 °C (7.26 ppm). [b] The H atoms *β1* and *β2* are those on the pyrrole groups nearest and farthest, respectively, from the carboxylate group. [c] Returned to 25 °C from 50 °C.

VT-NMR spectra of **3** in $C_6D_3Cl_3$ from 25 °C to 100 °C are shown in Figure 6.3 and the changes in the chemical shifts of the resonances are in Table 6.15. All shifts are reported relative to the $C_6HD_2Cl_3$ solvent residual at 25 °C (6.94 ppm). As the temperature increases from 25 °C to

100 °C, small downfield shifts, 0.04 ppm and 0.02 ppm, are observed for the CH_2, and CH_3 protons, respectively, with no shift in the *meso* (OEP) protons. The H_2BCP protons exhibit discrepant effects with the *meso* H (BCP) and the *β1* protons exhibiting upfield shifts of 0.07 ppm, the *β2* protons exhibiting no shift, and the NH protons exhibiting a downfield shift of 0.14 ppm. While **3** was determined to be in a partially extended conformation in TCB in Chapter 3, the direction of the temperature dependent changes observed here are not consistent with the expected changes for either folding or moving towards a completely extended structure. In addition to the changes in the chemical shifts a decrease in the coupling constant of the complex multiplet observed for the CH_2 protons is observed at elevated temperatures. It has previously been determined in studies of mercury[15] and thallium[16] octaethylporphyrins that the complex multiplet of the CH_2 protons is a result of diastereotopicity from the metal center being located above the plane of the porphyrin. This suggests that the doming distortion of the gallium metal center may decrease as the temperature increases. Overall, the VT-NMR experiments demonstrate that only minor conformational changes occur at elevated temperatures and interconversion between the folded and extended structures is not possible in the temperature range explored.

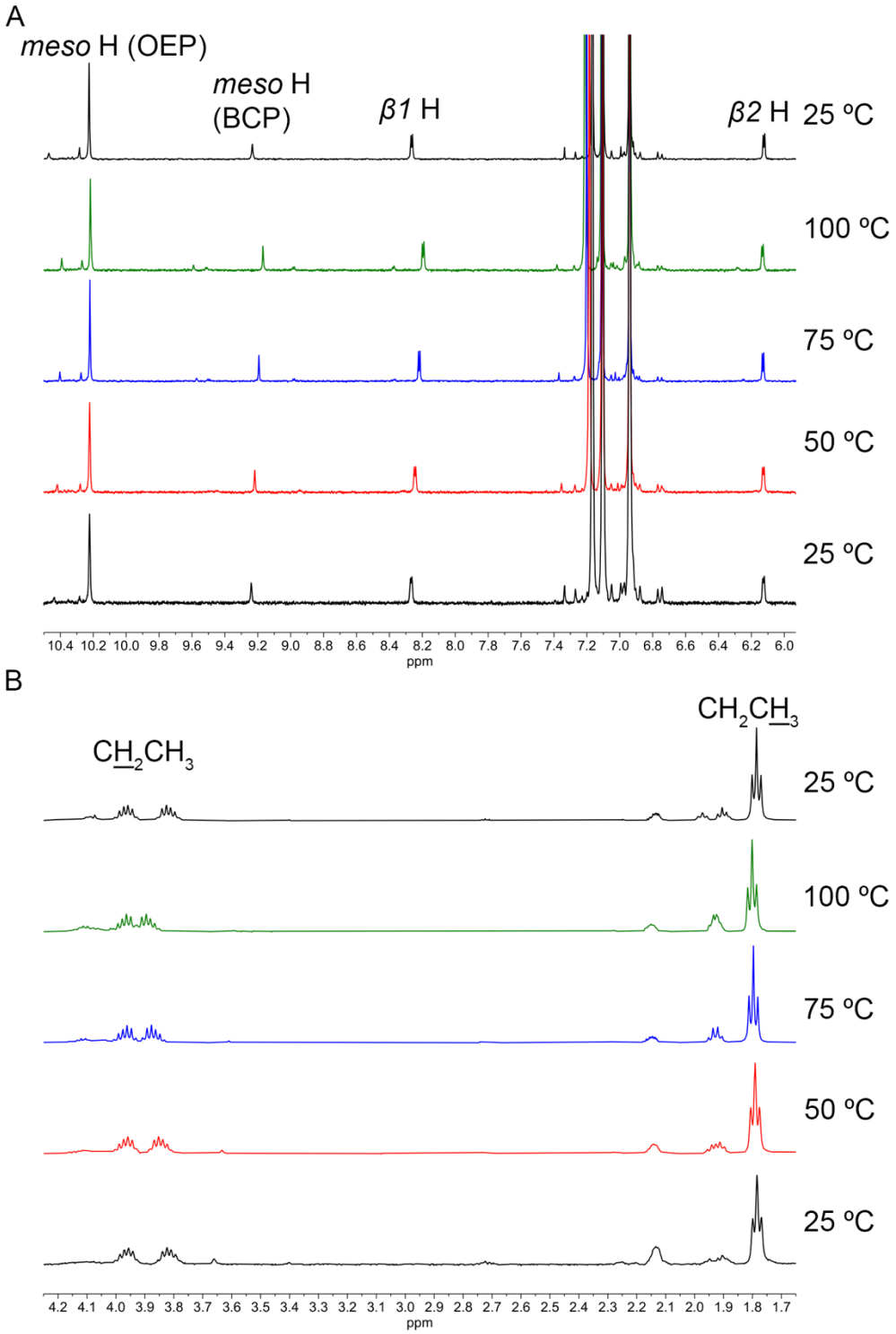

Figure 6.3. ^{1}H-NMR spectra (500.13 MHz) of **3** in $C_6D_3Cl_3$ at various temperatures. Spectra are corrected to $C_6HD_2Cl_3$ solvent residual at 25 °C (6.94 ppm). (a) Aromatic region; (b) aliphatic region; (c) porphyrin NH region.

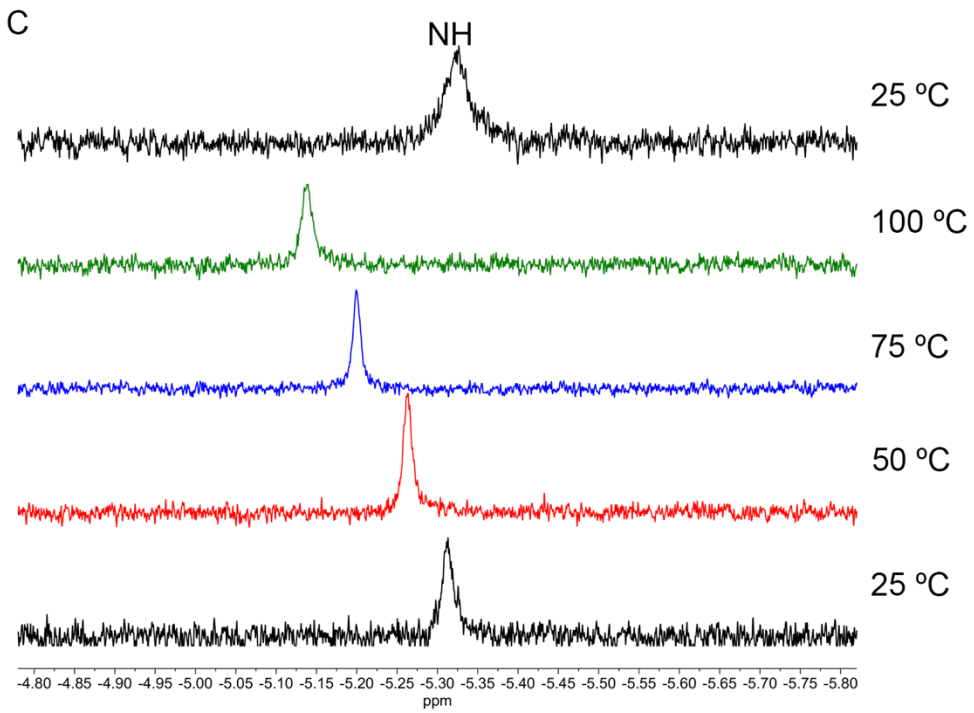

Figure 6.3, continued. ^{1}H-NMR spectra (500.13 MHz) of **3** in $C_6D_3Cl_3$ at various temperatures. Spectra are corrected to $C_6HD_2Cl_3$ solvent residual at 25 °C (6.94 ppm). (a) Aromatic region; (b) aliphatic region; (c) porphyrin NH region.

Table 6.15. Temperature Dependence of ^{1}H-NMR Chemical Shifts of **3** in $C_6D_3Cl_3$.[a]

Resonance	**25 °C**	**50 °C**	**75 °C**	**100 °C**	**25 °C**[c]
meso H (OEP)	10.22	10.22	10.22	10.22	10.22
CH_2 (OEP)	3.89	3.91	3.92	3.93	3.89
CH_3 (OEP)	1.78	1.79	1.80	1.80	1.78
meso H (BCP)	9.24	9.22	9.19	9.17	9.23
β1 (BCP)[b]	8.27	8.25	8.22	8.20	8.27
β2 (BCP)[b]	6.13	6.13	6.13	6.13	6.13
NH (BCP)	–5.31	–5.26	–5.20	–5.14	–5.32

[a] All shifts are reported with respect to the $C_6HD_2Cl_3$ solvent residual at 25 °C (6.94 ppm). [b] The H atoms *β1* and *β2* are those on the pyrrole groups nearest and farthest, respectively, from the carboxylate group. [c] Returned to 25 °C from 100 °C.

6.3. Chapter 4 Supplementary Information

6.3.1. *Z*-Coordinate Dependence of Simulated STM Images. In the Tersoff-Hamann approximation for simulating STM images, one of the parameters that must be chosen is the *z*-

coordinate at which the *xy* plane of the charge density is sampled in order to generate an STM image that corresponds to an experimentally acquired constant-height image. Typically, this coordinate is chosen to be within a few Å of the vdW surface of the uppermost atoms, in line with predictions of the physical distance between the tip and surface in STM images.[17,18] Using the **2**:C_{60} system shown in Figure 4.13, the dependence of these simulated images on the *z*-coordinate was investigated. Simulated STM images with three different *z*-coordinates are shown in Figure 6.4. In the simulated images sampled with a *z*-coordinate above the plane of the porphyrin (Figure 6.4a), a central feature emerges as the bias voltage is switched from –600 mV to –1200 mV. While this initially appears to be a result of the fullerene, this feature is also observed in simulated images in the absence of the fullerene (Figure 6.5). Both of the features in these images arise from the four pyrrole rings of the porphyrin, where a slight tilt in the upper porphyrin macrocycle with respect to the lower macrocycle (3.1° angle between the planes of best fit of the $C_{20}N_4$ macrocycles) results in an asymmetric distance from the sampling plane leading to the appearance of two features. In simulated images with the *z*-coordinate through the plane of the off-surface porphyrin (Figure 6.4b), both features are clearly observed with the fullerene appearing as a ring-like feature as the sampling plane intersects the C_{60} sphere. Finally, when the *z*-coordinate passes through the center of the fullerene (Figure 6.4c), the porphyrin is no longer observed and the terephthalate moiety appears; the C_{60} appears as a larger ring in accordance with the larger diameter in this plane. Given these observations, we chose to simulate images with the *z*-coordinate at the plane of the off-surface porphyrin.

While an STM tip at this position is obviously non-physical, this choice allows for concurrent investigation of the bias voltage dependence of both the porphyrin and fullerene. Furthermore, we note that because both the position in the *z*-direction of the uppermost atoms and

the tunneling probability at any given bias voltage vary between porphyrin and fullerene, experimental STM images of these systems are acquired in constant-current mode rather than constant-height mode; as a result, any physically meaningful choice of *z*-coordinate will misrepresent the system as it appears when interrogated by an STM in constant-current mode, where the position of the tip is not fixed. Using a *z*-coordinate that passes through both the porphyrin and fullerene eliminates the contribution of the positional variance between the two components, allowing for exclusive interrogation of the bias voltage dependence and, in our view, a better approximation of the experimentally acquired images. Modules for generating simulated constant-current STM images with data from the Tersoff-Hamann approximation have been developed but are not incorporated into the simulation package used here.[19]

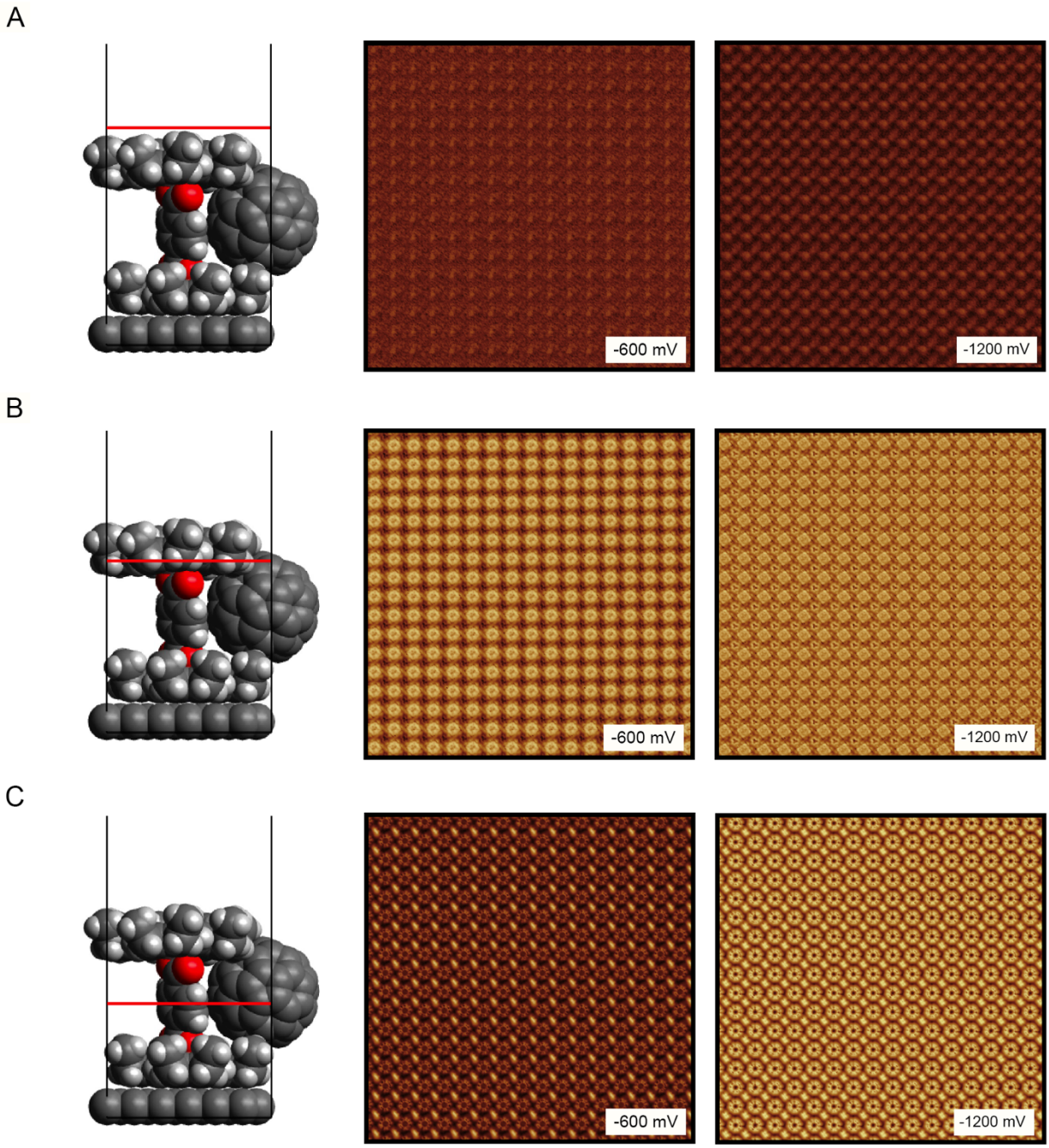

Figure 6.4. Simulated STM images of **2**:C_{60} calculated with a *z*-coordinate (a) above the plane of the porphyrin; (b) through the plane of the porphyrin; (c) bisecting the C_{60}. Space-filling model of **2**:C_{60} and graphene (left) with red line indicating plane used in simulating STM images at bias voltages of –600 mV (middle) and –1200 mV (right). The color mapping is constant throughout these images.

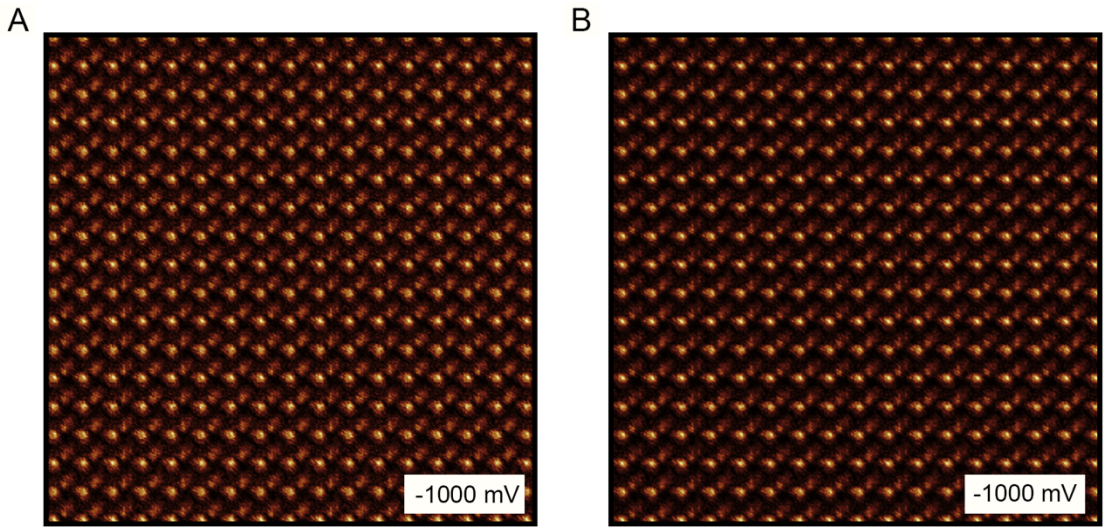

Figure 6.5. Simulated STM images of (a) **2** and (b) **2**:C_{60} calculated at the *z*-coordinate of Figure 6.4a.

6.3.2. Bias Voltage Dependence of TCB within Monolayers of Ni(OEP). The bias voltage dependence of 1,2,4-trichlorobenzene (TCB) was investigated as a means of identifying and distinguishing features resulting from the coadsorption of the solvent from those that are attributed to C_{60} within the bicomponent monolayers **2**:C_{60} and **4**:C_{60}. Deposition of a 1.5 mM solution of Ni(OEP) in TCB results in the formation of widespread monolayers adopting a square structure with tunneling density observed in the region between the Ni(OEP) features. The appearance of these features changes from a dim spot, considerably darker than the porphyrin feature, at –600 mV (Figure 6.6a), to a small bright dot at –900 mV (Figure 6.6b). At more negative bias voltages the porphyrin and TCB features show similar tunneling density (Figure 6.6c). In our experience, TCB has not been observed at bias voltages less negative than –500 mV, though literature reports have observed these features at bias voltages as low as –300 mV.[20,21] The bias voltage dependence observed here is similar to that observed for the C_{60} features in Chapter 4, suggesting that bias voltage alone cannot distinguish between these two features, though we

reiterate from Chapter 4 that TCB features have never been observed in STM images the porphyrin dimers.

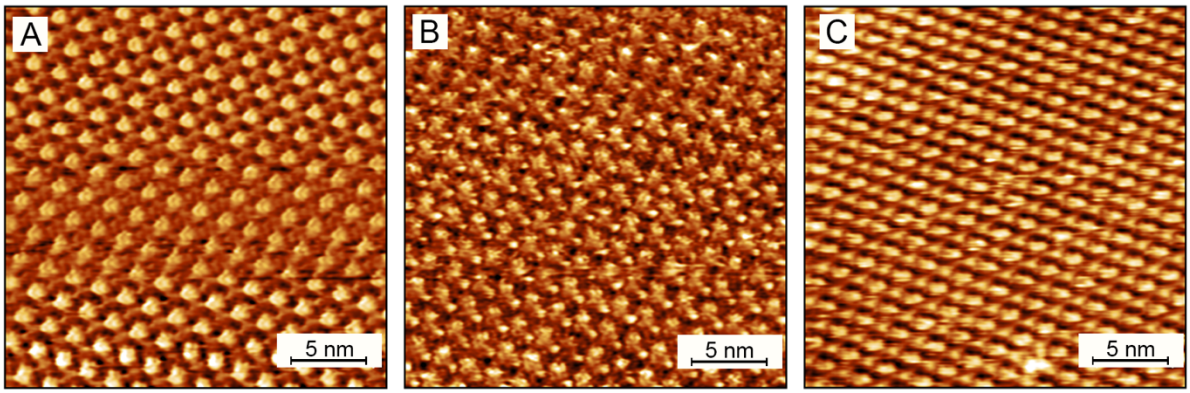

Figure 6.6. STM images of monolayer of Ni(OEP) on HOPG at the solid–liquid interface showing co-adsorbed TCB (1,2,4-TCB, [Ni(OEP)] = 1.5 mM, 25 nm × 25 nm) (a) I = 75 pA, V = –600 mV; (b) I = 75 pA, V = –900 mV; (c) I = 75 pA, V = –1200 mV.

6.3.3. STM Measurements of Ga(OEP)Cl in TCB at Various Concentrations. Given the very small quantities of material required to form a monolayer and that impurities with a concentration below the detection limit of ^{1}H-NMR spectroscopy have been observed to form monolayers,[22] the concentration thresholds for monolayer formation of small impurities of 5-coordinate porphyrins present in samples of **1**–**4** was investigated. At a concentration of 1 mM the Ga(OEP)Cl monolayers are clearly present over areas as large as 100 nm × 100 nm, showing the prototypical square structure observed in TCB (Figure 6.7a and b); however, within these monolayers are a relatively large amount of defects where porphyrins are not observed. Increasing the concentration of the deposited solution to 2 mM Ga(OEP)Cl results in the formation of monolayers without these defects (Figure 6.7c and d). At concentrations below 1.0 mM (ranging from 0.5 mM to 0.9 mM) monolayers of Ga(OEP)Cl have not been observed, despite substantial effort.

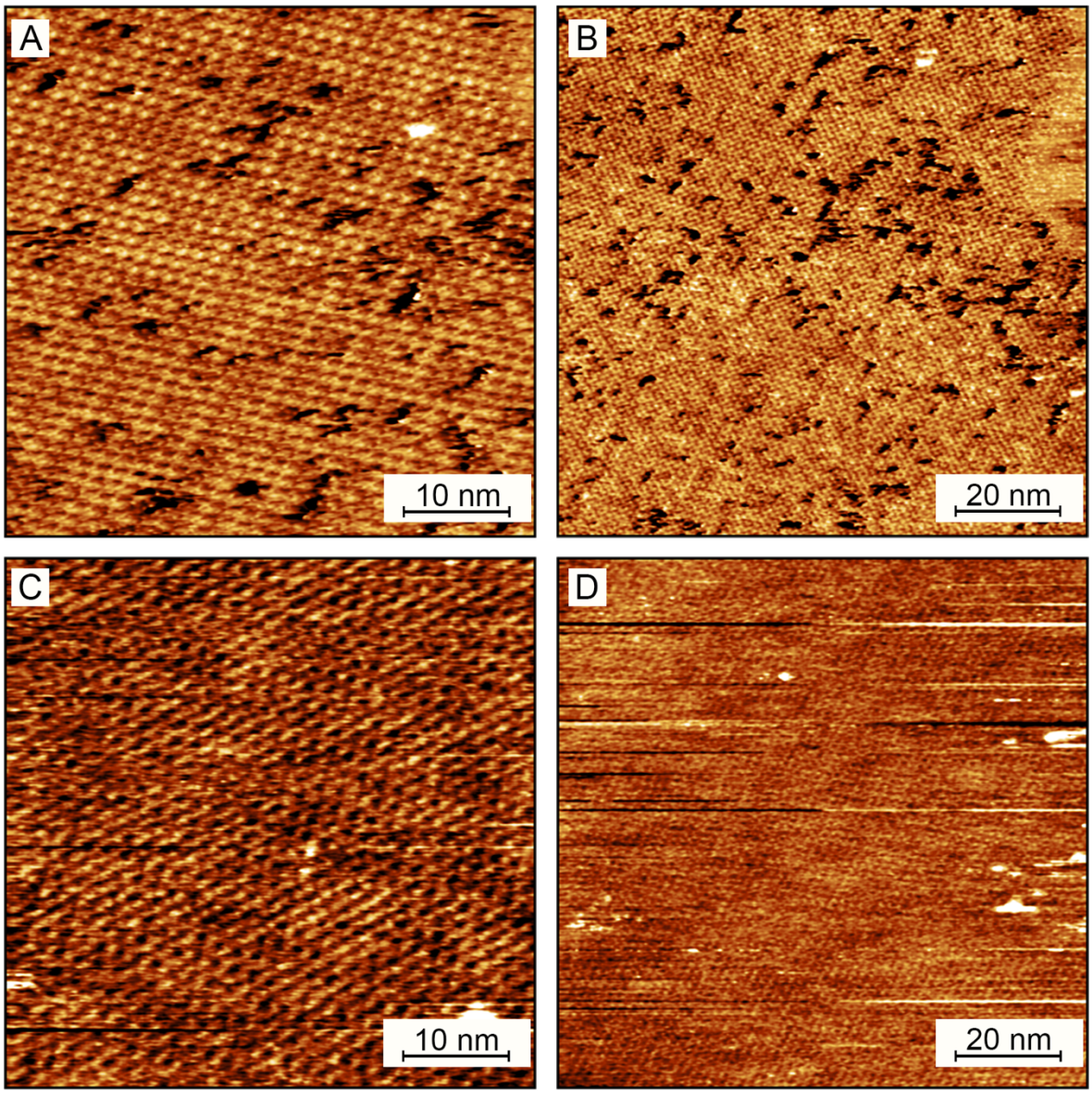

Figure 6.7. STM images of Ga(OEP)Cl on HOPG at the solid–liquid interface (TCB, I = 50 pA, V = –700 mV): (a) 50 nm × 50 nm, [Ga(OEP)Cl] = 1.0 mM; (b) 100 nm × 100 nm, [Ga(OEP)Cl] = 1.0 mM; (c) 50 nm × 50 nm, [Ga(OEP)Cl] = 2.0 mM; (d) 100 nm × 100 nm, [Ga(OEP)Cl] = 2.0 mM.

This concentration threshold for monolayer formation of around 1 mM for Ga(OEP)Cl in TCB is significantly higher than in 1-phenyloctane, and also in contrast with recent reports of Co(OEP) monolayers which were observed by STM when deposited from TCB solutions with concentrations as low as 10 μM.[20] While it should be noted that the concentration thresholds are

dependent on factors such as the free energy of solvation of the porphyrin and therefore 4- and 5-coordinate porphyrins would not be expected to be identical, such a gross difference is surprising and was investigated further. To establish that this difference is a result of porphyrin identity rather than an unknown experimental discrepancy, Ni(OEP) was deposited as a 50 μM solution from TCB resulting in the formation of monolayers as shown in Figure 6.8. The ability to image stable monolayers of Ni(OEP) at concentrations more than an order of magnitude lower than observed for Ga(OEP)Cl confirm that the high concentration threshold is intrinsic to this porphyrin. While these experiments are not perfectly analogous to those where a small concentration of 5-coordinate porphyrin is present along with large quantities of **1**–**4**, the gross differences between the concentration threshold observed for pristine monolayers of Ga(OEP)Cl and that of the samples of **1**–**4** make it highly improbable that the monolayers observed with these samples are due to the selective adsorption of porphyrin impurities.

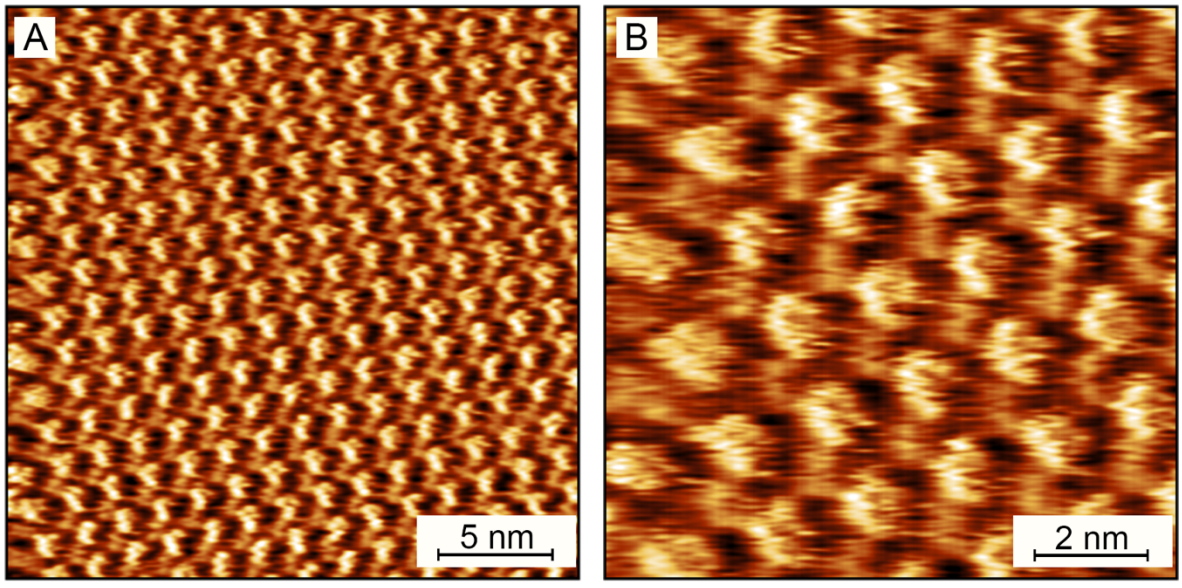

Figure 6.8. STM images of Ni(OEP) on HOPG at the solid–liquid interface (TCB, [Ni(OEP)] = 50 μM, I = 120 pA, V = –600 mV): (a) 25 nm × 25 nm; (b) 10 nm × 10 nm.

6.4. Chapter 5 Supplementary Information

6.4.1. Influence of Graphene on the Adsorption Energy of C_{60} within Monolayers of Ga(OEP)(R) Complexes. Including surface atoms within simulations of adsorbed molecules drastically increases the computational cost of performing these calculations. We hypothesized that removing graphene after determining the optimized structure of an adsorbed Ga(OEP)(R) complex would not drastically alter the relative adsorption energies of C_{60}, as the graphene would be expected to provide a constant influence on the geometry of the adsorbed Ga(OEP) subunit and would not be expected to have a discrepant contribution towards the adsorption energy of C_{60} between Ga(OEP)(R) systems. The adsorption energy of C_{60} within monolayers of Ga(OEP)(CC-*n*-Pyrene) and Ga(OEP)(CCPh) with and without a 1L sheet of graphene (Table 6.16) shows that the graphene contributes –0.07 eV to –0.08 eV to the adsorption energy—a small but virtually identical contribution across the three systems. Based on this we conclude that calculating the adsorption energy of C_{60} without the presence of graphene is justified given the substantial computational resources required to model such a layer.

Table 6.16. Comparison of Adsorption Energies of C_{60} with Ga(OEP)(R) Complexes with and without a 1L Sheet of Graphene at the Bridge Binding Site.

	$E_{ads(gas)}$ (eV)	
System	With Graphene	Without Graphene
Ga(OEP)(CC-1-Pyrene)	–1.84	–1.77
Ga(OEP)(CC-2-Pyrene)	–1.72	–1.64
Ga(OEP)(CCPh)	–1.22	–1.15

6.4.2. Rotational Orientation Dependence of the Adsorption Energy of C_{60} with CC-1-Pyrene. It was determined during initial calculations of C_{60} with Ga(OEP)(R) complexes that the optimized structures did not consistently relax to any particular rotational orientation of the C_{60} with respect to the axial ligand. In order to determine whether there was a significant dependence of the adsorption energy of C_{60} on the rotational orientation, the adsorption energy of C_{60} with CC-

1-Pyrene was determined at five rotational orientations (Figure 6.9). The dependence of the adsorption energy of C_{60} on the rotational orientation was determined to be only 0.04 eV (Table 6.17). As this effect is quite small, rather than attempting to enforce the rotational orientation of C_{60}, we take this as the lower bound for meaningful differences in adsorption energy in these systems.

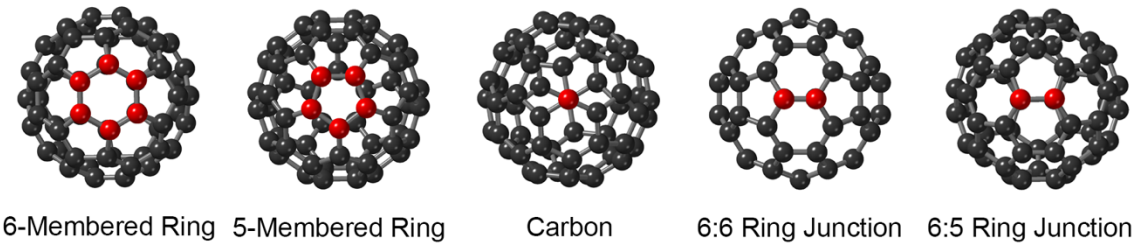

Figure 6.9. Rotational orientations where the adsorption energy of C_{60} with 1-pyrene was calculated. The closest carbon atom(s) to the 1-pyrene (not shown) are displayed in red for clarity.

Table 6.17. Rotational Orientation Dependence of the Adsorption Energy of C_{60} with 1-Pyrene.

Orientation	$E_{ads(gas)}$ (eV)
6-Membered Ring	–0.62
5-Membered Ring	–0.61
Carbon	–0.61
6:6 Ring Junction	–0.59
6:5 Ring Junction	–0.58

6.4.3. Deconvolution of the Contributions of the Axial Ligand and the Porphyrin Substituents to the Adsorption Energy of C_{60}. In the optimized structure of C_{60} within monolayers of Ga(OEP)(R) complexes, close contact between both the axial ligand and the upturned ethyl groups of the porphyrin with C_{60} are observed. In order to deconvolute the contributions of these two components and determine whether differences in binding sites were due solely to the axial ligand or in part due to the porphyrin substituents, the adsorption energies of C_{60} at the bridge and center sites were calculated with the corresponding Ga(Por)(CC-Pyrene) (Por = porphine) complexes, where all the peripheral substituents are hydrogens. The calculations

show that the upturned ethyl groups contribute 0.44 eV of the gas-phase adsorption energy for the Ga(OEP)(CC-1-Pyrene) systems and 0.36 eV – 0.38 eV of the gas-phase adsorption energy for the Ga(OEP)(CC-2-Pyrene) (Table 6.18; Tables 5.3 and 5.5 for Ga(OEP)(CC-Pyrene)). This demonstrates that the difference in adsorption energies for Ga(OEP)(CC-1-Pyrene) and Ga(OEP)(CC-2-Pyrene) is in part due to differing contributions from the ethyl groups of the underlying porphyrins.

Table 6.18. Adsorption Energies of C_{60} within Monolayers of Ga(Por)(CC-Pyrene) at the Bridge and Center Binding Sites.

	$\Delta E_{ads(gas)}$ (eV)	
System	Bridge	Center
Ga(Por)(CC-1-Pyrene)	–1.33	–1.16
Ga(Por)(CC-2-Pyrene)	–1.26	–0.91

6.4.4. Effect of Independent Optimization of Axial Ligands on the Adsorption Energy of C_{60}. In order to minimize computational resources, the minimum number of Ga(OEP)(R) complexes required to model a specific adsorption site was used. This corresponds to one Ga(OEP)(R) molecule per axial ligand orientation. This results in a system where the axial ligands at binding sites where multiple orientations are required have a potentially advantageous relaxation pathway that is not possible in systems where only one axial ligand orientation is present, such as the leaning of the CC-1-pyrene ligands towards C_{60} at the center rotated binding site of Ga(OEP)(CC-1-Pyrene). As these relaxations will destabilize the adjacent binding sites, this could lead to an overestimation of the adsorption energy of C_{60} at this site compared to the intended tileable structure. In order to determine the magnitude of this effect, the adsorption energy of C_{60} within monolayers of several Ga(OEP)(R) complexes was calculated at the bridge site with two Ga(OEP)(R) molecules explicitly modeled to allow for independent optimization of the axial ligands. The adsorption energies demonstrate that the independent optimization of the axial ligands

substantially increase the gas-phase adsorption energy by 0.14 eV, 0.15 eV, and 0.06 eV for Ga(OEP)(CC-1-Pyrene), Ga(OEP)(CC-2-Pyrene), and Ga(OEP)(CCPh), respectively (Table 6.19). The increased gas-phase adsorption energy is offset somewhat by an increased solvation energy for Ga(OEP)(CC-1-Pyrene) and Ga(OEP)(CC-2-Pyrene), resulting in solvated-phase adsorption energies that are 0.03 eV–0.08 eV greater than those calculated with identical axial ligands. As a result, when the adsorption energy of a structure where axial ligand equivalence is enforced is similar to that with non-identical axial ligands, the structure with identical axial ligands will be considered lower in energy in the gas-phase.

Table 6.19. Adsorption energies of C_{60} at the bridge site of Ga(OEP)(R) monolayers with independently optimized axial ligands.

Parameter	Ga(OEP)(CC-1-Pyrene)	Ga(OEP)(CC-2-Pyrene)	Ga(OEP)(CCPh)
$E_{ads(gas)}$ (eV)	–1.91	–1.79	–1.21
E_{solv} (eV)	0.47	0.42	0.23
$E_{ads(solv)}$ (eV)	–1.44	–1.37	–0.98

6.5. References

1. Chilukuri, B.; Mazur, U.; Hipps, K. W. Effect of Dispersion on Surface Interactions of Cobalt(II) Octaethylporphyrin Monolayer on Au(111) and HOPG(0001) Substrates: A Comparative First Principles Study. *Phys. Chem. Chem. Phys.* **2014**, *16*, 14096–14107.

2. Kamm, J. M.; Iverson, C. P.; Lau, W. Y.; Hopkins, M. D. Axial Ligand Effects on the Structures of Self-Assembled Gallium–Porphyrin Monolayers on Highly Oriented Pyrolytic Graphite. *Langmuir* **2016**, *32*, 487–495.

3. Brennan, T. D.; Scheidt, W. R.; Shelnutt, J. A. New Crystalline Phase of (Octaethylporphinato)Nickel(II) - Effects of π–π Interactions on Molecular-Structure and Resonance Raman Spectra. *J. Am. Chem. Soc.* **1988**, *110*, 3919–3924.

4. Brancato-Buentello, K. E.; Coutsolelos, A. G.; Scheidt, W. R. Chloro(2,3,7,8,12,13,17,18-Octaethylporphinato)Gallium(III). *Acta Crystallogr., Sect. C: Cryst. Struct. Commun.* **1996**, *52*, 2707–2710.

5. Tumino, F.; Casari, C. S.; Li Bassi, A.; Tosoni, S. Nature of Point Defects in Single-Layer MoS_2 Supported on Au(111). *J. Phys. Chem. C* **2020**, *124*, 12424–12431.

6. Müller, T.; Flynn, G. W.; Mathauser, A. T.; Teplyakov, A. V. Temperature-Programmed Desorption Studies of *n*-Alkane Derivatives on Graphite: Desorption Energetics and the Influence of Functional Groups on Adsorbate Self-Assembly. *Langmuir* **2003**, *19*, 2812–2821.

7. Paserba, K. R.; Gellman, A. J. Effects of Conformational Isomerism on the Desorption Kinetics of *N*-Alkanes from Graphite. *J. Chem. Phys.* **2001**, *115*, 6737–6751.

8. Manz, T. A.; Sholl, D. S. Chemically Meaningful Atomic Charges That Reproduce the Electrostatic Potential in Periodic and Nonperiodic Materials. *J. Chem. Theory Comput.* **2010**, *6*, 2455–2468.

9. Manz, T. A.; Sholl, D. S. Methods for Computing Accurate Atomic Spin Moments for Collinear and Noncollinear Magnetism in Periodic and Nonperiodic Materials. *J. Chem. Theory Comput.* **2011**, *7*, 4146–4164.

10. Manz, T. A.; Sholl, D. S. Improved Atoms-in-Molecule Charge Partitioning Functional for Simultaneously Reproducing the Electrostatic Potential and Chemical States in Periodic and Nonperiodic Materials. *J. Chem. Theory Comput.* **2012**, *8*, 2844–2867.

11. Limas, N. G.; Manz, T. A. Introducing DDEC6 Atomic Population Analysis: Part 2. Computed Results for a Wide Range of Periodic and Nonperiodic Materials. *RSC Adv.* **2016**, *6*, 45727–45747.

12. Manz, T. A.; Limas, N. G. Introducing DDEC6 Atomic Population Analysis: Part 1. Charge Partitioning Theory and Methodology. *RSC Adv.* **2016**, *6*, 47771–47801.

13. Manz, T. A. Introducing DDEC6 Atomic Population Analysis: Part 3. Comprehensive Method to Compute Bond Orders. *RSC Adv.* **2017**, *7*, 45552–45581.

14. Hoffman, R. E.; Becker, E. D. Temperature Dependence of the ^{1}H Chemical Shift of Tetramethylsilane in Chloroform, Methanol, and Dimethylsulfoxide. *J. Magn. Reson.* **2005**, *176*, 87–98.

15. Hudson, M. F.; Smith, K. M. Novel Mercury(II) Complexes of Porphyrins. *Tetrahedron* **1975**, *31*, 3077–3083.

16. Abraham, R. J.; Barnett, G. H.; Smith Synthesis and Properties of Thallium(III) Porphyrin Chelates. *J. Chem. Soc., Perkin Trans. 1* **1973**, 2142–2148.

17. Tersoff, J.; Hamann, D. R. Theory of the Scanning Tunneling Microscope. *Phys. Rev. B* **1985**, *31*, 805–813.

18. Binnig, G.; Rohrer, H. Scanning Tunneling Microscopy. *Surf. Sci.* **1983**, *126*, 236–244.

19. Larsen, A. H.; Mortensen, J. J.; Blomqvist, J.; Castelli, I. E.; Christensen, R.; Dulak, M.; Friis, J.; Groves, M. N.; Hammer, B.; Hargus, C.; Hermes, E. D.; Jennings, P. C.; Jensen, P. B.; Kermode, J.; Kitchin, J. R.; Kolsbjerg, E. L.; Kubal, J.; Kaasbjerg, K.; Lysgaard, S.; Maronsson, J. B.; Maxson, T.; Olsen, T.; Pastewka, L.; Peterson, A.; Rostgaard, C.; Schiotz, J.; Schutt, O.; Strange, M.; Thygesen, K. S.; Vegge, T.; Vilhelmsen, L.; Walter, M.; Zeng, Z. H.; Jacobsen, K. W. The Atomic Simulation Environment — a Python Library for Working with Atoms. *J. Phys.: Condens. Matter* **2017**, *29*, 273002.

20. Gurdumov, K.; Mazur, U.; Hipps, K. W. Self-Assembly Dynamics and Stability through Concentration Control at the Solution/HOPG Interface. *J. Phys. Chem. C* **2022**, *126*, 12916–12927.

21. Lee, S.; Hirsch, B. E.; Liu, Y.; Dobscha, J. R.; Burke, D. W.; Tait, S. L.; Flood, A. H. Multifunctional Tricarbazolo Triazolophane Macrocycles: One-Pot Preparation, Anion Binding, and Hierarchical Self-Organization of Multilayers. *Chem. – Eur. J.* **2016**, *22*, 560–569.

22. Lau, W.-Y. Ph. D. Thesis. The University of Chicago, Chicago, IL, 2016.